

University of Central Florida

**STARS**

---

Electronic Theses and Dissertations

---

2010

## Heat Transfer Augmentation In A Narrow Rectangular Duct With Dimples Applied To A Single Wall

Carson Slabaugh

*University of Central Florida*



Part of the [Mechanical Engineering Commons](#)

Find similar works at: <https://stars.library.ucf.edu/etd>

University of Central Florida Libraries <http://library.ucf.edu>

This Masters Thesis (Open Access) is brought to you for free and open access by STARS. It has been accepted for inclusion in Electronic Theses and Dissertations by an authorized administrator of STARS. For more information, please contact [STARS@ucf.edu](mailto:STARS@ucf.edu).

---

### STARS Citation

Slabaugh, Carson, "Heat Transfer Augmentation In A Narrow Rectangular Duct With Dimples Applied To A Single Wall" (2010). *Electronic Theses and Dissertations*. 4359.

<https://stars.library.ucf.edu/etd/4359>

HEAT TRANSFER AUGMENTATION IN A NARROW  
RECTANGULAR DUCT WITH DIMPLES APPLIED TO A  
SINGLE WALL

by

CARSON DANIEL SLABAUGH  
B.S. M.E., University of Central Florida, 2009

A thesis submitted in partial fulfillment of the requirements  
for the degree of Master of Science  
in the Department of Mechanical, Materials, and Aerospace Engineering  
in the College of Engineering and Computer Science  
at the University of Central Florida  
Orlando, FL

Summer Term 2010

© 2010 Carson Daniel Slabaugh

## **ABSTRACT**

Establishing a clean and renewable energy supply is the preeminent engineering challenge of our time. Turbines, in some form, are responsible for more than 98 percent of all electricity generated in the United State and 100 percent of commercial and military air transport. The operation of these engines is clearly responsible for significant consumption of hydrocarbon fuels and, in turn, emission of green house gases into the atmosphere. With such wide-scale implementation, it is understood that even the smallest increase in the operating efficiency of these machines can lead to enormous improvements over the current energy situation. These effects can extend from a reduction in the emission of greenhouse gases to lessening the nation's dependence of foreign energy sources to lower energy prices for the consumer.

The prominent means of increasing engine efficiency is by raising the 'Turbine Inlet Temperature' – the temperature of the mainstream flow after combustion, entering the first stage of the turbine section. The challenge is presented when these temperatures are forced beyond the allowable limits of the materials inside the machine. In order to protect these components, active cooling and protection methods are employed. The focus of this work is the development of more efficient means of cooling 'hot' turbine components. In doing so, the goal is to maximize the amount of heat removed by the coolant while minimizing the coolant mass flow rate: by removing a greater amount of heat with a lower coolant mass flow rate, more compressed air is left in the mainstream gas flow for combustion and power generation.



This study is an investigation of the heat transfer augmentation through the fully-developed portion of a narrow rectangular duct ( $AR=2$ ) characterized by the application of dimples to the bottom wall of the channel. Experimental testing and numerical modeling is performed for full support and validation of presented findings. The geometries are studied at channel Reynolds numbers of 20000, 30000, and 40000. The purpose is to understand the contribution of dimple geometries in the formation of flow structures that improve the advection of heat away from the channel walls. Experimental data reported includes the local and Nusselt number augmentation of the channel walls and the overall friction augmentation throughout the length of the duct. Computational results validate local Nusselt number results from experiments, in addition to providing further insight to local flow physics causing the observed surface phenomena. By contributing to a clearer understanding of the effects produced by these geometries, the development of more effective channel-cooling designs can be achieved.

To my wife, Hannah

“May the words of my mouth and the meditation of my heart be pleasing in your sight,

O Lord, my Rock and my Redeemer.” Psalm 19:14 (NIV)

## ACKNOWLEDGMENTS

I would like to express my sincere gratitude to my advisor, Dr. Jay Kapat, for his support and guidance through my research and for putting up with my hundreds of questions throughout the process of earning this degree and moving on to the next.

Thanks also to the members of my committee for their advice and assistance, Dr. Bijay Sultanian, Dr. Jihua Gou, and Dr. Ali Gordon.

I would like to extend my deepest gratitude to my good friend Lucky Tran. After countless all-nighters in the lab, volunteering every PC in his possession for data processing runs, and numerous runs to Dominoes Pizza well-after midnight, he has gone far beyond the duties of an undergraduate: he will always be my great colleague and friend.

I would also like to acknowledge the graduate students, post-docs, and others from the lab for their friendship, advice, and support. Specifically, I would like to thank Dr. Mark Ricklick, Dr. Vaidyanathan Krishnan, Jeff Nguyen, and Michelle Valentino.

As I depart from Orlando, I remember all of my family and friends who have played a major part in my making it this far: my Grandpa and Grandma Driskill, my Grandma Slabaugh, Mike and Fran Therber, John Fuoco, James Hart, Larry Teague (Dude), John and Ashley Kirkman, Brandon and Rachel Lutz, Seth Hammond, Danny and J-Rod. I will miss you all very much.

The support of knowledge and funding from the Laboratory for Turbine Aerodynamics, Heat Transfer, and Durability as a part of the Center for Advanced

Turbine and Energy Research at the University of Central Florida is gratefully acknowledged. Also, I would like to thank Dr. Guha for generously donating time on his cluster for me to perform the computational studies presented in this work.

Finally, I would be remiss to not acknowledge the love and support of my family. The foundation provided by my amazing wife, my parents, grandparents, loving sister, and my in-laws has played a major role in my successes, thus far, and those still to come. They are the giants on whose shoulders I stand.

# TABLE OF CONTENTS

LIST OF FIGURES .....	xiv
LIST OF TABLES .....	xxxviii
LIST OF PUBLICATIONS .....	xl
Conference Proceedings .....	xl
In Print .....	xl
In Preparation .....	xli
Journal Publications .....	xlii
In Preparation .....	xlii
Other Scholarly Accomplishments.....	xlii
In Print .....	xlii
In Preparation .....	xliii
NOMENCLATURE .....	xliv
CHAPTER 1:    INTRODUCTION.....	1
The Energy Challenge.....	1
Efficiency of Gas Turbine Engines .....	1
Internal Cooling.....	5
Literature Review of Related Works.....	12
Internal Cooling – Transport Enhancing Features.....	12
Dimples.....	16
Overview of the Present Work .....	28
Motivation and Objectives.....	28

Details and Outline of the Study.....	32
CHAPTER 2: OVERVIEW OF EXPERIMENTAL STUDY .....	39
Test Setup for Average Data .....	39
Background.....	39
Methods and Concepts.....	39
Design Details.....	40
Data Reduction .....	45
Experimental Uncertainty.....	49
Smooth Wall Validation .....	53
Test Setup for Local Data.....	56
Background.....	56
Methods and Concepts.....	56
Design Development – Mesh Heater.....	62
Design Development – Test Section .....	70
Design Development – Supporting Hardware.....	73
Design Development – Instrumentation .....	79
Final Design Details .....	91
Data Reduction .....	97
Experimental Uncertainty.....	103
Smooth Wall Validation .....	105

Summary of Experimental Setups.....	113
Validation Complete.....	113
Application to Study.....	114
<b>CHAPTER 3:    OVERVIEW OF COMPUTATIONAL STUDY .....</b>	<b>116</b>
Background .....	116
Response Surface Methodology.....	116
Geometry Creation and Meshing .....	117
Use of Journal Files.....	117
Generation of Computational Domain .....	118
Grid Dependence Study.....	125
Solution Details.....	130
Solution Details .....	130
Reynolds Average Navier-Stokes.....	132
Large Eddy Simulation.....	133
Solution Processing .....	134
Relevance and Application of Computational Results.....	134
Validation .....	134
Insight to Flow Physics.....	134
<b>CHAPTER 4:    EXPERIMENTAL RESULTS .....</b>	<b>136</b>
Background .....	136
Reported Data .....	136

Large Single Dimples .....	137
Local Experimental Data .....	137
Regionally Averaged Heat Transfer Data .....	139
Small Single Dimples .....	144
Local Experimental Data .....	144
Regionally Averaged Heat Transfer Data .....	146
Double Dimples.....	151
Local Experimental Data .....	151
Regionally Averaged Heat Transfer Data .....	154
Stream-wise Averaged Heat Transfer Data.....	159
Friction Data.....	163
Comparison to Literature .....	164
Double Dimple Summary.....	165
Conclusions Drawn from Experimental Study.....	166
<b>CHAPTER 5:    COMPUTATIONAL STUDY OF THE DOUBLE-DIMPLE .....</b>	<b>167</b>
Overview .....	167
Large Domain RANS Study.....	168
Geometry .....	168
Meshing .....	168
Boundary Conditions .....	168
Results and Findings.....	169
Reduced Domain, Refined RANS Study .....	174



Validation .....	174
Reynolds Number = 40000.....	175
Reynolds Number = 30000.....	188
Reynolds Number = 20000.....	191
Large Eddy Simulation.....	192
Conclusions from Computational Study .....	202
CHAPTER 6: DEVELOPMENT OF THE TRANSIENT TECHNIQUE.....	207
Background .....	207
Contribution of Non-Ideal Region .....	207
Surface Area Correction.....	208
Results and Findings .....	209
CHAPTER 7: CONCLUSIONS AND FUTURE WORK.....	212
Conclusions .....	212
Future Study .....	213
APPENDIX A: FACILITY.....	215
A.1. Experimental Facility .....	217
A.2. Computational Infrastructure .....	223
APPENDIX B: MESH HEATER ANALYSIS.....	226
APPENDIX C: IMAGE PROCESSING CODES .....	244
C.1. Image Importing Code .....	245
C.2. Image Cropping and Stitching Code .....	251
C.3. Filtering and Averaging Code .....	256
C.4. Nusselt Number Solution .....	263

C.5.	Bulk Temperature Calculation Function .....	274
C.6.	Superposition Summation Function .....	276
C.7.	Image Display Function .....	279
C.8.	Spanwise and Streamwise Averaging Code.....	284
C.9.	Flipping Code.....	288
APPENDIX D: JOURNAL FILES .....		291
D.1.	Double Dimple Meshing Journal .....	292
D.2.	Fluent Run Setup Journal (RANS).....	329
D.3.	LES ‘Rampup’ Journal.....	331
D.4.	LES ‘Statistic’ Journal .....	333
D.5.	LES ‘Pictures-Out’ Journal .....	335
APPENDIX E: REDUCED DOMAIN RANS – FULL RESULT SET .....		337
E.1.	Reynolds Number = 40000 .....	338
E.2.	Reynolds Number = 30000 .....	350
E.3.	Reynolds Number = 20000 .....	363
APPENDIX F: LARGE EDDY SIMULATION – TRANSIENT RESULT SET .....		375
F.1.	Velocity Contours – Positive x Streamwise Plane .....	376
F.2.	Velocity Contours – Spanwise Centerplane.....	384
F.3.	Velocity Contours – Negative x Streamwise Plane .....	392
F.4.	Vorticity Contours – Positive x Streamwise Plane .....	400
F.5.	Vorticity Contours – Negative x Streamwise Plane.....	408
APPENDIX G: VITA .....		416
REFERENCES .....		418

## LIST OF FIGURES

Figure 1.1: Gas Turbine Variations in Three Major Applications – Aircraft, Power Generation, and Marine Applications, Respectively .....	2
Figure 1.2: Air Standard Cycle of a Gas-Turbine Energy - Ideal (Left) and with Known Inefficiencies (Right) (Sultanian, 2009) .....	3
Figure 1.3: Air Standard Cycle Represented by Common Turbine Components.....	4
Figure 1.4: Increased in Safe Operating Temperature of Metals (Suo, 1985).....	6
Figure 1.5: Increase in Turbine Inlet Temperature with Advances in Cooling Techniques (Lakshminarayana, 1996) .....	7
Figure 1.6: Photograph of a Cooled Transition Piece in a Gas-Turbine with Shrouding Removed (Sultanian, 2009) .....	8
Figure 1.7: Illustration of Possible Turbine Blade Design Including a Combination of Cooling Techniques (Gladden & Simoneau).....	9
Figure 1.8: Example of a Turbine Nozzle Guide Vane with Endwall Film-Cooling and Endwall Impingement Cooling. ....	10
Figure 1.9: Increasing Cooling Effectiveness (Dailey, 2000).....	11
Figure 1.10: Illustration of Three-Dimensional Flow Structure Caused by a Surface Cavity (Mahmood, Hill, Nelson, Ligrani, Moon, & Glezer, 2001) .....	17
Figure 1.11: Flow Structure inside a Dimple (Griffith, Al Hadhrami, & Han, 2003) .....	26
Figure 1.12: Recirculation of Flow Due to Dimple Geometry (Kim & Choi, 2005) .....	27
Figure 1.13: Summary of Dimple Feature Contributions (Ligrani, Oliveira, & Blaskovich, 2003).....	31

Figure 1.14: Illustration of Dimple Nomenclature .....	34
Figure 1.15: Project Flow Diagram .....	35
Figure 1.16: Example of Local Heat Transfer Coefficient Data from Transient TLC Experiment.....	36
Figure 1.17: Three-Dimensional Local Contours of Heat Transfer of Heat Transfer Coefficient from RANS Numerical Solution.....	38
Figure 1.18: Vorticity Contours Showing Streamwise Variation in the Flow at One Instant in Time. ....	38
Figure 2.1: Schematic of Experimental Apparatus .....	40
Figure 2.2: Photo of a Single Module with a Feature Case Installed .....	41
Figure 2.3: Photo of Data Acquisition System .....	42
Figure 2.4: Schematic of Heat Supply System .....	43
Figure 2.5: Photo of Heat Supply System.....	43
Figure 2.6: Schematic of Module Design .....	44
Figure 2.7: Assembled Modular Channel .....	45
Figure 2.8: Illustration of Ambient Heat Loss .....	46
Figure 2.9: Uncertainty Trees for Basic Experiment – Nusselt Number Augmentation ..	49
Figure 2.10: Uncertainty Trees for Basic Experiment – Friction Factor Augmentation ..	49
Figure 2.11: Uncertainty Trees for Basic Experiment – Reynolds Number.....	50
Figure 2.12: Uncertainty Trees for Basic Experiment – Heat Transfer Coefficient.....	50
Figure 2.13: Uncertainty Trees for Basic Experiment – Friction Factor .....	51
Figure 2.14: Uncertainty Trees for Basic Experiment – Bulk Temperature.....	51

Figure 2.15: Regionally Averaged Heat Transfer Coefficient Plotted Against X/Dh: Re = 20000.....	53
Figure 2.16: Regionally Averaged Heat Transfer Coefficient Plotted Against X/Dh: Re = 30000.....	54
Figure 2.17: Regionally Averaged Heat Transfer Coefficient Plotted Against X/Dh: Re = 40000.....	55
Figure 2.18: Raw Temperature Data and Processed Local HTC Topography (Stasiek & Kowalewski, 2002) .....	59
Figure 2.19: Recorded RGB Values for Thermochromic Liquid Crystal (Farina, Hacker, Moffat, & Eaton, 1994).....	61
Figure 2.20: Plot of Nusselt Number as a Function of Wire Diameter.....	64
Figure 2.21: Plot of Heat Transfer Coefficient over wire as a Function of Wire Diameter .....	65
Figure 2.22: Temperature History as a Function of Wire Diameter and Power Input to Flow .....	65
Figure 2.23: Predicted Time History of Heat Addition to the Flow (Watts) .....	66
Figure 2.24: Pressure Loss across Mesh as a Function of Wire Diameter .....	68
Figure 2.25: Voltage across Wire Mesh as a Function of Power Added, Wire Diameter, and Number of Wires.....	69
Figure 2.26: Current across Wire Mesh as a Function of Power Added, Wire Diameter, and Number of Wires.....	70
Figure 2.27: Pressure Measurement Test Section with 0.5 inch Thick Acrylic Insert .....	71
Figure 2.28: Illustration of Counter-Bore Pressure Tap Design.....	72

Figure 2.29: Pressure Measurement Test Section with Pressure Taps Installed.....	72
Figure 2.30: 80-20 Aluminum Support Structure .....	73
Figure 2.31: Mirror Schematic.....	74
Figure 2.32: Mirror Supported in Machined Mounts.....	75
Figure 2.33: Power Supply Wiring Schematic .....	76
Figure 2.34: Photo of Author-Developed High-Current, Three-Way Switch and Power-Supply Setup .....	77
Figure 2.35: Photo of Experimental Setup with Lighting and Cameras .....	78
Figure 2.36: The Smectic Liquid Crystal Structure .....	80
Figure 2.37: The Nematic Liquid Crystal Structure .....	80
Figure 2.38: Schematic of Cholesteric Nature of Liquid Crystals [Ireland and Jones, 2000]. The Arrow is Indicative of the Helical Path within the Medium .....	81
Figure 2.39: Relation between Temperature and Reflected Wavelength .....	82
Figure 2.40: 3D RGB Color Chromaticity Diagram (Basu, 2009).....	86
Figure 2.41: Schematic of Calibration Setup.....	89
Figure 2.42: Photo of Calibration Setup During a Test .....	90
Figure 2.43: Schematic of Calibration Process.....	91
Figure 2.44: Experimental Apparatus .....	92
Figure 2.45: Complete Experiment.....	93
Figure 2.46: Vortex Blower .....	94
Figure 2.47: Panasonic NVGS240 3CCD Digital-Video Recorder .....	95
Figure 2.48: Single Snapshot of TLC Color Change (One Instant in Time) .....	96

Figure 2.49: Time History of a Mainstream Temperature with Superposition of Step Changes.....	99
Figure 2.50: Time History of a G Signal: Before and After Filtering and Averaging....	102
Figure 2.51: Local Heat Transfer Coefficient Contours - Smooth Wall, Re = 20000....	105
Figure 2.52: Regionally Averaged Heat Transfer Coefficient Plotted Against X/Dh - Smooth Wall, Re = 20000.....	106
Figure 2.53: Local Heat Transfer Coefficient Contours - Smooth Wall, Re = 30000....	107
Figure 2.54: Regionally Averaged Heat Transfer Coefficient Plotted Against X/Dh - Smooth Wall, Re = 30000.....	108
Figure 2.55: Local Heat Transfer Coefficient Contours - Smooth Wall, Re = 40000....	109
Figure 2.56: Regionally Averaged Heat Transfer Coefficient Plotted Against X/Dh - Smooth Wall, Re = 40000.....	110
Figure 2.57: Static Pressure Profile vs. Channel Length - Smooth Wall, Re = 20000...	111
Figure 2.58: Static Pressure Profile vs. Channel Length - Smooth Wall, Re = 30000...	112
Figure 2.59: Static Pressure Profile vs. Channel Length - Smooth Wall, Re = 40000...	112
Figure 3.1: Illustrations of Factorial Design Process.....	117
Figure 3.2: Complete Computational Domain as One Fluid Volume .....	118
Figure 3.3: Double Dimple Broken Down into Topological Squares .....	119
Figure 3.4: Dimple Break-Down Scheme is Extended to other Surfaces of the Channel .....	119
Figure 3.5: Channel Broken into Hexagonal Volumes .....	120
Figure 3.6: Boundary Layers and Transition Regions Applied .....	120

Figure 3.7: Double-Dimple Surface Feature with Boundary Layers and Edge Meshing Complete.....	121
Figure 3.8: Double-Dimple Face Meshed.....	121
Figure 3.9: Bottom Wall and Dimples Face Meshed.....	122
Figure 3.10: Normal View of Face Meshed Bottom Wall and Dimples .....	122
Figure 3.11: Channel Face-Meshing Complete .....	123
Figure 3.12: Final Mesh – Dimple.....	123
Figure 3.13: Final Mesh – Bottom Wall and Dimple .....	124
Figure 3.14: Final Mesh.....	124
Figure 3.15: Grid Dependence Study – Static Temperature .....	127
Figure 3.16: Grid Dependence Study – Velocity Magnitude .....	128
Figure 3.17: Grid Dependence Study – Net Heat Rate (Bottom Wall) .....	129
Figure 4.1: Local Heat Transfer Coefficient Data – Large Dimples, Re = 20000.....	137
Figure 4.2: Local Heat Transfer Coefficient Data – Large Dimples, Re = 30000.....	138
Figure 4.3: Local Heat Transfer Coefficient Data – Large Dimples, Re = 40000.....	139
Figure 4.4: Span-wise Averaged Nusselt Number Data – Large Dimples, Re = 20000	140
Figure 4.5: Regionally Averaged Nusselt Number Data from Copper-Block Experiment – Large Dimples, Re = 20000.....	141
Figure 4.6: Span-wise Averaged Nusselt Number Data – Large Dimples, Re = 30000	142
Figure 4.7: Regionally Averaged Nusselt Number Data from Copper-Block Experiment – Large Dimples, Re = 30000.....	142
Figure 4.8: Span-wise Averaged Nusselt Number Data – Large Dimples, Re = 40000	143



Figure 4.9: Regionally Averaged Nusselt Number Data from Copper-Block Experiment – Large Dimples, $Re = 40000$ .....	144
Figure 4.10: Local Heat Transfer Coefficient Data – Small Dimples, $Re = 20000$ .....	145
Figure 4.11: Local Heat Transfer Coefficient Data – Small Dimples, $Re = 30000$ .....	145
Figure 4.12: Local Heat Transfer Coefficient Data – Small Dimples, $Re = 40000$ .....	146
Figure 4.13: Span-wise Averaged Nusselt Number Data – Small Dimples, $Re = 20000$ .....	147
Figure 4.14: Regionally Averaged Nusselt Number Data from Copper-Block Experiment – Small Dimples, $Re = 20000$ .....	147
Figure 4.15: Span-wise Averaged Nusselt Number Data – Small Dimples, $Re = 30000$ .....	148
Figure 4.16: Regionally Averaged Nusselt Number Data from Copper-Block Experiment – Small Dimples, $Re = 30000$ .....	149
Figure 4.17: Span-wise Averaged Nusselt Number Data – Small Dimples, $Re = 40000$ .....	150
Figure 4.18: Regionally Averaged Nusselt Number Data from Copper-Block Experiment – Small Dimples, $Re = 40000$ .....	151
Figure 4.19: Local Heat Transfer Coefficient Data – Double Dimples, $Re = 20000$ ....	152
Figure 4.20: Local Heat Transfer Coefficient Data – Double Dimples, $Re = 30000$ ....	153
Figure 4.21: Local Heat Transfer Coefficient Data – Double Dimples, $Re = 40000$ ....	154
Figure 4.22: Span-wise Averaged Nusselt Number Data – Double Dimples, $Re = 20000$ .....	155

Figure 4.23: Regionally Averaged Nusselt Number Data from Copper-Block Experiment – Double Dimples, $Re = 20000$ .....	155
Figure 4.24: Span-wise Averaged Nusselt Number Data – Double Dimples, $Re = 30000$ .....	156
Figure 4.25: Regionally Averaged Nusselt Number Data from Copper-Block Experiment – Double Dimples, $Re = 30000$ .....	157
Figure 4.26: Span-wise Averaged Nusselt Number Data – Double Dimples, $Re = 40000$ .....	158
Figure 4.27: Regionally Averaged Nusselt Number Data from Copper-Block Experiment – Double Dimples, $Re = 40000$ .....	158
Figure 4.28: Regionally Averaged Heat Transfer Coefficient Data from Transient TLC Experiment Plotted Against the Channel Reynolds Number.....	159
Figure 4.29 Channel Averaged Nusselt Number Plotted Against the Channel Reynolds Number .....	162
Figure 4.30: Experimental Friction Factor Plotted Against the Channel Reynolds Number .....	163
Figure 4.31: Channel Nusselt Number from the Transient TLC Experiment Plotted Against the Friction Factor Augmentation .....	165
Figure 5.1: Consecutive Spanwise Profiles of Velocity Magnitude Cut Across one Double Dimple – $Re = 40000$ .....	170
Figure 5.2: Streamwise Profiles of Velocity Magnitude – Full Domain RANS, $Re =$ $40000$ .....	171

Figure 5.3: Streamwise Profiles of Vorticity Magnitude – Full Domain RANS, Re = 40000.....	172
Figure 5.4: Spanwise Profile of Vorticity Magnitude for Boundary Condition Validation – Full Domain RANS, Re = 40000.....	173
Figure 5.5: Spanwise Profile of Velocity Magnitude for Boundary Condition Validation – Full Domain RANS, Re = 40000.....	173
Figure 5.6: Spanwise Profiles of Vorticity Magnitude – Re = 40000 .....	174
Figure 5.7: Spanwise Profiles of Velocity Magnitude – Re = 40000 .....	175
Figure 5.8: Surface Heat Transfer Coefficient Contours, Bottom Wall – Re = 40000.	177
Figure 5.9: Surface Heat Transfer Coefficient Contours – Re = 40000 .....	177
Figure 5.10: Surface Heat Transfer Coefficient as a Function of Streamwise Distance – Re = 40000.....	178
Figure 5.11: Static Pressure Distribution over the Bottom Wall of the Channel – Re = 40000.....	179
Figure 5.12: Spanwise Profiles of Static Temperature – Re = 40000.....	180
Figure 5.13: Spanwise Profiles of Turbulent Kinetic Energy – Re = 40000 .....	182
Figure 5.14: Spanwise Profiles of Velocity Magnitude – Re = 40000 .....	183
Figure 5.15: Spanwise Profiles of Vorticity Magnitude – Re = 40000 .....	184
Figure 5.16: Streamwise Profiles of Static Temperature – Re = 40000 .....	185
Figure 5.17: Streamwise Profiles of Turbulent Kinetic Energy – Re = 40000.....	186
Figure 5.18: Streamwise Profiles of Velocity Magnitude – Re = 40000.....	187
Figure 5.19: Streamwise Profiles of Vorticity Magnitude – Re = 40000 .....	188
Figure 5.20: Surface Heat Transfer Coefficient Contours, Bottom Wall– Re = 30000.	189

Figure 5.21: Surface Heat Transfer Coefficient Contours, Side and Top Walls– Re = 30000.....	190
Figure 5.22: Surface Heat Transfer Coefficient as a Function of Streamwise Distance – Re = 30000.....	190
Figure 5.23: Surface Heat Transfer Coefficient Contours, Bottom Wall– Re = 20000.	191
Figure 5.24: Surface Heat Transfer Coefficient as a Function of Streamwise Distance – Re = 20000.....	192
Figure 5.25: Transient Contours of Velocity – (+)X Plane, Time Step = 0.000726s, Re = 40000.....	193
Figure 5.26: Transient Contours of Velocity – Spanwise Centerplane, Time Step = 0.000484s, Re = 40000 .....	194
Figure 5.27: Transient Contours of Velocity – (-)X Plane, Time Step = 0.001936s, Re = 40000.....	194
Figure 5.28: Transient Contours of Velocity – (-)X Plane, Time Step = 0.002178s, Re = 40000.....	195
Figure 5.29: Transient Contours of Velocity – (-)X Plane, Time Step = 0.00242s, Re = 40000.....	195
Figure 5.30: Transient Contours of Velocity – (-)X Plane, Time Step = 0.002662s, Re = 40000.....	195
Figure 5.31: Transient Contours of Velocity – (-)X Plane, Time Step = 0.002904s, Re = 40000.....	196
Figure 5.32: Transient Contours of Velocity – (-)X Plane, Time Step = 0.003146s, Re = 40000.....	196

Figure 5.33: Transient Contours of Velocity – (-)X Plane, Time Step = 0.003388s, Re = 40000.....	196
Figure 5.34: Transient Contours of Velocity – (-)X Plane, Time Step = 0.00363s, Re = 40000.....	197
Figure 5.35: Transient Contours of Velocity – (-)X Plane, Time Step = 0.003872s, Re = 40000.....	197
Figure 5.36: Transient Contours of Vorticity – (+)X Plane, Time Step = 0.000484s, Re = 40000.....	198
Figure 5.37: Transient Contours of Vorticity – (+)X Plane, Time Step = 0.001452s, Re = 40000.....	198
Figure 5.38: Transient Contours of Vorticity – (+)X Plane, Time Step = 0.001694s, Re = 40000.....	198
Figure 5.39: Transient Contours of Vorticity – (+)X Plane, Time Step = 0.004598s, Re = 40000.....	199
Figure 5.40: Transient Contours of Vorticity – (-)X Plane, Time Step = 0.001936s, Re = 40000.....	199
Figure 5.41: Transient Contours of Vorticity – (-)X Plane, Time Step = 0.002178s, Re = 40000.....	200
Figure 5.42: Transient Contours of Vorticity – (-)X Plane, Time Step = 0.00242s, Re = 40000.....	200
Figure 5.43: Transient Contours of Vorticity – (-)X Plane, Time Step = 0.002662s, Re = 40000.....	200

Figure 5.44: Transient Contours of Vorticity – (-)X Plane, Time Step = 0. 002904s, Re = 40000.....	201
Figure 5.45: Transient Contours of Vorticity – (-)X Plane, Time Step = 0.003146s, Re = 40000.....	201
Figure 5.46: Transient Contours of Vorticity – (-)X Plane, Time Step = 0.003388s, Re = 40000.....	201
Figure 5.47: Transient Contours of Vorticity – (-)X Plane, Time Step = 0. 00363s, Re = 40000.....	202
Figure 5.48: Transient Contours of Vorticity – (-)X Plane, Time Step = 0. 003872s, Re = 40000.....	202
Figure 6.1: Illustration of the Contaminated Data Region.....	208
Figure A.1: Frontal View of CATER Laboratory for Turbine Aerodynamics, Heat Transfer, and Durability.....	216
Figure A.2: Quincy Three-Piston, Two-Stage Air Compressor, Maximum Output of 0.01 kg/s at 250 psi .....	219
Figure A.3: Modine Heat Exchanger, Directly out of Compressor .....	220
Figure A.4: Condenser and Reheater .....	220
Figure A.5: Three Inch Diameter, Black Iron Supply Line .....	221
Figure A.6: Five-Thousand Gallon Compressed Air Storage Tank .....	222
Figure A.7: Snap-Shots of CECS Ariel Cluster.....	224
Figure E.1: Surface Heat Transfer Coefficient Contours, Bottom Wall – Re = 40000	339
Figure E.2: Surface Heat Transfer Coefficient Contours – Re = 40000.....	339

Figure E.3: Surface Heat Transfer Coefficient as a Function of Streamwise Distance – Re = 40000.....	340
Figure E.4: Static Pressure Distribution over the Bottom Wall of the Channel – Re = 40000.....	341
Figure E.5: Spanwise Profiles of Static Temperature – Re = 40000 .....	342
Figure E.6: Spanwise Profiles of Turbulent Kinetic Energy – Re = 40000.....	343
Figure E.7: Spanwise Profiles of Velocity Magnitude – Re = 40000.....	344
Figure E.8: Spanwise Profiles of Vorticity Magnitude – Re = 40000.....	345
Figure E.9: Streamwise Profiles of Static Temperature – Re = 40000.....	346
Figure E.10: Streamwise Profiles of Turbulent Kinetic Energy – Re = 40000 .....	347
Figure E.11: Streamwise Profiles of Velocity Magnitude – Re = 40000 .....	348
Figure E.12: Streamwise Profiles of Vorticity Magnitude – Re = 40000.....	349
Figure E.13: Surface Heat Transfer Coefficient Contours, Bottom Wall– Re = 30000	351
Figure E.14: Surface Heat Transfer Coefficient Contours, Side and Top Walls– Re = 30000.....	352
Figure E.15: Surface Heat Transfer Coefficient as a Function of Streamwise Distance – Re = 30000.....	352
Figure E.16: Static Pressure Distribution over the Bottom Wall of the Channel – Re = 30000.....	353
Figure E.17: Static Pressure on the Dimple Surface as a Function of Streamwise Distance – Re = 30000.....	354
Figure E.18: Spanwise Profiles of Static Temperature – Re = 30000 .....	355
Figure E.19: Spanwise Profiles of Turbulent Kinetic Energy – Re = 30000.....	356

Figure E.20: Spanwise Profiles of Velocity Magnitude – Re = 30000.....	357
Figure E.21: Spanwise Profiles of Vorticity Magnitude – Re = 30000.....	358
Figure E.22: Streamwise Profiles of Static Temperature – Re = 30000.....	359
Figure E.23: Streamwise Profiles of Turbulent Kinetic Energy – Re = 30000 .....	360
Figure E.24: Streamwise Profiles of Velocity Magnitude – Re = 30000 .....	361
Figure E.25: Streamwise Profiles of Vorticity Magnitude – Re = 30000.....	362
Figure E.26: Surface Heat Transfer Coefficient Contours, Bottom Wall– Re = 20000	364
Figure E.27: Surface Heat Transfer Coefficient as a Function of Streamwise Distance – Re = 20000.....	364
Figure E.28: Static Pressure Distribution over the Bottom Wall of the Channel – Re = 20000.....	365
Figure E.29: : Static Pressure on the Dimple Surface as a Function of Streamwise Distance – Re = 20000.....	366
Figure E.30: Streamwise Profiles of Static Temperature – Double Dimples, Re = 20000 .....	367
Figure E.31: Streamwise Profiles of Turbulent Kinetic Energy : Double Dimples, Re = 20000.....	368
Figure E.32: Streamwise Profiles of Velocity Magnitude : Double Dimples, Re = 20000 .....	369
Figure E.33: Streamwise Profiles of Vorticity Magnitude : Double Dimples, Re = 20000 .....	370
Figure E.34: Spanwise Profiles of Static Temperature : Double Dimples, Re = 20000371	



Figure E.35: Spanwise Profiles of Turbulent Kinetic Energy : Double Dimples, Re = 20000.....	372
Figure E.36: Spanwise Profiles of Velocity Magnitude : Double Dimples, Re = 20000 .....	373
Figure E.37: Spanwise Profiles of Vorticity Magnitude – Double Dimples, Re = 20000 .....	374
Figure F.1: Transient Contours of Velocity – (+)X Plane, Time Step = 0s, Re = 40000 .....	377
Figure F.2: Transient Contours of Velocity – (+)X Plane, Time Step = 0.000242s, Re = 40000.....	377
Figure F.3: Transient Contours of Velocity – (+)X Plane, Time Step = 0.000484s, Re = 40000.....	377
Figure F.4: Transient Contours of Velocity – (+)X Plane, Time Step = 0.000726s, Re = 40000.....	378
Figure F.5: Transient Contours of Velocity – (+)X Plane, Time Step = 0.000968s, Re = 40000.....	378
Figure F.6: Transient Contours of Velocity – (+)X Plane, Time Step = 0.00121s, Re = 40000.....	378
Figure F.7: Transient Contours of Velocity – (+)X Plane, Time Step = 0.001452s, Re = 40000.....	379
Figure F.8: Transient Contours of Velocity – (+)X Plane, Time Step = 0.001694s, Re = 40000.....	379

Figure F.9: Transient Contours of Velocity – (+)X Plane, Time Step = 0.1936s, Re = 40000.....	379
Figure F.10: Transient Contours of Velocity – (+)X Plane, Time Step = 0.2178s, Re = 40000.....	380
Figure F.11: Transient Contours of Velocity – (+)X Plane, Time Step = 0.00242s, Re = 40000.....	380
Figure F.12: Transient Contours of Velocity – (+)X Plane, Time Step = 0.002662s, Re = 40000.....	380
Figure F.13: Transient Contours of Velocity – (+)X Plane, Time Step = 0.002904s, Re = 40000.....	381
Figure F.14: Transient Contours of Velocity – (+)X Plane, Time Step = 0.003146s, Re = 40000.....	381
Figure F.15: Transient Contours of Velocity – (+)X Plane, Time Step = 0.003388s, Re = 40000.....	381
Figure F.16: Transient Contours of Velocity – (+)X Plane, Time Step = 0.00363s, Re = 40000.....	382
Figure F.17: Transient Contours of Velocity – (+)X Plane, Time Step = 0.003872s, Re = 40000.....	382
Figure F.18: Transient Contours of Velocity – (+)X Plane, Time Step = 0.004114s, Re = 40000.....	382
Figure F.19: Transient Contours of Velocity – (+)X Plane, Time Step = 0.004356s, Re = 40000.....	383

Figure F.20: Transient Contours of Velocity – (+)X Plane, Time Step = 0.004598s, Re = 40000.....	383
Figure F.21: Transient Contours of Velocity – Spanwise Centerplane, Time = 0s, Re = 40000.....	385
Figure F.22: Transient Contours of Velocity – Spanwise Centerplane, Time = 0.000242s, Re = 40000.....	385
Figure F.23: Contours of Velocity – Spanwise Centerplane, Time = 0.000484s, Re = 40000.....	385
Figure F.24: Transient Contours of Velocity – Spanwise Centerplane, Time = 0.000726s, Re = 40000.....	386
Figure F.25: Transient Contours of Velocity – Spanwise Centerplane, Time = 0.000968s, Re = 40000.....	386
Figure F.26: Transient Contours of Velocity – Spanwise Centerplane, Time = 0.00121s, Re = 40000.....	386
Figure F.27: Transient Contours of Velocity – Spanwise Centerplane, Time = 0.001452s, Re = 40000.....	387
Figure F.28: Transient Contours of Velocity – Spanwise Centerplane, Time = 0.001694s, Re = 40000.....	387
Figure F.29: Transient Contours of Velocity – Spanwise Centerplane, Time = 0.001936s, Re = 40000.....	387
Figure F.30: Transient Contours of Velocity – Spanwise Centerplane, Time = 0.002178s, Re = 40000.....	388

Figure F.31: Transient Contours of Velocity – Spanwise Centerplane, Time = 0.0024 s, Re = 40000.....	388
Figure F.32: Transient Contours of Velocity – Spanwise Centerplane, Time = 0.002662s, Re = 40000.....	388
Figure F.33: Transient Contours of Velocity – Spanwise Centerplane, Time = 0.002904s, Re = 40000.....	389
Figure F.34: Transient Contours of Velocity – Spanwise Centerplane, Time = 0.003146s, Re = 40000.....	389
Figure F.35: Transient Contours of Velocity – Spanwise Centerplane, Time = 0.003388s, Re = 40000.....	389
Figure F.36: Transient Contours of Velocity – Spanwise Centerplane, Time = 0.00363s, Re = 40000.....	390
Figure F.37: Transient Contours of Velocity – Spanwise Centerplane, Time = 0.003872s, Re = 40000.....	390
Figure F.38: Transient Contours of Velocity – Spanwise Centerplane, Time = 0.004114s, Re = 40000.....	390
Figure F.39: Transient Contours of Velocity – Spanwise Centerplane, Time = 0.004356s, Re = 40000.....	391
Figure F.40: Transient Contours of Velocity – Spanwise Centerplane, Time = 0.004598s, Re = 40000.....	391
Figure F.41: Transient Contours of Velocity – (-)X Plane, Time Step = 0s, Re = 40000 .....	393

Figure F.42: Transient Contours of Velocity – (-)X Plane, Time Step = 0.000242s, Re = 40000.....	393
Figure F.43: Transient Contours of Velocity – (-)X Plane, Time Step = 0.000484s, Re = 40000.....	393
Figure F.44: Transient Contours of Velocity – (-)X Plane, Time Step = 0.000726s, Re = 40000.....	394
Figure F.45: Transient Contours of Velocity – (-)X Plane, Time Step = 0.000968s, Re = 40000.....	394
Figure F.46: Transient Contours of Velocity – (-)X Plane, Time Step = 0.00121s, Re = 40000.....	394
Figure F.47: Transient Contours of Velocity – (-)X Plane, Time Step = 0.001452s, Re = 40000.....	395
Figure F.48: Transient Contours of Velocity – (-)X Plane, Time Step = 0.001694s, Re = 40000.....	395
Figure F.49: Transient Contours of Velocity – (-)X Plane, Time Step = 0.001936s, Re = 40000.....	395
Figure F.50: Transient Contours of Velocity – (-)X Plane, Time Step = 0.002178s, Re = 40000.....	396
Figure F.51: Transient Contours of Velocity – (-)X Plane, Time Step = 0.00242s, Re = 40000.....	396
Figure F.52: Transient Contours of Velocity – (-)X Plane, Time Step = 0.002662s, Re = 40000.....	396

Figure F.53: Transient Contours of Velocity – (-)X Plane, Time Step = 0.002904s, Re = 40000.....	397
Figure F.54: Transient Contours of Velocity – (-)X Plane, Time Step = 0.003146s, Re = 40000.....	397
Figure F.55: Transient Contours of Velocity – (-)X Plane, Time Step = 0.003388s, Re = 40000.....	397
Figure F.56: Transient Contours of Velocity – (-)X Plane, Time Step = 0.00363s, Re = 40000.....	398
Figure F.57: Transient Contours of Velocity – (-)X Plane, Time Step = 0.003872s, Re = 40000.....	398
Figure F.58: Transient Contours of Velocity – (-)X Plane, Time Step = 0.00411 s, Re = 40000.....	398
Figure F.59: Transient Contours of Velocity – (-)X Plane, Time Step = 0.004356s, Re = 40000.....	399
Figure F.60: Transient Contours of Velocity – (-)X Plane, Time Step = 0.004598s, Re = 40000.....	399
Figure F.61: Transient Contours of Vorticity – (+)X Plane, Time Step = 0s, Re = 40000 .....	401
Figure F.62: Transient Contours of Vorticity – (+)X Plane, Time Step = 0.000242s, Re = 40000.....	401
Figure F.63: Transient Contours of Vorticity – (+)X Plane, Time Step = 0.000484s, Re = 40000.....	401

Figure F.64: Transient Contours of Vorticity – (+)X Plane, Time Step = 0.000726s, Re = 40000.....	402
Figure F.65: Transient Contours of Vorticity – (+)X Plane, Time Step = 0.000968s, Re = 40000.....	402
Figure F.66: Transient Contours of Vorticity – (+)X Plane, Time Step = 0.00121s, Re = 40000.....	402
Figure F.67: Transient Contours of Vorticity – (+)X Plane, Time Step = 0.001452s, Re = 40000.....	403
Figure F.68: Transient Contours of Vorticity – (+)X Plane, Time Step = 0.001694s, Re = 40000.....	403
Figure F.69: Transient Contours of Vorticity – (+)X Plane, Time Step = 0.001936s, Re = 40000.....	403
Figure F.70: Transient Contours of Vorticity – (+)X Plane, Time Step = 0.002178s, Re = 40000.....	404
Figure F.71: Transient Contours of Vorticity – (+)X Plane, Time Step = 0.00242s, Re = 40000.....	404
Figure F.72: Transient Contours of Vorticity – (+)X Plane, Time Step = 0.002662s, Re = 40000.....	404
Figure F.73: Transient Contours of Vorticity – (+)X Plane, Time Step = 0.002904s, Re = 40000.....	405
Figure F.74: Transient Contours of Vorticity – (+)X Plane, Time Step = 0.003146s, Re = 40000.....	405

Figure F.75: Transient Contours of Vorticity – (+)X Plane, Time Step = 0.003388s, Re = 40000.....	405
Figure F.76: Transient Contours of Vorticity – (+)X Plane, Time Step = 0.00363s, Re = 40000.....	406
Figure F.77: Transient Contours of Vorticity – (+)X Plane, Time Step = 0.003872s, Re = 40000.....	406
Figure F.78: Transient Contours of Vorticity – (+)X Plane, Time Step = 0.004114s, Re = 40000.....	406
Figure F.79: Transient Contours of Vorticity – (+)X Plane, Time Step = 0.004356s, Re = 40000.....	407
Figure F.80: Transient Contours of Vorticity – (+)X Plane, Time Step = 0.004598s, Re = 40000.....	407
Figure F.81: Transient Contours of Velocity – (-)X Plane, Time Step = 0s, Re = 40000.....	409
Figure F.82: Transient Contours of Velocity – (-)X Plane, Time Step = 0.000242s, Re = 40000.....	409
Figure F.83: Transient Contours of Velocity – (-)X Plane, Time Step = 0.000484s, Re = 40000.....	409
Figure F.84: Transient Contours of Velocity – (-)X Plane, Time Step = 0.000726s, Re = 40000.....	410
Figure F.85: Transient Contours of Velocity – (-)X Plane, Time Step = 0.000968s, Re = 40000.....	410



Figure F.86: Transient Contours of Velocity – (-)X Plane, Time Step = 0.00121s, Re = 40000.....	410
Figure F.87: Transient Contours of Velocity – (-)X Plane, Time Step = 0.001452s, Re = 40000.....	411
Figure F.88: Transient Contours of Velocity – (-)X Plane, Time Step = 0.001694s, Re = 40000.....	411
Figure F.89: Transient Contours of Velocity – (-)X Plane, Time Step = 0.001936s, Re = 40000.....	411
Figure F.90: Transient Contours of Velocity – (-)X Plane, Time Step = 0.002178s, Re = 40000.....	412
Figure F.91: Transient Contours of Velocity – (-)X Plane, Time Step = 0.00242s, Re = 40000.....	412
Figure F.92: Transient Contours of Velocity – (-)X Plane, Time Step = 0.002662s, Re = 40000.....	412
Figure F.93: Transient Contours of Velocity – (-)X Plane, Time Step = 0.002904s, Re = 40000.....	413
Figure F.94: Transient Contours of Velocity – (-)X Plane, Time Step = 0.003146s, Re = 40000.....	413
Figure F.95: Transient Contours of Velocity – (-)X Plane, Time Step = 0.003388s, Re = 40000.....	413
Figure F.96: Transient Contours of Velocity – (-)X Plane, Time Step = 0.00363s, Re = 40000.....	414

Figure F.97: Transient Contours of Velocity – (-)X Plane, Time Step = 0.003872s s, Re = 40000 .....	414
Figure F.98: Transient Contours of Velocity – (-)X Plane, Time Step = 0.004114s, Re = 40000.....	414
Figure F.99: Transient Contours of Velocity – (-)X Plane, Time Step = 0.004356s, Re = 40000.....	415
Figure F.100: Transient Contours of Velocity – (-)X Plane, Time Step = 0.004598s, Re = 40000.....	415

## LIST OF TABLES

Table 1: Dimple Flow Structure Illustrations (Ligrani, Harrison, Mahmood, & Mill, 2001).....	24
Table 2: Three Tested Cases.....	34
Table 3: Test Matrix.....	34
Table 4: Uncertainties - Copper Block Experiment, $Re = 30000$ .....	52
Table 5: Table of Constants to Characterize the Bulk Temperature as a Function of Time and Streamwise Location in the Channel.....	101
Table 6: Uncertainties – Transient TLC Experiment: Double Dimple, $Re = 30000$ .....	104
Table 7: Smooth Wall Friction Factor Validation Summary.....	113
Table 8: Validation Summary.....	114
Table 9: Comparison of Channel-Averaged Heat Transfer Results.....	160
Table 10: Comparison of Channel-Averaged Heat Transfer Results – Reynolds Number = 30000.....	161
Table 11: Comparison of Channel-Averaged Heat Transfer Results – Reynolds Number = 40000.....	161
Table 12: Percentage Difference Channel-Averaged Nusselt number Augmentation between Two Experiments – Before Correction.....	162
Table 13: Comparison Friction Factor Augmentation.....	164
Table 14: Legend to LES Plane Descriptions.....	
Table 15: Comparison of Bottom Wall Surface .....	203
Table 16: Comparison of Surface Averaged Heat Transfer Coefficients.....	204
Table 17: Wall-to-Wall Comparison of Nusselt Number from Transient TLC Experiment (Before Area Correction).....	204
Table 18: Final Results Comparison (Before Final Transient TLC Corrections)...	206
Table 19: Nusselt Number Augmentation – Percentage Difference Between Basic and Transient TLC Experiments (After Area Correction).....	208

Table 20: Comparison of Channel-Averaged Nusselt Number – After Area Correction.....	209
Table 21: Nusselt Number Augmentation – Percentage Difference Between Basic and Transient TLC Experiments (After Area Correction).....	210
Table 22: Final Results Comparison – Double Dimple.....	211

## LIST OF PUBLICATIONS

### Conference Proceedings

#### In Print

- Carson D. Slabaugh, Lucky V. Tran, J. S. Kapat, "A Study of Heat Transfer and Friction Augmentation in a Rectangular Channel with Dimples Applied to the Bottom Wall," 46th AIAA/ASME/SAE/ASEE Joint Propulsion Conference & Exhibit, July 25-28, 2010, Nashville, TN
- Carson D. Slabaugh, Michelle Valentino, J. S. Kapat, "Heat Transfer and Friction Augmentation in a Rectangular Channel with Features Applied to a Single Wall," 46th AIAA/ASME/SAE/ASEE Joint Propulsion Conference & Exhibit, July 25-28, 2010, Nashville, TN.
- Lucky V. Tran, Carson D. Slabaugh, J. S. Kapat, "Thermal Performance of High Aspect Ratio Internal Cooling Channels Manufactured with Different Techniques," 46th AIAA/ASME/SAE/ASEE Joint Propulsion Conference & Exhibit, July 25-28, 2010, Nashville, TN.
- Carson D. Slabaugh, Lucky V. Tran, J. S. Kapat, "Heat Transfer and Friction Augmentation in High Aspect Ratio, Ribbed Channels with Dissimilar Inlet Conditions," ASME Paper IHTC14-23219, ASME International Heat Transfer Conference 2010, August 8-13, 2010, Washington D. C., USA.
- Carson D. Slabaugh, A. P. Le, J. S. Kapat, "A Study of Side Wall Heat Transfer Augmentation in a Narrow Rectangular Duct," AIAA Paper AIAA-2009-5377, 45th AIAA/ASME/SAE/ASEE Joint Propulsion Conference & Exhibit, August 2-5, 2009, Denver, CO.

A. P. Le, Carson D. Slabaugh, J. S. Kapat, B. Warren, "A Study of Heat Transfer Enhancement, in a High Aspect Ratio Channel, Using Rib-Turbulators and Varying Inlet Conditions," ASME Paper HT2009-59314, ASME Summer Heat Transfer Conference, July 19-23, 2009, San Francisco, CA.

#### In Preparation

Michelle Valentino, Carson D. Slabaugh, Mark Ricklick, J. S. Kapat, "Study on Rib Turbulators for Heat Transfer and Friction Augmentation in a Narrow Rectangular Duct," 49th AIAA Aerospace Sciences Meeting, January 4-7, 2011, Orlando, FL, USA.

Lucky V. Tran, Carson D. Slabaugh, Mark Ricklick, J. S. Kapat, "A Parametric Design Study of the Double Dimple Surface Feature for Heat Transfer Augmentation in Internal Cooling Channels," 49th AIAA Aerospace Sciences Meeting, January 4-7, 2011, Orlando, FL, USA.

Carson D. Slabaugh, Lucky V. Tran, J. S. Kapat, "An Experimental and Numerical Study of Dimples for Heat Transfer Augmentation in 2:1 Aspect Ratio Internal Cooling Channels," ASME Paper HT2009-59314, ASME Summer Heat Transfer Conference, July 19-23, 2011, San Francisco, CA.

## Journal Publications

### In Preparation

Carson D. Slabaugh, Lucky V. Tran, J. S. Kapat, “Heat Transfer and Friction Augmentation in High Aspect Ratio, Ribbed Channels with Dissimilar Inlet Conditions,” *ASME Journal of Heat Transfer*

Carson D. Slabaugh, Lucky V. Tran, J. S. Kapat, “An Experimental and Numerical Study of Dimples for Heat Transfer Augmentation in 2:1 Aspect Ratio Internal Cooling Channels,” *ASME Journal of Heat Transfer*

Carson D. Slabaugh, Lucky V. Tran, J. S. Kapat, “A Study of Heat Transfer and Friction Augmentation in a Rectangular Channel with Dimples Applied to the Bottom Wall,” *AIAA Journal of Thermophysics and Heat Transfer*

## Other Scholarly Accomplishments

### In Print

Carson D. Slabaugh, Lucky V. Tran, J. S. Kapat, “Radial Vent – Phase III, Final Report,” Siemens Energy, Inc., May 2010.

Carson D. Slabaugh, Lucky V. Tran, J. S. Kapat, “Radial Vent – Phase II, Final Report,” Siemens Energy, Inc., May 2010.

Carson D. Slabaugh, Lucky V. Tran, J. S. Kapat, “Radial Vent – Phase I, Addendum to Final Report,” Siemens Energy, Inc., April 2010.

C. D. Slabaugh, “An Experimental Study of the Effect of a Scratch/Dig on the Operational Function of Arrowhead’s Optical Flats,” Lockheed Martin, Missiles and Fire Control, Inc., August, 2007.

In Preparation

Carson D. Slabaugh, Michelle Valentino, J. S. Kapat, “Siemens Transition Duct Cooling,  
Final Report,” Siemens Energy, Inc., December 2010.



# NOMENCLATURE

## *Roman Symbols*

A	Wetted Area
$C_s$	Smagorinski Constant
D	Diameter
H	Channel Height
L	Characteristic Length
M	Blowing Ratio
Nu	Nusselt Number
P	Static Pressure
P	Perimeter
Pr	Prandtl Number
$Q''$	Surface Heat Transfer Flux
$Q_{\text{added}}$	Power Input to the Flow
$Q_{\text{input}}$	Power Input
$Q_{\text{loss\_amb}}$	Ambient Heat Loss
Re	Reynolds Number
U	Mean Velocity
T	Temperature
V	Voltage
W	Width
c	Specific Heat Capacity
d	Dimple Footprint Diameter

$f$	Darcy Friction Factor
$g$	Acceleration due to Gravity
$h$	Convective Heat Transfer Coefficient
$k$	Thermal Conductivity
$k$	Turbulent Kinetic Energy
$m^*$	Heat Load Parameter
$p$	Pitch
$t$	Time
$v$	Fluid Velocity
$u, v, w$	Longitudinal, Vertical, and Transverse Velocity Components in Fractions of U
$x, y, z$	Axial Coordinate

*Greek Symbols*

$\alpha$	Thermal Diffusivity
$\beta$	Non-Dimensional Time
$\delta$	Dimple Depth
$\Delta$	LES Length Scale Filter Width
$\varepsilon$	Cooling Efficiency
$\eta$	Cooling Effectiveness
$\theta$	Non-Dimensional Temperature
$\nu$	Kinematic Viscosity
$\rho$	Density
$\tau$	Stress [ $\text{Nm}^{-2}$ ]

$\eta$	Thermal Performance Factor
$\mu$	Fluid Dynamic Viscosity

*Superscripts*

-	Averaged Value
$\rightarrow$	Vector

*Subscripts*

air	Air
Blasius	Value Predicted by Blasius Correlation
bulk	Local Bulk Temperature
DB	Value Predicted by Dittus-Boelter Correlation
GN	Value Predicted by Gnielinski Correlation
ci	Coolant Inlet
g	Gas
h	Hydraulic
o	Baseline Value
p	Constant Pressure
T	Thermal
w	Wall

*Abbreviations*

AR	Aspect Ratio
----	--------------

CCD	Charge Coupled Device
CFD	Computational Fluid Dynamics
DNS	Direct Numerical Simulation
HSI	Hue, Saturation, Intensity
LES	Large Eddy Simulation
PIV	Particle Image Velocimetry
RANS	Reynolds-Averaged Navier-Stokes
RGB	Red, Green, Blue
RIT	Rotor Inlet Temperature
QUICK	Quadratic Upwind Interpolation for Convective Kinematics
SST	Stress Shear Transport
TBC	Thermal Barrier Coating
TIT	Turbine Inlet Temperature
TLC	Thermochromic Liquid Crystal

# CHAPTER 1: INTRODUCTION

## The Energy Challenge

Establishing a clean and renewable energy supply is the preeminent engineering challenge of our time. With the increased national focus on the environmental as well as the economic impacts of this issue, funding has been allocated from industry, government, and academia alike to promote greater understanding of the situation and work towards effective solutions. The development of new 'green' technologies is a crucial component of these efforts with monumental implications for the industries of power generation, transportation, and many more. In addition, it is crucial the continued focus is maintained on the improvement of existing technologies. It will take several decades for today's cutting edge technologies to be understood, trusted, commercialized and implemented to any considerable scale. In the mean time, it is crucial that diligent efforts be maintained, working with what we already have to improve the situations until the next technology is ready to come on line.

## Efficiency of Gas Turbine Engines

Turbines, in some form, are responsible for more than 98 percent of all electricity generated in the United State and 100 percent of commercial and military air transport. The operation of these engines is clearly responsible for significant consumption of hydrocarbon fuels and, in turn, emission of green house gases into the atmosphere. With such wide-scale implementation, it is understood that even the smallest increase in the operating efficiency of these machines can lead to enormous improvements over the

current energy situation. These effects can extend from a reduction in the emission of greenhouse gases to lessening the nation's dependence of foreign energy sources to lower energy prices for the consumer.

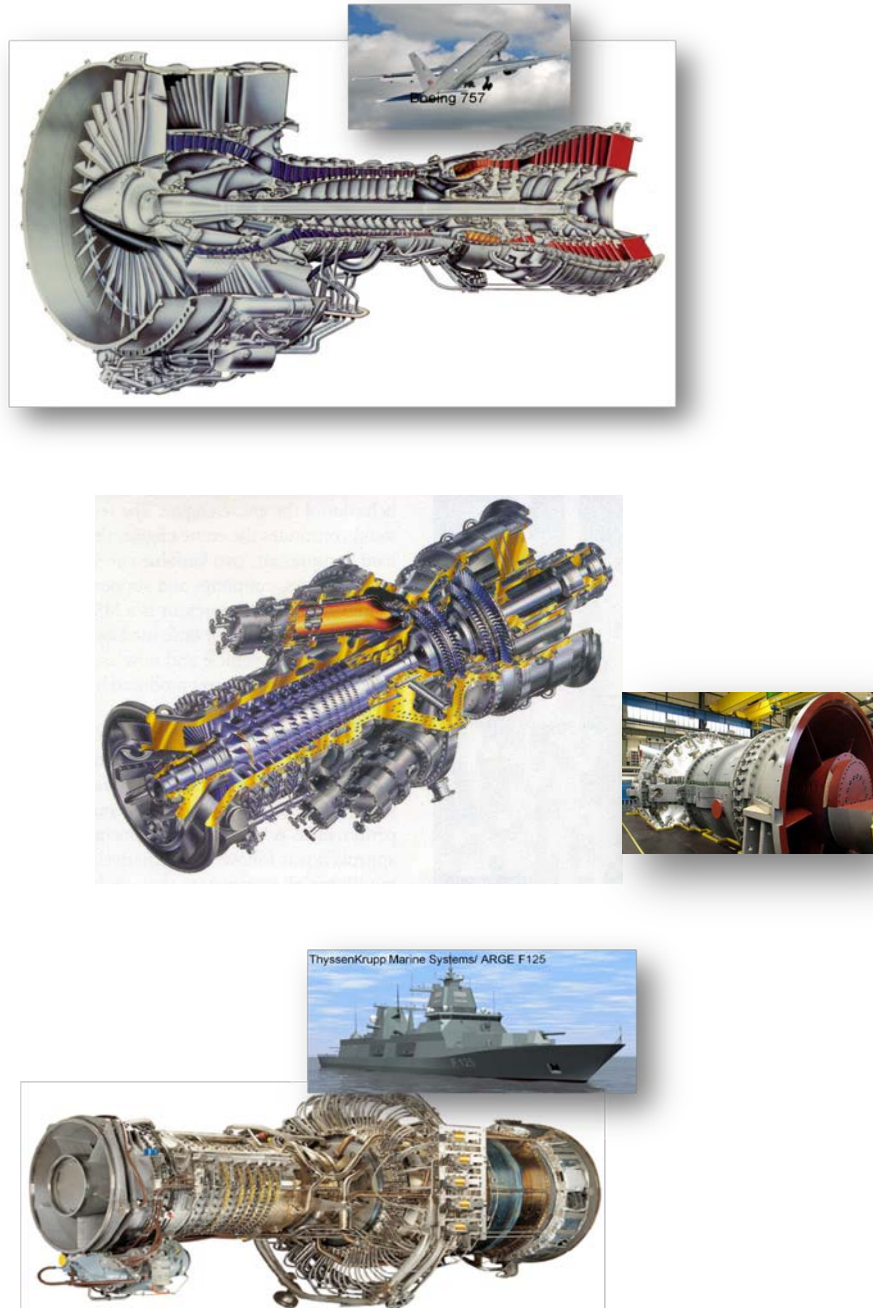


**Figure 1.1: Gas Turbine Variations in Three Major Applications – Aircraft, Power Generation, and Marine Applications, Respectively**

It is important to comprehend that vastness that, because of the widely-implemented use of these technologies in the world today, what some may consider a very minor contribution can have a vast impact on the world's energy situation. According to Randy Zwirn, President and CEO of Siemens Energy, just a one-percent gain in the efficiency of a land-based gas-turbine can provide enough extra power to supply 1800 homes with electricity. When keeping in mind that this is achieved using the same amount of fuel, it is easy to understand why research and development in this field is so fundamentally important.

The T-S diagram of a typical open loop Brayton cycle is presented in Figure 1.2, below. The figure on the left illustrates the ideal case, with no losses through the compressor or turbine stages and no thermal losses. Figure 1.3 represents this cycle in a more physical sense by showing the actual turbine components that complete the cycle.

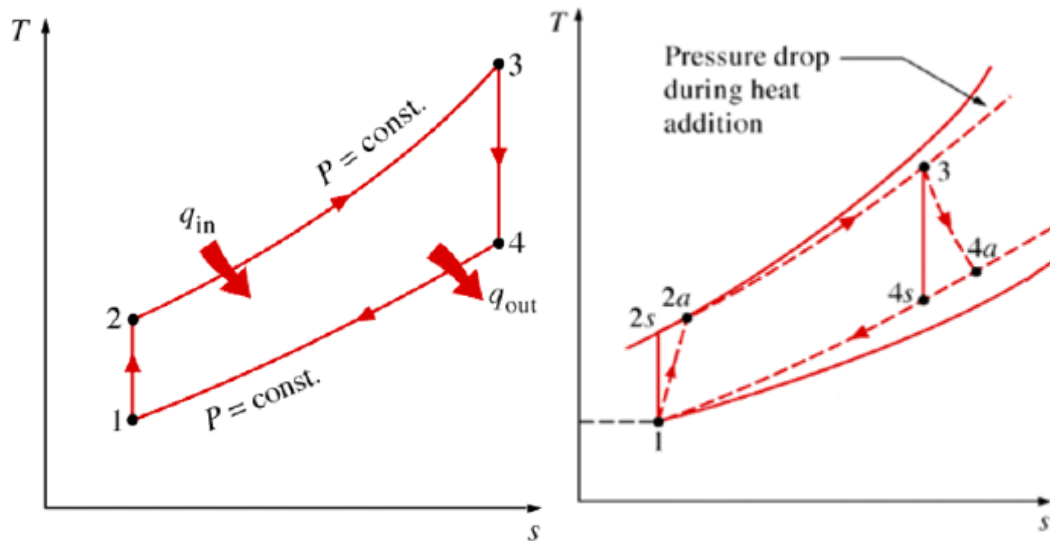


**Figure 1.2: Air Standard Cycle of a Gas-Turbine Energy - Ideal (Left) and with Known Inefficiencies (Right) (Sultanian, 2009)**

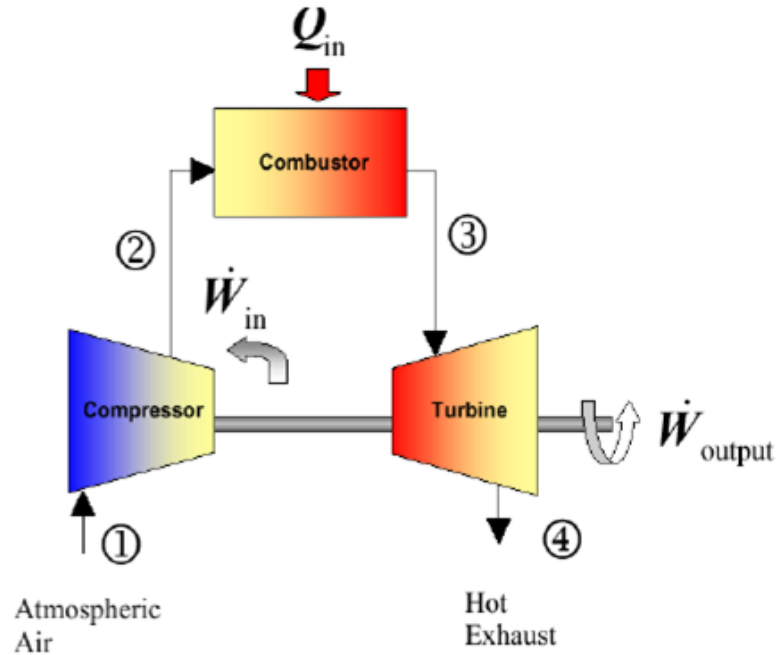


Figure 1.3: Air Standard Cycle Represented by Common Turbine Components

From analysis of the cycle and equation for cycle efficiency (1), it can be seen that an increase in the overall efficiency of the cycle can be achieved by mainly by two main methods.

$$\eta_{th,Brayton} = 1 - \frac{T_4 - T_1}{T_3 - T_2} \quad (1)$$

$$\text{and } 1 - \frac{T_4 - T_1}{T_3 - T_2} = 1 - \frac{T_4}{T_3} \text{ for an ideal cycle (no losses)}$$

First, an increase in pressure ratio would, in theory, lead to a greater power output from the engine by increasing the span between the high and low pressure isobars (Figure 1.2, Left). With increased pressure ratio, however, comes the need for more efficient compressor and turbine stages, where losses will become exaggerated using current technology (Figure 1.2, Right). In practice, increased pressure ratio is not enough to



drive the efficiency of the turbine up, alone. It is also necessary to increase the Turbine Inlet Temperature (T3).

The prominent means of increasing engine efficiency is by raising the ‘Turbine Inlet Temperature’ – the temperature of the mainstream flow after combustion, entering the first stage of the turbine section. The challenge is presented when these temperatures are forced beyond the allowable limits of the materials inside the machine. In order to protect these components, active cooling and protection methods are employed. The focus of this work is the development of more efficient means of cooling ‘hot’ turbine components.

### Internal Cooling

As shown in Figure 1.3, the Turbine Inlet Temperature (TIT) is the temperature of the flow directly after the combustor, and is a measure of the amount of enthalpy, or the amount of thermal energy potential that present in the flow available to be extracted by the turbine stages of the engine. Of course, there are restrictions that prevent the infinite increase in the TIT of the engine, the most obvious being the melting temperatures of the blades, vanes, and other components of the engine. It stands to reason that as the temperature of the mainstream flow is increased, the temperatures of all of the engine components in contact with the flow in driven up as well.

Development of advanced metal alloys has played a significant role in increasing the TIT of gas turbine engines. Figure 1.4 presents the increase in allowable operating temperature of metals used to fabricate gas turbine components such as blades and vanes.

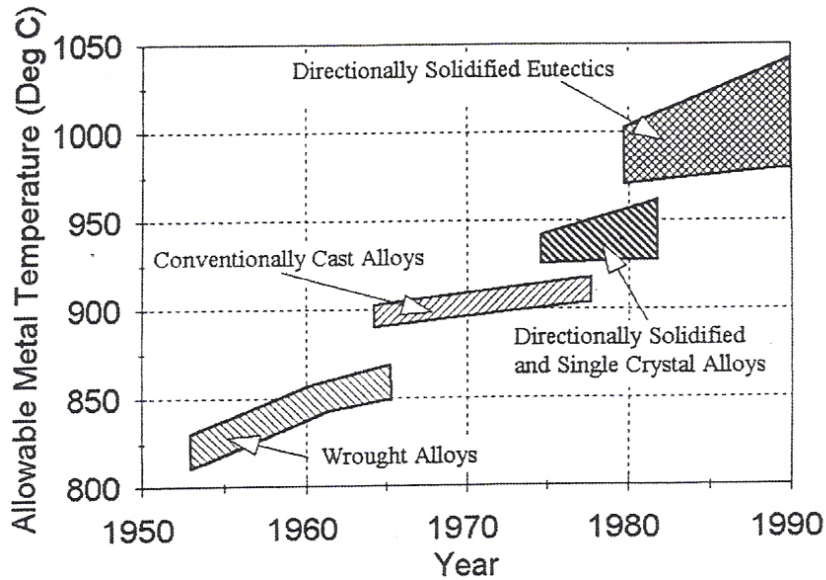


**Figure 1.4: Increased in Safe Operating Temperature of Metals (Suo, 1985)**

Also, the development of heat resistant coatings such as Thermal Barrier Coating has played a major role in the ability of these materials to withstand the high temperature, high stress environment to which they are subjected in an actual engine.

While these advancements in material science have been vital to the rise in turbine efficiency over the past thirty years, this technology, alone, has not been able to satisfy the requirements of design engineers increasing TIT. To solve this engineering challenge, active cooling methods are designed to remove heat from the engine components in an effort to maintain the part life and overall reliability. For this reason, the development of these advanced technologies has become a truly multi-disciplinary effort and every degree increase in TIT has been the result of enormous effort, passion, and focus of thousands of researchers and engineers worldwide. With this in mind, Figure 1.5 shows the increase in TIT over the past half-century with the development and refinement of active cooling techniques applied to turbine components.

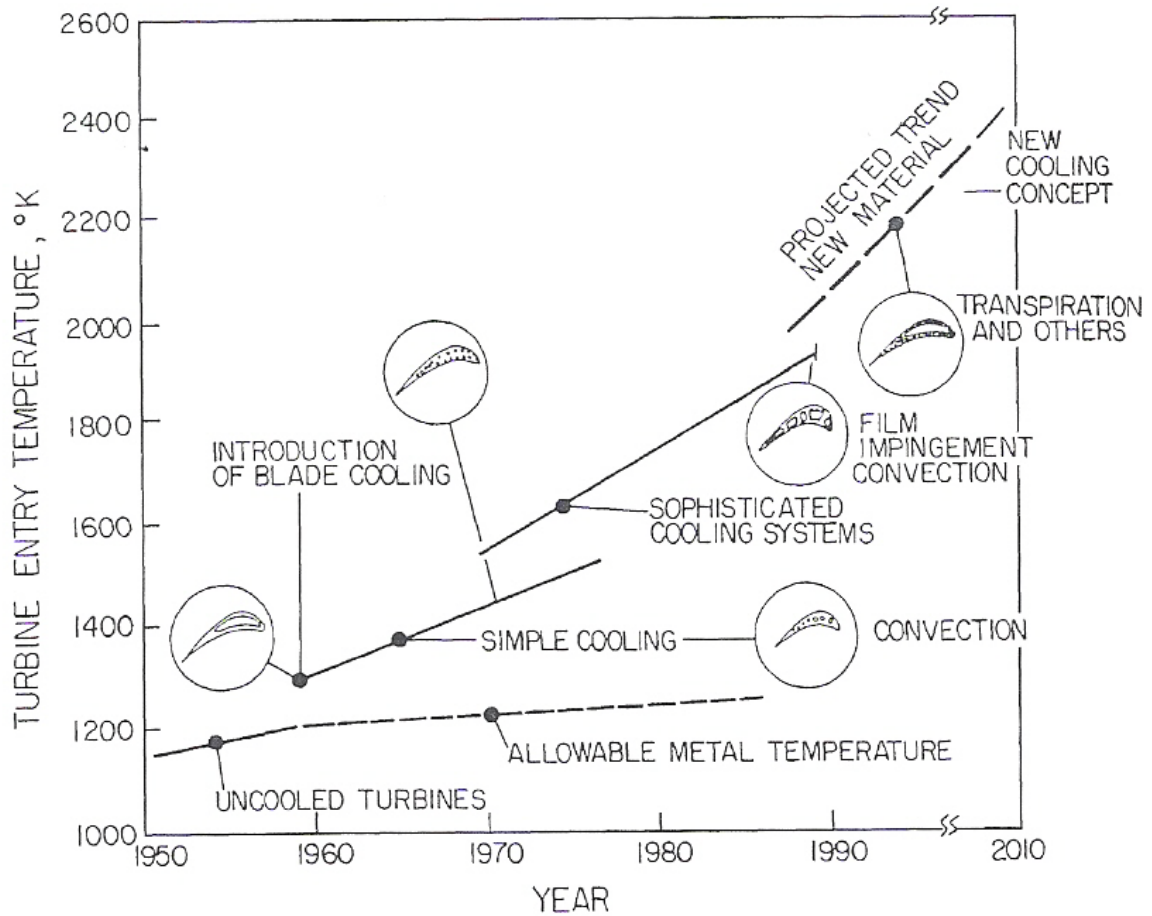


**Figure 1.5: Increase in Turbine Inlet Temperature with Advances in Cooling Techniques (Lakshminarayana, 1996)**

It is very interesting to note that for over forty years now, mainstream gas temperatures leaving the combustor have been several hundred degrees higher than the allowable metal temperature of the material. In fact, then operating conditions of today's most advanced engines are more than 300 K higher than the melting temperatures of the component materials. An interesting fact from Hany Moustapha's book, *Axial and Radial Turbines*, "The amount of ... heat that needs to be removed from the blades (of an aircraft engine) ... is enough to power fourteen average homes per blade (Moustapha, Zelesky, Baines, & Japikse, 2003)."

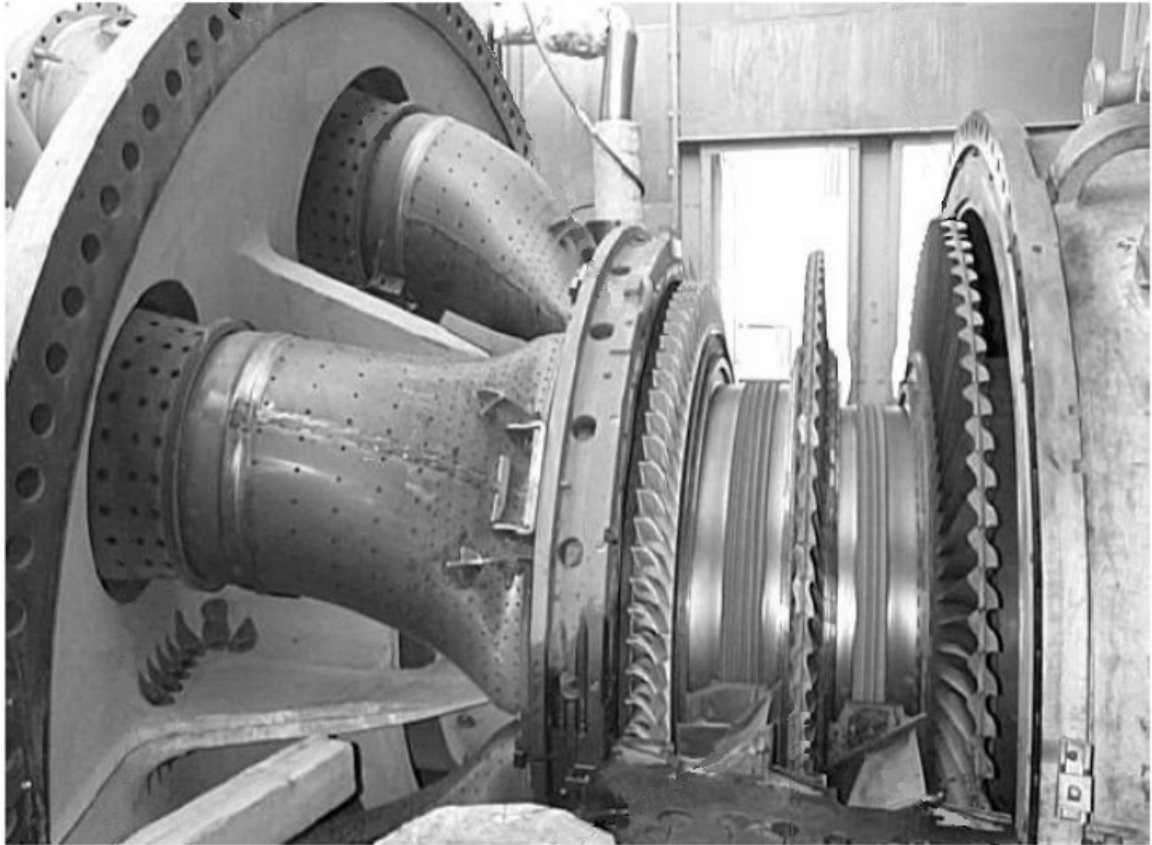


**Figure 1.6: Photograph of a Cooled Transition Piece in a Gas-Turbine with Shrouding Removed (Sultanian, 2009)**

While cooling engine components is absolutely necessary to withstand the thermal and mechanical loads of advanced systems, there is a penalty for coolant air used in the secondary air system. In some cases, as much as 20% of the total incoming mass-flow rate from the compressor is ducted away to cool the hot components of the engine (Jeal, 1988). Removing high pressure air from the compressor is an ‘expensive’ process because it reduces the amount of air available for combustion. This is air which has already had a large amount of work done to raise the pressure, but will no longer make any contribution to the power generation in the subsequent expansion stages through the following stages. It has been shown that improvements in overall cycle efficiency with increasing TIT are also heavily dependent on the amount of cooling air required

(Horlock, Watson, & Jones, 2001). Therefore, it is crucial that the cooling system designed for each component of the hot stages of the turbine be carefully planned in order to maximize the amount of heat removed while minimizing the flow-rate required. Figure 1.7 illustrates a blade cooling design that uses a combination of several different techniques to effectively remove heat from the component using three key technologies: Film Cooling for protection of the outer surface, Internal Passage Cooling with turbulence promoters, and Impingement Cooling on the leading edge of the blade.

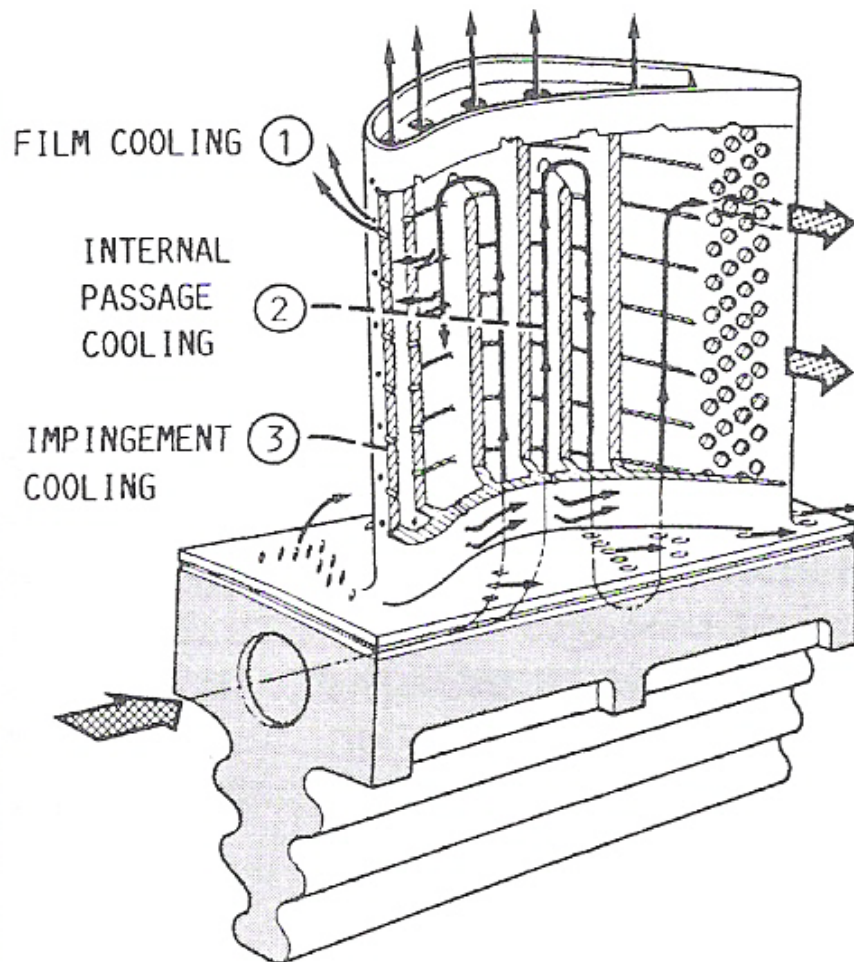


**Figure 1.7: Illustration of Possible Turbine Blade Design Including a Combination of Cooling Techniques (Gladden & Simoneau)**

Figure 1.8 provides a visual understanding of what an actual part looks like with the aforementioned cooling technologies implemented.

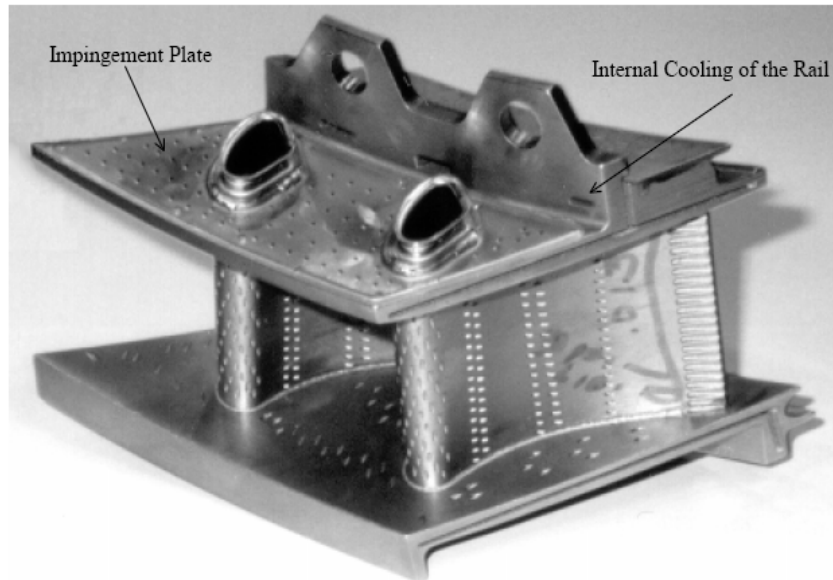


**Figure 1.8: Example of a Turbine Nozzle Guide Vane with Endwall Film-Cooling and Endwall Impingement Cooling.**

It is the combined influence of multiple factors, including advancement in the efficiency of active cooling techniques, that allows for the continual increase in the TIT and hence the overall efficiency of the engine. Therefore, it is the goal of the design engineer in this field is to maximize the amount of heat removed by the coolant while minimizing the coolant mass flow rate: by removing a greater amount of heat with a lower coolant mass flow rate, more compressed air is left in the mainstream gas flow for combustion and power generation. Figure 1.9 shows the increase in turbine cooling effectiveness and efficiency over the past several decades as a function of non-dimensional mass flow through the cooling system (Dailey, 2000).

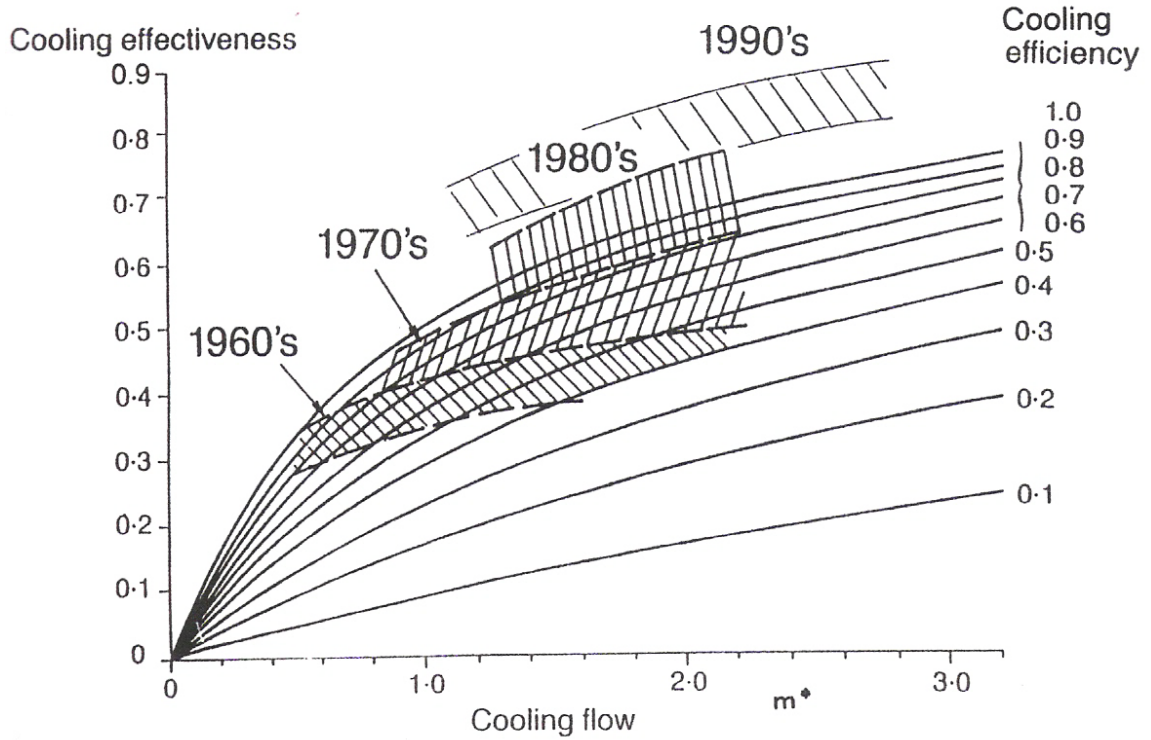


Figure 1.9: Increasing Cooling Effectiveness (Dailey, 2000)

Cooling effectiveness, convective cooling efficiency, and the dimensionless mass flow (or heat load parameter) are defined by [2], [3], and [4], respectively, where  $T_{gas}$  is the mainstream gas temperature,  $T_{metal}$  is the maximum temperature of the metal component,  $T_{ce}$  is the coolant exit temperature,  $T_{ci}$  is the coolant inlet temperature,  $m$  is the coolant mass flow rate,  $A$  is the outside surface area of the component, and  $\bar{h}_0$  is the area-weighted averaged hot-gas-path heat transfer coefficient with the shortest distance to the wall exposed to the hot gas.

$$\epsilon_0 = \frac{T_{gas} - T_{metal}}{T_g - T_{ci}} = \frac{\eta_c * m^*}{1 + \eta_c * m^*} \quad (2)$$

$$\eta_c = \frac{T_{ce} - T_{ci}}{T_{metal} - T_{ci}} \quad (3)$$

$$m^* = \frac{m * c_p}{h_0 * A} \quad (4)$$

In order to continue driving the efficiencies of these turbines up, it is imperative that the efficiencies of the active cooling designs increased simultaneously. It is today's research and development in the fields of Heat Transfer, Fluid Mechanics, and Thermodynamics that are absolutely crucial for the continued improvement and development of the technologies that will shape the way this country meets the energy needs of generations to come.

### Literature Review of Related Works

#### Internal Cooling – Transport Enhancing Features

Optimization of internal channel cooling has been the subject of a great deal of study in past years. One of the most common ways of improving the performance of any internal channel cooling design is application of a transport enhancing geometries to the channel walls. The added roughness of the surface geometries promote turbulence and heat transfer enhancement. Effectively increasing secondary flows and unsteady turbulent flow phenomena, these features act to disrupt formation of the viscous sub-layer and promote more intense mixing. The price paid, however, is an increase in pressure loss throughout the length of the channel. Therefore, to improve the efficiency of these ducts, one must optimize the various aspects of the channel design, such as pressure drop and



heat transfer performance, to remove the maximum amount of heat while requiring the minimum amount of coolant. Researchers have studied a great deal of geometries including ribs, dimples, pin fins, and scales with limitless variations of each.

Different components are designed with different cooling schemes based on the specific design requirements applicable there. For example, dimples typically applied in areas where a low pressure-drop is desired to allow more favorable pressure margins for other regions of the cooling design because of their notably low pressure-drop characteristics. Therefore, it is important to find a configuration that provides the best balance between heat transfer and friction augmentation for the specific channel configuration. For this reason, wall surface geometries found in literature are vast and diverse in nature; including dimples, pin fins, ribs, and numerous derivatives of these designs.

Ribs are positive features that act to trip the flow, disrupting boundary layer formation and causing the formation of complex vortices and secondary flow patterns. This increased turbulence leads to a greater mixing of the flow and improvement in the advection of heat away from the channel walls. Typically, rib turbulators are rectangular in cross-section. Many other parameters such as rib aspect ratio, channel blockage ratio, orientation to the flow direction, and rib spacing (pitch) can be varied such that an optimal design is achieved. A great deal of studied has been devoted to the application of these features to internal channel cooling designs.

The earliest studies of transport enhancement by adding ribs to channels walls were performed on single-pass, stationary channels (no rotation). Han et al. (Han, Glicksman, & Rohsenow, 1978) presented the effects of rib orientation, rib shape, and pitch to rib-height ratio on the heat transfer performance of the channel. This study concluded that for the same pumping power, ribs with a forty-five degree orientation the flow yield better results than those oriented perpendicular to flow direction. Han et al. (Han, Park, & Lie, 1984) investigate the effects of channel aspect ratio on the heat transfer characteristics of the channel with angled ribs. It was concluded that the cooling channels perform best with an aspect ratio of one and a rib-orientation angle in the range of 30-45 degrees. It was, in fact, found that the same range of angles is also optimal for rectangular channels, but overall performance is still surpassed by the square channel.

Han et al. (Han, Huang, & Lee, 1993) provided Nusselt number augmentation and friction factor augmentation data for wedge shaped and delta shaped transport promoters in a square channel. The authors compared the performance of broken wedge and delta configurations to the full-length configurations. It was found that the broken arrangements perform better than the full-length case. Taslim et al. (Taslim, Li, & Spring, 1998) studied twelve different rib geometries, with square as well as trapezoidal cross-section, applied to all four walls of a channel. This work characterized the heat transfer and flow characteristics of each geometry. Casarsa et al (Casarsa, M., & Arts, 2002) characterized the hydrodynamic and heat transfer performance of square ribs oriented perpendicular to the flow in a rectangular cooling channel. The ribs studied were

comparatively very large, creating a 30% blockage ratio. Reported results included time-averaged distributions of mean velocity components, and Nusselt number values.

Ligrani and Mahmood (Ligrani & Mahmood) present spatially resolved Nusselt Numbers and Friction Factors for a channel with an aspect ratio of 4 and 45 degree angled ribs. The ribs were arranged such that they were oriented perpendicular to each other on opposite wall. The rib height to Hydraulic diameter was 0.078, rib pitch to height was 10, and blockage ratio is 25%. This work concluded that the highest spatially resolved Nusselt numbers are present on the top surface of the rib with the lowest values being found on the flat surfaces in between the ribs where flow separation and shear layer reattachment have a pronounced effect.

Other studies performed include Wang et al. (Wang, Ireland, Kohler, & Chew, 1998) who studied heat transfer in a square duct with ribs oriented at 45 degree angles. Cho et al (Cho, Lee, & Wu, 2001) investigated a combination of continuous and discrete, parallel and cross arrays of ribs in a single pass square channel.

Pin Fins are typically applied to turbine airfoils where higher levels of heat transfer augmentation are required and the expense of increased pressure loss is not an issue. Pin Fins typically extend between two opposite walls of an internal cooling passage and are most often found in the trailing edge of the turbine blade. They are typically applied to this portion to satisfy two purposes. The high pressure drop across the pin fin array is used to regulate the flow of coolant upstream of the array. This design feature is crucial

as it keeps the pressure high throughout the rest of cooling system, which is desirable for improved heat transfer performance. Also, by the point at which the flow has reached the trailing edge of the blade, the coolant has picked up a substantial amount of heat. It is therefore necessary to apply a transport enhancing feature to this portion of the cooling system that is capable of removing as much heat as possible, even with a small temperature difference.

Van Fossen (Van Fossen, 1982) studied circular pin fins made of different materials placed in a channel of rectangular cross section. Heat transfer coefficients on the pin surface are measured for varying plate-to-flow temperature differences. Results are given as a function of Reynolds number. Researchers also considered the effects of different pin-fin shapes on heat transfer and flow in internal passages including circular pin-fins with endwall fillets (Chyu, 1990), and cross-sections including four-sided diamond, cubic, and elliptical. (Chyu & Natarajan, 1996)(Chyu, Hsing, & Natarajan, 1998)(Hwang & Lu, 2000)(Uzol & Camci, 2001)(Mahmood, Won, & Ligrani, 2002)

Several other studies have been performed that report large heat transfer augmentation of a surface having pin fin arrays compared to flat surfaces with none (Zukauskas, 1972)(Sparrow, Ramsey, & Altemani, 1980)(Metzger & Haley, 1982)(Metzger, Barry, & Bronson, 1982).

## Dimples

Dimples are negative features that are machined into a surface to promote turbulent mixing of the flow by breaking up the formation of the viscous sub-layer along the wall-

surface. This layer acts as a thermally resistive boundary, where the turbulent advection effects are negligible and heat transfer takes place primarily through the modes of conduction and laminar convection. In this layer, the fluid is heated to a temperature very near the temperature of the wall itself. This reduces the temperature difference that is driving the flow of heat from the surface to the fluid and, therefore, hinders the removal of heat from the channel wall.

Dimples are a very attractive method of increasing internal cooling because they trigger the formation of multiple vortex pairs that produce substantial Nusselt number augmentation as they are swept downstream. Figure 1.10 shows the three-dimensional flow structure of the multiple vortex pairs created by the flow over a dimple.

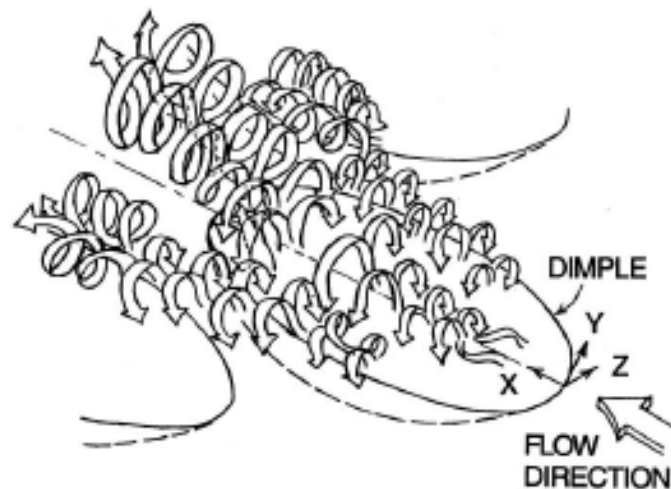


**Figure 1.10: Illustration of Three-Dimensional Flow Structure Caused by a Surface Cavity (Mahmood, Hill, Nelson, Ligrani, Moon, & Glezer, 2001)**

The diagram was created by Mahmood, et al. (Mahmood, Hill, Nelson, Ligrani, Moon, & Glezer, 2001) based on smoke visualization studies performed over a staggered array of dimples on a flat plate through a range of Reynolds numbers between 1250 and 61500.

The diagram shows a primary vortex pair that is located along the longitudinal line of symmetry and advected up into the mainstream flow downstream of the dimple as it is lifted up off the surface by the large upwash region at the trailing edge of the dimple. Using smoke visualization, the authors also observed two additional secondary vortices form periodically on each side of the primary vortex. The formation and ejection of these secondary vortex structures causes a lifting and lowering of the primary vortex pair. This periodic shedding of vortical packets of fluid is an important feature of the flow structure produced by a dimple. As one vortex is shed, there is an inrush of fluid to take its place, followed by another shedding event, and so on. These events take place alternatively on one side or the other in order to satisfy continuity at the surface of the dimple. As a result, using infrared thermography to measure the local Nusselt numbers, it was concluded that these vortex flow structures augment heat transfer from the wall near the downstream rims of the dimple. The authors concluded that this was due to the advection of cooler mainstream fluid down to the channel wall, which was caused by the actions of the vortical fluid ejected from the dimple.

Dimples are particularly desirable because of their characteristically low-pressure drop penalties. This can be partially credited to the fact that they are a negative feature, and therefore, do not produce significant form drag. For this reason, they have proven to be of particular usefulness in low pressure sections of the turbine cooling system. Leinhart et al (Leinhart, Breuer, & Koksoy, 2008) performed a complimentary experimental and numerical investigation of the turbulent flow over a dimpled surface with the objective of determining if dimples, when applied to the walls of a channel, can actually lead to a

reduction in the skin-friction drag. Experimental measurement of boundary layer profiles confirmed by DNS simulations of smooth and dimpled walls (on both accounts) proved that the feasibility of an observed drag reduction is not realistic. However, the observed increase in pressure drop was very small; in fact, within experimental uncertainties. The experimental work of Zhao et al. (Zhao, Chew, & Khoo, 2004) also found that the friction coefficient of a hydraulically smooth channel compared to that of a channel with dimples applied to the surface yielded a difference well within the range of experimental uncertainty. The takeaway: it is possible to achieve appreciable heat transfer augmentation without significant pressure losses encountered by other transport enhancing geometries.

The earliest contribution to the understanding of flow behavior in hemispherical indentation was from strictly an aerodynamics standpoint. Researchers, Snedeker and Donaldson (Snedeker & Donaldson, 1966), from the Aeronautical Research Associates of Princeton performed an experimental study of the flow induced inside a full-hemispherical cavity fastened to the floor of a subsonic wind tunnel. By traversing a tuft through the flow-field, the authors observed a random, but steady vortex ejected from the feature at an angle ‘considerably skewed’ with respect to the direction of the free stream.

Putting this phenomenon to good use, the concept of using dimples to promote heat transfer augmentation was pioneered in the late USSR in the 1980’s. Murzin et al (Murzin, Stoklitskii, & Chebotarev, 1986) performed an experimental study to further characterize the flow behavior caused by the presence of a hemispherical indentation in the

channel wall. The study reports that the flow consists of a steady, recirculating region with the feature itself and a stable, symmetric streamline separation in the mainstream flow. It was also observed that “the pressure gradient due to rotation requires an outflow along the rotation axis and an inflow of liquid toward it in the boundary layer.” This aspect of the flow physics caused by a dimple was observed to be a major contributor to the heat transfer augmentation caused by the feature

Soon after, Gromov et al. (Gromov, Zobnin, Rabinovich, & Sushchik, 1986) contributed results from detailed flow visualizations studies of the flow in a channel over a shallow, hemispherical surface feature. They confirmed Murzin’s observations of stable, symmetric flow and vortex structures for low Reynolds numbers. However, as Reynolds number is increased, the authors report a transition in the flow physics to an unstable solitary vortex structure. This vortex was observed to randomly switch between two stable positions, forming an equal angle on either side of the dimples center axis to the direction of the mainstream flow. The frequency of the switching between the two positions was observed to increase with Reynolds number.

In the work by Afanasyev et al. (Afanasyev, Chudnovsky, Leontiev, & Roganov, 1993), the mechanism of heat transfer enhancement created by flow over a dimpled wall is studied with particular focus on the observed effects on the hydrodynamic and thermal boundary layers. Heat transfer performance was measured to be increased by approximately 30-40% with a negligible increase in pressure loss. The authors attributed this improvement to the combined influence of 1) a reduction in the thickness of the



viscous sublayer and 2) the spherical shape of the cavities. Flow over this shape is known to produce a wall pressure gradient that triggers the formation of the vortex flows that are the primary mechanism of heat transfer enhancement in the region.

Belen'kiy et al. (Belen'kiy, Gotovskiy, Lekakh, Fokin, & Dolgushin, 1993) present improvement in heat transfer from a staggered array of surface indentions applied to a shell-and-tube heat exchanger. Testing was performed through a range of Reynolds numbers between 5000 and 20000 (based on the channel height). Deeper cavities tested showed a maximum increase of 150% while shallow cavities exhibited a maximum improvement of 100%. In some cases, the authors reported that the improvement in heat transfer from the shallow cavities was actually accompanied by a decrease in pressure loss throughout the length of the channel compared to the smooth wall case.

Terekhov et al. (Terekhov, Kalinina, & Mshvidobadze, 1995) provided the first quantitative measurements of dimple flow physics using laser diagnostics. Detailed velocity measurements in the symmetry plane of the dimple are provided along with pressure fields and heat transfer created by a single dimple on a single surface of an internal channel. Results showed that 'auto-oscillations' of the flow arise from the dimpled surface for all of the experimental conditions tested, with a single monovortex structure switching between two positions (as observed in previous studies as well). The authors also performed a frequency analysis of the oscillations, discovering two dominant modes of oscillation exist: a low frequency and a high frequency. The low-frequency mode is reported to only occur for flow in transition and fully-turbulent flows. The high-

frequency mode is always observed. It was also shown that pressure losses increase with increasing cavity depth and increasing Reynolds number. This was concluded to be a result of the changes in flow structure produced by changes in dimple shape.

Kesarev and Kozlov (Kesarav & Kozlov, 1995) studied dimples flows and their local heat transfer coefficients when applied to a flat surface. An interesting analogy was drawn describing the flow streamlines around the cavity; a source and a sink are observed, where the source originate from with the dimple itself and the acting sink is an eddy entraining air from the cavity into the mainstream flow. From their work, the authors concluded that the heat advected from a dimpled surface is higher than that of a flat surface of the same surface area as the 'foot-print' of the applied dimple.

Average heat transfer results measured from a heat plate located directly downstream of a single dimple are reported by Shuckin et al. (Schukin, Kozlov, & Agachev, 1995). This work was unique in that the dimples were applied to a converging nozzle and a diffuser. The author's report the effects of mainstream turbulence intensity and expansion or contraction angle on heat transfer augmentation. It was concluded that heat transfer performance is increased in both applications, regardless of the direction of the pressure gradient. It was also observed that the heat transfer within the concavity itself exhibited stronger dependence on the mainstream turbulence level than the channel walls around the dimple.

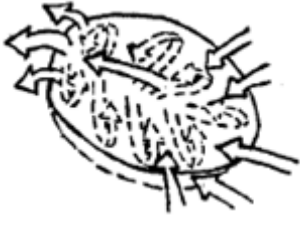
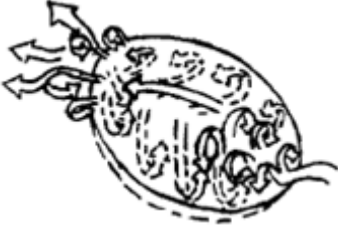
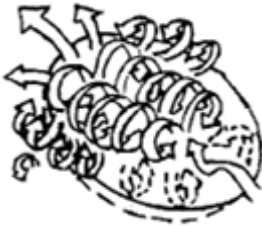
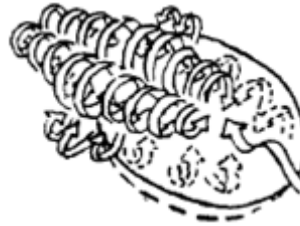
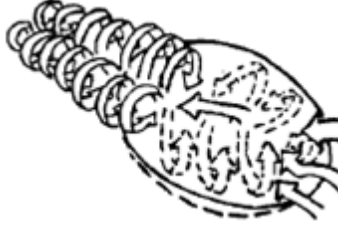

Using a Transient TLC technique, Chyu et al. (Chyu, Yu, Ding, Downs, & Soechting, 1997) studied the overall channel heat transfer enhancement caused by an staggered array of concavities applied to a the channel walls. Two dimple designs were studied: a hemispherical shape and a tear-drop shaped geometry. Channel Aspect ratio was varied from approximately two to twelve and the range of Reynolds numbers tested was from 10000 to 50000. Other key dimple parameters were:  $\delta/d = 0.29$ ,  $H/d = 0.38-2.3$ ,  $P/d = 1.15$ , and  $S/d = 1.15$ . Reported results include profiles of local heat transfer augmentation along with channel averaged heat transfer and friction augmentation. The authors claimed to observe heat transfer augmentation values as high as 2.5 time the values predicted by Dittus-Boelter for a smooth walled channel. This improvement was accompanied by as little as a fifty-percent increase in friction augmentation.

At the 1999 International Gas Turbine Conference and Exposition, Lin et al. (Lin, Shih, & Chyu, 1999) presented their computational work studying the flow structure and resulting heat transfer distributions for hemispherical and tear-drop shaped indentions applied to two opposing wall of an internal channel. The authors divided the computational domain, assuming symmetry along the dimple centerplane, to conserve computational resources. The results showed two vortical structures forming as the flow enters the dimple.

The effects of channel height on the heat transfer and friction characteristics of a dimpled passage were investigated by Moon et al. (Moon, O'Connell, & Glezer, 2000). They studied a range of  $H/d$  ratios from 0.37 to 1.49. It was found that the average heat

transfer enhancement ( $Nu/Nu_0$ ) remained a constant value of approximately 2.1 for the entire range of  $H/d$  ratios.

**Table 1: Dimple Flow Structure Illustrations (Ligrani, Harrison, Mahmood, & Mill, 2001)**

		
<b>0.000 s</b>	<b>0.017 s</b>	<b>0.033 s</b>
		
<b>0.050 s</b>	<b>0.067 s</b>	<b>0.083 s</b>

Mahmood and Ligrani (Mahmood & Ligrani, 2002) studied the influence of  $H/d$ , temperature ratio, and Reynolds number on the flow structure and heat transfer performance of a dimpled channel. Channel aspect ratio was also varied as a consequence of the varying  $H/d$  holding  $W$  constant. The following parameters were held constant:  $\delta/d = 0.2$ ,  $P/d = S/d = 0.81$ .  $H/d$  was varied from 0.2 to 1. Reynolds number (based on channel height because of the nature of the computational domain) was varied between 600 and 11000. Using flow visualization for the lower Reynolds numbers, it was discovered that as the  $H/d$  was decreased the strength of the local vortices increased. This, in turn, results in increased augmentation of local Nusselt number values, which

were measured to be as high as 5.0 in some locations. Using a smoke visualization, Ligrani et al. also studied unsteady formation of flow structure from the same dimple structure (Ligrani, Harrison, Mahmood, & Mill, 2001).

One of the most productive contributors to the science of dimple flows in the last ten years has been the Russian research group from the Civil Aviation Academy in Saint Petersburg, Russia. In their work (Isaev, Leontiev, Kudryatsev, & Pysnyi, 2003), the results of numerical simulations of turbulent convective heat transfer promoted by a single spherical dimple on a smooth wall are presented. By varying the dimple depth, the authors found, by increasing dimple depth, there is a transition point in the structure of the flow where the structure departs from the stable, symmetric formations observed by other researchers, to an unsteady, sweeping monovortex. This transition was computed to result in significant intensification of the heat transfer within the dimple itself as well as in the channel wake behind the feature: approximately sixty and forty-five percent respectively.

With specific application to the cooling of turbines and other rotating machinery, Griffith et al. (Griffith, Al Hadhrami, & Han, 2003) studied the effects of rotation on a 4:1 aspect ratio channel with dimples applied to the two large walls. Testing was performed at Reynolds number between 5000 and 40000 with rotation numbers varying from 0.04 to 0.3. The staggered array of 131 dimples was maintained with equal streamwise and spanwise pitch with a  $\delta/d = 0.2$ . The channel was tested at two orientations to the plane of rotation:  $\beta = 90^\circ$  and  $135^\circ$ . It was concluded that, compared to the stationary case, a  $\beta$

$= 90^\circ$  produces nearly 100% increase in heat transfer from the trailing edge at the highest rotation number. This increase is accompanied by a similar increase in heat transfer on the outer dimpled surfaces. At a  $\beta = 135^\circ$ , the high rotation number increased heat transfer from the trailing edge by more than 120% with lowest augmentation of any wall being greater than 50%.

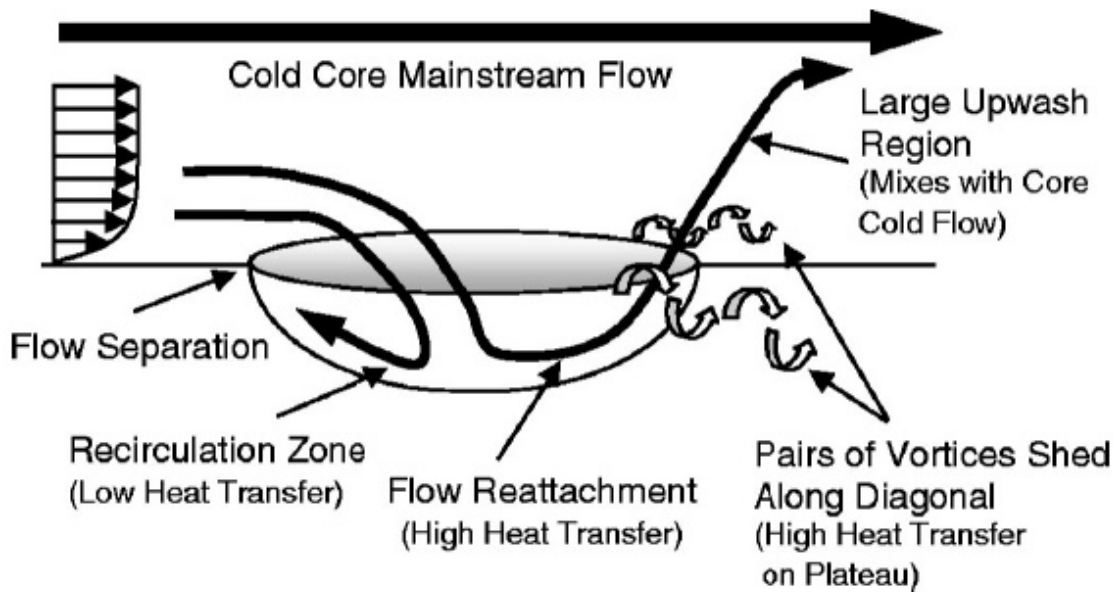


**Figure 1.11: Flow Structure inside a Dimple (Griffith, Al Hadhrami, & Han, 2003)**

A numerical study of the flow structures and heat transfer performance of a dimpled channel was performed by Patrick for his M.S. work at Virginia Tech (Patrick, 2005). Using the Virginia Tech HPCFD Direct Numerical Simulation code, Patrick studied a dimple feature with the following parameters:  $\delta/d = 0.2$ ,  $H/d = 0.5$ ,  $P/d = S/d = 0.81$ . Reynolds number (based on channel height because of the nature of the computational domain) was varied between 25 and 2000. The author reports that flow transition occurs between Reynolds numbers 1020 and 1130. Nusselt number augmentation is seen to be as high as 3.22 accompanied by a friction factor increase of 150 percent. It is also observed that, in this study, the presence of the vertical structures generated by the

dimples dominates the flow through the channel; augmenting not only the flow of heat from the featured surface, to the smooth walls as well.

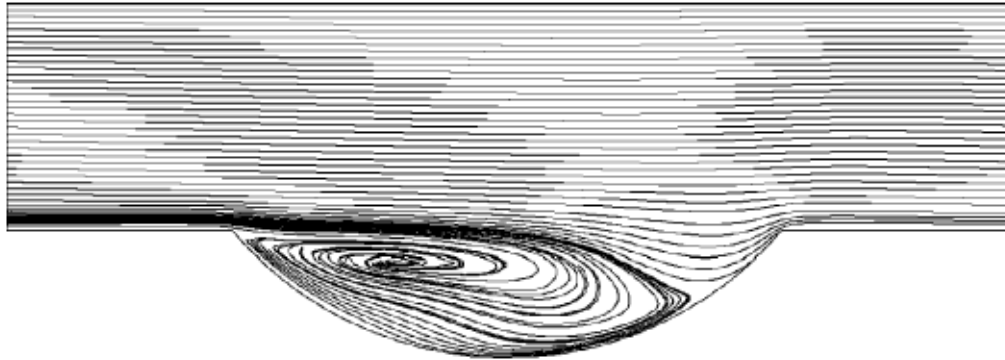


**Figure 1.12: Recirculation of Flow Due to Dimple Geometry (Kim & Choi, 2005)**

The heat transfer and pressure drop characteristics of dimples and protrusions patterned along the walls of a straight, 7:1 aspect ratio rectangular channel were investigated by Hwang et al. (Hwang, Kwon, & Cho, 2008). The characteristic values of the feature were as follows:  $\delta/d = 0.288$ ,  $H/d = 1.15$ ,  $P/d = S/d = 0.81$ . Parameters varied were the channel Reynolds number (from 1000 to 10000), and the number of dimpled walls. Using a Transient TLC technique, it was determined that the overall heat transfer coefficient is higher when dimples are applied to two walls versus just one with enhancement values as high as fourteen times that of a smooth duct. These results were found to be accompanied by as much as a 300% increase in the channel friction factor.

Among the most recent contributions on this topic is the study released by the Russian research group led by Isaev (Isaev, Kornev, Leontiev, & Hassel, 2010). In this work, a numerical investigation is performed on the nature of turbulent flow generated/augmented by a single dimple present in a narrow channel. In this case, the

term ‘narrow’ is referring to the height ( $h$ ) of the channel: i.e. the distance from the wall on which the dimple is applied to the opposite, parallel wall ( $h/d = 0.66$ ). The observed effects of varying dimple depth and Reynolds number is reported via surface heat transfer coefficient profiles and a detailed look at local flow phenomena causing the observed behavior. Dimple depth is studied at two values:  $\delta/d = 0.13$  and  $0.26$ . Reynolds number is varied from 20000 to 60000. Results were observed to match well with previous LES studies performed by the same group on the same geometry. Velocity profiles from both models were validated by experimental results using an LDV measurement technique. Nusselt number augmentation (based on smooth wall) is broken into three sections. First, inside the dimple itself: 1.06 and 1.09 for  $\delta/d = 0.13$  and  $0.26$ , respectively, invariant with Reynolds number. In the square region immediately surrounding the circular dimple footprint: 1.05 to 1.08, again, showing very little change with respect to either factor. In the region downstream of the dimples trailing edge: a range of 1.07 to 1.14 with the deeper dimple outperforming the more shallow design. Also, in this region, Nusselt number augmentation observed to be slightly higher for the lowest Reynolds number studied, with no observed difference in the computed solution for the higher values.

## Overview of the Present Work

### Motivation and Objectives

The overall goal of this research is to make a valuable contribution to the understanding and application of dimples to promote turbulent convective heat transfer in internal channels. Unlike more aggressive turbulence-promoting features, dimple flows generate their effect almost entirely by promotion of unsteadiness in the flow. Their effective



promotion of heat transfer caused by a dimple originates from the nature of the reaction of the flow to the presence of the feature – no fin effects, no protrusions, etc. It is this key fact that makes these features so interesting.

The shedding of multiple vortex pairs from dimples arrays increases turbulence within the flow improves turbulent mixing of the fluid within the channel. This phenomena can lead to drastic improvements in heat transfer performance by reestablishing a larger temperature gradient between the flow and the channel wall. Creation of strong secondary fluid motions within these vortical packets of fluid promotes this effect by advecting the warmer fluid from the boundary layers up into the faster-moving mainstream flow and replacing it with colder fluid that has not yet felt the effect of the wall. Two additional secondary vortices form periodically on each side of the primary vortex. The formation and ejection of these secondary vortex structures causes a lifting and lowering of the primary vortex pair. This periodic shedding of turbulent flow eddies is an important feature of the flow structure produced by a dimple. As one vortex is shed, there is an inrush of fluid to take its place, followed by another shedding event, and so on. These events take place alternatively on one side or the other in order to satisfy continuity at the surface of the dimple.

Flow reattachment inside the dimple can also cause a similar effect, where the boundary layer is very thin in the region where the fluid impinges onto the wall. Lastly, the unsteady nature of the vortex generation and ejection from the indentation causes a periodic dissipation and reformation of the thermal boundary layer downstream of the

dimple over the affected area. This unsteadiness is the key phenomena of the dimple feature as it allows with significant improvement in heat removed from the wall. These effects have been proven to produce appreciably increased performance in channel heat transfer coefficient.

Another key aspect of the channel flow physics is that, as opposed to many ‘academic’ studies, in a real applications more than one dimple is applied to the heat transfer surface, in which case, there will be many more vortex interactions taking place. For example, if the dimples are closely spaced in the lateral direction, the secondary vortex formations could interact with each other from both dimples. It is also possible to have interactions of the primary vortices in the longitudinal direction for consecutive rows of dimples.

In their work, ‘A Comparison of Heat Transfer Augmentation Techniques,’ (Ligrani, Oliveira, & Blaskovich, 2003) Ligrani et al. present a comprehensive survey of dimple literature. Figure 1.13 is a comparison of the heat transfer and friction augmentation results observed in the applicable papers from the aforementioned review; many of which were given in the detailed review of the preceding section. After careful review of this and the works presented in the previous section of this work, it is immediately apparent that there is still room for significant improvement on the understanding of dimple-induced flow dynamics and the subsequent heat transfer augmentation. There is an unacceptably large spread in the results observed from different researchers studying, what are essentially, the same geometry.

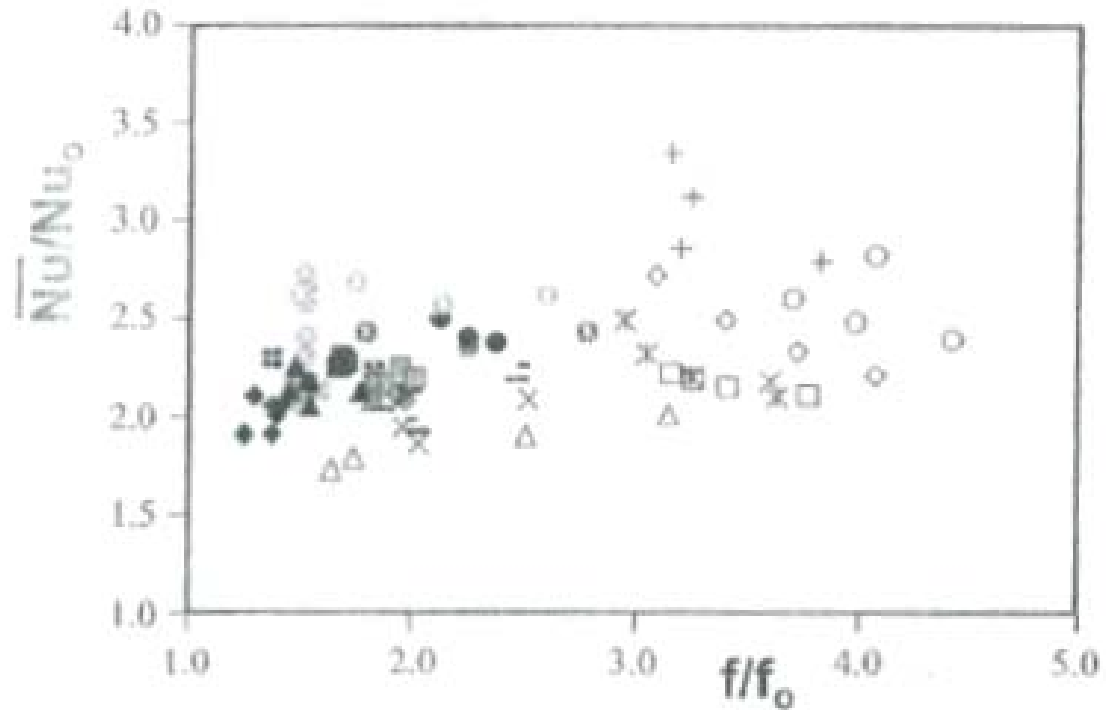


**Figure 1.13: Summary of Dimple Feature Contributions (Ligrani, Oliveira, & Blaskovich, 2003)**

The theory and motivation behind this work is that the physics governing the behavior of flows over a dimple are some complex that it is extremely difficult to obtain repeatable results from one study to the next. By nature, the performance of dimples is highly dependent on a slew of external factors that govern the physics behind their observed behavior, such as mainstream turbulence levels, proximity to channel walls, upstream boundary layer profiles, developing length, etc. Adding in the transition from steady symmetric vortex generation to the unsteady, oscillating monovortex structure observed by first by Terekhov et al. (Terekhov, Kalinina, & Mshvidobadze, 1995) and the need for more detailed characterization of this feature is immediately apparent.

This study is intended to meet three objectives. The first – to understand dimple flow physics on a first-principles level when applied in a staggered array to a single wall of a

2:1 aspect ratio rectangular channel. The primary end of this work is to understand the actual phenomena leading to the observed heat transfer augmentation that makes these features so attractive. Second – to design, analyze, develop, validate, and employ a new method of experimentally determining local surface heat transfer coefficients. At the start of this project, there existed no suitable means to perform the experiments required for this study, within the UCF-CATER lab. In response, a total design process is completed to develop an accurate experimental rig for the collection of local heat transfer data using the transient liquid crystal technique. Third and last – this study will provide a full characterization of a completely novel turbulator concept, the double dimple feature, employing a combination of experimental and numerical techniques to understand the performance of this feature and the underlying flow physics producing the observed phenomena.

### Details and Outline of the Study

The research performed in this study has direct implications to the knowledge and understanding of the fields of heat transfer and fluid mechanics as they apply to the gas turbine industry. By adding to this knowledge base, the results of this project will shed light to a more effective cooling design to satisfy the needs of this demanding industry where thermal performance is the goal of any design. However, this study is also intended to be a contribution to the scientific community, as well, not the simple generation of an industrial dataset. Focus will be given to an understanding of the physics behind the recorded results. For this reason, experimental cases will be run in parallel with a numerical solution to gain a clearer understanding of the full-field profile

of the flow physics throughout the entire design. This work will add further clarity to the local surface measurements obtained from the experiments performed.

Specifically, this study is an investigation of the heat transfer augmentation through the fully-developed portion of a narrow rectangular duct ( $AR=2$ ) characterized by the application of dimples to the bottom wall of the channel. Experimental testing and numerical modeling is performed for full support and validation of presented findings. The geometries are studied at channel Reynolds numbers of 20000, 30000, and 40000. The purpose is to understand the contribution of dimple geometries in the formation of flow structures that improve the advection of heat from the channel walls.

Three dimple cases were chosen. As mentioned earlier in this section, this work is aiming to accomplish two major contributions to dimple literature: 1) full characterization of two dimple geometries under the unique testing conditions in our study and 2) complete development and initial analysis of a novel double-dimple feature. The details of these three features were chosen based on combined influences including published data in the open literature and industry input from related projects.

Table 2 illustrates the final designs being tested. The first dimple shape is the largest of the three. The second augmentation geometry is very similar to the first geometry in that the axial and lateral spacing of the individual dimples is maintained. The key difference in this case is that the difference in the radius of the dimple itself. In this case, not only is the circular ‘foot-print’ of the dimple on the channel surface decreased, but the depth of

the dimple itself is reduced as well. The final geometry is a pair of two small dimples manufactured such that there is a ridge separating the two entities at the bottom of the pit. The radius is maintained from the second geometry as well as the lateral and axial spacing of the dimple pairs.

**Table 2: Three Tested Cases**

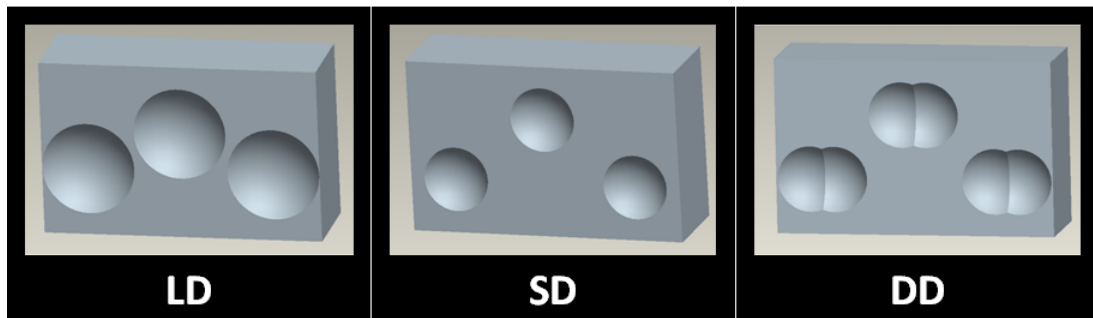
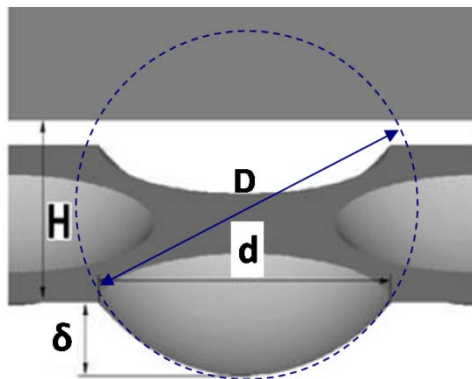


Table 3 gives the details of each design and Figure 1.14 offers clarification of the dimple nomenclature used to characterize the geometry.



**Figure 1.14: Illustration of Dimple Nomenclature**

**Table 3: Test Matrix**

DESIGNATION	DIMPLE CLASSIFICATION	DIMPLE PARAMETERS				
		R/Dh	H/d	$\delta/d$	P/d	S/d
LD	Single	0.533	0.946	0.236	0.775	1.001
SD	Single	0.358	1.333	0.250	1.000	1.411
DD	Double	0.358	1.010	0.189	0.758	1.069

1) Each geometry is studied at three flow-rates with channel Reynolds numbers ranging from 20,000 to 40,000.  
**NOTE:** All Reynolds numbers based on the hydraulic diameter of the channel. Area and Perimeter calculated at the non-featured portion of the channel.  
*\* All other channel parameters (AR, W, L, H, etc.) are held constant for ALL cases tested*  
*\*\*Streamwise Dimple Pitch is held constant for all cases*

With multiple interdependent objectives, the process of completing this study significant planning and multiple parallel efforts to be completed in a two semester timeframe.

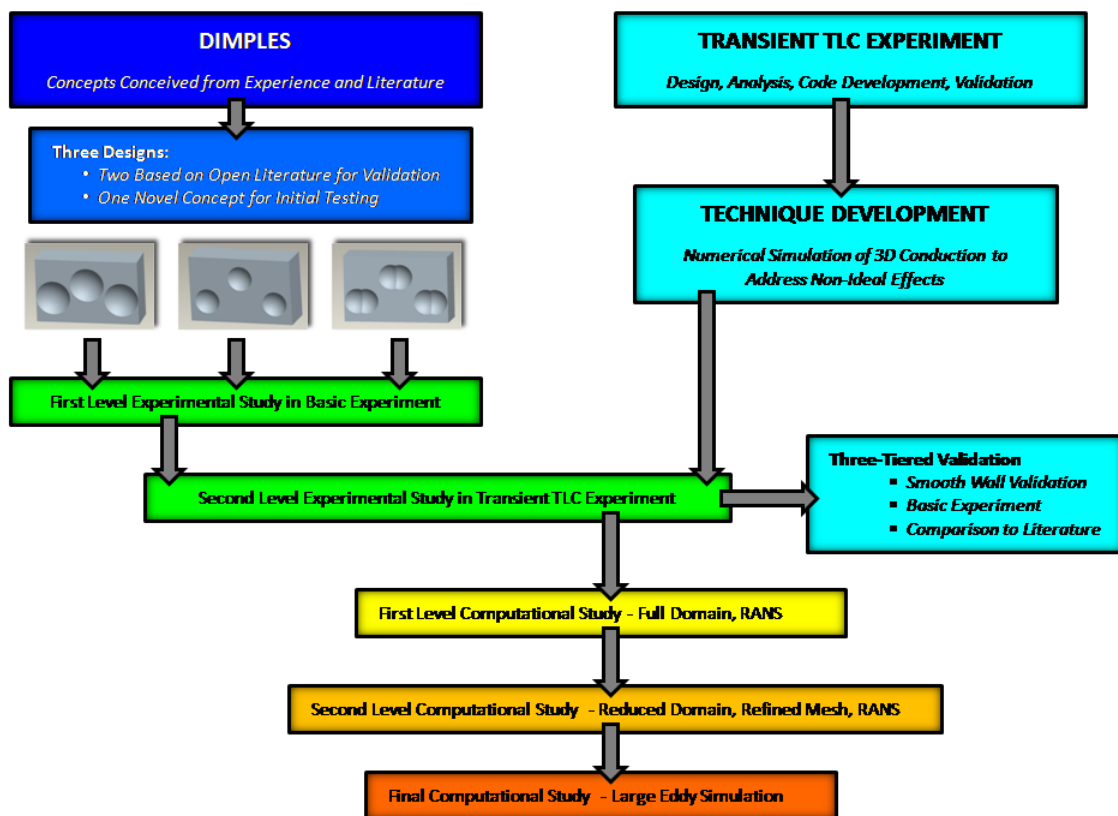
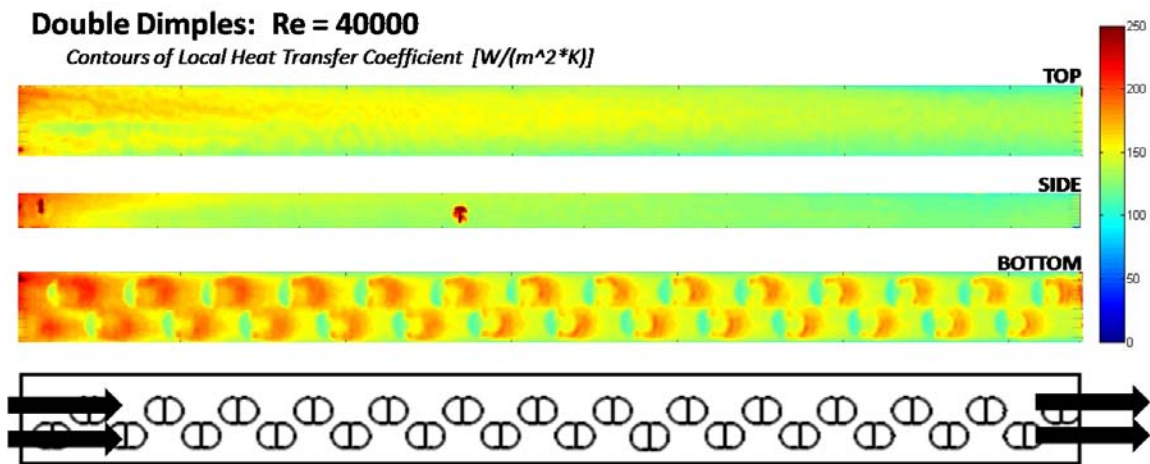


Figure 1.15: Project Flow Diagram

Figure 1.15 is a schematic representation of the tasks completed through this work. To meet the three objectives outlined in the previous section, a unanimous parallel effort was

required right from the start. Design development of the new experiment was started immediately, with a full design analysis performed, uncertainty analysis, and code development well underway as initial testing was being performed on the copper block rig for the three geometries. As part of the development of the transient experiment, a numerical model of the conduction through the channel walls was developed to address the known weaknesses of the technique that have previously been overlooked by other researchers (this falls under the technique development box in Figure 1.15).

After initial testing of the three dimple geometries was completed and the transient experiment had passed the initial smooth wall validation, the dimple geometries were tested in the new rig. After further debugging of the data reduction codes and application of the newly developed technique corrections, the results from the two experiments were found to be within acceptable agreement of each other (see CHAPTER 6:).



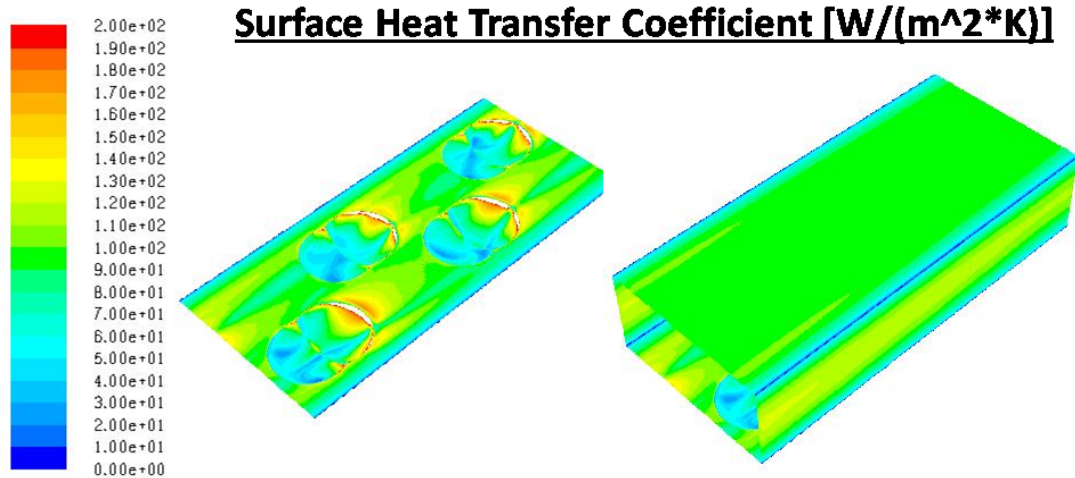
**Figure 1.16: Example of Local Heat Transfer Coefficient Data from Transient TLC Experiment**

Figure 1.16 is a sample of the local surface heat transfer coefficient data that is attainable with the new experiment.



As discussed further in CHAPTER 4:, an interesting phenomena that was discovered was the performance of the double-dimple feature. In both experiments, it was found to promote increased higher heat transfer from the surface with a very low cost in pressure drop. The details of this phenomena is to be discussed in the upcoming sections of this document. However, it was this result that prompted that author to pursue a numerical simulation of the flow over this feature for further validation and understanding of this result.

Initial computational modeling consisted of the entire experimental test section to gain broad understanding of the aerodynamics within the channel. This model served to provide a baseline understanding of the boundary conditions for further, refined modeling. The second-level of computational modeling included a reduced domain, with a periodic inlet and exit condition and a body-force term to simulate the linear pressure drop through the fully-developed portion of the channel. The steady RANS solver was used with the SST turbulence model. Further details on the setup and results will be provided in CHAPTER 3: of this document. Figure 1.17 shows an example of the contours of surface heat transfer coefficient obtained from the solution. The surface-averaged results of this solution were also found to be within acceptable agreement with both previous experiments with some explainable differences



**Figure 1.17: Three-Dimensional Local Contours of Heat Transfer of Heat Transfer Coefficient from RANS Numerical Solution**

After successful validation of the previous numerical simulations and the reduced domain model, a further refined mesh was solved using the unsteady Large Eddy Simulation turbulence model. These results of this simulation provide a highly detailed look into the flow structures caused by a dimple surface feature and provide a clear understanding of the effects that have on surface heat transfer.

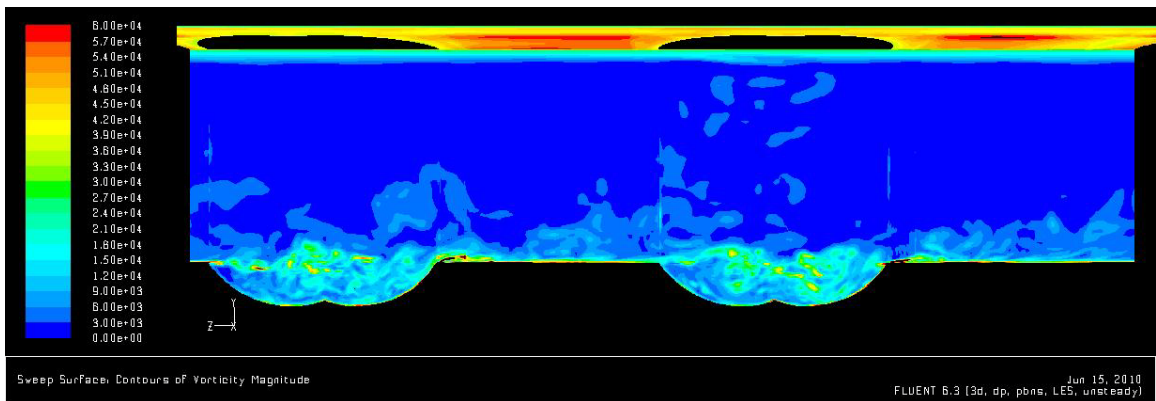


**Figure 1.18: Vorticity Contours Showing Streamwise Variation in the Flow at One Instant in Time.**

By following the outline given in Figure 1.15, this study was able to meet all three of its objectives.

## **CHAPTER 2: OVERVIEW OF EXPERIMENTAL STUDY**

### Test Setup for Average Data

#### Background

Inherent in the nature of scientific research is the fact that, in a majority of cases, the results obtained are the first of their kind, novel, and new. For this reason, it is necessary for the researcher to perform similar studies of reduced complexity in an effort to provide support to the more elaborate efforts of the work. Validation is the key to gaining a thorough understanding of complex physical phenomena that could be too difficult, in and of themselves, to explain from a first-principles level. Whether the means of study is theoretical, computational, or experimental, these simplified studies provide the stepping-stones to gaining further insight into new physics.

With these ideas in mind, this section describes the design, development, and initial testing of an experimental setup that is used to gain a ‘10,000 foot view’ of the tested geometries performance. This rig is used to provide the foundation of understanding on which all other subsequent observation and conclusions are built.

#### Methods and Concepts

The first set of experiments is run on a basic setup to provide regionally-averaged heat transfer coefficient data for all four channel walls over the length of the channel. Employing one of the fundamental principles of convection heat transfer, the experiment is based on Newton’s Law of cooling.

$$q'' = h * (T_h - T_c) \tag{5}$$

The experiment is designed such that a known supply of heat is generated and transferred to the flow through the channel. By measuring the wall temperature and calculating a known flow temperature, the surface heat transfer coefficient can be easily deduced. While more extensive calculations are brought into use for more accurate interpretation of the data, it is this basic principle on which the experimental method is based.

### Design Details

The fluid used in all tests is air, supplied from an external compressor and dehumidified by an inline condenser and reheater. The flow rate of the air is regulated by the inline pressure regulator. The flow-rate is measured by the inline venturi flow-meter.

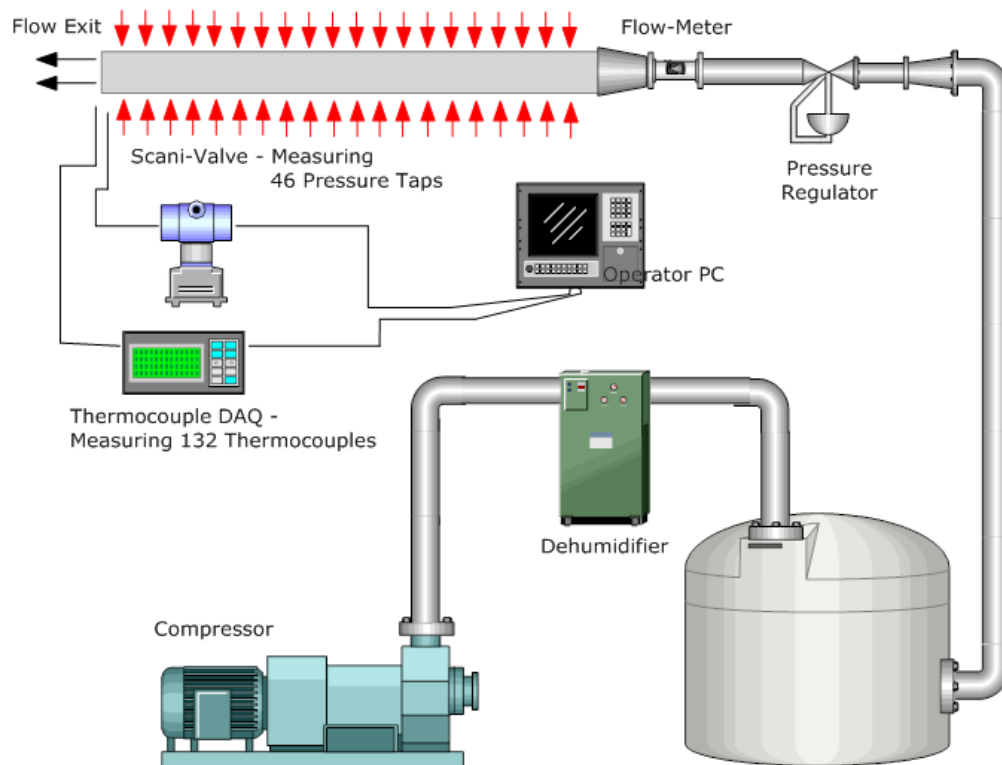


**Figure 2.1: Schematic of Experimental Apparatus**

The temperature of the inlet air is monitored with multiple thermocouples located at the entrance of the duct (for redundancy). In order to identify the fully developed region and to isolate the entrance and exit effects, the duct wall is longitudinally divided into a number of identical modules each with a length of approximately two and one-half hydraulic diameters. Each test module contains four pieces of copper that form the walls of the internal channel.

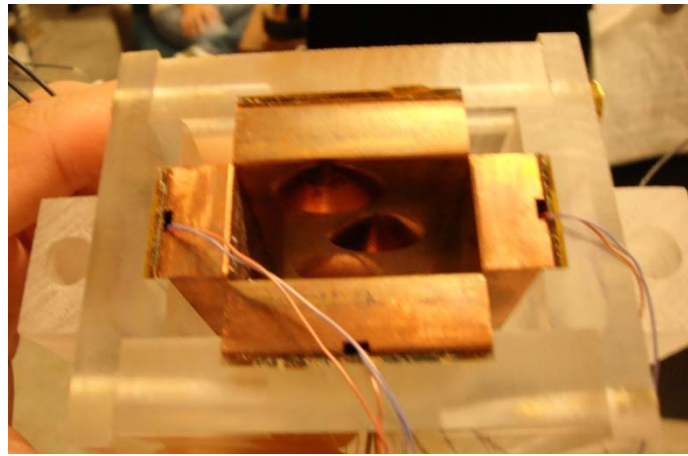


**Figure 2.2: Photo of a Single Module with a Feature Case Installed**

Copper was chosen as the wall material because of its favorable thermal properties. The high thermal conductivity results in a low calculated Biot number (assuming a value of  $h$  from the lowest Reynolds number calculated using the Dittus-Boelter correlation).

$$Bi = \frac{h * L}{k} \quad (6)$$

With  $Bi \ll 1$ , it can be assumed that the temperature profile throughout the thickness of the block can be considered flat. This criteria must be met in order to assume that the temperature of the Copper block measured by the thermocouple is representative of the wall temperature driving the heat transfer.

Two type-T thermocouples are assembled into machined holes in the back of each copper block using high thermal conductivity paste. Data is collected by a Measurement Computing© data acquisition system (Figure 2.3) over a period of period of time. Recorded values are then averaged to reduce the contribution to the experimental uncertainty by precision error.

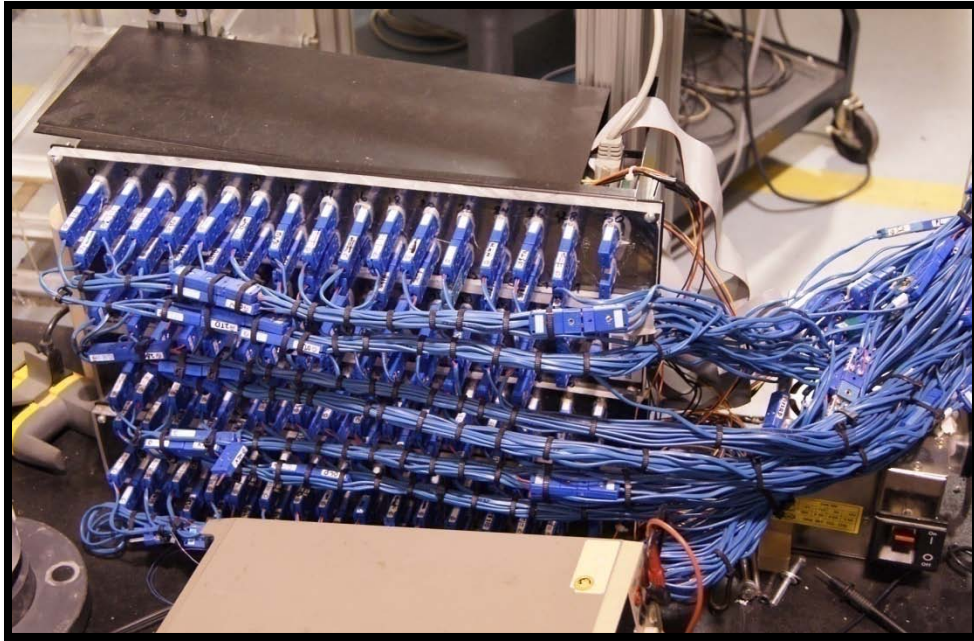


**Figure 2.3: Photo of Data Acquisition System**

Heat is supplied to the flow by an array of foil heaters that are bonded to the back of the copper blocks with high thermal conductivity, double-sided Kapton™ tape. The heaters are manufactured to cover the surface of the copper block exactly. Power is supplied to the heaters by an 1800 Watt DC power source. Additionally, the top bottom, and side heaters are each controlled by an array of rheostats such that the power to each surface of each heater can be adjusted individually to achieve constant heat flux throughout the

length of the channel. Figure 2.4 is a schematic of this system and Figure 2.5 gives an actual picture of the setup.

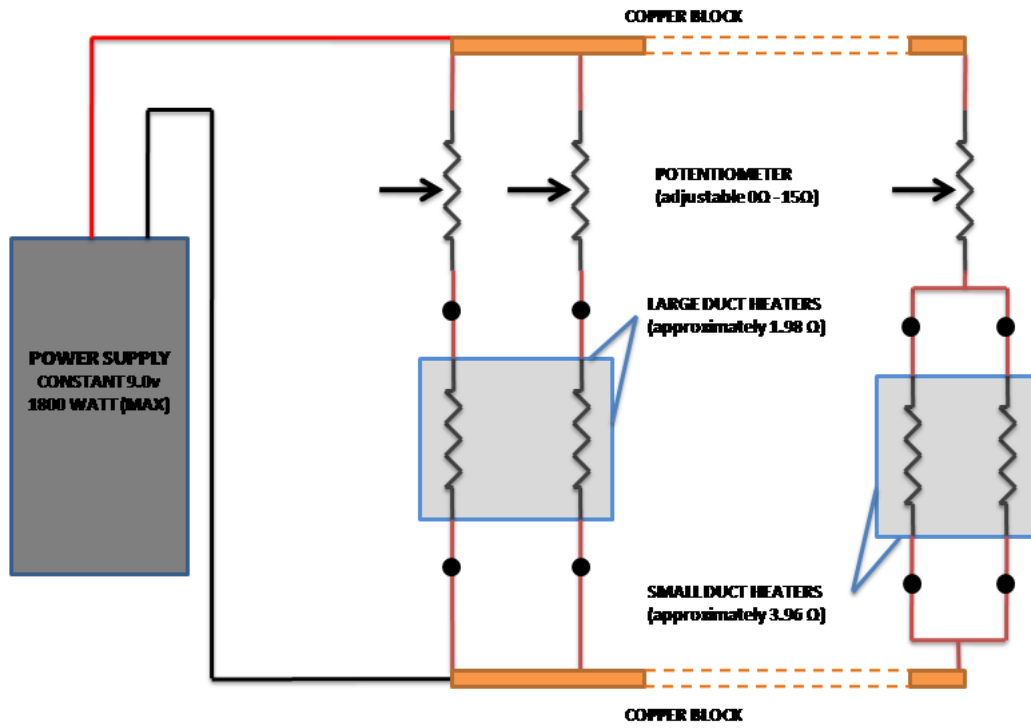


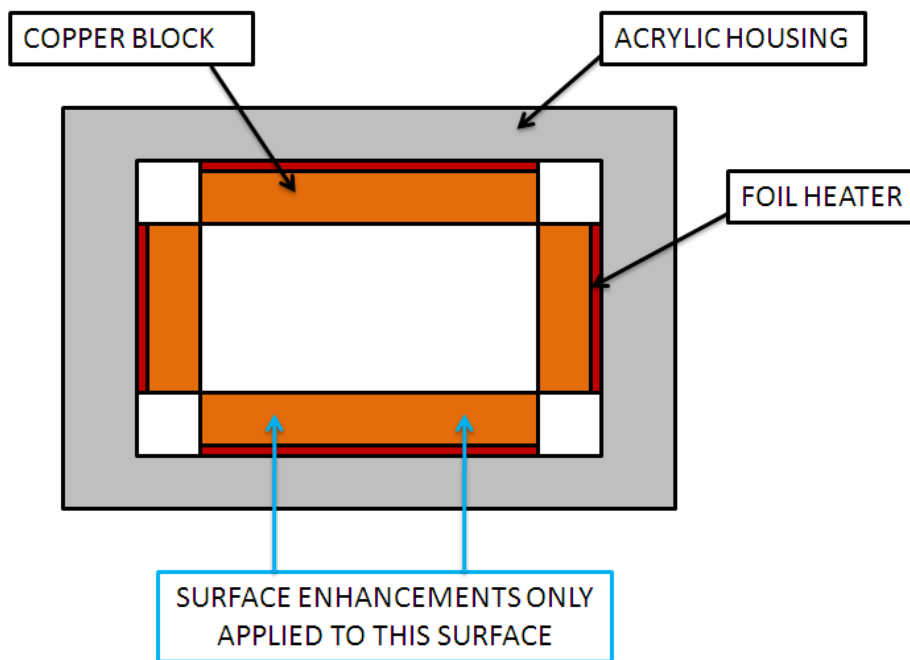
Figure 2.4: Schematic of Heat Supply System



Figure 2.5: Photo of Heat Supply System



It is also important to note that the copper blocks are assembled into and acrylic housing and insulated to minimize heat leakage as shown in Figure 2.6.



**Figure 2.6: Schematic of Module Design**

The acrylic is shaped in a way as to provide interconnectivity between modules so that it is easy to keep the shape of the channel under any testing condition. The acrylic is also meant to provide a structure that will allow the copper to form a channel, but without directly linking the copper pieces. This, in effect disrupts any lateral conduction between copper pieces. Alignment of the channel is guaranteed during the assembly process by inserting a long aluminum alignment bar into the channel being assembled. The assembled channel is shown in Figure 2.7



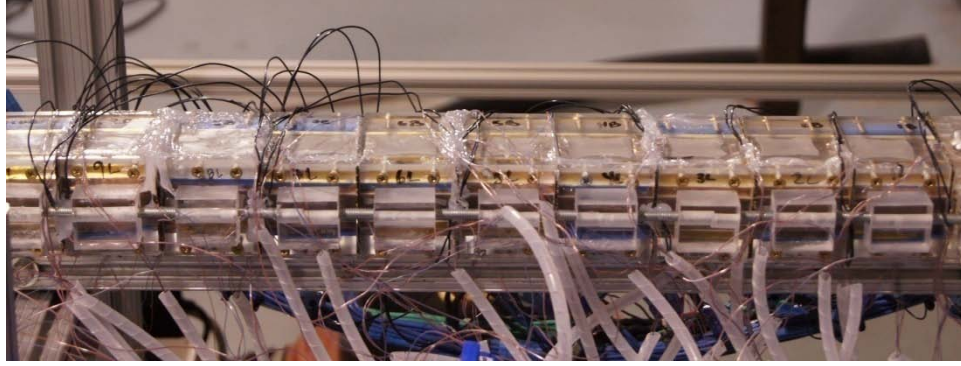


**Figure 2.7: Assembled Modular Channel**

### Data Reduction

Detailed analysis of the pressure drop through the channel is a key component of the performance of transport-enhancing feature. Initial smooth wall validation is compared to the Blasius correlation (7) for a smooth round pipe – using the hydraulic diameter of the rectangular duct as the characteristic length for the Reynolds number calculation.

$$f_0 = 0.316 * Re^{-\frac{1}{4}} \quad (7)$$

The experimental pressure drop, hydraulic diameter, mass flow rate, and local density are used to calculate the experimental friction factor using (8).

$$f = \frac{\frac{dP}{dl} * D_h}{0.5 * \rho * v^2} \quad (8)$$

$\frac{dP}{dl}$  is measured across the fully developed portion of the channel. This criterion is known to be met by examining the pressure profile data collected from the array of pressure taps placed along the stream-wise direction on the vertical center-plane of the channel side walls.

To determine the average Nusselt number of the channel first the power generated by the foil heaters was found knowing that

$$Q_{input} = \frac{V^2}{R} \quad (9)$$

where V is measured for each test and adjusted such that a constant wall temperature is maintained circumferentially in each module as well as throughout the streamwise length of the channel. The resistance of each heater is known, as a function of temperature, and is therefore calculated for each wall of each module for each test as well.

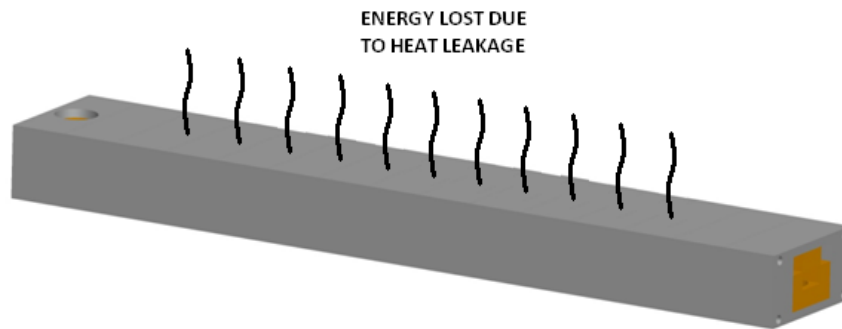


**Figure 2.8: Illustration of Ambient Heat Loss**

The heat leakage from each wall of each heating module is also known as a function of the temperature difference between the ambient air and the copper wall. It is also calculated for each wall of each module for each test. Lateral conduction is also accounted for by assuming that the flow of heat from one module to the next is well approximated using the one-dimensional heat conduction model with a known value of the thermal conductivity of the module to module insulation and the measured wall temperature between contiguous walls of contiguous modules, an energy balance is used to determine the net heat addition contributed or lost to the adjacent modules. Thus, the final equation for heat added to the channel is established by subtracting the ambient heat

loss from the total heat generated, then accounting for the lateral conduction through the channel walls from module to module.

After applying all of the aforementioned corrections, it is then known that the power actually added to the flow is the sum of the total heat generated minus the heat lost plus the balance had the lateral heat conduction through each wall (Equation (10)).

$$Q_{actual} = Q_{input} - Q_{loss} + Q_{lateral} \quad (10)$$

It is important to note that, due to the very low Biot number of the copper blocks forming the channel walls of each module, the channel wall temperature-profile is assumed to a step function, where the temperature of each wall of each module is the average of the measured values taken by the two thermocouples. This assumption is verified by the fact that the temperatures measured by the two thermocouples are invariably within 1.5°C of each other, which is within the  $\pm 1^\circ\text{C}$  range of accuracy for the thermocouples being used. It is therefore assumed that the wall temperature of each wall of each module is the temperature at the center-point of that surface.

In order to quantify the temperature difference driving the heat transfer from the wall to the fluid, the local flow temperature must be calculated. Starting from the temperature of the flow, measured by a thermocouple at the channel entrance, the temperature of the bulk flow is calculated throughout the entire length of the channel knowing the power added, the channel mass flow rate and the local fluid properties.

$$T_{bulk_i} = T_{bulk_{i-1}} + \frac{Q_{added_i}}{\dot{m} * c_p} \quad (11)$$

Due to the location of the thermocouples, this power calculation must be modified slightly in order to correctly find the amount of power added before the point in the stream-wise direction where the temperature different is assumed to be known. This value is found to be the sum of the heat transferred to the flow from the second half of the preceding copper block and the first half of the down-stream copper block where the specific thermocouple is located.

$$Q_{added_i} = 0.5 * Q_{actual_{i-1}} + 0.5 * Q_{actual_i} \quad (12)$$

Applied to the individual walls of each module:

$$Q_{added_i} = 0.5 * (Q_{top_{i-1}} + Q_{bottom_{i-1}} + Q_{left_{i-1}} + Q_{right_{i-1}}) + 0.5 * (Q_{top_i} + Q_{bottom_i} + Q_{left_i} + Q_{right_i}) \quad (13)$$

Bulk temperature change throughout the channel was maintained at approximately 20°C and local variation of fluid properties was taken into account. In order to minimize experimental uncertainty, the temperature different between the wall and the fluid was maintained at approximately 50°C.

Knowing the bulk temperature throughout the flow and the exact value of the power added to the flow at each point of temperature measurement, the heat transfer coefficient can be calculated for each individual wall of each module throughout the length of the channel. The experimental results for Nusselt number are compared to values calculated from two correlations for turbulent internal flow in a round pipe:

the Dittus-Boelter correlation

$$Nu_0 = 0.023 * Re^{0.8} * Pr^{0.4} \quad (14)$$

and the Gnielenski correlation.

$$Nu_0 = 0.0214 * (Re^{0.8} - 100) * Pr^{0.4} \quad (15)$$

The results from the smooth wall testing are compared to both correlations for the purpose of validation. From that point forward, the most appropriate value is selected for calculation of Nusselt number augmentation provided by the feature.

### Experimental Uncertainty

The experimental uncertainty in the reported values was calculated using the second-power equation for the estimation of uncertainty given in Kline and McClintock (Kline & McClintock, 1953).

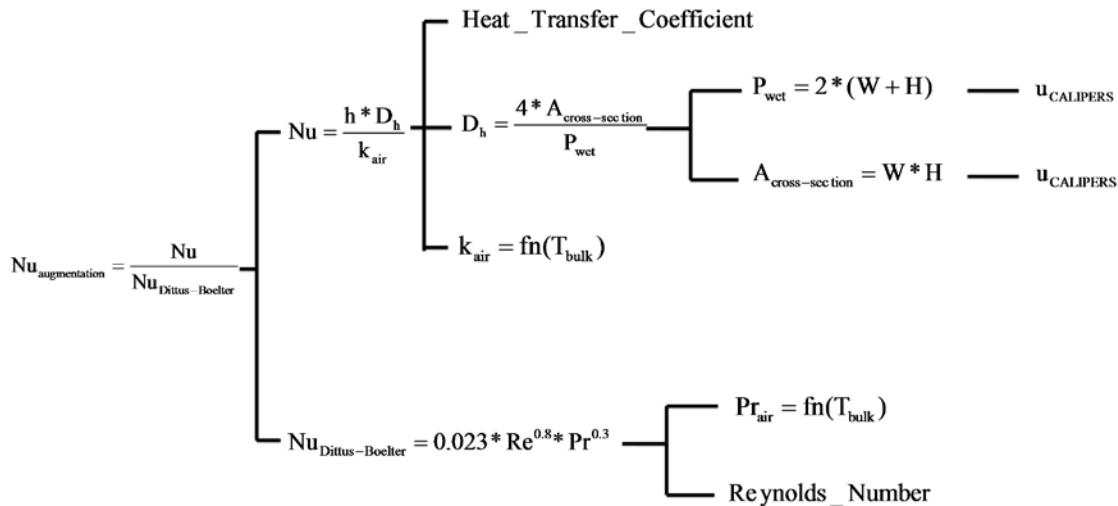


Figure 2.9: Uncertainty Trees for Basic Experiment – Nusselt Number Augmentation

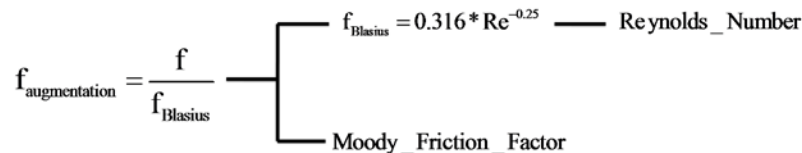


Figure 2.10: Uncertainty Trees for Basic Experiment – Friction Factor Augmentation

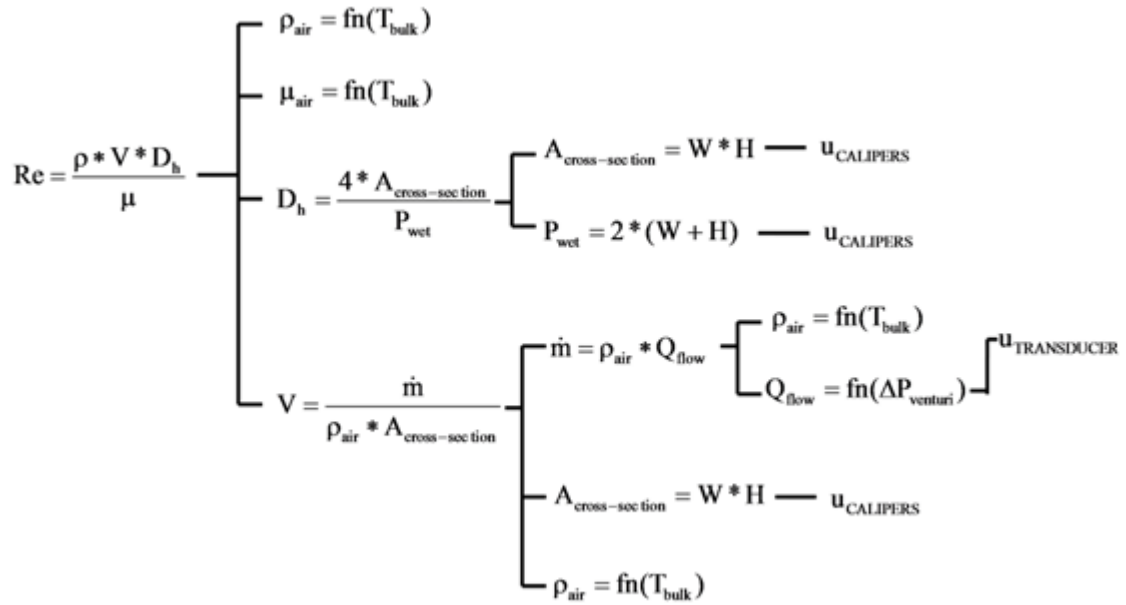


Figure 2.11: Uncertainty Trees for Basic Experiment – Reynolds Number

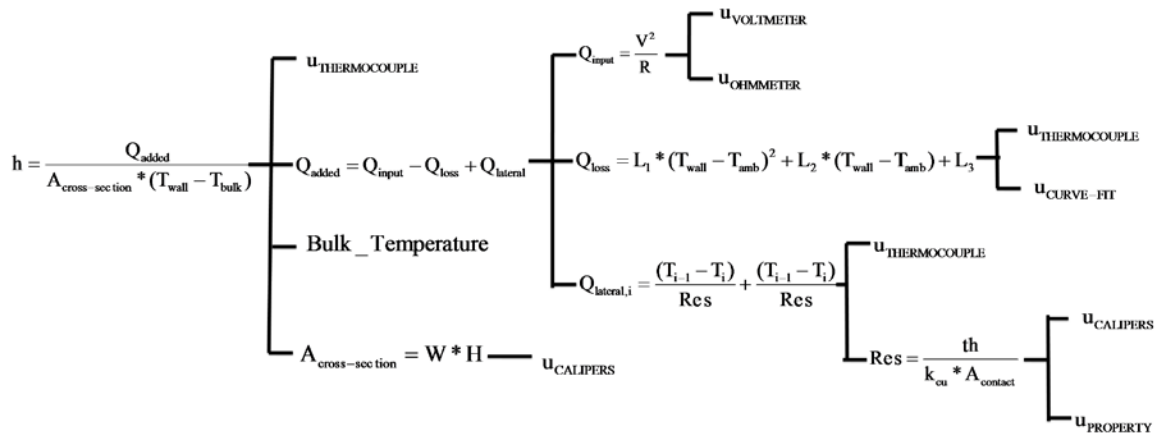


Figure 2.12: Uncertainty Trees for Basic Experiment – Heat Transfer Coefficient

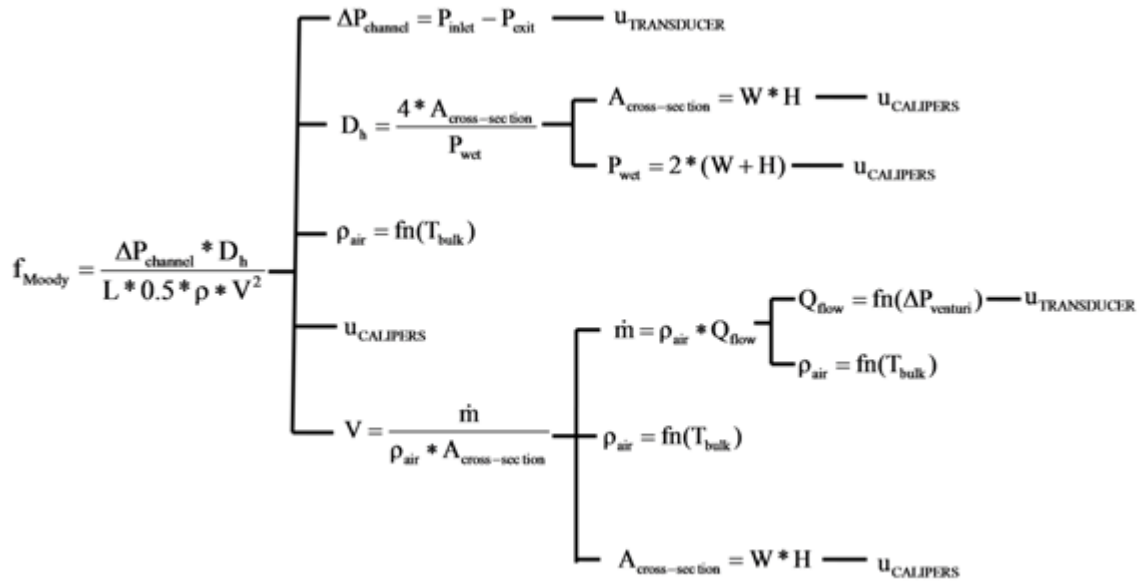


Figure 2.13: Uncertainty Trees for Basic Experiment – Friction Factor

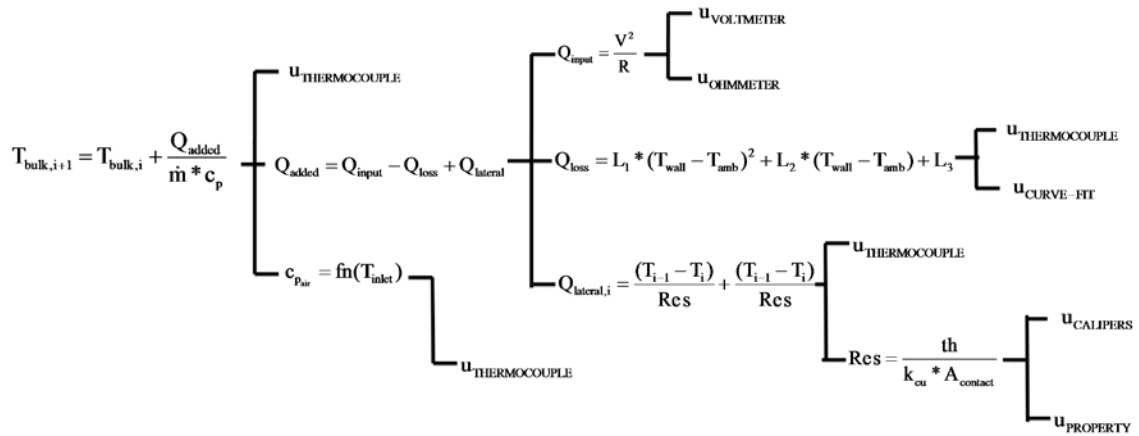


Figure 2.14: Uncertainty Trees for Basic Experiment – Bulk Temperature

Figure 2.13 illustrates the complex interdependence of the final calculated results on the accuracies of the base-level measurements taken during the experiment. This diagram proved to very extremely useful in the original development and debugging of the

experiments, as it provides a visual understanding of where the final solutions are actually coming from. Table 4, below, gives uncertainties in the final calculated values as well as the uncertainties of the key components building up the final solution.

<b>Table 4: Uncertainties - Copper Block Experiment, Re = 30000</b>						
	<b>Calculated Value</b>		<b>Calculated Uncertainty</b>		<b>Percentage Uncertainty (%)</b>	
$Q$	5.20	±	0.039	$W$		0.749
$\Delta T$	27.4	±	1.2	°C		4.383
$\Delta P$ (venturi)	3289	±	32	Pa		0.988
$\dot{m}$	0.01756	±	0.00008826	kg/s		0.503
Re No.	29860	±	387			1.296
$\Delta P$ (channel)	225.447	±	0.49	Pa		0.218
$f_B$	0.0240	±	0.0001			0.325
$Nu_{DB}$	76.20	±				1.051
$f$	0.0198	±	0.0005			2.700
$Nu$	77.27	±	5.12			6.630
<b><math>f/f_B</math></b>	<b>0.83</b>	<b>±</b>	<b>0.02</b>			<b>2.720</b>
<b><math>Nu/Nu_{DB}</math></b>	<b>1.01</b>	<b>±</b>	<b>0.07</b>			<b>6.713</b>

The experimental uncertainty in the test section Reynolds number was calculated to be a maximum of 1.3% of the calculated value. Excluding the inherent uncertainty in the Dittus-Boelter correlation, the uncertainty in  $Nu/Nu_0$  was calculated to approximately 6.7%. The calculated uncertainty for  $f/f_0$  was calculated to be approximately 2.7% for the lowest flow rate tested. The table shows that the highest contributor to the experimental uncertainty in heat transfer augmentation is the temperature measurement. This is expected due to the fact that calibrated thermocouples were not practical for use in the tests on this experiment – the cost would have been simply too high. Instead, a random sample of the lab’s in-house thermocouples were tested for their accuracy. It was determined that  $\pm 1^\circ\text{C}$  was a safe estimate of the bias error associated with measurements



using these devices. Also, by taking over 1000 samples of steady-state temperature data, the author was able to reduce the precision components of uncertainty down to a negligible value.

### Smooth Wall Validation

For the purposes of validation, smooth copper blocks were machined and installed into the modules. Testing was performed at all three Reynolds numbers and the calculated results were compared to established correlations.

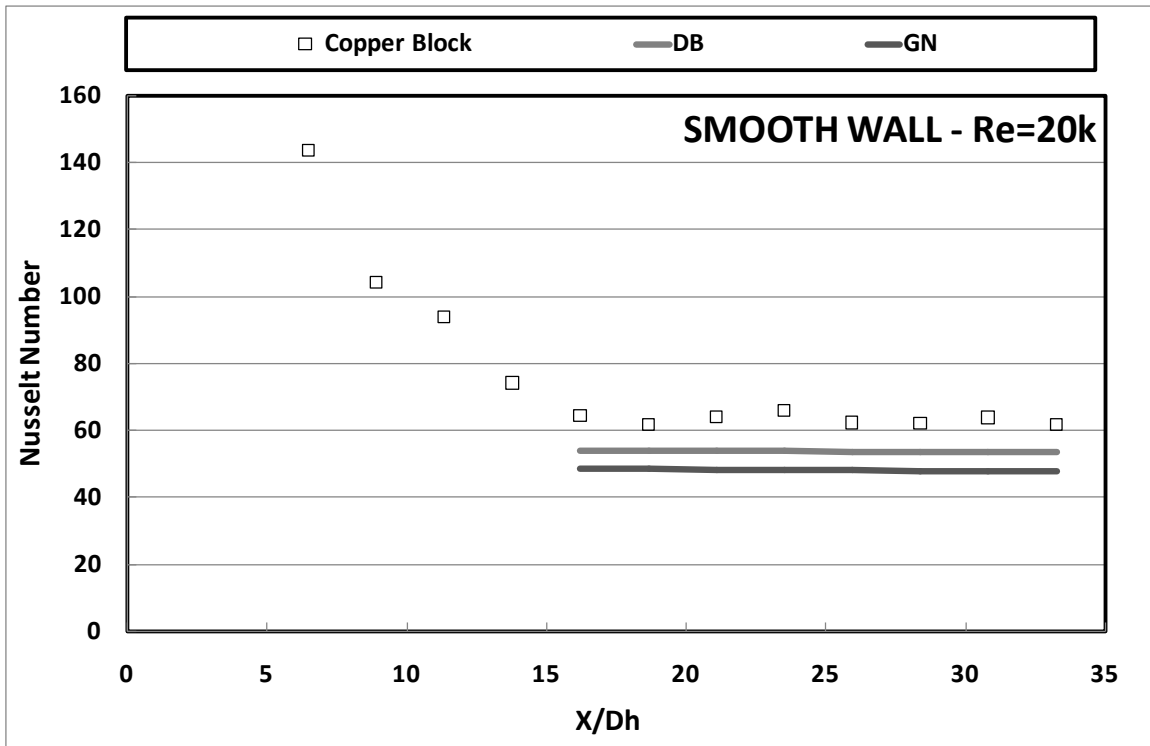


**Figure 2.15: Regionally Averaged Heat Transfer Coefficient Plotted Against X/Dh: Re = 20000**

Figure 2.15 shows the regionally (surface-area weighted) averaged (module-to-module) Nusselt number as a function of channel length. The flow is fully-developed within approximately 15 hydraulic diameters, which is typical of turbulent flows. A strict arithmetic mean of the module Nusselt numbers throughout the fully-developed portion

reveals that the channel Nusselt number is approximately seventeen percent greater than the value predicted by the Dittus-Boelter correlation and thirty-one percent greater than the value predicted by the Gnielinski correlation (see Table 8). These discrepancies are justified by the fact that the modular design of the channel has a tendency to promote increased turbulent mixing in the near-wall region, disturbing the viscous sublayer and causing an observed increase in heat transfer coefficient. Also, the Dittus-Boelter correlation has an inherent uncertainty of  $\pm 25\%$ , within which these results comfortably fall.

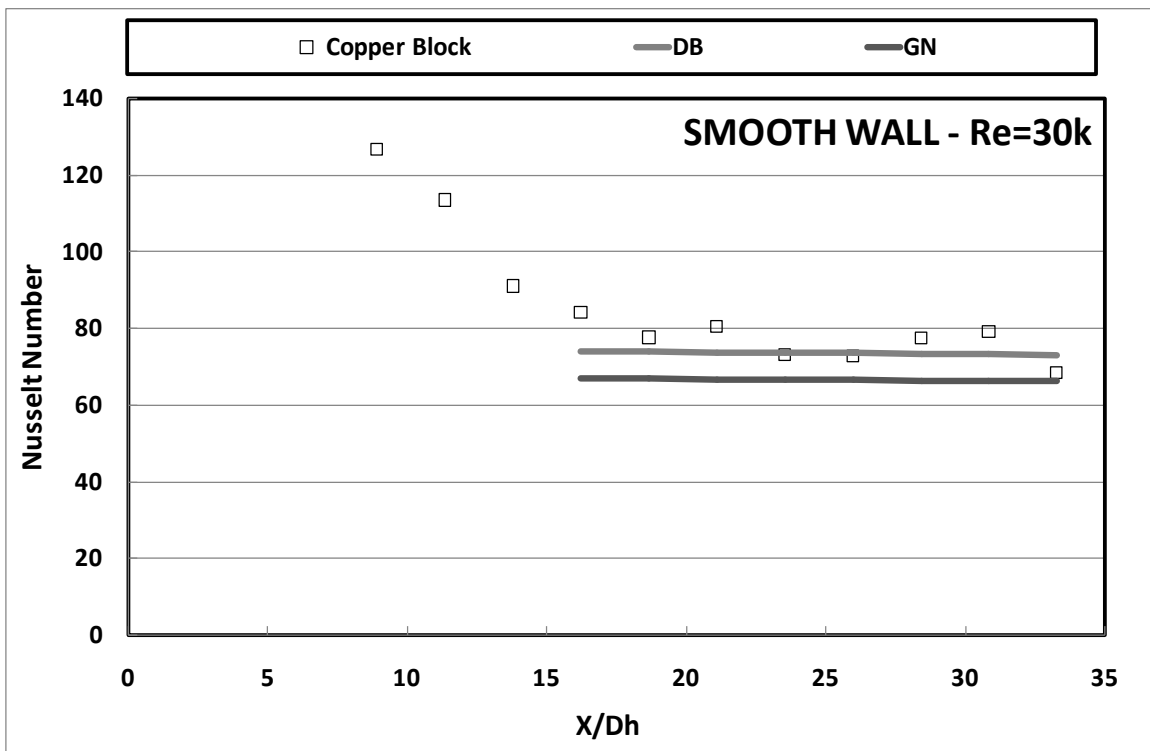


**Figure 2.16: Regionally Averaged Heat Transfer Coefficient Plotted Against X/Dh: Re = 30000**

Figure 2.16 gives the module-to-module Nusselt number profile as a function of channel length (in hydraulic diameters) for the channel Reynolds number of 30000. As given in Table 8, the average Nusselt number (through the fully-developed portion) is five percent

greater than that predicted by the Dittus-Boelter Correlation and sixteen percent greater than that predicted by the Gnielinski correlation.

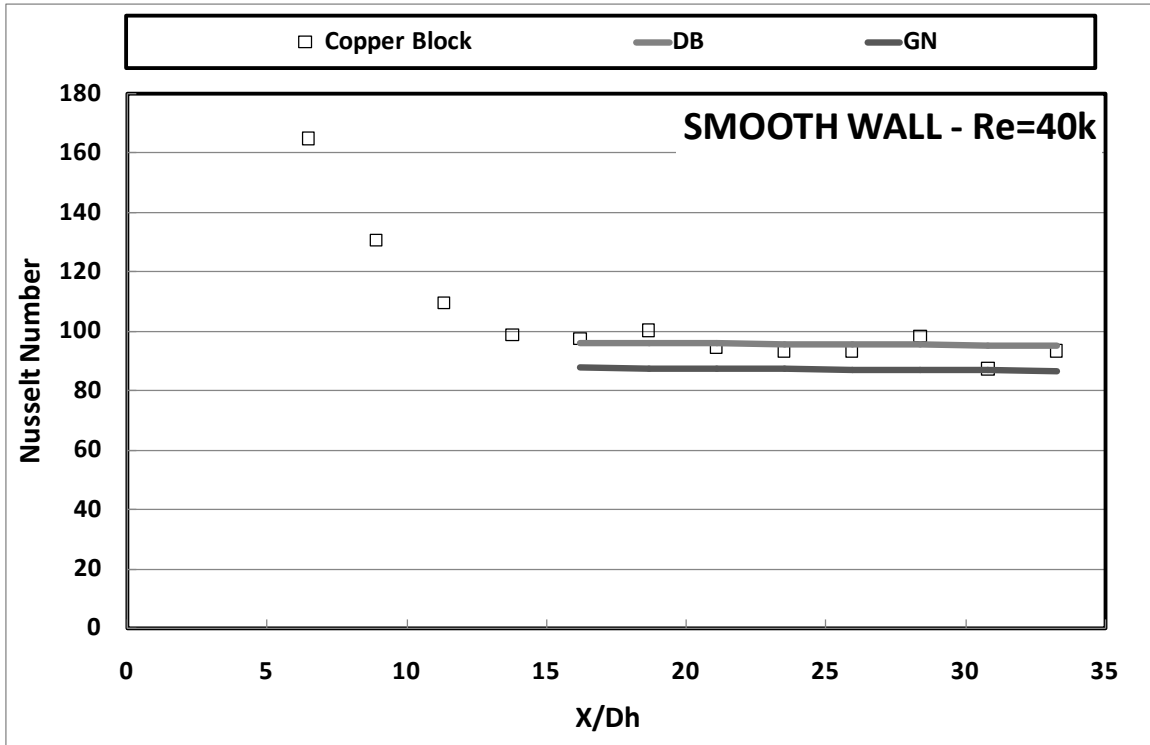


**Figure 2.17: Regionally Averaged Heat Transfer Coefficient Plotted Against X/Dh: Re = 40000**

Figure 2.17 gives the module-to-module Nusselt number profile as a function of channel length (in hydraulic diameters) for the channel Reynolds number of 40000. As given in Table 8, the average Nusselt number (through the fully-developed portion) is just one percent greater than that predicted by the Dittus-Boelter Correlation and eleven percent greater than that predicted by the Gnielinski correlation. The Dittus-Boelter correlation is chosen as the baseline value prediction for all tests performed on the Copper block rig throughout the remainder of this study.

As Reynolds number increases, it is observed that the measured values are converging on the predicted values. This is again justified by the idea that the module-to-module

transitions are tripping the flow, resetting the boundary layer and promoting turbulent heat transfer from the channel walls. As the channel Reynolds number is increased, the inherent mainstream turbulence is increased, resulting in a reduction of the augmentation caused by the module transitions.

## Test Setup for Local Data

### Background

As discussed in great detail closing out chapter one, this study is intended to meet three objectives. This section is to provide a complete description of the efforts made toward the completion of the second objective: to design, analyze, develop, validate, and employ a new method of experimentally determining local surface heat transfer coefficients. Reiterating, at the start of this project, there existed no suitable means to perform the experiments required for this study. In response, a total design process is completed to develop an accurate experimental rig for the collection of local heat transfer data using the transient liquid crystal technique. This method has been effectively employed by other competing labs around the world and has proved to be an accurate and efficient means of studying the phenomena that is the subject of this research. It will be an asset to the lab to have an experimental setup operating on this technique.

### Methods and Concepts

Initially, steady-state techniques were used most commonly used in heat transfer research to determine the average values of the heat transfer coefficients of the cooling design. One of the simplest methods of measuring the heat transfer coefficients of a channel is a steady-state method using copper blocks, and thermocouples (the level-one experimental

setup employed in this work. While these methods remain very useful in determining the average temperature of the cooled component or calculating the thermal performance of the cooling system design, many researchers have turned to more advanced techniques. It is known that, in some engine components, the rate of heat conduction is not fast enough to maintain a uniform temperature distribution when a non-uniform heat transfer distribution is employed (Hucek, 1985)(Dailey, 2000).

The Transient Liquid Crystal technique provides a full-surface local measurement of temperature in a very short duration test. In this case, flow is established over a surface being studied. At the start of the test, a step-change in the flow temperature is induced. The local color change history of the flow surface is recorded by a digital video camera. The recorded images are broken up by a digital frame grabber and processed translated into temperature values by a MatLAB™ image-processing code (see APPENDIX C:) in conjunction with a predefined calibration curve. This develops a time history of the temperature at each camera pixel. This information can then be used to quickly determine the local heat transfer coefficients of the flow under study (the mathematics behind process will be covered in great detail in the data reduction section of this chapter). Knowledge of this information allows engineers to better understand of physical phenomena present in the cooling channel. This knowledge is crucial to design an efficient, high performance cooling system that is capable of achieving the desired wall temperatures while minimizing the temperature gradients which play such a detrimental role in the fatigue and life of the component.

There are aspects of transient testing that caused early concerns and questioning of validity of result obtained from transient testing methods. One of the main concerns was the development of the thermal boundary layer during transient testing which would be a steady factor in steady-state testing. Hippensteele, Baughn, and Son all concluded that while transient testing does complicate some aspects of the experiment, the overall accuracy of the method is valid and acceptable (Hippensteele, Russell, & Stepka, 1981)(Baughn, 1995)(Son, Michaleis, Roberston, & Ireland, 1998). Also, the issue of three-dimensional non-uniformities on the channel wall (such as the dimple features of this study), can cause the heat conduction characteristics of the wall to change, breaking down the physics on which this technique relies. This phenomenon will be taken under detailed study in the later sections of this chapter. It is the goal of the author to address this matter for the purposes of this work as well as the interpretation of other work who have failed to address the topic.

By having the ability to perform full-surface temperature measurements, researchers are able to gain a far better understanding of the physical phenomena that simply would never have been realized with a more primitive method. Figure 2.18, below, is an example of the side wall temperature distributions near and impinging jet.

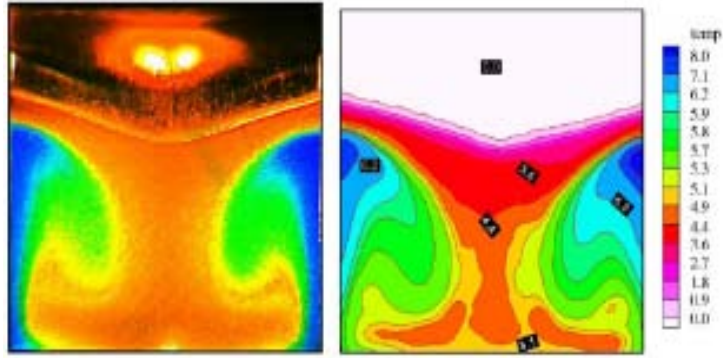


**Figure 2.18: Raw Temperature Data and Processed Local HTC Topography (Stasiek & Kowalewski, 2002)**

Also, transient methods have a vast advantage over steady state methods in data collection time. After establishing the correct flow through the channel, a transient test can be completed in as little as forty-five seconds of elapsed time. Steady state methods can very easily last over three hours before data can even be collected. Also, in a transient test, the rig is designed such that the channels walls can be assumed to be a semi-infinite solid and analyzed using a one-dimensional conduction approach.

In some situations it is difficult to create the needed step-change in the flow temperature. This can be the result of factors such as flow velocity that may not be controlled by the researcher. In answer to this issue, Newton et al. (Newton, Youyou, Stevens, Evatt, Lock, & Owen, 2003) developed a ‘slow transient’ method in response to the fact that it is not possible to produce a perfect step change in the temperature of the flow. This method was proven to yield accurate results using a narrow band liquid crystal (1°C). Also, Ekkad and Han (Ekkad & Han, 2000) employ a superposition of small temperature steps to the actual flow temperature step. The details of this process are covered in greater detail in section 3.8.

There are several well-developed methods to determine local heat transfer coefficients using a transient test with the TLC temperature measurement system. The Transient HSI technique uses an RGB to HSI converter to determine local temperatures from a recorded image. The local convective heat transfer coefficients are determined using the equation for a semi-infinite solid at a chosen time, knowing the temperature at every single pixel on the test surface from recorded image and a Hue-Temperature calibration curve.

The Transient Single Color Capturing Technique measures the time appearance of a certain color band at every pixel location on the test surface during the experiment. In other words, the single color method measures the time required for each pixel to reach a certain temperature. The temperature is translated from the reflected color of the TLC coating using an established calibration curve. Because this method only watches for the intensity of one color, the recorded image is far less sensitive to variations in viewing angle and lighting angle that plague Hue-based methods. It is therefore also true that the calibration process is also much less rigorous for the single-color technique than the HSI technique. This work will employ the Transient, Single Color Capturing Technique to capture the local heat transfer coefficients over the walls of the internal channels being studied.



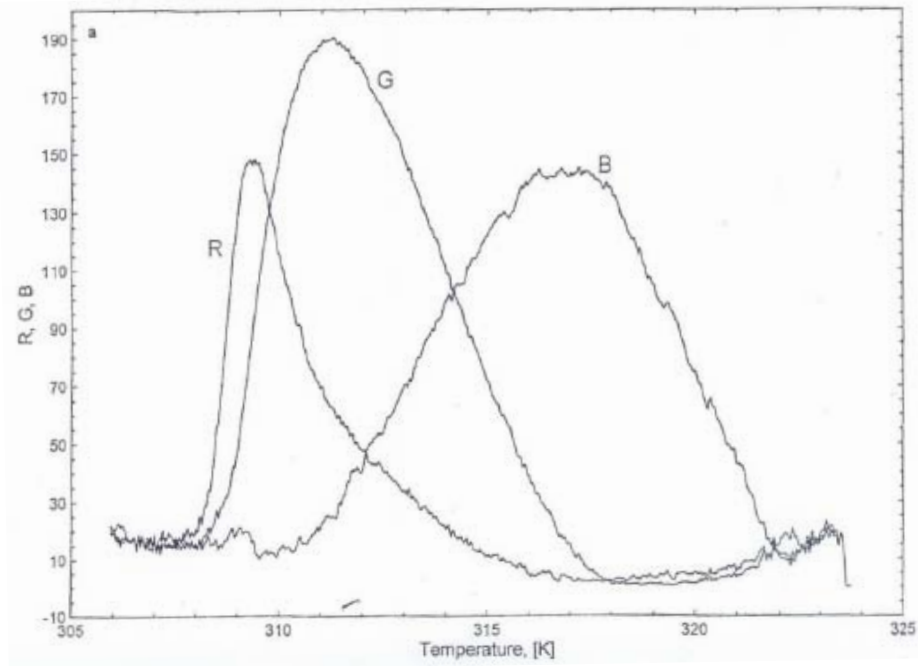


**Figure 2.19: Recorded RGB Values for Thermochromic Liquid Crystal (Farina, Hacker, Moffat, & Eaton, 1994)**

Observed color comes from a combination of characteristics of electromagnetic radiation that give the sensation of color to the human eye or video device. The change in reflected color of a liquid crystal coating as a function of temperature comes from the reorientation of the crystal lattice, and the spectral characteristics of the incident light source. Color-change data is collected with a digital video camcorder. The image processing code then looks for the appearance of green, which is found at the point where the G value is maximum (see Figure 2.19 and Figure 2.50). Green is chosen due to that, when green is reflected, the intensity of Green is higher than any other color. The increased intensity is more accurate to track.

Knowing the temperature at some point on the surface of the test section and the time to it took reach that temperature from the start of the transient test, the local heat transfer coefficient can be calculated using the solution for the semi-infinite solid, 1-D transient conduction problem:

$$\frac{(T_w - T_i)}{T_\infty - T_i} = 1 - \exp(\beta^2) \operatorname{erfc}(\beta) \quad \text{where} \quad \beta = h * \left( \frac{t}{\rho c k} \right) \quad (16)$$

Where  $T_w$  is the wall temperature read from the reflected color of the TLC at every pixel location,  $T_i$  is the initial temperature of the test section, and  $T_\infty$  is the temperature of the oncoming air after the temperature step. The thermophysical properties,  $\rho$ ,  $c$ , and  $k$ , are those of the tests section wall, which is made of a material with a low thermal conductivity so the semi-infinite solid approach can be used and heat loss to the atmosphere can be neglected.

### Design Development – Mesh Heater

Open literature presents a wide variety of methods to produce a step change in flow temperature during a transient test. After extensive reading, it was concluded that the best-suited design to accomplish this task in the current study would be to use a wire-mesh heater. The concept is simply to pass flow over an array of wires through which and electric current is passed. As the wire heat up, they will transfer heat to the flow, creating the desired change in flow temperature.

Though seemingly simple, the mesh heater component of this design was found to be the most complicated. This component encompasses so many different branches of engineering that it would be impossible to use one's 'engineering intuition' to simply

guess what is going to be the best design. For this reason, an extensive amount of analysis was performed on the heater mesh to determine what the best design would actually be.

The analytical model was made such that the wire mesh was modeled as an array of cylinders. This simplification is one that can easily be analyzed using common correlations for the subjects of heat transfer, fluid flow, and even electrical power. The entire analysis is given in Appendix A of this report. For this reason, this following section will provide only a brief overview of the line of thinking that was followed for this process.

To begin, analysis was performed to determining the Nusselt Number of the flow over the wire. This was found using correlations from the Incropera and Dewitt Heat and Mass Transfer book (Incropera & Dewitt, 2006) and assuming the flow through the mesh to be well-approximated as flow around a cylinder. The correlation was given to be a function of the Reynolds number of the flow around the wire (with the wire diameter taken as the characteristic length) and the Prandtl Number of the flow itself (taken as a constant).

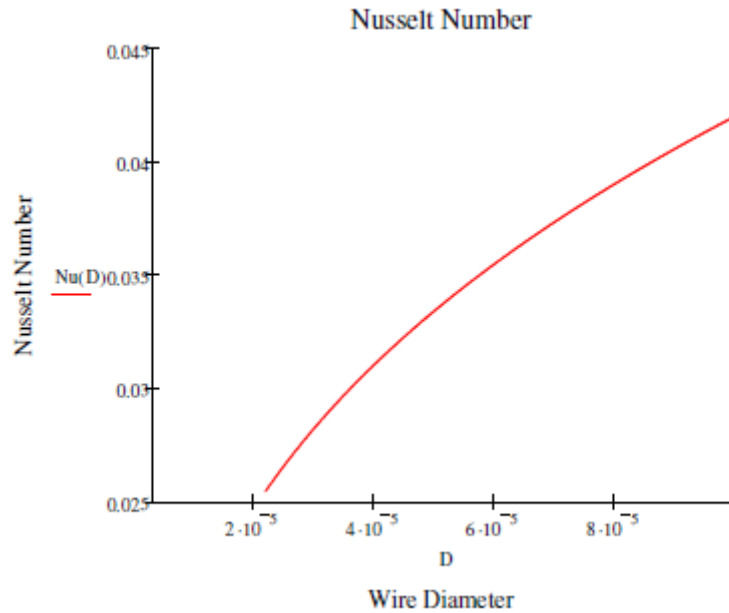


**Figure 2.20: Plot of Nusselt Number as a Function of Wire Diameter**

Knowing the Nusselt Number, it was then just a simple calculation to find the heat transfer coefficient of the wire itself. This information is given on the following page in Figure 2.21. It can be seen that the Convection Coefficient of the wire actually decreases with increasing wire diameter. This indicates a strong reliance of the overall effectiveness of the mesh on the design input of the actual wire diameter; the smaller the better.

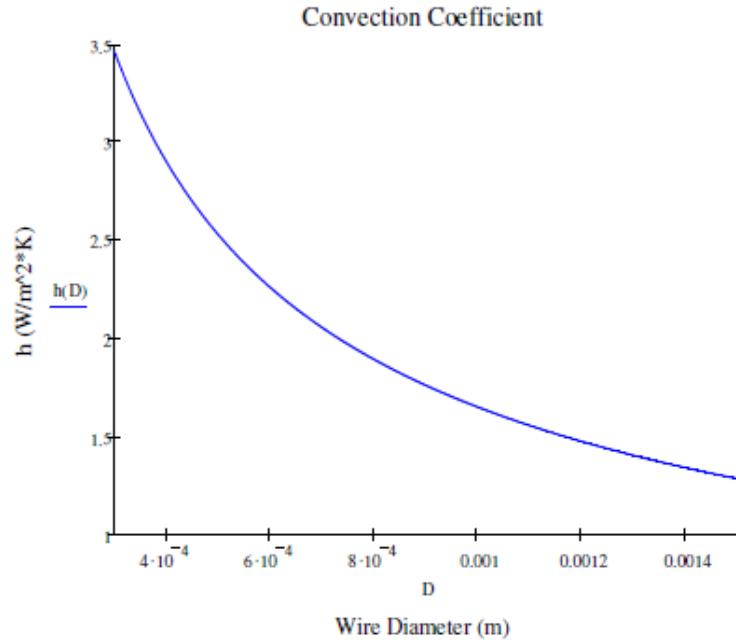


Figure 2.21: Plot of Heat Transfer Coefficient over wire as a Function of Wire Diameter

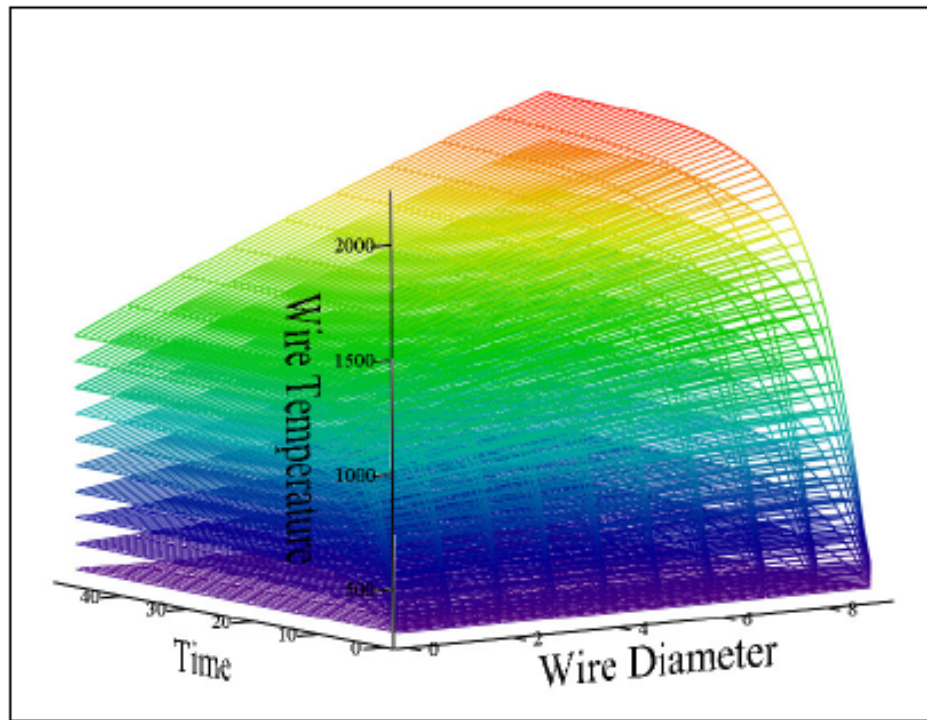
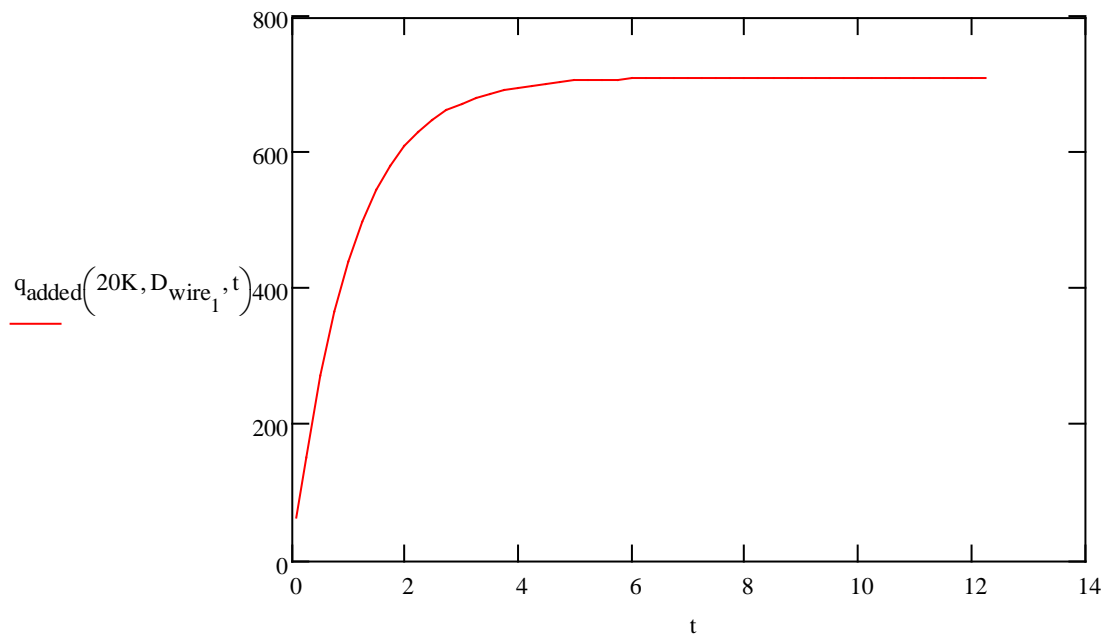


Figure 2.22: Temperature History as a Function of Wire Diameter and Power Input to Flow

The surface plot in Figure 2.22 gives a lot of design information. Based on the heat transfer coefficient, the thermal conductivity of the wire, and several other factors, this plot yields the predicted temperature history of the mesh wire using approximately one hundred different combinations of wire diameter and temperature step across the mesh. It is known that for stainless steel, our decided mesh materials, that the softening point is approximately 1400°C. However, this really is not a realistic temperature to set as a maximum value because the material actually begins to anneal at approximately 1100°C. The information given in this chart allows for the selection of a wire and a final decision on the power generated by the wire, such that this value is not over-stretched. Additionally, the transient development of the wire temperature is very important as it needs to be as close to a step change in temperature as possible. This value can also be known and ‘tuned’ using the information presented above.



**Figure 2.23: Predicted Time History of Heat Addition to the Flow (Watts)**

Figure 2.23 is a plot of the transient development of power addition to the flow. Thinking physically, it is easy to understand that at the first instant that the power is turned on to the wire mesh, zero heat will be transferred. This is simply because the wire, when no power is being generated, is at the same temperature as the flow. When two bodies are isothermal, there will obviously be no heat transferred. From the energy balance it is known that the heat generated by the flow must equal the sum of the heat output by the flow (by convection) and the heat stored in the wire itself. Therefore, it can be deduced that at that first instant, when power button is pushed, all of the energy generated by the wire will be stored in the wire itself, causing a very rapid rise in temperature. As soon as this temperature rises, heat will begin transferring to the flow by convection as well. These competing effects are what determine the transient response of the wire temperature. The figure above is a plot of the power added to the flow, which is exactly the energy out term of the energy balance, being pulled away from the wire by the flow from convection.

The pressure drop across the mesh is a relatively important consideration in the mesh design Figure 2.24. This analysis took into consideration the form drag on the body, but neglected the friction drag associated with the flow. It was found that the coefficient of drag decreased with increasing Reynolds number around the cylinder, where Reynolds number increases with increasing wire diameter. Thus it was determined that the force that would be exerted on the mesh was actually going to increase as the wire diameter of the mesh decreased. This is an important trend to note due to the fact that, as the wire diameter decreases, the internal stress in the wire itself would increase with decreasing

area, even if the force exerted on the wire was held constant. This is, then, further amplified when the force is increasing in an exponential manner as well. This is a key design factor due to the fact that, as mentioned above, the heat transfer characteristics of the mesh are best when the wire diameter is minimized. If not for the restriction of the strength of the wire itself, the design criteria would simply be to purchase the smallest wire diameter that is available. After considering the structural integrity of the mesh itself, however, it is realized that there must be a balance found between the two effects.

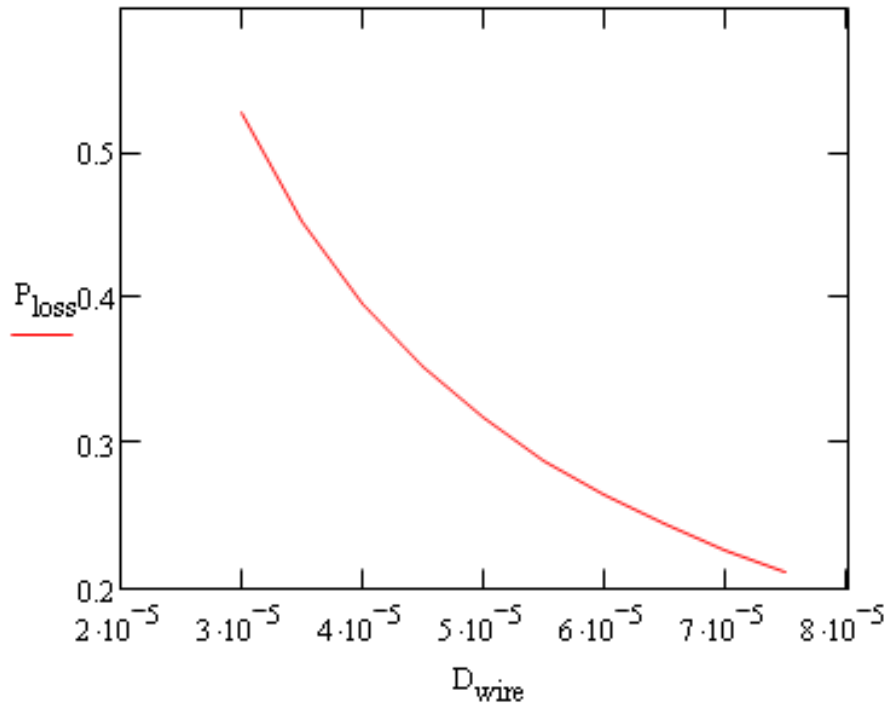


**Figure 2.24: Pressure Loss across Mesh as a Function of Wire Diameter**

Electrical calculations had to be performed on the heater mesh itself to determine the appropriate power supply requirements and overall feasibility of the project. First the temperature-dependant resistance of the mesh was found. Then, knowing the power



needed to achieve and specified step-change in the temperature of the flow, the voltage and current were calculated as functions of wire diameter and the number of wires in the mesh. These two parameters were chosen because they are the two most flexible when ordering a wire mesh/cloth from a manufacturer. These results shown indicate that our design can feasibly induce a forty Kelvin temperature step in the existing flow with power consumption below two kilowatts. This is an ideal situation as our existing power supplies in the lab are capable of producing three-hundred Amps of current at potential difference of seven Volts.

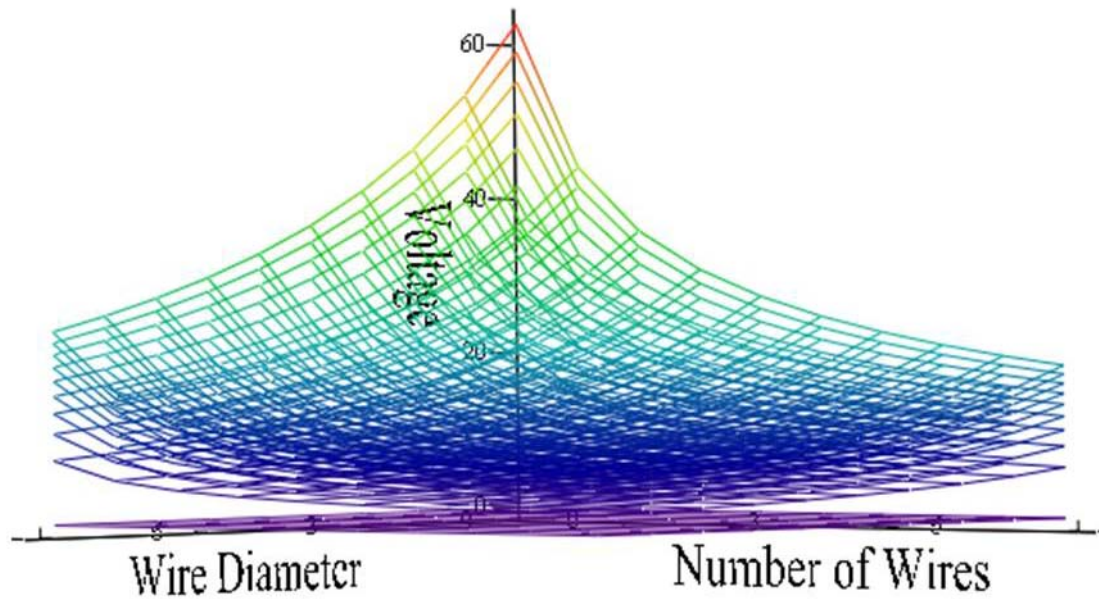


**Figure 2.25: Voltage across Wire Mesh as a Function of Power Added, Wire Diameter, and Number of Wires**

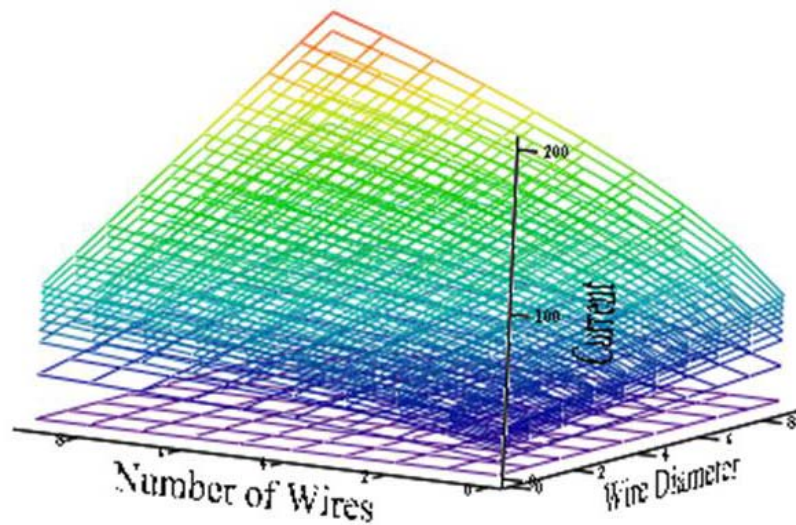


**Figure 2.26: Current across Wire Mesh as a Function of Power Added, Wire Diameter, and Number of Wires**

### Design Development – Test Section

The raw material used for the construction of the channel inserts, heater module housing, test section housing, and transition pieces is clear Perspex® acrylic. This was the optimal material choice for appearance, functionality, and strength for this project. Additionally, its thermophysical properties made it the perfect candidate for a transient HTC test.

In order to safely neglect heat loss and use the semi-infinite solid model to find the surface heat transfer coefficient, the total duration of the experiment has to be complete before reaching the maximum time value for the given materials properties and material thickness. This is determined from simply analysis of the propagation of thermal information through the solid using the non-dimensional parameter – the Fourier number

a common modification is made to the equation for transient tunnel designs by adding a factor of safety (set at 16 in equation (17), below).

$$t_{max} = \frac{d^2}{16 * \alpha} \quad (17)$$

where  $t_{max}$  is the maximum test duration for which the semi-infinite model holds,  $d$  is the wall thickness, and  $\alpha$  is the thermal diffusivity of the wall material.

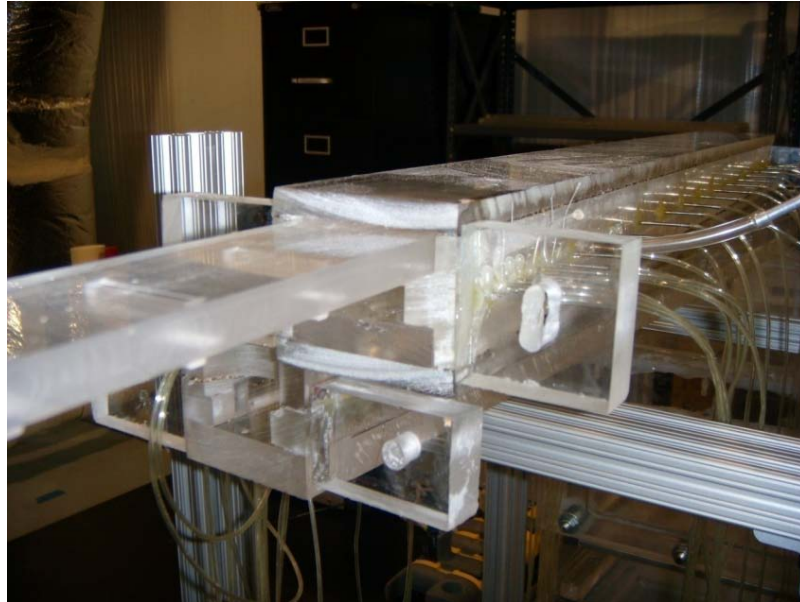


**Figure 2.27: Pressure Measurement Test Section with 0.5 inch Thick Acrylic Insert**

After performing the above calculation it was determined that the plenum wall should be constructed of acrylic walls with a thickness of 0.75 inches. It was also determined that the channel inserts should be constructed from acrylic 0.5 inches thick. These parameters allow for a  $t_{max}$  of greater than 90 seconds, more than twice the intended test time for this study.

Pressure measurements are taken from the array of pressure taps oriented on the height-wise center-plane along the entire stream-wise length of the channel. As shown in Figure

2.28, the holes for the pressure taps are counter-bored to the appropriate diameter to approximately half of the channel thickness. This provides the dual benefit of maintaining a smooth inner-wall and also ensuring accurate static pressure measurement.

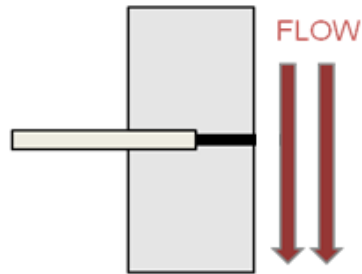


**Figure 2.28: Illustration of Counter-Bore Pressure Tap Design**

Figure 2.29 is a photo of the assembled channel with the pressure tap array installed. The taps are spaced at one inch intervals over the length of the channel and at one-half inch intervals near the channel entrance to capture the development effects. This information is crucial for isolation of the channels fully-developed flow region for calculation of the Moody friction factor.



**Figure 2.29: Pressure Measurement Test Section with Pressure Taps Installed**

## Design Development – Supporting Hardware

The tunnel is supported by an aluminum structure designed for the purpose of supporting the tunnel as well as accurate placement and support of the other necessary equipment such as lighting for the TLC test section, the digital video camcorders, and power supplies.

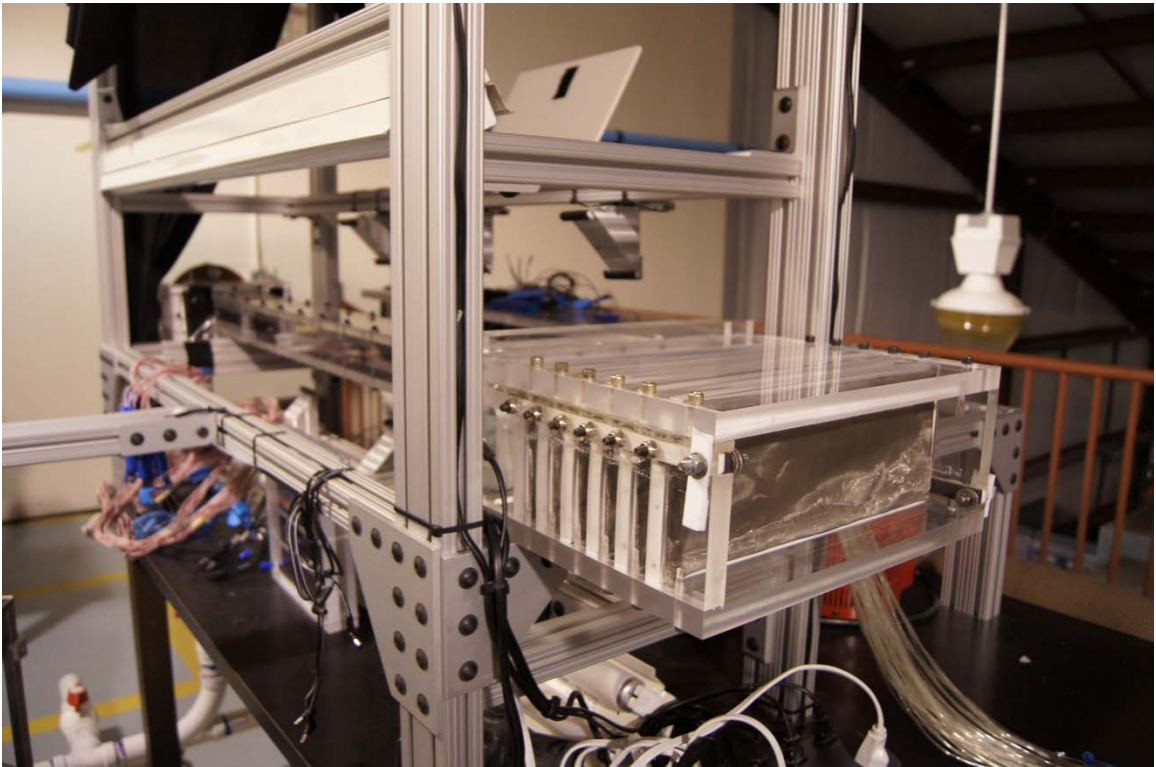


**Figure 2.30: 80-20 Aluminum Support Structure**

The channel is supported by a frame at the inlet and exit, with the heater supported separately. This allows for easy repairs and test section changes without major adjustments being performed. It also allows for clear optical access to three walls of the test section as is required to obtain the necessary pictures for data processing. An outer cage was designed for all of the peripheral equipment. This outer cage, when testing, is covered with a blackout material to avoid any light unknown lighting conditions from the



affecting of the tests. The ability to subject the test section to only a controlled lighting environment is crucial to accurate calibration and experimental data collection.

As part of the frame, two beams are placed just above and below the temperature measurement test section. These beams will serve to hold fast a series of mirrors used reflect the TLC image of the top and bottom surfaces of the test section to. The mirrors will be set at an angle of 45 degrees to transmit the images of the top and bottom surface to s single set of cameras aligned with the side of the channel. Figure 2.31 is a schematic of the design and a photograph is given in Figure 2.32.

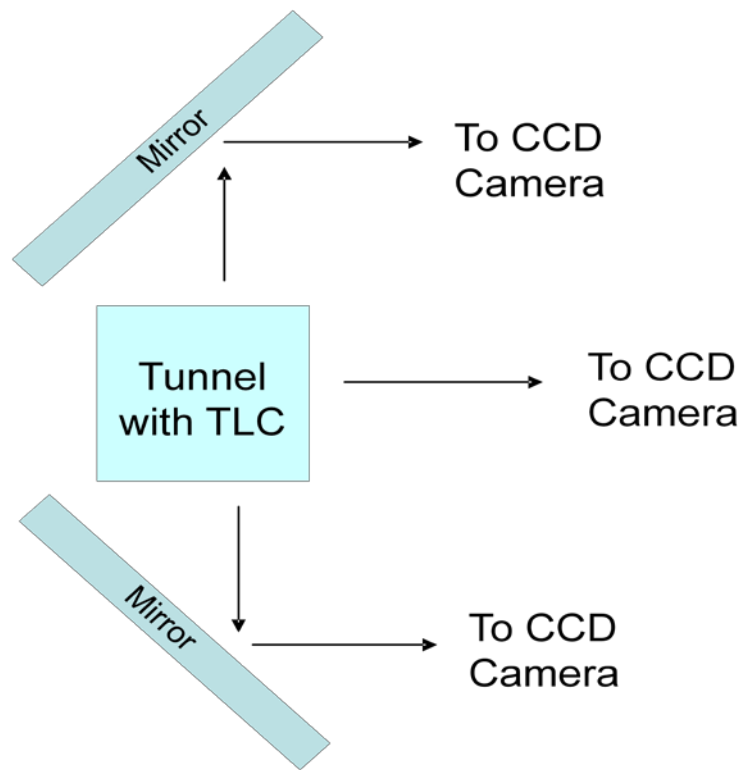


**Figure 2.31: Mirror Schematic**

This design will allow for the collection of temperature measurements on three surfaces of the channel with the use of only one camera instead of six. The flow is assumed to be

symmetric along the stream-wise direction, therefore eliminating the need to collect data on both of the side walls.

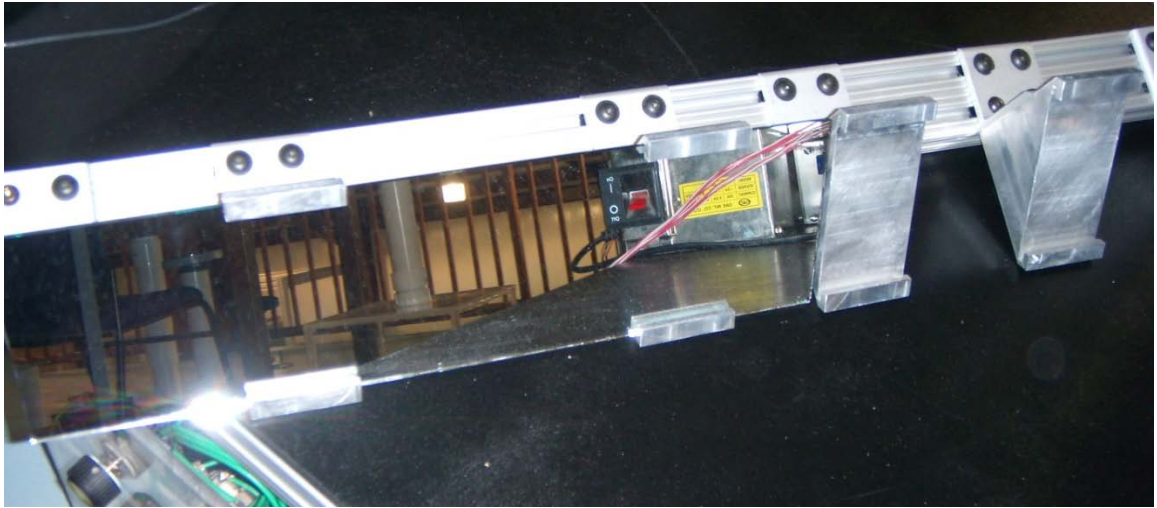


**Figure 2.32: Mirror Supported in Machined Mounts**

These mirrors will be front surface as opposed to the more common back surface mirrors. Having the reflective surface on the front minimizes any loss in image quality through the glass structure. Furthermore the mirrors used will be of optical grade (S/D 80-50), ensuring high image quality. The implementation of these components into the design will reduce the image processing (data-reduction) time by approximately 60% and therefore, will be very useful in the overall functionality of the rig for future use.

The heater mesh is powered by a DC power supply capable of producing up to 2.1 kW at a maximum voltage of 7.3 Volts. The final design decisions were made based on the analytical solution developed in section 3.3.1 of this thesis to work with this power supply. The final heater design contains a total of six meshes wired in parallel, summing up to a total resistance of 0.019 Ohm. At this value, the mesh heater can induce a 40°C step change in the flow temperature (at a Reynolds number of 40,000 – the highest flow-

rate supported by the lab's current compressed air infrastructure) at 7.39 Volts passing 305.2 Amps.

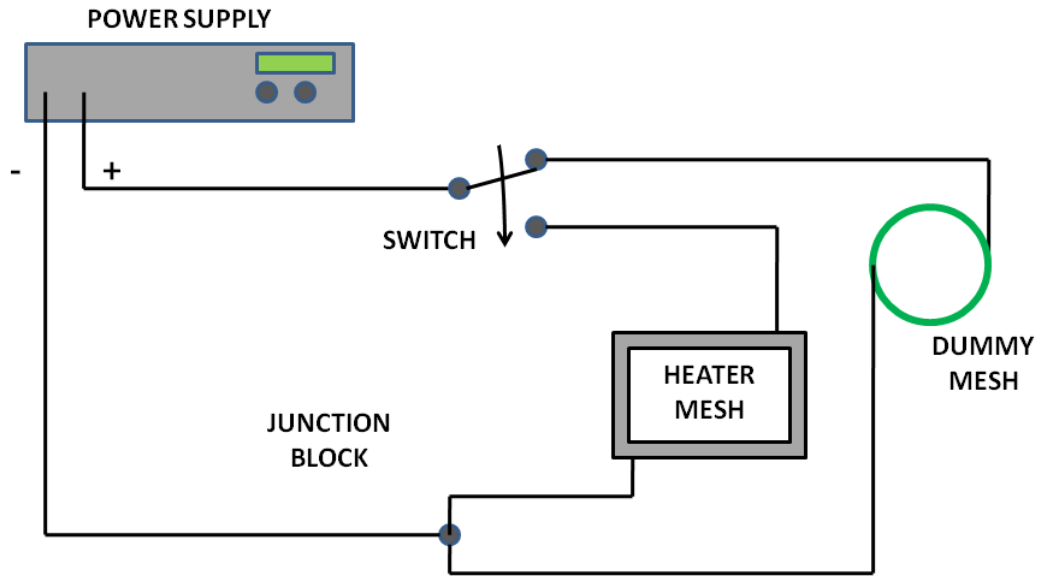


**Figure 2.33: Power Supply Wiring Schematic**

To account for the ramp up period of the digitally controlled power supply, a simulator mesh was created from an 11 meter length of 8 AWG insulated copper wire that was calculated and tested to have a resistance identical to that of the heater mesh. The positive lead of the power supply is connected to an and/or switch that sends current only to the mesh simulator or only to the heater mesh. This allows the tester to start the power supply while sending power to the mesh simulator, adjust the power setting and allow the power supply to reach a stable value before turning the current over to the heater mesh. This allows for a much more accurate test by facilitating change in temperature more closely resembling the ideal case of an instantaneous change in flow temperature



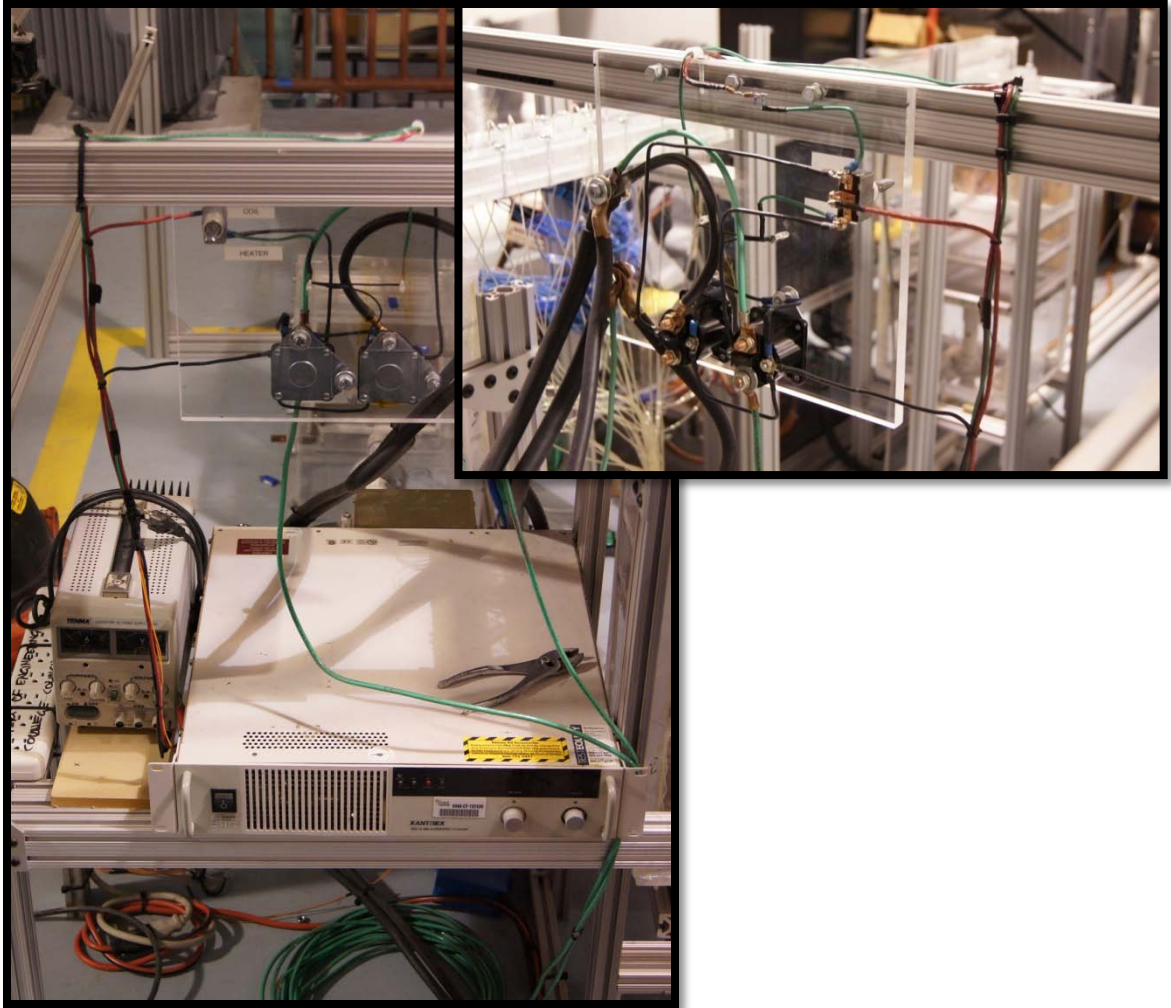


**Figure 2.34: Photo of Author-Developed High-Current, Three-Way Switch and Power-Supply Setup**

Proper illumination of the TLC surface requires only a collimated source of white light. Fluorescent Lights were mounted to the 80-20 aluminum frame to illuminate the test section with white light. A bulb temperature of 4100 Kelvin was chosen as this most puts off the coolest, white light. The lights were mounted in such a way as to avoid any shadows or glare that could be created problems. The cameras were mounted in the same plane as the lights to eliminate the possibility of shadows. After setting up the 80-20 support structure, the plenums and channels were assembled. The inserts for the heat transfer test sections are coated with a thin layer of Thermochromic liquid crystals using

an airbrush. The lighting is arranged so that the test section is uniformly lit and no shadows or glares are produced on the test section walls or mirrors).



**Figure 2.35: Photo of Experimental Setup with Lighting and Cameras**

While the lighting arrangement is not as crucial when using the RGB, single-color capturing system, it remains important to verify that the background intensity of the black surface behind the liquid crystals is at a satisfactory level. If the background intensity is too low, then the reflected image is too dark and the camera cannot capture the actual color. If the background intensity is too high, the reflected image too bright and the reflected color is lost due to the white light effect.

## Design Development – Instrumentation

In recent years, liquid crystal measurements have been developed into a very accurate and reliable means of collecting local surface temperature measurement. These crystals are highly anisotropic liquids with a phase of matter that can be classified between solid phase and the conventional isotropic liquid phase.

The Mesomorphic (Liquid Crystalline) state is between that of a crystalline solid and an isotropic liquid therefore, liquid crystals possess a combination of characteristics from both. When heated beyond its melting point, a crystalline solid transforms into an isotropic liquid. In contrast, liquid crystals do not pass directly from a crystalline solid into an isotropic liquid. Rather, they adapt an intermediate state with a chemical structure that possesses greater order than that of an isotropic liquid, but not equal to that of a crystalline solid. These materials possess the mechanical properties of liquids such as fluidity and surface tension, and the optical properties of a crystalline solid such as anisotropy to light.

There are two types of liquid crystals, Lyotropic and Thermotropic. For the purposes of this study, focus will only be given to the Thermotropic liquid crystals, which are thermally activated mesophases which are products of melting a mesogenic solid by heating the material to a temperature where the crystal lattice of the solid become unstable. Thermotropic liquid crystals are divided into two different classifications based on their optical properties: Smectic and Nematic. Smectic Mesophases possess a greater deal of organization than the Nematic mesophases. They can be described as long axes

of parallel sheets or planes of molecules in a two-dimensional, layered structure with all of the molecules long axes aligned (see Figure 2.36).

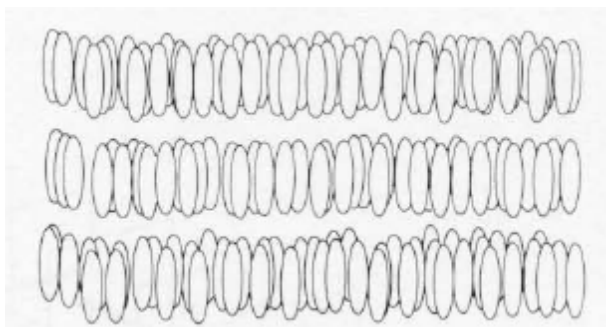


**Figure 2.36: The Smectic Liquid Crystal Structure**

The Nematic mesophase is characterized to possess a more random, disorderly structure than that of the Smectic mesophase. While the long axes of the molecules tend to remain aligned, the molecules themselves are no longer seen to be constrained to the two-dimensional sheets, or layers seen in the Smectic mesophase. Figure 2.37, below, presents the structure clearly.

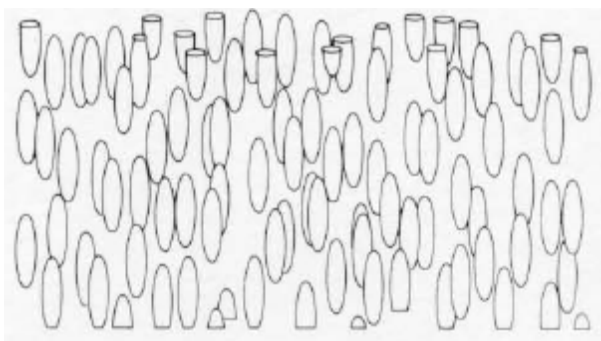


**Figure 2.37: The Nematic Liquid Crystal Structure**

The Cholesteric and Chiral-Nematic mesophases are an optically-active types of Thermotropic, Nematic Liquid crystals. These two liquid crystal forms possess the most desirable properties for application dealing with thermal science such as this work. Cholesteric and Chiral-Nematic liquid crystals possess very similar properties while

having different chemical compositions. Cholesteric liquid crystals are comprised entirely of cholesterol and other sterol-derived chemicals. Chiral-Nematic formulations are comprised entirely of non-sterol based chemicals. The Thermochromic liquid crystals used in this study are a combination of the two forms and therefore exhibit a combination of the chemical and physical properties of the two pure forms.

The optically active Nematic liquid crystal mesophases are comprised of helical aggregates of molecules whose longitudinal dimensions are on the order of the wavelength of visible light. One important characteristic of these helical structures is the degree of rotation or ‘twist’ they exhibit. To quantify this value, a parameter called pitch,  $p$ , is defined as the longitudinal distance between two points between which the helix has rotated exactly  $360^\circ$ . Therefore, depending on the pitch of the helical structure, each molecule within the structure is rotated at some angle  $\theta$  with respect to the neighboring planes of molecules directly above and below. The angle,  $\theta$ , is referred to as the displacement angle.

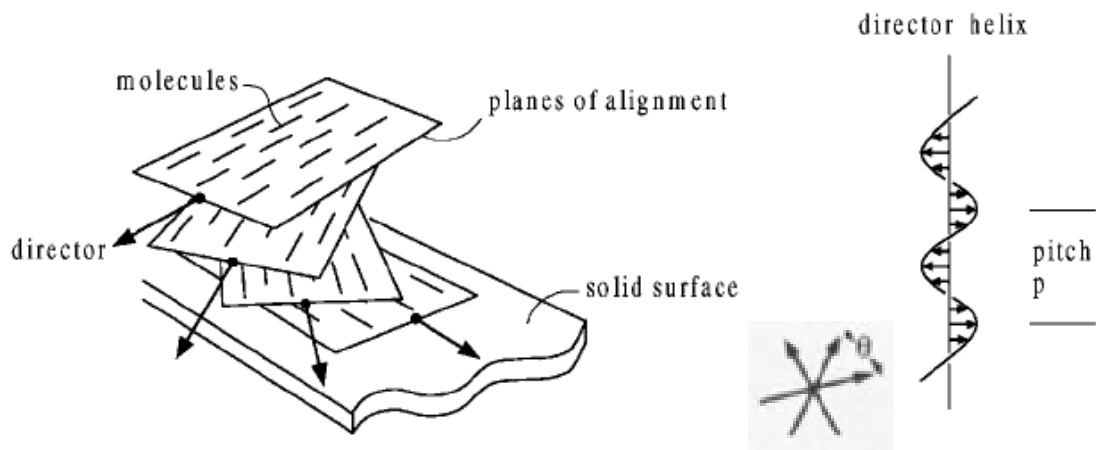


**Figure 2.38: Schematic of Cholesteric Nature of Liquid Crystals [Ireland and Jones, 2000]. The Arrow is Indicative of the Helical Path within the Medium**

As the name implies, these optically active, Thermochromic liquid crystals react to a change in temperature by a change in reflected, visible light (change in color). Thermochromic liquid crystals modify incident white light, changing the reflected wavelength as a function of temperature. Starting from a colorless form at a temperature below the starting temperature of the mixture, the mixture remains colorless until the start temperature is reached. At this point, the color red is reflected. The reflected color passes through the entire visible spectrum in sequence as temperature is continually increased until transitioning back to a colorless form to the top of the color-play bandwidth. Figure 2.39 shows a typical color (wavelength) response as a function of temperature.

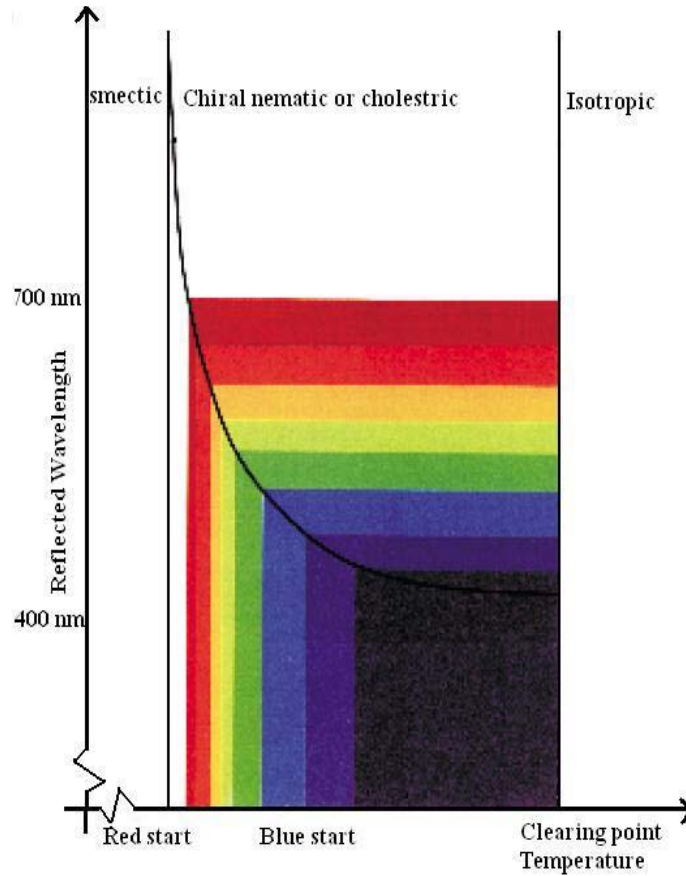


**Figure 2.39: Relation between Temperature and Reflected Wavelength**

The color-play bandwidth of a Thermochromic liquid crystal is defined as the blue-start temperature minus the red start temperature. The ‘color play’ of the mixture is defined by specifying either the red-start temperature, or both the mid-green temperature and the bandwidth. For example, the narrow-band liquid crystal slurry employed in this work has the LCR Hallcrest™ identification number of BM/R32C5W. R32 indicates a red-start temperature of 32°C with and C5 indicates a color-play interval of 5°C. The active temperature of the liquid crystals is limited by the isotropic liquid phase at the high temperature region, and the solid state or the smectic mesophase at the low temperature. The spectral dependence of the maximum reflectivity of incident light reflected is governed by the approximately by the Bragg diffraction equation (18).

$$\lambda_o = 2 * d * \hat{n} * \sin \phi \quad (18)$$

Where n is the mean refractive index, 2d is equal to P, the Cholesteric helical pitch length,  $\phi$  is the angle of incidence normal to the surface of the mesophase, and  $\lambda_o$  is the wavelength of the selectively reflected light (the reflected wavelength).

The illuminating light, incident on the liquid crystal surface must be within an acceptable range of deviation from the direction normal to the liquid crystal surface. When incident light is propagated at an angle to the helical axis, the reflected wavelength will naturally decrease with increasing angle. This effect is explained by the Bragg Theory

As the temperature increases, the thermal motion of the molecules increases, resulting in an increase in their molar volume, which can affect the helical structure in two, opposing ways. First, as molecular energy increases, the intermolecular spacing along the helical

axis (the distance between neighboring planes) increases, tending to increase the pitch and therefore, increase the reflected wavelength. However, as the displacement angle,  $\theta$ , increases between the long axes of neighboring planes of molecules in the helical aggregates of molecules increases, the pitch and reflected wavelength is decreased. Between the two competing effects, the second is dominant, such that pitch and reflected wavelength almost invariably decrease with increasing temperature. It is important to note that only about one-tenth of a degree change in  $\theta$  causes the reflected wavelength to move from one end of the visible spectrum to the other.

The planar liquid crystal structure of the Cholesteric (or Chiral-Nematic) mesophase possesses a number of properties that give rise to the unique optical effects referred to above. Liquid crystals possess the optical properties of birefringence, optical activity, Circular Dichroism, and Bragg Scattering, the details of which are irrelevant to the purposes of this study. However, it is the combination of these effects which yields a material that, when illuminated with white light, selectively reflects a narrow portion of the visible spectrum while either absorbing or transmitting the rest of the rest of the illuminating light. Because of the fact that only a very small range of incident light is reflected by the liquid crystals, a black background is typically applied to absorb any light transmitted through the liquid crystal mixture and to provide the optimum visual image of light reflected from the liquid crystal surface.

Liquid crystals, in the pure form, are essentially oils and depending on their formulation can vary from a thin, light oil to a dense, viscous, greasy liquid. Regardless, in this form,



they are very difficult to use in a laboratory setting. In addition, they are also sensitive to mechanical stress and are susceptible to degradation by exposure to UV light as well as other common chemicals like greases and solvents. In order to make these materials conducive to any sort of closed process, research-level application, a micro-encapsulation process was developed in order to stabilize these crystals to provide some appreciable longevity and repeatability. This process encloses small portions of the liquid crystal material into a polymeric (gum arabic) sphere with a diameter of approximately 5-10  $\mu\text{m}$ . Encapsulation of the crystals is a direct solution to the issues of stress sensitivity and chemical deterioration of the materials.

In order for the Liquid crystals to be of any use in a research environment, there must be a way to directly translate the color visible light reflected from them into an actual temperature. A calibration curve establishes a relationship between the temperature of the crystal and the measured Hue of the reflected light. This curve is established using a calibration rig is known temperature distribution. The relation between temperature and Hue is a non-linear one and therefore, its accuracy varies with color.

The spatial resolution of the microencapsulated TLC is reported on the same order as the thickness of the liquid crystal coating, approximately 10 microns. The response time of a thin film of microencapsulated TLC's found to be only a few milliseconds with a film thickness of approximately 25 microns and a heating rate of 2000°C per second (Ireland & Jones, 2000). This response time is found to be acceptable for the purposes of this study.

As mentioned in Section 3.2, there are two techniques for analyzing the qualitative color data of the liquid crystals and translating them into the quantitative data needed to continued data reduction and processing. The first considered here is the RGB technique. The RGB color model has three basic primary colors; Red, Green, and Blue. All of the other colors in the entire visible spectrum can be obtained by some combination of these three colors. White light is reflected when all of the colors are present and black is seen in the absence of any other color. This model is the same as that employed in many common household electronics such as LCD televisions, computer monitors, and the three CCD digital video cameras used for data collection in this work.

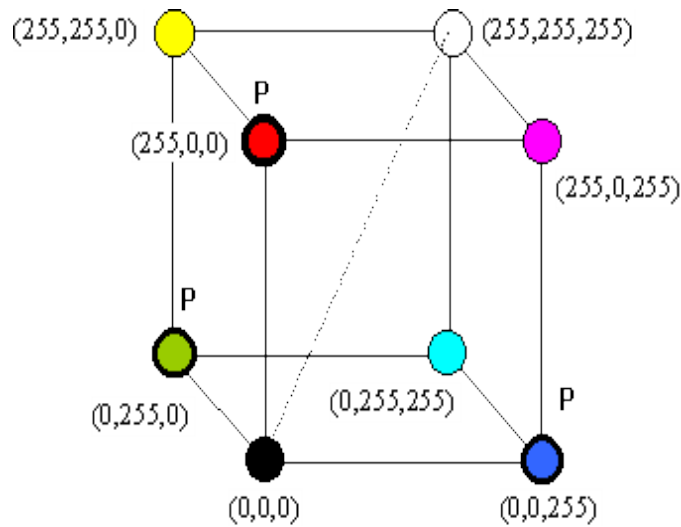


**Figure 2.40: 3D RGB Color Chromaticity Diagram (Basu, 2009)**

The RGB color model is shown above in Figure 2.40 where every color in the spectrum is represented by three values. This system is comparable to a point in space located by the Cartesian coordinate system with an x, y, and z value. The Red, Green, and Blue values are on a scale from 0 to 255 because of the fact that they are stored on an 8-bit data storage scale which is only capable of 256 different values ( $2^8$ ).

Temperature measurement data is recorded by taking a time history of the visible color change of the TLC coating applied to the channel walls. A Panasonic NVGS240 3CCD digital-video recorder with a resolution of 2.4 megapixels and a capture frame-rate of 30 frames per second will be used for this task. The images are stored on a custom-built, AMD 64-bit PC running 64-bit Windows Professional. A FPG 32-bit color frame-grabber is installed into a PCI slot on the motherboard and is connected directly to the video cameras using a standard USB cable. These images are analyzed, frame-by-frame, using a MATLAB code to determine the time history of the recorded RGB values of the color present at each individual pixel. The quantitative RGB values are compared to a calibration curve established using thermocouples. This process generates a time-history of the temperature development in the channel. Knowing the temperature of the wall at a specific small point on the wall of the channel and knowing the local flow temperature as caused by the instantaneous mesh heater (a controlled value to achieve a specific step change in temperature for a specific mass-flow rate), it is possible to calculate the local heat transfer coefficient at this small point on the wall of the channel (section 3.8 covers this process in greater detail). These local temperature measurements will allow for the detailed study of the actual physical phenomena caused by the various testing configurations being studied by calculating the local heat transfer coefficient. This will allow or an even greater understanding of the effectiveness of these geometries and the implication that hold to the main goal of this project, increased turbine efficiency.

The liquid crystals used for this experiment were custom made by Hallcrest™ Inc.; R32C5W. The batch is formulated by the manufacturer to have a 5°C color-play interval and a Red-start temperature of 32°C. The band temperatures are also known to be the following: Red – 31.6°C, Green – 32.8°C, Blue – 37.2°C. A calibration test must be run in order to confirm the color change temperatures of the band in the actual laboratory lighting conditions.

To confirm the color change temperatures, a thick, polished copper plate is fitted with a foil heater on one side. On the other side, a small array of type-T thin foil thermocouples is applied to the surface: one in each of the four corners and six more arranged in two perpendicular lines across the center of the plate surface. The smooth surface is then coated with the blackening surface coating before applying the Thermochromic liquid crystal coating.

The camera is placed such that the lens is approximately 0.3m from the plate surface to include the entire plate surface with the camera-zoom completely out (see Figure 2.41). The plate is lit by two fluorescent lights, identical to those used on the actual test, placed the same distance away as they are on the actual test. A light-blackout material is placed over the calibration apparatus during the test to eliminate light pollution from the lab overhead lights. The same precaution is also taken on the actual test rig, increasing accuracy by minimizing possible discrepancies between the calibration test and the actual experiment.

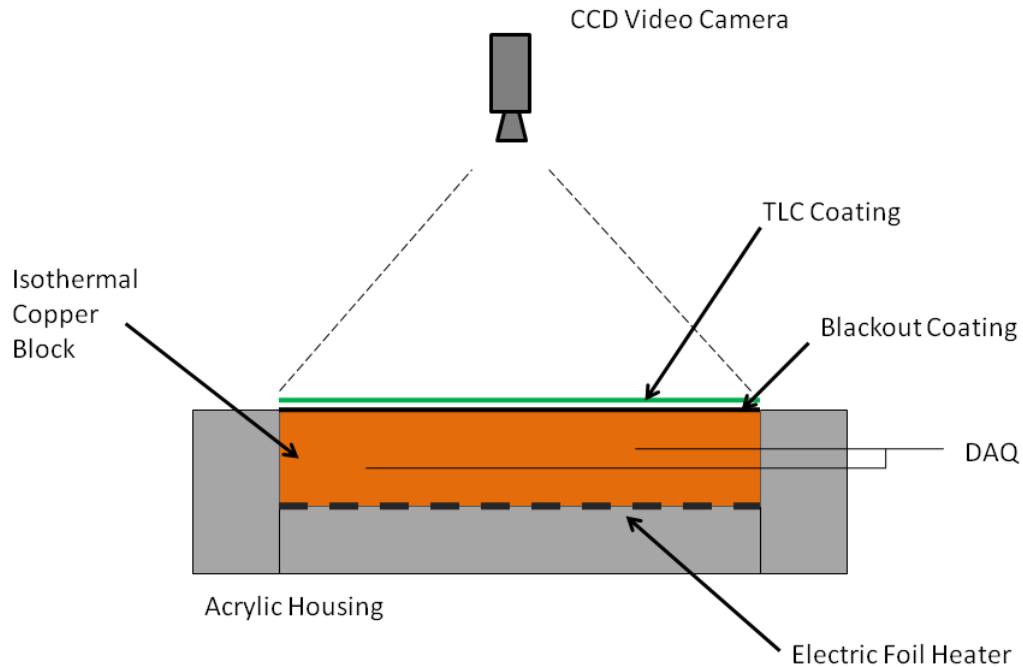


**Figure 2.41: Schematic of Calibration Setup**

The heater is turned on and the plate is heated up to a temperature of approximately 50°C. At this point, the heater is turned off and the plate is allowed to slowly cool. The calculated Biot number for natural convection from the plate was found to be very small and the thermal conductivity of the acrylic block is very high. It is therefore assumed that the temperature gradient in the direction of the thickness of the block is flat. The cool-down time for the block is typically around 50 minutes. During this time, the color change of the liquid crystals is recorded (see Figure 2.42) using a digital video recorder while simultaneously recording the output from the thermocouples with a National Instruments LabView Data Acquisition system which is also connected to the same PC described for TLC image processing. To create the discrete points needed for the curve-fit, a spatial average is taken of the recorded temperatures from the six centrally-located thermocouples. Also, the recorded green intensity of all of the pixels in a prescribed

region in the center of the surface is filtered and averaged as a part of the calibration image processing code.

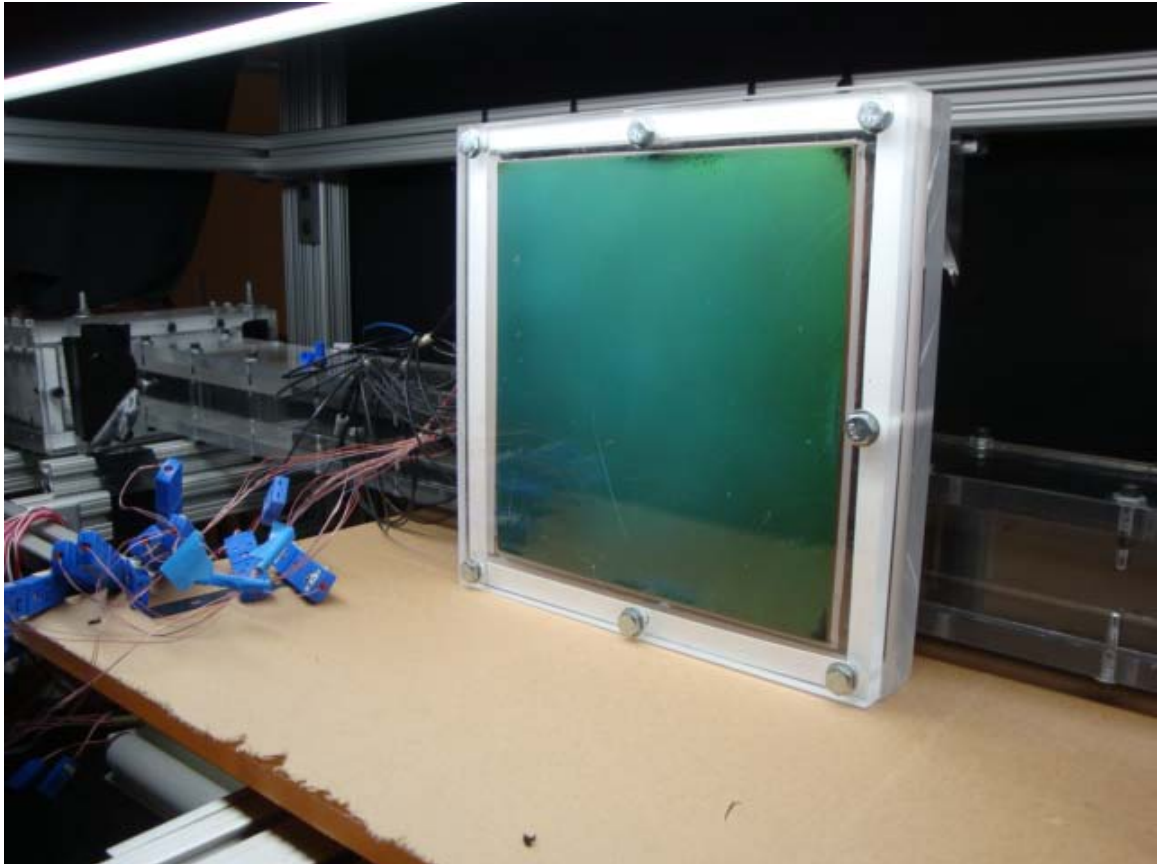


**Figure 2.42: Photo of Calibration Setup During a Test**

After averaging the recorded color change and the temperature history from the thermocouples, the averaged Green signal is fit to a curve as a function of the plate temperature recorded from the thermocouples. This is the calibration curve used to translate the reflected color from the test section to a quantitative value of temperature. Figure 2.43, below is a schematic of the TLC calibration process.

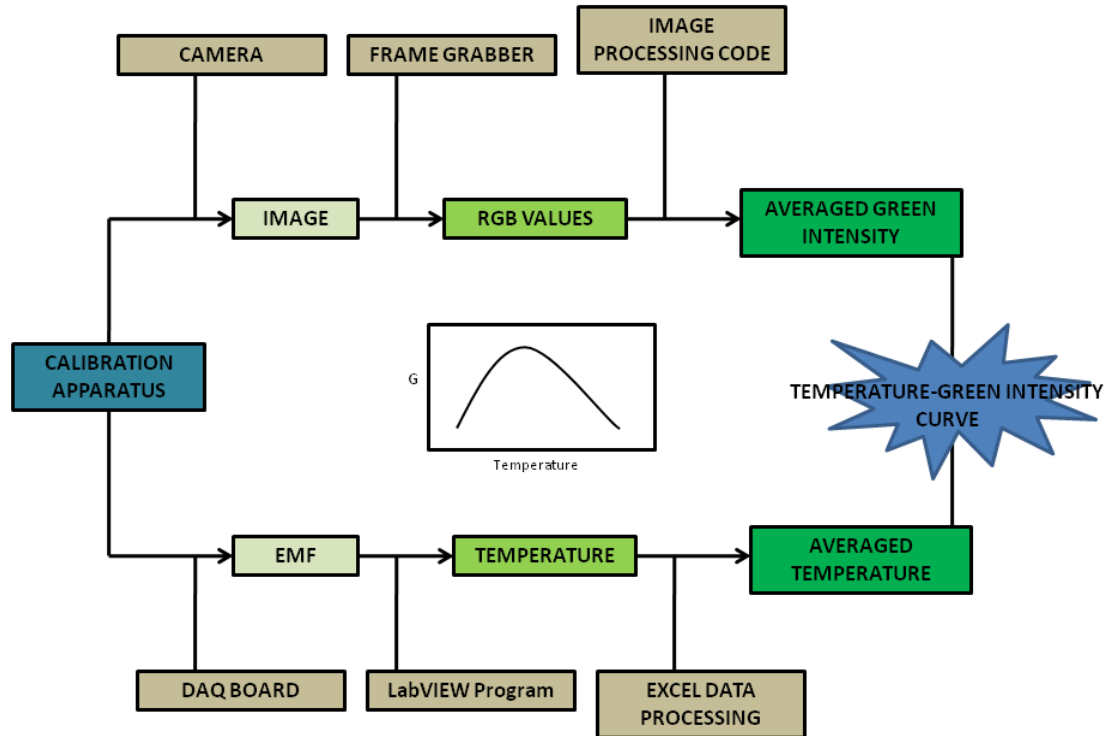


**Figure 2.43: Schematic of Calibration Process**

It is important to perform these calibration procedures with every new application of Thermo-chromic liquid crystals to ensure accurate color change and time information. This is shown, in later sections of this chapter, to be one of the most crucial steps of the entire experiment.

### Final Design Details

A CAD model as well as an actual picture of the final assembly is given in Figure 2.44. It has been designed in such a way to allow for easy changes in channel aspect ratio for future testing in the lab. A schematic of the complete system is shown in Figure 2.45.

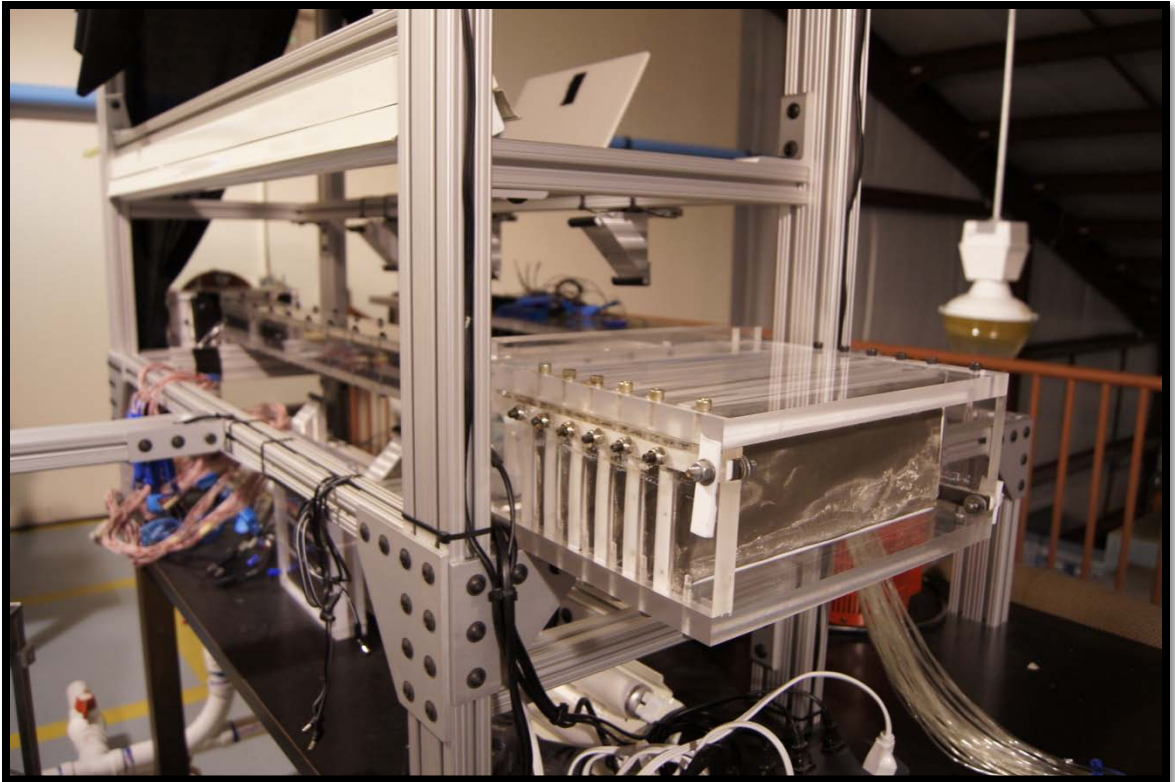
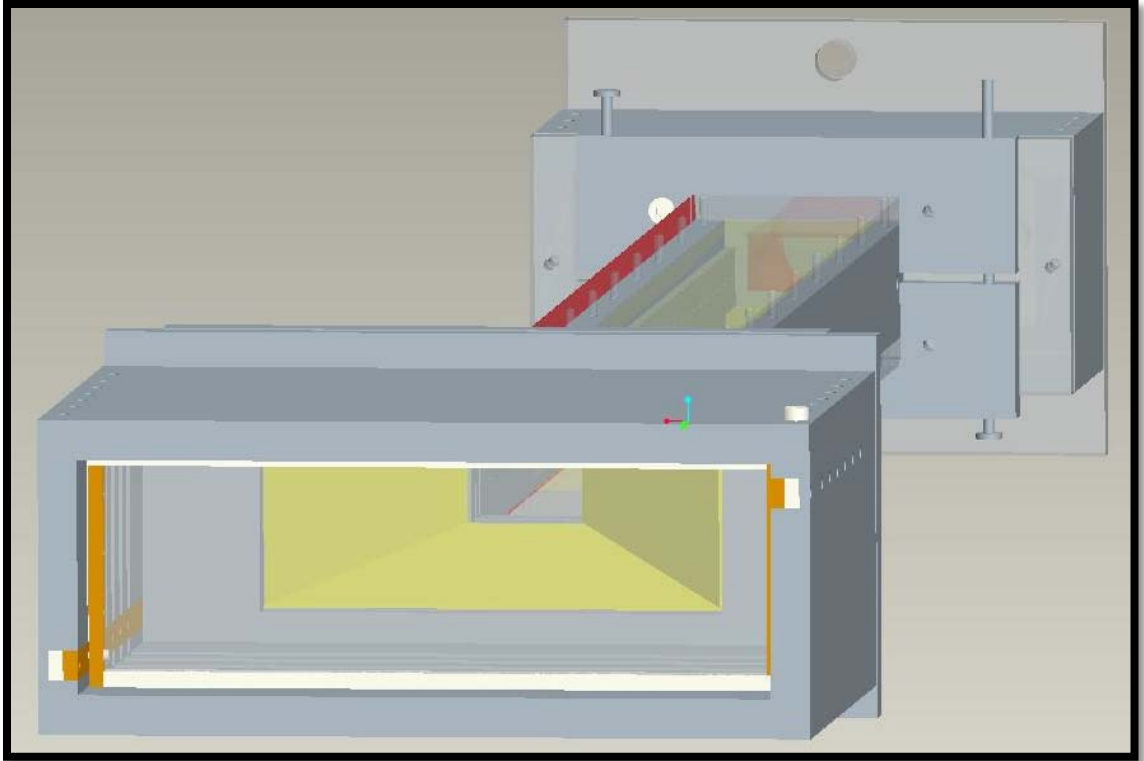


Figure 2.44: Experimental Apparatus



The flow path of the experimental setup to test this cooling channel design is shown in Figure 2.45, below. When operating as designed, the air is pulled through the test section on a vacuum provided by a vortex blower (Figure 2.46). Air enters through the heater module on the left side of the supply enters through the left side of the heated test section and exits to atmospheric conditions. Testing is performed using a Transient Liquid Crystal Technique in which the step change in temperature is provided using an instantaneous mesh heater. The heater module is power by a high current, DC power supply which is switched on at the start of the test. This is  $t=0$  for the test.

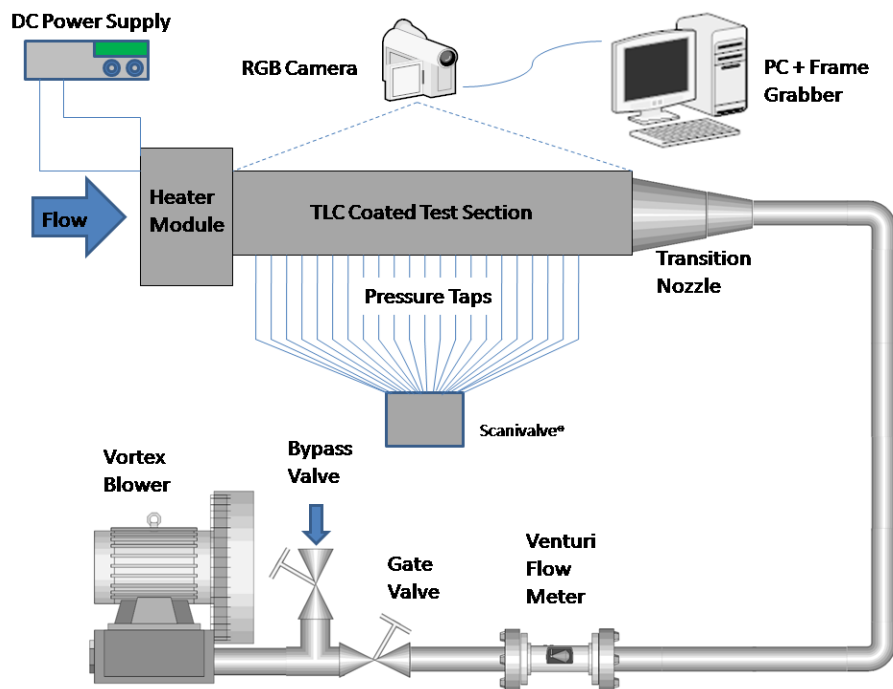


Figure 2.45: Complete Experiment



**Figure 2.46: Vortex Blower**

Temperature data is recorded by taking a time history of the visible color change of the TLC coating applied to the channel walls. A Panasonic NVGS240 3CCD digital-video recorder with a resolution of 2.4 megapixels and a capture frame-rate of 30 frames per second will be used for this task. Spatial resolution is approximately one pixel per millimeter. The images are stored on a custom-built, AMD 64-bit PC running 64-bit Windows Professional. A FPG 32-bit color frame-grabber is installed into a PCI slot on the motherboard and is connected directly to the video cameras using a standard USB

cable. These images are analyzed, frame-by-frame, using a MATLAB code to determine the time history of the recorded RGB values of the color present at each individual pixel. The quantitative RGB values are compared to a calibration curve established using thermocouples.



**Figure 2.47: Panasonic NVGS240 3CCD Digital-Video Recorder**

This process generates a time-history of the temperature development in the channel. Knowing the temperature of the wall at a specific small point on the wall of the channel and knowing the local flow temperature as caused by the instantaneous mesh heater (a controlled value to achieve a specific step change in temperature for a specific mass-flow rate), it is possible to calculate the local heat transfer coefficient at this small point on the wall of the channel (The data reduction section of this work covers this process in greater

detail). These local temperature measurements will allow for the detailed study of the actual physical phenomena caused by the various testing configurations being studied by calculating the local heat transfer coefficient. This will allow for an even greater understanding of the effectiveness of these geometries and the implications that hold to the main goal of this project, increased turbine efficiency.

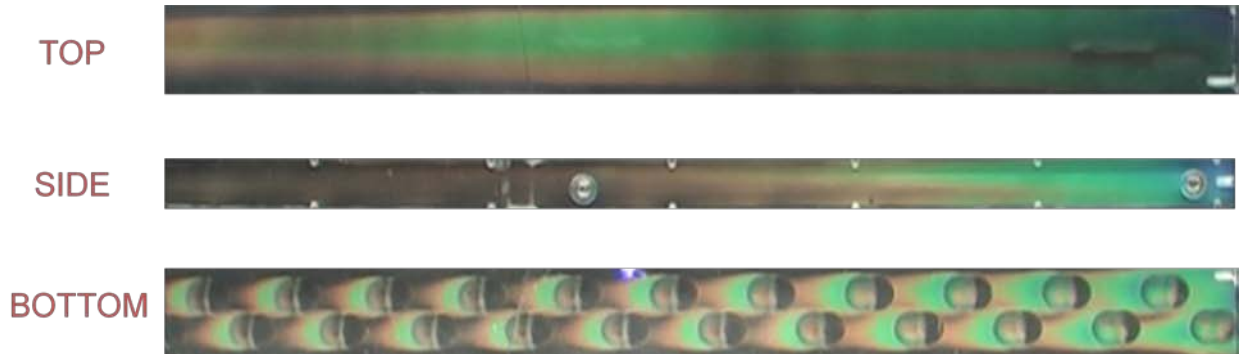


**Figure 2.48: Single Snapshot of TLC Color Change (One Instant in Time)**

To test the friction factor augmentation, the flow is first set to desired Reynolds number in the test section. Static pressure measurements are taken using a Scanivalve® device throughout the length of the channel, to determine the static pressure profile throughout the fully developed region of the channel. To test the Heat Transfer Coefficient of the channel walls, the flow is first set up according to the flow distribution for the desired Reynolds number in the Heat Transfer test section. Recording is started with the digital video cameras and the entire experiment is isolated from any surrounding light sources by a blackout material, which is draped over the support frame. With the flow running and the cameras recording, the power supply is switched on and allowed to stabilize with current is being diverted through the dummy mesh. Once the power supply has reached a steady value, power is diverted to the heater mesh inside the plenum providing a step in the temperature of the flow. At that very instant, the starting time in the recorded video is

marked by an LED light source wired into the heater mesh circuit that is placed in the viewing pane of the recorded image. The test is continued until the entire channel has reached a temperature higher than the color-play bandwidth. At which point the power supply is turned off and the channel is allowed to cool before testing the next Reynolds Number. Testing is always performed at the highest Reynolds Number first, and in decreasing order. This is done to minimize the impact of any hysteresis effects that may be present in the flow regulation system.

### Data Reduction

To characterize the pressure loss data in the channel, the Darcy friction factor is calculated through the fully developed portion of the channel. For validation purposes, and for any pure-channel tests performed, this valued is compared to a theoretical value established by the Blasius solution for Friction Factor in a fully-developed, smooth-wall pipe flow, calculated using.

$$f_0 = 0.316 * Re^{-\frac{1}{4}} \quad (19)$$

The experimental friction factor is determined from the static pressure measurements recorded by the Scanivalve™® using

$$f = \frac{\frac{dP}{dl} * D_h}{0.5 * \rho * V^2} \quad (20)$$

where  $\frac{dP}{dl}$  is determined experimentally to determine the Moody friction factor of the dimpled channel. Flow velocity is known by the continuity equation and the known mass flow-rate from the venturi measurement. The venturi is calibrated and known to accurate within  $\pm 0.01\%$ . This and the contributions from the manometer accuracy are found to

create an overall uncertainty in mass flow rate of less than 0.5%. After validation, the value of  $f$  from the Blasius solution will be used as the baseline  $f_o$  for augmentation purposes in all of the featured cases.

The local heat transfer coefficient ( $h$ ) over a surface coated with liquid crystals can be obtained from a transient test using the 1D semi-infinite solid model. This assumption is made with the prior knowledge or calculation of a sufficiently high heat transfer coefficient, acceptable thermophysical properties of the fluid/wall, and a sufficiently short test duration. The heat diffusion equation, for the one-dimensional case, reduces to:

$$k^* \frac{\partial^2 T}{\partial x^2} = \rho c_p \frac{\partial T}{\partial t} \quad (21)$$

The known boundary conditions are as follows:

$$\text{at } t = 0, T = T_i$$

$$\text{at } x = 0, -k \frac{\partial T}{\partial x} = h^*(T_w - T_m)$$

$$\text{at } x \rightarrow \infty, T = T_i$$

From Incropera and Dewitt (Incropera & Dewitt, 2006), (21) can be solved with the initial and boundary conditions can be used to obtain the non-dimensional surface temperature at the convective channel surface.

$$\frac{(T_w - T_i)}{T_\infty - T_i} = 1 - \exp(\beta^2) \operatorname{erfc}(\beta) \quad (22)$$

$$\text{where } \beta = h^* \left( \frac{t}{\rho c k} \right)$$

After initial smooth wall validation testing, it was determined that the experiment was exhibiting some non-ideal effects and an actual temperature step was not an accurate assumption. This is attributed to such things as energy storage in the mesh, heat lost to the channel walls, and the pass-through time of the heater mesh. To account for this, Duhamel's superposition theorem is applied as suggested by Metzger and Larsen (Metzger & Larson, 1986). By segmenting the overall temperature change into a number of smaller temperature steps (Figure 2.49), the accuracy of the method can be maintained by use of (23).  $T_w$  is the wall temperature read from the reflected color of the TLC at every pixel location based on the calibration curve determine previously The Initial temperature,  $T_i$ , of the test surface is measured using a thin-foil thermocouple attached to the channel whose output is recorded before the test is begun.

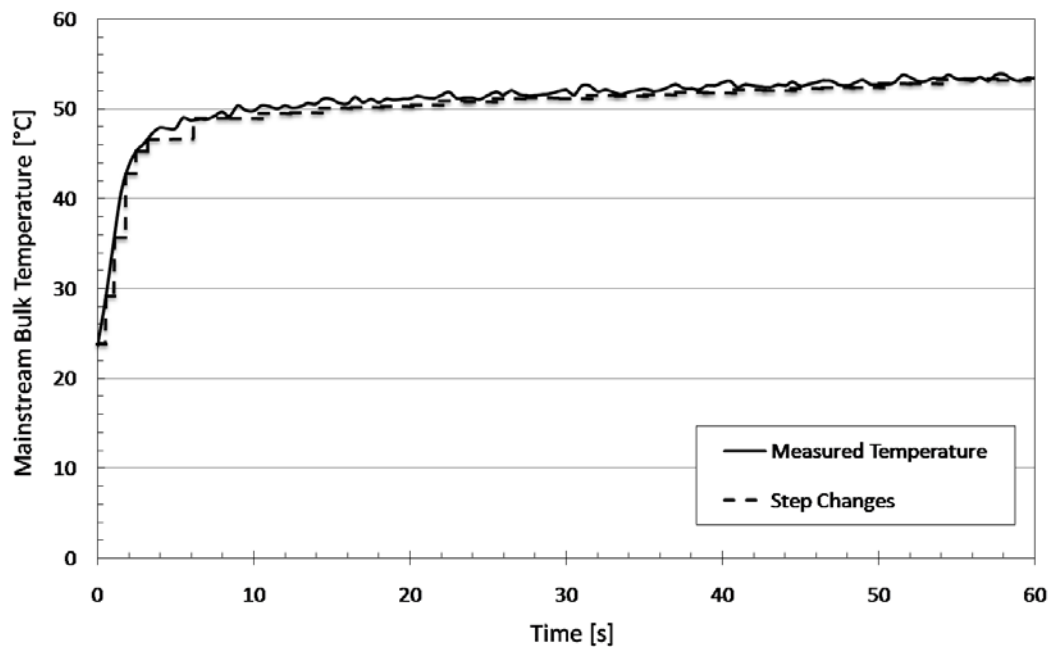


Figure 2.49: Time History of a Mainstream Temperature with Superposition of Step Changes

Thermocouples are placed in the mainstream flow at several locations throughout the length of the channel. Using the superposition method, the mainstream temperature as a function of time had to be known throughout the entire length of the test for proper discretization. Also, it was determined that the initial assumption of negligible heat loss (and therefore temperature drop) throughout the length of the channel was unrealistic. Therefore, a non-linear regression analysis is performed on the data recorded from these probes to develop a representative equation for the mainstream bulk temperature as a function of both time and the streamwise location in the flow. This was found to be crucial component of the data reduction process because if the exponential relationship between the temperature components and the final heat transfer coefficient calculation.

$$T_w - T_i = \sum_{j=1}^N \left[ 1 - \exp\left(\frac{h^2 * \alpha * (t - \tau_j)}{k^2}\right) * \operatorname{erfc}\left(\frac{h * (\alpha * (t - \tau_j))^{\frac{1}{2}}}{k}\right) \right] * [\Delta T_{m(j,j-1)}] \quad (23)$$

Based on the relationship for log mean temperature difference, to determine the temperature driving force for heat transfer throughout the channel equation (24) is taken as the basic form.

$$\frac{T(x,t) - T_w}{T_{in} - T_w} = e^{-(A*x)} * (1 - e^{(B*t)}) \quad (24)$$

where  $A = \frac{h*A}{m*c_p}$  and B is a constant for the transient response of the system. Taking the

series expansion yields:

$$\frac{T(x,t) - T_w}{T_{in} - T_w} = \left(1 - A * x + \frac{A^2 * x^2}{2} - \frac{A^3 * x^3}{6} + \dots\right) * (1 - e^{(B*t)}) \quad (25)$$

Knowing that  $|A * x| \ll 1$ , it is safe to ignore the higher order terms, yielding the form:



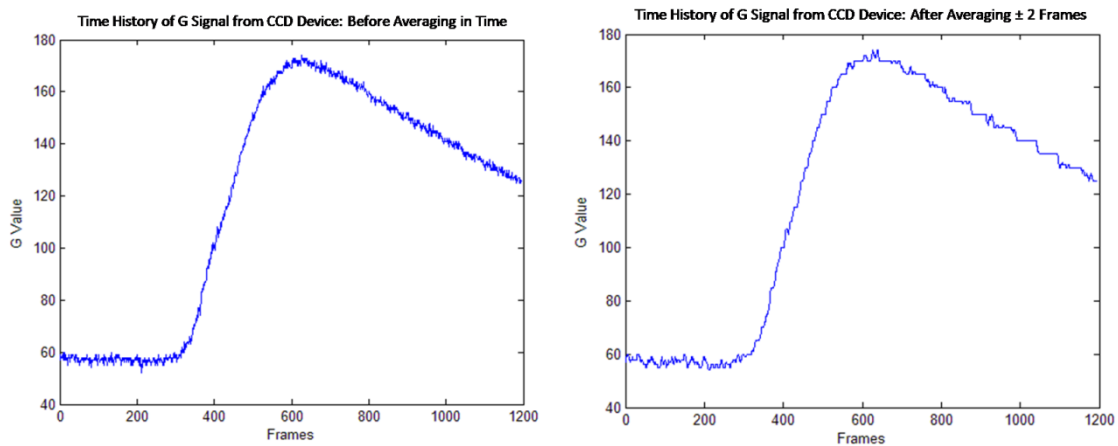
$$\frac{T(x,t)-T_w}{T_{in}-T_w} = (1 + A * x) * (1 - e^{(B*t)}) \quad (26)$$

Table 5 summarizes the results from the regression analysis performed for each test of this study.

**Table 5: Table of Constants to Characterize the Bulk Temperature as a Function of Time and Streamwise Location in the Channel**

$\frac{T_{\text{bulk}} - T_{\text{initial}}}{T_{\text{bulk,max}} - T_{\text{initial}}} = \frac{\theta}{\theta_{\text{max}}} = (1 - Ax) * (1 - e^{B*t})$				
T <sub>initial</sub> (°C)		T <sub>bulk,max</sub> (°C)	A (in <sup>-1</sup> )	B (s <sup>-1</sup> )
SW – 20k	23.56	53.14	0.0067779	-0.345062
SW – 30k	23.21	55.16	0.0053791	-0.499282
SW – 40k	23.13	53.25	0.0044729	-0.523222
SD – 20k	23.18	57.52	0.0051261	-0.541903
SD – 30k	23.17	61.46	0.0051453	-0.394418
SD – 40k	23.15	62.81	0.0070719	-0.277271
LD – 20k	22.99	51.99	0.0072317	-0.288007
LD – 30k	22.99	53.56	0.008084	-0.398872
LD – 40k	22.95	54.60	0.006035	-0.492071
DD – 20k	23.11	54.65	0.008393	-0.302179
DD – 30k	23.05	55.03	0.007576	-0.372101
DD – 40k	23.04	55.88	0.007397	-0.502996

The recorded video is imported to a frame grabber on the data acquisition computer. The images are first run through a MATLAB processing code to crop the images down to include only the regions of interest, reducing processing time and the likelihood of error. The cropped images are then used to generate a three-dimensional matrix in of the G signal values for each pixel in the X-Y spatial coordinates and time. To minimize noise in the data, a filtering procedure is performed on every pixel in the entire array using the `imfilter()` command.



**Figure 2.50: Time History of a G Signal: Before and After Filtering and Averaging**

Spatial averaging is performed between the nine surrounding pixels of each image pixel. Averaging in time was very carefully considered, as any ‘blurring’ in this dimension could drastically effect the calculation of the final heat transfer coefficient. It was determined that  $\pm 2$  frames would lead to effective filtering of the data with only a negligible consequence on the final solution.

Once filtered, the time-history of each pixel is scanned for the presence of a maximum in the value of G. At this point, the values of all three components of the color-space are taken and the value of  $T_{\text{wall}}$  and  $t$  are determined for that pixel at that discrete point in

time. Knowing  $T_i$  and  $T_{bulk}(x,t)$ , it is a simple computation to find the local values of the surface heat transfer coefficient at every pixel recorded from the surface temperature measurement. For the purpose of comparison to the literature, Nusselt Number is also found using the form in equation (27).

$$Nu = \frac{h * D_h}{k_{fluid}} \quad (27)$$

Similar to the friction factor testing, for validation purposes, and for any pure-channel tests performed, this value is compared to a theoretical value established by the Dittus-Boelter and Gnielinski Correlations, calculated using (28) and (29) respectively. The power added to the Prandtl number term in this case is chosen as 0.3 because in transient testing, the heat is flowing from the fluid into the wall.

$$Nu_{DB} = 0.023 * Re^{0.8} * Pr^{0.3} \quad (28)$$

$$Nu_{GN} = 0.0214 * (Re^{0.8} - 100) * Pr^{0.4} \quad (29)$$

Upon completion of the smooth wall validation, the correlation with the best fit will be chosen as the baseline for all augmentation calculations.

### Experimental Uncertainty

The experimental uncertainty in the reported values was calculated using the second-power equation for the estimation of uncertainty given in Kline and McClintock (Kline & McClintock, 1953) on the semi-infinite conduction equation (22). Bias and precision errors were considered for all contributions from instrumentation, data acquisition, calibration, and curve-fits included in the analysis with 95% confidence interval. Table 6

gives the calculated values and uncertainties of a representative case along with the respective percentages.

**Table 6: Uncertainties – Transient TLC Experiment: Double Dimple, Re = 30000**

	<i>Experimental Value</i>	<i>Calculated Uncertainty</i>	<i>Percentage Uncertainty (%)</i>
$T_{WALL}$	308 ± 0.4	K	0.129
$T_{\infty}$	328 ± 2.13	K	0.649
$T_{INIT}$	296 ± 0.5	K	0.169
$t$ (time)	28.3 ± 0.066	s	0.233
$\dot{m}$	0.0214 ± 0.00008793	kg/s	0.411
Re No.	29957 ± 912		3.044
$\Delta P$ (channel)	626 ± 27	Pa	4.313
$f_0$	0.02402 ± 0.000184		0.767
$Nu_0$	81.67 ± 2.01		2.458
$f$	0.03934 ± 0.002152		5.471
$Nu$	121.45 ± 7.04		5.819
$f/f_0$	<b>1.64 ± 0.09</b>		<b>5.524</b>
$Nu/Nu_0$	<b>1.49 ± 0.09</b>		<b>6.297</b>

Lower level-uncertainties were calculated and output for better understanding of the experimental uncertainty of the final values. Using an eight-bit representation of the RGB values, measurement of the Green signal is assured to be better than 1% accurate (Stasiek & Kowalewski, 2002). After calibration, an uncertainty of approximately  $\pm 0.6^{\circ}\text{C}$  is calculated at the peak green temperature. This yields a percentage uncertainty in the value of  $T_{wall}$  of approximately 0.17%, which is comparable to the values predicted calculated by Farina et al. (Farina, Hacker, Moffat, & Eaton, 1994) for the low temperature bandwidths of a narrow-band liquid crystal.

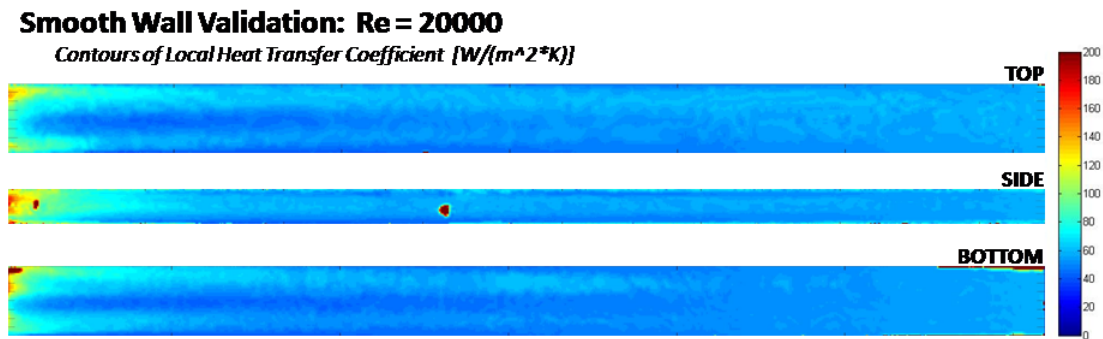
Excluding the inherent uncertainty in the Dittus-Boelter correlation, the uncertainty in  $Nu/Nu_0$  was calculated to approximately 6.3%. The calculated uncertainty for  $f/f_0$  was calculated to be approximately 5.5%. The table shows that the highest contributor to the

experimental uncertainty in heat transfer augmentation stems from the calculated bulk temperature. Though the percentage uncertainty in the value of the temperature itself is less than one percent, the exponential relationship between the temperature differences results in a high sensitivity to this value. The primary source of error in the calculated friction factor is the measured pressure drop. By nature, dimples have a very low pressure drop penalty. As a result, the measured pressure drop is seen to inherit as much as five percent uncertainty. This effect is seen in the increased uncertainty in the calculated friction factor for the feature channel.

## Smooth Wall Validation

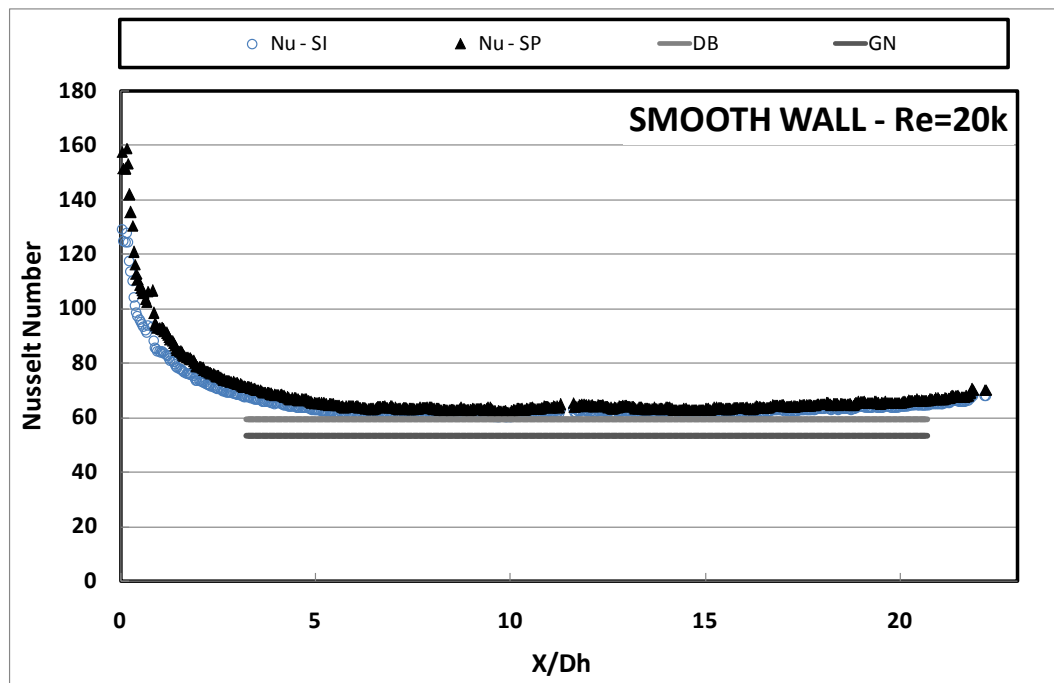
### Heat Transfer

Figure 2.51 presents the local contours of the smooth wall validation test performed at a Reynolds number of 20000. The flow enters the channel from the left and exits on the right. All four walls were observed to have the same spanwise averaged heat transfer coefficient (within  $\pm 1\%$ , which is well within the range of experimental uncertainty) at each location throughout the streamwise length of the fully-developed portion of the channel.



**Figure 2.51: Local Heat Transfer Coefficient Contours - Smooth Wall, Re = 20000**

The spanwise averaged Nusselt number for each row of pixels is given as a function of channel length in hydraulic diameters in Figure 2.52. The flow is fully-developed within approximately five hydraulic diameters, which is typical of turbulent flows. A strict arithmetic mean of the area-weighted, spanwise averaged Nusselt numbers throughout the fully-developed portion reveals that the channel Nusselt number is approximately eight percent greater than the value predicted by the Dittus-Boelter correlation and twenty percent greater than the value predicted by the Gnielinski correlation (see Table 8).



**Figure 2.52: Regionally Averaged Heat Transfer Coefficient Plotted Against X/Dh - Smooth Wall, Re = 20000**

Similar to the copper-block experiments smooth wall validation, the Dittus-Boelter correlation has an inherent uncertainty of  $\pm 25\%$  ((Incropera & Dewitt, 2006), Equation 8.6, Page 514), within which these results comfortably fall. Also, in the calculation of the Dittus-Boelter correlation, the hydraulic diameter assumption is made in the calculation of the channel Reynolds number. Though widely accepted, this assumption can be

misleading. Because the channel used in this study is rectangular, secondary flows are present due to the corner effects that can lead to increased convective heat transfer that is not present in a circular pipe.

Figure 2.51 presents the local contours of the smooth wall validation test performed at a Reynolds number of 30000. The flow enters the channel from the left and exits on the right. All four walls were observed to have the same spanwise averaged heat transfer coefficient (within  $\pm 2.2\%$ , which is well within the range of experimental uncertainty) at each location throughout the streamwise length of the fully-developed portion of the channel.

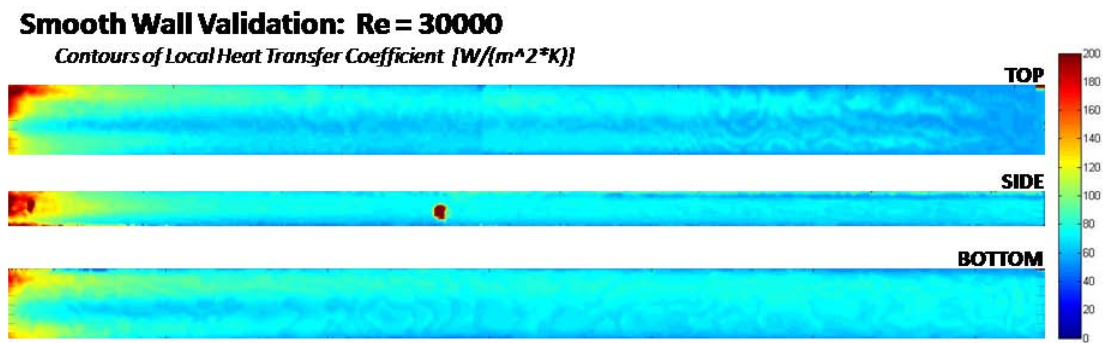


**Figure 2.53: Local Heat Transfer Coefficient Contours - Smooth Wall, Re = 30000**

The spanwise averaged Nusselt number for each row of pixels is given as a function of channel length in hydraulic diameters in Figure 2.54. The flow is fully-developed within approximately five hydraulic diameters, which is typical of turbulent flows. An arithmetic mean of the area-weighted, spanwise averaged Nusselt numbers throughout the fully-developed portion reveals that the channel Nusselt number is less than one percent greater than the value predicted by the Dittus-Boelter correlation and

approximately eleven percent greater than the value predicted by the Gnielinski correlation (see Table 8).

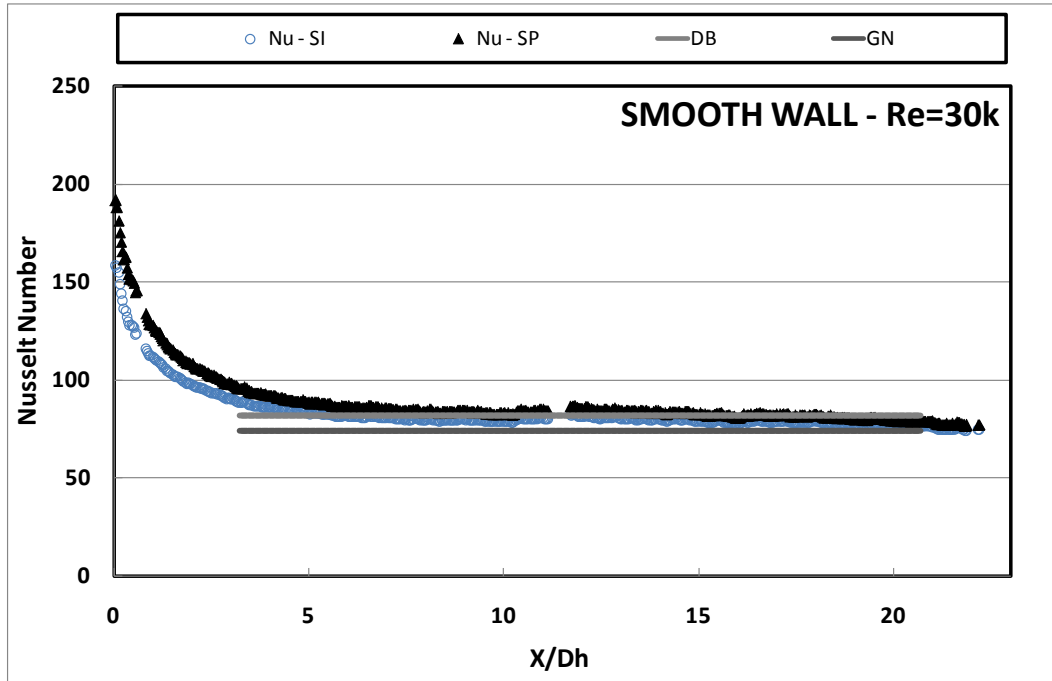


**Figure 2.54: Regionally Averaged Heat Transfer Coefficient Plotted Against X/Dh - Smooth Wall, Re = 30000**

Figure 2.55 presents the local contours of the smooth wall validation test performed at a Reynolds number of 40000. The flow enters the channel from the left and exits on the right. All four walls were observed to have the same spanwise averaged heat transfer coefficient (within  $\pm 1.8\%$  - well within the range of experimental uncertainty) at each location throughout the streamwise length of the fully-developed portion of the channel.



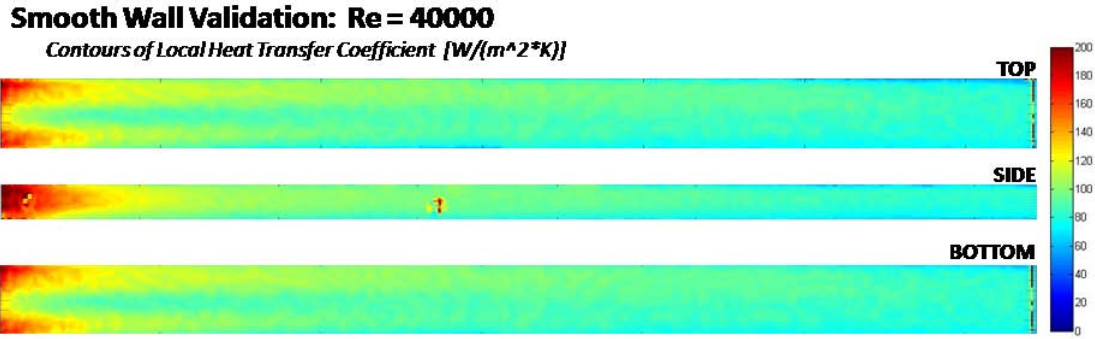


**Figure 2.55: Local Heat Transfer Coefficient Contours - Smooth Wall, Re = 40000**

The spanwise averaged Nusselt number for each row of pixels is given as a function of channel length in hydraulic diameters in Figure 2.56. The flow is fully-developed within approximately five hydraulic diameters, which is typical of turbulent flows. A strict arithmetic mean of the area-weighted, spanwise averaged Nusselt numbers throughout the fully-developed portion reveals that the channel Nusselt number is approximately one percent greater than the value predicted by the Dittus-Boelter correlation and eleven percent greater than the value predicted by the Gnielinski correlation (see Table 8).

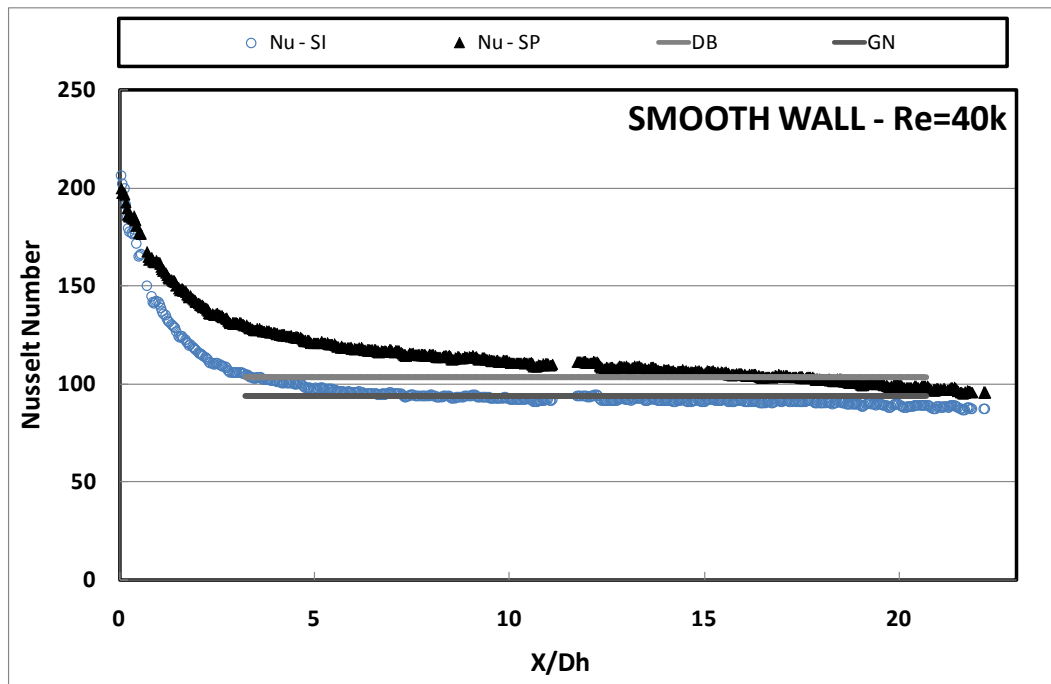


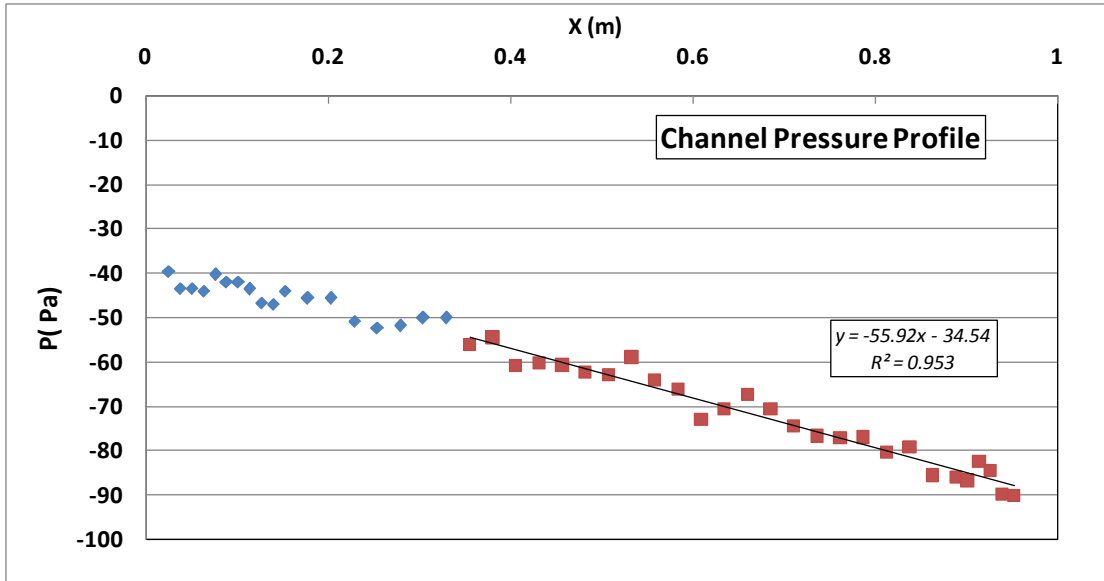
**Figure 2.56: Regionally Averaged Heat Transfer Coefficient Plotted Against X/Dh - Smooth Wall, Re = 40000**

As Reynolds number increases, it is observed that the measured values are converging on the predicted values. As the channel Reynolds number is increased, the inherent mainstream turbulence is increased, resulting in a reduction of the augmentation caused by secondary wall effects.

Another interesting phenomena is the departure of the spanwise averaged Nusselt number curves from each, processed with and without the assumption of a step-change in temperature, as the channel Reynolds number is increased. This is explained by the fact that, as the flow-rate through the mesh heat is increased, the response of the bulk temperature to the power step from the heat is increasingly delayed.

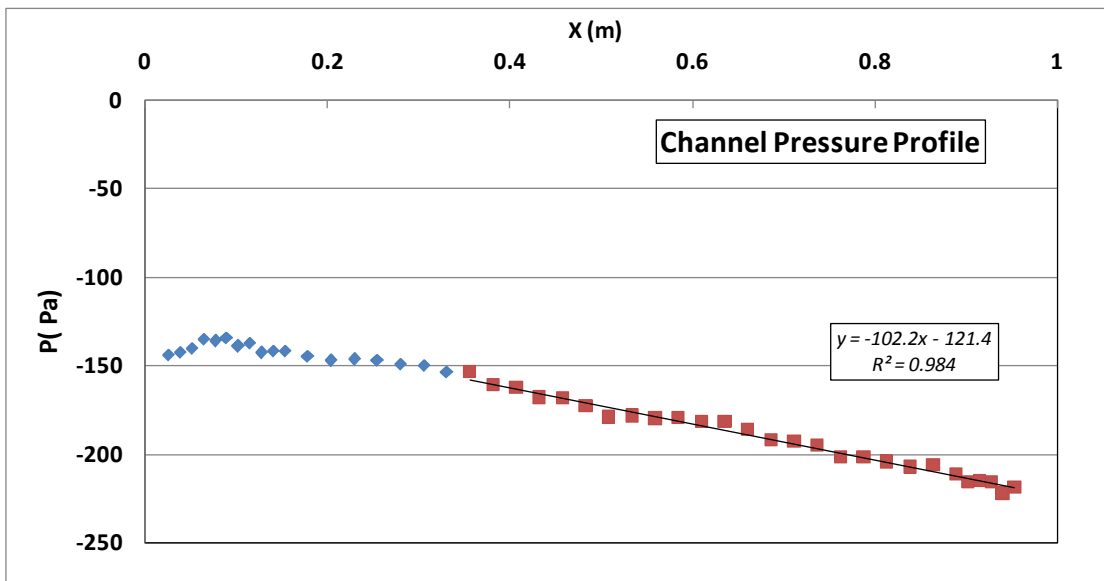
#### Friction Factor

Figure 2.57 is the static pressure profile as plotted as a function of the channel length for 20000 Reynolds number, smooth wall validation. The developing portion is signified by the blue markers. The fully-developed portion is marked by the red squared and the linear curve-fit is taken from this portion to represent the  $dp/dx$  used in the calculation of the channel friction factor.



**Figure 2.57: Static Pressure Profile vs. Channel Length - Smooth Wall, Re = 20000**

Similarly, Figure 2.58 is the static pressure profile as plotted as a function of the channel length for 30000 Reynolds number, smooth wall validation. The developing portion is signified by the blue markers. The fully-developed portion is marked by the red squared and the linear curve-fit is taken from this portion to represent the  $dp/dx$  used in the calculation of the channel friction factor.



**Figure 2.58: Static Pressure Profile vs. Channel Length - Smooth Wall, Re = 30000**

Finally, Figure 2.59 is the static pressure profile as plotted as a function of the channel length for 40000 Reynolds number, smooth wall validation. The developing portion is signified by the blue markers. The fully-developed portion is marked by the red squared and the linear curve-fit is taken from this portion to represent the  $dp/dx$  used in the calculation of the channel friction factor.

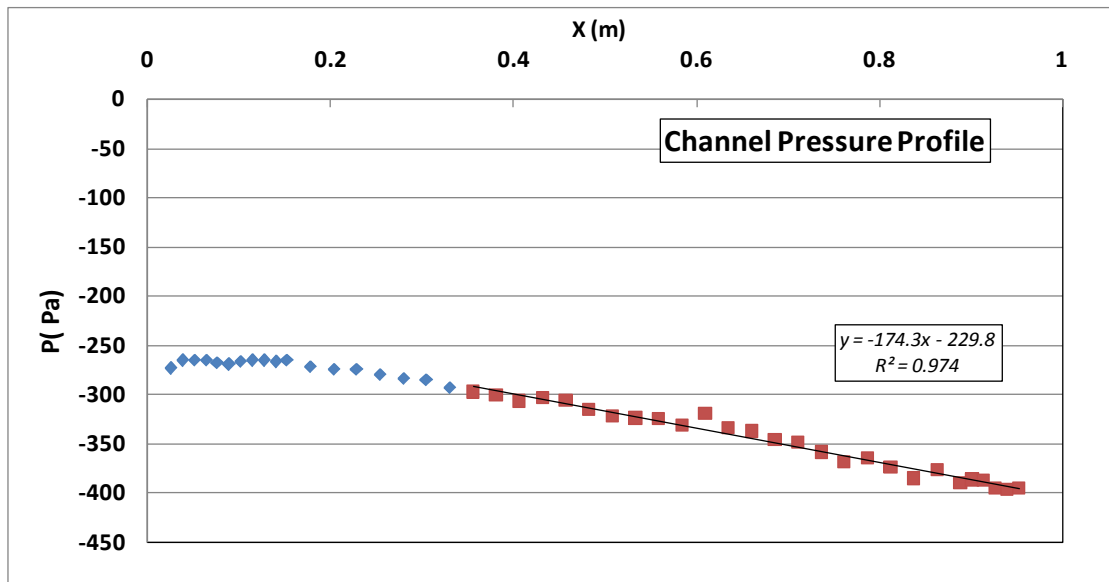


**Figure 2.59: Static Pressure Profile vs. Channel Length - Smooth Wall, Re = 40000**

Table 7 gives the calculated smooth wall friction factors calculated from the experimentally-determined static pressure drop and from the Blasius solution. Moody friction is decreasing with increasing Reynolds number as expected. An important observation to take from this table is that there is a baseline friction factor augmentation (offset) in the rig that is caused by the rectangular cross-section of the channel. The Reynolds number calculation assumes that the channel is round using the hydraulic diameter approximation to establish an appropriate characteristic length. The error of

this assumption is most evident in the friction calculation because, in the direction of the channel height (where  $H < W$ ), the boundary layer is squeezed to a lesser thickness that would be present in a circular duct with the same hydraulic diameter. In this case, the velocity gradient in the direction of the thickness of the boundary layer will be more severe, causing an increase in the wall shear stress. This increase in wall shear stress is the reason for the baseline friction factor augmentation seen in Table 7.

**Table 7: Smooth Wall Friction Factor Validation Summary**

<b>Reynolds Number</b>	<b>dP/dx [Pa/m]</b>	$f$ (experimental)	$f_0$ (Blasius)	$\frac{f}{f_0}$
<b>20078</b>	-55.92	0.0359	0.02654	1.35
<b>30009</b>	-102.9	0.02964	0.02401	1.23
<b>40077</b>	-174.3	0.02815	0.02233	1.26

### Summary of Experimental Setups

#### Validation Complete

As Reynolds number increases, the experimental values for the smooth wall validation approach those predicted by the correlations. Table 8 is a summary of the validation cases run on both experimental setups.

**Table 8: Validation Summary**

<b>SMOOTH WALL VALIDATION SUMMARY</b>										
		Reynolds Number	Nu	$f$	Nuo [Dittus-Boelter]	Nuo [Gnielinski]	$f_0$ [Blasius]	Nu/Nuo [Dittus-Boelter]	Nu/Nuo [Gnielinski]	$f/f_0$ [Blasius]
T-TLC	SI - Super Position	20078	64.03	0.03598	59.3	53.18	0.03	1.08	1.2	1.35
	SI - Single Step		62.23					1.05	1.17	
Copper-Block Setup		19455	63.11					53.87	48.25	
T-TLC	SI - Super Position	30010	82.02	0.02964	81.79	74.11	0.02	1.00	1.11	1.24
	SI - Single Step		79.10					0.97	1.07	
Copper-Block Setup		28881	77.27					73.89	66.88	
T-TLC	SI - Super Position	40078	104.37	0.02815	103.09	93.92	0.02	1.01	1.11	1.26
	SI - Single Step		91.19					0.88	0.97	
Copper-Block Setup		39941	97.08					95.85	87.32	

As we discussed with each rig individually, it is observed that the measured values are converge on the predicted values as the channel Reynolds number increases. Increasing turbulence isotropy, corner secondary flows, and module-to-module transitions provide logical explanations to this observation. Based on the results of the validation, all future cases will be compared to the Dittus-Boelter and Blasius correlations as baseline values for Nusselt number and friction factor augmentation, respectively. Also, the Superposition method of processing the transient local data will be the only method from this point forward for processing data from the transient TLC experiment.

### Application to Study

With two complete experiments complete developed and validated, the laboratory now possesses the appropriate facilities for detailed study of wall-surface features and their heat transfer augmentation characteristics. The experiments detailed in this section will also provide means of self-validation of any measured results: adding support and improved confidence for publication and defense. With the capability of a three-tiered

validation, this setup will also prove to be invaluable for validation of computational models as well.

## **CHAPTER 3: OVERVIEW OF COMPUTATIONAL STUDY**

### Background

Computational Fluid Dynamics (CFD) is a means of solving the equations that govern the flow of mass, momentum, and energy in a computational domain. Stemming from conservation of momentum, the point of departure almost all fluid mechanics problem is the famed Navier-stokes equations; Partial Differential equations containing a nonlinear dissipation term. Numerical solutions of the Navier-Stokes equations are obtained using the finite-volume method, where the computational domain is broken down into a multitude of smaller domains for refined analysis. The algorithms needed to enforce the governing equations on these domains is basis of the science of CFD today.

Over the past decade, high-speed parallel computing has completely changed the scenery of numerical simulation, providing a more clear understanding of complicated flow physics than ever before possible. Through the application of advanced, physics-based modeling, researchers now have new insight and understanding of new physics and processes that can never be measured in experiments.

### Response Surface Methodology

In statistics, Response Surface Methodology explores the relationships between several explanatory variables and one or more response variables. Introduced by George E. P. Box (Box, Hunter, & Hunter, 2005), the beauty in the method is the development of an approximated, second-degree polynomial model to estimate the response of a measured



output to an array of given design inputs. In this way, the research is able to perform a group of designed experiments to gain a thorough understanding of the system under study with minimal cost/investment.

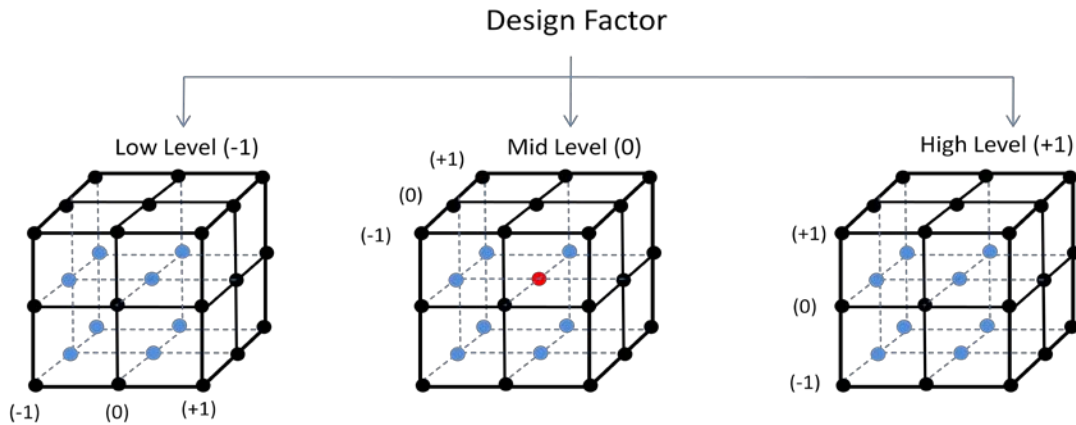


**Figure 3.1: Illustrations of Factorial Design Process**

## Geometry Creation and Meshing

### Use of Journal Files

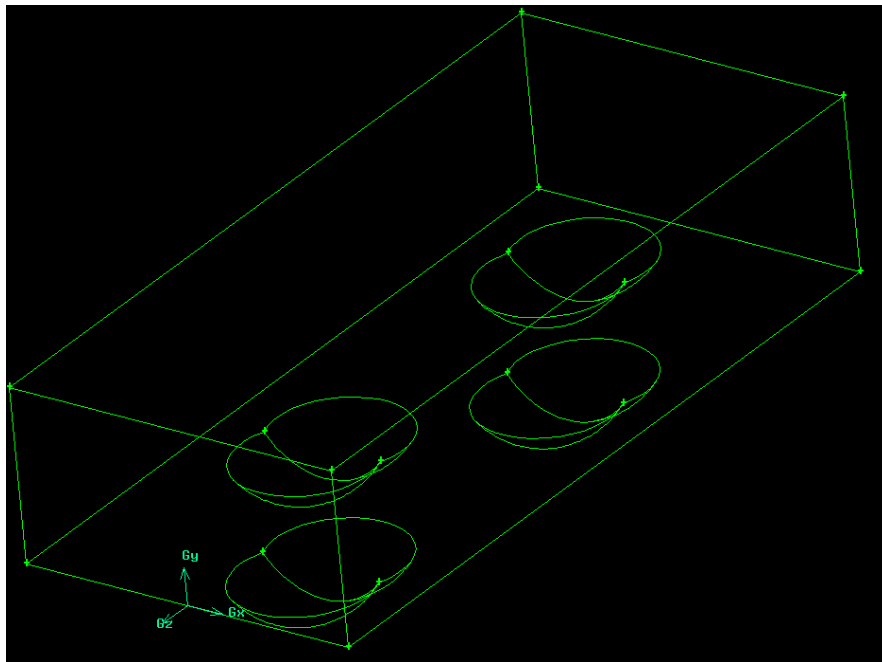
All computational domains generated for this study were developed using the GAMBIT software (v2.4.6). The program maintains a record of all command-line inputs from the user to the program and can, at any time be operated from such an interface. Within the journal file, values can be stored under user-defined variable names and recalled at any time during the journal files run, which proves to be a very useful tool when making any changes to the computational domain. An example would be, when running a grid-dependence study, meshing parameters can be precisely controlled by altering the values of a given meshing parameter, then running the journal file to generate the domain. This tool has also proven to be extremely useful with applications to parametric design studies,

where many combinations of parameters are tested to study the response of the desired performance factor. An example of a GAMBIT journal file is included in APPENDIX D:.

### Generation of Computational Domain

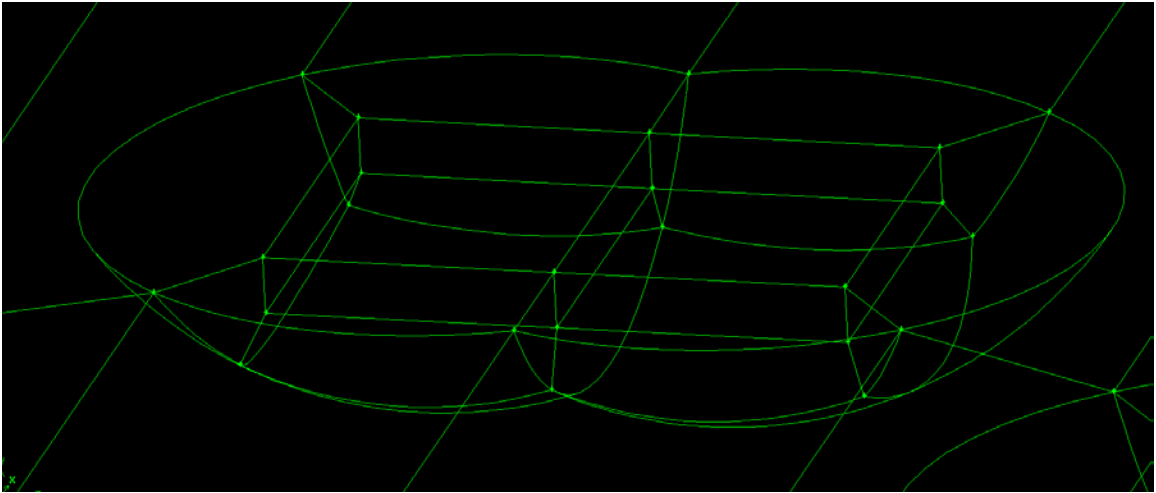
The computational domain was carefully created to enable absolute control over the meshing process. A set of intersecting hemispherical indentions can be very difficult for any meshing algorithm to accurately resolve. To compensate, the features and broken into an arrangement of topological squares and cubes for natural accommodation of a fully-controllable mapped mesh scheme.

The domain was first generated using modeling tools within the GAMBIT software



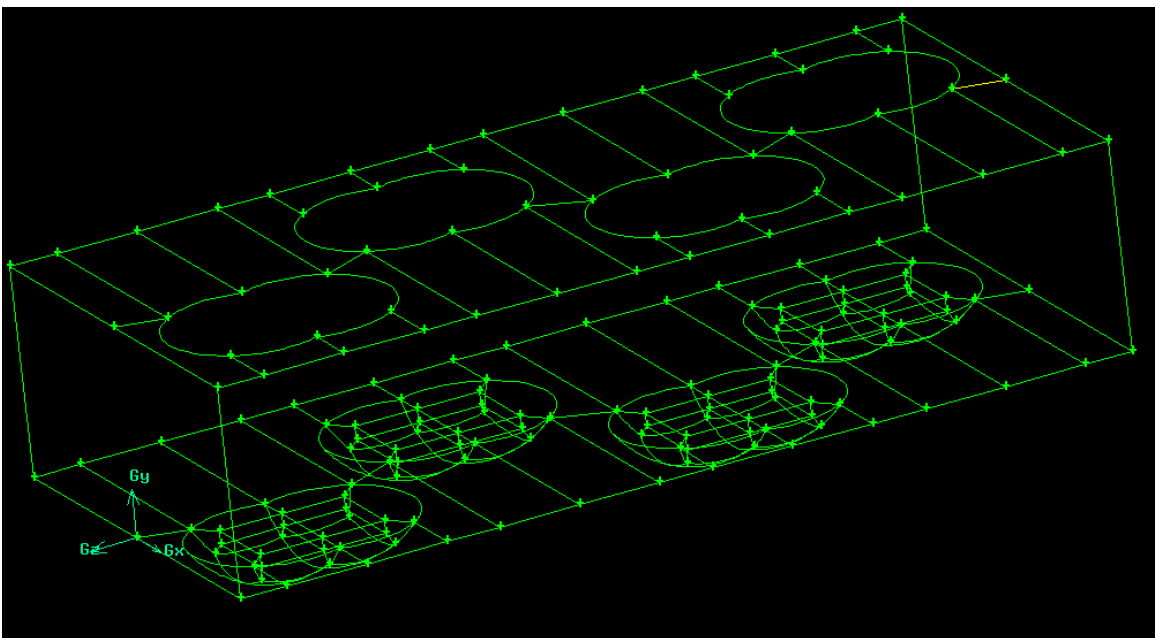
**Figure 3.2: Complete Computational Domain as One Fluid Volume**

Figure 3.3 shows the double dimple surface feature broken into a number of pseudo-hexagonal volumes to aid in the proper application of a mapped mesh.



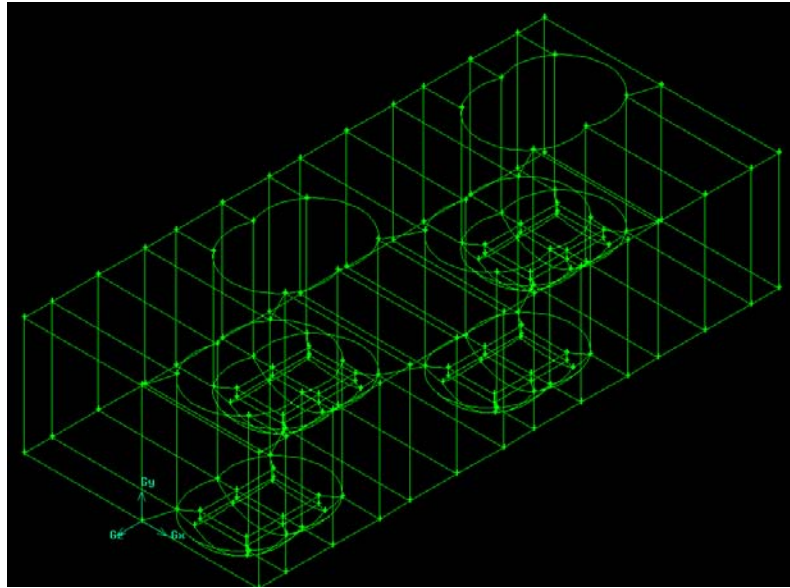
**Figure 3.3: Double Dimple Broken Down into Topological Squares**

The break-up scheme of the dimple must then be extended over the remainder of the channel faces for continuity of mapped meshing scheme (Figure 3.4).



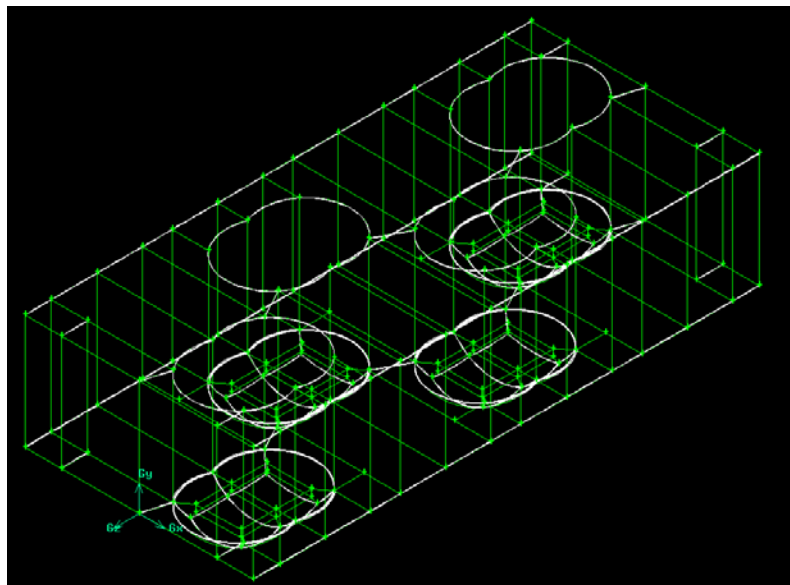
**Figure 3.4: Dimple Break-Down Scheme is Extended to other Surfaces of the Channel**

After dividing the top and bottom faces, the volume of the channel itself is broken down into a multitude of hexagonal volumes Figure 3.5.



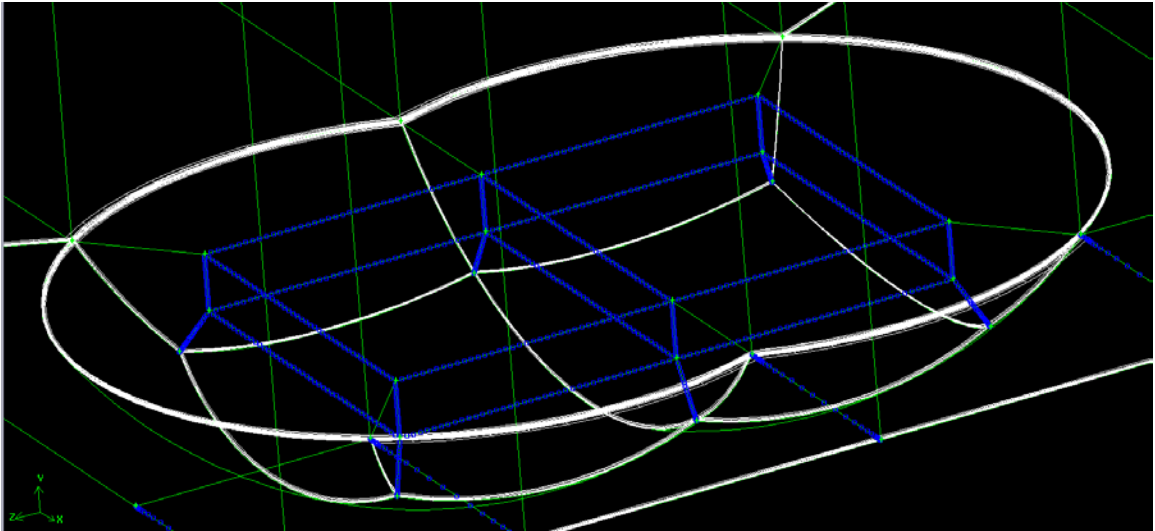
**Figure 3.5: Channel Broken into Hexagonal Volumes**

Figure 3.6 shows the numerical domain after the addition of the boundary layer and transition regions.



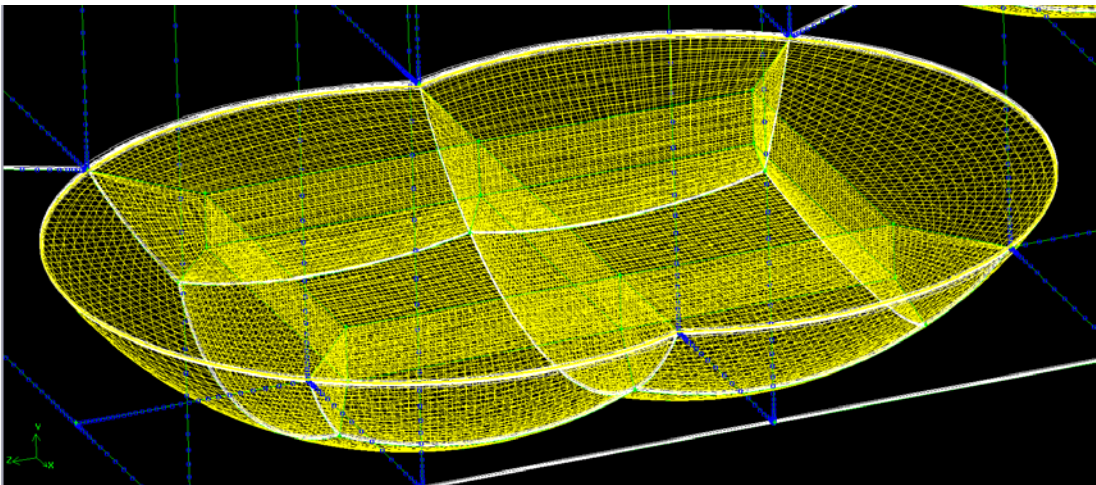
**Figure 3.6: Boundary Layers and Transition Regions Applied**

The double-dimple surface feature with the boundary layers and edge meshing complete is shown in Figure 3.7, below.



**Figure 3.7: Double-Dimple Surface Feature with Boundary Layers and Edge Meshing Complete**

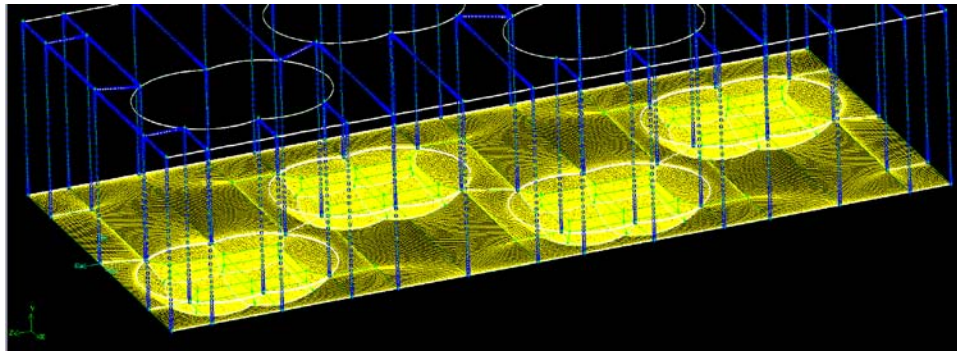
With strategic edge meshing and face mesh generation, all upper-level meshing is fully-constrained and is generated automatically. A fully face-meshed double dimple feature is shown in Figure 3.8.



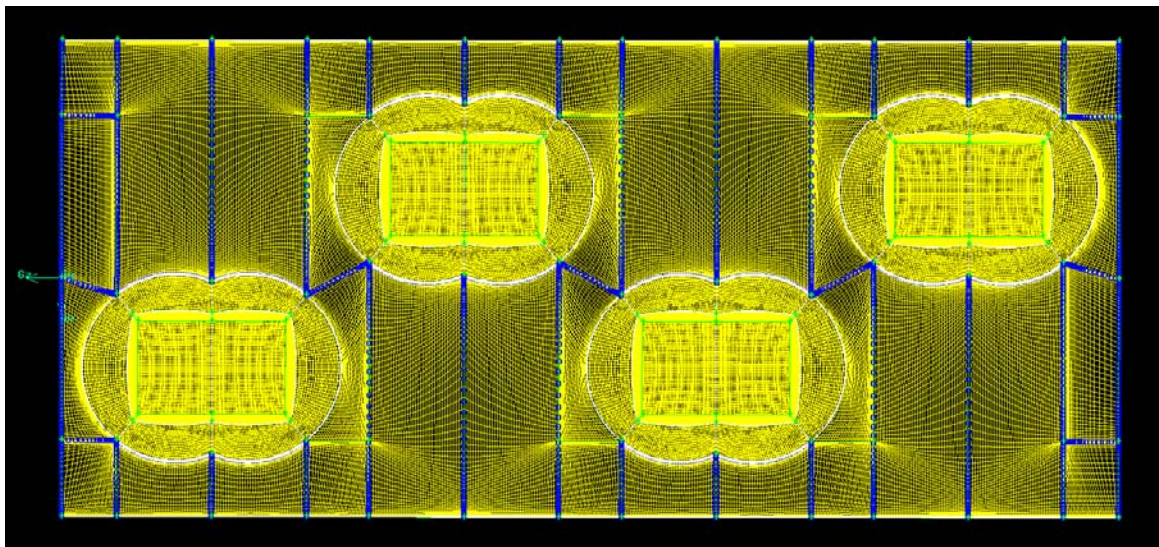
**Figure 3.8: Double-Dimple Face Meshed**



The bottom wall of the channel is the most crucial component of the entire numerical domain as it will be the subject of a majority of the heat transfer study performed in this work. Accurate and detailed solutions are required of this area. The completed face mesh of the dimples and bottom wall is shown in Figure 3.9 and Figure 3.10.

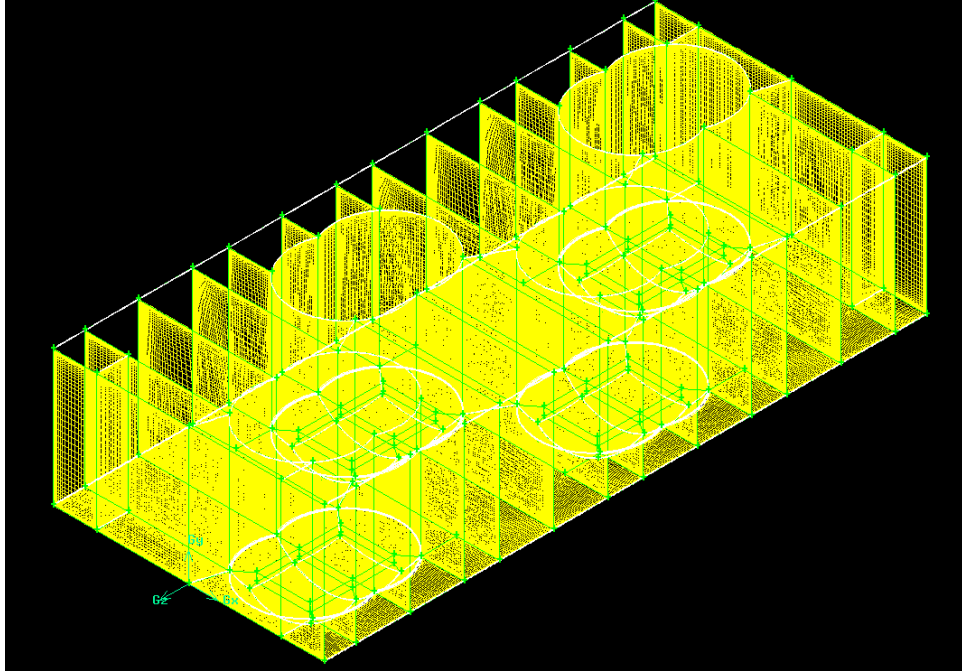


**Figure 3.9: Bottom Wall and Dimples Face Meshed**



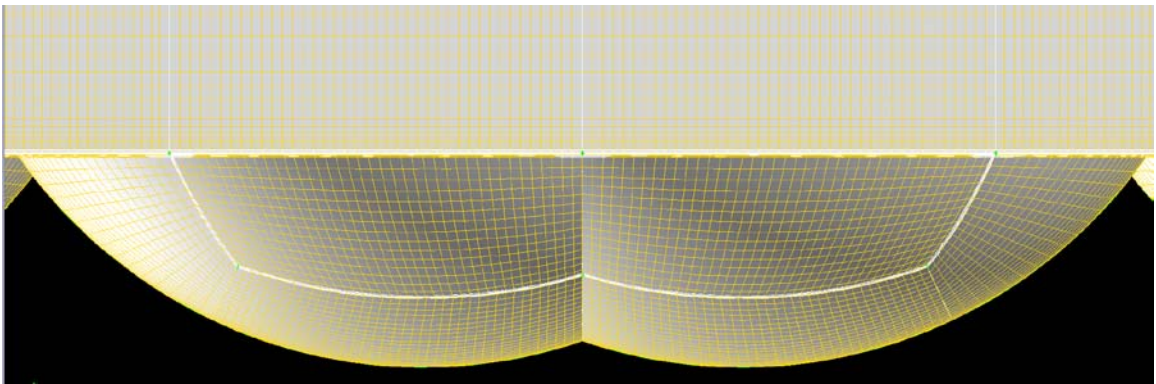
**Figure 3.10: Normal View of Face Meshed Bottom Wall and Dimples**

Figure 3.11 is a view of the entire channel after all face meshing has been completed.



**Figure 3.11: Channel Face-Meshing Complete**

Figure 3.12 is a snapshot of the final mesh of one of the dimple features after all volume meshing has been completed and the boundary conditions have been assigned.



**Figure 3.12: Final Mesh – Dimple**

Figure 3.13 is a similar snapshots taken to also shows the intersection of the bottom wall with the dimple feature mesh.



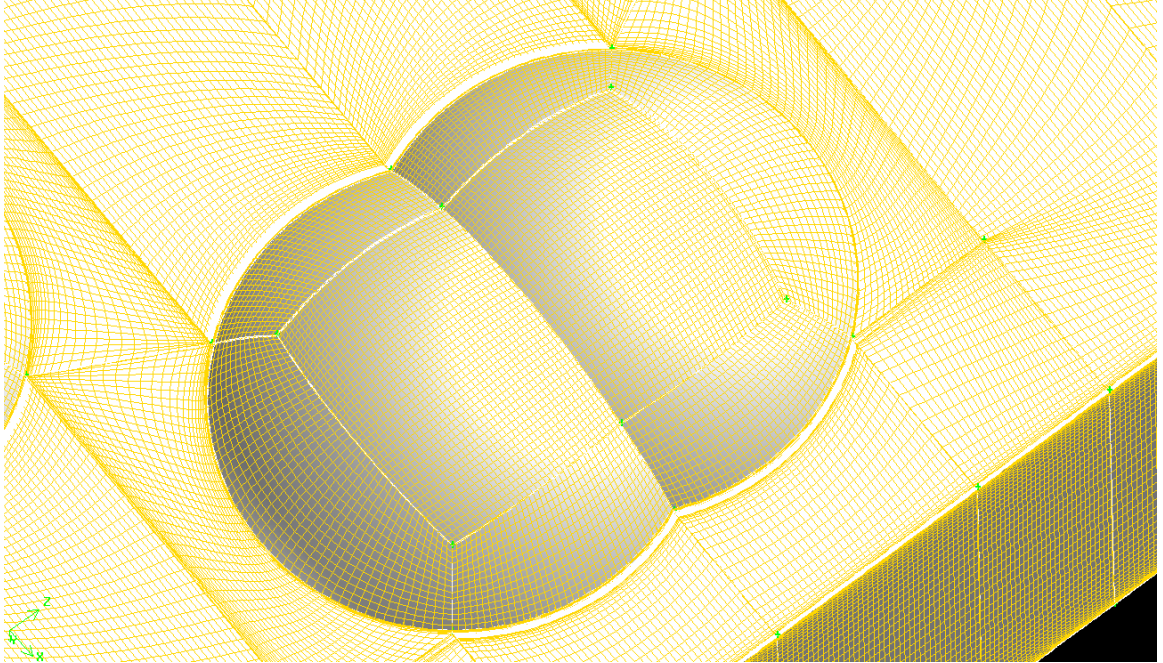


**Figure 3.13: Final Mesh – Bottom Wall and Dimple**

Figure 3.14 is a side view of the final numerical domain.

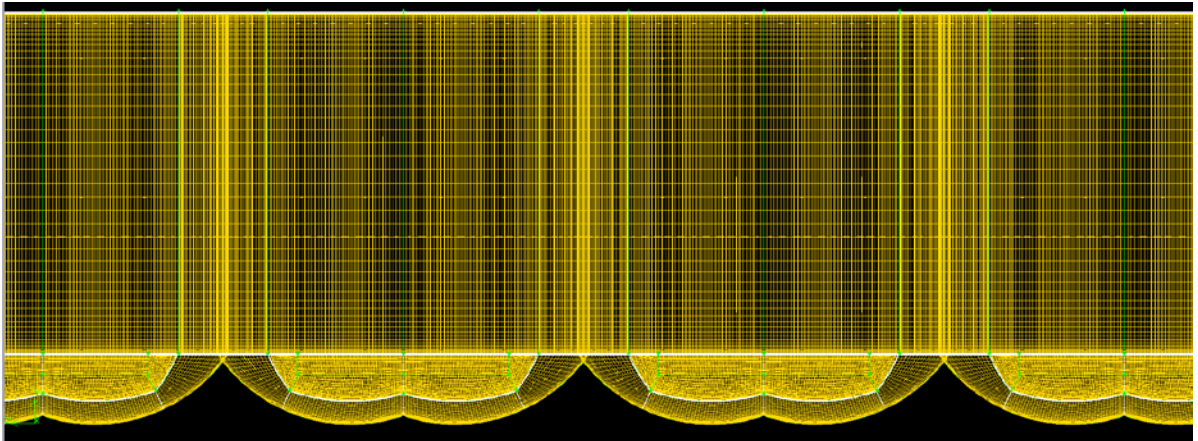


**Figure 3.14: Final Mesh**

In summary, a computational domain was generated to represent the fully-developed portion of a rectangular channel with a Double-Dimple surface feature applied to the bottom wall. The parameters of the feature were modeled as identical to those tested in the experimental study of this work. Great care was taken during mesh generation to



maintain quality without overrunning available computational resources. Total cell counts for the full domain and reduced domain RANS simulations were 2.8 and 3.6 million, respectively. The total cell count for the LES mesh was approximately 6.2 million cells. A quality check on the latter two domains revealed more than ninety-eight percent of the domain had an equisize skew of less than 0.3 and a maximum value of 0.6. Cell aspect ratio and size change were minimized in the near-wall regions by use of transition cells: values of each measure were kept below fifteen and two, respectively.

Periodic boundary conditions were assigned to the inlet and exit planes of the channel and an appropriate body force term was imposed to simulate the driving pressure difference pushing the fluid motion. This term was solved in a sub-iterative procedure in order to maintain the desired fluid mass flow rate. Simulations were performed for three channel Reynolds numbers (based on hydraulic diameter) for direct comparison to experimental results.

Boundary layer features were added to the mesh domain for a first layer thickness of approximately  $0.9 y^+$  or less to accurately resolve the high gradients present in the near wall region that are so critical to accurate solutions of turbulent convective heat transfer from the wall surface. All wall faces were assigned no slip conditions and a constant temperature of 353 Kelvin.

### Grid Dependence Study

A grid-dependence study was performed on the reduced domain RANS mesh. Total cell count was varied from approximately 400,000 cells to 3.7 million; nearly an order of

magnitude change within which an optimal point was chosen as a balance of computational resources and simulation accuracy. Three sampling points were placed in each domain to determine trends in the measured values as a function of the total cell count. GDS\_1 is in the near wall region on the streamwise channel centerplane in between two dimple surface features in the streamwise direction. GDS\_2 is directly above GDS\_1 in the direction of the bottom wall area-normal vector on the channel mid-plane in the direction of the channel height. GDS\_3 is placed in the mainstream flow just above the first dimple, in plane with the bottom wall of the channel.

Total cell count was varied using multiple control variables set in the GAMBIT journal file (see APPENDIX D:). Using this tool, meshing quality was able to be maintained to an acceptable level, even at the lowest total cell counts by performing incremental adjustments to boundary layer thickness and transitioning tools to accommodate the increased cell sizes.

Figure 3.15 shows the relationship between the calculated static temperature at each point and the total cell count of the domain. As expected, the mainstream flow temperatures have slightly lower static temperatures because of their distance from the wall and position within the thermal boundary layer. The saturation point appears to be around 3 million cells.

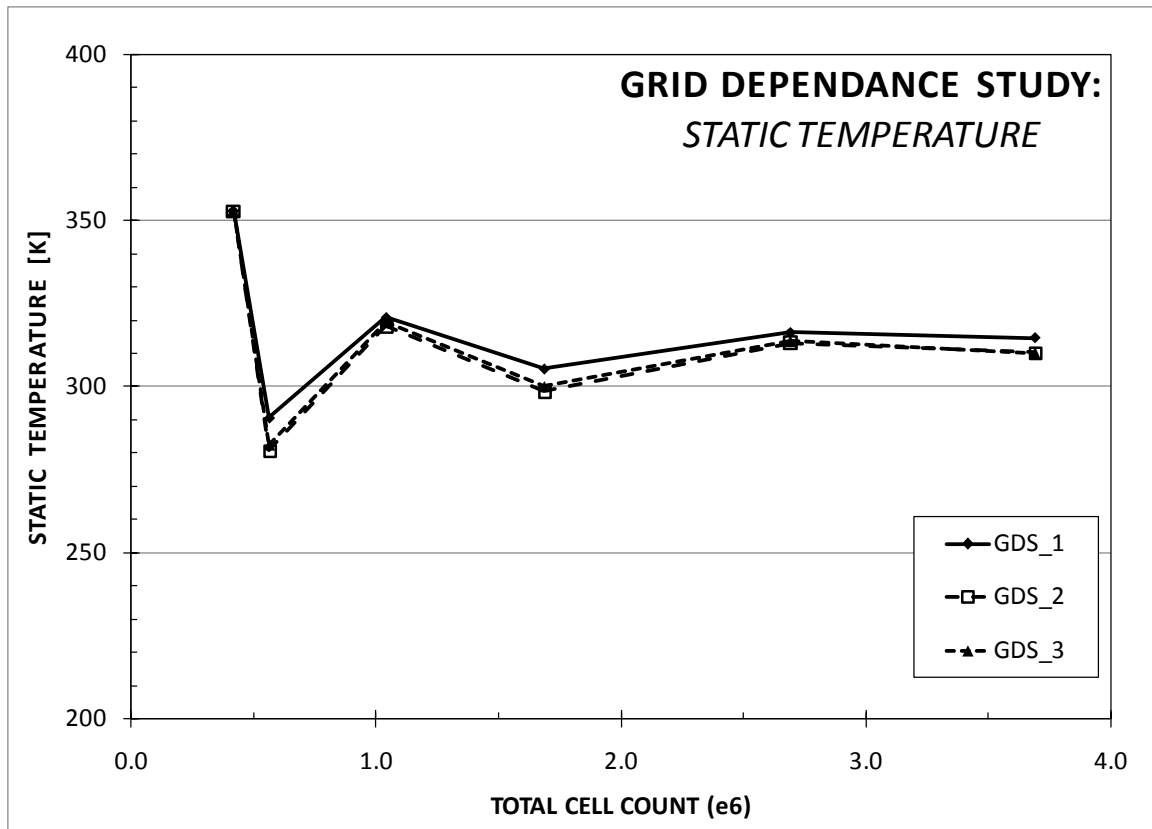


**Figure 3.15: Grid Dependence Study – Static Temperature**

Figure 3.16 indicates a similar trend, with a saturation point of approximately three million cells for the GDS\_1 and GDS\_2 sampling points. While the change in GDS\_3 is decreasing, it is possible that increased grid resolution could be needed for this change to lay completely flat. It was decided, instead, that because of the location of the point in the shearing region of the dimple-mainstream interaction, it should be disregarded for this aspect of the study.

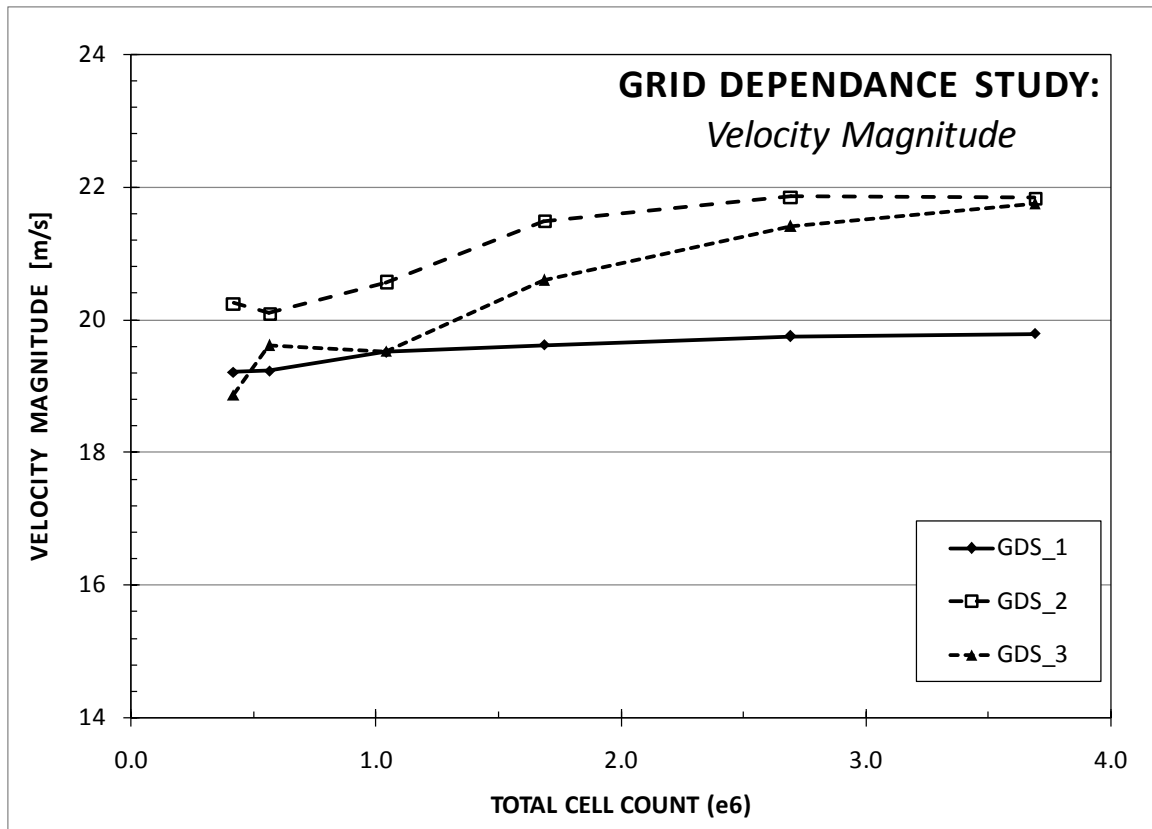
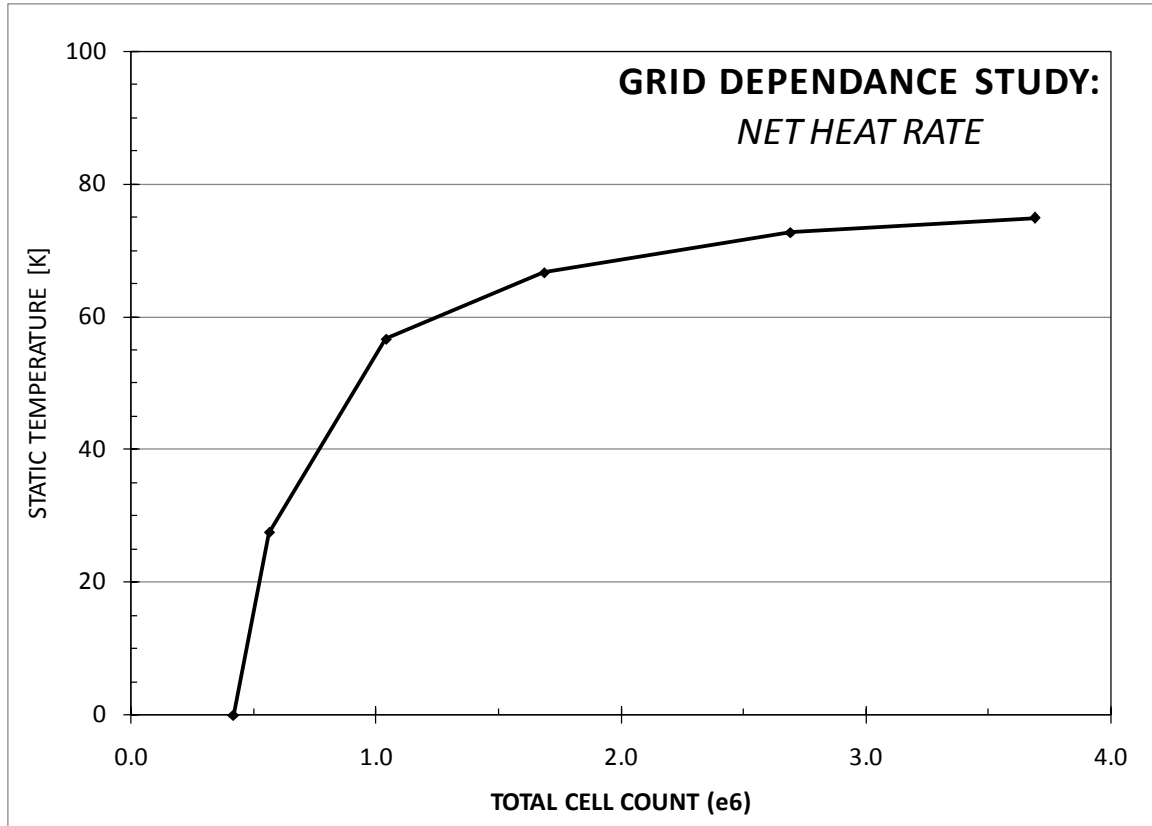


Figure 3.16: Grid Dependence Study – Velocity Magnitude

The net heat flux from the bottom wall is plotted in Figure 3.17 as a function of the total cell count in the computational domain. The trend is seen to increase drastically initially and begin to flatten out around three million cells. Based on the trend of GDS\_1 Figure 3.16, this relationship is expected as that velocity in the near-wall region increasing to promote advection of heat from the channel surface. In addition, increasingly improved resolution of the large temperature and velocity gradients found in the turbulent boundary layer are also known to contribute to such improved accuracies.



**Figure 3.17: Grid Dependence Study – Net Heat Rate (Bottom Wall)**

Due to the recirculating effect that could be caused by the periodic inlet and exit conditions, an initialization dependence study was also performed to determine the residual effect of different initialization values on the final solution. Of particular interest were the dependencies of the turbulent kinetic energy and turbulent dissipation terms. It was determined that, aside from increased required run times, no appreciable difference could be observed by varying these parameters within an order of magnitude of their eventual converged values.

A grid-dependence study was not performed on the numerical mesh employed for the LES solution due to the extreme requirement of computational resources. However, the

generation of the LES mesh was guided by the parameters used in other similar studies published in the open literature. Along the streamwise centerplane, a comparison of the ratio of the characteristic control volume height to the Kolmogorov length scale showed values ranging from 1.6 next to the wall to a maximum value of approximately 20 in the mainstream flow. Based on these values, and the eventual validation of converged solution, it was determined that the numerical mesh was fully appropriate for the LES simulation

### Solution Details

#### Solution Details

The goal of the computational efforts of this work is to capture physics of scales of interaction occurring inside the channel to provide validation and support to experimental findings. Additionally, through the use of unsteady Large Eddy Simulations of turbulence, new insight is gained into the physical phenomena resulting in the improved heat transfer performance.

The FLUENT (v6.3.26) CFD solver is used for this study. FLUENT uses a centered computational pattern, where discrete scalar values of the dependent variable are stored at the center of the cell. Interpolation between contiguous cell-centers is necessary to solve values at the face for convective terms.

A second-order pressure interpolation scheme was used, which interpolates the pressure values at the cell faces using the momentum equation coefficients. This process has been

shown to work well in the absence of sharp changes in pressure between adjacent cell centers. A second-order upwind discretization scheme is applied for momentum, energy, turbulent kinetic energy, and dissipation (upwind meaning that the face value is calculated from the values in the ‘cell-upstream’ direction relative to the normal velocity). Both convective and diffusive terms of the discretized equations are approximated by a second-order central difference scheme. This approach allows second order accuracy to be achieved through a Taylor series expansion of the cell-centered solutions about the cell centroid. In this scheme, the upwind terms are solved for implicitly while the difference between the central-difference and upwind values is treated explicitly. This approach has been proven to exhibit ‘meritoriously low numerical diffusion (Leonard),’ which is ideal for LES runs exhibiting very low subgrid-scale turbulent diffusivity. For incompressible flow applications, FLUENT simply uses arithmetic averaging for density interpolation.

The SIMPLE pressure-velocity coupling scheme is used to save computational resources. It operates by employing the relationship between the velocity and pressure corrections to enforce mass conservation and to obtain the pressure field and therefore, does not require an additional sub-iterative procedure. The SIMPLE algorithm substitutes the flux correction equations into the discrete continuity equation to obtain the pressure correction. It is also more stable in complex domains.

The unsteady LES solutions employ a Bounded Central Differencing scheme in time. The temporal discretization of every term requires the integration of each term in the

governing differential equation over a time step  $\Delta t$ . In all cases run, the characteristic time step was chosen such  $CFL_{\max} < 0.6$  throughout the entire domain.

The temporal discretization of the transient derivative is broken up in time using the same fully-implicit second-order scheme that is used for spatial discretization. FLUENT's pressure-based solver uses an implicit discretization of the transport equation (30), where all convective, diffusive, and source terms are evaluated from the fields for time step  $n+1$ .

$$\int_V \frac{\partial \rho \phi}{\partial t} dV + \oint \rho \phi \vec{v} \cdot d\vec{A} = \int_V S_\phi dV + \oint \Gamma_\phi \nabla \phi \cdot d\vec{A} \quad (30)$$

### Reynolds Average Navier-Stokes

The Reynolds-averaged equations used to solve for turbulent flows that exhibit a statistically-steady mean are developed by substitution of the velocity and scalar decompositions into the unsteady governing equations, then applying time-averaging operation. In equation (31),  $f(\mathbf{x})$  represents the statistical mean value of the variable or property at the vector location  $\mathbf{x} = (x_1, x_2, x_3)$ .

$$\bar{f}(\mathbf{x}) = \lim_{t \rightarrow \infty} \frac{1}{t} \int_{t_0}^{t_0+t} f(\mathbf{x}, t) dt \quad (31)$$

A RANS simulation provides a time-averaged solution to the Navier-Stokes equations. Over the years, a number of closure models have been developed to solve for the second-order tensor of unknowns to quantifying the apparent stresses (Reynolds Stresses) in the flow. Different models have come up with different ways to solve for these unknowns, and choosing the 'correct' model can make the difference between a right and wrong solution.



For this study, Stress Shear Transport model was employed. The SST model is a hybrid that activates the  $k-\omega$  model in the near-wall region and the  $k-\epsilon$  in the bulk flow. It has been shown that, in applications such the present study, when the flow is faced with an adverse pressure gradient,  $k-\epsilon$  alone will over-predict the turbulence length scale in the near-wall region. This will lead to an over-prediction of the heat transfer at the reattachment point. The hybrid SST model instead uses the  $k-\omega$  model to solving a turbulence/frequency-based model in the near-wall region and  $k-\epsilon$  throughout the rest of the bulk flow to capture the separation effects. This, in turn, allows it to more accurately predict the near-wall turbulence that can make or break a computational solutions of turbulent heat transfer.

### Large Eddy Simulation

Large-Eddy Simulation is an unsteady model that provides detailed solutions to the equations governing the flow of fluid and heat through a domain in computationally effective manner. In turbulent flow, LES tries to partition a flow physics into large scale motion (large eddies) and small scale motion (small eddies). The large eddies are characterized outright, using no representative models. The smaller eddies are simulated using a closure model to save computational resources, making LES a more useful model for everyday problems than a DNS solution.

The FLUENT LES solver used in this study is based on the Smagorinski model - assuming that the behavior of the small scale eddies is completely determined by the large-scale motion. This method employs a one-equation model in which the kinetic

energy of the small scale motion ( $k$ ) is introduced taken to be unknown and is solved for iteratively. In the Smagorinski model, there is also second-order dissipation equation for the Reynolds stress of the small scale motions that is solve for directly.

### Solution Processing

Post-processing of computed solutions is initially performed within Fluent itself. Contour plots, vector fields, and other forms of local data are all analyzed using the natural software. Hardcopy images are exported for future referencing. Additionally, Fluent has the capability to export data in the form of an ASCII file, which can then be uploaded into a program, such as Excel™ for further analysis. This process was employed for the surface averaging needed for validation/comparison with experimental data.

## Relevance and Application of Computational Results

### Validation

Local surface heat transfer coefficient contours are compared to those obtained through experimental results. Surface-averaged, channel-averaged, and featured averaged results are also anchored to experimental works to provide a foundation for future development and work with the computational model.

### Insight to Flow Physics

Results from the computational study performed in this work will be used for further validation and support of experimental findings. Modeling of time-averaged turbulent convective heat transfer is performed using the RANS equations for fluid flow with the

SST turbulence closure model. Surface contours of heat transfer coefficient are compared to experimental results along with a detailed quantitative comparison of the surface-averaged values. The streamwise pressure gradient is the subject of analysis. A Large Eddy Simulation study is also performed to gain insight into new flow physics of the unsteady turbulent flow over a dimple surface feature.

## CHAPTER 4: EXPERIMENTAL RESULTS

### Background

This thesis is an investigation of the heat transfer and friction performance of 2:1 aspect ratio internal cooling channel with dimples applied to a single wall. This chapter describes the experimental efforts of this work. Each geometry was tested in two separate experiments: the first to establish a baseline understanding of the features performance and the second to gain a more detailed understanding of heat transfer characteristics on the channel wall. The latter provide contours of the local surface heat transfer coefficients for three channel walls. The technique is still under development in the UCF-CATER lab and throughout this chapter, discussion is provided concerning the calculated results and the possible issues associated with them. Final results from the experimental studies covered in this chapter are provided in Table 20 and Table 22 in CHAPTER 6:.

### Reported Data

Local Data from the channel surfaces is reported for understanding of the local flow phenomena and to gain a detailed understand of the convective heat transfer from the channel surface. This data is averaged across the pixels in the Spanwise direction and plotted against the channel length in units of channel hydraulic diameters. The spanwise averaged data is then compared to a similar plot of the regionally averaged data from the basic experiment plotted against the same x-axis. This provides a valuable comparison between the two experiments as well as established correlations and the fundamentals of

turbulent flow. The fully-developed portion of the channel can be established. This region is then averaged (in the Streamwise direction) and used in the calculation of the channel performance parameters: Nusselt number and friction factor augmentation based on the smooth wall baseline, calculated from the Dittus-Boelter correlation.

### Large Single Dimples

#### Local Experimental Data

The contours of the local surface heat transfer coefficients for the Large Dimple geometry are shown in Figure 4.1 for the 20000 Reynolds number test. As indicated, flow enters the channel from the left and exits on the right side. At low Reynolds numbers, the distribution of the heat transfer coefficients is relatively uniform. A peak occurs on the downstream edge of each dimple: this is the location of an impingement region where high momentum flow from the mainstream reacts to the void in the channel wall and diverts into the indentation. Heat transfer performance is relatively high in this region where the stagnation streamlines intersect the wall (Figure 1.12).

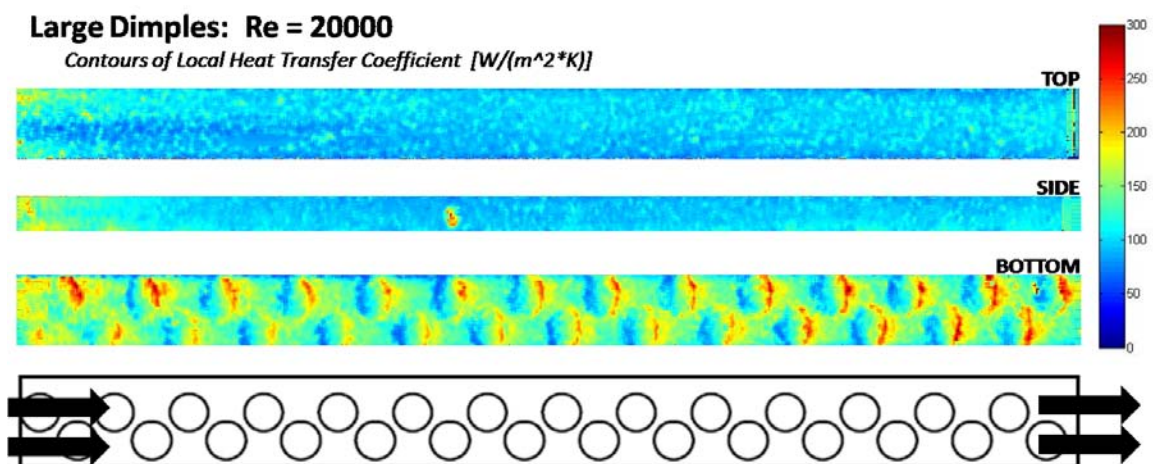
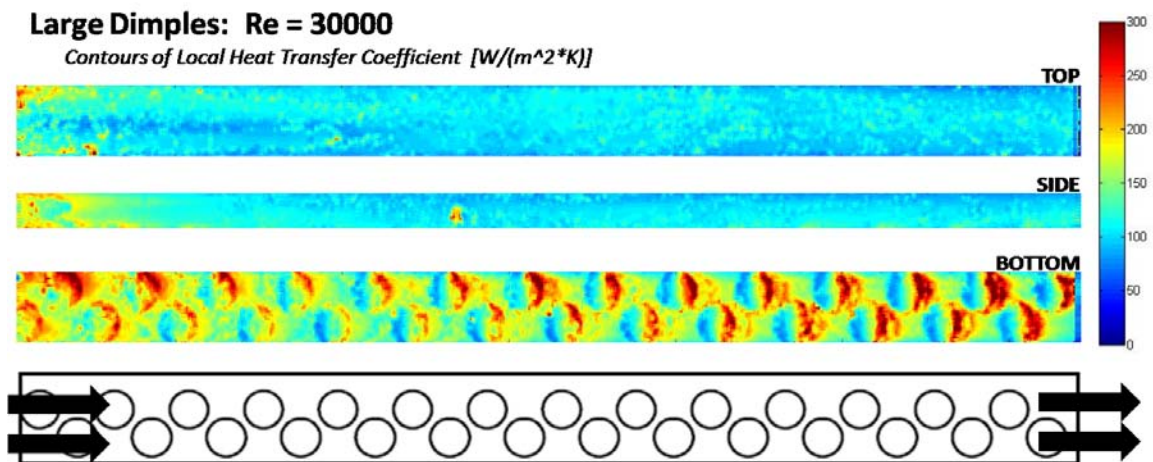


Figure 4.1: Local Heat Transfer Coefficient Data – Large Dimples, Re = 20000

As the channel Reynolds number is increased, increasing nonuniformity is observed due to the sharp contrast in convective heat transfer taking place between the stagnation and the recirculation zone within the dimple. Recirculation zones are known to have characteristically low measured convection coefficients; the flow in recirculation pockets is heated up to the temperature of the wall and the driving temperature difference causing the flow of heat is reduced.



**Figure 4.2: Local Heat Transfer Coefficient Data – Large Dimples, Re = 30000**

Figure 4.2 shows the local contours of the surface heat transfer coefficients on all four walls of the channel. As expected, there is an increase in the Nusselt number on all three walls. The dimples on the bottom wall have notably high performance, with increased sized and performance of the participating surface area within the dimple.

The local heat transfer coefficient data of the channel walls, when tested at a channel Reynolds number of 40000 is shown in Figure 4.3. The performance of the unfeatured walls is seen to increase significantly over the lower Reynolds number cases. As the strength and promotion of turbulence in the channel by the dimple features increases,

these results explain that participation of the non-featured walls can be invoked with an aggressive feature design. Close observation of the side wall contours in Figure 4.3 will reveal slight increases in surface Nusselt number near the dimple feature.

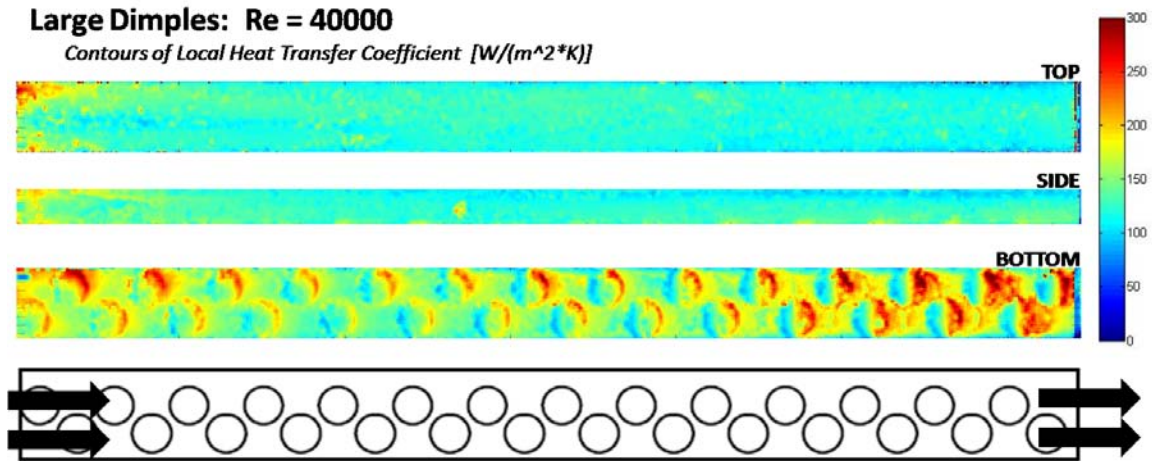


**Figure 4.3: Local Heat Transfer Coefficient Data – Large Dimples, Re = 40000**

It should also be noted that the performance in the upstream region of the dimple is improved due to the increase in the level of turbulence in the mainstream. This observation was also made in the studies reported by Shukin et al. (Schukin, Kozlov, & Agachev, 1995).

### Regionally Averaged Heat Transfer Data

With increasing channel length, the hydrodynamic boundary layer becomes increasingly developed. In this experiment, the flow becomes fully-developed at approximately eight hydraulic diameters. In this region, the heat transfer coefficient of a smooth walled channel is assumed to be constant.

Figure 4.4 is a plot of the area-weighted average of the spanwise-averaged Nusselt number contours in Figure 4.1. The saw-tooth trend is a result of the periodic

nonuniformity of the Nusselt number profiles on the bottom wall. Reiterating, this is caused by the combination of stagnation-recirculation zones that are characteristic of a hemispherical indentation. Through the fully-developed portion, an average value of 88.20 was recorded; approximately fifty percent augmentation over the smooth wall case.

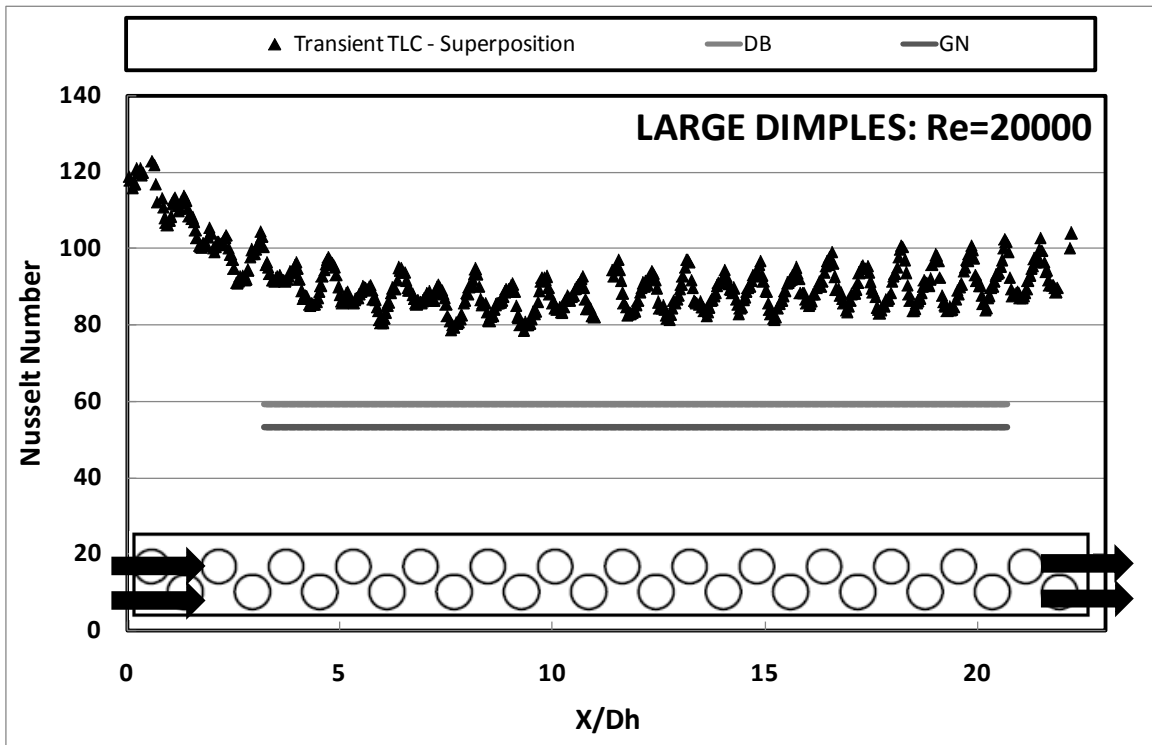
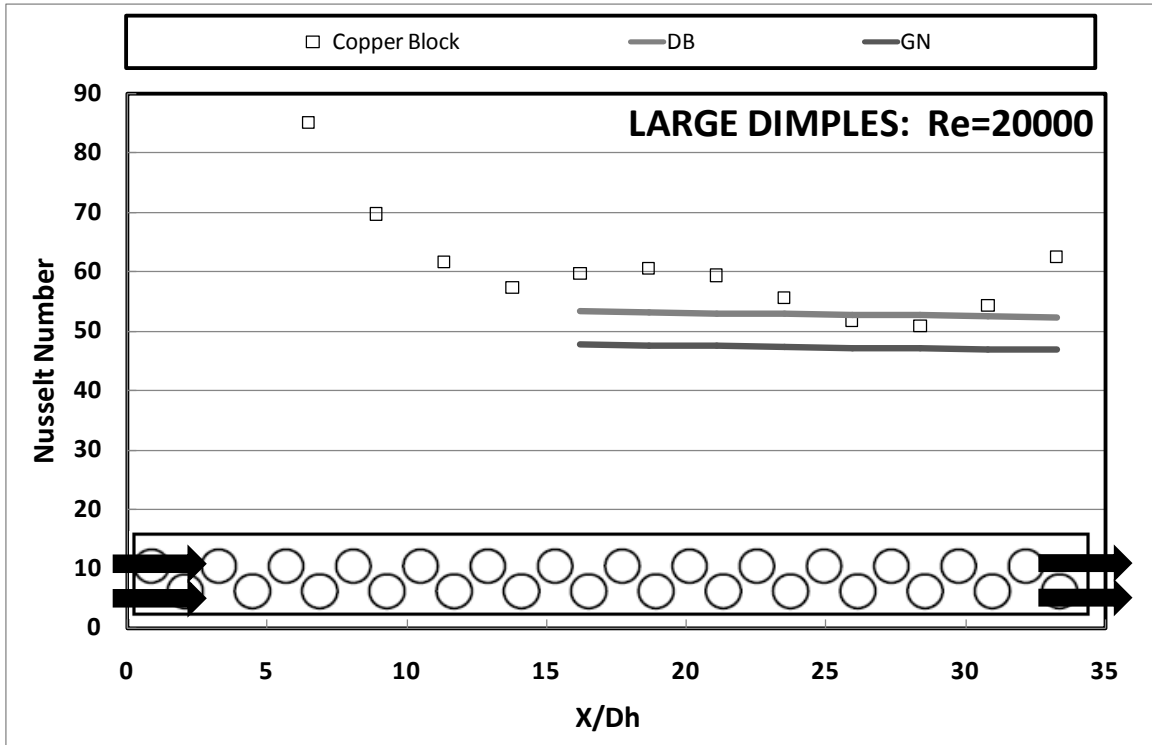


Figure 4.4: Span-wise Averaged Nusselt Number Data – Large Dimples, Re = 20000

Comparing this result to Figure 4.5, the results from the basic experiment are not as promising with an average augmentation of approximately six percent. Over-prediction of the heat transfer coefficient on a featured surface is a known issue with a transient TLC experiment. In the past, results from such experiments have been accepted and validated repeatedly (Hippensteele, Russell, & Stepka, 1981)(Ireland P. T., 1987)(Chyu, Yu, Ding, Downs, & Soechting, 1997)(Kim & Choi, 2005). The focus of CHAPTER 6: is the development of a correction factor to resolve this issue and serve as a guide for interpretation of the transient TLC results of this work as well as others. Based on these



results a detailed comparison of the corrected channel-averaged values is presented in CHAPTER 6:



**Figure 4.5: Regionally Averaged Nusselt Number Data from Copper-Block Experiment – Large Dimples, Re = 20000**

Figure 4.6 is a plot of the spanwise averaged Nusselt number profiles for the large dimple case, tested at a channel Reynolds number of 30000. As was observed in the surface contours, the nonuniformity of the surface heat transfer coefficient has a pronounced effect for the large dimple feature when tested at this flow rate. The channel-averaged augmentation is measured to be as high as eighty percent for the transient TLC experiment. This increased performance was also recorded with the copper block experiment. Though the two trends are offset from each other, for the reasons discussed, the basis experiment still recorded a heat transfer augmentation more than twenty-five percent greater than the 20000 and 40000 Reynolds number cases.

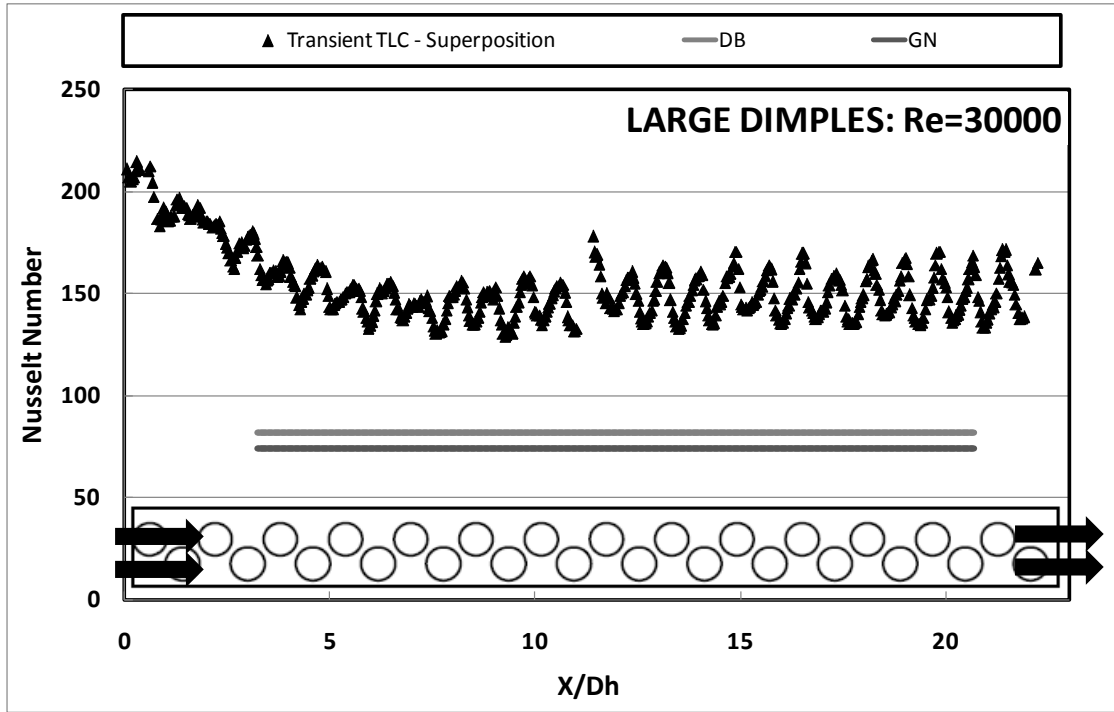


Figure 4.6: Span-wise Averaged Nusselt Number Data – Large Dimples, Re = 30000

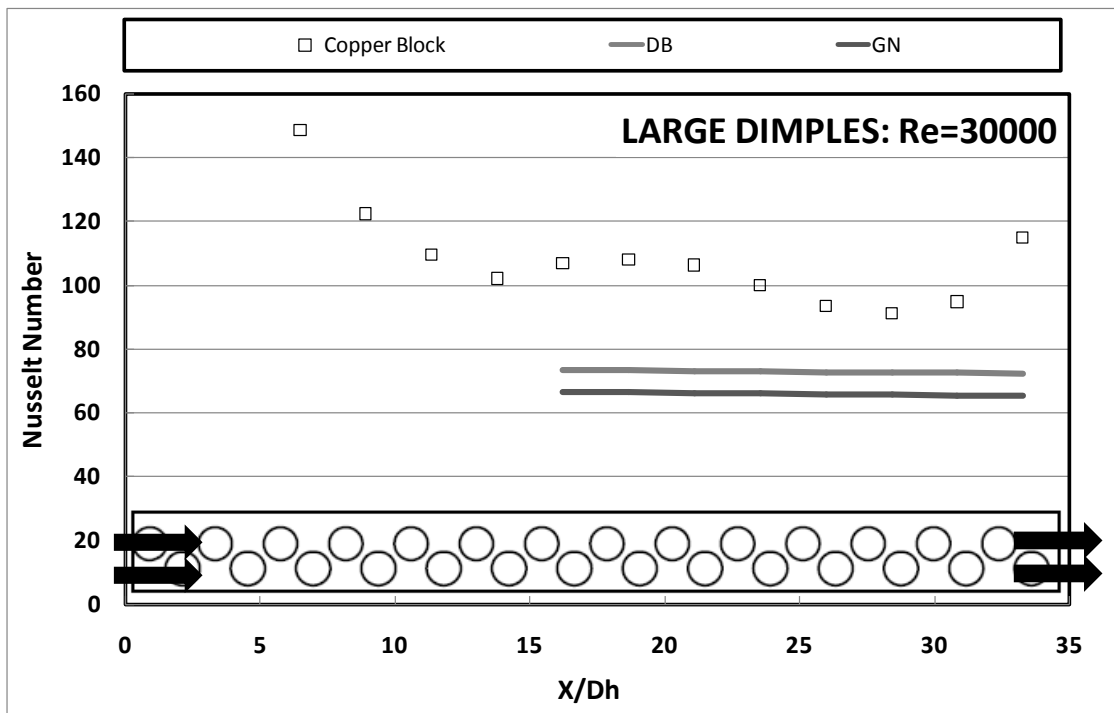


Figure 4.7: Regionally Averaged Nusselt Number Data from Copper-Block Experiment – Large Dimples, Re = 30000

As seen in Figure 4.3, the uniformity of the surface Nusselt number is improved in the 40000 Reynolds number case over the 30000 Reynolds number case. Figure 4.8 also shows this fact by a reduction in the amplitude of the peaks and valleys of the spanwise averaged Nusselt number trend through the fully-developed portion of the channel. The averaged Nusselt number was recorded as 161 with an augmentation of fifty-six percent over the smooth wall case.

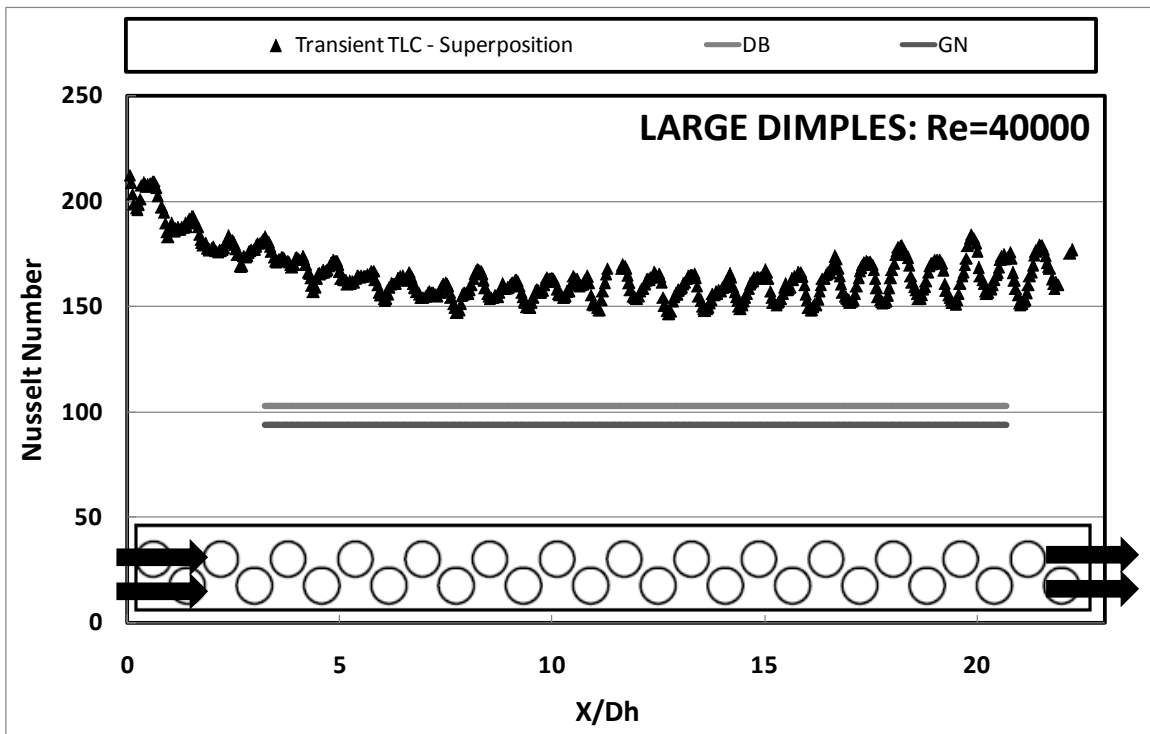
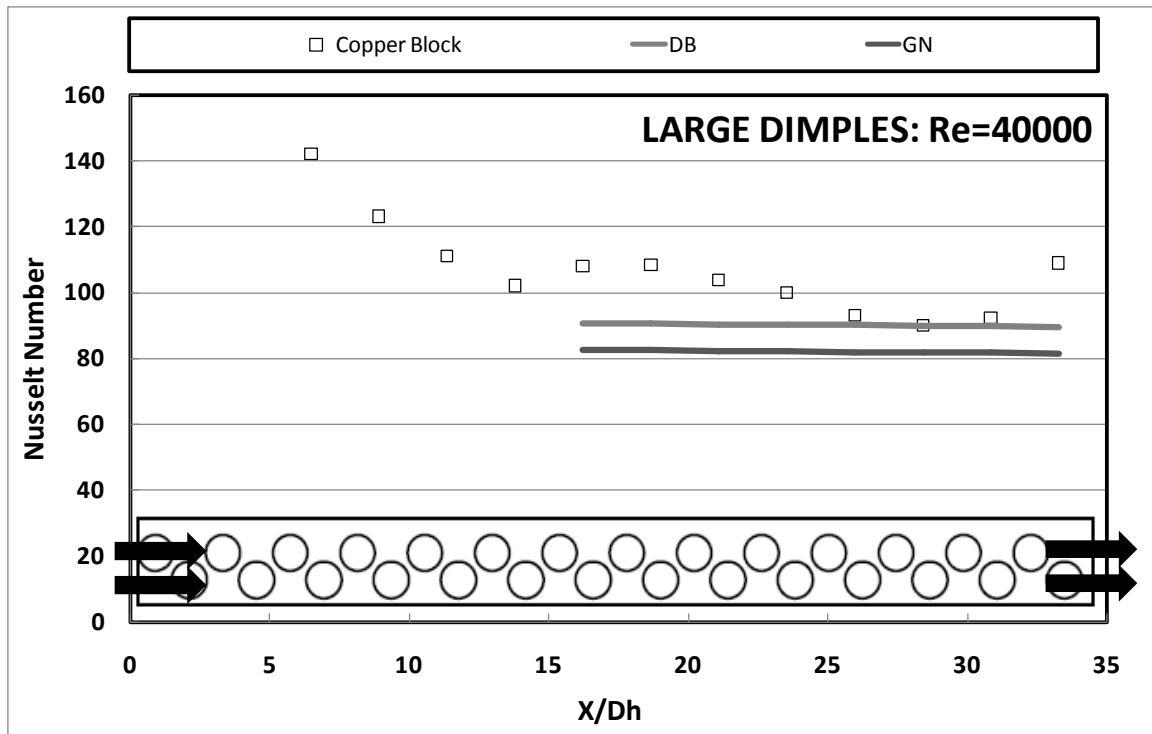


Figure 4.8: Span-wise Averaged Nusselt Number Data – Large Dimples, Re = 40000

Figure 4.9 shows that an average Nusselt number of 100 was recorded through the fully-developed portion of the channel. This resulted in a value of approximately eleven percent for the Nusselt number augmentation through the channel.

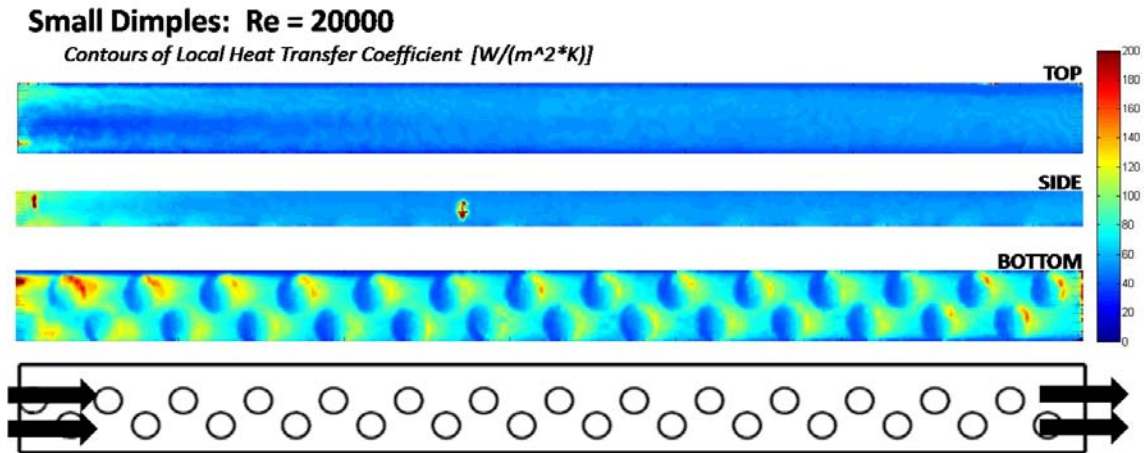


**Figure 4.9: Regionally Averaged Nusselt Number Data from Copper-Block Experiment – Large Dimples, Re = 40000**

### Small Single Dimples

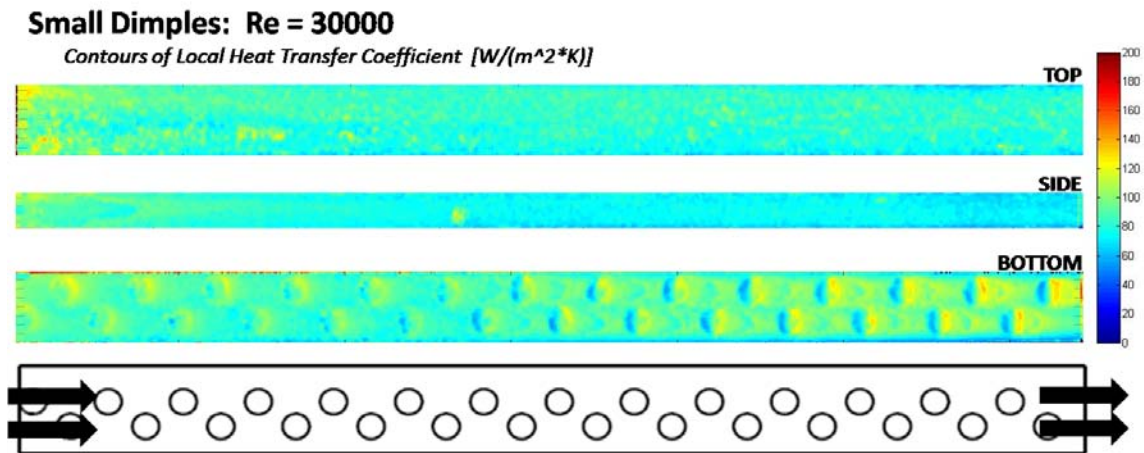
#### Local Experimental Data

Figure 4.10 describes the local heat transfer coefficients of the small dimple case tested at a channel Reynolds number of 20000. Examination of the bottom wall reveals a comparatively large recirculation zone within the feature itself. Comparing the bottom surface to the side and top walls, the dimples are, in fact, causing the promotion of convection heat transfer over the bottom surface as a whole. However, relative to the performance of the large dimples, this modest feature is not considered to be effective at a channel Reynolds number of 20000.



**Figure 4.10: Local Heat Transfer Coefficient Data – Small Dimples, Re = 20000**

The local contours of surface heat transfer coefficient in Figure 4.11 reiterate this fact. The bottom wall was observed to outperform the nonfeatured side and top walls by as little as ten percent. It is interesting to note the nearly homogenous levels of convective heat transfer over the featured wall.



**Figure 4.11: Local Heat Transfer Coefficient Data – Small Dimples, Re = 30000**

In Figure 4.12 the performance of the small dimples is seen to drastically improve at a channel Reynolds number of 40000. The size of the recirculation zone within the dimple is reduced to nearly half the size of that observed when the channel was tested at 20000

Reynolds number. The downstream advection of turbulent eddies promoting convective heat transfer over the wall is apparent in the regions of high convection coefficients immediately downstream of each dimple.

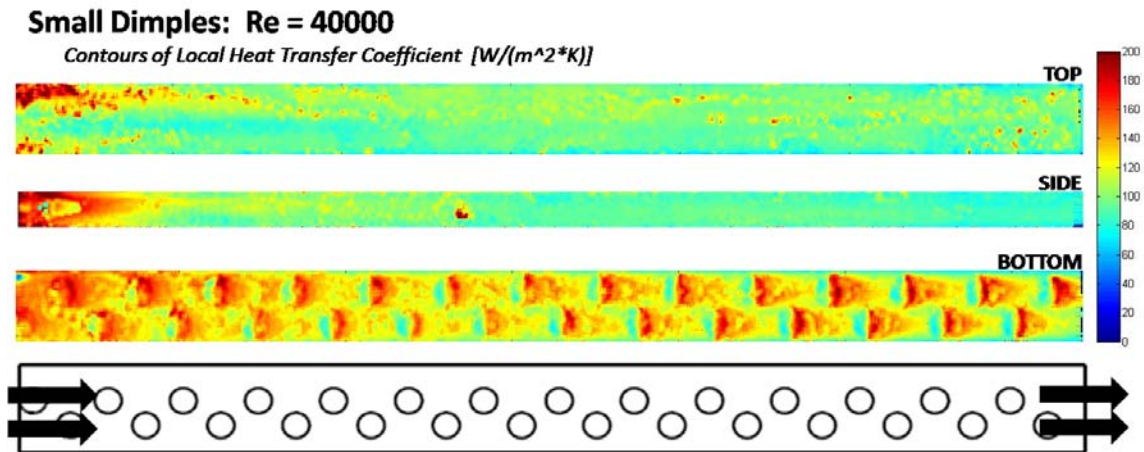


Figure 4.12: Local Heat Transfer Coefficient Data – Small Dimples, Re = 40000

### Regionally Averaged Heat Transfer Data

Figure 4.13 presents the spanwise averaged data of the small dimple Nusselt number profiles as a function of the channel length in units of hydraulic diameters. Again, the flow is fully-developed in approximately five hydraulic diameters, as is expected for a fully-turbulent flow. The nonuniformity caused by the large recirculation regions seen in Figure 4.10 is seen in the sharp peaks of the spanwise averaged plot. The area-weighted average of the spanwise averaged surface Nusselt number through the fully-developed portion is 70.60 before any corrections have been applied. The Nusselt number augmentation over the smooth wall baseline was calculated to be 1.19.

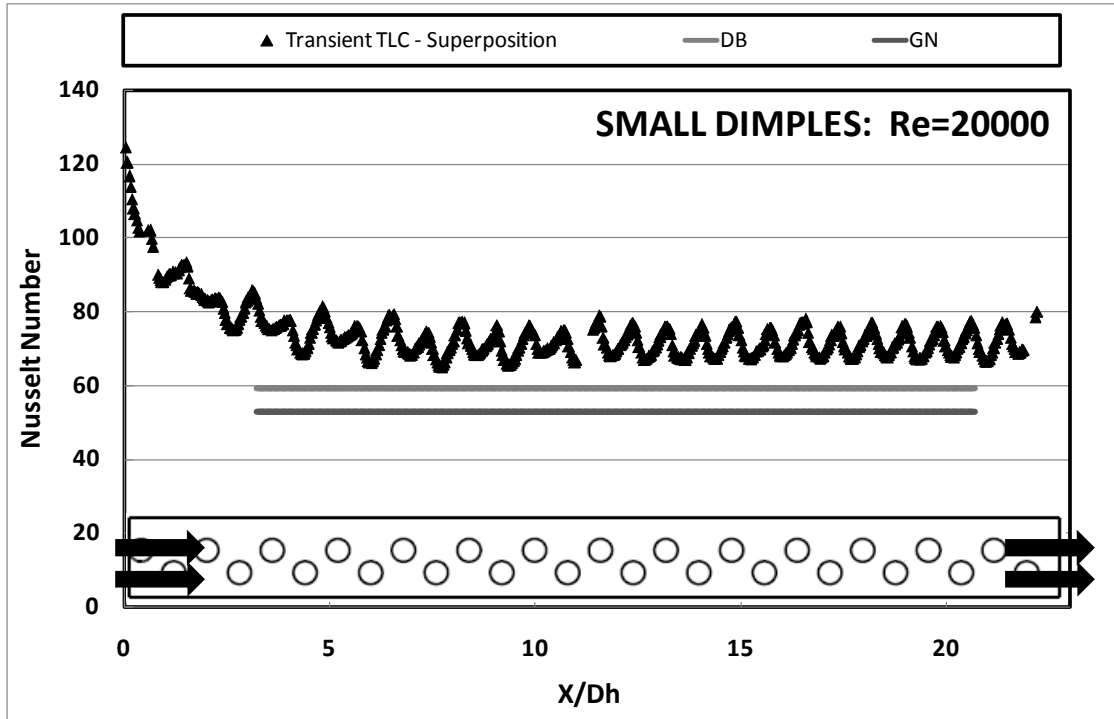


Figure 4.13: Span-wise Averaged Nusselt Number Data – Small Dimples, Re = 20000

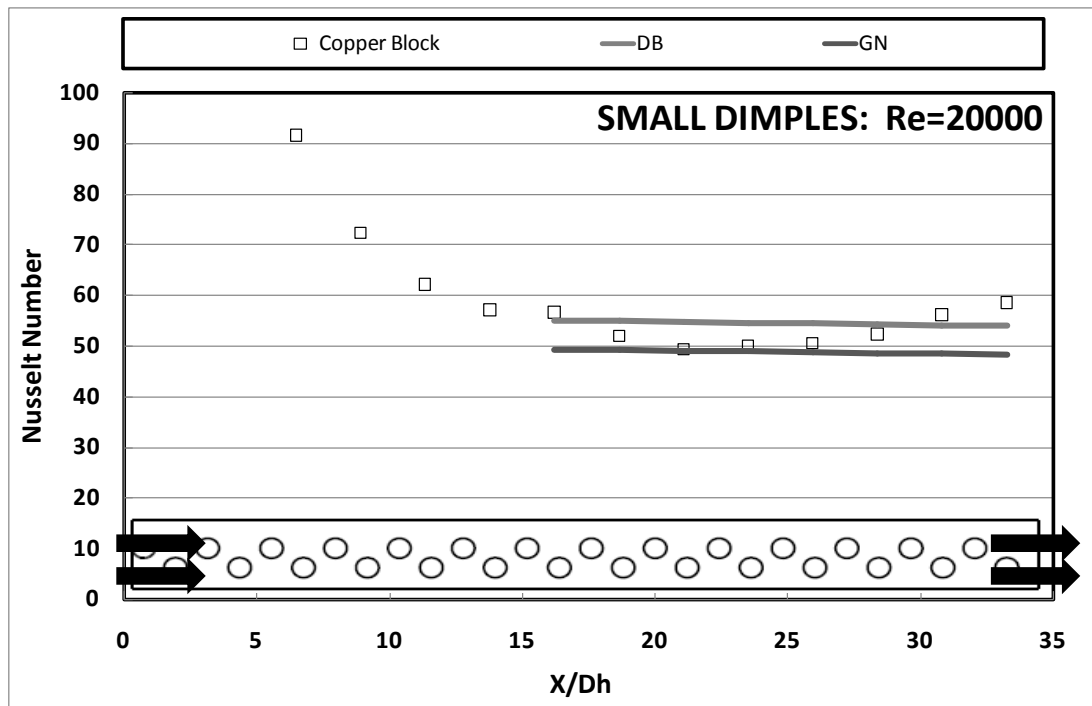


Figure 4.14: Regionally Averaged Nusselt Number Data from Copper-Block Experiment – Small Dimples, Re = 20000

Figure 4.14 is a plot of the regionally averaged surface Nusselt number measured by the Copper Block experiment. The channel-averaged Nusselt number is 52.81 for the small dimple feature tested at a channel Reynolds number of 20000. This value leads to a heat transfer augmentation value of 0.97 over the smooth wall case. Although a *decrease* in channel performance is possible, it is unlikely. Instead, considering the uncertainty of the experiment is approximately 6.7 percent (Table 4), the small dimple feature is considered to simply have no appreciable effect at this flow rate.

The spanwise averaged Nusselt numbers of the channel with the small dimples are present in Figure 4.15. The channel averaged Nusselt number is approximately 97, yielding an augmentation of eighteen percent over the smooth wall-channel.

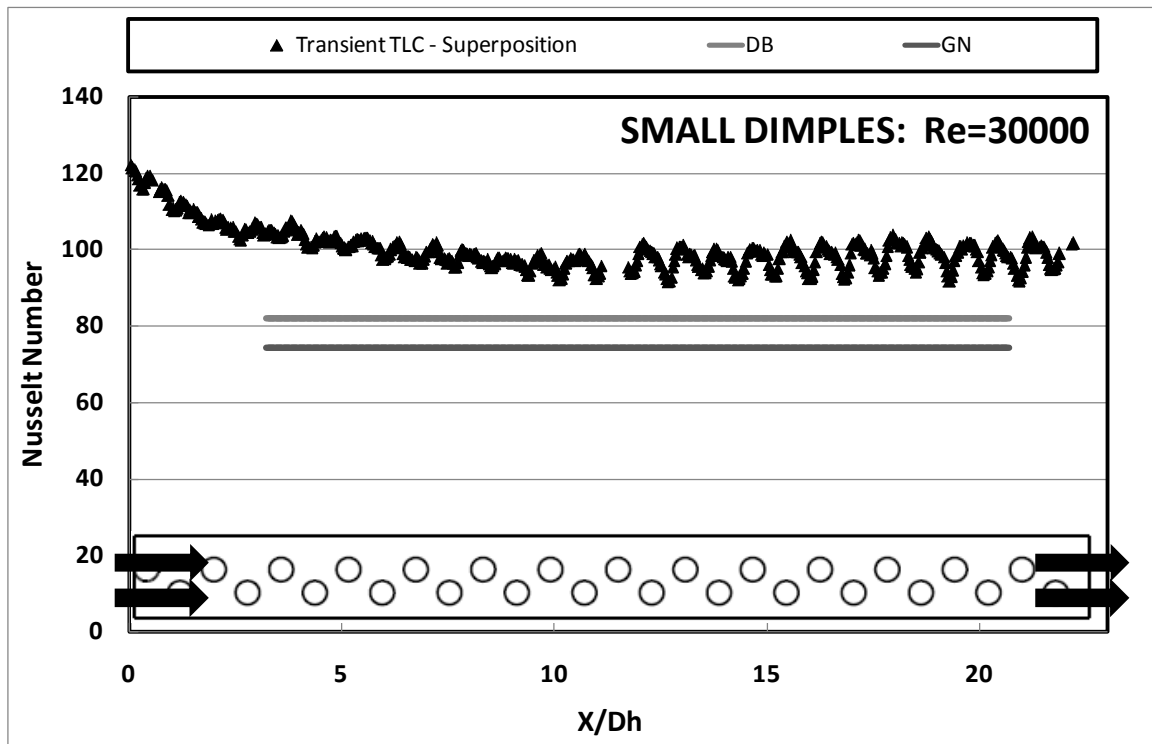
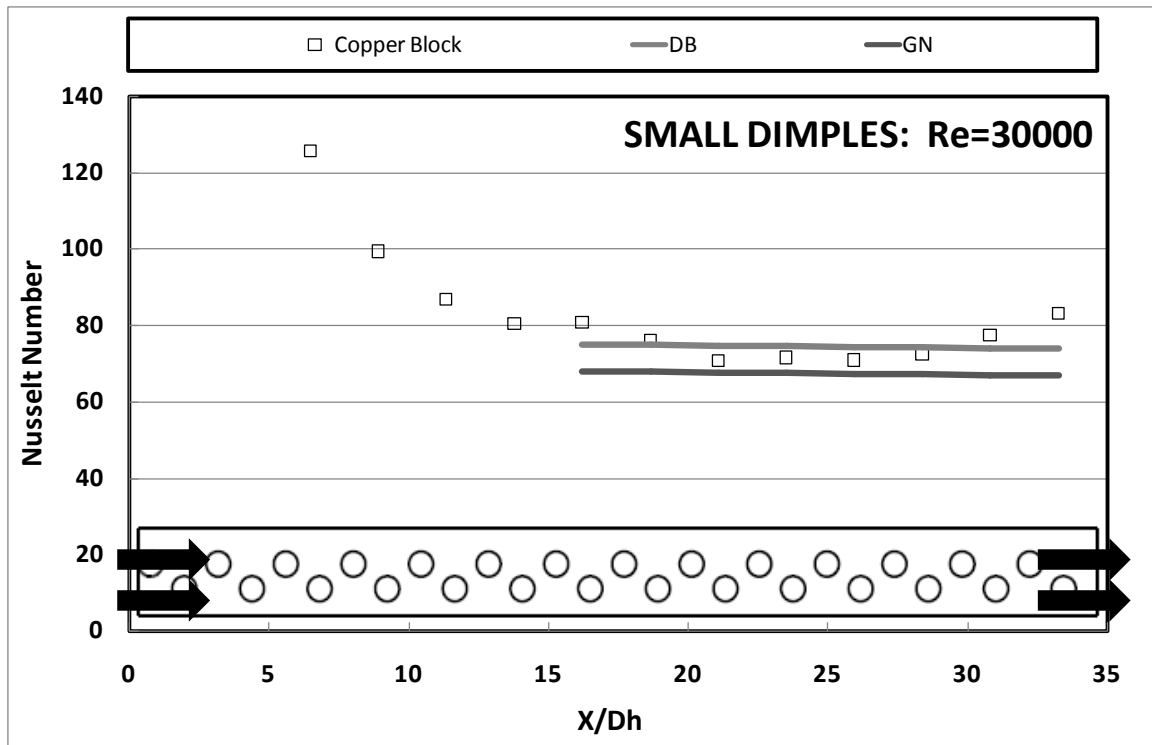


Figure 4.15: Span-wise Averaged Nusselt Number Data – Small Dimples, Re = 30000





**Figure 4.16: Regionally Averaged Nusselt Number Data from Copper-Block Experiment – Small Dimples, Re = 30000**

The channel averaged Nusselt number calculated from the basic experiment for the small dimples tested at a Reynolds number of 30000 is 74.98. Similar to the 20000 Reynolds number case, this leads to an augmentation of unity. The same conclusion is also applicable: because the calculated heat transfer augmentation is within the experimental uncertainty for the test, the small dimple is considered to have no appreciable effect on the heat transfer performance of a narrow channel when tested at a Reynolds number of 30000 under our experimental conditions.

The uniformity of the surface Nusselt number is seen to also improve with increasing channel Reynolds number. This is due to the increased level of the mainstream turbulence that tends to smooth out any non-uniformities along the channel wall due to a

reduction in turbulent eddy size. From Figure 4.17, the channel-averaged Nusselt number is calculated to be 124.05. The Nusselt number augmentation is twenty percent above that of the smooth wall channel. Figure 4.18 presents the regionally averaged Nusselt number data as a function of the streamwise location in the channel. The average Nusselt number through the fully-developed portion of the channel is 95.70, which yields an increase of just three percent.

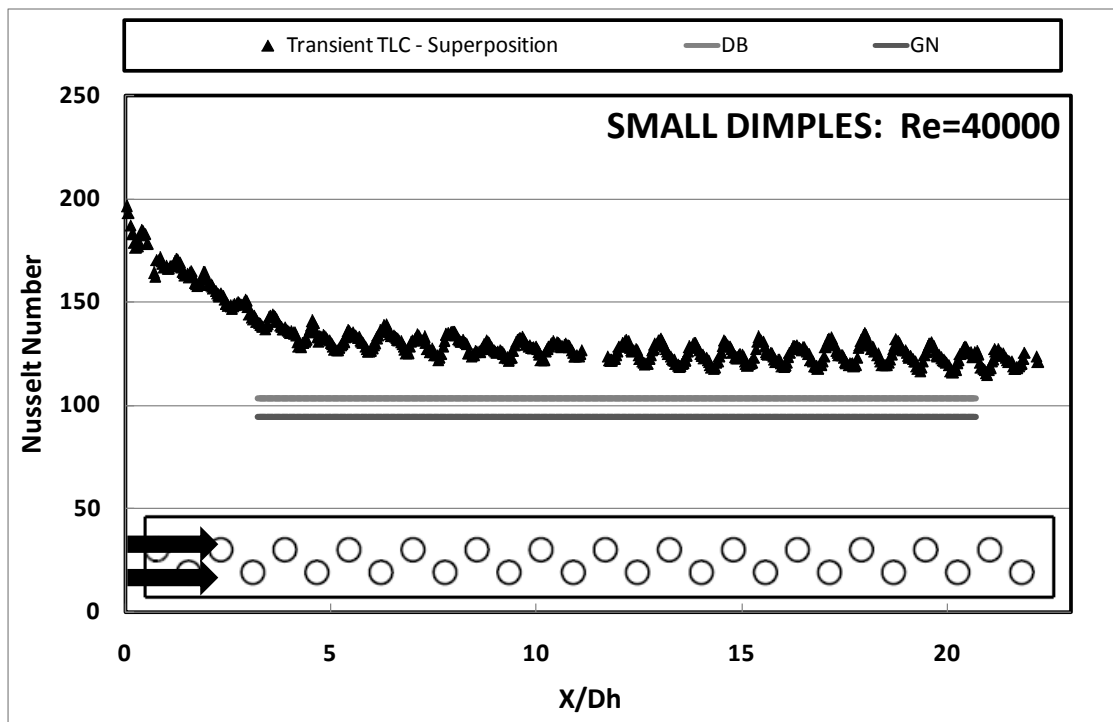


Figure 4.17: Span-wise Averaged Nusselt Number Data – Small Dimples, Re = 40000

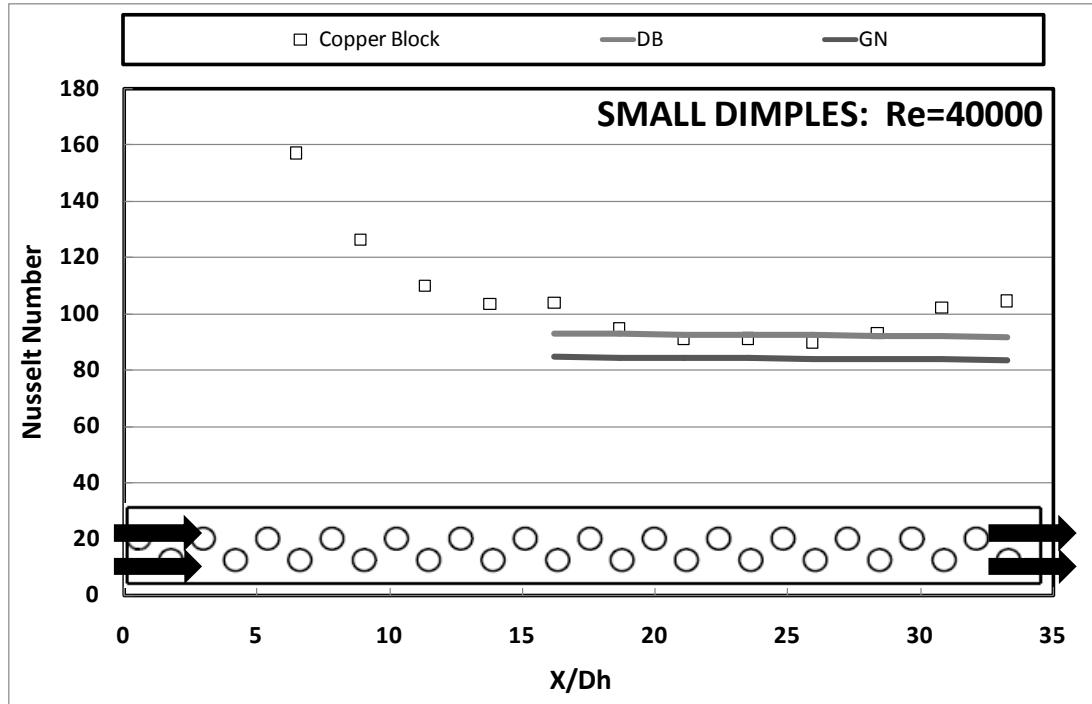


Figure 4.18: Regionally Averaged Nusselt Number Data from Copper-Block Experiment – Small Dimples, Re = 40000

### Double Dimples

#### Local Experimental Data

The double dimple surface feature is a combination of two small dimples machined in pair with a center-to-center distance that is smaller than the footprint diameter ( $d$ ). In interesting phenomena is observed in Figure 4.19 through Figure 4.21; the size of the recirculation zone is reduced to a very small percentage of the overall dimple surface area, much less than any single dimple feature tested in this study. This results in high heat transfer uniformity and overall high performance of the channel as a whole.

At a channel Reynolds number of 20000, the double dimples are seen to function well in the promotion of turbulent advection of heat from the channel surface in the downstream region near the edge of the dimple. At this Reynolds number, no significant Nusselt number augmentation is recorded on the unfeathered walls. This is because the mainstream flow does not possess the needed kinetic energy for the augmentation features to promote such an effect.

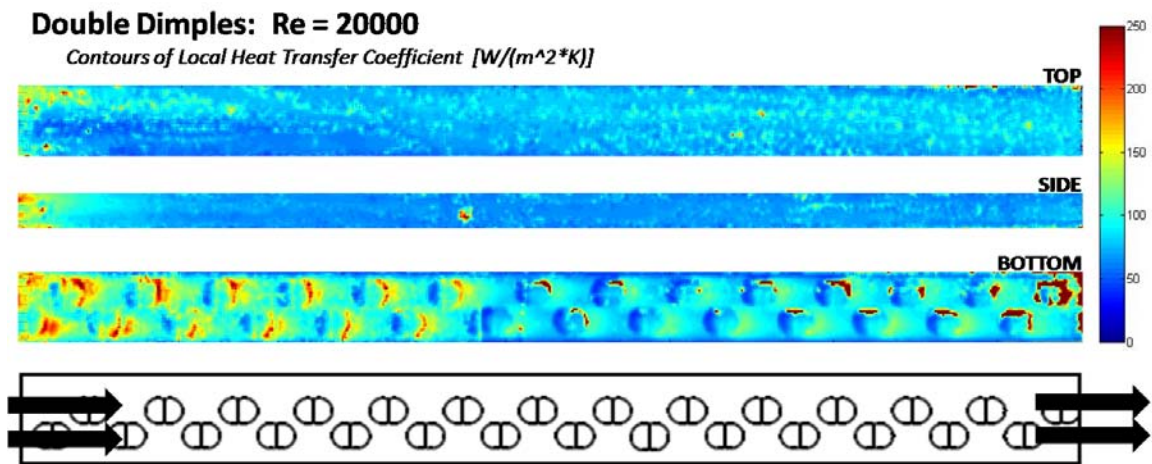
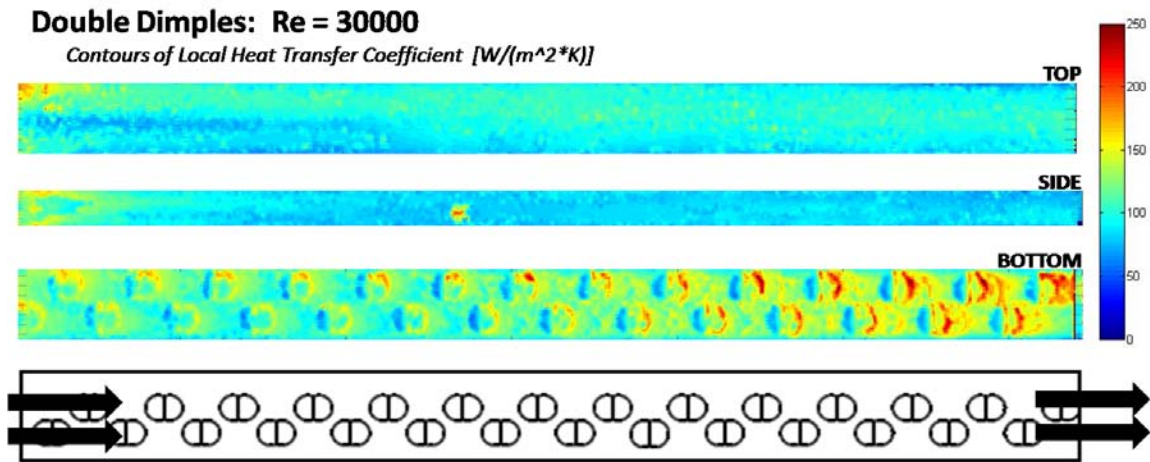


Figure 4.19: Local Heat Transfer Coefficient Data – Double Dimples, Re = 20000

As the channel Reynolds number is increased, the inherent turbulence of the flow is increased and the heat transfer performance of the side and top walls is increased. In Figure 4.20, the top wall is observed to have higher average heat transfer coefficient through the fully-developed portion than the side wall. At first, this is counter-intuitive when considering the wall's proximity to the feature. It is the channel aspect ratio that causes this to take place. In this study, the height of the channel one half of the channel width; resulting in a more extreme velocity gradient through the hydrodynamic boundary layer between the top and bottom walls than the boundary layer between the

two side walls. The result is that higher velocity fluid is within closer proximity to the top wall than the side walls; resulting in a higher heat transfer coefficient.



**Figure 4.20: Local Heat Transfer Coefficient Data – Double Dimples, Re = 30000**

At a channel Reynolds number of 40000, the double dimples promote significant gains in surface Nusselt number on the bottom walls of the channel. In Figure 4.21, the downstream dimple of the double-dimple pair is seen to exhibit Nusselt number values as high as those recorded on the bottom wall just downstream of the dimple. The combination seems to be working in harmony: the first dimple exhibits the same stagnation-recirculation characteristics observed from the single small dimple, then the second dimple uses the increased turbulent kinetic energy for increased convection heat transfer from its own walls then further promotes increased vortex generation to be swept downstream. The evidence of these phenomena can be clearly seen in Figure 4.21, where the Nusselt number in each dimple throughout the fully-developed portion is seemingly staged – green, yellow, red – as the flow transitions through the three stages described above. These conjectures will be further supported by means of numerical simulation in CHAPTER 5: of this work.

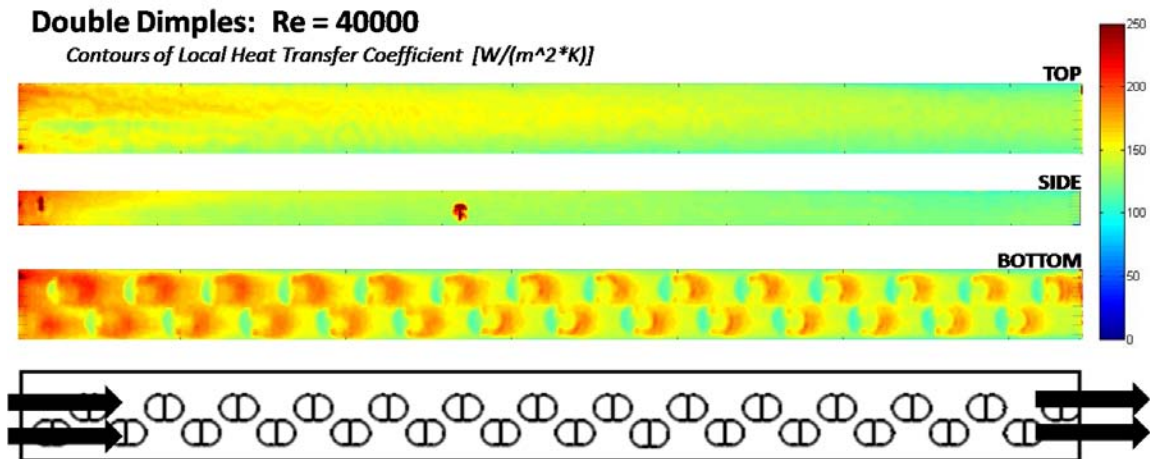


Figure 4.21: Local Heat Transfer Coefficient Data – Double Dimples, Re = 40000

### Regionally Averaged Heat Transfer Data

Figure 4.22 presents the area-weighted spanwise averaged Nusselt number data for the double dimple surface feature tested at a channel Reynolds number of 20000. The channel Nusselt number averaged through the fully-developed portion of the channel is 84.38 yielding a Nusselt number augmentation of forty-two percent. In Figure 4.23, the regionally-averaged Nusselt number of each module shows a full-developed flow occurring at approximately fifteen hydraulic diameters. Through this portion, the average Nusselt number is calculated to be approximately 64.55. The heat transfer augmentation, normalized by the smooth wall Nusselt number established by the Dittus-Boelter correlation, was found to be 1.17.

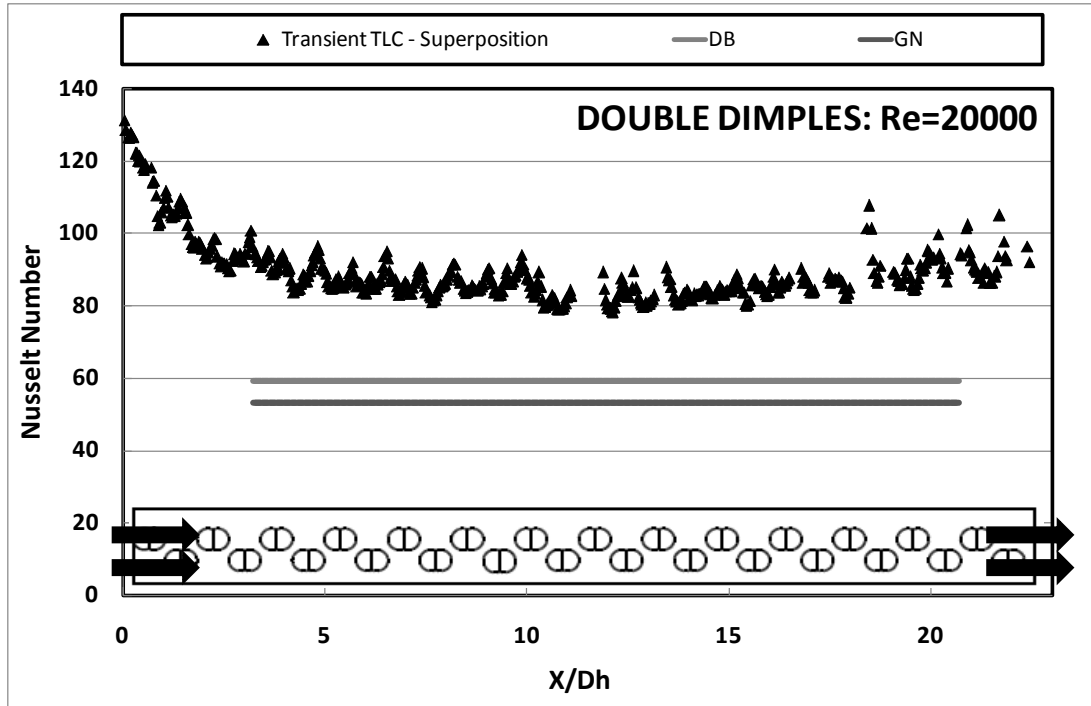


Figure 4.22: Span-wise Averaged Nusselt Number Data – Double Dimples, Re = 20000

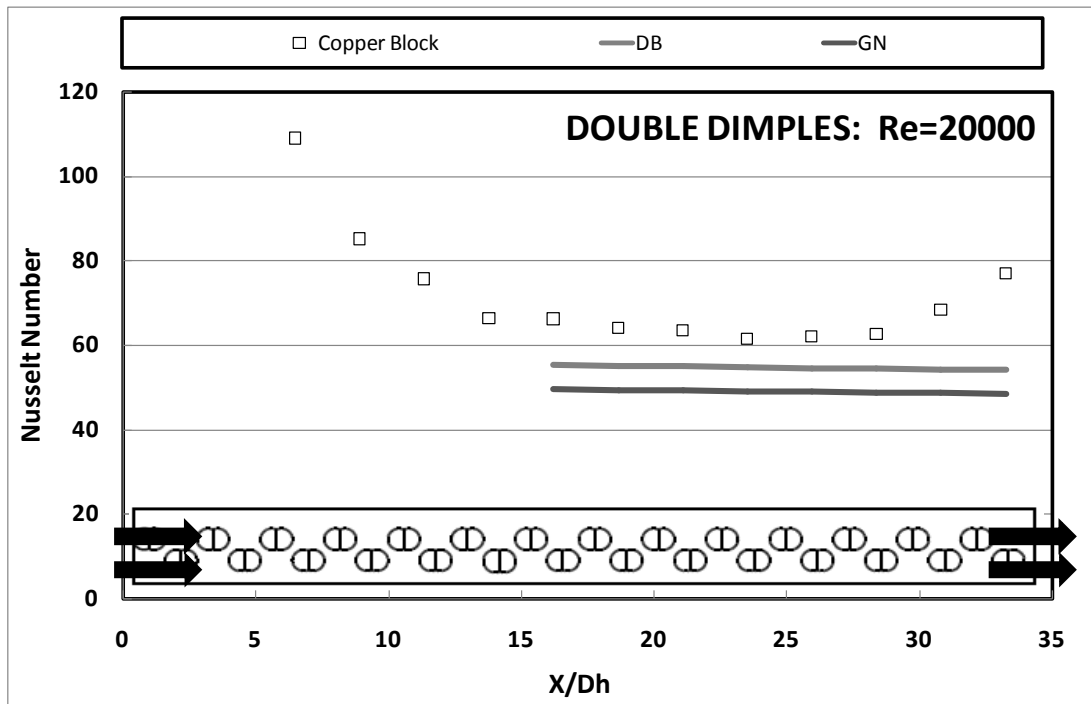
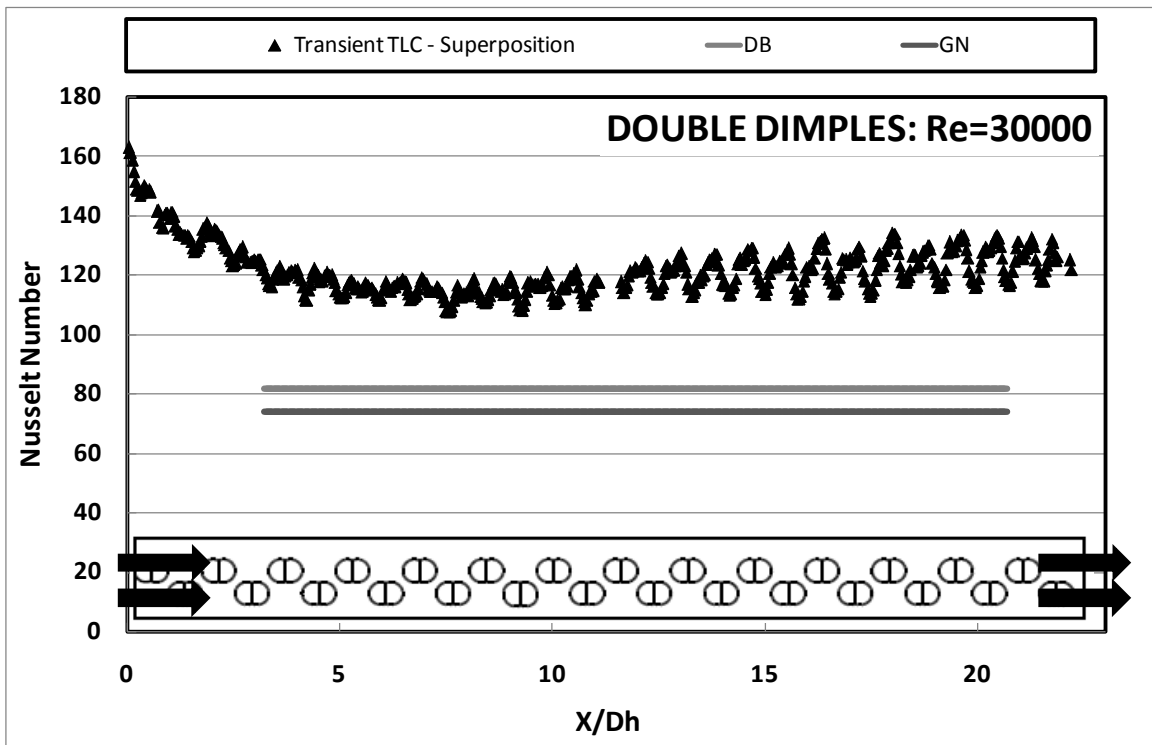


Figure 4.23: Regionally Averaged Nusselt Number Data from Copper-Block Experiment – Double Dimples, Re = 20000

Figure 4.24 indicates an increase in the spanwise averaged Nusselt number towards the end of the channel length. This is not a physically explainable phenomenon, but due to the small magnitude, it is dismissed as part of the uncertainty, contributed by the bulk temperature component (see Test Setup for Local Data, Data Reduction and Test Setup for Local Data, Experimental Uncertainty). The channel-averaged Nusselt number is 120.86, which leads to an augmentation of 1.48.



**Figure 4.24: Span-wise Averaged Nusselt Number Data – Double Dimples, Re = 30000**

These regionally-averaged Nusselt number data from the basic experiment is shown in Figure 4.25, shows a fully developed flow after approximately fifteen hydraulic diameters and an average Nusselt number of approximately 91.48 through that portion. The Nusselt number augmentation for the double dimple geometry, tested at a Reynolds number of 30000 on this experiment is 1.23.



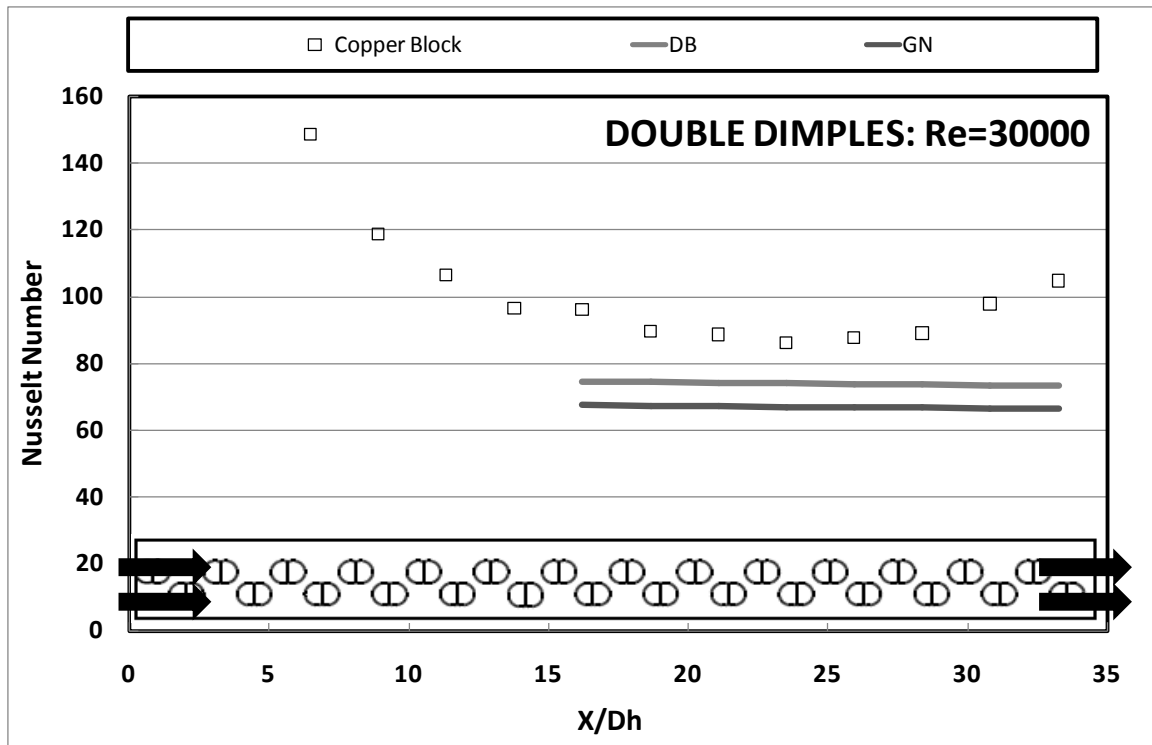


**Figure 4.25: Regionally Averaged Nusselt Number Data from Copper-Block Experiment – Double Dimples, Re = 30000**

The spanwise averaged Nusselt number data for the double dimple feature tested at a channel Reynolds of 40000 is shown in Figure 4.26. An interesting feature of this plot is the smoothness of the curve. As was discussed in the previous section, the overlapping phases of the flow regions from the staggered dimple array cause an extremely uniform surface Nusselt number. The channel averaged value through the fully-developed portion was determined to be 165.54 with an augmentation of sixty percent over the predicted smooth wall value. Figure 4.27 presents the module-to-module values determined by the basic experiment. Averaging from fifteen to thirty-two hydraulic diameters, the channel averaged Nusselt number and Nusselt number augmentation were calculated to be 112.72 and 1.21, respectively.

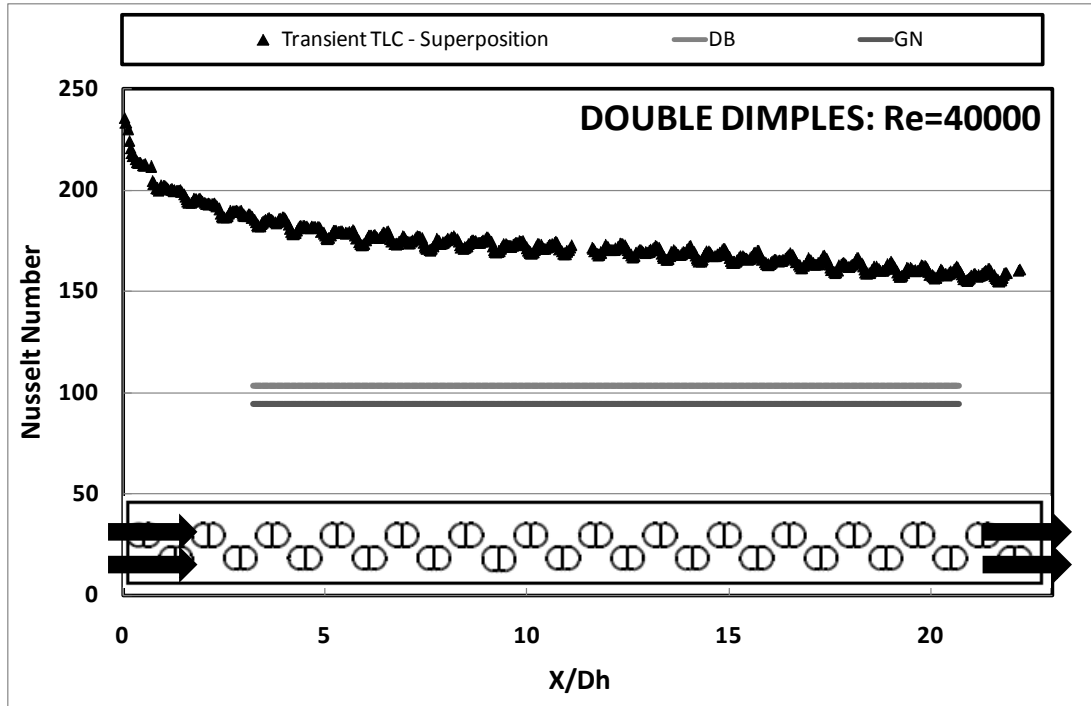


Figure 4.26: Span-wise Averaged Nusselt Number Data – Double Dimples, Re = 40000

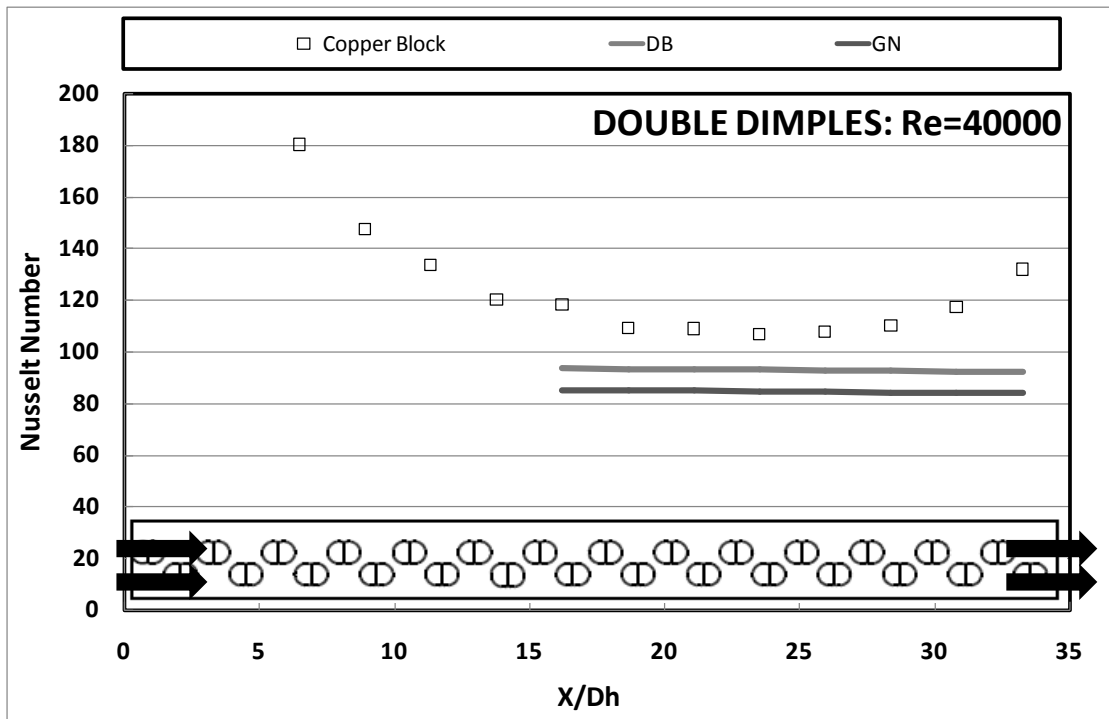
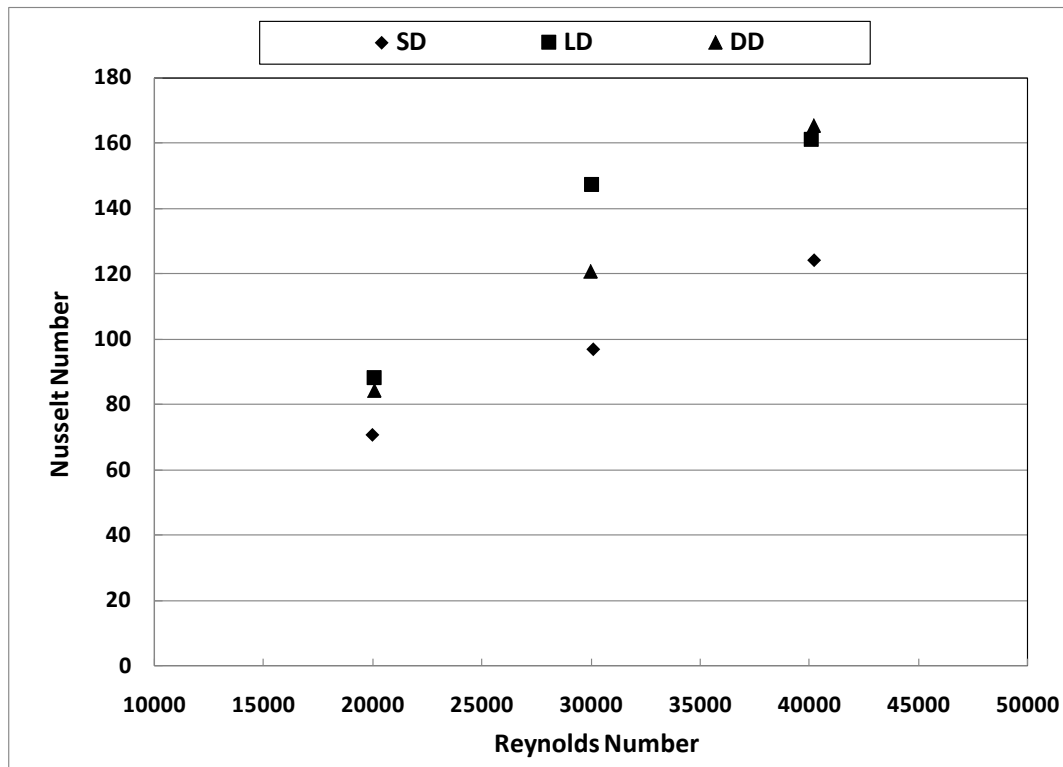


Figure 4.27: Regionally Averaged Nusselt Number Data from Copper-Block Experiment – Double Dimples, Re = 40000

### Stream-wise Averaged Heat Transfer Data

The channel-averaged Nusselt number is plotted against the channel Reynolds number in Figure 4.28, below. As expected, Nusselt number is increasing with Reynolds number. In fact, for the small dimple and double dimple cases, the trend is nearly linear; this would be expected as most correlations for internal flows have exponents that are near unity describing the Reynolds number dependence of the channel Nusselt number.



**Figure 4.28: Regionally Averaged Heat Transfer Coefficient Data from Transient TLC Experiment Plotted Against the Channel Reynolds Number**

As discussed in the previous sections (Large Single Dimples), the large dimple case is seen to have a ‘sweet spot’ at a channel Reynolds number of 30,000. This same trend was also observed in the basic experiment. In general, the double dimples are capable of producing Nusselt number values comparable with those of the large dimple surface feature.

Table 9 is a comparison of the Nusselt number, Baseline Nusselt number, and Nusselt number augmentation for each feature, tested in both experiments at a target Reynolds number of 20000. Note that the discrepancy between the Nusselt number augmentations calculated from the two experiments for the same feature increases with the increasing surface area of the feature:  $\Delta LD = 0.43$ ,  $\Delta SD = 0.25$ ,  $\Delta DD = 0.23$ . This is the subject of CHAPTER 6:.

**Table 9: Comparison of Channel-Averaged Heat Transfer Results – Reynolds Number = 20000**

		Reynolds Number	Nusselt Number	Nuo [Dittus-Boelter]	Nu/Nuo [Dittus-Boelter]
LD	Transient TLC	20078	88.20	59.30	1.49
	Copper-Block	19083	56.27	53.04	1.06
SD	Transient TLC	20002	70.60	59.12	1.19
	Copper-Block	19835	52.81	54.74	0.96
DD	Transient TLC	20087	84.38	59.30	1.42
	Copper-Block	19932	64.55	54.94	1.17

Table 10 is a comparison of the Nusselt number, Baseline Nusselt number, and Nusselt number augmentation for each feature, tested in both experiments at a target Reynolds number of 30000. The same trend (and coincidentally, the same values) are seen:  $\Delta LD = 0.43$ ,  $\Delta SD = 0.25$ ,  $\Delta DD = 0.18$ . It is particularly interesting that, even with the significant offset of the large dimple feature at this Reynolds number, the difference between the Nusselt number augmentations measured by both experiments is very

similar. This is indicative of a systematic error somewhere in the experiment or post-processing, rather than a hardware or a physics-based issue.

**Table 10: Comparison of Channel-Averaged Heat Transfer Results – Reynolds Number = 30000**

		Reynolds Number	Nusselt Number	Nuo [Dittus-Boelter]	Nu/Nuo [Dittus-Boelter]
LD	Transient TLC	30010	147.35	81.79	1.80
	Copper-Block	28592	100.68	73.32	1.37
SD	Transient TLC	30116	96.97	82.02	1.18
	Copper-Block	29214	74.98	74.68	1.00
DD	Transient TLC	29957	120.86	81.67	1.48
	Copper-Block	29036	91.48	74.31	1.23

Table 11 is a comparison of the Nusselt number, Baseline Nusselt number, and Nusselt number augmentation for each feature, tested in both experiments at a target Reynolds number of 40000. Again, a similar trend is seen:  $\Delta LD = 0.45$ ,  $\Delta SD = 0.39$ ,  $\Delta DD = 0.17$ .

**Table 11: Comparison of Channel-Averaged Heat Transfer Results – Reynolds Number = 40000**

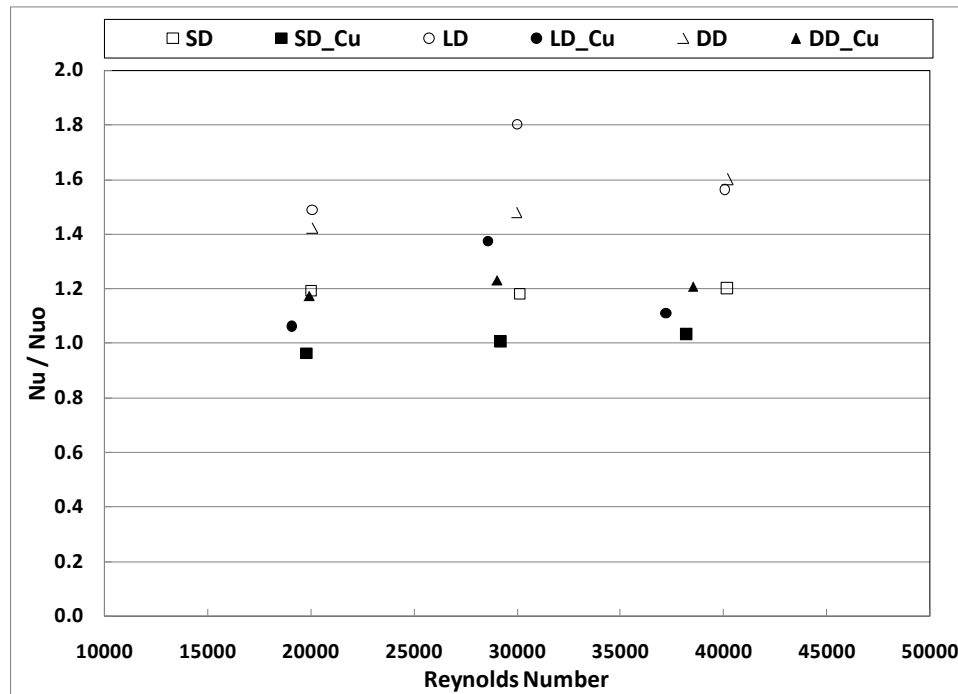
		Reynolds Number	Nusselt Number	Nuo [Dittus-Boelter]	Nu/Nuo [Dittus-Boelter]
LD	Transient TLC	40078	161.01	103.90	1.56
	Copper-Block	37216	100.55	90.60	1.11
SD	Transient TLC	40201	124.05	103.34	1.20
	Copper-Block	38228	95.70	92.67	1.03
DD	Transient TLC	40201	165.54	103.34	1.60
	Copper-Block	38502	112.72	93.19	1.21

Table 12 is a summary of these differences, calculated as a percentage difference between the Transient TLC experiment and the copper block experiment.

**Table 12: Percentage Difference Channel-Averaged Nusselt number Augmentation between Two Experiments – Before Correction**

DIMPLE GEOMETRY	Reynolds Number		
	20000	30000	40000
Large Dimple	0.321	0.238	0.287
Small Dimple	0.140	0.151	0.192
Double Dimple	0.245	0.168	0.174

Figure 4.29 is a plot of the channel-averaged Nusselt number augmentation as a function of the channel Reynolds number.



**Figure 4.29 Channel Averaged Nusselt Number Plotted Against the Channel Reynolds Number**

### Friction Data

The Moody friction factor calculated from the static pressure drop over the length of the channel is plotted against Reynolds number in Figure 4.30. As expected the trend in friction factor is decreasing with Reynolds number (reference the Moody diagram of any basic Fluid Mechanics book). What is important to take from this diagram is the performance of the double dimple feature. Figure 4.30 shows that the channel friction factor of the double dimple feature is directly comparable to that of the small dimples. Recalling the previous section (Stream-wise Averaged Heat Transfer Data), it was observed that the heat transfer performance of the double dimple feature was on the level of the large dimples, around forty percent higher than that of the small dimples.

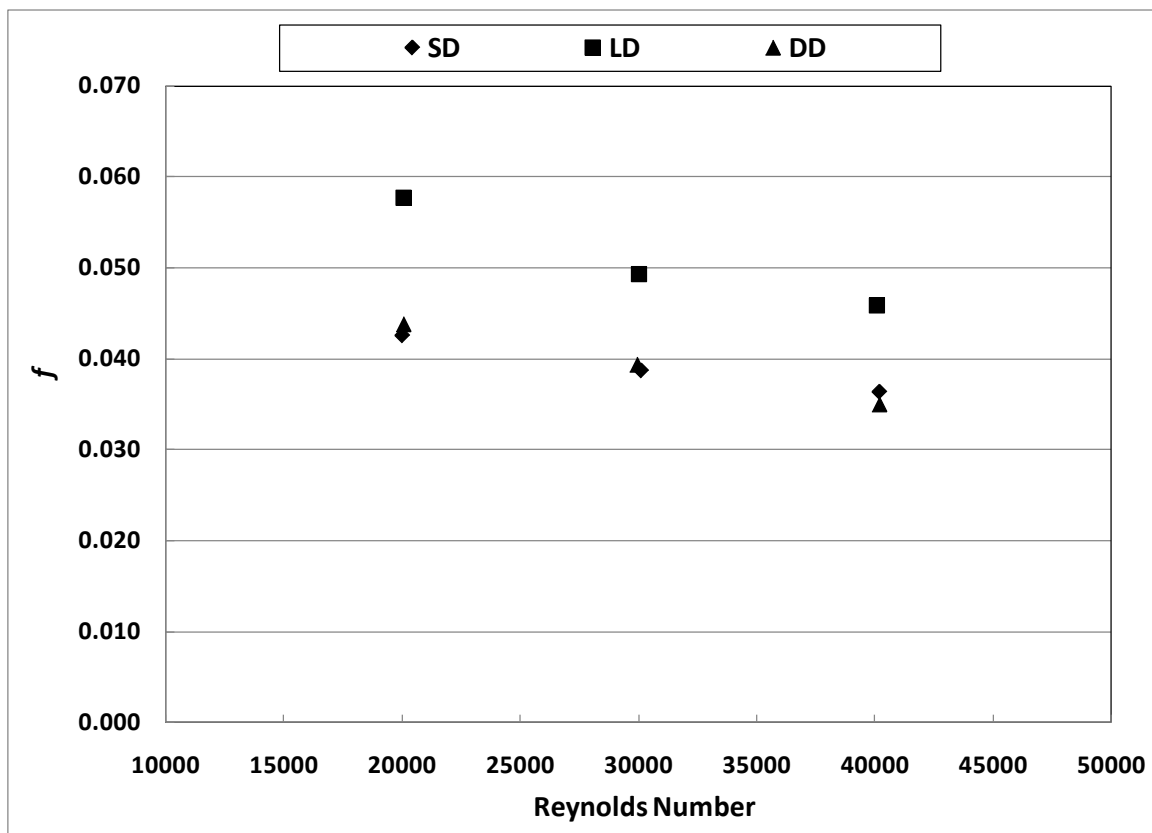


**Figure 4.30: Experimental Friction Factor Plotted Against the Channel Reynolds Number**

**Table 13: Comparison Friction Factor Augmentation**

	Reynolds Number		
DIMPLE GEOMETRY	20000	30000	40000
Large Dimple	2.17	2.05	2.06
Small Dimple	1.60	1.61	1.63
Double Dimple	1.65	1.64	1.57

Table 13 provides a summary of the Moody friction factor augmentation based on the Blasius correlation for the three Reynolds numbers tested.

#### Comparison to Literature

Comparison of the Nusselt number and friction factor augmentation values to those available in the literature, the results from these experiments compare directly with a majority of the comparable published works (Figure 1.13). However, for a direct comparison, there is no immediately related work (see those described in Literature Review of Related Works, Dimples). Nearly all existing studies have been performed in one of two configurations: a staggered array with data collected only in an isolated region (away from wall effects), or a single dimple on a flat plate. In summary, the arrangement under study in this work, a staggered array applied to a single wall of a narrow channel (where wall effects are non-negligible) has not been studied. Therefore, the presence of this data in the general vicinity of the other cited works is taken to be ample confirmation of the legitimacy of this work. Instead, heavy reliance is placed on



the cross-validation of the data between the two different experiments, which were both successfully validated with a smooth wall test. Additionally, as described in the upcoming sections, extensive computational efforts have been performed for further support and validation of experimental data.

### Double Dimple Summary

Based on the results from the experimental efforts discussed in this chapter, the performance of the double dimple surface feature has been seen to exhibit a marked improvement over the conventional single dimple design.

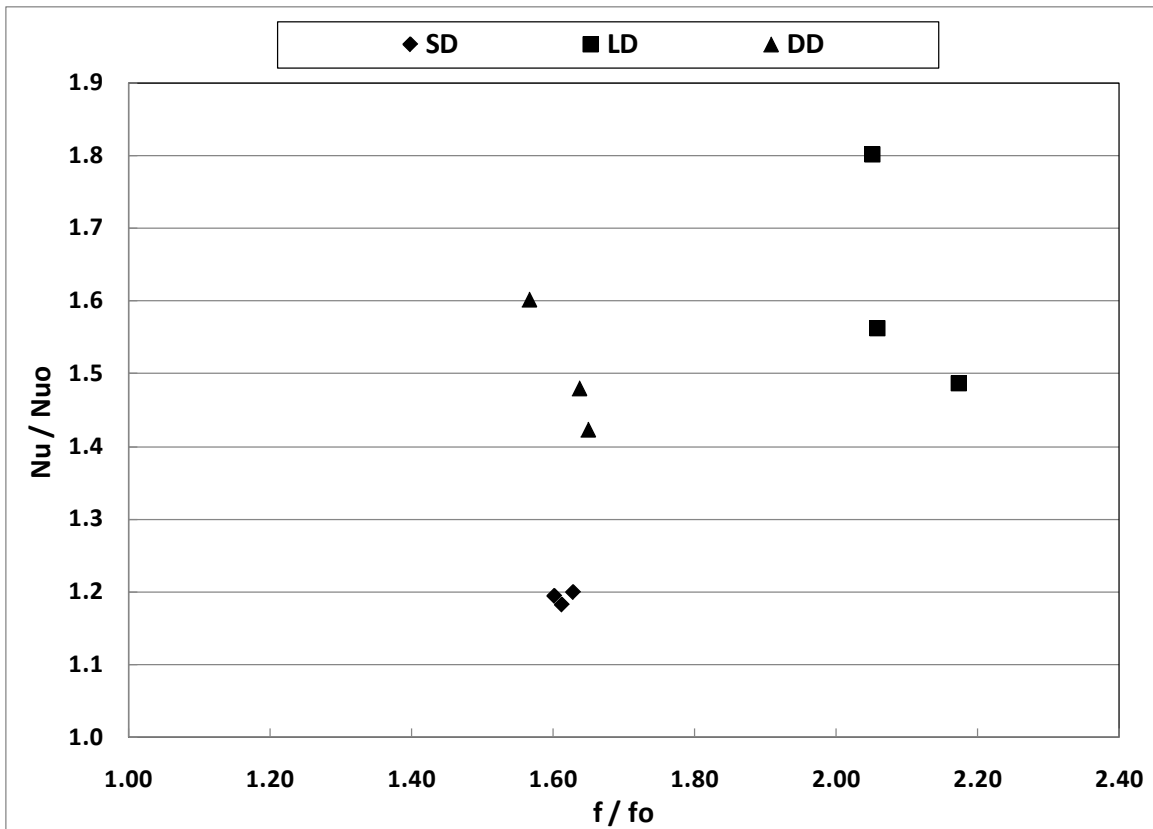


**Figure 4.31: Channel Nusselt Number from the Transient TLC Experiment Plotted Against the Friction Factor Augmentation**

As shown in Figure 4.31, the double-dimple improves the channel-averaged Nusselt number by as much as sixty percent, while accompanied by only sixty percent increase in friction factor when compared to smooth wall correlations. In summary, the double dimples gain the performance of the large dimples, with the cost of the small dimples. This finding has proven to be quite valuable and is the subject of a detailed computational study to understand the physics behind the improved performance of the feature.

### Conclusions Drawn from Experimental Study

As was pointed out throughout the chapter, further work is needed in the development of the transient technique. All of the results from the Transient TLC experiment thus far have been calculated using the accepted, proven methods published in the open literature. However, the curvature and the intersecting edges of the negative feature are known to play a significant role in the measurement and calculation of the surface heat transfer coefficient in when employing the technique. In response, further development and processing of these results will be the continued as the subject of CHAPTER 6:.

## CHAPTER 5: COMPUTATIONAL STUDY OF THE DOUBLE-DIMPLE

### Overview

The performance of the double dimple geometry inspires curiosity about the physics behind this marked improvement in performance over the previously well-characterized single dimple feature. Due to its novelty, extensive validation is necessary to gain a full understanding of this feature and its potential for real-world applications. In this chapter, extensive numerical analysis is performed on the flow over the double dimple feature. The motive of this work is to anchor the flow-field conjectures of the previous chapter that were based on local heat transfer coefficient contours and good old engineering intuition.

Computational Fluid Dynamics is used in this chapter to understand complex flow phenomena that, without accurate simulation, cannot be confirmed or denied. In this case, since no previous works exist to serve as a baseline for comparison, the study starts simple, using only what is known. With repeated validation and review, the model is built up with increasing complexities before reaching the point of the most physical model possible with existing resources. This process of repeated check-pointing and cross-validation serves to generate trustworthy results and inspire confidence in this work's findings of a completely novel design.

## Large Domain RANS Study

### Geometry

The initial development of the computational model was a model of entire experiment test section. The purpose of this large-scale model was to gain a broad understanding of the flow from an aerodynamic standpoint. The computational model was built in GAMBIT in an identical manner as that outline in CHAPTER 3: Geometry Creation and Meshing for the reduced domain study. The dimple was broken down and a mapped mesh was generated for the entire computational domain.

### Meshing

The numerical mesh generated for the full domain study contained a total of 3.73 million cells. Reiterating, as opposed to the upcoming, more detailed model, the purpose of this simulation was to gain an understanding of the aerodynamics within the channel. Therefore, in order to maintain overall cell quality, the first-layer thickness of the wall boundary layers was kept at  $y^+ = 20$ . Skewness and cell aspect ratio were also kept within acceptable values for such a study

### Boundary Conditions

The boundary conditions for this study were taken directly from the experiment. A 'Velocity-Inlet' condition was set to maintain the desired mass flow rate and a 'Pressure-Outlet' based on the static pressure at the exit of the test section. The boundary conditions for the SST  $k-\omega$  model were set based on the channel hydraulic diameter and the percentage turbulence intensity that were also determined from the experimental

setup. Turbulence intensity was found to be approximately three percent, based on values taken with a hot-wire anemometer.

## Results and Findings

Profiles of ten consecutive spanwise cuts through the flow-field of one double-dimple feature are shown in Figure 5.1. The Streamwise location of these planes is approximately eighty percent of the channel length downstream from the channel inlet. One of the key observations to pull from this illustration is the reduced boundary layer thickness on the bottom wall. Due to the course grid, the resolution of the turbulent vortices advected downstream of the dimple is blurred. However, it can still be seen that the flow into the dimple is reattaching at some point near the ridge that is separating the upstream and downstream hemispherical indentions. The streamwise profiles of velocity, traversed across the half-width of the channel also support this conjecture (Figure 5.2).

Figure 5.2 and Figure 5.3 indicate that flow, throughout the fully-developed portion is periodic and symmetric in nature. This was expected based on the definition of fully developed flow; specifically, the pressure drop through this portion of the channel is linear. By observing this to be true in the full-domain computational model, a more detailed model can be developed using these flow features to our advantage. Rather than modeling the entire domain, a reduced model can be generated, with periodic inlet and exit conditions; whatever flow comes in, goes out (satisfying continuity). The computed pressure drop can then be converted to a body-force term that will be applied to simulate the pressure difference that is driving the fluid motion.

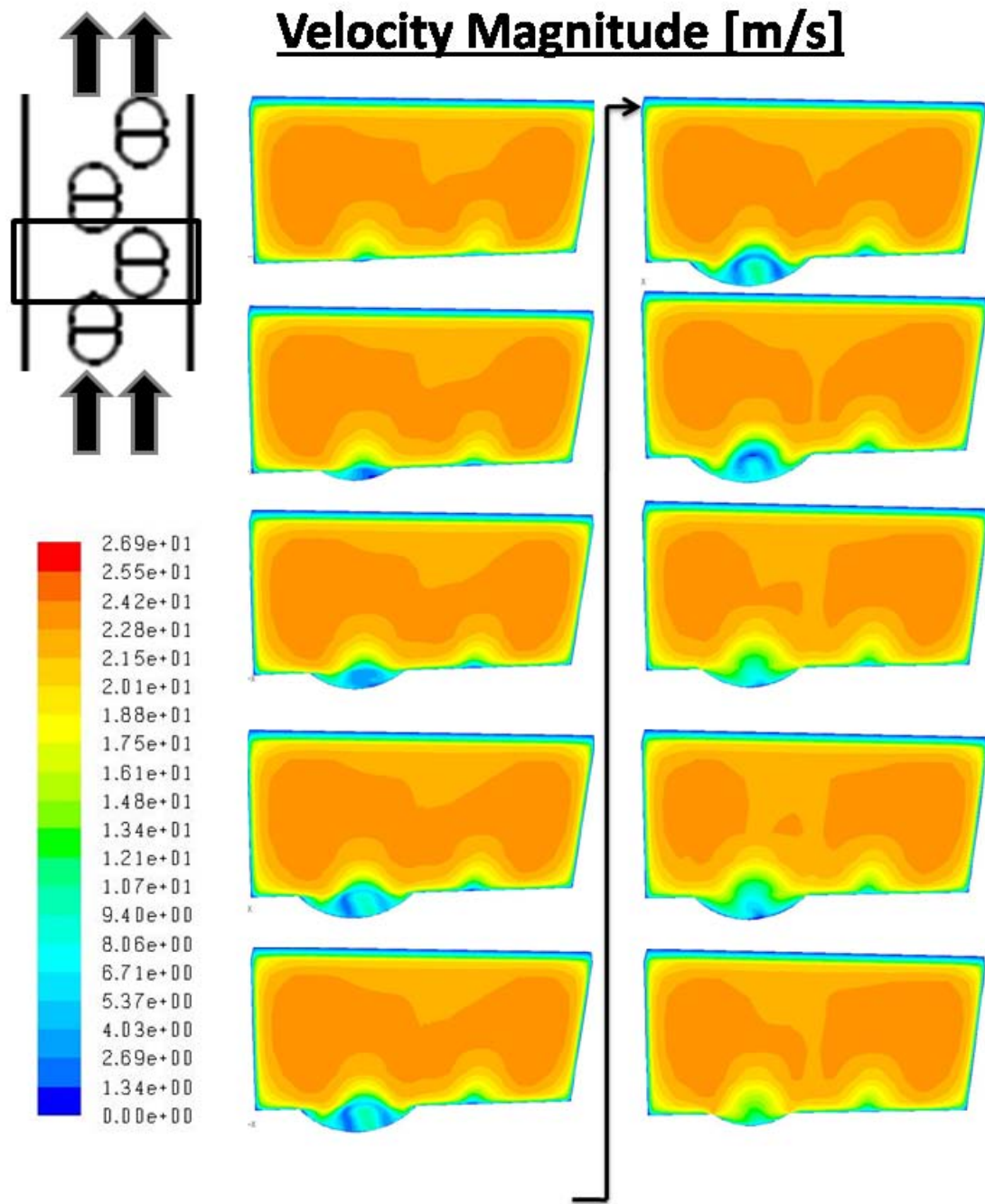
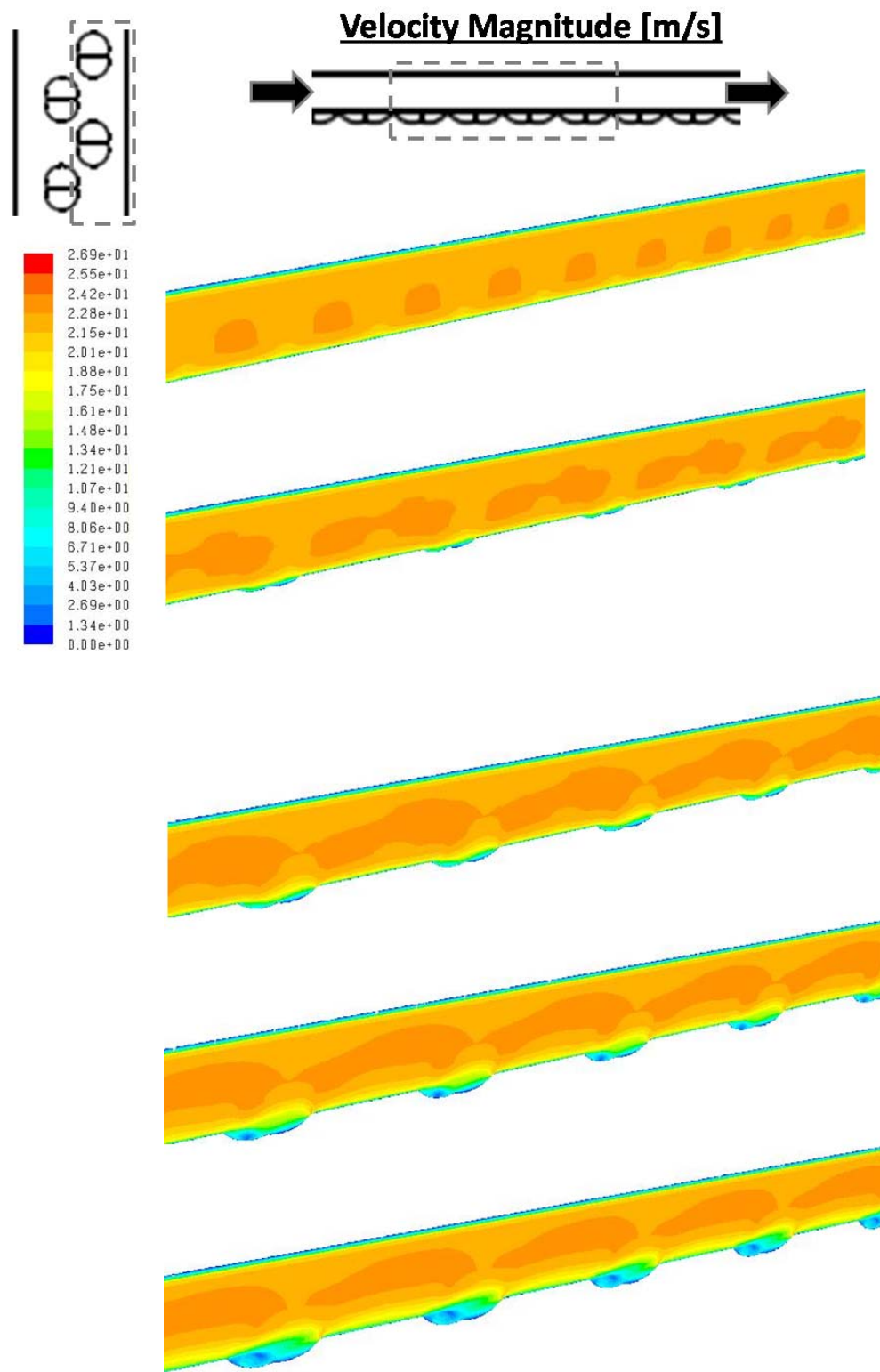


Figure 5.1: Consecutive Spanwise Profiles of Velocity Magnitude Cut Across one Double Dimple –  
 $Re = 40000$



**Figure 5.2: Streamwise Profiles of Velocity Magnitude – Full Domain RANS, Re = 40000**

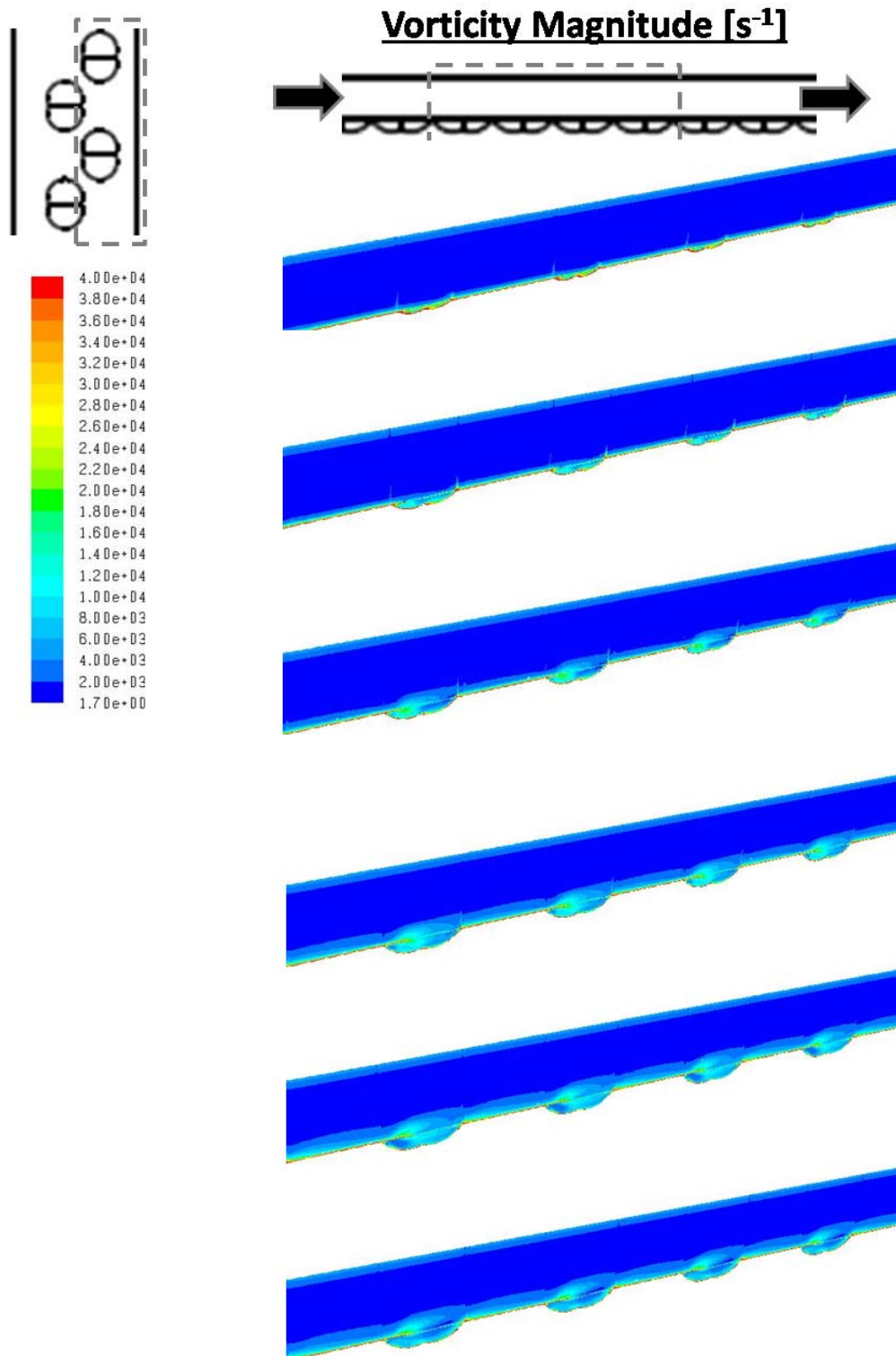
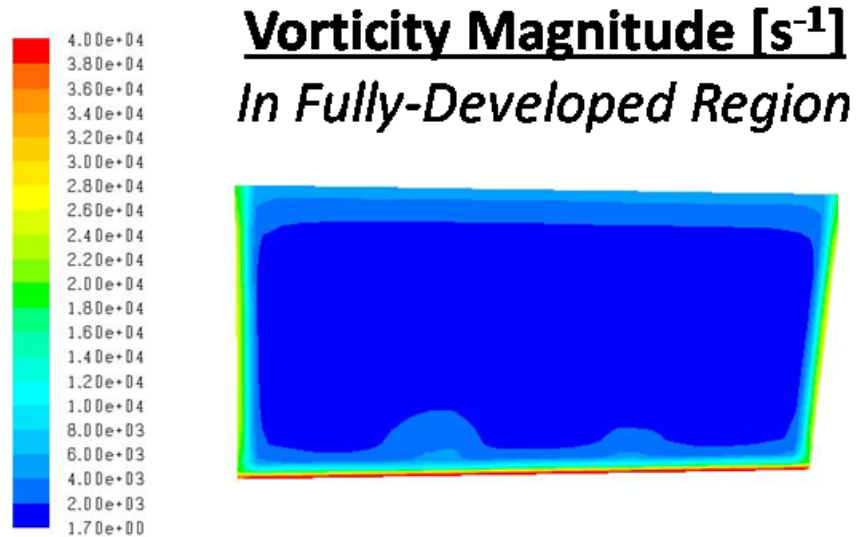


Figure 5.3: Streamwise Profiles of Vorticity Magnitude – Full Domain RANS, Re = 40000



For the purposes of validation the periodic boundary condition assumption, Figure 5.4 and Figure 5.5 were taken for comparison to the solutions of the reduced domain RANS study at the same dimple-to-dimple location.



**Figure 5.4: Spanwise Profile of Vorticity Magnitude for Boundary Condition Validation – Full Domain RANS, Re = 40000**

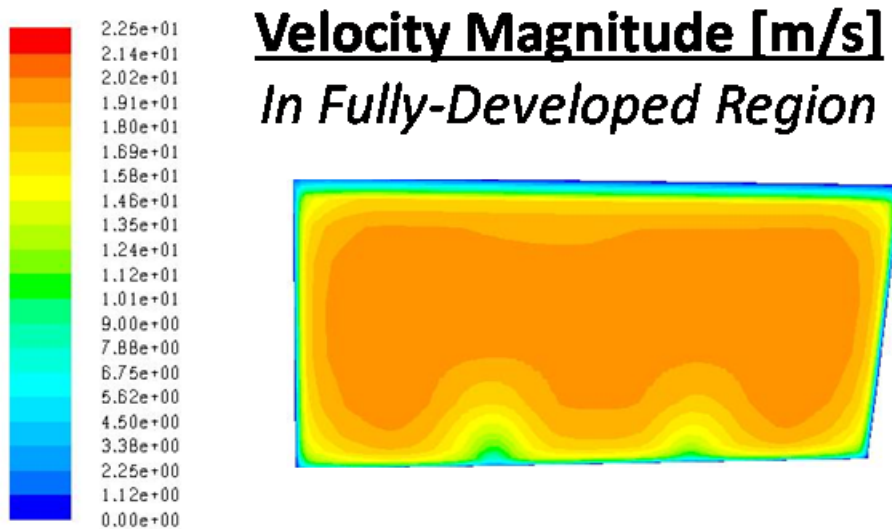


**Figure 5.5: Spanwise Profile of Velocity Magnitude for Boundary Condition Validation – Full Domain RANS, Re = 40000**

## Reduced Domain, Refined RANS Study

### Validation

The immediate observation taken from the reduced domain RANS study is the validation of the boundary conditions with the full domain study. Comparing Figure 5.6 to Figure 5.4, the results are very similar. The increased resolution in the near-wall region yields much higher resolution, which is crucial in the calculation of vorticity because of the added uncertainty in the calculation of the derivative. However, it is determined that these results are in good agreement based on their overall scale and minor, justifiable deviations.

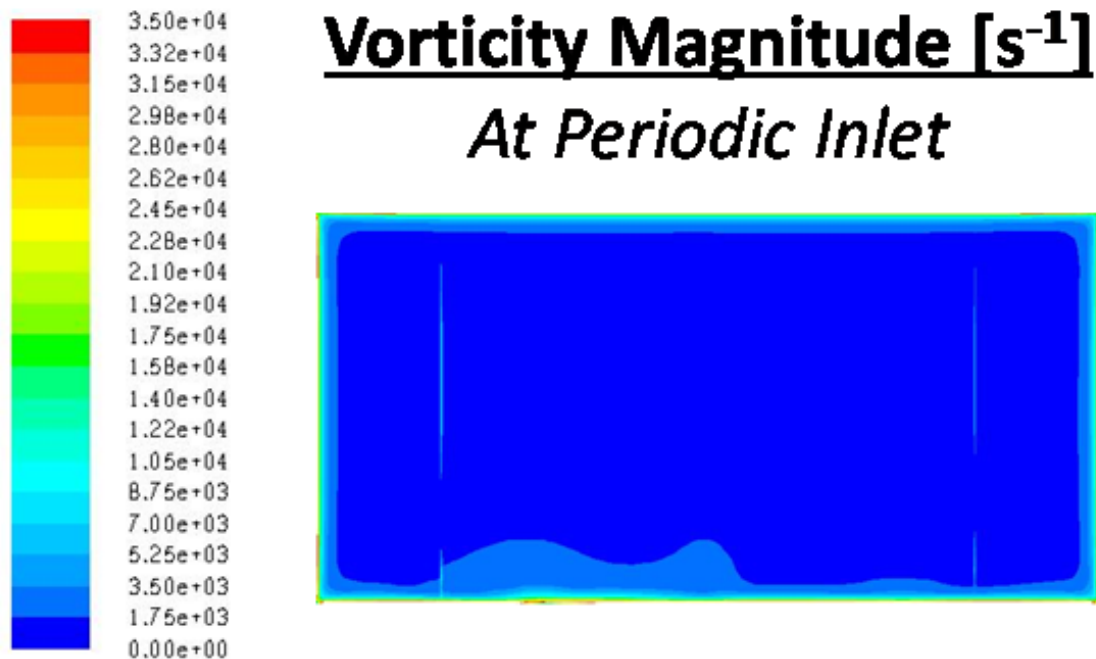


**Figure 5.6: Spanwise Profiles of Vorticity Magnitude – Re = 40000**

A similar conclusion is reached when comparing Figure 5.7 to Figure 5.5. increased near-wall resolution allows for more accurate simulation of the boundary layer flows. However, the same flow features are still resolved by both models: low velocity flow

downstream of the dimples, reduced boundary layer thickness on the top and bottom walls compared to the side walls, and high velocity core flow away from the effects of the boundary layers. These comparisons provide full validation of the periodic boundary condition assumption and clear the way for further simulation with the model.

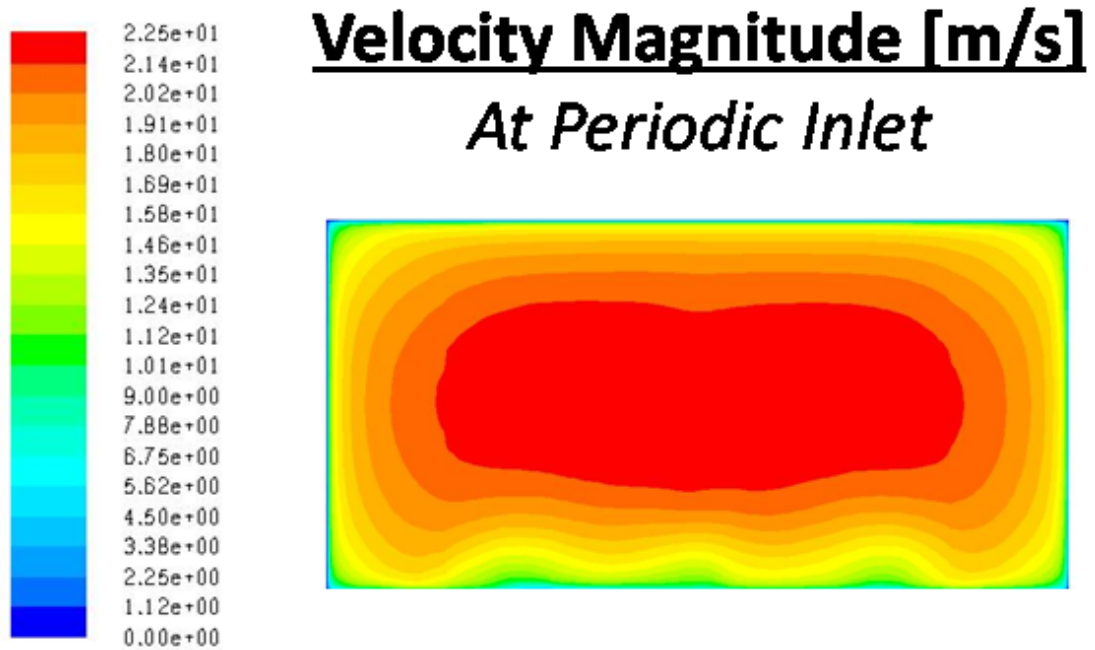


**Figure 5.7: Spanwise Profiles of Velocity Magnitude – Re = 40000**

Reynolds Number = 40000

A key feature of the reduced domain RANS study is the solution of the energy equation in addition to the time-averaged Navier-Stokes equations that model the fluid flow. This allows for further study and validation of the experimental results through comparison of the local surface heat transfer coefficients as well as the averaged values. A detailed comparison is presented in the final section of this chapter (Conclusions from Computational Study).

Figure 5.8 shows the contours of the local surface Nusselt number. The default configuration for this calculation did not yield accurate results due to programs default length scale. However, after establishing the characteristic length as the hydraulic diameter of the channel, the values were found to be within close proximity to the experimental works.

The numerical simulations provide far greater resolution of surface results than ever possible with the current data acquisition system. In comparison to Figure 4.21, one key difference is the presence of a split in the downstream enhancement, behind the dimple. This feature has been observed by other researchers working with the conventional single dimple designs (Isaev, Leontiev, Kudryatsev, & Pyshnyi, 2003). Also, the appearance of 'hot spots' on the floor of the dimple is a new feature that was not resolved in the experimental efforts.

As described in detail in CHAPTER 2:, RANS simulations solve the time-averaged Navier-Stokes equations in order to reduce computational expense. The penalty is lost resolution of unsteady flow features and the resulting surface effects caused by these fluctuations. Dimples, by nature, generate unsteady fluctuations the flow. This is believed to be the reason for which no two dimples are observed to have an identical solution. Therefore, as the resolution of the numerical model is increased, new insight into the performance of these features is gained and a deeper understanding of the true flow physics is possible.

## Surface Nusselt Number

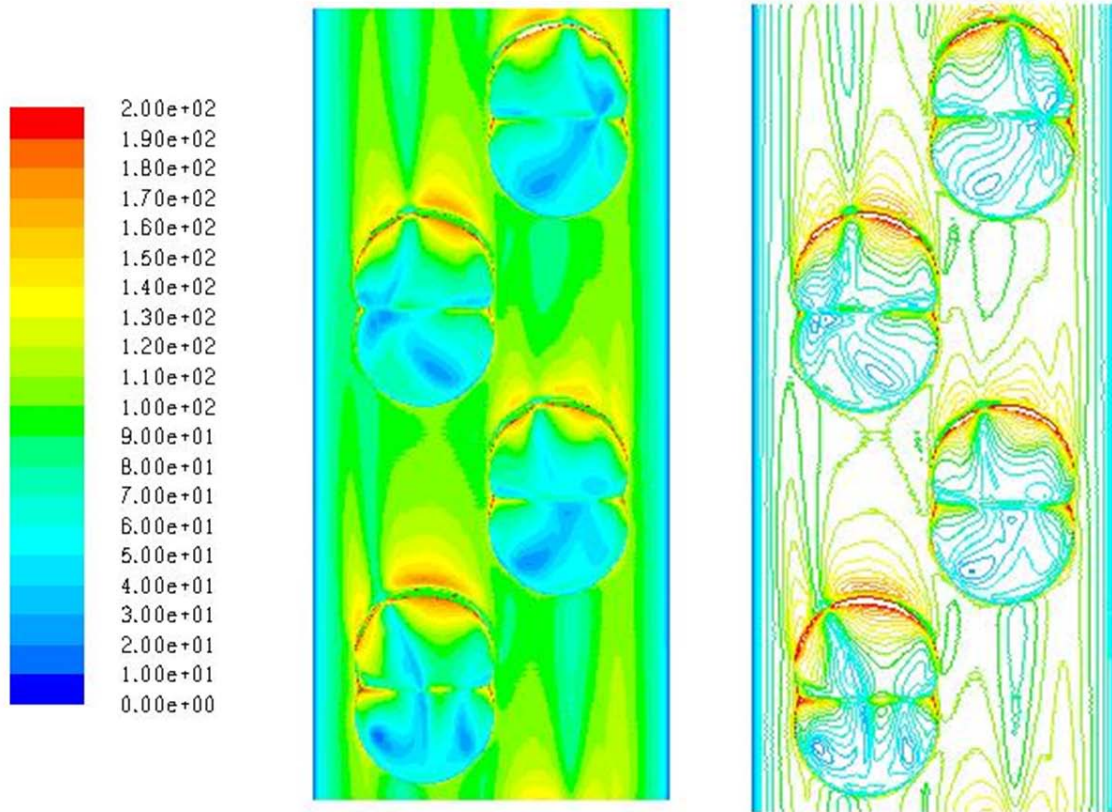


Figure 5.8: Surface Heat Transfer Coefficient Contours, Bottom Wall –  $Re = 40000$

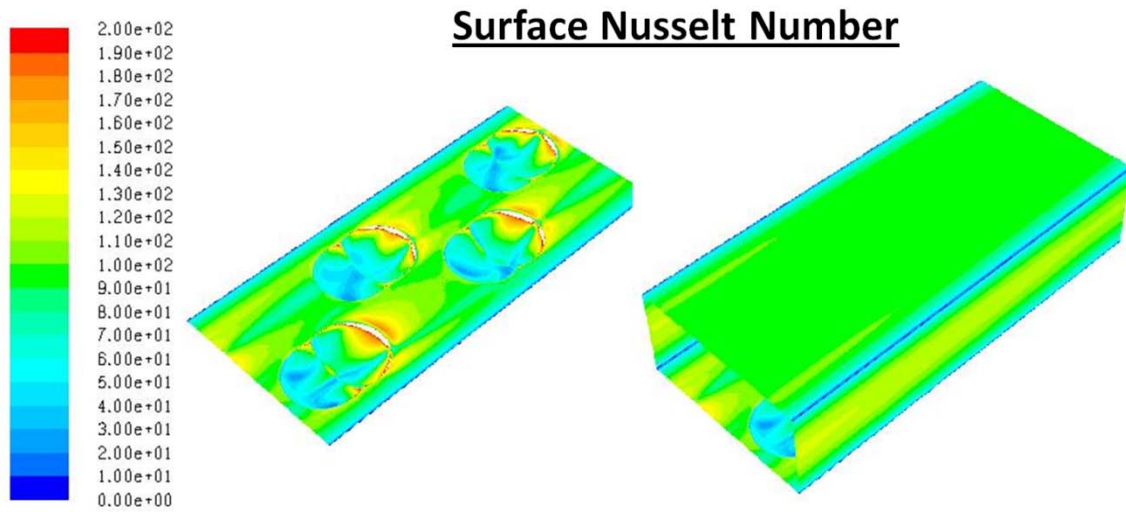
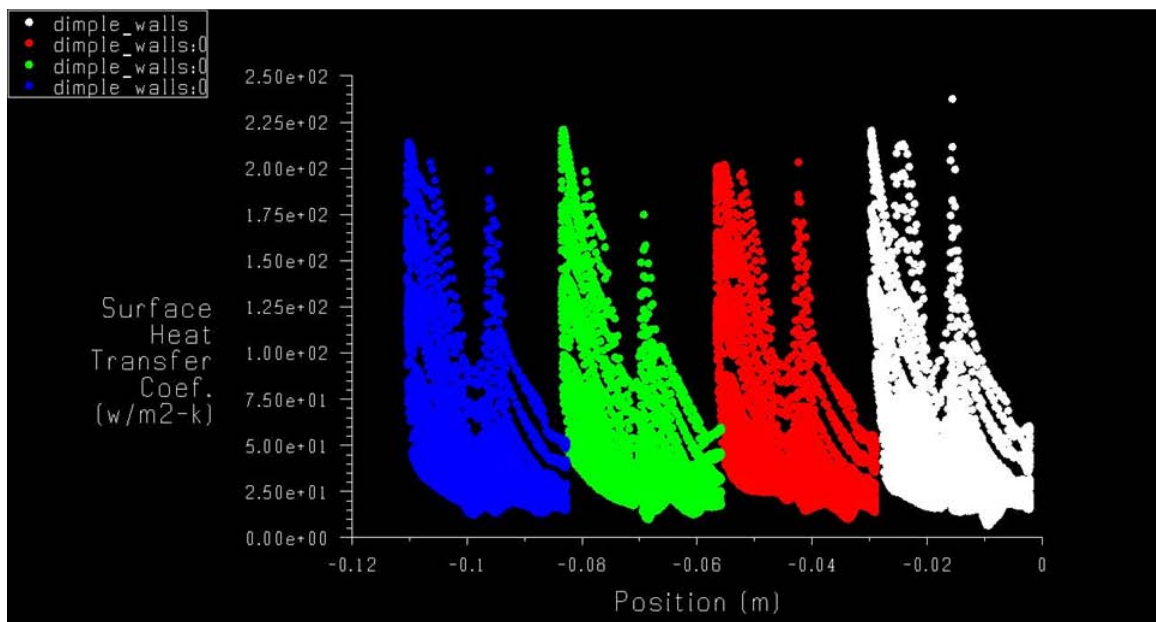


Figure 5.9: Surface Heat Transfer Coefficient Contours –  $Re = 40000$

Figure 5.9 shows the surface Nusselt number of the side and top walls, relative to the bottom wall. An interesting observation from this image is that the channel side walls have a higher surface Nusselt number than the top wall. This is in contrast with the experimental results presented in the previous chapter. It is possible the eminent location of the surface features is causing the increased advection of heat from the side walls through ejected vortices that are not strong enough to jump the mainstream flow and affect the top wall.



**Figure 5.10: Surface Heat Transfer Coefficient as a Function of Streamwise Distance –  $Re = 40000$**

Figure 5.10 is a plot of the local surface heat transfer coefficients *inside the dimples* versus the streamwise location (note that HTC, for this experiment, is approximately twenty percent lower than Nusselt number). The flow is entering from the right and exiting on the left. There is a distinct peak in the channel performance at the dividing ridge between the two dimples with a more pronounced increase at the dimple exit. This adds further confirmation to the conjecture that, even at the highest flow rate, the

momentum of the mainstream flow is still low enough to react to the low pressure region. This is evident in the flows reattachment, confirmed by this peak.

## Static Pressure (Gauge) [Pa]

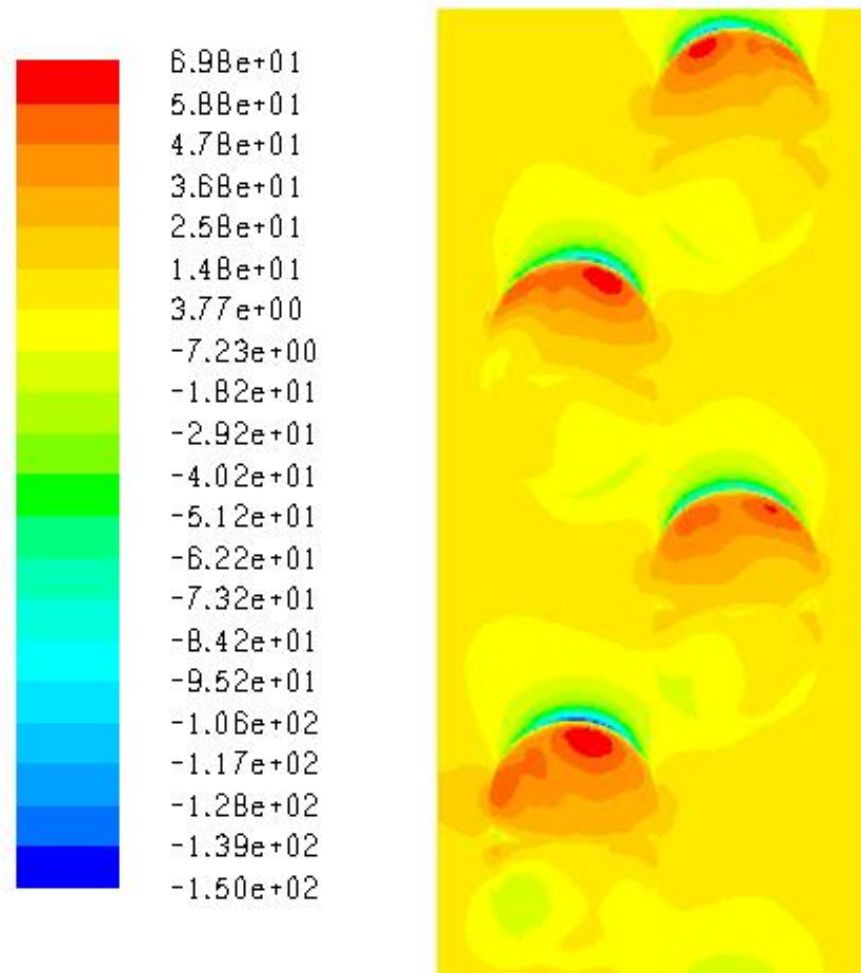


**Figure 5.11: Static Pressure Distribution over the Bottom Wall of the Channel –  $Re = 40000$**

Figure 5.11 provides detailed information about the reattachment location of the flow over the dimple. In most cases, full reattachment does not take place until the downstream dimples, as indicated by the impingement-like high pressure region.



However, the orange regions in the upstream indentation are indication of some minor reattachment taking place upstream of the more dominant feature.

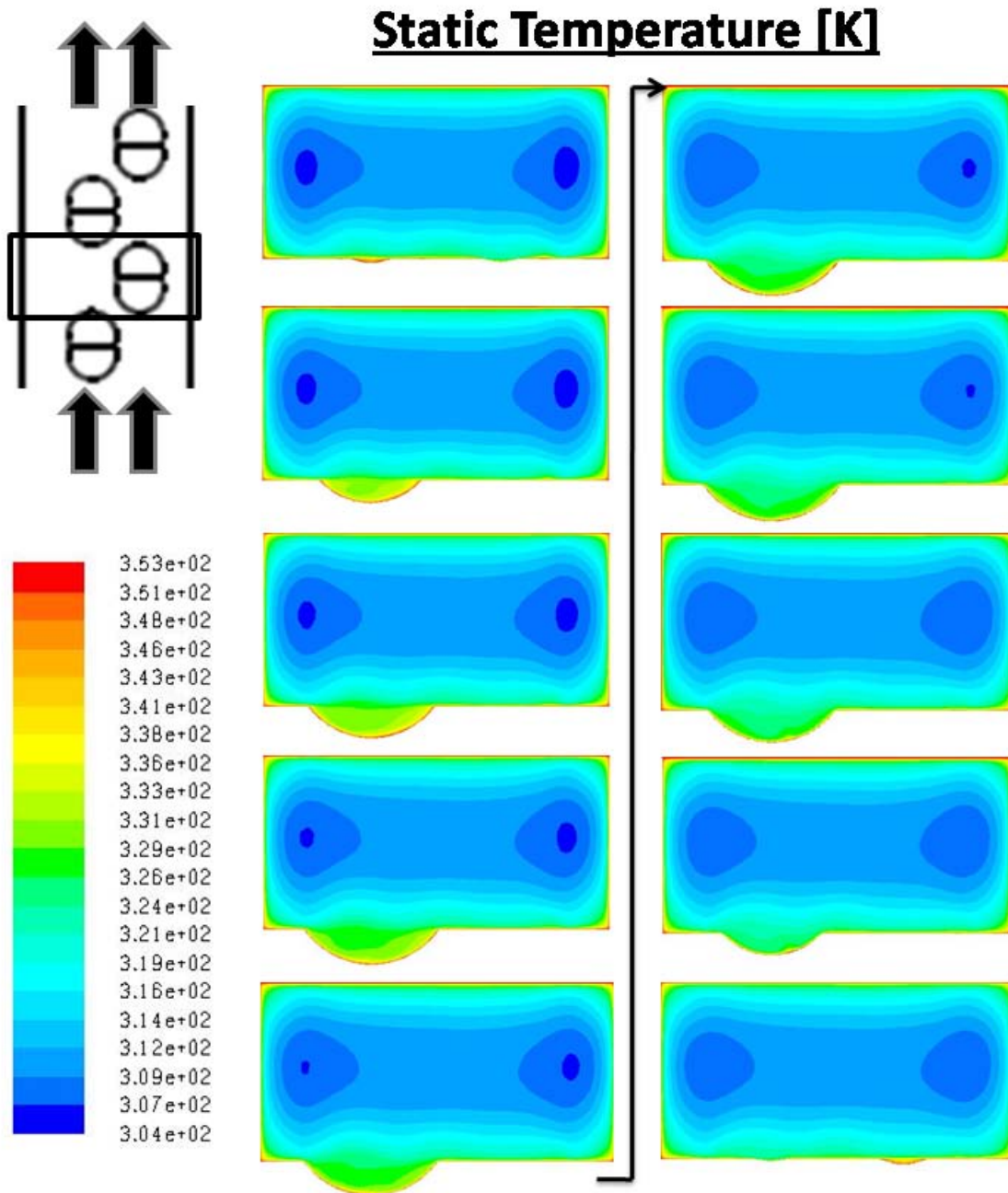


Figure 5.12: Spanwise Profiles of Static Temperature –  $Re = 40000$

The spanwise contours of the Figure 5.12 static temperature indicate a high temperature region near the upstream edge of the feature, which is indicative of the recirculation zone



conjectured to exist there. Looking farther downstream, within the feature, the thickness of the thermal boundary layer is reduced lower than what is observed in the mainstream flow.

Another key feature of this diagram is the presence of low temperature zones near the side walls. The streamtubes of cold flow are pushed toward the side wall by the slower moving, highly turbulent flow near the bottom wall that is advecting up into the mainstream. The existence of these low temperature regions explain the solutions prediction of increased Nusselt number on the channel side walls.

Two aspects of the flow physics generated by a dimple feature are shown in Figure 5.13. The first is the downstream advection of turbulent kinetic energy immediately after the double dimple, which is seen on the flat portion of the bottom wall. The first profile indicates a value of  $k$  as approximately 17.5 in a dense region next to the channel wall. As this vortical packet of fluid is swept downstream, the energy-containing eddies are diffused into the surrounding mainstream flow as the boundary layer begins to develop over the flat surface. Understanding this rate of dissipation is extremely valuable in designing an array with the proper dimple-to-dimple pitch. The second aspect of the dimple flows that is resolved in Figure 5.13 is the shear layer that is formed between the slow-moving recirculation zone of the leading edge of the dimple and the faster, high momentum flow of the mainstream (Figure 5.14). This results in the generation of vorticity (Figure 5.15), or flow rotation, and a spike in the turbulent kinetic energy in the region. The increased turbulent kinetic energy of the shear layer is advected downstream,

gaining energy before it is ejected from the downstream edge of the dimple. After removing the shearing force that serves as a source for this flow structure, the pocket of turbulence is quickly dissipated, in the same manner as the flow from the preceding dimple captured in the same images.

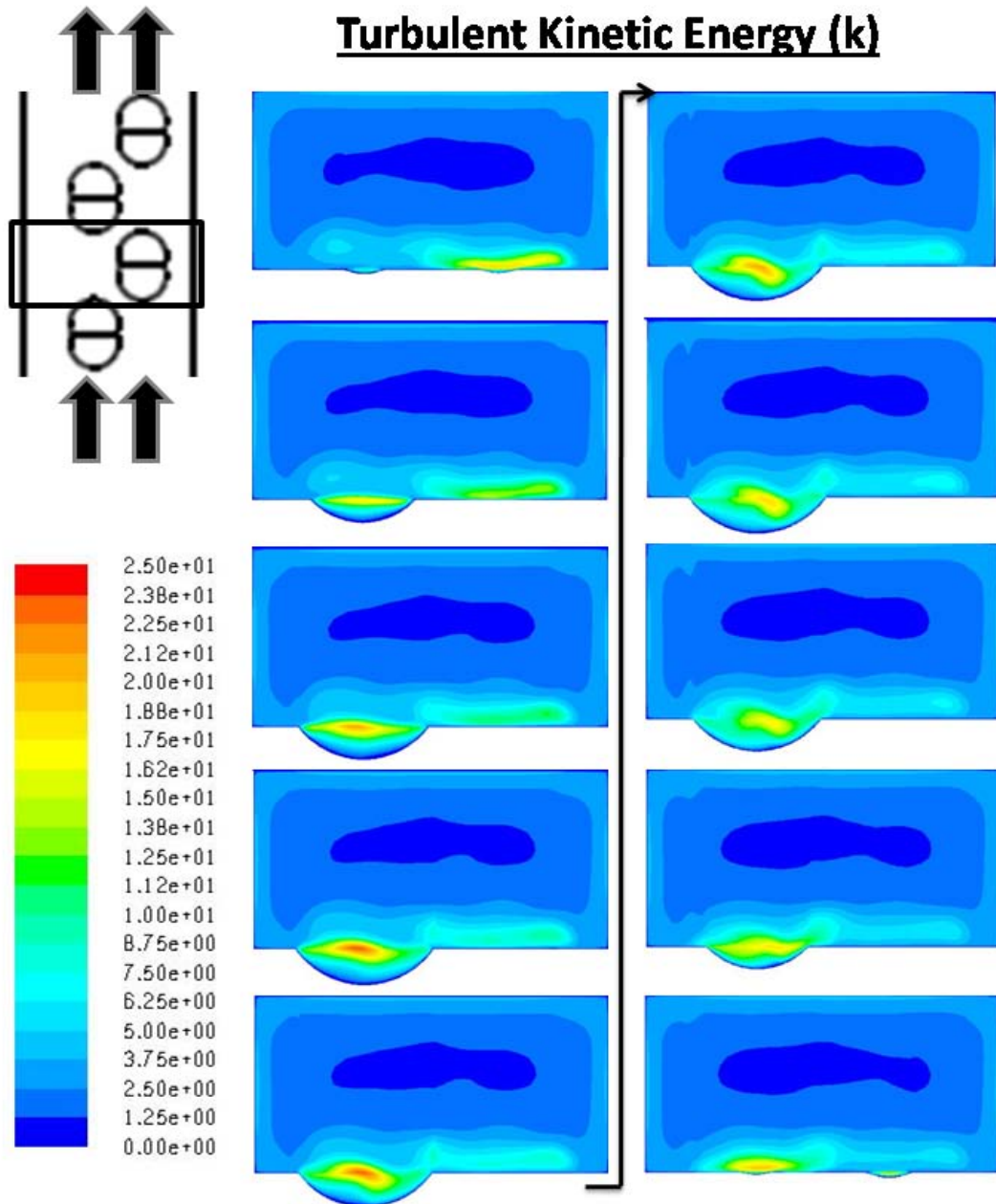


**Figure 5.13: Spanwise Profiles of Turbulent Kinetic Energy – Re = 40000**

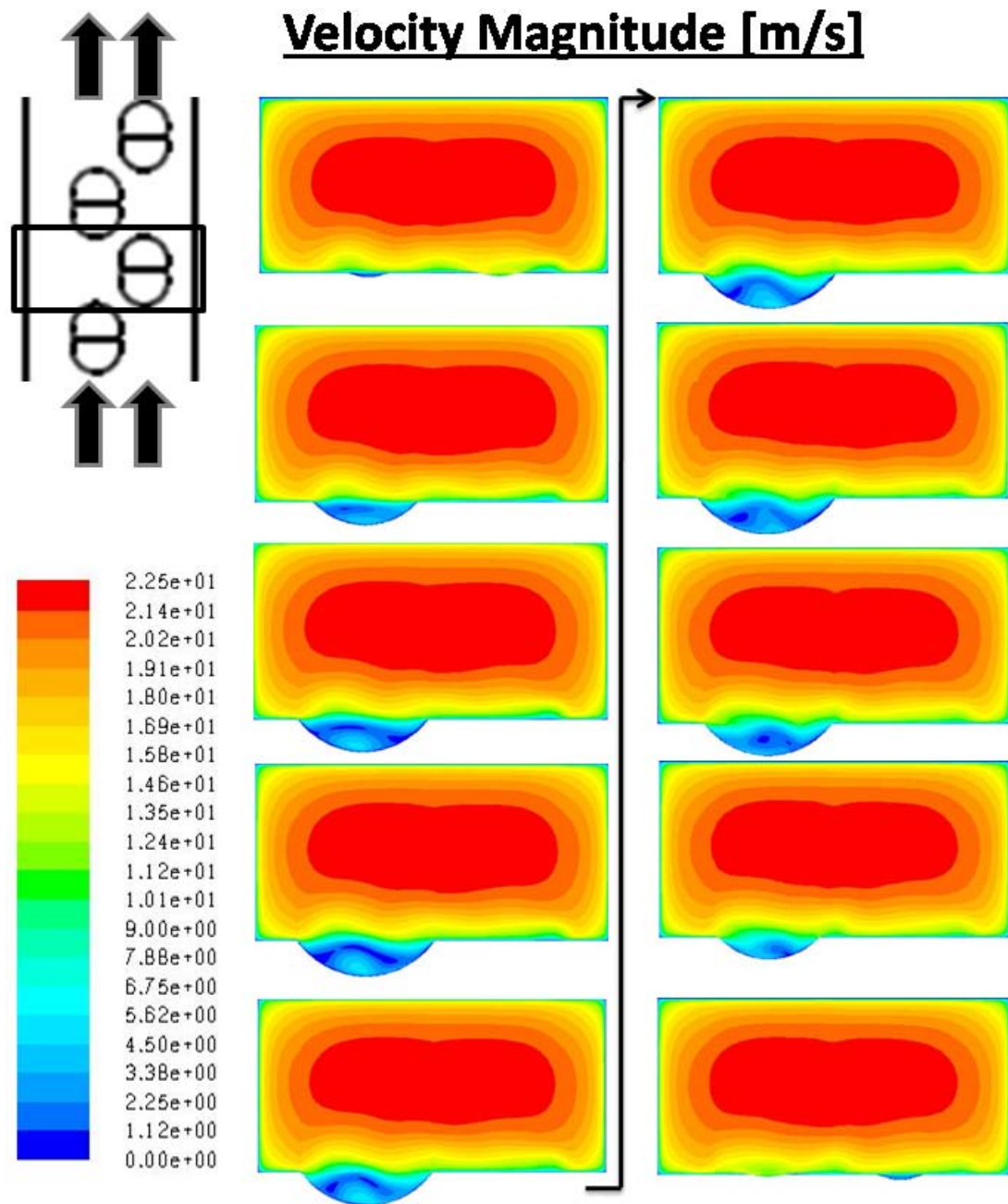


**Figure 5.14: Spanwise Profiles of Velocity Magnitude –  $Re = 40000$**

The sharp velocity gradient in the upstream regions of the flow over the dimple is the source of the shearing force that generates the vorticity in this region of the flow field.

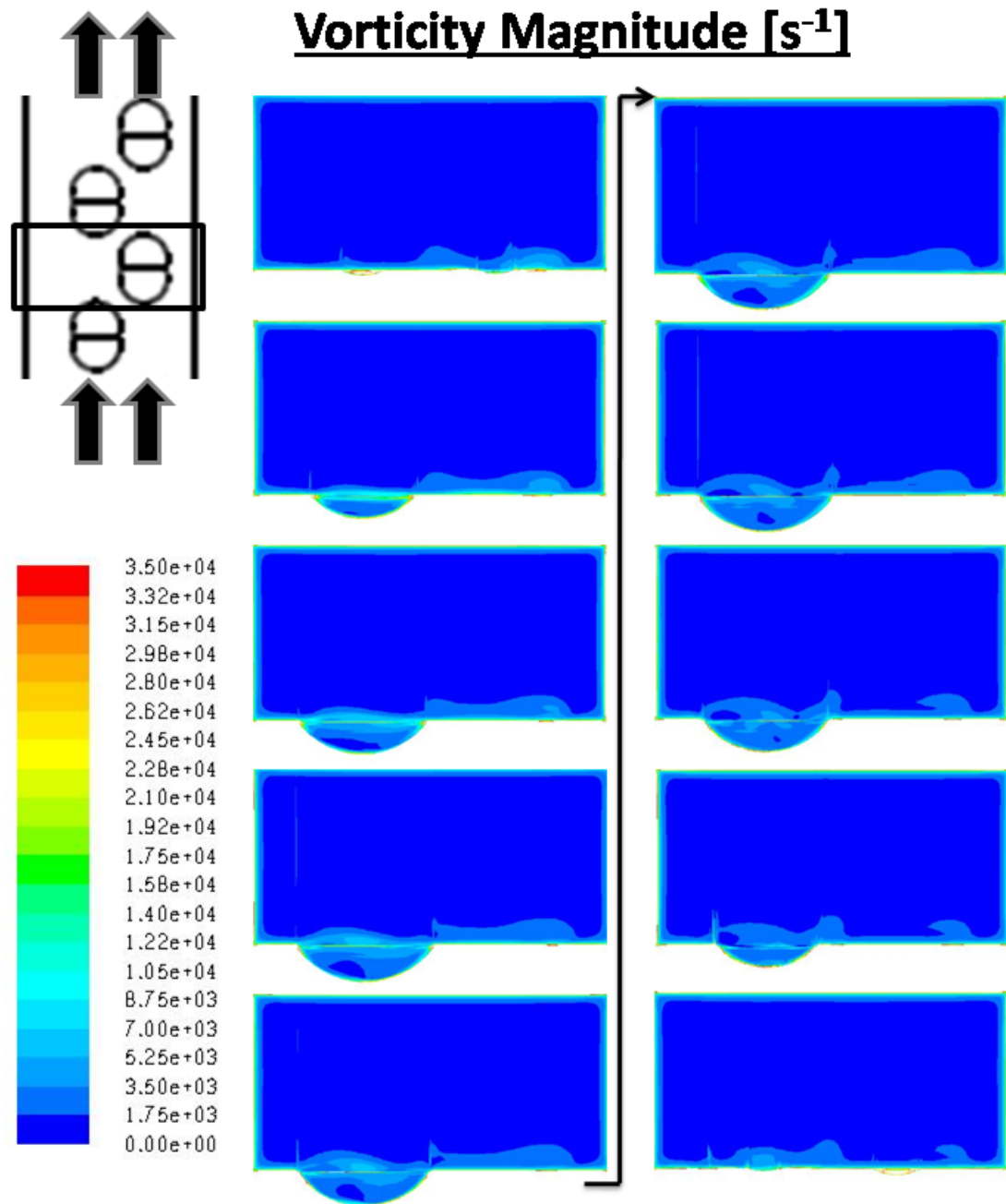


**Figure 5.15: Spanwise Profiles of Vorticity Magnitude – Re = 40000**

The spanwise contours of vorticity do not offer a great deal of information beyond the general location of the source. To conserve computational resources, the mesh for the reduced domain RANS study is still too coarse to accurately resolve the curl of the

velocity field and provide detailed information in this region. Instead, the details of this aspect of dimple flow physics is reserved for the capstone - large eddy simulation.

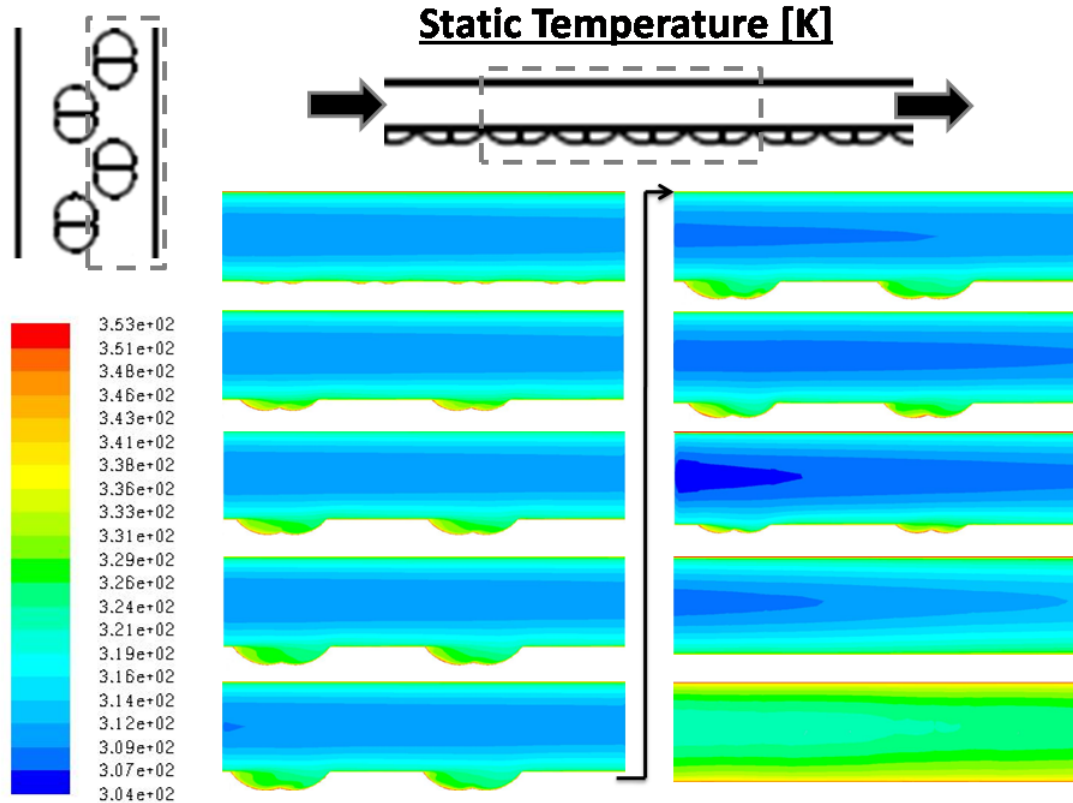


**Figure 5.16: Streamwise Profiles of Static Temperature – Re = 40000**

The streamwise contours of static temperature given in Figure 5.16 add further understanding to the reason behind the side wall heat transfer augmentation . The static temperature profiles of the stream tube in the near-wall region nearly mimic the trends in the surface Nusselt number on the side wall. The reduction in the thickness of the thermal boundary layer is also apparent in the flat regions directly downstream of the feature. As with the spanwise contours of static temperature, these streamwise contours confirm the existence of the recirculation zone as well as supporting the previous

conjecture that it is completely contained within the upstream indentation of the double dimple surface feature.

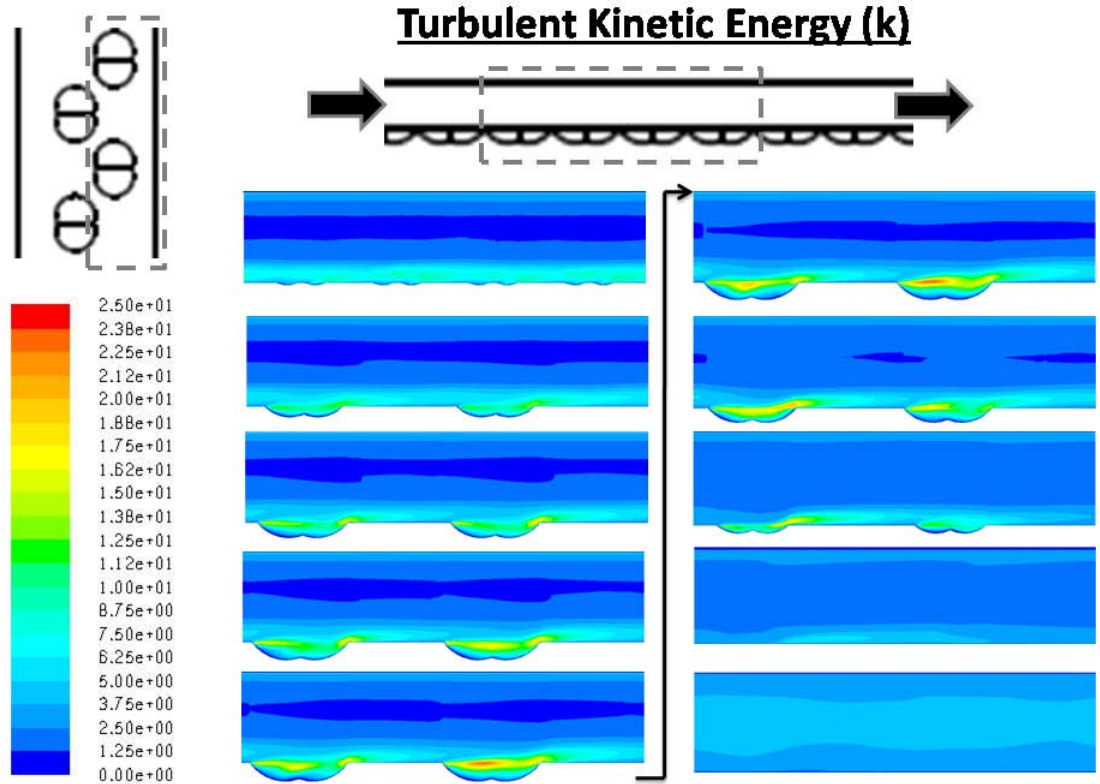


**Figure 5.17: Streamwise Profiles of Turbulent Kinetic Energy –  $Re = 40000$**

The streamwise contours of turbulent kinetic energy, in Figure 5.17, illustrate the successful realization of the fundamental purpose behind the application of any transport enhancing feature. With reference to the top left image, the turbulent kinetic energy within the near wall region of the bottom wall is approximately 800 percent higher than the boundary layer region of the top wall.

Furthermore, Figure 5.17 adds clarity to the previous description of a prominent shear layer present in the intersecting region between the mainstream flow and the slower,

recirculating flow within the upstream cavity of the dimple. There is a notable variation if the distribution of the turbulent kinetic energy between the two dimples; though the same features are present, they are quite different. Reiterating, this is because a time-averaged model is being applied to an inherently unsteady problem. The two dimples are both being modeled correctly, as possible solutions to the flow field – they are simply different solutions within the same domain.

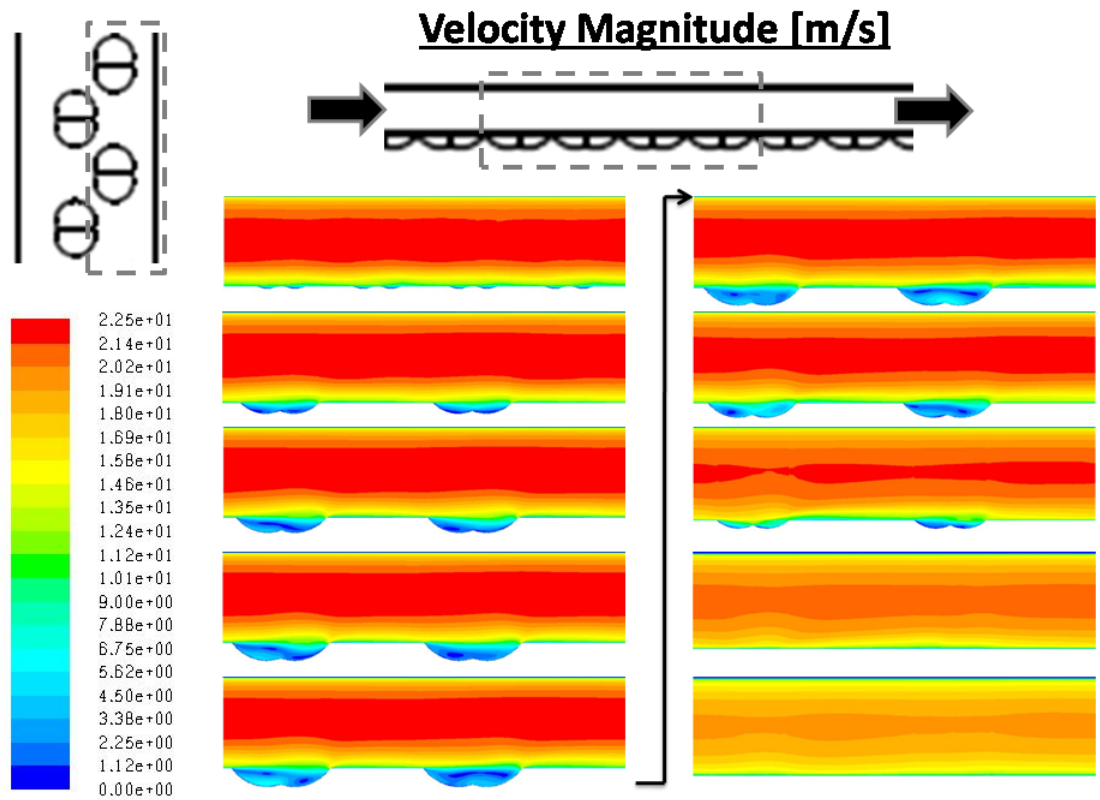


**Figure 5.18: Streamwise Profiles of Velocity Magnitude – Re = 40000**

The streamwise contours of velocity as the plane of interest is traversed in the spanwise direction across the positive half of the domain is shown in Figure 5.18. The dissipation of the velocity gradient in the shear layer is seen in the region above the dimple. This



dissipation is the source of the vorticity generation, shown in Figure 5.19, where the kinetic energy of the flow in the axial direction is converted to rotational energy.

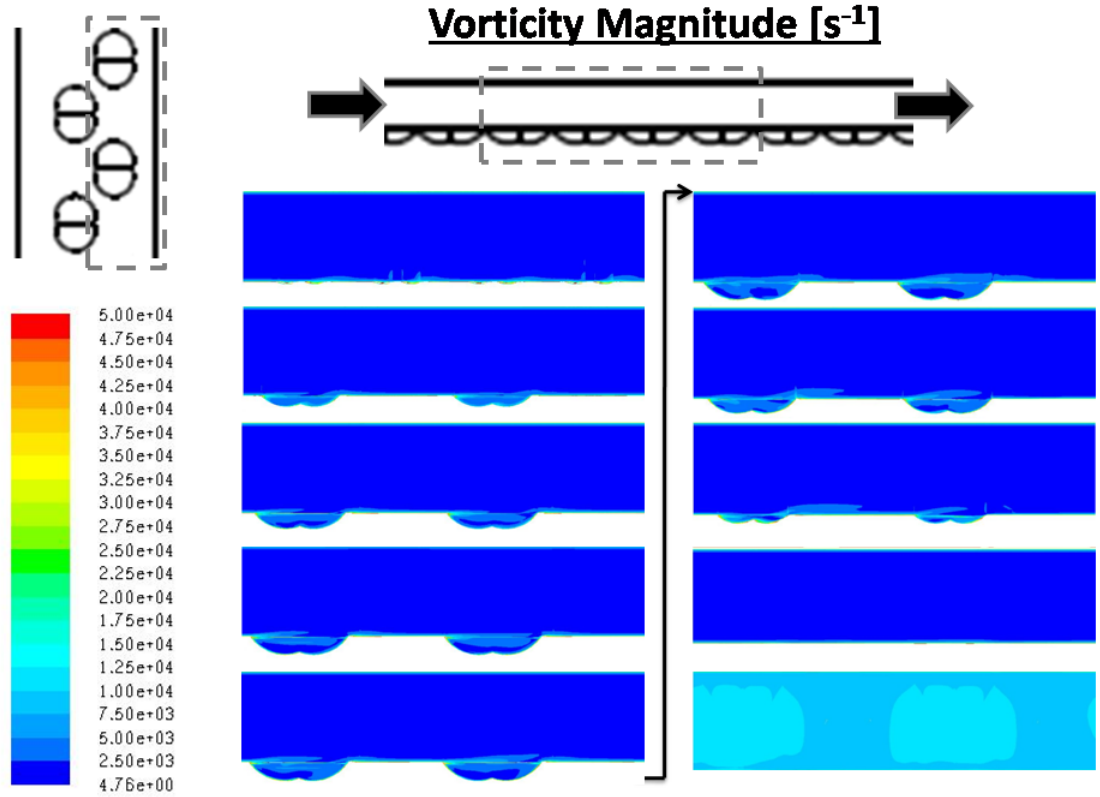


**Figure 5.19: Streamwise Profiles of Vorticity Magnitude – Re = 40000**

Reynolds Number = 30000

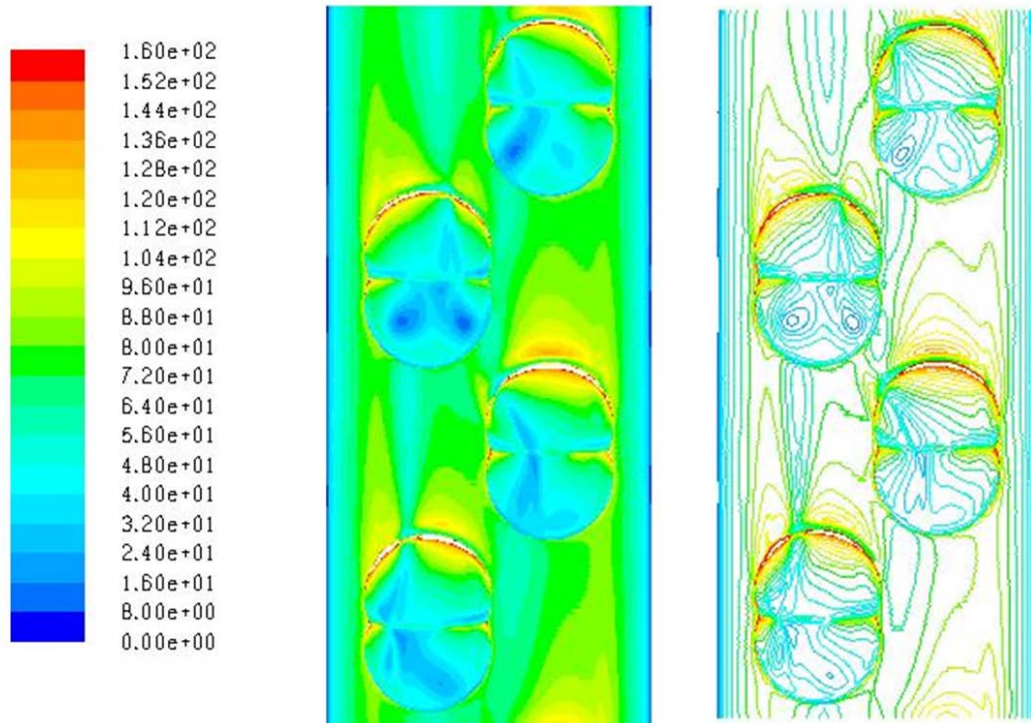
After close examination and post-processing, it was determined that the level of detail revealed by the RANS simulation yielded no new insight to the local flow physics when subject to a change in Reynolds number. Therefore, for the purposes of this work, they have been relocated to APPENDIX E: and will be the subject of any further discussion to avoid redundancy. For the remaining two Reynolds numbers, only the surface Nusselt



number data will be subject to scrutiny and discussion as there will be continued analysis and focus placed on the information contained therein.

The surface Nusselt number contours in Figure 5.20 and Figure 5.21 are seen to closely mimic those the 40000 Reynolds number solution. The split downstream augmentation is observed on multiple dimples and the general non-uniformity from feature to feature remains present.

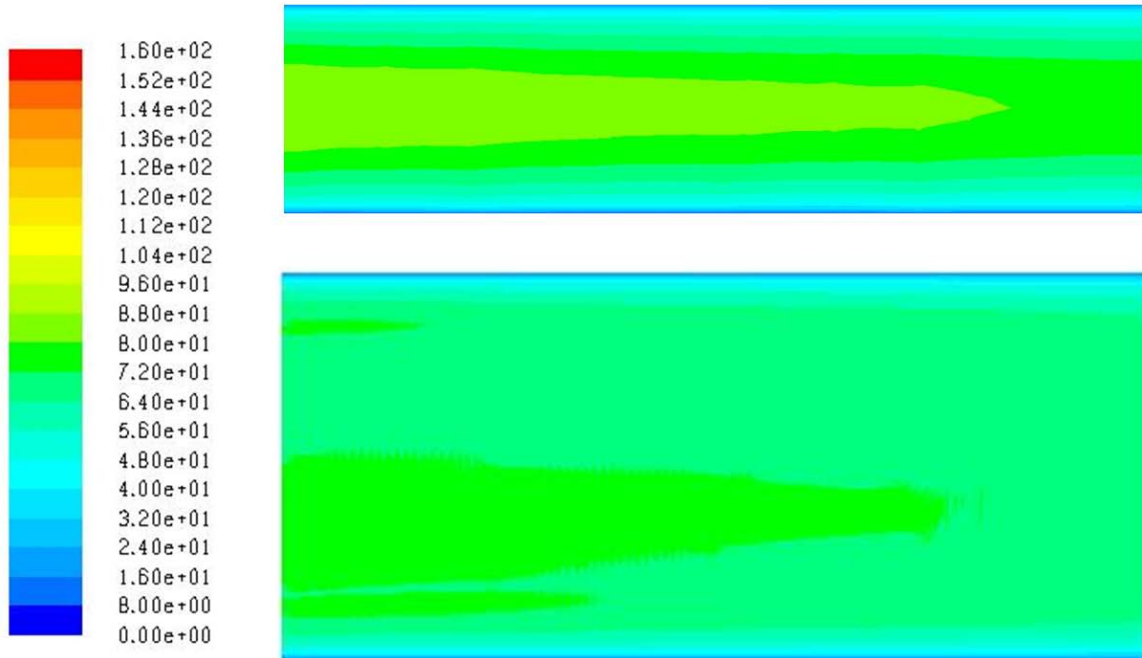
## Surface Nusselt Number



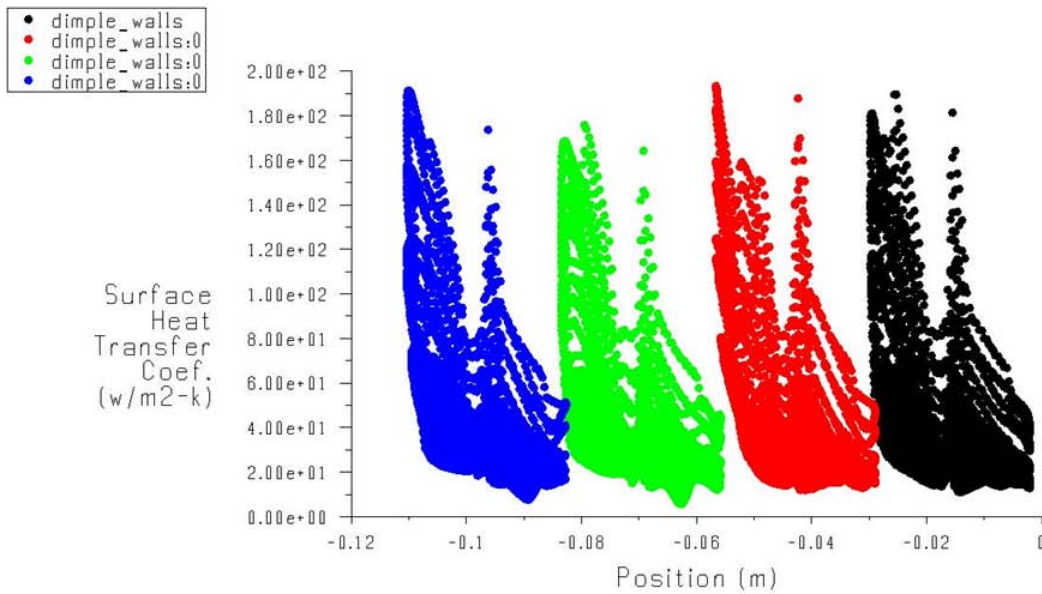
**Figure 5.20: Surface Heat Transfer Coefficient Contours, Bottom Wall-  $Re = 30000$**

Figure 5.22 indicates a slight increase in the surface area participation within the feature. This is due to the reduced tendency of the flow to ‘jump’ the dimple, having a late reattachment zone due to the increase momentum of the mainstream flow.

## Surface Nusselt Number



**Figure 5.21: Surface Heat Transfer Coefficient Contours, Side and Top Walls– Re = 30000**



**Figure 5.22: Surface Heat Transfer Coefficient as a Function of Streamwise Distance – Re = 30000**

Reynolds Number = 20000

As the channel Reynolds number is reduced to the minimum value of 20000, the average Nusselt number inside the dimple and the Nusselt number on the bottom wall begin to converge. As the momentum of the mainstream flow is reduced, the flow has a greater tendency to fall into the dimple, reattaching at increasingly upstream locations within the feature. With a steady mainstream flow temperature, the response of the flow to a change in pressure is constant throughout the range of Reynolds numbers studied. With this in mind, the time scale of the flow's response to the change in pressure should remain constant (the acoustic speed). Therefore, it is the velocity of the fluid with respect to the ability of the flow to respond to the presence of a void that governs this phenomena.

## Surface Nusselt Number

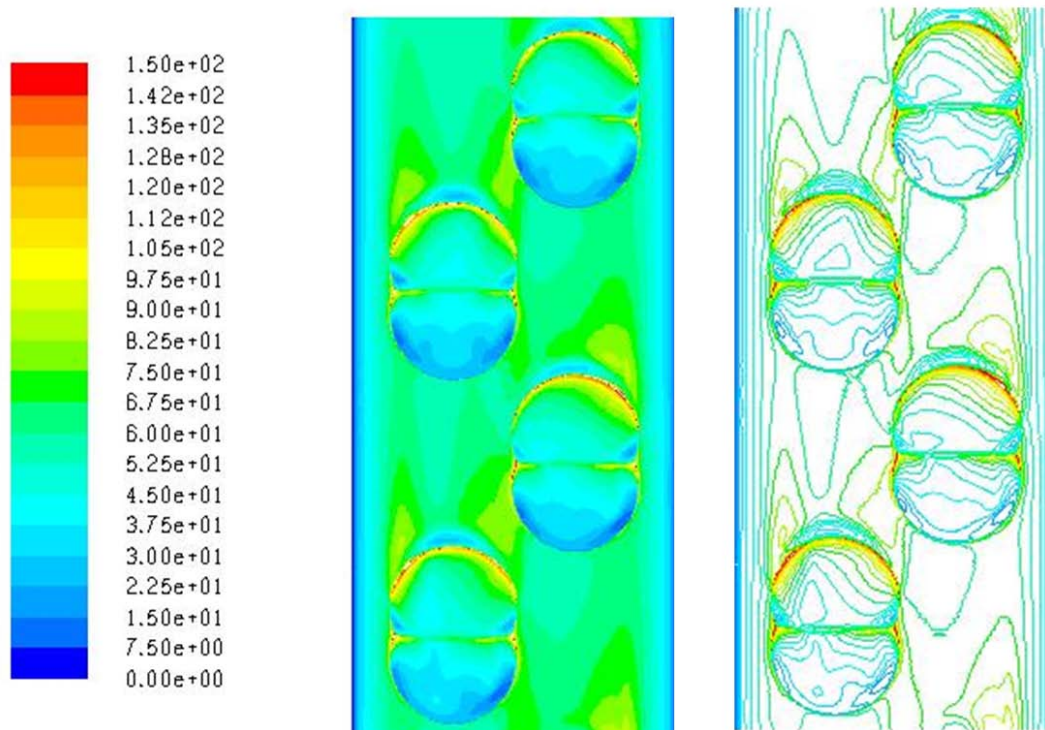
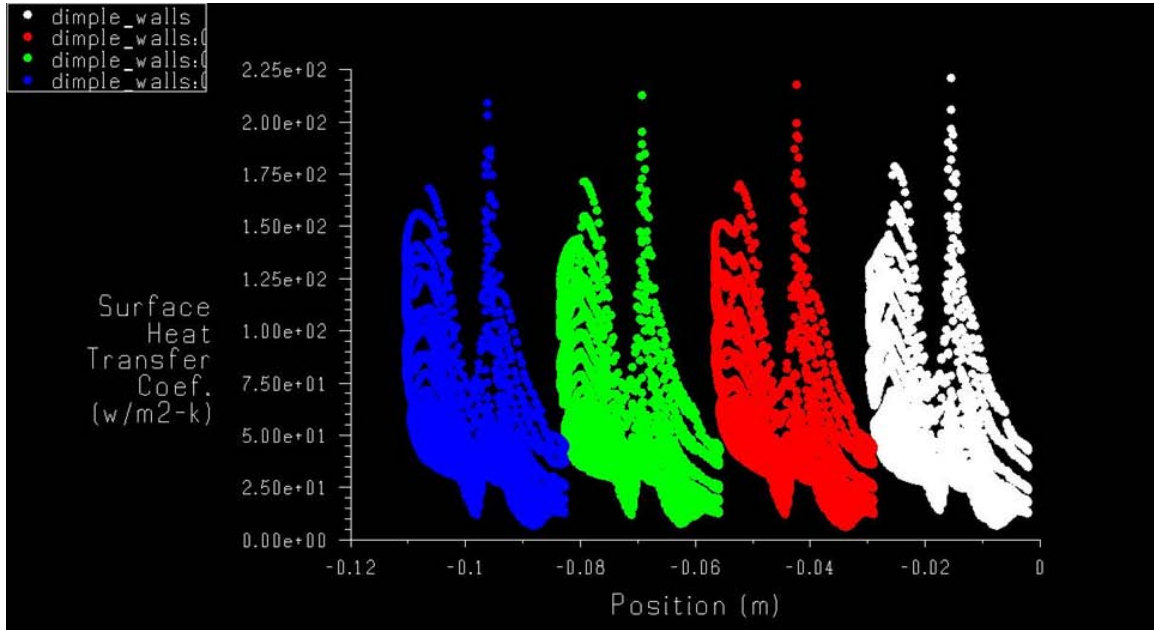


Figure 5.23: Surface Heat Transfer Coefficient Contours, Bottom Wall- Re = 20000

Accompanying a decrease in the kinetic energy of the mainstream flow is a decrease in the strength of the stagnation region of the back wall of the feature. This in turn, causes a reduction in the strength of the vortices ejected from the dimple as well.



**Figure 5.24: Surface Heat Transfer Coefficient as a Function of Streamwise Distance – Re = 20000**

### Large Eddy Simulation

The results of the large eddy simulation are present in Figure 5.25 through Figure 5.48. An unsteady simulation, this solution generated a massive amount of raw data. Again, it was determined that the 40000 Reynolds number cases revealed, most clearly showed the flow physics present in a double dimple. Therefore, to remain concise, only a selection will be discussed in this section. For reference, a full transient dataset was generated for all three flow rates; the 40000 Reynolds case is included in APPENDIX F: of this work.

The locations of the planes interrogated for the data presented in this section are as described in Table 14, below.

**Table 14: Legend to LES Plane Descriptions**

(+) X	Full plane cut in the streamwise direction along the longitudinal centerplane of dimples one and three
Spanwise Centerplane	Centerplane of the channel, dividing the entire domain into two equal volumes maintaining full streamwise length
(-) X	Full plane cut in the streamwise direction along the longitudinal centerplane of dimples two and four

Figure 5.25 shows the inherent pockets of velocity that are observed in a fully isotropic turbulent flow. As reported by Patrick in his DNS study of transition regime flows over single dimple features (Patrick, 2005), the transition to a fully-turbulent flow regime take place at a Reynolds number of approximately 1100.

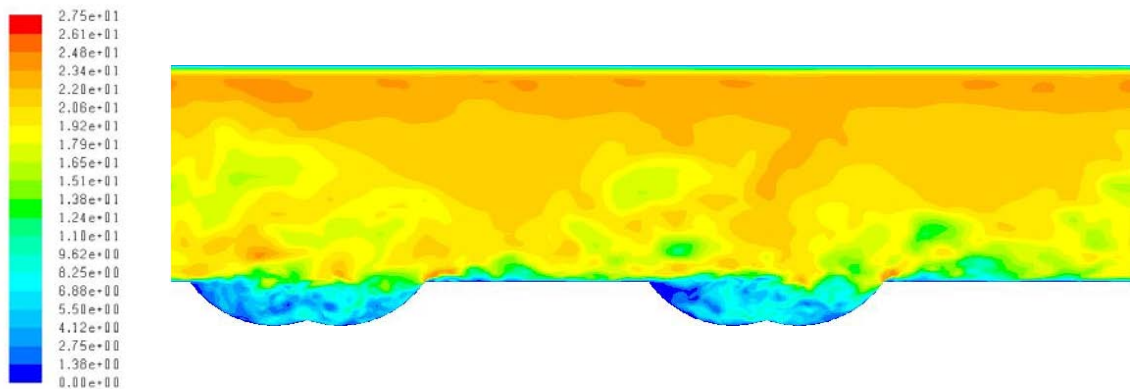


**Figure 5.25: Transient Contours of Velocity – (+)X Plane, Time Step = 0.000726s, Re = 40000**

Figure 5.26 is a snapshot of the turbulent flow activity along the spanwise centerplane of the channel. This region of the domain is seen to contain some of the most active flow structures because of the inextricable interaction of the unsteady flow between adjacent features in the staggered dimple array.



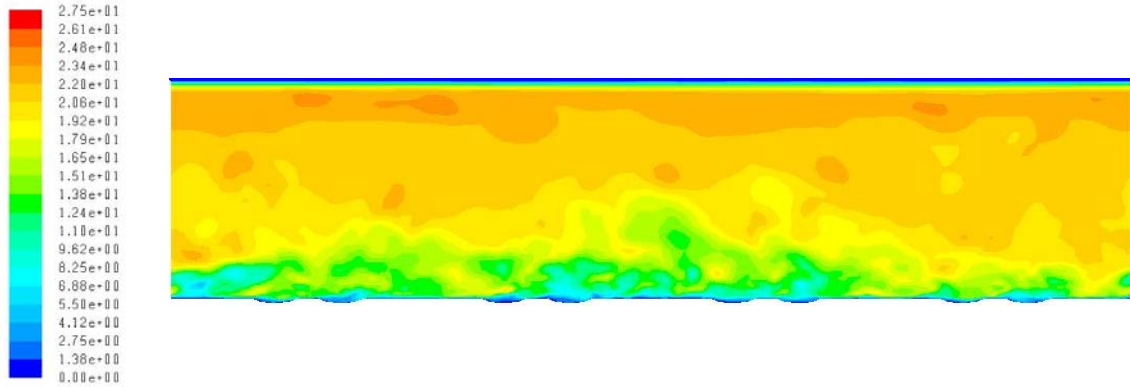


**Figure 5.26: Transient Contours of Velocity – Spanwise Centerplane, Time Step = 0.000484s, Re = 40000**

Figure 5.27 through Figure 5.35 is a sequence of snapshots to illustrate the unsteady fluctuations in the velocity field in and around the surface features. One key aspect of this illustration is the unsteady interaction of the fluid within the dimple itself and the mainstream flow. The periodic raising and lowering of the shear layer results in the generation of low velocity eddies. As these eddies are pulled away from the dimple by the mainstream flow, they create a boundary layer disturbance. This disturbance is responsible for a further increase in surface Nusselt number as an added benefit over the default boundary layer reset.

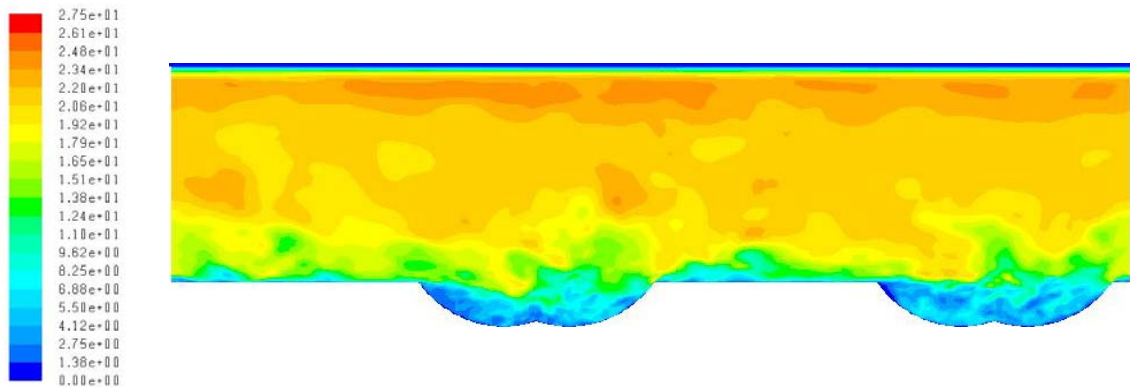


**Figure 5.27: Transient Contours of Velocity – (-)X Plane, Time Step = 0.001936s, Re = 40000**

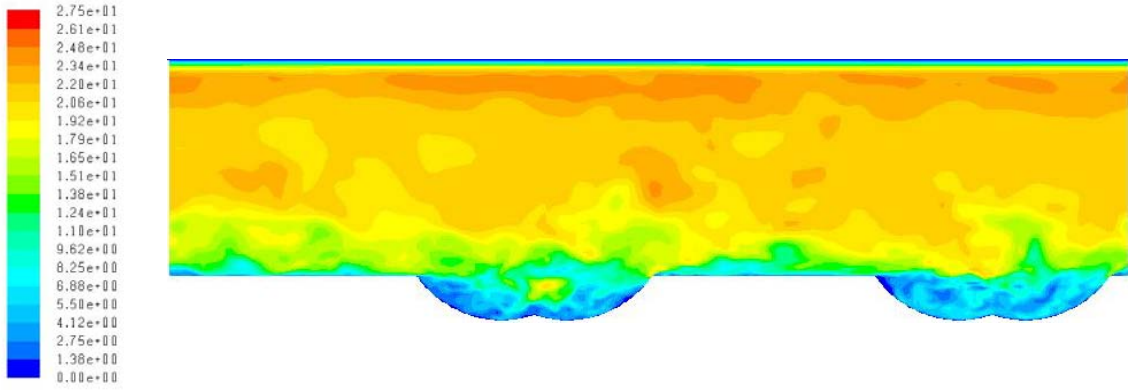


**Figure 5.28: Transient Contours of Velocity – (-)X Plane, Time Step = 0.002178s, Re = 40000**

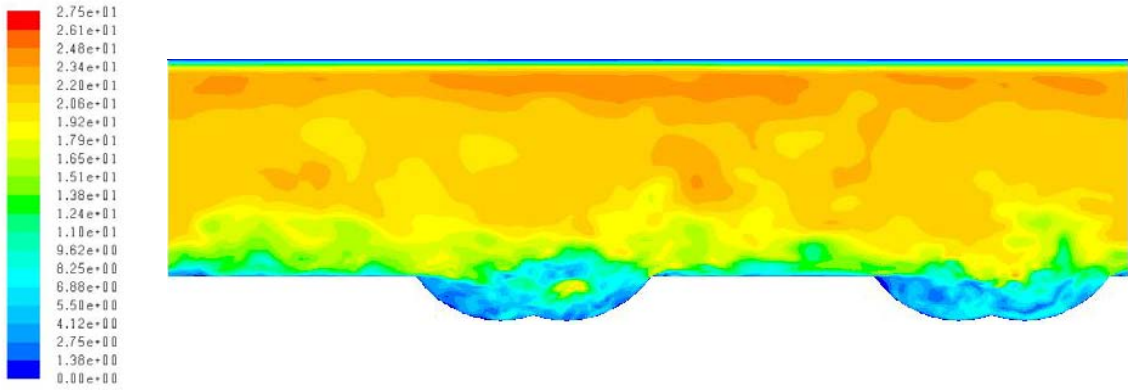


**Figure 5.29: Transient Contours of Velocity – (-)X Plane, Time Step = 0.00242s, Re = 40000**

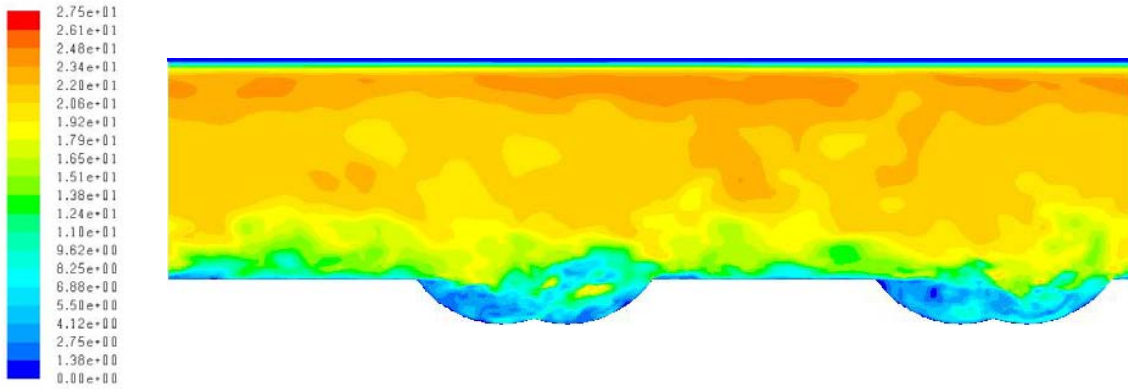


**Figure 5.30: Transient Contours of Velocity – (-)X Plane, Time Step = 0.002662s, Re = 40000**

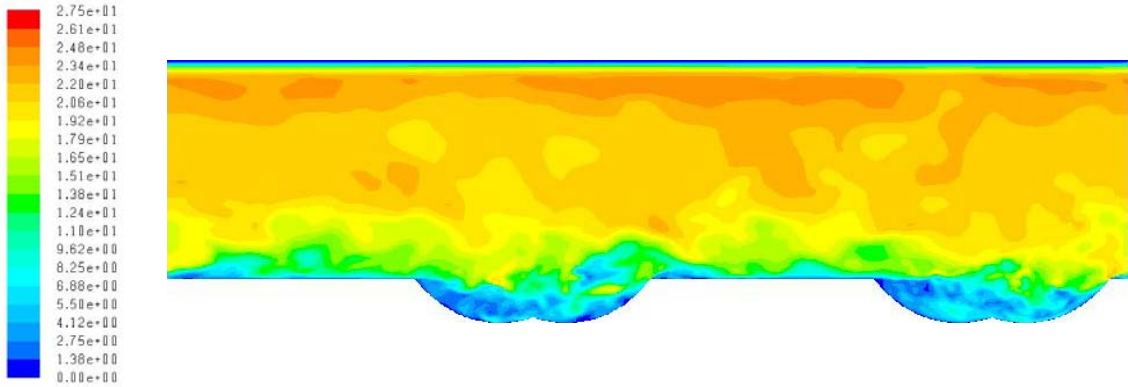


**Figure 5.31: Transient Contours of Velocity – (-)X Plane, Time Step = 0.002904s, Re = 40000**

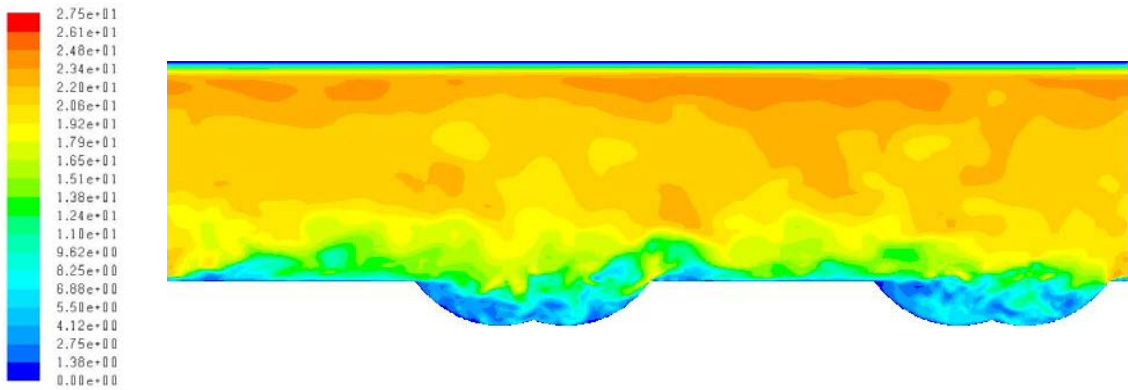


**Figure 5.32: Transient Contours of Velocity – (-)X Plane, Time Step = 0.003146s, Re = 40000**

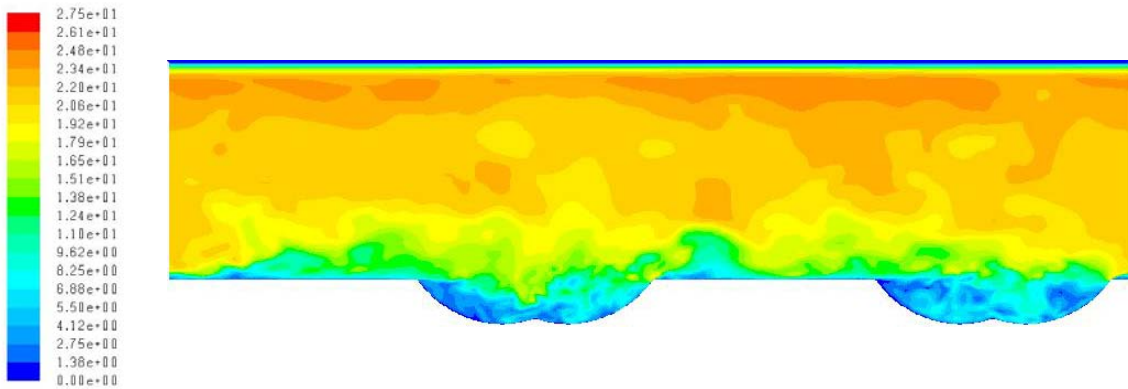


**Figure 5.33: Transient Contours of Velocity – (-)X Plane, Time Step = 0.003388s, Re = 40000**



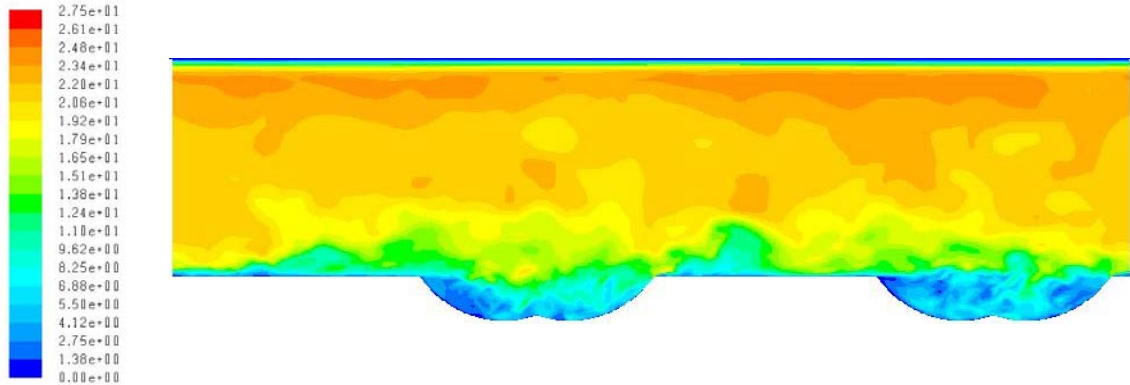


**Figure 5.34: Transient Contours of Velocity – (-)X Plane, Time Step = 0.00363s, Re = 40000**

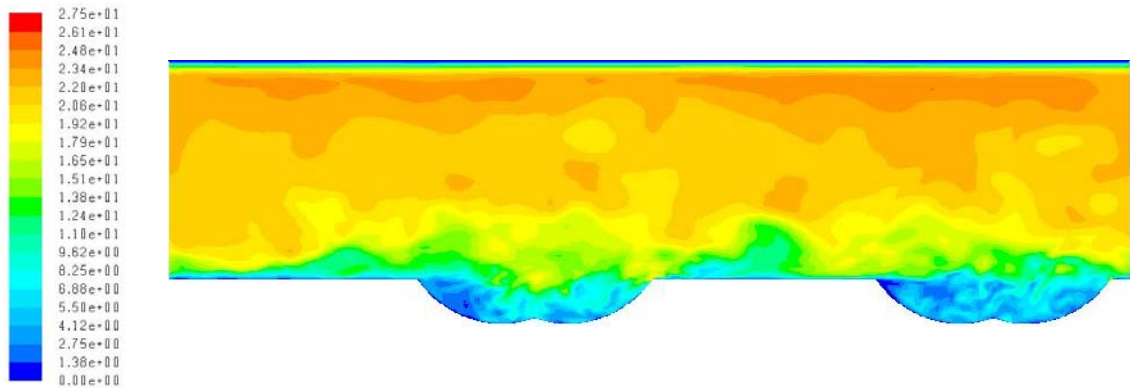


**Figure 5.35: Transient Contours of Velocity – (-)X Plane, Time Step = 0.003872s, Re = 40000**

Figure 5.36 illustrates a particular instant in time where the flow structure in the two dimples are very different; the same phenomena was observed in the RANS solutions. Figure 5.36 through Figure 5.39 is an accelerated sequence of frames animating the unsteady formation and breakup of the high vorticity regions within the shear layer. By comparing these images with those showing the unsteady velocity contours, it is easily understood how the generation of vorticity is directly related to the dissipation of the velocity gradient discussed in detail throughout the previous section.

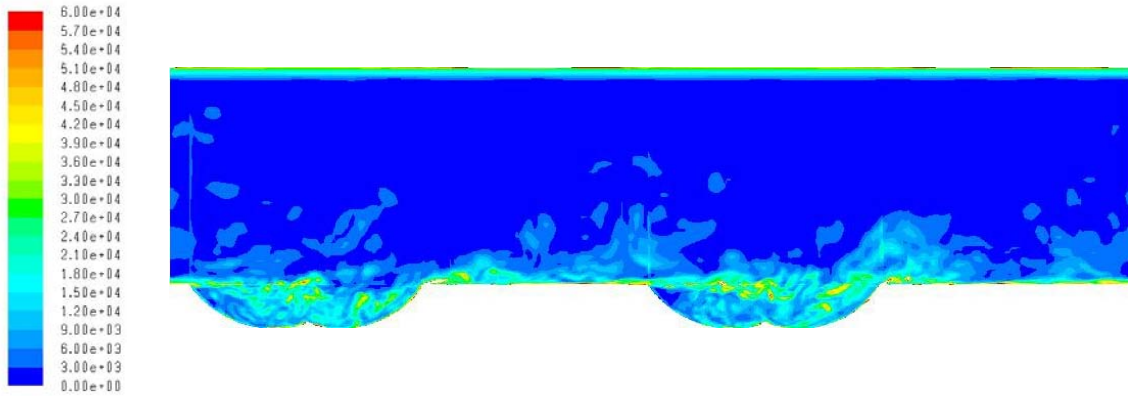


**Figure 5.36: Transient Contours of Vorticity – (+)X Plane, Time Step = 0.000484s, Re = 40000**

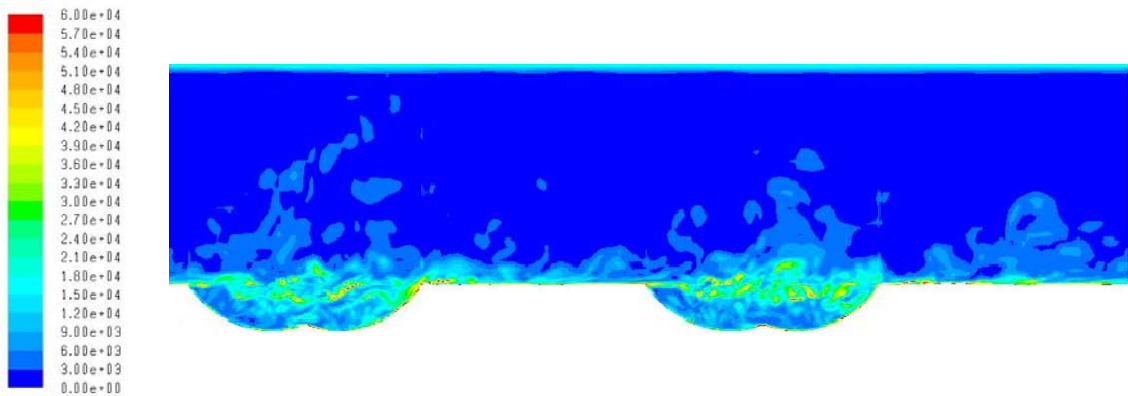


**Figure 5.37: Transient Contours of Vorticity – (+)X Plane, Time Step = 0.001452s, Re = 40000**

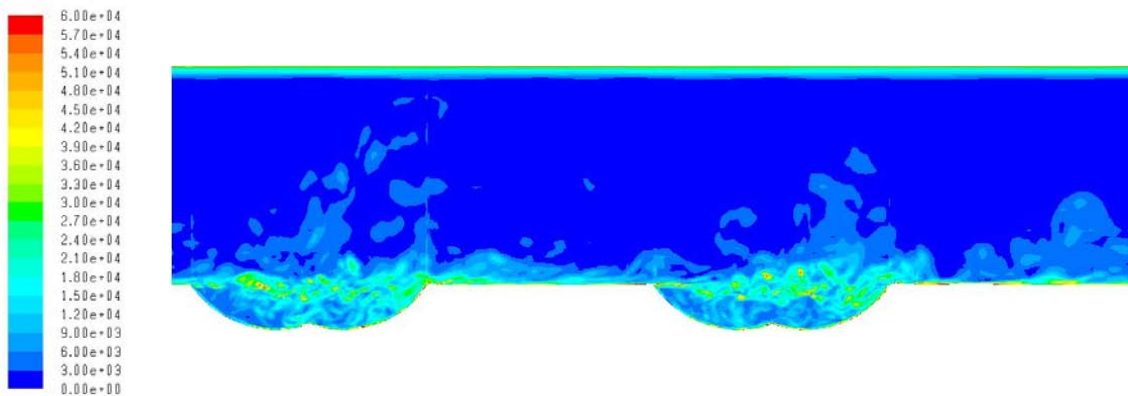


**Figure 5.38: Transient Contours of Vorticity – (+)X Plane, Time Step = 0.001694s, Re = 40000**

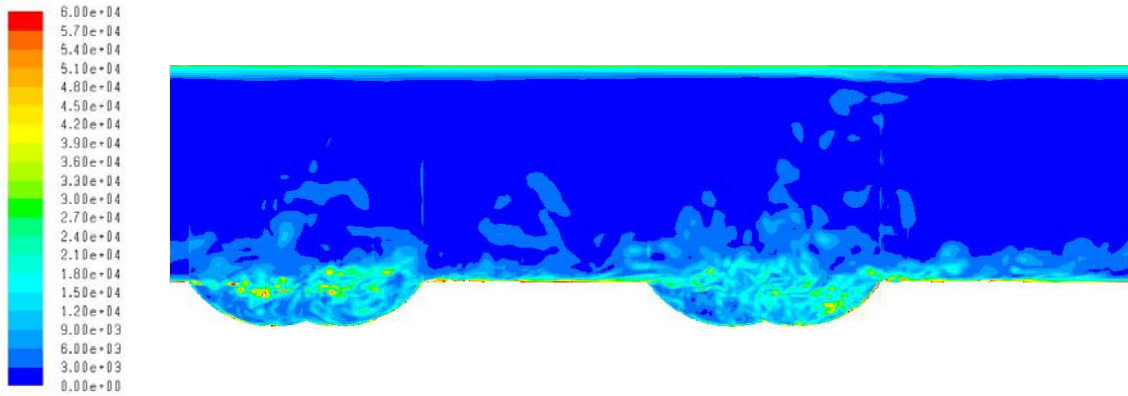


**Figure 5.39: Transient Contours of Vorticity – (+)X Plane, Time Step = 0.004598s, Re = 40000**

Figure 5.40 through Figure 5.48 is an extended time sequence following the complete formation, breakup, ejection, and downstream advection of a pocket of high vorticity fluid. Careful study of the upstream dimple in each image will illustrate the complex phenomena. This insight provides unparalleled depth and understanding to the true physics behind the performance of this geometry.

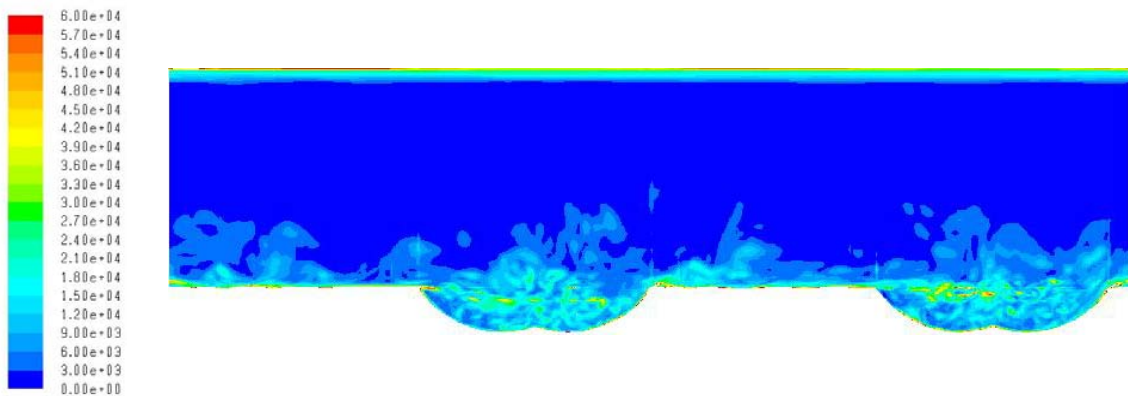


**Figure 5.40: Transient Contours of Vorticity – (-)X Plane, Time Step = 0.001936s, Re = 40000**

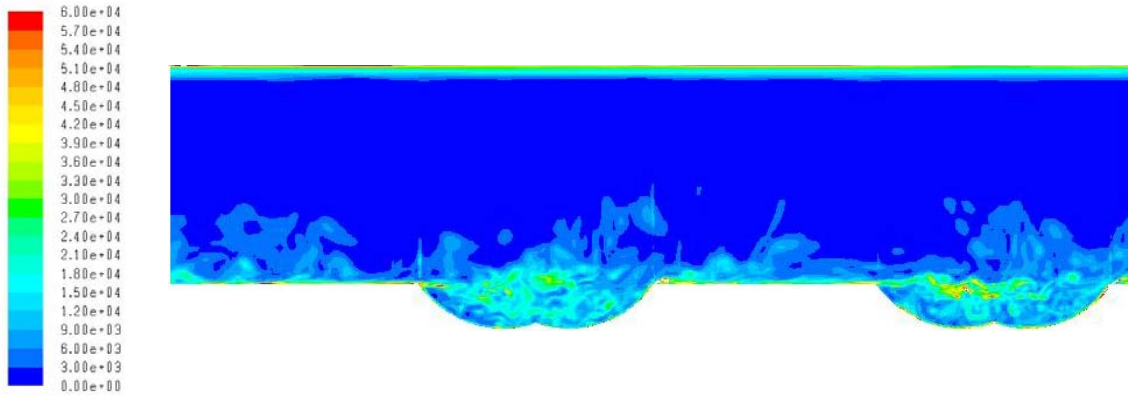


**Figure 5.41: Transient Contours of Vorticity – (-)X Plane, Time Step = 0002178s, Re = 40000**

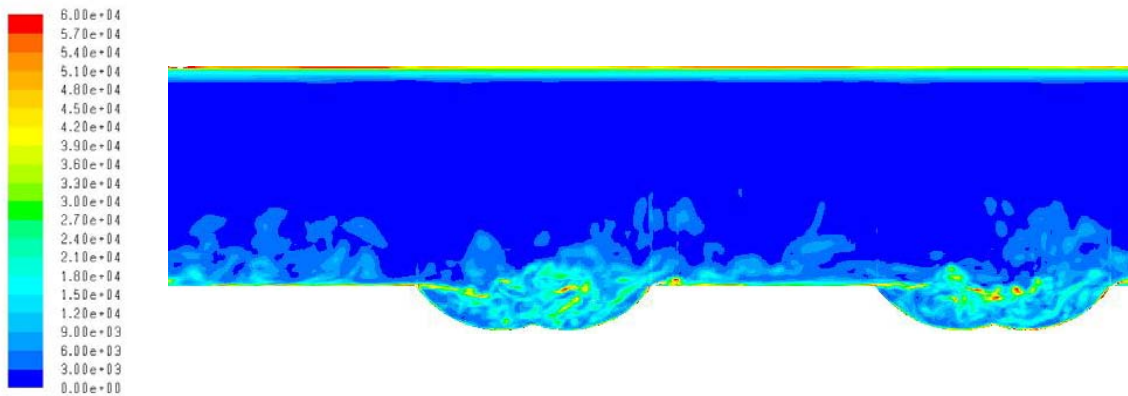


**Figure 5.42: Transient Contours of Vorticity – (-)X Plane, Time Step = 0.00242s, Re = 40000**

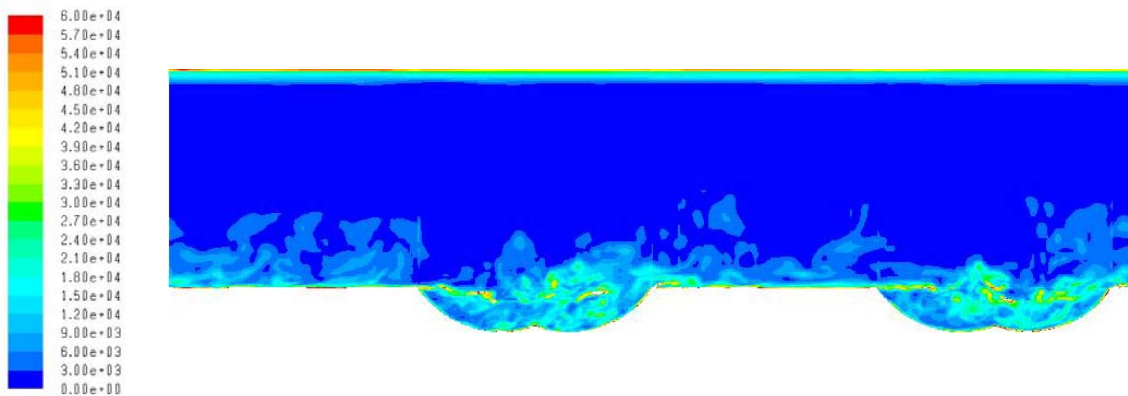


**Figure 5.43: Transient Contours of Vorticity – (-)X Plane, Time Step = 0.002662s, Re = 40000**

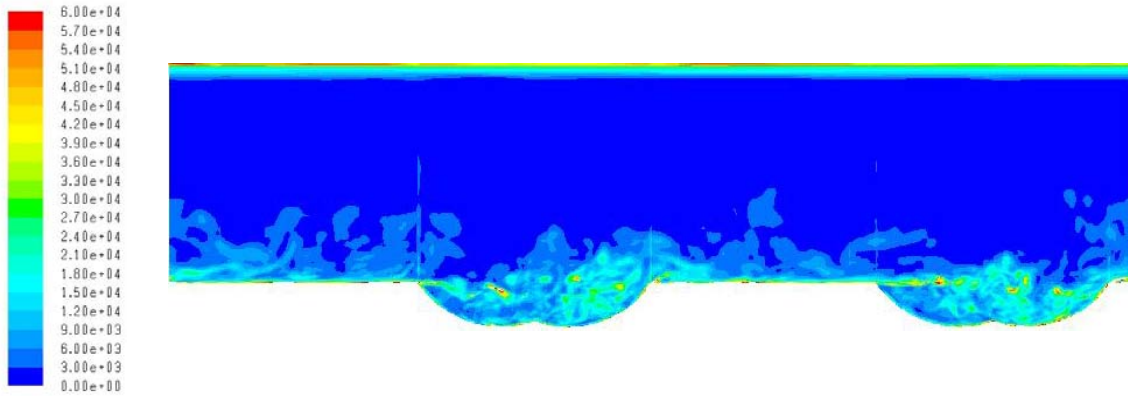


**Figure 5.44: Transient Contours of Vorticity – (-)X Plane, Time Step = 0.002904s, Re = 40000**

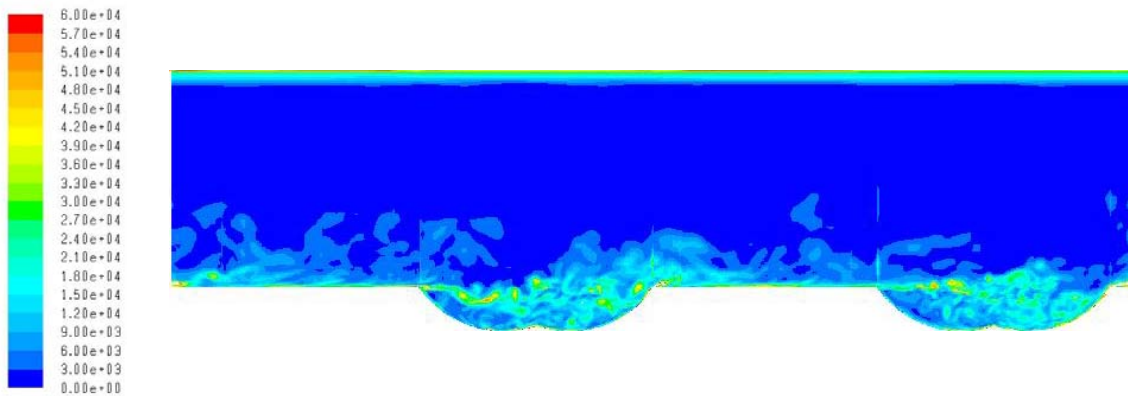


**Figure 5.45: Transient Contours of Vorticity – (-)X Plane, Time Step = 0.003146s, Re = 40000**

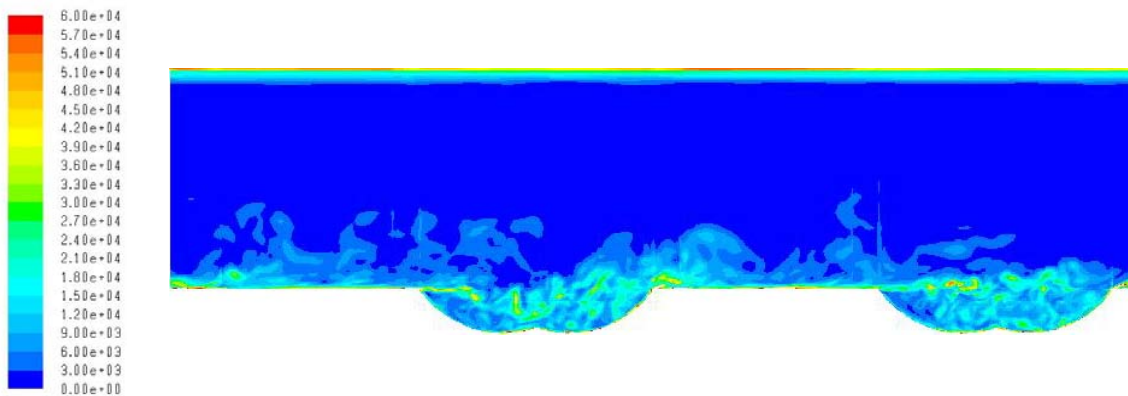


**Figure 5.46: Transient Contours of Vorticity – (-)X Plane, Time Step = 0.003388s, Re = 40000**



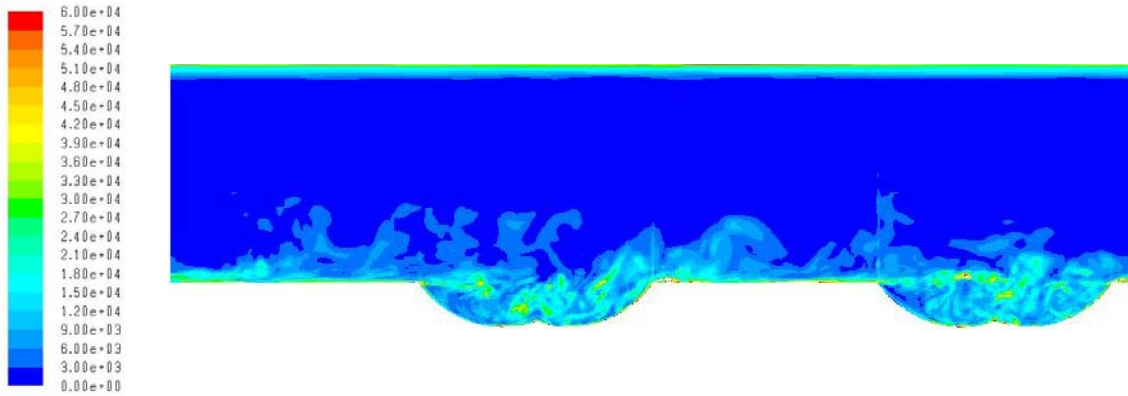


**Figure 5.47: Transient Contours of Vorticity – (-)X Plane, Time Step = 0.00363s, Re = 40000**

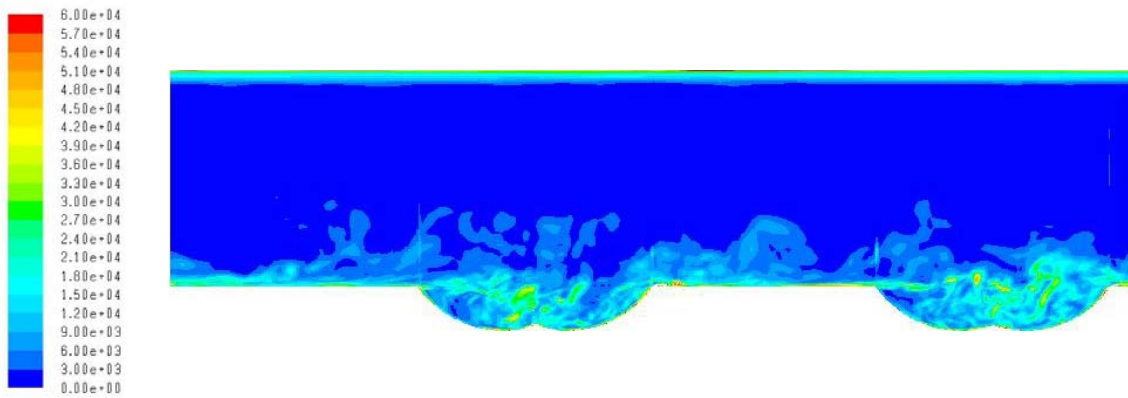


**Figure 5.48: Transient Contours of Vorticity – (-)X Plane, Time Step = 0.003872s, Re = 40000**

### Conclusions from Computational Study

Table 15 provides a comparison of the Surface Nusselt numbers between the bottom wall of the channel and wall-surface within the feature itself. The channel Reynolds numbers are exact because channel mass flow rate was specified as an imposed boundary condition.

**Table 15: Comparison of Bottom Wall Surface Nusselt Numbers**

Channel Wall		Reynolds Number	Nusselt Number
BOTTOM	DIMPLE	20000	41.1
	WALL		72.34
BOTTOM	DIMPLE	30000	46.62
	WALL		93.16
BOTTOM	DIMPLE	40000	48.84
	WALL		112.86

Table 15 shows that, as the Reynolds number is increased, the average Nusselt number within the dimple itself stays nearly constant. Although it was observed that the local trends shows some variation, it is important to note that the numerical simulation does not predict what was observed through the experimental testing of this feature.

Table 16 presents a wall-to-wall surface Nusselt number comparison with an area-weighted average performed on the bottom wall for accurate inclusion of the featured surface. At low Reynolds numbers, the numerical simulation over-predicts the side wall Nusselt number and severely under-predicts the average Nusselt number of the featured wall. As the channel Reynolds number is increased, this trend becomes increasingly pronounced. This erroneous trend is thought to be caused almost entirely by the models inability to accurately predict the Nusselt number with the feature itself.

**Table 16: Comparison of Surface Averaged Heat Transfer Coefficients for Each Wall**

Channel Wall	Reynolds Number	Nusselt Number
TOP	20000	61.84
SIDE		69.69
BOTTOM		61.03
TOP	30000	74.37
SIDE		89.16
BOTTOM		76.39
TOP	40000	89.78
SIDE		107.45
BOTTOM		91.62

Table 17 provides a comparison of the surface-averaged Nusselt number for the individual walls of the channel tested in the transient TLC tunnel. The wall to wall trend is observed to be the reverse of that predicted by the RANS simulation

**Table 17: Wall-to-Wall Comparison of Nusselt Number from Transient TLC Experiment (Before Area Correction)**

CHANNEL WALL	Reynolds Number		
	20000	30000	40000
TOP	93.27	113.80	163.36
SIDE	81.35	98.06	152.77
BOTTOM	108.66	151.82	178.74



The explanation for this issue is that the time-averaged RANS solution is incapable of accurately resolving the contribution of the unsteady flow created by the dimple feature to the convective heat transfer from the downstream surface. The simple boundary layer restart and modeled production of turbulence is determined to be unsuitable for the unique unsteadiness of the double-dimple flow problem.

Table 18 provides a final comparison of the channel averaged Nusselt number and friction factor data present thus far. It is encouraging to note that the pressure loss from the numerical simulation was found to be very comparable to that determined experimentally. With the difference between the experimental and numerically-predicted values of friction factor augmentation as low as four percent, we can be confident in the solution of the force-momentum balance, to say the least.

It is also interesting to note that, at a Reynolds number of 20000, the channel averaged Nusselt number is in close agreement with that of the value determined experimentally by the basic experiment. This adds further support to the theory that the error in the RANS-calculated Nusselt number is stemming from its inability to accurately simulate the unsteady flow within the dimple itself. As channel Reynolds number increases, the severity of the under-prediction increases as well.

**Table 18: Final Results Comparison (Before Final Transient TLC Corrections)**

	Reynolds Number	Nusselt Number	Friction Factor [Moody]	Nu/Nuo [Dittus-Boelter]	$f/f_0$ [Blasius]
Copper-Block	19932	64.55	0.04378	<b>1.17</b>	<b>1.65</b>
Transient TLC	20078	84.38		<b>1.42</b>	
CFD-RANS	20000	64.08	0.04088	<b>1.13</b>	<b>1.54</b>
Copper-Block	29036	91.48	0.03934	<b>1.23</b>	<b>1.64</b>
Transient TLC	29957	120.86		<b>1.48</b>	
CFD-RANS	30000	79.57	0.03706	<b>1.02</b>	<b>1.54</b>
Copper-Block	38502	112.72	0.03497	<b>1.21</b>	<b>1.57</b>
Transient TLC	40201	165.54		<b>1.60</b>	
CFD-RANS	40000	96.05	0.03426	<b>0.97</b>	<b>1.53</b>

## CHAPTER 6: DEVELOPMENT OF THE TRANSIENT TECHNIQUE

### Background

As described in detail in the Test Setup for Local Data section of CHAPTER 2:, the Transient TLC experimental technique is based on the assumption of one-dimensional semi-infinite conduction of heat into the channel wall. In the case of a feature channel wall, such as in this case, a dimple, this assumption breaks down in the regions near the feature, where the conduction of heat is known to be more complex. Two aspects must be understood: the contribution of the non-ideal conduction region to the overall, wall averaged Nusselt number and the effect of the increased wall surface area caused by presence of the feature.

### Contribution of Non-Ideal Region

A calculation of the penetration depth of the thermal information into the wall revealed a maximum value of 1.98 mm. This calculation was performed using a simple Fourier number analysis with the maximum time recorded for a pixel to reach its green peak in the area of interest: approximately 38 seconds. As illustrated by Figure 6.1, the only region that this problem occurs in is the brim around the outside edge of the dimple. Therefore, taking the large dimple case to be the worst case scenario (largest diameter), the region containing contaminated data, at any point in the test, was found not to exceed 13 percent of the feature itself. Furthermore, under the same conditions, a maximum of 8 percent of the bottom wall of the channel and just 2.8 percent of the overall channel is lost.

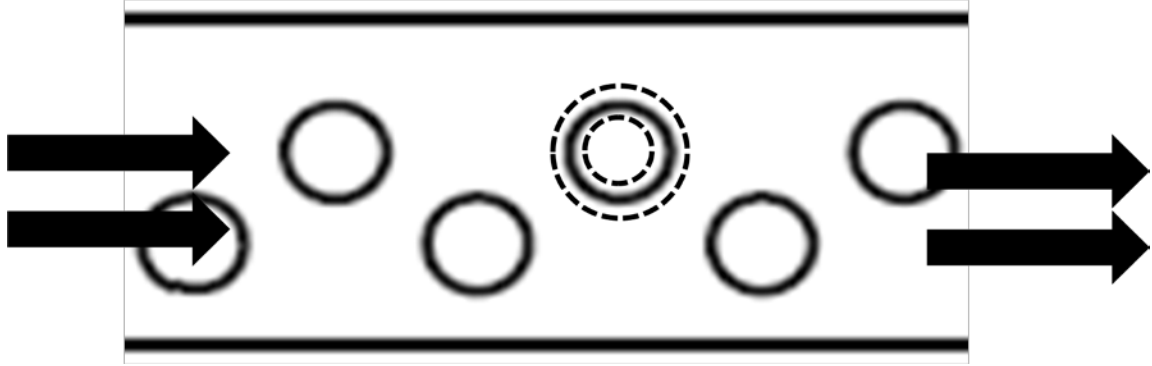


**Figure 6.1: Illustration of the Contaminated Data Region**

Surface Area Correction

Table 19 presents the percentage difference between the experimental Nusselt number augmentation determined by the basic experiment and the transient TLC experiment. With variations as high as nearly thirty percent and nearly constant differences across the range of Reynolds numbers, it inspires suspicion that some systematic error exists.

**Table 19: Nusselt Number Augmentation – Percentage Difference Between Basic and Transient TLC Experiments (After Area Correction)**

	Reynolds Number		
DIMPLE GEOMETRY	20000	30000	40000
Large Dimple	0.287	0.238	0.289
Small Dimple	0.192	0.151	0.140
Double Dimple	0.174	0.168	0.245

In response, a simple, physical correction was developed to account for the added surface area of the dimple features. The correction factor is simply multiplied by the final channel-averaged Nusselt number.

$$Nu_{CF} = (W * L) - (N * \frac{\pi d^2}{4}) + (N * (\frac{d^2}{4} + \delta^2)) \quad (32)$$

### Results and Findings

Table 20 provides the final, channel-averaged results after the application of the area correction to the bottom wall of the channel.

**Table 20: Comparison of Channel-Averaged Nusselt Number – After Area Correction**

	Reynolds Number		
DIMPLE GEOMETRY	20000	30000	40000
Large Dimple	79.01	132.01	144.24
Small Dimple	63.24	86.87	111.13
Double Dimple	75.59	108.27	148.30

Table 21 shows the percentage difference between the final Nusselt number augmentation values for the Transient TLC experiments and those determined by the basic experiment. Augmentation is the parameter chosen for this comparison because it is normalized by the smooth wall values to account for any variation in testing condition such as channel Reynolds number. After application of this factor, the difference

between the two experiments is, in most cases, brought within the range of experimental uncertainty.

**Table 21: Nusselt Number Augmentation – Percentage Difference Between Basic and Transient TLC Experiments (After Area Correction)**

	Reynolds Number		
DIMPLE GEOMETRY	20000	30000	40000
Large Dimple	0.204	0.149	0.207
Small Dimple	0.098	0.052	0.040
Double Dimple	0.078	0.071	0.157

Table 22 is a final comparison of all of the final data for the double dimple surface feature. After the correction, the channel averaged Nusselt number augmentation from the Transient TC experiment is found to be within overlapping bands of uncertainty with the basic experiment. The steady RANS numerical solution under-predicts Nusselt number of the within the dimple itself because it is unable to resolve the unsteady fluctuations of the flow which play a major role in the performance of this region. Friction factor augmentation is found to be in good agreement between the experimental values and the RANS calculated value based on the imposed body-force term.

**Table 22: Final Results Comparison – Double Dimple**

	Reynolds Number	Nusselt Number	Friction Factor [Moody]	Nu/Nuo [Dittus-Boelter]	$f/f_0$ [Blasius]
Copper-Block	19932	64.55	0.04378	<b>1.17</b>	<b>1.65</b>
Transient TLC	20078	75.59		<b>1.27</b>	
CFD-RANS	20000	64.08	0.04088	<b>1.13</b>	<b>1.54</b>
Copper-Block	29036	91.48	0.03934	<b>1.23</b>	<b>1.64</b>
Transient TLC	29957	108.27		<b>1.33</b>	
CFD-RANS	30000	79.57	0.03706	<b>1.02</b>	<b>1.54</b>
Copper-Block	38502	112.72	0.03497	<b>1.21</b>	<b>1.57</b>
Transient TLC	40201	148.30		<b>1.43</b>	
CFD-RANS	40000	96.05	0.03426	<b>0.97</b>	<b>1.53</b>

## CHAPTER 7: CONCLUSIONS AND FUTURE WORK

### Conclusions

The first chapter of this work provided an explanation of the need for advanced active cooling of gas turbine components in engineering design. The literature review provided an overview of internal channel cooling with the application of transport-enhancing surface features. A specific focus was placed on the use of dimples for the promotion to turbulent convective heat transfer within the channel. Three designs were proposed and an outline of the work was described.

The second chapter thoroughly described the details of both experiments employed during this study. Detailed design information, data reduction, and experimental uncertainty calculations were presented. Great detail was also given on the design of the transient TLC experiment, as its development composed a major portion of this project.

The third chapter provided the details of the computational study performed in this work. Geometry generation and meshing were covered in detail along with the solution details such as discretization schemes, turbulence models, and unsteady time step calculations.

The fourth chapter describes the experimental efforts of the work. Results from both experiments are discussed and continued development of the transient TLC experiment is outlined based on the findings. A detailed look at the surface heat transfer enhancement



is also provided by the local heat transfer coefficient profiles obtained from the Transient rig.

The fifth chapter walks through the complete development of the computational study performed in this work. The surface Nusselt number data is determined to have some complications because of the difficulty associated with modeling the unsteady turbulence within the feature itself. The large eddy simulation results provided a detailed look at these aspects of dimple flow physics to provide greater depth in understanding of observed surface phenomena.

The sixth chapter established some final development and corrections to the transient liquid crystal experiment. It was determined that the contribution of the non-ideal regions would have only a negligible effect on the calculated overall performance of the channel. A correction factor for the increased surface area of a featured wall was also developed and applied to the bottom wall Nusselt number data. The results were a reduction in the difference in calculated Nusselt number augmentation (between the two experiments) to a value within the combined experimental uncertainties.

### Future Study

The work is the first stage of an ongoing research project. With successful design, fabrication, and validation of the experimental setup, this study was able to provide a detailed characterization of three dimple geometries. To continue, a computational parametric design study varying the non-dimensional parameters of the dimples and

response of the physics through the surface Nusselt number augmentation would provide valuable information to cooling system designers in the gas-turbine field. With the current setup, these results can then be subjected to a two-level validation as well as a more detailed computational study using unsteady RANS as well as Large-Eddy Simulation for validation and deeper understanding of the physics behind observed results.

## **APPENDIX A: FACILITY**

All of the work performed for this thesis was completed at the Laboratory for Turbine Heat Transfer and Aerodynamics within the Center for Advanced Turbine and Energy Research at the University of Central Florida.



**Figure A.1: Frontal View of CATER Laboratory for Turbine Aerodynamics, Heat Transfer, and Durability**

The lab is an 11,000 ft<sup>2</sup> building located on the outside edges of the UCF campus. The students and faculty there are committed to expanding the knowledge and understanding of the physical phenomena that is so crucial to meeting the energy needs of society in the future. The Center for Advanced Turbines and Energy Research is located within the Siemens Energy Center and is a valuable asset to UCF. It not only provides unique, ground-breaking studies for the leading design engineers of the world today, but it also maintains a rich, nurturing environment, producing some of the best engineers the college has to offer.

## A.1. Experimental Facility

The experiment was constructed on the second floor of the new building expansion. It is at an elevation of approximately seventy-five feet above sea-level at this location. Ambient Temperature in the Building is maintained at  $23^{\circ}\text{C} \pm 1^{\circ}\text{C}$ . The Atmospheric Pressure at the Setup Location is monitored by a Digital Barometer. Additionally, Ambient Conditions are always measured by the Data acquisition system by adding a minimum of three additional pressure taps or thermocouples to established a bias for pressure and temperature measurements, respectively.

The compressed air supply for the experiment was generated by a Quincy Three-Piston, Two Stage Air Compressor that is setup outside of the building. The compressor was part of the pre-existing infrastructure prior to the conception of this project. It is capable of a maximum mass flow rate of 0.01 kg/s of air at a pressure of 250 psi. The compressor shaft is driven by a 50 HP Baldor Electric Motor. Figure A.2 shows the compressor in its enclosure behind the building.

Immediately after the compressor, the high-pressure air is run through a Modine® heat exchanger to cool the air. This is a must because the compressed air becomes very hot from the work input by the compressor. It is then run through a Zeks® ‘Heat-Sink’ Condenser and Reheater (Figure A.4). The condenser cools the air below the dew point and removes the moisture from the compressed air entering the system. It then reheats the air back above the dew point in order to keep any remaining moisture from condensing out downstream as the air cools flowing through the system. This component

is very important to in the sub-tropical Central Florida environment with humidity levels as high as ninety percent in the summer months.



**Figure A.2: Quincy Three-Piston, Two-Stage Air Compressor, Maximum Output of 0.01 kg/s at 250 psi**



**Figure A.3: Modine Heat Exchanger, Directly out of Compressor**



**Figure A.4: Condenser and Reheater**



After the condenser, the actual air supply system begins. The entire system is plumbed with three-inch diameter pipe. In the old-wing of the building, the pipe is three-inch black iron and extends a length of approximately 100 feet before switching over to a Stainless/Aluminum alloy line in the new building section. There are several drops throughout the overall length, each with an individual regulator and Moisture Filter ( Figure A.5).



**Figure A.5: Three Inch Diameter, Black Iron Supply Line**

For the purposes of dampening pressure fluctuations and flow continuity, a five-thousand gallon storage tank is in-line, in parallel with the Air Distribution System. It is shown in Figure A.6.



**Figure A.6: Five-Thousand Gallon Compressed Air Storage Tank**

## A.2. Computational Infrastructure

For the computational solutions in this work, the sixteen-node Sunfire V20Z cluster on the UCF College of Engineering Network was employed. These resources were donated to this work by Dr. Guha. His contributions are gratefully acknowledged and appreciated. Also, the efforts of Steven Dick are appreciated.



**Figure A.7: Snap-Shots of CECS Ariel Cluster**

Meshes were generated on a quad-core, Dell XPS personal computer with eight gigabytes of memory using GAMBIT (Version 2.4.16) employing rigorously maintained journal files. These domains were solved using the commercial CFD solver, ANSYS-FLUENT (Version 6.3.26) in a parallel computing environment on the CECS Ariel cluster. Various features of the twin SunRack machine are listed below:

**Hardware Features:**

- 64 SunFire v20z 1U boxes, each with 4 to 8 GB of ram, and two 64-bit Opteron processors
- 4 Cisco Catalyst Gigabit Ethernet Switches, to provide for a full gigabit of bandwidth for each port

- 2 Terminal Multiplexers, for serial administration of all boxes
- Full Ethernet management with an ethernet cascade
- A Dell 2850 frontend, for hosting shells and administrative programs
- An additional 3 TB of mobile storage attached to the frontend

**Software Features:**

- Rocks / CentOS Linux
- GNU C and Fortran compilers
- MPI and MPICH
- 30 total licenses of Fluent (v6.3.26) (parallel and interface)

## **APPENDIX B: MESH HEATER ANALYSIS**

## ASSUMPTIONS MADE

- Incompressible Flow
- Constants for Air taken at 350 K
- Wire Properties taken at 500K
- Negligible Natural Convection
- Wire can be Analyzed as an Infinite Cylinder for Heat Transfer Purposes
- Negligible Viscous Dissipation
- Minimal Change in Elevation

## GLOBALLY NECESSARY CONSTANTS AND DESIGN PARAMETERS

### Properties of Air

$$\mu_{\text{air}} := 1.86 \cdot 10^{-5} \frac{\text{N} \cdot \text{s}}{\text{m}^2}$$

$$\rho_{\text{air}} := 1.18 \frac{\text{kg}}{\text{m}^3}$$

$$R_{\text{air}} := 286.9 \frac{\text{J}}{\text{kg} \cdot \text{K}}$$

$$T_{\text{amb}} := 298\text{K}$$

$$c_{p\text{air}} := 1006 \frac{\text{J}}{\text{kg} \cdot \text{K}}$$

$$Q_{\text{flow}} := \frac{m_{\text{dot}}}{\rho_{\text{air}}}$$

$$Q_{\text{flow}} = 0.06 \frac{\text{m}^3}{\text{s}}$$

$$Q_{\text{flow}} = 127.251 \frac{\text{ft}^3}{\text{min}}$$

### Channel Conditions

$$H_{\text{channel}} := 0.0254\text{m}$$

$$Re_{\text{channel}} := 100000$$

$$W_{\text{channel}} := 2 \cdot H_{\text{channel}}$$

$$H_{\text{channel}} = 1 \text{ in}$$

$$W_{\text{channel}} = 2 \text{ in}$$

$$A_{\text{channel}} := W_{\text{channel}} \cdot H_{\text{channel}}$$

$$P_{\text{channel}} := (2 \cdot W_{\text{channel}}) + (2 \cdot H_{\text{channel}})$$

$$D_{h,\text{channel}} := \frac{4 \cdot A_{\text{channel}}}{P_{\text{channel}}}$$

$$\frac{0.5 \cdot D_{h,\text{channel}}}{H_{\text{channel}}} = 0.667$$

$$m_{\text{dot}} := \frac{Re_{\text{channel}} \cdot \mu_{\text{air}} \cdot A_{\text{channel}}}{D_{h,\text{channel}}}$$

$$m_{\text{dot}} = 0.071 \frac{\text{kg}}{\text{s}}$$

$$V_{\text{channel}} := \frac{m_{\text{dot}}}{\rho_{\text{air}} \cdot (A_{\text{channel}})}$$

$$V_{\text{channel}} = 46.543 \frac{\text{m}}{\text{s}}$$

### Heater Conditions

$$H_{\text{plenum}} := 0.1016\text{m}$$

$$T_{\text{inlet\_plenum}} := (27 + 273)\text{K}$$

$$W_{\text{plenum}} := 0.3048\text{m}$$

$$T_{\text{inlet\_plenum}} = 300\text{K}$$

$$A_{\text{plenum}} := W_{\text{plenum}} \cdot H_{\text{plenum}}$$

$$H_{\text{plenum}} = 4\text{in}$$

$$P_{\text{plenum}} := 2 \cdot W_{\text{plenum}} + 2 \cdot H_{\text{plenum}}$$

$$W_{\text{plenum}} = 12\text{in}$$

$$D_{\text{h,plenum}} := \frac{4 \cdot A_{\text{plenum}}}{P_{\text{plenum}}}$$

$$\text{HC\_ratio} := \frac{D_{\text{h,plenum}}}{D_{\text{h,channel}}}$$

$$V_{\text{plenum}} := \frac{\dot{m}}{\rho_{\text{air}} \cdot A_{\text{plenum}}}$$

$$\text{HC\_ratio} = 4.5$$

$$V_{\text{plenum}} = 1.939 \frac{\text{m}}{\text{s}}$$

### Mesh Spacing

$$\text{mesh}_{\text{step}} := 0.1 \cdot D_{\text{h,plenum}}$$

$$\text{time}_{\text{step\_d}} := \frac{\text{mesh}_{\text{step}}}{V_{\text{plenum}}}$$

$$\text{mesh}_{\text{step}} = 0.6\text{in}$$

### Number of Meshes

$$\text{num}_{\text{mesh}} := 6$$

$$\text{time}_{\text{step}} := \frac{\text{time}_{\text{step\_d}}}{s}$$



## Mesh Parameters

Wire Dimensions can be input for up to 5 different wire diameters at one time, but the material properties/open area ratio can only be included for one metal. Allowing multiple sizes to be studied for one heater material.

Wire Diameter

$$D_{\text{wire}} := \begin{pmatrix} 0.00001403 \\ 1.0 \times 10^{-5} \\ 1.5 \times 10^{-5} \\ 2.0 \times 10^{-5} \\ 2.5 \times 10^{-5} \end{pmatrix} \text{m}$$

Selection

64 gauge

49 gauge

unknown

316 Stainless

Open Area Ratio (OR)

$$\text{OR} := 0.25$$

Wire Properties

$$L_{\text{wire}} := W_{\text{plenum}}$$

$$X_{\text{wire}} := H_{\text{plenum}}$$

$$D_{\text{wire\_nd}} := \frac{D_{\text{wire}}}{\text{m}}$$

$$\rho_{\text{wire}} := 7854 \frac{\text{kg}}{\text{m}^3}$$

$$c_{p_{\text{wire}}} := 500 \frac{\text{J}}{\text{kg} \cdot \text{K}}$$

$$k_{\text{wire}} := 60.5 \frac{\text{W}}{\text{m} \cdot \text{K}}$$

$$\alpha_{\text{wire}} := 17.7 \cdot 10^{-6} \cdot \frac{\text{m}^2}{\text{s}}$$

Number of Wires

$$w(D_{\text{wire}}) := \frac{D_{\text{wire}}}{1 - \text{OR}^{0.5}}$$

$$T_{\text{initial}} := T_{\text{amb}}$$

$$\text{num}_{\text{wire}}(D_{\text{wire}}) := \frac{\frac{X_{\text{wire}}}{\text{m}}}{w(D_{\text{wire}})}$$

$$\rho_{\text{reso}} := 15.9 \cdot 10^{-8} \Omega \cdot \text{m}$$

$$\alpha_{\text{res}} := \frac{0.0016}{\text{K}}$$

$$\text{num}_{\text{wire\_all}}(D_{\text{wire}}) := \text{num}_{\text{wire}}(D_{\text{wire}}) \cdot \text{num}_{\text{mesh}}$$

$$T_{\text{wire}} := 500\text{K}$$

## CALCULATION OF PRESSURE DROP

- Pressure Drop across the Heater Mesh

$$K_{\text{mesh}} := \frac{1 - \text{OR}}{\text{OR}^2} \quad \text{in}_{\text{h2o}} := 249.252 \cdot \text{Pa}$$

$$\Delta P_{\text{mesh}} := \text{num}_{\text{mesh}} \cdot \left( K_{\text{mesh}} \cdot 0.5 \cdot \rho_{\text{air}} \cdot V_{\text{plenum}}^2 \right)$$

$$\Delta P_{\text{mesh}} = 159.764 \text{ Pa}$$

$$\Delta P_{\text{mesh\_in}} := \frac{\Delta P_{\text{mesh}}}{\text{in}_{\text{h2o}}}$$

$$\Delta P_{\text{mesh\_in}} = 0.641 \text{ Inches of Water}$$

- Pressure Drop across the Pipe System

$$D_{\text{pipe}} := 3 \text{ in}$$

$$K_{\text{elbow}} := 1.5$$

$$A_{\text{pipe}} := \frac{\pi}{4} D_{\text{pipe}}^2$$

$$\text{Area}_{\text{ratio}} := \frac{D_{\text{h.channel}}}{D_{\text{pipe}}}$$

$$\text{Area}_{\text{ratio}} = 0.444$$

$$V_{\text{pipe}} := \frac{\dot{m}}{\rho_{\text{air}} \cdot A_{\text{pipe}}}$$

$$K_{\text{diffuser}} := 0.41 \text{ Fox McDonald, Pg. 343}$$

$$\Delta P_{\text{pipe}} := 2 \cdot \left( K_{\text{elbow}} \cdot 0.5 \cdot \rho_{\text{air}} \cdot V_{\text{pipe}}^2 \right)$$

$$\Delta P_{\text{diffuser}} := 2 \cdot \left( K_{\text{diffuser}} \cdot 0.5 \cdot \rho_{\text{air}} \cdot V_{\text{channel}}^2 \right)$$

$$\Delta P_{\text{total}} := \Delta P_{\text{mesh}} + \Delta P_{\text{pipe}} + \Delta P_{\text{diffuser}}$$

$$\Delta P_{\text{total\_in}} := \frac{\Delta P_{\text{total}}}{\text{in}_{\text{h2o}}}$$

$$\Delta P_{\text{total\_in}} = 6.077 \text{ Inches of Water}$$

## CALCULATION OF MINIMUM HEAT ADDITION

- This is the amount of heat that must be transferred to the flow to initiate the desired step change in the temperature of the flow.

- This calculation is taking into account the change in the specific heat of the air

$$\alpha := 3.653$$

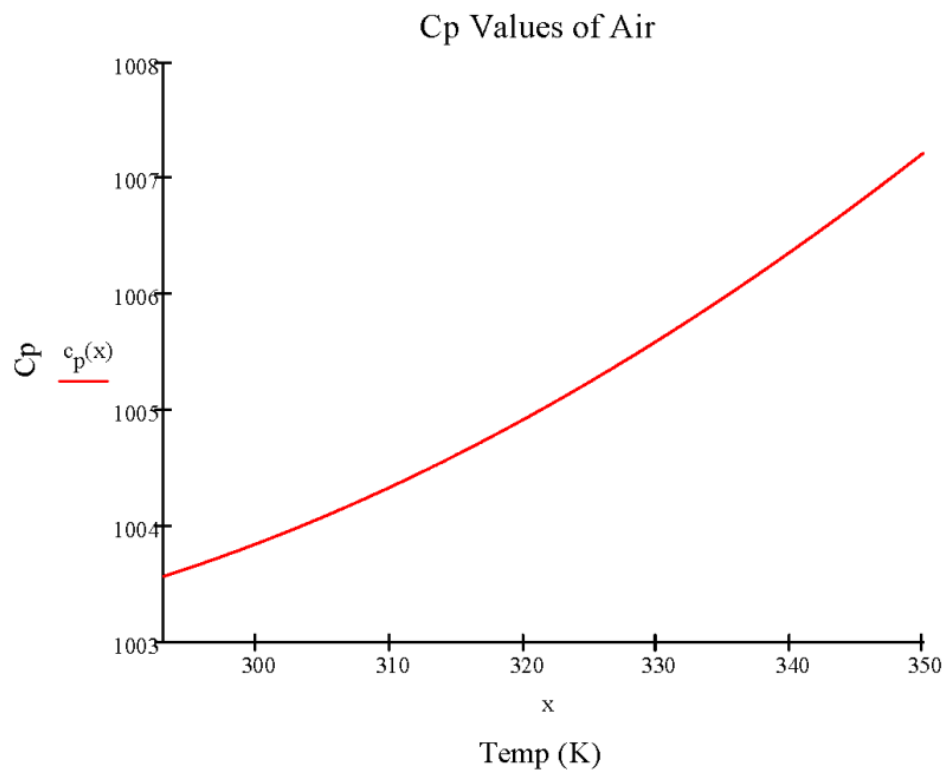
$$\beta := -1.337 \cdot 10^{-3}$$

$$\gamma := 3.294 \cdot 10^{-6}$$

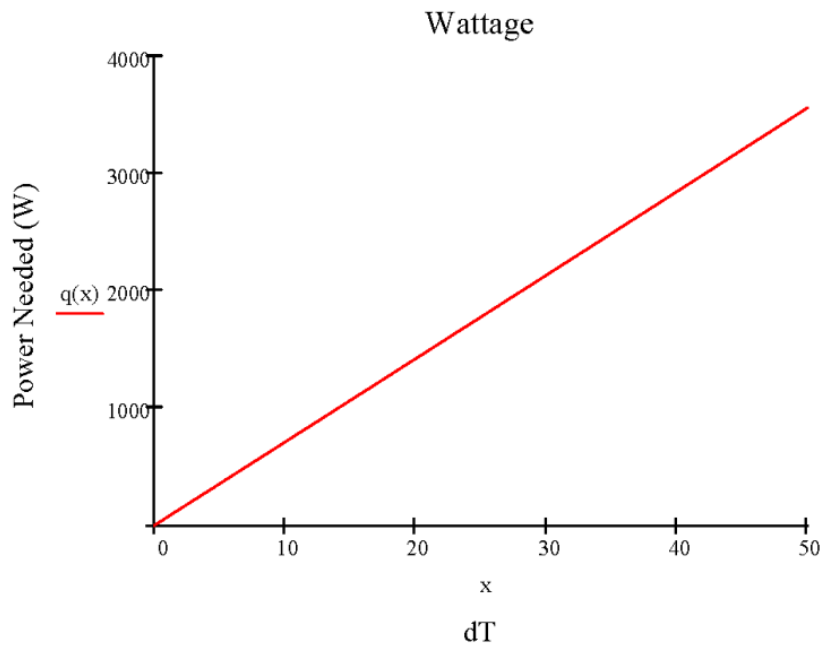
$$\delta := -1.913 \cdot 10^{-9}$$

$$\varepsilon := .2763 \cdot 10^{-12}$$

$$c_p(T) := (\alpha + \beta \cdot T + \gamma \cdot T^2 + \delta \cdot T^3 + \varepsilon \cdot T^4) \cdot R_{\text{air}}$$



$$q(dT) := m\_dot \cdot c_p \left( \frac{dT + T\_inlet\_plenum}{K} \right) \cdot (dT)$$



$$dT := \begin{pmatrix} 20 \\ 25 \\ 30 \\ 35 \\ 40 \end{pmatrix} \cdot K$$

$$q_{input}(dT) := \begin{cases} \text{for } i \in 0..4 \\ q_{in_i} \leftarrow q(dT_i) \\ q_{in} \end{cases}$$

$$q_{input}(dT) = \begin{pmatrix} 1.424 \times 10^3 \\ 1.781 \times 10^3 \\ 2.138 \times 10^3 \\ 2.495 \times 10^3 \\ 2.853 \times 10^3 \end{pmatrix} W$$

## ELECTRICAL CALCULATIONS

- These calculations will look into the electrical aspects of the heater mesh and the effects of various parameters on the electrical loading.

$$A_{\text{wire}}(D_{\text{wire}}) := \left( \frac{\pi \cdot D_{\text{wire}}^2}{4} \right)$$

$$\text{Res}_{\text{mesh}}(D_{\text{wire}}) := \left[ \frac{(L_{\text{wire}}) \cdot [\rho_{\text{reso}} [1 + \alpha_{\text{res}}(T_{\text{wire}})]]}{A_{\text{wire}}(D_{\text{wire}})} \right]^{-1} \cdot \text{num}_{\text{wire\_all}} \left( \frac{D_{\text{wire}}}{m} \right)^{-1}$$

$$I(dT, D_{\text{wire}}) := \sqrt{\frac{q(dT)}{\text{Res}_{\text{mesh}}(D_{\text{wire}})}}$$

$$V_o(dT, D_{\text{wire}}) := \sqrt{q(dT) \cdot \text{Res}_{\text{mesh}}(D_{\text{wire}})}$$

$$V_{\text{all}} := \begin{cases} \text{for } j \in 0..4 \\ \text{for } k \in 0..4 \\ V_{0,j,k} \leftarrow V_o(dT_j, D_{\text{wire}_k}) \\ V_0 \end{cases}$$

$$I_{\text{all}} := \begin{cases} \text{for } j \in 0..4 \\ \text{for } k \in 0..4 \\ I_{0,j,k} \leftarrow I(dT_j, D_{\text{wire}_k}) \\ I_0 \end{cases}$$

$$V_{\text{all}} = \begin{pmatrix} 6.082 & 7.204 & 5.882 & 5.094 & 4.556 \\ 6.801 & 8.056 & 6.578 & 5.696 & 5.095 \\ 7.452 & 8.826 & 7.207 & 6.241 & 5.582 \\ 8.05 & 9.535 & 7.786 & 6.742 & 6.031 \\ 8.608 & 10.196 & 8.325 & 7.209 & 6.448 \end{pmatrix} \text{ V}$$

$$I_{\text{all}} = \begin{pmatrix} 234.174 & 197.701 & 242.134 & 279.592 & 312.593 \\ 261.857 & 221.073 & 270.758 & 312.644 & 349.547 \\ 286.9 & 242.215 & 296.652 & 342.544 & 382.976 \\ 309.944 & 261.671 & 320.48 & 370.058 & 413.738 \\ 331.41 & 279.793 & 342.675 & 395.686 & 442.391 \end{pmatrix} \text{ A}$$

## CONVECTION COEFFICIENT CALCULATIONS

- These calculations will look into different aspects of the heater mesh and there effect on its overall effectiveness.

### Necessary Constants for Heat Transfer Analysis

Comparing Voltages with a Wire Diameter of 0.001m as a function of Wire Diameter and the Number of Wires.

$$Pr_{\text{air}} := .700$$

$$k_{\text{air}} := .0292 \frac{\text{W}}{\text{m}\cdot\text{K}}$$

### Plenum Conditions Refreshed

$$m_{\text{dot}} = 0.071 \frac{\text{kg}}{\text{s}}$$

$$A_{\text{plenum}} = 0.031 \text{ m}^2$$

$$V_{\text{plenum}} = 1.939 \frac{\text{m}}{\text{s}}$$

### Channel Conditions Refreshed

$$D_{\text{h.channel}} = 0.034 \text{ m}$$

$$\rightarrow A_{\text{channel}} := \frac{\pi \cdot D_{\text{h.channel}}^2}{4}$$

$$\rightarrow V_{\text{channel}} = 46.543 \frac{\text{m}}{\text{s}}$$

$$ReNo_{\text{wire}}(D) := \frac{\rho_{\text{air}} \cdot V_{\text{plenum}} \cdot (D \cdot m)}{\mu_{\text{air}}}$$

<-- D is the Diameter of the Wire (the characteristic length for the flow around a cylinder)

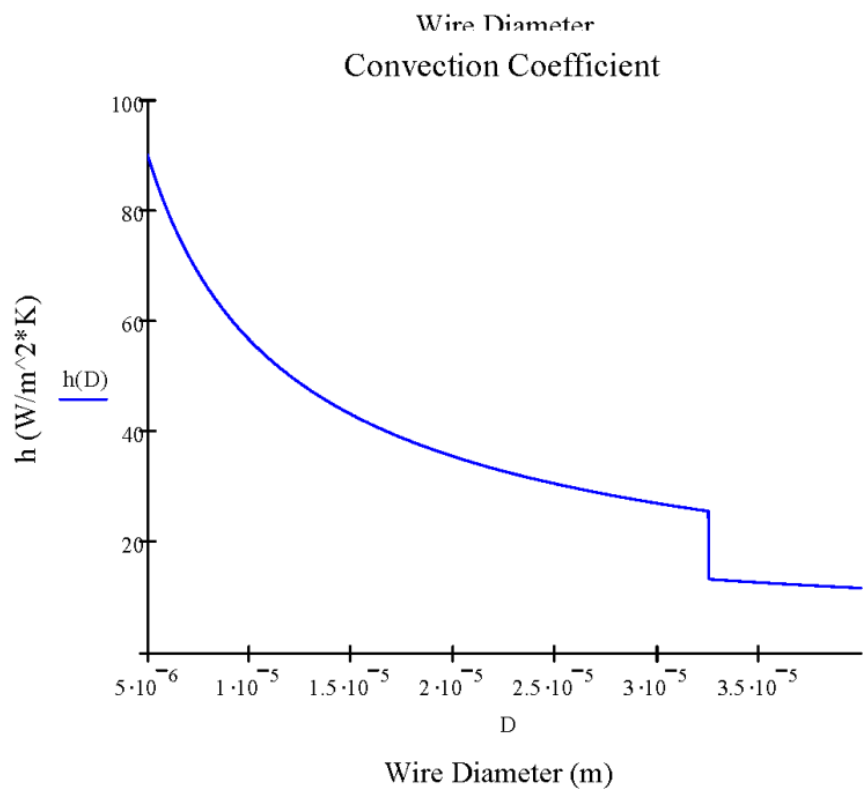
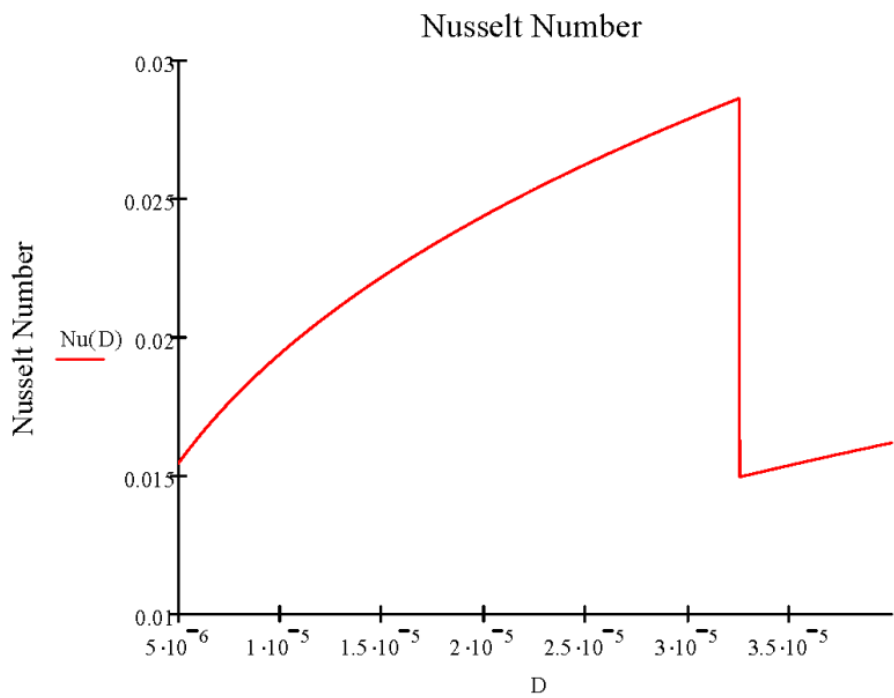
$$m_{\text{h}}(D) := \begin{cases} .330 & \text{if } 0.4 < ReNo_{\text{wire}}(D) < 4 \\ .385 & \text{if } 4 \leq ReNo_{\text{wire}}(D) < 40 \\ .466 & \text{if } 40 \leq ReNo_{\text{wire}}(D) < 4000 \\ .618 & \text{if } 4000 \leq ReNo_{\text{wire}}(D) < 40000 \\ .805 & \text{if } 40000 \leq ReNo_{\text{wire}}(D) < 400000 \end{cases}$$

$$C_{\text{h}}(D) := \begin{cases} .989 & \text{if } 0.4 < ReNo_{\text{wire}}(D) < 4 \\ .911 & \text{if } 4 \leq ReNo_{\text{wire}}(D) < 40 \\ .683 & \text{if } 40 \leq ReNo_{\text{wire}}(D) < 4000 \\ .193 & \text{if } 4000 \leq ReNo_{\text{wire}}(D) < 40000 \\ .027 & \text{if } 40000 \leq ReNo_{\text{wire}}(D) < 400000 \end{cases}$$

*From Pg 426 in Incropera and Dewitt*

$$Nu(D) := C_{\text{h}}(D) \cdot Re(D)^{m_{\text{h}}(D)} \cdot Pr_{\text{air}}^{0.37}$$

$$h(D) := \frac{k_{\text{air}} \cdot Nu(D)}{D \cdot m}$$



## TEMPERATURE CALCULATIONS - Mesh

- These calculations will look into the time-development of the wire and flow temperatures

$$\text{htc\_wire} := \begin{cases} \text{for } i \in 0..4 \\ \text{htc}_i \leftarrow h(D_{\text{wire\_nd}_i}) \\ \text{htc} \end{cases}$$

$$\text{htc\_wire} = \begin{pmatrix} 45.158 \\ 56.659 \\ 43.18 \\ 35.61 \\ 30.665 \end{pmatrix} \frac{\text{W}}{\text{m}^2 \cdot \text{K}}$$

$$A_{\text{s\_wire}}(D_{\text{wire}}) := L_{\text{wire}} \cdot (\pi) \cdot (D_{\text{wire}} \cdot \text{m})$$

$$\text{Vol\_wire}(D_{\text{wire}}) := \frac{\pi \cdot (D_{\text{wire}} \cdot \text{m})^2}{4} \cdot L_{\text{wire}}$$

$$\text{mass\_wire}(D_{\text{wire}}) := \rho_{\text{wire}} \cdot \text{Vol\_wire}(D_{\text{wire}})$$

$$L_{\text{c\_wire}}(D_{\text{wire}}) := \frac{\text{Vol\_wire}(D_{\text{wire}})}{A_{\text{s\_wire}}(D_{\text{wire}})}$$

$$\text{Bi}(D_{\text{wire}}) := \frac{\text{htc\_wire} \cdot (D_{\text{wire}})}{k_{\text{wire}}}$$

Bi << 1 - Assume a Uniform Temperature Distribution within the Wire

$$\text{Biot} := \begin{cases} \text{for } i \in 0..4 \\ \text{bio}_{0,i} \leftarrow \text{Bi}(D_{\text{wire}_i}) \\ \text{bio} \end{cases}$$

$$\text{Biot} = \begin{pmatrix} \begin{pmatrix} 1.047 \times 10^{-5} \\ 1.314 \times 10^{-5} \\ 1.001 \times 10^{-5} \\ 8.258 \times 10^{-6} \\ 7.111 \times 10^{-6} \end{pmatrix} & \begin{pmatrix} 7.464 \times 10^{-6} \\ 9.365 \times 10^{-6} \\ 7.137 \times 10^{-6} \\ 5.886 \times 10^{-6} \\ 5.069 \times 10^{-6} \end{pmatrix} & \begin{pmatrix} 1.12 \times 10^{-5} \\ 1.405 \times 10^{-5} \\ 1.071 \times 10^{-5} \\ 8.829 \times 10^{-6} \\ 7.603 \times 10^{-6} \end{pmatrix} & \begin{pmatrix} 1.493 \times 10^{-5} \\ 1.873 \times 10^{-5} \\ 1.427 \times 10^{-5} \\ 1.177 \times 10^{-5} \\ 1.014 \times 10^{-5} \end{pmatrix} & \begin{pmatrix} 1.866 \times 10^{-5} \\ 2.341 \times 10^{-5} \\ 1.784 \times 10^{-5} \\ 1.471 \times 10^{-5} \\ 1.267 \times 10^{-5} \end{pmatrix} \end{pmatrix}$$



## TEMPERATURE CALCULATIONS - Mainstream (Bulk) Flow Temperature

- These calculations look into the time-development of the flow temperatures

```

Powers := | t ← 0
           | i ← 1
           | j ← 2
           | k ← 0
           | t_delt ← 0.0001·s
           | qheateri ← 1 W
           | Twire0 ← T_inletplenum
           | while t ≤ 2
           |   | z ←  $\frac{t}{\text{time}_{\text{step}}}$ 
           |   | timecode ← t·s
           |   | Twirei ← Twirei-1 +  $\frac{t\_delt \cdot q_{\text{heater}}_{i-1}}{c_{\text{pwire}} \cdot \text{mass}_{\text{wire}}(D_{\text{wire\_nd}_k})}$ 
           |   | while z < 1
           |   |   | Tb6i ← T_inletplenum
           |   |   | qin_6 ← h(Dwire_ndk) · (numwire(Dwire_ndk) · Aswire(Dwire_ndk)) · (Twirei - Tb6i)
           |   |   | Tbbulki ← T_inletplenum +  $\frac{q_{\text{in\_6}}}{m\_dot \cdot c_{\text{pair}}}$ 
           |   |   | qtotali ← nummesh · qin_6

```

```

| break
while 1 ≤ z < 2
| qin_1 ← h(Dwire_ndk) · (numwire(Dwire_ndk) · Aswire(Dwire_ndk)) · (Twirei - Tinletplenum)
| Tb_2i ← Tinletplenum +  $\frac{q_{in\_1}}{m\_dot \cdot c_{p\_air}}$ 
| qin_2 ← h(Dwire_ndk) · (numwire(Dwire_ndk) · Aswire(Dwire_ndk)) · (Twirei - Tb_2i)
| Tb_3i ← Tb_2i +  $\frac{q_{in\_2}}{m\_dot \cdot c_{p\_air}}$ 
| qin_3 ← h(Dwire_ndk) · (numwire(Dwire_ndk) · Aswire(Dwire_ndk)) · (Twirei - Tb_3i)
| Tb_4i ← Tb_3i +  $\frac{q_{in\_3}}{m\_dot \cdot c_{p\_air}}$ 
| qin_4 ← h(Dwire_ndk) · (numwire(Dwire_ndk) · Aswire(Dwire_ndk)) · (Twirei - Tb_4i)
| Tb_5i ← Tb_4i +  $\frac{q_{in\_4}}{m\_dot \cdot c_{p\_air}}$ 
| qin_5 ← h(Dwire_ndk) · (numwire(Dwire_ndk) · Aswire(Dwire_ndk)) · (Twirei - Tb_5i)
| Tb_6i ← Tb_5i +  $\frac{q_{in\_5}}{m\_dot \cdot c_{p\_air}}$ 
| qin_6 ← h(Dwire_ndk) · (numwire(Dwire_ndk) · Aswire(Dwire_ndk)) · (Twirei - Tb_6i)
| Tbulki ← Tb_6i +  $\frac{q_{in\_6}}{m\_dot \cdot c_{p\_air}}$ 
| qtotali ← qin_1 + qin_2 + qin_3 + qin_4 + qin_5 + qin_6

```

```

| break
while 2 ≤ z < 3
| qin_1 ← h(Dwire_ndk) · (numwire(Dwire_ndk) · Aswire(Dwire_ndk)) · (Twirei - Tinletplenum)
| Tb_2i ← Tinletplenum +  $\frac{q_{in\_1}}{m\_dot \cdot c_{p\_air}}$ 
| qin_2 ← h(Dwire_ndk) · (numwire(Dwire_ndk) · Aswire(Dwire_ndk)) · (Twirei - Tb_2i)
| Tb_3i ← Tb_2i +  $\frac{q_{in\_2}}{m\_dot \cdot c_{p\_air}}$  +  $\frac{q_{in\_1}}{m\_dot \cdot c_{p\_air}}$ 
| qin_3 ← h(Dwire_ndk) · (numwire(Dwire_ndk) · Aswire(Dwire_ndk)) · (Twirei - Tb_3i)
| Tb_4i ← Tb_3i +  $\frac{q_{in\_3}}{m\_dot \cdot c_{p\_air}}$  +  $\frac{q_{in\_2}}{m\_dot \cdot c_{p\_air}}$ 
| qin_4 ← h(Dwire_ndk) · (numwire(Dwire_ndk) · Aswire(Dwire_ndk)) · (Twirei - Tb_4i)
| Tb_5i ← Tb_4i +  $\frac{q_{in\_4}}{m\_dot \cdot c_{p\_air}}$  +  $\frac{q_{in\_3}}{m\_dot \cdot c_{p\_air}}$ 
| qin_5 ← h(Dwire_ndk) · (numwire(Dwire_ndk) · Aswire(Dwire_ndk)) · (Twirei - Tb_5i)
| Tb_6i ← Tb_4i +  $\frac{q_{in\_5}}{m\_dot \cdot c_{p\_air}}$  +  $\frac{q_{in\_4}}{m\_dot \cdot c_{p\_air}}$ 
| qin_6 ← h(Dwire_ndk) · (numwire(Dwire_ndk) · Aswire(Dwire_ndk)) · (Twirei - Tb_6i)
| Tbulki ← Tb_6i +  $\frac{q_{in\_6}}{m\_dot \cdot c_{p\_air}}$  +  $\frac{q_{in\_5}}{m\_dot \cdot c_{p\_air}}$ 
| qtotali ← qin_1 + qin_2 + qin_3 + qin_4 + qin_5 + qin_6

```





```

| break
|
| 
$$q_{\text{heater}_i} \leftarrow \frac{V_{\text{all}_{j,k}} \cdot I_{\text{all}_{j,k}} - q_{\text{total}_i}}{\text{num\_wire\_all}(D_{\text{wire\_nd}_k})}$$

|
|  $i \leftarrow i + 1$ 
|
|  $t \leftarrow t + \frac{t\_delt}{s}$ 
|
| (qheater qin_6 qtotal)

```

$$\text{Powers} := \text{Powers}^T$$

$$\text{Temperatures} := \text{Temperatures}^T$$

$$q_{\text{stored}} := \text{Powers}_0$$

$$T_{\text{wire}} := \text{Temperatures}_0$$

$$q_{\text{in}_5} := \text{Powers}_1$$

$$T_{\text{bulk}} := \text{Temperatures}_1$$

$$q_{\text{total}} := \text{Powers}_2$$

```

time_plot := | tim ← 0
| for i ∈ 0 .. 20000
| | t_i ← tim
| | tim ← tim + 0.0001
| t

```

$$\text{time\_plots} := \text{time\_plot} \cdot s$$

$$T_{\text{max}} := 450$$

$q_{\text{stored}} =$

	0
0	0
1	0.098
2	0.098
3	0.098
4	0.098
5	0.098
6	0.098
7	0.098
8	0.098
9	0.098
10	0.098
11	0.098
12	0.098
13	0.098
14	0.098
15	0.098

W

$q_{\text{total}} =$

	0
0	0
1	0
2	0.701
3	1.402
4	2.102
5	2.802
6	3.502
7	4.202
8	4.902
9	5.601
10	6.3
11	6.999
12	7.697
13	8.396
14	9.094
15	9.792

W

$q_{\text{in}_5} = 244.038 \text{ W}$

$T_{\text{wire}} =$

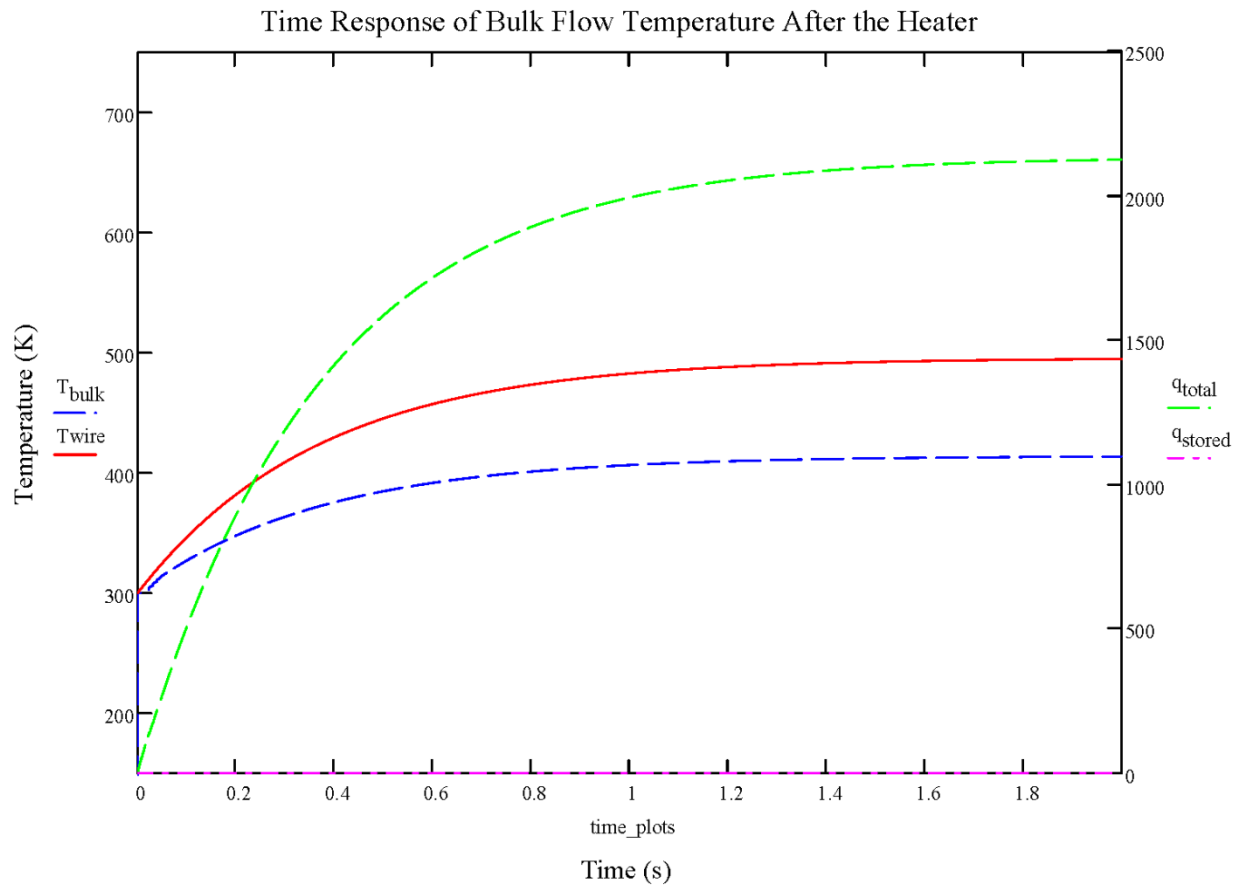
	0
0	300
1	300
2	300.053
3	300.106
4	300.159
5	300.213
6	300.266
7	300.319
8	300.372
9	300.425
10	300.478
11	300.531
12	300.584
13	300.637
14	300.69
15	300.743

K

$T_{\text{bulk}} =$

	0
0	0
1	300
2	300.002
3	300.003
4	300.005
5	300.007
6	300.008
7	300.01
8	300.011
9	300.013
10	300.015
11	300.016
12	300.018
13	300.02
14	300.021
15	300.023

K



## APPENDIX C: IMAGE PROCESSING CODES



## C.1. Image Importing Code

```

%-----%
% TRANSIENT STRAIGHT DUCT PROJECT
%   Processing Step 1
%   Reading Sequenced Images from Video Files
%       - All Cameras

% CARSON SLABAUGH
% M.S. M.E. Thesis and Open Publication Project
% 05/01/2010
%-----%

clc
close all

%Inputs Required:
%   Sequenced Images from Video Files
%   -- From T1, '[Caseinfo]_T1'
%   -- From T2, '[Caseinfo]_T2'
%   -- From S1, '[Caseinfo]_S1'
%   -- From S2, '[Caseinfo]_S2'
%   -- From B1, '[Caseinfo]_B1'
%   -- From B2, '[Caseinfo]_B2'

%   Number of Sequenced Images
%   -- numT1
%   -- numT2
%   -- numS1
%   -- numS2
%   -- numB1
%   -- numB2

%INPUTS
numT1 = 1500;
numT2 = 1500;
numS1 = 1500;
numS2 = 1500;
numB1 = 1500;
numB2 = 1500;

%READING IMAGES
%Pulling the green value from the image scanned into 'oneFile'
%into an array of green values for each individual picture
%sequenced into a three-dimensional array where the z is in
%time.

%z variable controls the loop for each case ( T1 T2 S1 S2 B1 B2 )
=> ( 1 2 3 4 5 6 )

for z = 1:6 %set to 1:6
    if z == 1

```

```

        currentFolder = 'C:\Users\Lucky\Desktop\Transient Straight
Duct\V_SW_2\40k_run1\Images\T1\';
    else if z == 2
        currentFolder = 'C:\Users\Lucky\Desktop\Transient Straight
Duct\V_SW_2\40k_run1\Images\T2\';
    else if z == 3
        currentFolder = 'C:\Users\Lucky\Desktop\Transient Straight
Duct\V_SW_2\40k_run1\Images\S1\';
    else if z == 4
        currentFolder = 'C:\Users\Lucky\Desktop\Transient Straight
Duct\V_SW_2\40k_run1\Images\S2\';
    else if z == 5
        currentFolder = 'C:\Users\Lucky\Desktop\Transient Straight
Duct\V_SW_2\40k_run1\Images\B1\';
    else if z == 6
        currentFolder = 'C:\Users\Lucky\Desktop\Transient Straight
Duct\V_SW_2\40k_run1\Images\B2\';
    end % z == 6
    end % z == 5
    end % z == 4
    end % z == 3
    end % z == 2
end % z == 1

index = 0;

for i = 0:9
    for j= 0:9
        for k = 0:9
            for l = 0:9
                bmpfilename = sprintf('_00%d%d%d%d.bmp', i, j, k, l);
                fullFileName = fullfile(currentFolder,bmpfilename);
                oneFile= imread(fullfile(currentFolder,bmpfilename));
                index = index + 1;
                [h w r] = size(oneFile) ;
                for x = 1:h
                    for y = 1:w

%copies the image in the open file into the array
%one file is the current open image containing an
%array of rgb values
%only the g values are used here
                    if z == 1
                        T1(x,y,index) = oneFile(x,y,2);
                    else if z == 2
                        T2(x,y,index) = oneFile(x,y,2);
                    else if z == 3
                        S1(x,y,index) = oneFile(x,y,2);
                    else if z == 4
                        S2(x,y,index) = oneFile(x,y,2);
                    else if z == 5
                        B1(x,y,index) = oneFile(x,y,2);
                    else if z == 6
                        B2(x,y,index) = oneFile(x,y,2);

                    end % z == 6
                end
            end
        end
    end
end

```

```

        end % z == 5
        end % z == 4
        end % z == 3
        end % z == 2
    end % z == 1
    end %for y
end % for x
if z == 1
    if index == numT1
        break
    end
else if z == 2
    if index == numT2
        break
    end
else if z == 3
    if index == numS1
        break
    end
else if z == 4
    if index == numS2
        break
    end
else if z == 5
    if index == numB1
        break
    end
else if z == 6
    if index == numB2
        break
    end
end

    end % z == 6
    end % z == 5
    end % z == 4
    end % z == 3
    end % z == 2
end % z == 1
end % for l
if z == 1
    if index == numT1
        break
    end
else if z == 2
    if index == numT2
        break
    end
else if z == 3
    if index == numS1
        break
    end
else if z == 4
    if index == numS2
        break
    end
else if z == 5
    if index == numB1

```

```

        break
    end
else if z == 6
    if index == numB2
        break
    end

    end % z == 6
end % z == 5
end % z == 4
end % z == 3
end % z == 2
end % z == 1
end % for k
if z == 1
    if index == numT1
        break
    end
else if z == 2
    if index == numT2
        break
    end
else if z == 3
    if index == numS1
        break
    end
else if z == 4
    if index == numS2
        break
    end
else if z == 5
    if index == numB1
        break
    end
else if z == 6
    if index == numB2
        break
    end

    end % z == 6
end % z == 5
end % z == 4
end % z == 3
end % z == 2
end % z == 1
end % for j
if z == 1
    if index == numT1
        break
    end
else if z == 2
    if index == numT2
        break
    end
else if z == 3
    if index == numS1

```

```

        break
    end
else if z == 4
    if index == numS2
        break
    end
else if z == 5
    if index == numB1
        break
    end
else if z == 6
    if index == numB2
        break
    end

    end % z == 6
    end % z == 5
    end % z == 4
    end % z == 3
    end % z == 2
end % z == 1
end % for i
end % for z

%Clean Workspace
%Clears Variables that are no longer needed
clear numT1 numT2 numS1 numS2 numB1 numB2;
clear bmpfilename;
clear currentFolder;
clear oneFile;
clear fullFileName;
clear i j k l z h w r x y index;

```

## C.2. Image Cropping and Stitching Code

```

%-----%
% TRANSIENT STRAIGHT DUCT PROJECT
%   Processing Step 2
%   Cropping ALL Images and Stitching

% CARSON SLABAUGH
% M.S. M.E. Thesis and Open Publication Project
% 05/01/2010
%-----%

%Inputs Required:
%   T1 Image Matrix      <-- From Previous Codes (named 'T1')
%   T2 Image Matrix      <-- From Previous Codes (named 'T2')
%   S1 Image Matrix      <-- From Previous Codes (named 'S1')
%   S2 Image Matrix      <-- From Previous Codes (named 'S2')
%   B1 Image Matrix      <-- From Previous Codes (named 'B1')
%   B2 Image Matrix      <-- From Previous Codes (named 'B2')

%   Number of Sequenced Images in T    <-- numT
%   Number of Sequenced Images in S    <-- numS
%   Number of Sequenced Images in B    <-- numB
%   Crop Ranges                      <-- T1, T2, S1, S2, B1, and B2
%                                     <-- w and h range variables

%INPUTS
% num images
numT = 1500;
numS = 1500;
numB = 1500;

%Stitching Parameters
%Set Stitching Limits

%Top Wall Crop Areas
T1_w = 196:507;
T1_h = 4:41;
T2_w = 1:330;
T2_h = 4:41;

%Side Wall Crop Areas
S1_w = 230:543;
S1_h = 5:26;
S2_w = 1:434;
S2_h = 4:25;

%Bottom Wall Crop Areas
B1_w = 207:419;
B1_h = 1:39;
B2_w = 1:321;
B2_h = 2:40;

%Needed Values
index = 0;

```



```

Glow = 0;
Ghigh = 255;

%CROP
%Crops images based on defined Crop Areas
%Stores cropped image in a new variable Var_Crop
T1_Crop = T1(T1_h,T1_w,:);
T2_Crop = T2(T2_h,T2_w,:);
S1_Crop = S1(S1_h,S1_w,:);
S2_Crop = S2(S2_h,S2_w,:);
B1_Crop = B1(B1_h,B1_w,:);
B2_Crop = B2(B2_h,B2_w,:);

%STITCH
%Grabs dimensions of cropped images and stores them in new vars
%NOTE: Vertical crop height must match in image pairs

[xT1,yT1,zT1] = size(T1_Crop);
[xT2,yT2,zT2] = size(T2_Crop);
[xS1,yS1,zS1] = size(S1_Crop);
[xS2,yS2,zS2] = size(S2_Crop);
[xB1,yB1,zB1] = size(B1_Crop);
[xB2,yB2,zB2] = size(B2_Crop);

% Left to Right stitching
% Stitch Pattern [1]|[2]

% for i = 1:5
%   T(1:xT1,1:yT1,i) = T1_Crop(1:xT1,1:yT1,i);
%   T(1:xT1,yT1+1:yT1+yT2,i) = T2_Crop(1:xT2,1:yT2,i);
% end
%
% for i = 1:numS
%   S(1:xS1,1:yS1,i) = S1_Crop(1:xS1,1:yS1,i);
%   S(1:xS1,yS1+1:yS2+yS2,i) = S2_Crop(1:xS2,1:yS2,i);
% end
%
% for i = 1:numB
%   B(1:xB1,1:yB1,d) = B1_Crop(1:xB1,1:yB1,d);
%   B(1:xB1,yB1+1:yB2+yB2,d) = B2_Crop(1:xB2,1:yB2,d);
% end

% Right to Left stitching
% Stitch Pattern [2]|[1]
for i = 1:numT
    T(1:xT2,1:yT2,i) = T2_Crop(1:xT2,1:yT2,i);
    T(1:xT2,yT2+1:yT1+yT2,i) = T1_Crop(1:xT1,1:yT1,i);
end

for i = 1:numS
    S(1:xS2,1:yS2,i) = S2_Crop(1:xS2,1:yS2,i);
    S(1:xS2,yS2+1:yS2+yS1,i) = S1_Crop(1:xS1,1:yS1,i);
end

```

```

for i = 1:numB
    B(1:xB2,1:yB2,i) = B2_Crop(1:xB2,1:yB2,i);
    B(1:xB2,yB2+1:yB2+yB1,i) = B1_Crop(1:xB1,1:yB1,i);
end

%Display stitched image
imagesc(T(:, :, 1000));
imagemenu;
colorbar;
lims = get(gca, 'CLim');
set(gca, 'CLim', [Glow Ghigh]);
phch =
get(findall(gcf, 'type', 'image', 'tag', 'TMW_COLORBAR'), {'parent'});
for i=1:length(phch);
    phud = get(phch{i}, 'userdata');
    if isfield(phud, 'PlotHandle');
        if isequal(gca, phud.PlotHandle);
            colorbar;
        end
    end
end
end

figure;
imagesc(S(:, :, 1000));
imagemenu;
colorbar;
lims = get(gca, 'CLim');
set(gca, 'CLim', [Glow Ghigh]);
phch =
get(findall(gcf, 'type', 'image', 'tag', 'TMW_COLORBAR'), {'parent'});
for i=1:length(phch);
    phud = get(phch{i}, 'userdata');
    if isfield(phud, 'PlotHandle');
        if isequal(gca, phud.PlotHandle);
            colorbar;
        end
    end
end
end

figure;
imagesc(B(:, :, 1000));
imagemenu;
colorbar;
lims = get(gca, 'CLim');
set(gca, 'CLim', [Glow Ghigh]);
phch =
get(findall(gcf, 'type', 'image', 'tag', 'TMW_COLORBAR'), {'parent'});
for i=1:length(phch);
    phud = get(phch{i}, 'userdata');
    if isfield(phud, 'PlotHandle');
        if isequal(gca, phud.PlotHandle);
            colorbar;
        end
    end
end
end

```

end

```
%Clean Workspace
%Clears Variables that are no longer needed
clear numT numS numB;
clear T1_w T1_h T2_w T2_h S1_w S1_h S2_w S2_h B1_w B1_h B2_w B2_h;
clear xT1 yT1 zT1 xT2 yT2 zT2 xS1 yS1 zS1 xS2 yS2 zS2 xB1 yB1 zB1 x2
yB2 zB2;
clear index Glow Ghigh;
clear i lims phch phud xB2
% clear T1 T2 S1 S2 B1 B2;
% clear T1_Crop T2_Crop S1_Crop S2_Crop B1_Crop B2_Crop
```

### C.3. Filtering and Averaging Code

```

%-----%
% TRANSIENT STRAIGHT DUCT PROJECT
%   Processing Step 3
%   Image Filtering and Averaging
%   Build Time Matrix (t)

% CARSON SLABAUGH
% M.S. M.E. Thesis and Open Publication Project
% 05/01/2010
%-----%

clc;
close all;

%Inputs Required:
%   Top Wall G(x,y,t) Array      <-- From Previous Codes (named 'Top')
%   Side Wall G(x,y,t) Array    <-- From Previous Codes (named 'Side')
%   Bottom Wall G(x,y,t) Array  <-- From Previous Codes (named
'Bottom')
%   Number of Frames to Average in Time      <-- t_num_avg = 5 (+2 and -
2)
%   Camera Speed                    <-- Frames Per Second (Hz)

%INPUTS

%Number of frames to average
%Enter odd numbers of frames to stay symmetric
t_num_avg = 9;
s_num_avg = 9;
b_num_avg = 9;

%Frame offset

t_offset = (t_num_avg + 1)/2;
s_offset = (t_num_avg + 1)/2;
b_offset = (t_num_avg + 1)/2;

%Camera Frame Rate
cam_speed = 29;

%FIND SIZES OF INPUT ARRAYS
[Ty Tx Tz] = size(T);
[Sy Sx Sz] = size(S);
[By Bx Bz] = size(B);

tlow = 0;
thigh = Tz;

%AVERAGING IN TIME

%Top

```

```

%Fetch images that can't be filtered at ends
for i = 1:t_offset-1
    T_avgt(:,:,i) = T(:,:,i);
    T_avgt(:,:,Tz-i+1) = T(:,:,Tz-i+1);
end

%fills the rest of the array with zeroes
T_avgt(:,:,t_offset:Tz-t_offset+1)=0;

% T_avgt(:,:,1) = (T(:,:,1));
% T_avgt(:,:,2) = (T(:,:,1));
% T_avgt(:,:,Tz-1) = (T(:,:,Tz-1));
% T_avgt(:,:,Tz) = (T(:,:,Tz));

%arithmetic operation on uint8 will overflow
%must pre-divide to remain in unit8 space
for i = 1:Ty
    for j = 1:Tx
        for k = t_offset:Tz-t_offset
            for l = (k-t_offset+1):(k+t_offset-1)
                T_avgt(i,j,k) = T_avgt(i,j,k)+T(i,j,l)/t_num_avg;
            end
        end
    end
end

%Side
%Fetch images that can't be filtered at ends
for i = 1:s_offset-1
    S_avgt(:,:,i) = S(:,:,i);
    S_avgt(:,:,Sz-i+1) = S(:,:,Sz-i+1);
end

%fills the rest of the array with zeroes
S_avgt(:,:,s_offset:Sz-s_offset+1)=0;

for i = 1:Sy
    for j = 1:Sx
        for k = s_offset:Sz-s_offset
            for l = (k-s_offset+1):(k+s_offset-1)
                S_avgt(i,j,k) = S_avgt(i,j,k)+S(i,j,l)/s_num_avg;
            end
        end
    end
end

%Bottom
%Fetch images that can't be filtered at ends
for i = 1:b_offset-1
    B_avgt(:,:,i) = B(:,:,i);
    B_avgt(:,:,Bz-i+1) = B(:,:,Bz-i+1);
end

%fills the rest of the array with zeroes
B_avgt(:,:,b_offset:Bz-b_offset+1)=0;

```

```

for i = 1:By
    for j = 1:Bx
        for k = t_offset:Bz-b_offset
            for l = (k-b_offset+1):(k+b_offset-1)
                B_avgt(i,j,k) = B_avgt(i,j,k)+B(i,j,l)/b_num_avg;
            end
        end
    end
end

% %Plot Selected Time-Averaged Data
for i=1:k
    T_plot(i) = T_avgt(12,250,i);
    T_plot_old(i) = T(12,250,i);
    S_plot(i) = S_avgt(12,250,i);
    S_plot_old(i) = S(12,250,i);
    B_plot(i) = B_avgt(12,250,i);
    B_plot_old(i) = B(12,250,i);
    t(i)=i;
end

plot(t,T_plot); %1
figure
plot(t,T_plot_old); %2
figure
plot(t,S_plot); %3
figure
plot(t,S_plot_old); %4
figure
plot(t,B_plot); %5
figure
plot(t,B_plot_old); %6
figure

%BUILD Z MATRICES
%Top
z_T(Ty,Tx) = zeros;
for i = 1:Ty
    for j = 1:Tx
        for k = 1:Tz
            if T_avgt(i,j,k)>z_T(i,j)
                z_T(i,j) = k;
            end
        end
    end
end

%Side
z_S(Sy,Sx) = zeros;
for i = 1:Sy
    for j = 1:Sx
        for k = 1:Sz
            if S_avgt(i,j,k)>z_S(i,j)
                z_S(i,j) = k;
            end
        end
    end
end

```

```

        end
    end
end

%Bottom
z_B(By,Bx) = zeros;
for i = 1:By
    for j = 1:Bx
        for k = 1:Bz
            if B_avgt(i,j,k)>z_B(i,j)
                z_B(i,j) = k;
            end
        end
    end
end

end

%AVERAGING IN SPACE
%    Looping through every index
%    Average z value of surrounding points to the center
%    Outside edge of single pixels is excluded

%Top
%
%Fetch edges
z_T_avg_space(:, :) = z_T(:, :);
z_T_avg_space(2:Ty-1, 2:Tx-1) = 0;

for i = 2:Ty-1
    for j = 2:Tx-1
        z_T_avg_space(i, j) = (z_T(i-1, j-1)+z_T(i, j-1)+z_T(i+1, j-1)+z_T(i-1, j)+z_T(i, j)+z_T(i+1, j)+z_T(i-1, j+1)+z_T(i, j+1)+z_T(i+1, j+1))/s_num_avg;
    end
end

% Side
%
%Fetch edges
z_S_avg_space(:, :) = z_S(:, :);
z_S_avg_space(2:Sy-1, 2:Sx-1) = 0;

for i = 2:Sy-1
    for j = 2:Sx-1
        z_S_avg_space(i, j) = (z_S(i-1, j-1)+z_S(i, j-1)+z_S(i+1, j-1)+z_S(i-1, j)+z_S(i, j)+z_S(i+1, j)+z_S(i-1, j+1)+z_S(i, j+1)+z_S(i+1, j+1))/s_num_avg;
    end
end

%Bottom
%
%Fetch edges
z_B_avg_space(:, :) = z_B(:, :);

```



```

z_B_avg_space(2:By-1,2:Bx-1) = 0;

for i = 2:By-1
    for j = 2:Bx-1
        z_B_avg_space(i,j) = (z_B(i-1,j-1)+z_B(i,j-1)+z_B(i+1,j-1)+z_B(i-1,j)+z_B(i,j)+z_B(i+1,j)+z_B(i-1,j+1)+z_B(i,j+1)+z_B(i+1,j+1))/s_num_avg;
    end
end

%CONVERT FROM FRAMES TO TIME
t_T = z_T_avg_space(:,:)/cam_speed;
t_S = z_S_avg_space(:,:)/cam_speed;
t_B = z_B_avg_space(:,:)/cam_speed;

%PLOTTING
%Display Final t matrices
imagesc(t_T(:,:));
imagemenu;
colorbar;
lims = get(gca, 'CLim');
set(gca, 'CLim', [tlow thigh]);
phch =
get(findall(gcf,'type','image','tag','TMW_COLORBAR'),{'parent'});
for i=1:length(phch);
    phud = get(phch{i},'userdata');
    if isfield(phud,'PlotHandle');
        if isequal(gca, phud.PlotHandle);
            colorbar;
        end
    end
end
end

figure;
imagesc(t_S(:,:));
imagemenu;
colorbar;
lims = get(gca, 'CLim');
set(gca, 'CLim', [tlow thigh]);
phch =
get(findall(gcf,'type','image','tag','TMW_COLORBAR'),{'parent'});
for i=1:length(phch);
    phud = get(phch{i},'userdata');
    if isfield(phud,'PlotHandle');
        if isequal(gca, phud.PlotHandle);
            colorbar;
        end
    end
end
end

figure;

```

```

imagesc(t_B(:,:));
imagemenu;
colorbar;
lims = get(gca, 'CLim');
set(gca, 'CLim', [tlow thigh]);
phch =
get(findall(gcf,'type','image','tag','TMW_COLORBAR'),{'parent'});
for i=1:length(phch);
    phud = get(phch{i},'userdata');
    if isfield(phud,'PlotHandle');
        if isequal(gca, phud.PlotHandle);
            colorbar;
        end
    end
end
end

%Clean Workspace
%Clears Variables that are no longer needed
clear i j k l;
clear cam_speed;
clear t_num_avg s_num_avg b_num_avg;
clear t_offset s_offset b_offset;
clear Ty Tx Tz;
clear Sy Sx Sz;
clear By Bx Bz;
clear tlow thigh;
clear lims phch phud;
clear T_plot T_plot_old;
clear S_plot S_plot_old;
clear Z_plot Z_plot_old;
clear t;
clear T S B;

```

#### C.4. Nusselt Number Solution

```

%-----%
% TRANSIENT STRAIGHT DUCT PROJECT
%   Processing Step 4
%   Heat Transfer Coefficient and Nusselt Number Processing Code
%   Semi-Infinite and Superposition Solutions

% CARSON SLABAUGH
% M.S. M.E. Thesis and Open Publication Project
% 05/16/2010
%-----%

clc;
close all;

%Inputs Required:
%   Time Matrix (t)           <-- From Previous Codes (named 't')
%   Dimensions of Time Matrix <-- [x,y] - Value of Time (t) in space
%   Wall Temperature (T_wall) <-- From TLC Calibration
%   (T_MaxG)(Kelvin)
%   Initial Temperature (T_init)<-- From DAQ (One Value)(Kelvin)
%   Inlet Temperature (T_inlet) <-- From DAQ (T_inlet)(Kelvin)
%   Bulk Temp Curve (T_bulk)   <-- From Excel Fit (fn(x))
%   Channel Mass Flow-Rate     <-- Input From Venturi Sheet
%   (m_dot)(kg/s)
%   Channel Wetted Perimeter   <-- Specific to Case Tested

% Code Stuff

%FIND SIZES OF INPUT ARRAYS
[Ty Tx] = size(t_T);
[Sy Sx] = size(t_S);
[By Bx] = size(t_B);

%L = length of the channel
L = 30; % in.

%Resolutions
RT = L/Tx;
RS = L/Sx;
RB = L/Bx;

%INPUTS
T_wall = 35.76229 + 273.15; %From Calibration Don't Touch
T_init = 23.14677 + 273.15;

tlow = 0;
thigh = 250;

%Flow Values
m_dot = 0.02880543; %flow rate, kg/s
P_wet = 0.1524; %wetted perimeter: 6 inches in meters
A_x = 2*0.0254*0.0254;
Dh = 4*A_x/P_wet; %hydraulic diameter 4/3 in

%Acrylic Properties

```

```

rho_a = 1190 ; % kg/m^3
cp_a = 1440; % J/kg/K
k_a = 0.184; % W/m/K
alpha_a = k_a/(rho_a*cp_a); %m^2/s

%TOP SOLUTION
%Semi-Infinite Solid
%=====
%Create Identically Sized Matrix of Temperature Factors (Eta)
eta = (T_wall - T_init)/(T_inf - T_init);
for i = 1:Tx
    for j = 1:Ty
        eta(j,i) = (T_wall - T_init)/(T_bulk_SP(RT,L,i, t_T(j,i)) -
T_init);
        Beta_T(j,i) = fsolve(@(Beta)(1-(exp(Beta^2)*erfc(Beta))-
eta(j,i)),1,optimset('Display','iter'));
        T_h(j,i) = sqrt((Beta_T(j,i)^2*rho_a*cp_a*k_a)/(t_T(j,i)));
    end
end

%TOP SOLUTION
%Superposition
%=====
for i = 1:Tx
    for j = 1:Ty
        h_T(j,i) = T_h(j,i);
        h_T(j,i) = fsolve(@(HTC)( T_init - T_wall + SPfun(t_T(j,i), HTC
, RT , L , i ) ), h_T(j,i),optimset('Display','off'));
        % [j i h_T(j,i)] % Print Out Results
    end %end j loop
end %end i loop

%SIDE SOLUTION
%Semi-Infinite Solid
%=====
% Create Identically Sized Matrix of Temperature Factors (Eta)
eta = (T_wall - T_init)/(T_inf - T_init);
for i = 1:Sx
    for j = 1:Sy
        eta(j,i) = (T_wall - T_init)/(T_bulk_SP(RS,L,i, t_S(j,i)) -
T_init);
        Beta_S(j,i) = fsolve(@(Beta)(1-(exp(Beta^2)*erfc(Beta))-
eta(j,i)),0.55,optimset('Display','iter'));
        S_h(j,i) = sqrt((Beta_T(j,i)^2*rho_a*cp_a*k_a)/(t_S(j,i)));
    end
end

%SIDE SOLUTION
%Superposition
%=====
for i = 1:Sx
    for j = 1:Sy
        h_S(j,i) = S_h(j,i);
        h_S(j,i) = fsolve(@(HTC)( T_init - T_wall + SPfun(t_S(j,i), HTC
, RS , L , i ) ), h_S(j,i),optimset('Display','off'));

```

```

%           [j i h_S(j,i)] % Print Out Results
    end %end j loop
end %end i loop

%BOTTOM SOLUTION
%Semi-Infinite Solid
%=====
% Create Identically Sized Matrix of Temperature Factors (Eta)
eta = (T_wall - T_init)/(T_inf - T_init);
for i = 1:Bx
    for j = 1:By
        eta(j,i) = (T_wall - T_init)/(T_bulk_SP(RB,L,i, t_B(j,i)) -
T_init);
        Beta_B(j,i) = fsolve(@(Beta)(1-(exp(Beta^2)*erfc(Beta))-
eta(j,i)),0.55,optimset('Display','iter'));
        B_h(j,i) = sqrt((Beta_B(j,i)^2*rho_a*cp_a*k_a)/(t_B(j,i)));
    end
end

%BOTTOM SOLUTION
%Superposition
%=====
for i = 1:Bx
    for j = 1:By
        h_B(j,i) = B_h(j,i);
        h_B(j,i) = fsolve(@(HTC)( T_init - T_wall + SPfun(t_B(j,i), HTC
, RB , L , i ) ), h_B(j,i),optimset('Display','off'));
%           [j i h_B(j,i)] % Print Out Results
    end %end j loop
end %end i loop

PLOTTING
Display Final HTC matrices
imagesc(h_T(:,,:));
imagemenu;
colorbar;
lims = get(gca, 'CLim');
set(gca, 'CLim', [tlow thigh]);
phch =
get(findall(gcf,'type','image','tag','TMW_COLORBAR'),{'parent'});
for i=1:length(phch);
    phud = get(phch{i},'userdata');
    if isfield(phud,'PlotHandle');
        if isequal(gca, phud.PlotHandle);
            colorbar;
        end
    end
end
end

figure;
imagesc(S_h(:,,:));
imagemenu;

```

```

colorbar;
lims = get(gca, 'CLim');
set(gca, 'CLim', [0 120]);
phch =
get(findall(gcf, 'type', 'image', 'tag', 'TMW_COLORBAR'), {'parent'});
for i=1:length(phch);
    phud = get(phch{i}, 'userdata');
    if isfield(phud, 'PlotHandle');
        if isequal(gca, phud.PlotHandle);
            colorbar;
        end
    end
end
end

```

```

figure;
imagesc(B_h(:, :));
imagemenu;
colorbar;
lims = get(gca, 'CLim');
set(gca, 'CLim', [0 120]);
phch =
get(findall(gcf, 'type', 'image', 'tag', 'TMW_COLORBAR'), {'parent'});
for i=1:length(phch);
    phud = get(phch{i}, 'userdata');
    if isfield(phud, 'PlotHandle');
        if isequal(gca, phud.PlotHandle);
            colorbar;
        end
    end
end
end

```

```

figure;
imagesc(B_h(:, :));
imagemenu;
colorbar;
lims = get(gca, 'CLim');
set(gca, 'CLim', [0 120]);
phch =
get(findall(gcf, 'type', 'image', 'tag', 'TMW_COLORBAR'), {'parent'});
for i=1:length(phch);
    phud = get(phch{i}, 'userdata');
    if isfield(phud, 'PlotHandle');
        if isequal(gca, phud.PlotHandle);
            colorbar;
        end
    end
end
end

```

```

%Nu Plot
Nu_low = 0;
Nu_high = 3;

```

```

figure;
imagesc(T_Nu_aug(:, :));
imagemenu;
colorbar;

```

```

lims = get(gca, 'CLim');
set(gca, 'CLim', [Nu_low Nu_high]);
phch =
get(findall(gcf, 'type', 'image', 'tag', 'TMW_COLORBAR'), {'parent'});
for i=1:length(phch);
    phud = get(phch{i}, 'userdata');
    if isfield(phud, 'PlotHandle');
        if isequal(gca, phud.PlotHandle);
            colorbar;
        end
    end
end
end

```

```

figure;
imagesc(S_Nu_aug(:, :));
imagemenu;
colorbar;
lims = get(gca, 'CLim');
set(gca, 'CLim', [Nu_low Nu_high]);
phch =
get(findall(gcf, 'type', 'image', 'tag', 'TMW_COLORBAR'), {'parent'});
for i=1:length(phch);
    phud = get(phch{i}, 'userdata');
    if isfield(phud, 'PlotHandle');
        if isequal(gca, phud.PlotHandle);
            colorbar;
        end
    end
end
end

```

```

figure;
imagesc(B_Nu_aug(:, :));
imagemenu;
colorbar;
lims = get(gca, 'CLim');
set(gca, 'CLim', [Nu_low Nu_high]);
phch =
get(findall(gcf, 'type', 'image', 'tag', 'TMW_COLORBAR'), {'parent'});
for i=1:length(phch);
    phud = get(phch{i}, 'userdata');
    if isfield(phud, 'PlotHandle');
        if isequal(gca, phud.PlotHandle);
            colorbar;
        end
    end
end
end

```

```

Clean Workspace
Clears Variables that are no longer needed
clear x y i j;
clear lims phch phud;
clear T_bulk T_film;
clear eta B;
clear rho cp mu nu k alpha Pr;
clear rho_f cp_f mu_f nu_f k_f alpha_f Pr_f;
clear Nu_0 Re_f;

```



```

clear Ty Tx;
clear Sy Sx;
clear By Bx;
clear T_wall T_init T_inlet;

clear m_dot P_wet Dh;
clear thigh tlow;

clc;
close all;

%Inputs Required:
%   Time Matrix (t)           <-- From Previous Codes (named 't')
%   Dimensions of Time Matrix <-- [x,y] - Value of Time (t) in space
%   Wall Temperature (T_wall) <-- From TLC Calibration
%   (T_MaxG)(Kelvin)
%   Initial Temperature (T_init)<-- From DAQ (One Value)(Kelvin)
%   Inlet Temperature (T_inlet) <-- From DAQ (T_inlet)(Kelvin)
%   Bulk Temp Curve (T_bulk)   <-- From Excel Fit (fn(x))
%   Channel Mass Flow-Rate     <-- Input From Venturi Sheet
%   (m_dot)(kg/s)
%   Channel Wetted Perimeter   <-- Specific to Case Tested

%FIND SIZES OF INPUT ARRAYS
[Ty Tx Tz] = size(t_T);
[Sy Sx Sz] = size(t_S);
[By Bx Bz] = size(t_B);

%Choose *_x smallest to avoid out of bounds error
x=min( [Tx Sx Bx]);

%INPUTS
T_wall = 35 + 273.15; %From Calibration Don't Touch

T_init = 23 + 273.15;
T_inlet = 50.91 + 273.15;
T_exit = 45.6 + 273.15;

tlow = 0;
thigh = 250;

%Flow Values
m_dot = 0.028712486; %flow rate, kg/s
P_wet = 0.1524; %wetted perimeter: 6 inches in meters
A_x = 2*0.0254*0.0254;
Dh = 4*A_x/P_wet; %hydraulic diameter 4/3 in =

%Acrylic Properties
rho_a = 1190 ; % kg/m^3
cp_a = 1440;
k_a = 0.184;
alpha_a = .0011; %cm^2/s

```

```

%Create Matrices of Fluid Properties
for i = 1:x
    %Bulk Temperature Calculation (Kelvin)
    T_bulk(i) = 0.000214*(30-i*30/x)^3-0.010083*(30-i*30/x)^2-
0.071322*(30-i*30/x)+55.258305 + 273.15;

    %Film Temperature Calculation (Kelvin)
    T_film(i) = 0.5*(T_bulk(i)+T_wall);

    %Properties of Air as a Function of Bulk Temperature
    %Properties Curve-Fit
    rho(i) = 368.38*(T_bulk(i)^(-1.008));
    cp(i) = (0.0000005*T_bulk(i)^2 - 0.0003*T_bulk(i) + 1.0499)*1000;
    mu(i) = -0.00000000003*T_bulk(i)^2 + 0.00000007*T_bulk(i) +
0.0000008;
    nu(i) = 0.0000000001*T_bulk(i)^2 + 0.00000003*T_bulk(i) - 0.000002;
    k(i) = -0.00000003*T_bulk(i)^2 + 0.0001*T_bulk(i) - 0.00007;
    alpha(i) = 0.000000002*T_bulk(i)^2 + 0.00000004*T_bulk(i) -
0.000004;
    Pr(i) = 0.0000006*T_bulk(i)^2 - 0.0006*T_bulk(i) + 0.8373;

    %Properties of Air as a Function of Film Temperature
    %Properties Curve-Fit
    rho_f(i) = 368.38*(T_film(i)^(-1.008));
    cp_f(i) = (0.0000005*T_film(i) - 0.0003*T_film(i) + 1.0499)*1000;
    mu_f(i) = -0.00000000003*T_film(i) + 0.00000007*T_film(i) +
0.0000008;
    nu_f(i) = 0.0000000001*T_film(i) + 0.00000003*T_film(i) - 0.000002;
    k_f(i) = -0.00000003*T_film(i) + 0.0001*T_film(i) - 0.00007;
    alpha_f(i) = 0.000000002*T_film(i) + 0.00000004*T_film(i) -
0.000004;
    Pr_f(i) = 0.0000006*T_film(i) - 0.0006*T_film(i) + 0.8373;
end

%SOLUTION

%Solve for the Predicted Surface Nusselt Number Using the
% Dittus-Boelter Correlation
for i = 1:x
    Re = (4*m_dot)/(P_wet*mu(i));
    Re_f = (4*m_dot)/(P_wet*mu_f(i));
    Nu_0(i) = 0.023*Re_f^0.8*(Pr_f(i))^0.4;
end

%Create Identically Sized Matrix of Temperature Factors (Eta)
% eta = (T_wall - T_init)/(T_inf - T_init)
for i = 1:x
    T_inf = T_bulk(i);
    eta(i) = (T_wall - T_init)/(T_inf - T_init);
end

%Solve for Betas
% eta = 1 - (exp(Beta^2)*erfc(Beta))
% Values of matrix B set at value found for Beta at every pixel

```

```

for i = 1:x
    Be(i) = fsolve(@(Beta)(1-(exp(Beta^2)*erfc(Beta))-eta(i)),25);
end

%Solve for h, Nu, and Nu Augmentation

%Top
for i = 1:Ty
    for j = 1:x
        T_h(i,j) = sqrt((Be(i)^2*rho_a*cp_a*k_a)/(t_T(i,j)));
        T_Nu(i,j) = (T_h(i,j)*Dh)/(k(i));
        T_Nu_aug(i,j) = T_Nu(i,j)/Nu_0(i);
    end
end

%Side
for i = 1:Sy
    for j = 1:x
        S_h(i,j) = sqrt((Be(i)^2*rho_a*cp_a*k_a)/(t_S(i,j)));
        S_Nu(i,j) = (S_h(i,j)*Dh)/(k(i));
        S_Nu_aug(i,j) = S_Nu(i,j)/Nu_0(i);
    end
end

% %Bottom
for i = 1:By
    for j = 1:x
        B_h(i,j) = sqrt((Be(i)^2*rho_a*cp_a*k_a)/(t_B(i,j)));
        B_Nu(i,j) = (B_h(i,j)*Dh)/(k(i));
        B_Nu_aug(i,j) = B_Nu(i,j)/Nu_0(i);
    end
end

%PLOTTING
%Display Final htc matrices
imagesc(T_h(:, :));
imagemenu;
colorbar;
lims = get(gca, 'CLim');
set(gca, 'CLim', [tlow thigh]);
phch =
get(findall(gcf, 'type', 'image', 'tag', 'TMW_COLORBAR'), {'parent'});
for i=1:length(phch);
    phud = get(phch{i}, 'userdata');
    if isfield(phud, 'PlotHandle');
        if isequal(gca, phud.PlotHandle);
            colorbar;
        end
    end
end
end

figure;
imagesc(S_h(:, :));
imagemenu;
colorbar;
lims = get(gca, 'CLim');

```

```

set(gca, 'CLim', [tlow thigh]);
phch =
get(findall(gcf, 'type', 'image', 'tag', 'TMW_COLORBAR'), {'parent'});
for i=1:length(phch);
    phud = get(phch{i}, 'userdata');
    if isfield(phud, 'PlotHandle');
        if isequal(gca, phud.PlotHandle);
            colorbar;
        end
    end
end

figure;
imagesc(B_h(:, :));
imagemenu;
colorbar;
lims = get(gca, 'CLim');
set(gca, 'CLim', [tlow thigh]);
phch =
get(findall(gcf, 'type', 'image', 'tag', 'TMW_COLORBAR'), {'parent'});
for i=1:length(phch);
    phud = get(phch{i}, 'userdata');
    if isfield(phud, 'PlotHandle');
        if isequal(gca, phud.PlotHandle);
            colorbar;
        end
    end
end

%Nu_aug limits to plot
Nu_low = 1;
Nu_high = 3;

figure;
imagesc(T_Nu_aug(:, :));
imagemenu;
colorbar;
lims = get(gca, 'CLim');
set(gca, 'CLim', [Nu_low Nu_high]);
phch =
get(findall(gcf, 'type', 'image', 'tag', 'TMW_COLORBAR'), {'parent'});
for i=1:length(phch);
    phud = get(phch{i}, 'userdata');
    if isfield(phud, 'PlotHandle');
        if isequal(gca, phud.PlotHandle);
            colorbar;
        end
    end
end

figure;
imagesc(S_Nu_aug(:, :));
imagemenu;
colorbar;
lims = get(gca, 'CLim');
set(gca, 'CLim', [Nu_low Nu_high]);

```

```

phch =
get(findall(gcf,'type','image','tag','TMW_COLORBAR'),{'parent'});
for i=1:length(phch);
    phud = get(phch{i},'userdata');
    if isfield(phud,'PlotHandle');
        if isequal(gca, phud.PlotHandle);
            colorbar;
        end
    end
end
end

figure;
imagesc(B_Nu_aug(:,,:));
imagemenu;
colorbar;
lims = get(gca, 'CLim');
set(gca, 'CLim', [Nu_low Nu_high]);
phch =
get(findall(gcf,'type','image','tag','TMW_COLORBAR'),{'parent'});
for i=1:length(phch);
    phud = get(phch{i},'userdata');
    if isfield(phud,'PlotHandle');
        if isequal(gca, phud.PlotHandle);
            colorbar;
        end
    end
end
end

%Clean Workspace
%Clears Variables that are no longer needed
% clear x y i j;
clear lims phch phud;
%clear T_bulk T_film;
%clear eta Be;
% clear rho cp mu nu k alpha Pr;
% clear rho_f cp_f mu_f nu_f k_f alpha_f Pr_f;
%clear Nu_0 Re_f;
clear Ty Tx Tz;
clear Sy Sx Sz;
clear By Bx Bz;
clear T_wall T_init T_inlet;

%clear m_dot P_wet Dh;
clear thigh tlow;
clc

```

## C.5. Bulk Temperature Calculation Function

```

function [ output ] = T_bulk_SP( R , L , i , t )
%BULK TEMPERATURE CALCULATION
%Solving for Bulk Temperature as a function of Streamwise position and
%time.

%Needed Constants
% T_init = 23.1378+273.15;
% T_max = T_init + 33.1224;

%From Curve-Fits
% A = -0.006060;
% B = -0.2795;
%
% theta = ((A*(-i*R+L)) + 1)*(1 - exp(B*t));
% output = (theta*(T_max-T_init)) + T_init;

T_init = 23.14677 + 273.15;
T_max = 60.7288967 + 273.15;
A = -0.00739740588;
B = -0.502996778;

output = (((A*(-i*R+L)) + 1)*(1 - exp(B*t))*(T_max-T_init)) +
T_init;
end

```

## C.6. Superposition Summation Function



```

function [ output ] = SPfun( t_max , h, RT , L , i )
%UNTITLED Summary of this function goes here
% Detailed explanation goes here

%Acrylic Properties
rho_a = 1190 ; % kg/m^3
cp_a = 1440; % J/kg/K
k_a = 0.184; % W/m/K
alpha_a = k_a/(rho_a*cp_a); %m^2/s

%Split the total time calculation into a 1:2 block
t_split = t_max / 3;

%if the first block is too small, split the time into a 1:1 block
if t_split < 5
    t_slit = t_max / 2;
end

tres = 100; % total number of time steps

% cr (ratio, value between 0 and 1)
% factor to determine how much of the calculation to spend in the
shorter time step
% use relatively high cr to have a higher resolution at earlier times

cr=0.75;
tres1 = tres*cr; %resolution in first part
tres2 = tres*cr; %resolution in second second

N1 = t_split * tres1; %num steps in first part
N2 = (t_max - t_split) * tres2; %num steps in second second

Tw = 0; %initialize wall temperature

%loop to calculate increase in wall temperature for first part
for n = 1:N1
    Tau = n/tres1;
    delT(n) = T_bulk_SP(RT, L , i ,Tau)-T_bulk_SP(RT , L , i,Tau -
1/tres1);
    Theta(n) = (1-exp(h^2*alpha_a*(t_max-
Tau)/k_a^2)*erfc(h*sqrt(alpha_a*(t_max-Tau))/k_a))*delT(n);
    Tw = Tw + Theta(n);
end

%loop to calculate increase in wall temperature for second part
for n = 1:N2
    Tau = n/tres2 + t_split;
    delT(n) = T_bulk_SP(RT, L , i ,Tau)-T_bulk_SP(RT , L , i,Tau -
1/tres2);
    Theta(n) = (1-exp(h^2*alpha_a*(t_max-
Tau)/k_a^2)*erfc(h*sqrt(alpha_a*(t_max-Tau))/k_a))*delT(n);
    Tw = Tw + Theta(n);
end

% clear rho_a cp_a k_a alpha_a;

```

```
output = Tw;  
end
```

## C.7. Image Display Function

```

function imagemenu(handle)
%IMAGEMENU adds a context menu to change image properties
%   IMAGEMENU(handle) creates a context menu for all images with the
parent
%   handle that allows image properties to be easily changed.
%   IMAGEMENU, without any input arguments, will create this context
menu
%   for all images that are found in the current figure.
%   This allows users to easily change image properties, and is
especially
%   useful for compiled programs, as users do not have access to
MATLAB's
%   property editor.
%
%
%   Example:
%   -----
%   imagesc(peaks)
%   axis image
%   imagemenu

if margin == 0
    % Use all images in current figure as default
    handle = gcf;
end

handle = findobj(handle, 'type', 'image');

% Define the context menu
cmenu = uicontextmenu;

% Define the context menu items
colormapmenu = uimenu(cmenu, 'Label', 'Colormap');
uimenu(cmenu, 'Label', 'Reverse current colormap', 'Callback',
'colormap(flipud(colormap))');
uimenu(cmenu, 'Label', 'Toggle colorbar', 'Callback', @togglecolorbar);
if exist('pixval.m')
    % Only show this to those who have it installed...
    uimenu(cmenu, 'Label', 'Toggle pixel values', 'Callback',
'pixval');
end
uimenu(cmenu, 'Label', 'Colormap length...', 'Callback',
@colormaplength);
uimenu(cmenu, 'Label', '3D plot...', 'Callback', @call3d);
uimenu(cmenu, 'Label', 'Image limits...', 'Callback', @imagelimits);
uimenu(cmenu, 'Label', 'Title...', 'Callback', @titlecallback);
uimenu(cmenu, 'Label', 'X-axis label...', 'Callback', @xaxiscallback);
uimenu(cmenu, 'Label', 'Y-axis label...', 'Callback', @yaxiscallback);

% Define colormap choices
uimenu(colormapmenu, 'Label', 'Jet', 'Callback', 'colormap(jet)');
uimenu(colormapmenu, 'Label', 'Gray', 'Callback', 'colormap(gray)');
uimenu(colormapmenu, 'Label', 'Hot', 'Callback', 'colormap(hot)');
uimenu(colormapmenu, 'Label', 'Bone', 'Callback', 'colormap(bone)');
uimenu(colormapmenu, 'Label', 'Cool', 'Callback', 'colormap(cool)');
uimenu(colormapmenu, 'Label', 'Color cube', 'Callback',
'colormap(colorcube)');

```

```

uimenu(colormapmenu, 'Label', 'HSV', 'Callback', 'colormap(hsv)');
uimenu(colormapmenu, 'Label', 'Prism', 'Callback', 'colormap(prism)');
uimenu(colormapmenu, 'Label', 'Spring', 'Callback',
'colormap(spring)');
uimenu(colormapmenu, 'Label', 'Summer', 'Callback',
'colormap(summer)');
uimenu(colormapmenu, 'Label', 'Winter', 'Callback',
'colormap(winter)');

% And apply menu to handle(s)
set(handle, 'uicontextmenu', cmenu);

% Menu callback
function togglecolorbar(obj, eventdata)
% Do we have a colorbar now?
phch =
get(findall(gcf, 'type', 'image', 'tag', 'TMW_COLORBAR'), {'parent'});
for i=1:length(phch)
    phud = get(phch{i}, 'userdata');
    if isfield(phud, 'PlotHandle')
        if isequal(gca, phud.PlotHandle)
            delete(phch{i})
            axis image
            return
        end
    end
end

% Nope
colorbar
axis image

% Menu callback
function colormaplength(obj, eventdata)
cmap = colormap;
oldlength = length(cmap);
clength = cellstr(num2str(oldlength));
new = inputdlg({'Enter new colormap length:'}, ...
'New colormap length', 1, clength);
newlength = str2double(new{1});
oldsteps = linspace(0, 1, oldlength);
newsteps = linspace(0, 1, newlength);
newmap = zeros(newlength, 3);

for i=1:3
    % Interpolate over RGB spaces of colormap
    newmap(:,i) = min(max(interp1(oldsteps, cmap(:,i), newsteps)', 0),
1);
end
colormap(newmap);
% And update the colorbar, if one exists
phch =
get(findall(gcf, 'type', 'image', 'tag', 'TMW_COLORBAR'), {'parent'});
for i=1:length(phch)
    phud = get(phch{i}, 'userdata');
    if isfield(phud, 'PlotHandle')

```

```

        if isequal(gca, phud.PlotHandle)
            colorbar
        end
    end
end

% Menu callback
function imagelimits(obj, eventdata)
lims = get(gca, 'CLim');
oldlower = num2str(lims(1));
oldupper = num2str(lims(2));
new = inputdlg({'Enter new lower limit:', 'Enter new upper limit:'},
    ...
    'New image limits', 1, {oldlower, oldupper});
if ~isnan(str2double(new{1})) & ~isnan(str2double(new{2}))
    set(gca, 'CLim', [str2double(new{1}) str2double(new{2})]);
end

% And update the colorbar, if one exists
phch =
get(findall(gcf, 'type', 'image', 'tag', 'TMW_COLORBAR'), {'parent'});
for i=1:length(phch)
    phud = get(phch{i}, 'userdata');
    if isfield(phud, 'PlotHandle')
        if isequal(gca, phud.PlotHandle)
            colorbar
        end
    end
end

% Menu callback
function titlecallback(obj, eventdata)
old = get(gca, 'title');
oldstring = get(old, 'string');
if ischar(oldstring)
    oldstring = cellstr(oldstring);
end
new = inputdlg('Enter new title:', 'New image title', 1, oldstring);
set(old, 'string', new);

% Menu callback
function xaxiscallback(obj, eventdata)
old = get(gca, 'xlabel');
oldstring = get(old, 'string');
if ischar(oldstring)
    oldstring = cellstr(oldstring);
end
new = inputdlg('Enter new X-axis label:', 'New image X-axis label', 1,
oldstring);
set(old, 'string', new);

% Menu callback
function yaxiscallback(obj, eventdata)
old = get(gca, 'ylabel');
oldstring = get(old, 'string');
if ischar(oldstring)

```

```

    oldstring = cellstr(oldstring);
end
new = inputdlg('Enter new Y-axis label:', 'New image Y-axis label', 1,
oldstring);
set(old, 'string', new);

% Menu callback
function call3d(obj, eventdata)
ax = gca;
temp = double(get(gca, 'CData'));

newfig = figure;
newax = axes;
if isempty(get(get(ax, 'Parent'), 'Name'))
    set(newfig, 'Name', '3D view');
else
    set(newfig, 'Name', [get(get(ax, 'Parent'), 'Name') ', 3D view']);
end
s = surf(temp, 'LineStyle', 'none');
hl = camlight;
xlabel('X distance [pixels]');
ylabel('Y distance [pixels]');
axis('tight');

```

## C.8. Spanwise and Streamwise Averaging Code



```

%-----%
% TRANSIENT STRAIGHT DUCT PROJECT
% Processing Step 5 (Final)
% Spanwise and Streamwise Averaging Nusselt Number

% CARSON SLABAUGH
% M.S. M.E. Thesis and Open Publication Project
% 05/01/2010
%-----%

```

```

clc;
close all;

```

```

[Ty Tx] = size(T_Nu);
[Sy Sx] = size(S_Nu);
[By Bx] = size(B_Nu);

```

```

%Span-wise Average

```

```

%Top
T_spn_avg = zeros(Tx-2,1);
for i = 2:Tx-1
    for j = 2:Ty-1
        T_spn_avg(i-1) = T_spn_avg(i-1) + T_Nu(j,i)/(Ty-2);
    end
end

```

```

%Side
S_spn_avg = zeros(Sx-2,1);
for i = 2:Sx-1
    for j = 2:Sy-1
        S_spn_avg(i-1) = S_spn_avg(i-1) + S_Nu(j,i)/(Sy-2);
    end
end

```

```

%Bottom
B_spn_avg = zeros(Bx-2,1);
for i = 2:Bx-1
    for j = 2:By-1
        B_spn_avg(i-1) = B_spn_avg(i-1) + B_Nu(j,i)/(By-2);
    end
end

```

```

%Stream-wise Average

```

```

%Top
T_strm_avg = zeros(Ty-2,1);
for i = 2:Ty-1
    for j = 2:Tx-1
        T_strm_avg(i-1) = T_strm_avg(i-1) + T_Nu(i,j)/(Tx-2);
    end
end

```

```

    end
end

% Side
S_strm_avg = zeros(Sy-2,1);
for i = 2:Sy-1
    for j = 2:Sx-1
        S_strm_avg(i-1) = S_strm_avg(i-1) + S_Nu(i,j)/(Sx-2);
    end
end

% Bottom
B_strm_avg = zeros(By-2,1);
for i = 2:By-1
    for j = 2:Bx-1
        B_strm_avg(i-1) = B_strm_avg(i-1) + B_Nu(i,j)/(Bx-2);
    end
end

fd_start = Tx-500;
fd_end = 1;

% Span-wise Stream-wise Average

%Top
T_spn_strm_avg = 15;
for i = fd_end:fd_start
    T_spn_strm_avg = T_spn_strm_avg + T_spn_avg(i)/(fd_start-fd_end+1);
end

%Side
S_spn_strm_avg = 15;
for i = fd_end:fd_start
    S_spn_strm_avg = S_spn_strm_avg + S_spn_avg(i)/(fd_start-fd_end+1);
end

%Bottom
B_spn_strm_avg = 15;
for i = fd_end:fd_start
    B_spn_strm_avg = B_spn_strm_avg + B_spn_avg(i)/(fd_start-fd_end+1);
end

%Plot Span-wise Averaged Data
figure;
plot(T_spn_avg);
figure;
plot(T_strm_avg);
figure;

```

```
plot(S_spn_avg);  
figure;  
plot(S_strm_avg);  
figure;  
plot(B_spn_avg);  
figure;  
plot(B_strm_avg);
```

```
T_spn_strm_avg  
S_spn_strm_avg
```

```
%clear T_spn_avg T_strm_avg T_spn_strm_avg;
```

## C.9. Flipping Code

```

%-----%
% TRANSIENT STRAIGHT DUCT PROJECT
%   Processing Step 5
%   Flipping Solution in Streamwise Direction

% CARSON SLABAUGH
% M.S. M.E. Thesis and Open Publication Project
% 05/16/2010
%-----%

clc;
close all;

%Inputs Required:
%   Heat Transfer Coefficient Matrices <-- Top, Side, and Bottom

% Code Stuff

%FIND SIZES OF INPUT ARRAYS
[Ty Tx] = size(h_T);
[Sy Sx] = size(h_S);
[By Bx] = size(h_B);

%Flipping Semi-Infinite Matrices
%Top
for i = 1:Tx
    for j = 1:Ty
        T_h_flip(j,i) = T_h(j,Tx+1-i);
    end
end

%Side
for i = 1:Sx
    for j = 1:Sy
        S_h_flip(j,i) = S_h(j,Sx+1-i);
    end
end

%Bottom
for i = 1:Bx
    for j = 1:By
        B_h_flip(j,i) = B_h(j,Bx+1-i);
    end
end

%Flipping Super-Position Matrices
%Top
for i = 1:Tx
    for j = 1:Ty
        h_T_flip(j,i) = h_T(j,Tx+1-i);
    end
end

```

```
%Side
for i = 1:Sx
    for j = 1:Sy
        h_S_flip(j,i) = h_S(j,Sx+1-i);
    end
end

%Bottom
for i = 1:Bx
    for j = 1:By
        h_B_flip(j,i) = h_B(j,Bx+1-i);
    end
end
```

## APPENDIX D: JOURNAL FILES

## D.1. Double Dimple Meshing Journal



```

/ Journal File for GAMBIT 2.3.16, Database 2.3.14, ntx86 SP2006032921
/ Identifier "default_id2728"
/ File opened for write Fri Dec 11 15:09:46 2009.
/ Journal File for GAMBIT 2.3.16, Database 2.3.14, ntx86 SP2006032921
/ Identifier "default_id3388"
/ File opened for write Fri Dec 11 14:22:53 2009.
window modify shade
default set "GRAPHICS.GENERAL.CONNECTIVITY_BASED_COLORING" numeric
1
default set "GRAPHICS.GENERAL.CONNECTIVITY_BASED_COLORING" numeric
0

/ EVERYTHING IN mm

/ Input Parameters
/ Dimple Radius, Height Offset, Spanwise Half-Pitch, Streamwise Pitch (Dimple to
Dimple)
$dr = 12.12
$h_d = 6.92
$d = $dr - $h_d
$D = 2*sqrt(($dr^2)-($h_d^2))
$dd = 7.78
$stw = 26.88
$spw = 19.05

/ Inner-Box Parameters
$dbox_str = 0.2*$D
$dbox_spn = 0.5*$D
$dbox_dep = 0.3*$d

/ Outer-Box Parameters
$strboff = 0.6
$spnboff = 0.6

/ Other Needed Parameters
$space = $stw-$dd-(2*$dr)
$stw_off = 0.5*$space
$end_offs = 0.5*(-$space)
$num_dimp = 4

/ Channel Parameters
/ Aspect Ratio (w/h), Height, Width, Length
$AR = 2
$ch_h = 25.4
$ch_w = $AR*$ch_h
$ch_l = ($num_dimp)*$stw + (2*$end_offs)

```

\$chsplit = 0.5

/ MESHING PARAMETERS

/ BOUNDARY LAYERS

/ DIMPLES

\$blds\_dimp = 0.0142

\$blgrow\_dimp = 1.2

  \$b11\_dimp = \$blds\_dimp

  \$b12\_dimp = \$blgrow\_dimp\*\$b11\_dimp

  \$b13\_dimp = \$blgrow\_dimp\*\$b12\_dimp

  \$b14\_dimp = \$blgrow\_dimp\*\$b13\_dimp

  \$b15\_dimp = \$blgrow\_dimp\*\$b14\_dimp

  \$bltotal\_dimp = \$b11\_dimp + \$b12\_dimp + \$b13\_dimp + \$b14\_dimp + \$b15\_dimp

\$blrows\_dimp = 5

\$bltrans\_dimp = 1

\$blthrows\_dimp = 0

/ CHANNEL

/ Bottom

\$blds\_chbot = 0.0142

\$blgrow\_chbot = 1.2

  \$b11\_chbot = \$blds\_chbot

  \$b12\_chbot = \$blgrow\_chbot\*\$b11\_chbot

  \$b13\_chbot = \$blgrow\_chbot\*\$b12\_chbot

  \$b14\_chbot = \$blgrow\_chbot\*\$b13\_chbot

  \$b15\_chbot = \$blgrow\_chbot\*\$b14\_chbot

  \$bltotal\_chbot = \$b11\_chbot + \$b12\_chbot + \$b13\_chbot + \$b14\_chbot + \$b15\_chbot

\$blrows\_chbot = 5

\$bltrans\_chbot = 1

\$blthrows\_chbot = 0

/ Side

\$blds\_chsid = 0.0142

\$blgrow\_chsid = 1.2

  \$b11\_chsid = \$blds\_chsid

  \$b12\_chsid = \$blgrow\_chsid\*\$b11\_chsid

  \$b13\_chsid = \$blgrow\_chsid\*\$b12\_chsid

  \$b14\_chsid = \$blgrow\_chsid\*\$b13\_chsid

  \$b15\_chsid = \$blgrow\_chsid\*\$b14\_chsid

  \$bltotal\_chsid = \$b11\_chsid + \$b12\_chsid + \$b13\_chsid + \$b14\_chsid + \$b15\_chsid

\$blrows\_chsid = 5

\$bltrans\_chsid = 1

\$blthrows\_chsid = 0

```

/ Top
$blds_chnop = 0.0142
$blgrow_chnop = 1.2
  $bl1_chnop = $blds_chnop
  $bl2_chnop = $blgrow_chnop*$bl1_chnop
  $bl3_chnop = $blgrow_chnop*$bl2_chnop
  $bl4_chnop = $blgrow_chnop*$bl3_chnop
  $bl5_chnop = $blgrow_chnop*$bl4_chnop
  $bltotal_chnop = $bl1_chnop + $bl2_chnop + $bl3_chnop + $bl4_chnop + $bl5_chnop
$blrows_chnop = 5
$bltrans_chnop = 1
$bltrows_chnop = 0

```

```

/ TRANSITIONS FROM DIMPLES

```

```

$transds_in = 0.0142
$transgrow_in = 1.2
  $bl1_in = $transds_in
  $bl2_in = $transgrow_in*$bl1_in
  $bl3_in = $transgrow_in*$bl2_in
  $bl4_in = $transgrow_in*$bl3_in
  $bl5_in = $transgrow_in*$bl4_in
  $stranstotal_in = $bl1_in + $bl2_in + $bl3_in + $bl4_in + $bl5_in
$transrows_in = 5
$transtrans_in = 1
$transtrows_in = 0

```

```

$transds_sid = 0.0142
$transgrow_sid = 1.8
  $bl1_sid = $transds_sid
  $bl2_sid = $transgrow_sid*$bl1_sid
  $bl3_sid = $transgrow_sid*$bl2_sid
  $bl4_sid = $transgrow_sid*$bl3_sid
  $bl5_sid = $transgrow_sid*$bl4_sid
  $stranstotal_sid = $bl1_sid + $bl2_sid + $bl3_sid + $bl4_sid + $bl5_sid
$transrows_sid = 5
$transtrans_sid = 1
$transtrows_sid = 0

```

```

/ EDGE MESHING

```

```

/ DIMPLES

```

```

$growrate_dimp_rad = 0.95
$edgenum_dimp_rad = 20 + $blrows_dimp
$growrate_dimp_theta = 1
$edgenum_dimp_theta = 30
$growrate_dimp_span = 1
$edgenum_dimp_span = 40

```

```

$growrate_dimp_strm = 1
$edgenum_dimp_strm = 45
$growrate_dimpbox = 1
$edgenum_dimpbox = 15 + $transrows_in

/ CHANNEL
/ Streamwise-Normal
$grow_ch_strm_short_bell = 0.85
$edgenum_ch_strm_short = $transrows_sid + $blrows_chsid + 25
$grow_ch_strm_med_bell = 0.6
$edgenum_ch_strm_med = $edgenum_dimp_strm
$grow_ch_strm_long1 = 1.1
$grow_ch_strm_long2 = 1.1
$edgenum_ch_strm_long = $edgenum_ch_strm_short + $edgenum_dimp_strm

/ Spanwise-Normal
$grow_ch_span_connect_bell = 0.8
$edgenum_ch_span_connect = 20 + (2*$blrows_chsid)
$grow_ch_span_ie = 1.15
$edgenum_ch_span_S = $transrows_sid + 20
$grow_ch_span_out = 0.95
$edgenum_ch_span_out = $edgenum_ch_span_connect

/ Channel Height
$Y = 50
$grow_ch_hght_bell = 0.75
$edgenum_ch_hght = $blrows_chbot + $blrows_chttop + $Y

/ HERE IT GOES. HERE IT GOES.

/ Channel Volume Creation
volume create "Channel" width $ch_w depth $ch_h height $ch_l offset 0 (0.5*$ch_h) (-
0.5*$ch_l) brick

/ Dimple Creation and Placement
volume create "Dimple_1u" radius $dr sphere
volume move "Dimple_1u" offset (0.5*$spw) $h_d -((0*$stw) + $dr + $stw_off +
$end_offs)
volume create "Dimple_1d" radius $dr sphere
volume move "Dimple_1d" offset (0.5*$spw) $h_d -((0*$stw) + $dr + $stw_off +
$end_offs + $dd)

volume create "Dimple_2u" radius $dr sphere

```

volume move "Dimple\_2u" offset  $-(0.5*\$spw)$   $\$h\_d$   $-((1*\$stw) + \$dr + \$stw\_off + \$end\_offs)$

volume create "Dimple\_2d" radius  $\$dr$  sphere

volume move "Dimple\_2d" offset  $-(0.5*\$spw)$   $\$h\_d$   $-((1*\$stw) + \$dr + \$stw\_off + \$end\_offs + \$dd)$

volume create "Dimple\_3u" radius  $\$dr$  sphere

volume move "Dimple\_3u" offset  $(0.5*\$spw)$   $\$h\_d$   $-((2*\$stw) + \$dr + \$stw\_off + \$end\_offs)$

volume create "Dimple\_3d" radius  $\$dr$  sphere

volume move "Dimple\_3d" offset  $(0.5*\$spw)$   $\$h\_d$   $-((2*\$stw) + \$dr + \$stw\_off + \$end\_offs + \$dd)$

volume create "Dimple\_4u" radius  $\$dr$  sphere

volume move "Dimple\_4u" offset  $-(0.5*\$spw)$   $\$h\_d$   $-((3*\$stw) + \$dr + \$stw\_off + \$end\_offs)$

volume create "Dimple\_4d" radius  $\$dr$  sphere

volume move "Dimple\_4d" offset  $-(0.5*\$spw)$   $\$h\_d$   $-((3*\$stw) + \$dr + \$stw\_off + \$end\_offs + \$dd)$

/ Unite Individual Dimple and Channel Volumes

volume unite volumes "Channel" "Dimple\_1u"

volume unite volumes "Channel" "Dimple\_1d"

volume unite volumes "Channel" "Dimple\_2u"

volume unite volumes "Channel" "Dimple\_2d"

volume unite volumes "Channel" "Dimple\_3u"

volume unite volumes "Channel" "Dimple\_3d"

volume unite volumes "Channel" "Dimple\_4u"

volume unite volumes "Channel" "Dimple\_4d"

/ Make Inner Box

vertex create coordinates  $((0.5*\$spw)+(0.5*\$dbox\_spn))$  0 -  
 $((0*\$stw)+\$stw\_off+\$dr+\$end\_offs)-(\$dbox\_str)$

vertex create coordinates  $((0.5*\$spw)-(0.5*\$dbox\_spn))$  0 -  
 $((0*\$stw)+\$stw\_off+\$dr+\$end\_offs)-(\$dbox\_str)$

vertex create coordinates  $((0.5*\$spw)+(0.5*\$dbox\_spn))$  0 -  
 $((0*\$stw)+\$stw\_off+\$dr+\$end\_offs)+\$dd+(\$dbox\_str)$

vertex create coordinates  $((0.5*\$spw)-(0.5*\$dbox\_spn))$  0 -  
 $((0*\$stw)+\$stw\_off+\$dr+\$end\_offs)+\$dd+(\$dbox\_str)$

vertex create coordinates  $-((0.5*\$spw)+(0.5*\$dbox\_spn))$  0 -  
 $((1*\$stw)+\$stw\_off+\$dr+\$end\_offs)-(\$dbox\_str)$

vertex create coordinates  $-((0.5*\$spw)-(0.5*\$dbox\_spn))$  0 -  
 $((1*\$stw)+\$stw\_off+\$dr+\$end\_offs)-(\$dbox\_str)$

vertex create coordinates  $-((0.5*\$spw)+(0.5*\$dbox\_spn))$  0 -  
 $((1*\$stw)+\$stw\_off+\$dr+\$end\_offs)+\$dd+(\$dbox\_str)$

vertex	create	coordinates	$-((0.5*\$spw)-(0.5*\$dbox\_spn))$	0	-
			$((1*\$stw)+\$stw\_off+\$dr+\$end\_offs)+\$dd+(\$dbox\_str)$		
vertex	create	coordinates	$((0.5*\$spw)+(0.5*\$dbox\_spn))$	0	-
			$((2*\$stw)+\$stw\_off+\$dr+\$end\_offs)-(\$dbox\_str)$		
vertex	create	coordinates	$((0.5*\$spw)-(0.5*\$dbox\_spn))$	0	-
			$((2*\$stw)+\$stw\_off+\$dr+\$end\_offs)-(\$dbox\_str)$		
vertex	create	coordinates	$((0.5*\$spw)+(0.5*\$dbox\_spn))$	0	-
			$((2*\$stw)+\$stw\_off+\$dr+\$end\_offs)+\$dd+(\$dbox\_str)$		
vertex	create	coordinates	$((0.5*\$spw)-(0.5*\$dbox\_spn))$	0	-
			$((2*\$stw)+\$stw\_off+\$dr+\$end\_offs)+\$dd+(\$dbox\_str)$		
vertex	create	coordinates	$-((0.5*\$spw)+(0.5*\$dbox\_spn))$	0	-
			$((3*\$stw)+\$stw\_off+\$dr+\$end\_offs)-(\$dbox\_str)$		
vertex	create	coordinates	$-((0.5*\$spw)-(0.5*\$dbox\_spn))$	0	-
			$((3*\$stw)+\$stw\_off+\$dr+\$end\_offs)-(\$dbox\_str)$		
vertex	create	coordinates	$-((0.5*\$spw)+(0.5*\$dbox\_spn))$	0	-
			$((3*\$stw)+\$stw\_off+\$dr+\$end\_offs)+\$dd+(\$dbox\_str)$		
vertex	create	coordinates	$-((0.5*\$spw)-(0.5*\$dbox\_spn))$	0	-
			$((3*\$stw)+\$stw\_off+\$dr+\$end\_offs)+\$dd+(\$dbox\_str)$		
vertex	create	coordinates	$((0.5*\$spw)+(0.5*\$dbox\_spn))$	$-\$dbox\_dep$	-
			$((0*\$stw)+\$stw\_off+\$dr+\$end\_offs)-(\$dbox\_str)$		
vertex	create	coordinates	$((0.5*\$spw)-(0.5*\$dbox\_spn))$	$-\$dbox\_dep$	-
			$((0*\$stw)+\$stw\_off+\$dr+\$end\_offs)-(\$dbox\_str)$		
vertex	create	coordinates	$((0.5*\$spw)+(0.5*\$dbox\_spn))$	$-\$dbox\_dep$	-
			$((0*\$stw)+\$stw\_off+\$dr+\$end\_offs)+\$dd+(\$dbox\_str)$		
vertex	create	coordinates	$((0.5*\$spw)-(0.5*\$dbox\_spn))$	$-\$dbox\_dep$	-
			$((0*\$stw)+\$stw\_off+\$dr+\$end\_offs)+\$dd+(\$dbox\_str)$		
vertex	create	coordinates	$-((0.5*\$spw)+(0.5*\$dbox\_spn))$	$-\$dbox\_dep$	-
			$((1*\$stw)+\$stw\_off+\$dr+\$end\_offs)-(\$dbox\_str)$		
vertex	create	coordinates	$-((0.5*\$spw)-(0.5*\$dbox\_spn))$	$-\$dbox\_dep$	-
			$((1*\$stw)+\$stw\_off+\$dr+\$end\_offs)-(\$dbox\_str)$		
vertex	create	coordinates	$-((0.5*\$spw)+(0.5*\$dbox\_spn))$	$-\$dbox\_dep$	-
			$((1*\$stw)+\$stw\_off+\$dr+\$end\_offs)+\$dd+(\$dbox\_str)$		
vertex	create	coordinates	$-((0.5*\$spw)-(0.5*\$dbox\_spn))$	$-\$dbox\_dep$	-
			$((1*\$stw)+\$stw\_off+\$dr+\$end\_offs)+\$dd+(\$dbox\_str)$		
vertex	create	coordinates	$((0.5*\$spw)+(0.5*\$dbox\_spn))$	$-\$dbox\_dep$	-
			$((2*\$stw)+\$stw\_off+\$dr+\$end\_offs)-(\$dbox\_str)$		
vertex	create	coordinates	$((0.5*\$spw)-(0.5*\$dbox\_spn))$	$-\$dbox\_dep$	-
			$((2*\$stw)+\$stw\_off+\$dr+\$end\_offs)-(\$dbox\_str)$		
vertex	create	coordinates	$((0.5*\$spw)+(0.5*\$dbox\_spn))$	$-\$dbox\_dep$	-
			$((2*\$stw)+\$stw\_off+\$dr+\$end\_offs)+\$dd+(\$dbox\_str)$		

```

vertex create coordinates ((0.5*$spw)-(0.5*$dbox_spn)) -$dbox_dep -
(((2*$stw)+$stw_off+$dr+$end_offs)+$dd+($dbox_str))

vertex create coordinates -((0.5*$spw)+(0.5*$dbox_spn)) -$dbox_dep -
(((3*$stw)+$stw_off+$dr+$end_offs)-($dbox_str))
vertex create coordinates -((0.5*$spw)-(0.5*$dbox_spn)) -$dbox_dep -
(((3*$stw)+$stw_off+$dr+$end_offs)-($dbox_str))
vertex create coordinates -((0.5*$spw)+(0.5*$dbox_spn)) -$dbox_dep -
(((3*$stw)+$stw_off+$dr+$end_offs)+$dd+($dbox_str))
vertex create coordinates -((0.5*$spw)-(0.5*$dbox_spn)) -$dbox_dep -
(((3*$stw)+$stw_off+$dr+$end_offs)+$dd+($dbox_str))

```

/ Project Vertices to Outer-Rim

```

vertex create project "vertex.22" "vertex.21" edge "edge.16" splitedge
vertex create project "vertex.24" "vertex.23" edge "edge.14" splitedge
vertex create project "vertex.25" "vertex.26" edge "edge.20" splitedge
vertex create project "vertex.28" "vertex.27" edge "edge.18" splitedge
vertex create project "vertex.29" "vertex.30" edge "edge.24" splitedge
vertex create project "vertex.31" "vertex.32" edge "edge.22" splitedge
vertex create project "vertex.33" "vertex.34" edge "edge.28" splitedge
vertex create project "vertex.35" "vertex.36" edge "edge.26" splitedge

```

/ Edge Generation - Break up the Dimples

```

edge create straight "vertex.24" "vertex.23"
edge create straight "vertex.40" "vertex.39"
edge create straight "vertex.39" "vertex.37" "vertex.38" "vertex.40"
edge create straight "vertex.23" "vertex.21" "vertex.22" "vertex.24"
edge create straight "vertex.24" "vertex.40"
edge create straight "vertex.23" "vertex.39"
edge create straight "vertex.21" "vertex.37"
edge create straight "vertex.22" "vertex.38"
edge create straight "vertex.23" "vertex.56"
edge create straight "vertex.21" "vertex.54"
edge create straight "vertex.22" "vertex.53"
edge create straight "vertex.24" "vertex.55"
edge create straight "vertex.27" "vertex.28"
edge create straight "vertex.43" "vertex.44"
edge create straight "vertex.44" "vertex.42" "vertex.41" "vertex.43"
edge create straight "vertex.28" "vertex.26" "vertex.25" "vertex.27"
edge create straight "vertex.28" "vertex.44"
edge create straight "vertex.26" "vertex.42"
edge create straight "vertex.25" "vertex.41"
edge create straight "vertex.27" "vertex.43"
edge create straight "vertex.28" "vertex.59"
edge create straight "vertex.26" "vertex.58"
edge create straight "vertex.25" "vertex.57"

```

edge create straight "vertex.27" "vertex.60"  
edge create straight "vertex.32" "vertex.31"  
edge create straight "vertex.48" "vertex.47"  
edge create straight "vertex.47" "vertex.45" "vertex.46" "vertex.48"  
edge create straight "vertex.31" "vertex.29" "vertex.30" "vertex.32"  
edge create straight "vertex.32" "vertex.48"  
edge create straight "vertex.31" "vertex.47"  
edge create straight "vertex.29" "vertex.45"  
edge create straight "vertex.30" "vertex.46"  
edge create straight "vertex.31" "vertex.63"  
edge create straight "vertex.29" "vertex.61"  
edge create straight "vertex.30" "vertex.62"  
edge create straight "vertex.32" "vertex.64"  
edge create straight "vertex.35" "vertex.36"  
edge create straight "vertex.51" "vertex.52"  
edge create straight "vertex.36" "vertex.34" "vertex.33" "vertex.35"  
edge create straight "vertex.52" "vertex.50" "vertex.49" "vertex.51"  
edge create straight "vertex.36" "vertex.52"  
edge create straight "vertex.34" "vertex.50"  
edge create straight "vertex.33" "vertex.49"  
edge create straight "vertex.35" "vertex.51"  
edge create straight "vertex.36" "vertex.68"  
edge create straight "vertex.34" "vertex.66"  
edge create straight "vertex.33" "vertex.65"  
edge create straight "vertex.35" "vertex.67"

/ divide up dimples

edge create straight "vertex.10" "vertex.11"  
edge create straight "vertex.13" "vertex.14"  
edge create straight "vertex.16" "vertex.17"  
edge create straight "vertex.19" "vertex.20"  
vertex create edgeints "edge.109" "edge.52" real  
vertex create edgeints "edge.109" "edge.50" real  
vertex create edgeints "edge.110" "edge.68" real  
vertex create edgeints "edge.110" "edge.66" real  
vertex create edgeints "edge.111" "edge.84" real  
vertex create edgeints "edge.111" "edge.82" real  
vertex create edgeints "edge.112" "edge.97" real  
vertex create edgeints "edge.112" "edge.95" real

vertex create project "vertex.70" edge "edge.47" splitedge  
vertex create project "vertex.69" edge "edge.49" splitedge  
vertex create project "vertex.72" edge "edge.63" splitedge  
vertex create project "vertex.71" edge "edge.65" splitedge  
vertex create project "vertex.73" edge "edge.81" splitedge



vertex create project "vertex.74" edge "edge.79" splitedge  
vertex create project "vertex.76" edge "edge.98" splitedge  
vertex create project "vertex.75" edge "edge.100" splitedge  
vertex create project "vertex.77" "vertex.78" edge "edge.15" splitedge  
vertex create project "vertex.79" "vertex.80" edge "edge.19" splitedge  
vertex create project "vertex.81" "vertex.82" edge "edge.23" splitedge  
vertex create project "vertex.83" "vertex.84" edge "edge.27" splitedge

edge split "edge.97" vertex "vertex.75" connected  
edge split "edge.95" vertex "vertex.76" connected  
edge split "edge.84" vertex "vertex.73" connected  
edge split "edge.82" vertex "vertex.74" connected  
edge split "edge.68" vertex "vertex.71" connected  
edge split "edge.66" vertex "vertex.72" connected  
edge split "edge.52" vertex "vertex.69" connected  
edge split "edge.50" vertex "vertex.70" connected  
edge split "edge.109" vertex "vertex.69" connected  
edge split "edge.137" vertex "vertex.70" connected  
edge split "edge.110" vertex "vertex.72" connected  
edge split "edge.110" vertex "vertex.71" connected  
edge split "edge.111" vertex "vertex.74" connected  
edge split "edge.111" vertex "vertex.73" connected  
edge split "edge.112" vertex "vertex.76" connected  
edge split "edge.112" vertex "vertex.75" connected

edge create project "edge.114" "edge.46" "edge.47" face "face.16" splitface  
edge create project "edge.113" "edge.48" "edge.49" face "face.7" splitface  
edge create project "edge.116" "edge.62" "edge.63" face "face.18" splitface  
edge create project "edge.115" "edge.64" "edge.65" face "face.17" splitface  
edge create project "edge.117" "edge.78" "edge.79" face "face.21" splitface  
edge create project "edge.81" "edge.80" "edge.118" face "face.20" splitface  
edge create project "edge.120" "edge.94" "edge.98" face "face.24" splitface  
edge create project "edge.100" "edge.99" "edge.119" face "face.23" splitface

edge create straight "vertex.39" "vertex.100" "vertex.56"  
edge create straight "vertex.70" "vertex.77" "vertex.85"  
edge create straight "vertex.37" "vertex.108" "vertex.54"  
edge create straight "vertex.38" "vertex.107" "vertex.53"  
edge create straight "vertex.69" "vertex.78" "vertex.86"  
edge create straight "vertex.40" "vertex.99" "vertex.55"  
edge create straight "vertex.78" "vertex.77"  
edge create straight "vertex.44" "vertex.116" "vertex.59"  
edge create straight "vertex.72" "vertex.79" "vertex.87"  
edge create straight "vertex.42" "vertex.124" "vertex.58"  
edge create straight "vertex.41" "vertex.123" "vertex.57"  
edge create straight "vertex.88" "vertex.80" "vertex.71"

edge create straight "vertex.43" "vertex.115" "vertex.60"  
edge create straight "vertex.80" "vertex.79"  
edge create straight "vertex.47" "vertex.132" "vertex.63"  
edge create straight "vertex.74" "vertex.82" "vertex.90"  
edge create straight "vertex.45" "vertex.140" "vertex.61"  
edge create straight "vertex.46" "vertex.139" "vertex.62"  
edge create straight "vertex.73" "vertex.81" "vertex.89"  
edge create straight "vertex.48" "vertex.131" "vertex.64"  
edge create straight "vertex.81" "vertex.82"  
edge create straight "vertex.52" "vertex.148" "vertex.68"  
edge create straight "vertex.76" "vertex.83" "vertex.91"  
edge create straight "vertex.50" "vertex.156" "vertex.66"  
edge create straight "vertex.49" "vertex.155" "vertex.65"  
edge create straight "vertex.92" "vertex.84" "vertex.75"  
edge create straight "vertex.51" "vertex.147" "vertex.67"  
edge create straight "vertex.84" "vertex.83"

edge create project "edge.204" "edge.194" face "face.16" splitface  
edge create project "edge.198" "edge.200" face "face.7" splitface  
edge create project "edge.217" "edge.207" face "face.18" splitface  
edge create project "edge.211" "edge.213" face "face.17" splitface  
edge create project "edge.230" "edge.220" face "face.21" splitface  
edge create project "edge.226" "edge.224" face "face.20" splitface  
edge create project "edge.243" "edge.233" face "face.24" splitface  
edge create project "edge.237" "edge.239" face "face.23" splitface

edge delete "edge.200" "edge.198" "edge.194" "edge.204" lowertopology  
edge delete "edge.213" "edge.211" "edge.207" "edge.217" lowertopology  
edge delete "edge.220" "edge.224" "edge.226" "edge.230" lowertopology  
edge delete "edge.243" "edge.233" "edge.237" "edge.239" lowertopology

/ Create Dimple Faces

/ Dimple 1

face create wireframe "edge.46" "edge.193" "edge.146" "edge.203" real  
face create wireframe "edge.47" "edge.193" "edge.147" "edge.196" real  
face create wireframe "edge.113" "edge.196" "edge.151" "edge.197" real  
face create wireframe "edge.48" "edge.197" "edge.152" "edge.199" real  
face create wireframe "edge.153" "edge.202" "edge.49" "edge.199" real  
face create wireframe "edge.114" "edge.202" "edge.145" "edge.203" real  
face create wireframe "edge.46" "edge.47" "edge.205" "edge.114" real  
face create wireframe "edge.205" "edge.113" "edge.48" "edge.49" real  
face create wireframe "edge.46" "edge.53" "edge.45" "edge.54" real  
face create wireframe "edge.54" "edge.47" "edge.195" "edge.50" real  
face create wireframe "edge.136" "edge.195" "edge.113" "edge.55" real  
face create wireframe "edge.51" "edge.55" "edge.48" "edge.56" real  
face create wireframe "edge.52" "edge.201" "edge.49" "edge.56" real

face create wireframe "edge.135" "edge.53" "edge.114" "edge.201" real  
 face create wireframe "edge.137" "edge.195" "edge.205" "edge.201" real  
 face create wireframe "edge.135" "edge.45" "edge.50" "edge.137" real  
 face create wireframe "edge.137" "edge.136" "edge.51" "edge.52" real  
 face create wireframe "edge.246" "edge.193" "edge.54" "edge.57" real  
 face create wireframe "edge.195" "edge.138" "edge.122" "edge.196" real  
 face create wireframe "edge.55" "edge.58" "edge.249" "edge.197" real  
 face create wireframe "edge.59" "edge.56" "edge.199" "edge.250" real  
 face create wireframe "edge.109" "edge.201" "edge.202" "edge.15" real  
 face create wireframe "edge.245" "edge.60" "edge.53" "edge.203" real  
 face create wireframe "edge.57" "edge.45" "edge.60" "edge.31" real  
 face create wireframe "edge.50" "edge.57" "edge.14" "edge.138" real  
 face create wireframe "edge.136" "edge.138" "edge.30" "edge.58" real  
 face create wireframe "edge.51" "edge.58" "edge.29" "edge.59" real  
 face create wireframe "edge.16" "edge.109" "edge.52" "edge.59" real  
 face create wireframe "edge.109" "edge.32" "edge.60" "edge.135" real  
 face create wireframe "edge.205" "edge.196" "edge.121" "edge.202" real

/ Dimple 2

face create wireframe "edge.62" "edge.206" "edge.158" "edge.216" real  
 face create wireframe "edge.63" "edge.206" "edge.159" "edge.209" real  
 face create wireframe "edge.115" "edge.209" "edge.163" "edge.210" real  
 face create wireframe "edge.64" "edge.210" "edge.164" "edge.212" real  
 face create wireframe "edge.65" "edge.212" "edge.165" "edge.214" real  
 face create wireframe "edge.216" "edge.116" "edge.214" "edge.157" real  
 face create wireframe "edge.218" "edge.209" "edge.123" "edge.214" real  
 face create wireframe "edge.61" "edge.69" "edge.62" "edge.72" real  
 face create wireframe "edge.66" "edge.69" "edge.63" "edge.208" real  
 face create wireframe "edge.134" "edge.208" "edge.115" "edge.70" real  
 face create wireframe "edge.67" "edge.70" "edge.64" "edge.71" real  
 face create wireframe "edge.68" "edge.215" "edge.65" "edge.71" real  
 face create wireframe "edge.133" "edge.72" "edge.116" "edge.215" real  
 face create wireframe "edge.140" "edge.208" "edge.218" "edge.215" real  
 face create wireframe "edge.73" "edge.254" "edge.206" "edge.69" real  
 face create wireframe "edge.208" "edge.139" "edge.124" "edge.209" real  
 face create wireframe "edge.70" "edge.74" "edge.257" "edge.210" real  
 face create wireframe "edge.75" "edge.71" "edge.212" "edge.258" real  
 face create wireframe "edge.110" "edge.215" "edge.214" "edge.19" real  
 face create wireframe "edge.76" "edge.72" "edge.216" "edge.253" real  
 face create wireframe "edge.62" "edge.63" "edge.218" "edge.116" real  
 face create wireframe "edge.218" "edge.115" "edge.64" "edge.65" real  
 face create wireframe "edge.61" "edge.66" "edge.140" "edge.133" real  
 face create wireframe "edge.140" "edge.134" "edge.67" "edge.68" real  
 face create wireframe "edge.73" "edge.61" "edge.76" "edge.35" real  
 face create wireframe "edge.73" "edge.18" "edge.139" "edge.66" real  
 face create wireframe "edge.139" "edge.34" "edge.74" "edge.134" real

face create wireframe "edge.67" "edge.74" "edge.33" "edge.75" real  
face create wireframe "edge.110" "edge.68" "edge.75" "edge.20" real  
face create wireframe "edge.36" "edge.76" "edge.133" "edge.110" real

/ Dimple 3

face create wireframe "edge.78" "edge.219" "edge.170" "edge.229" real  
face create wireframe "edge.79" "edge.219" "edge.171" "edge.222" real  
face create wireframe "edge.118" "edge.222" "edge.177" "edge.223" real  
face create wireframe "edge.80" "edge.223" "edge.176" "edge.225" real  
face create wireframe "edge.81" "edge.225" "edge.175" "edge.228" real  
face create wireframe "edge.229" "edge.117" "edge.228" "edge.169" real  
face create wireframe "edge.231" "edge.222" "edge.125" "edge.228" real  
face create wireframe "edge.78" "edge.79" "edge.231" "edge.117" real  
face create wireframe "edge.231" "edge.118" "edge.80" "edge.81" real  
face create wireframe "edge.77" "edge.86" "edge.78" "edge.85" real  
face create wireframe "edge.82" "edge.86" "edge.79" "edge.221" real  
face create wireframe "edge.132" "edge.221" "edge.118" "edge.87" real  
face create wireframe "edge.83" "edge.87" "edge.80" "edge.88" real  
face create wireframe "edge.84" "edge.88" "edge.81" "edge.227" real  
face create wireframe "edge.131" "edge.227" "edge.117" "edge.85" real  
face create wireframe "edge.131" "edge.77" "edge.82" "edge.142" real  
face create wireframe "edge.142" "edge.221" "edge.231" "edge.227" real  
face create wireframe "edge.142" "edge.132" "edge.83" "edge.84" real  
face create wireframe "edge.89" "edge.262" "edge.219" "edge.86" real  
face create wireframe "edge.141" "edge.126" "edge.222" "edge.221" real  
face create wireframe "edge.90" "edge.266" "edge.223" "edge.87" real  
face create wireframe "edge.91" "edge.88" "edge.225" "edge.265" real  
face create wireframe "edge.111" "edge.227" "edge.228" "edge.23" real  
face create wireframe "edge.92" "edge.85" "edge.229" "edge.261" real  
face create wireframe "edge.77" "edge.92" "edge.39" "edge.89" real  
face create wireframe "edge.82" "edge.89" "edge.22" "edge.141" real  
face create wireframe "edge.141" "edge.38" "edge.90" "edge.132" real  
face create wireframe "edge.83" "edge.90" "edge.37" "edge.91" real  
face create wireframe "edge.111" "edge.84" "edge.91" "edge.24" real  
face create wireframe "edge.40" "edge.92" "edge.131" "edge.111" real

/ Dimple 4

face create wireframe "edge.94" "edge.232" "edge.182" "edge.242" real  
face create wireframe "edge.98" "edge.232" "edge.183" "edge.235" real  
face create wireframe "edge.119" "edge.235" "edge.189" "edge.236" real  
face create wireframe "edge.99" "edge.236" "edge.188" "edge.238" real  
face create wireframe "edge.187" "edge.240" "edge.100" "edge.238" real  
face create wireframe "edge.181" "edge.242" "edge.120" "edge.240" real  
face create wireframe "edge.244" "edge.235" "edge.127" "edge.240" real  
face create wireframe "edge.98" "edge.244" "edge.120" "edge.94" real

face create wireframe "edge.244" "edge.119" "edge.99" "edge.100" real  
 face create wireframe "edge.144" "edge.234" "edge.244" "edge.241" real  
 face create wireframe "edge.93" "edge.101" "edge.94" "edge.104" real  
 face create wireframe "edge.95" "edge.101" "edge.98" "edge.234" real  
 face create wireframe "edge.130" "edge.234" "edge.119" "edge.102" real  
 face create wireframe "edge.96" "edge.102" "edge.99" "edge.103" real  
 face create wireframe "edge.97" "edge.103" "edge.100" "edge.241" real  
 face create wireframe "edge.129" "edge.241" "edge.120" "edge.104" real  
 face create wireframe "edge.93" "edge.95" "edge.144" "edge.129" real  
 face create wireframe "edge.144" "edge.130" "edge.96" "edge.97" real  
 face create wireframe "edge.105" "edge.270" "edge.232" "edge.101" real  
 face create wireframe "edge.143" "edge.128" "edge.235" "edge.234" real  
 face create wireframe "edge.102" "edge.106" "edge.273" "edge.236" real  
 face create wireframe "edge.107" "edge.103" "edge.238" "edge.274" real  
 face create wireframe "edge.112" "edge.241" "edge.240" "edge.27" real  
 face create wireframe "edge.108" "edge.104" "edge.242" "edge.269" real  
 face create wireframe "edge.43" "edge.105" "edge.93" "edge.108" real  
 face create wireframe "edge.105" "edge.26" "edge.143" "edge.95" real  
 face create wireframe "edge.143" "edge.42" "edge.106" "edge.130" real  
 face create wireframe "edge.96" "edge.106" "edge.41" "edge.107" real  
 face create wireframe "edge.107" "edge.28" "edge.112" "edge.97" real  
 face create wireframe "edge.112" "edge.44" "edge.108" "edge.129" real

/ Cut Out Dimple Volumes

volume split "Channel" faces "face.73" "face.74" "face.75" "face.76" \  
 "face.77" "face.78" "face.65" "face.66" connected  
 volume split "Channel" faces "face.102" "face.103" "face.105" "face.104" \  
 "face.109" "face.108" "face.107" "face.106" connected  
 volume split "Channel" faces "face.134" "face.135" "face.136" "face.137" \  
 "face.138" "face.139" "face.125" "face.127" connected  
 volume split "Channel" faces "face.156" "face.157" "face.165" "face.166" \  
 "face.167" "face.168" "face.169" "face.164" connected

/ Break Dimples

/ Volume Creation and Split

/ Dimple 1

volume create stitch "face.54" "face.79" "face.52" "face.53" "face.57" \  
 "face.27" real  
 volume create stitch "face.26" "face.50" "face.51" "face.79" "face.55" \  
 "face.56" real  
 volume create stitch "face.72" "face.16" "face.67" "face.58" "face.50" \  
 "face.73" real  
 volume create stitch "face.67" "face.35" "face.68" "face.59" "face.74" \  
 "face.51" real  
 volume create stitch "face.68" "face.37" "face.69" "face.60" "face.75" \  
 "face.51" real

"face.52" real  
volume create stitch "face.61" "face.69" "face.7" "face.70" "face.76" \  
"face.53" real  
volume create stitch "face.70" "face.62" "face.71" "face.36" "face.77" \  
"face.54" real

volume split "volume.2" faces "face.58" "face.59" "face.64" "face.63" \  
connected  
volume split "volume.2" faces "face.62" "face.61" "face.60" connected  
volume split "volume.2" volumes "volume.6" connected bidentity  
volume split "volume.2" volumes "volume.7" connected bidentity  
volume split "volume.2" volumes "volume.8" connected bidentity  
volume split "volume.2" volumes "volume.9" connected bidentity  
volume split "volume.2" volumes "volume.10" connected bidentity  
volume split "volume.2" volumes "volume.11" connected bidentity  
volume split "volume.2" volumes "volume.12" connected bidentity

/ Dimple 2

volume create stitch "face.99" "face.18" "face.94" "face.87" "face.80" \  
"face.104" real  
volume create stitch "face.94" "face.39" "face.95" "face.88" "face.105" \  
"face.81" real  
volume create stitch "face.95" "face.41" "face.96" "face.89" "face.82" \  
"face.106" real  
volume create stitch "face.90" "face.96" "face.17" "face.97" "face.107" \  
"face.83" real  
volume create stitch "face.91" "face.97" "face.40" "face.98" "face.108" \  
"face.84" real  
volume create stitch "face.98" "face.38" "face.99" "face.92" "face.109" \  
"face.85" real  
volume create stitch "face.80" "face.81" "face.86" "face.85" "face.28" \  
"face.100" real  
volume create stitch "face.86" "face.82" "face.83" "face.84" "face.101" \  
"face.29" real  
volume split "volume.3" volumes "volume.22" connected bidentity  
volume split "volume.3" volumes "volume.23" connected bidentity  
volume split "volume.3" volumes "volume.24" connected bidentity  
volume split "volume.3" volumes "volume.25" connected bidentity  
volume split "volume.3" volumes "volume.26" connected bidentity  
volume split "volume.3" volumes "volume.27" connected bidentity  
volume split "volume.3" volumes "volume.28" connected bidentity  
volume split "volume.3" volumes "volume.29" connected bidentity  
volume split "volume.3" faces "face.93" connected

/ Dimple 3

volume create stitch "face.133" "face.21" "face.128" "face.119" "face.110" \  
"

"face.134" real  
 volume create stitch "face.128" "face.43" "face.129" "face.120" "face.111" \  
 "face.135" real  
 volume create stitch "face.129" "face.45" "face.130" "face.121" "face.112" \  
 "face.136" real  
 volume create stitch "face.130" "face.20" "face.131" "face.122" "face.137" \  
 "face.113" real  
 volume create stitch "face.131" "face.44" "face.132" "face.123" "face.114" \  
 "face.138" real  
 volume create stitch "face.42" "face.133" "face.124" "face.132" "face.115" \  
 "face.139" real  
 volume create stitch "face.110" "face.111" "face.116" "face.115" "face.117" \  
 "face.30" real  
 volume create stitch "face.116" "face.112" "face.113" "face.114" "face.118" \  
 "face.31" real  
 volume split "volume.4" volumes "volume.39" connected bidentity  
 volume split "volume.4" volumes "volume.40" connected bidentity  
 volume split "volume.4" volumes "volume.41" connected bidentity  
 volume split "volume.4" volumes "volume.42" connected bidentity  
 volume split "volume.4" volumes "volume.43" connected bidentity  
 volume split "volume.4" volumes "volume.44" connected bidentity  
 volume split "volume.4" volumes "volume.45" connected bidentity  
 volume split "volume.4" volumes "volume.46" connected bidentity  
 volume split "volume.4" faces "face.126" connected

/ Dimple 4

volume create stitch "face.163" "face.24" "face.158" "face.150" "face.164" \  
 "face.140" real  
 volume create stitch "face.158" "face.47" "face.159" "face.151" "face.165" \  
 "face.141" real  
 volume create stitch "face.159" "face.49" "face.160" "face.152" "face.142" \  
 "face.166" real  
 volume create stitch "face.160" "face.23" "face.161" "face.153" "face.143" \  
 "face.167" real  
 volume create stitch "face.161" "face.48" "face.162" "face.154" "face.168" \  
 "face.144" real  
 volume create stitch "face.46" "face.163" "face.155" "face.162" "face.169" \  
 "face.145" real  
 volume create stitch "face.140" "face.141" "face.146" "face.145" "face.32" \  
 "face.147" real  
 volume create stitch "face.146" "face.142" "face.143" "face.144" "face.33" \  
 "face.148" real  
 volume split "volume.5" volumes "volume.56" connected bidentity  
 volume split "volume.5" volumes "volume.57" connected bidentity  
 volume split "volume.5" volumes "volume.58" connected bidentity  
 volume split "volume.5" volumes "volume.59" connected bidentity

```
volume split "volume.5" volumes "volume.60" connected bidentity
volume split "volume.5" volumes "volume.61" connected bidentity
volume split "volume.5" volumes "volume.62" connected bidentity
volume split "volume.5" volumes "volume.63" connected bidentity
volume split "volume.5" faces "face.149" connected
```

```
/ Break up the bottom wall
```

```
vertex create project "vertex.54" "vertex.11" "vertex.56" "vertex.58" \
"vertex.14" "vertex.59" "vertex.61" "vertex.17" "vertex.63" "vertex.66" \
"vertex.20" "vertex.68" edge "edge.6" splitedge
vertex create project "vertex.53" "vertex.10" "vertex.55" "vertex.57" \
"vertex.13" "vertex.60" "vertex.62" "vertex.16" "vertex.64" "vertex.65" \
"vertex.19" "vertex.67" edge "edge.5" splitedge
vertex create project "vertex.201" "vertex.202" "vertex.203" "vertex.204" \
"vertex.205" "vertex.206" "vertex.207" "vertex.208" "vertex.209" \
"vertex.210" "vertex.211" "vertex.212" edge "edge.8" splitedge
vertex create project "vertex.213" "vertex.214" "vertex.215" "vertex.216" \
"vertex.217" "vertex.218" "vertex.219" "vertex.220" "vertex.221" \
"vertex.222" "vertex.223" "vertex.224" edge "edge.7" splitedge
vertex create coordinates 0 0 0
vertex create coordinates 0 0 -$ch_1
```

```
edge split "edge.9" vertex "vertex.249" connected
edge split "edge.1" vertex "vertex.250" connected
```

```
edge create straight "vertex.54" "vertex.201"
edge create straight "vertex.11" "vertex.202"
edge create straight "vertex.56" "vertex.203"
edge create straight "vertex.58" "vertex.204"
edge create straight "vertex.14" "vertex.205"
edge create straight "vertex.59" "vertex.206"
edge create straight "vertex.61" "vertex.207"
edge create straight "vertex.17" "vertex.208"
edge create straight "vertex.63" "vertex.209"
edge create straight "vertex.66" "vertex.210"
edge create straight "vertex.20" "vertex.211"
edge create straight "vertex.68" "vertex.212"
edge create straight "vertex.67" "vertex.224"
edge create straight "vertex.19" "vertex.223"
edge create straight "vertex.65" "vertex.222"
edge create straight "vertex.64" "vertex.221"
edge create straight "vertex.16" "vertex.220"
edge create straight "vertex.62" "vertex.219"
edge create straight "vertex.60" "vertex.218"
edge create straight "vertex.13" "vertex.217"
edge create straight "vertex.57" "vertex.216"
```



```
edge create straight "vertex.55" "vertex.215"  
edge create straight "vertex.10" "vertex.214"  
edge create straight "vertex.53" "vertex.213"  
edge create straight "vertex.58" "vertex.55"  
edge create straight "vertex.59" "vertex.62"  
edge create straight "vertex.64" "vertex.66"  
edge create straight "vertex.53" "vertex.249"  
edge create straight "vertex.68" "vertex.250"
```

#### / Project Dimples Perimeters to Top Wall

```
edge create project "edge.16" "edge.32" "edge.31" "edge.14" "edge.30" \  
"edge.29" "edge.35" "edge.18" "edge.34" "edge.33" "edge.20" "edge.36" \  
"edge.24" "edge.40" "edge.39" "edge.22" "edge.38" "edge.37" "edge.44" \  
"edge.43" "edge.26" "edge.42" "edge.41" "edge.28" face "face.5" vector 0 1 \  
0 splitface
```

```
vertex create project "vertex.249" edge "edge.12" splitedge  
vertex create project "vertex.250" edge "edge.4" splitedge
```

#### / Edges to Break Up Top Wall

```
edge create straight "vertex.237" "vertex.321"  
edge create straight "vertex.238" "vertex.319"  
edge create straight "vertex.239" "vertex.317"  
edge create straight "vertex.315" "vertex.240"  
edge create straight "vertex.241" "vertex.313"  
edge create straight "vertex.242" "vertex.311"  
edge create straight "vertex.243" "vertex.309"  
edge create straight "vertex.244" "vertex.307"  
edge create straight "vertex.245" "vertex.305"  
edge create straight "vertex.246" "vertex.303"  
edge create straight "vertex.247" "vertex.301"  
edge create straight "vertex.248" "vertex.299"  
edge create straight "vertex.300" "vertex.236"  
edge create straight "vertex.302" "vertex.235"  
edge create straight "vertex.304" "vertex.234"  
edge create straight "vertex.306" "vertex.233"  
edge create straight "vertex.308" "vertex.232"  
edge create straight "vertex.310" "vertex.231"  
edge create straight "vertex.312" "vertex.230"  
edge create straight "vertex.314" "vertex.229"  
edge create straight "vertex.316" "vertex.228"  
edge create straight "vertex.318" "vertex.227"  
edge create straight "vertex.320" "vertex.226"  
edge create straight "vertex.322" "vertex.225"  
edge create straight "vertex.323" "vertex.321"  
edge create straight "vertex.317" "vertex.316"
```

```
edge create straight "vertex.312" "vertex.309"  
edge create straight "vertex.305" "vertex.304"  
edge create straight "vertex.300" "vertex.324"
```

/ Use Edges to Break Up Top and Bottom Walls into Faces

```
face split "face.25" edges "edge.445" "edge.441"  
face split "face.25" edges "edge.418"  
face split "face.25" edges "edge.419"  
face split "face.25" edges "edge.420"  
face split "face.25" edges "edge.440"  
face split "face.25" edges "edge.439"  
face split "face.25" edges "edge.442" "edge.421"  
face split "face.25" edges "edge.438"  
face split "face.25" edges "edge.422"  
face split "face.25" edges "edge.437"  
face split "face.25" edges "edge.423"  
face split "face.25" edges "edge.436"  
face split "face.25" edges "edge.435" "edge.443"  
face split "face.25" edges "edge.424"  
face split "face.25" edges "edge.425"  
face split "face.25" edges "edge.426"  
face split "face.25" edges "edge.434"  
face split "face.25" edges "edge.433"  
face split "face.25" edges "edge.444" "edge.427"  
face split "face.25" edges "edge.432"  
face split "face.25" edges "edge.428"  
face split "face.25" edges "edge.429"  
face split "face.25" edges "edge.431"  
face split "face.25" edges "edge.430"  
face split "face.25" edges "edge.446"  
face split "face.5" edges "edge.521" "edge.497"  
face split "face.5" edges "edge.520"  
face split "face.5" edges "edge.519"  
face split "face.5" edges "edge.518"  
face split "face.5" edges "edge.498"  
face split "face.5" edges "edge.499"  
face split "face.5" edges "edge.517" "edge.522"  
face split "face.5" edges "edge.500"  
face split "face.5" edges "edge.501"  
face split "face.5" edges "edge.502"  
face split "face.5" edges "edge.516"  
face split "face.5" edges "edge.515"  
face split "face.5" edges "edge.523" "edge.503"  
face split "face.5" edges "edge.514"  
face split "face.5" edges "edge.513"  
face split "face.5" edges "edge.512"
```

face split "face.5" edges "edge.504"  
face split "face.5" edges "edge.505"  
face split "face.5" edges "edge.524" "edge.511"  
face split "face.5" edges "edge.506"  
face split "face.5" edges "edge.507"  
face split "face.5" edges "edge.508"  
face split "face.5" edges "edge.510"  
face split "face.5" edges "edge.509"  
face split "face.5" edges "edge.582"

/ Cut Edges Through the Volume Connecting Top and Bottom Walls

/ Internals

edge create straight "vertex.323" "vertex.249"  
edge create straight "vertex.321" "vertex.53"  
edge create straight "vertex.319" "vertex.10"  
edge create straight "vertex.317" "vertex.55"  
edge create straight "vertex.316" "vertex.58"  
edge create straight "vertex.314" "vertex.14"  
edge create straight "vertex.312" "vertex.59"  
edge create straight "vertex.309" "vertex.62"  
edge create straight "vertex.307" "vertex.16"  
edge create straight "vertex.305" "vertex.64"  
edge create straight "vertex.304" "vertex.66"  
edge create straight "vertex.302" "vertex.20"  
edge create straight "vertex.300" "vertex.68"  
edge create straight "vertex.324" "vertex.250"  
edge create straight "vertex.322" "vertex.54"  
edge create straight "vertex.320" "vertex.11"  
edge create straight "vertex.318" "vertex.56"  
edge create straight "vertex.310" "vertex.61"  
edge create straight "vertex.308" "vertex.17"  
edge create straight "vertex.306" "vertex.63"  
edge create straight "vertex.315" "vertex.57"  
edge create straight "vertex.313" "vertex.13"  
edge create straight "vertex.311" "vertex.60"  
edge create straight "vertex.303" "vertex.65"  
edge create straight "vertex.301" "vertex.19"  
edge create straight "vertex.299" "vertex.67"

/ Walls

edge create straight "vertex.225" "vertex.201"  
edge create straight "vertex.226" "vertex.202"  
edge create straight "vertex.227" "vertex.203"  
edge create straight "vertex.228" "vertex.204"  
edge create straight "vertex.229" "vertex.205"  
edge create straight "vertex.230" "vertex.206"  
edge create straight "vertex.231" "vertex.207"

edge create straight "vertex.232" "vertex.208"  
edge create straight "vertex.233" "vertex.209"  
edge create straight "vertex.234" "vertex.210"  
edge create straight "vertex.235" "vertex.211"  
edge create straight "vertex.236" "vertex.212"  
edge create straight "vertex.237" "vertex.213"  
edge create straight "vertex.238" "vertex.214"  
edge create straight "vertex.239" "vertex.215"  
edge create straight "vertex.240" "vertex.216"  
edge create straight "vertex.241" "vertex.217"  
edge create straight "vertex.242" "vertex.218"  
edge create straight "vertex.243" "vertex.219"  
edge create straight "vertex.244" "vertex.220"  
edge create straight "vertex.245" "vertex.221"  
edge create straight "vertex.246" "vertex.222"  
edge create straight "vertex.247" "vertex.223"  
edge create straight "vertex.248" "vertex.224"

/ Create Faces to Cut Volumes

face create wireframe "edge.583" "edge.521" "edge.584" "edge.445" real  
face create wireframe "edge.584" "edge.447" "edge.585" "edge.16" real  
face create wireframe "edge.585" "edge.448" "edge.586" "edge.32" real  
face create wireframe "edge.522" "edge.587" "edge.442" "edge.586" real  
face create wireframe "edge.455" "edge.588" "edge.34" "edge.587" real  
face create wireframe "edge.454" "edge.589" "edge.18" "edge.588" real  
face create wireframe "edge.589" "edge.523" "edge.590" "edge.443" real  
face create wireframe "edge.459" "edge.591" "edge.24" "edge.590" real  
face create wireframe "edge.460" "edge.592" "edge.40" "edge.591" real  
face create wireframe "edge.524" "edge.593" "edge.444" "edge.592" real  
face create wireframe "edge.468" "edge.594" "edge.42" "edge.593" real  
face create wireframe "edge.467" "edge.595" "edge.26" "edge.594" real  
face create wireframe "edge.595" "edge.525" "edge.596" "edge.446" real  
face create wireframe "edge.31" "edge.586" "edge.449" "edge.599" real  
face create wireframe "edge.450" "edge.599" "edge.14" "edge.598" real  
face create wireframe "edge.451" "edge.598" "edge.30" "edge.597" real  
face create wireframe "edge.452" "edge.597" "edge.29" "edge.584" real  
face create wireframe "edge.456" "edge.587" "edge.33" "edge.603" real  
face create wireframe "edge.457" "edge.603" "edge.20" "edge.604" real  
face create wireframe "edge.458" "edge.604" "edge.36" "edge.605" real  
face create wireframe "edge.605" "edge.453" "edge.589" "edge.35" real  
face create wireframe "edge.590" "edge.464" "edge.600" "edge.37" real  
face create wireframe "edge.463" "edge.601" "edge.38" "edge.600" real  
face create wireframe "edge.462" "edge.602" "edge.22" "edge.601" real  
face create wireframe "edge.461" "edge.592" "edge.39" "edge.602" real  
face create wireframe "edge.469" "edge.593" "edge.41" "edge.606" real  
face create wireframe "edge.470" "edge.606" "edge.28" "edge.607" real

```

face create wireframe "edge.465" "edge.607" "edge.44" "edge.608" real
face create wireframe "edge.466" "edge.608" "edge.43" "edge.595" real
face create wireframe "edge.597" "edge.520" "edge.609" "edge.418" real
face create wireframe "edge.598" "edge.519" "edge.610" "edge.419" real
face create wireframe "edge.599" "edge.518" "edge.611" "edge.420" real
face create wireframe "edge.517" "edge.612" "edge.421" "edge.587" real
face create wireframe "edge.588" "edge.516" "edge.613" "edge.422" real
face create wireframe "edge.589" "edge.515" "edge.614" "edge.423" real
face create wireframe "edge.600" "edge.514" "edge.615" "edge.424" real
face create wireframe "edge.601" "edge.513" "edge.616" "edge.425" real
face create wireframe "edge.602" "edge.512" "edge.617" "edge.426" real
face create wireframe "edge.511" "edge.618" "edge.427" "edge.593" real
face create wireframe "edge.594" "edge.510" "edge.619" "edge.428" real
face create wireframe "edge.595" "edge.509" "edge.620" "edge.429" real
face create wireframe "edge.441" "edge.621" "edge.497" "edge.584" real
face create wireframe "edge.622" "edge.498" "edge.585" "edge.440" real
face create wireframe "edge.623" "edge.499" "edge.586" "edge.439" real
face create wireframe "edge.624" "edge.500" "edge.603" "edge.438" real
face create wireframe "edge.625" "edge.501" "edge.604" "edge.437" real
face create wireframe "edge.626" "edge.502" "edge.605" "edge.436" real
face create wireframe "edge.627" "edge.503" "edge.590" "edge.435" real
face create wireframe "edge.628" "edge.504" "edge.591" "edge.434" real
face create wireframe "edge.629" "edge.505" "edge.592" "edge.433" real
face create wireframe "edge.630" "edge.506" "edge.606" "edge.432" real
face create wireframe "edge.631" "edge.507" "edge.607" "edge.431" real
face create wireframe "edge.632" "edge.508" "edge.608" "edge.430" real

```

/ Break-Up Inlet and Exit Faces

```

face split "face.6" edges "edge.583"
face split "face.1" edges "edge.596"

```

/ Volume Time

/ Break Out Dimples First

```

volume split "Channel" faces "face.244" "face.229" "face.230" "face.241" \
"face.242" "face.243" connected
volume split "Channel" faces "face.246" "face.247" "face.248" "face.233" \
"face.232" "face.245" connected
volume split "Channel" faces "face.235" "face.236" "face.252" "face.251" \
"face.250" "face.249" connected
volume split "Channel" faces "face.253" "face.254" "face.255" "face.256" \
"face.239" "face.238" connected

```

/ Break Down the Rest of the Channel

```

volume split "Channel" faces "face.269" "face.228" connected
volume split "Channel" faces "face.257" connected
volume split "Channel" faces "face.258" connected

```

volume split "Channel" faces "face.270" connected  
 volume split "Channel" faces "face.259" connected  
 volume split "Channel" faces "face.271" connected  
 volume split "Channel" faces "face.260" "face.231" connected  
 volume split "Channel" faces "face.272" connected  
 volume split "Channel" faces "face.273" connected  
 volume split "Channel" faces "face.261" connected  
 volume split "Channel" faces "face.262" connected  
 volume split "Channel" faces "face.273" connected  
 volume split "Channel" faces "face.274" connected  
 volume split "Channel" faces "face.234" "face.275" connected  
 volume split "Channel" faces "face.263" connected  
 volume split "Channel" faces "face.264" connected  
 volume split "Channel" faces "face.276" connected  
 volume split "Channel" faces "face.265" connected  
 volume split "Channel" faces "face.277" connected  
 volume split "Channel" faces "face.266" "face.237" connected  
 volume split "Channel" faces "face.278" connected  
 volume split "Channel" faces "face.279" connected  
 volume split "Channel" faces "face.267" connected  
 volume split "Channel" faces "face.268" connected  
 volume split "Channel" faces "face.280" connected  
 volume split "Channel" faces "face.240" connected

/ Break up Odd Geometry for Meshing Convenience

vertex create project "vertex.54" edge "edge.416" splitedge  
 vertex create project "vertex.56" edge "edge.421" splitedge  
 vertex create project "vertex.57" edge "edge.439" splitedge  
 vertex create project "vertex.60" edge "edge.435" splitedge  
 vertex create project "vertex.61" edge "edge.423" splitedge  
 vertex create project "vertex.63" edge "edge.427" splitedge  
 vertex create project "vertex.65" edge "edge.433" splitedge  
 vertex create project "vertex.67" edge "edge.417" splitedge  
 edge create straight "vertex.54" "vertex.325"  
 edge create straight "vertex.56" "vertex.326"  
 edge create straight "vertex.57" "vertex.327"  
 edge create straight "vertex.60" "vertex.328"  
 edge create straight "vertex.61" "vertex.329"  
 edge create straight "vertex.63" "vertex.330"  
 edge create straight "vertex.65" "vertex.331"  
 edge create straight "vertex.67" "vertex.332"  
 face split "face.180" edges "edge.766"  
 face split "face.185" edges "edge.767"  
 face split "face.186" edges "edge.768"  
 face split "face.191" edges "edge.769"  
 face split "face.192" edges "edge.770"

face split "face.197" edges "edge.771"  
face split "face.198" edges "edge.772"  
face split "face.203" edges "edge.773"

vertex create project "vertex.327" edge "edge.9" splitedge  
vertex create project "vertex.333" edge "edge.441" splitedge  
vertex create project "vertex.333" edge "edge.495" splitedge  
vertex create project "vertex.335" edge "edge.497" splitedge  
vertex create project "vertex.325" edge "edge.12" splitedge  
vertex create project "vertex.332" edge "edge.4" splitedge  
vertex create project "vertex.330" edge "edge.1" splitedge  
vertex create project "vertex.339" edge "edge.429" splitedge  
vertex create project "vertex.340" edge "edge.509" splitedge  
vertex create project "vertex.341" edge "edge.496" splitedge  
edge create straight "vertex.325" "vertex.337" "vertex.322"  
edge create straight "vertex.334" "vertex.333" "vertex.335" "vertex.336"  
edge create straight "vertex.336" "vertex.334"  
edge create straight "vertex.299" "vertex.338" "vertex.332"  
edge create straight "vertex.342" "vertex.339"  
edge create straight "vertex.339" "vertex.340" "vertex.341" "vertex.342"  
face create wireframe "edge.800" "edge.801" "edge.802" "edge.803" real  
face create wireframe "edge.798" "edge.799" "edge.773" "edge.676" real  
face create wireframe "edge.635" "edge.766" "edge.792" "edge.793" real  
face create wireframe "edge.796" "edge.797" "edge.794" "edge.795" real  
volume split "volume.77" faces "face.319" connected  
volume split "volume.78" faces "face.318" connected  
volume split "volume.101" faces "face.316" connected  
volume split "Channel" faces "face.317" connected

/ GEOMETRY IS DONE. GEOMETRY IS DONE. GEOMETRY IS DONE.

/ MESHING MESHING MESHING

/ Linking

/ Link Edges

edge link "edge.10" "edge.2" directions 1 0 periodic  
edge link "edge.807" "edge.818" directions 0 1 periodic  
edge link "edge.633" "edge.634" directions 0 1 periodic  
edge link "edge.811" "edge.812" directions 0 1 periodic  
edge link "edge.11" "edge.3" directions 0 1 periodic  
edge link "edge.9" "edge.765" directions 1 0 periodic  
edge link "edge.784" "edge.4" directions 0 1 periodic  
edge link "edge.782" "edge.417" directions 1 0 periodic  
edge link "edge.495" "edge.787" directions 0 1 periodic  
edge link "edge.416" "edge.788" directions 0 1 periodic  
edge link "edge.786" "edge.496" directions 1 0 periodic

edge link "edge.758" "edge.1" directions 0 1 periodic  
edge link "edge.12" "edge.791" directions 1 0 periodic

/ Link Faces

face link "face.281" "face.330" edges "edge.807" "edge.765" vertices \  
"vertex.333" "vertex.332" reverse periodic  
face link "face.323" "face.282" edges "edge.633" "edge.417" vertices \  
"vertex.249" "vertex.250" reverse periodic  
face link "face.6" "face.326" edges "edge.633" "edge.496" vertices \  
"vertex.323" "vertex.324" reverse periodic  
face link "face.325" "face.1" edges "edge.811" "edge.791" vertices \  
"vertex.337" "vertex.342" reverse periodic

/ Boundary Layers

/ Dimple Faces

undo begingroup

blayer create first \$blds\_dimp growth \$blgrow\_dimp total \$bltotal\_dimp rows  
\$blrows\_dimp transition \$bltrans\_dimp \  
trows \$bltrows\_dimp uniform

blayer attach "b\_layer.1" volume "volume.8" "volume.9" "volume.10" \  
"volume.11" "volume.12" "volume.2" "volume.7" "volume.6" "volume.22" \  
"volume.23" "volume.24" "volume.25" "volume.26" "volume.27" "volume.28" \  
"volume.29" "volume.39" "volume.40" "volume.41" "volume.42" "volume.43" \  
"volume.44" "volume.45" "volume.46" "volume.56" "volume.57" "volume.58" \  
"volume.59" "volume.60" "volume.61" "volume.62" "volume.63" face "face.16" \  
"face.35" "face.37" "face.7" "face.36" "face.34" "face.26" "face.27" \  
"face.18" "face.39" "face.41" "face.17" "face.40" "face.38" "face.28" \  
"face.29" "face.21" "face.43" "face.45" "face.20" "face.44" "face.42" \  
"face.30" "face.31" "face.24" "face.47" "face.49" "face.23" "face.48" \  
"face.46" "face.32" "face.33" add

undo endgroup

/ Bottom Wall Edges

undo begingroup

blayer create first \$blds\_chbot growth \$blgrow\_chbot total \$bltotal\_chbot rows  
\$blrows\_chbot transition \$bltrans\_chbot \  
trows \$bltrows\_chbot uniform

blayer attach "b\_layer.2" face "face.228" "face.229" "face.230" "face.231" \  
"face.232" "face.233" "face.234" "face.235" "face.236" "face.237" \  
"face.238" "face.239" "face.240" edge "edge.445" "edge.16" "edge.32" \  
"edge.442" "edge.34" "edge.18" "edge.443" "edge.24" "edge.40" "edge.444" \  
"edge.42" "edge.26" "edge.446" add

undo endgroup

undo begingroup



```

blayer create first $blds_chbot growth $blgrow_chbot total $bltotal_chbot rows
$blrows_chbot transition $bltrans_chbot \
  trows $bltrows_chbot uniform
blayer attach "b_layer.3" face "face.244" "face.243" "face.242" "face.241" \
  "face.245" "face.246" "face.247" "face.248" "face.249" "face.250" \
  "face.251" "face.252" "face.253" "face.254" "face.255" "face.256" edge \
  "edge.29" "edge.30" "edge.14" "edge.31" "edge.33" "edge.20" "edge.36" \
  "edge.35" "edge.37" "edge.38" "edge.22" "edge.39" "edge.41" "edge.28" \
  "edge.44" "edge.43" add
undo endgroup

```

```

undo begingroup
blayer create first $blds_chbot growth $blgrow_chbot total $bltotal_chbot rows
$blrows_chbot transition $bltrans_chbot \
  trows $bltrows_chbot uniform
blayer attach "b_layer.4" face "face.4" "face.285" "face.284" "face.289" \
  "face.287" "face.293" "face.292" "face.297" "face.296" "face.301" \
  "face.304" "face.305" "face.299" "face.306" "face.303" "face.302" \
  "face.300" "face.298" "face.295" "face.294" "face.291" "face.290" \
  "face.288" "face.286" "face.3" "face.283" edge "edge.6" "edge.368" \
  "edge.369" "edge.370" "edge.371" "edge.372" "edge.373" "edge.374" \
  "edge.375" "edge.376" "edge.377" "edge.378" "edge.379" "edge.391" \
  "edge.390" "edge.389" "edge.388" "edge.387" "edge.386" "edge.385" \
  "edge.384" "edge.383" "edge.382" "edge.381" "edge.380" "edge.5" add
undo endgroup

```

```

undo begingroup
blayer create first $blds_chbot growth $blgrow_chbot total $bltotal_chbot rows
$blrows_chbot transition $bltrans_chbot \
  trows $bltrows_chbot uniform
blayer attach "b_layer.5" face "face.319" "face.318" "face.316" "face.317" \
  edge "edge.805" "edge.766" "edge.813" "edge.773" add
undo endgroup

```

/ Side Wall Edges

```

undo begingroup
blayer create first $blds_chsid growth $blgrow_chsid total $bltotal_chsid rows
$blrows_chsid transition $bltrans_chsid \
  trows $bltrows_chsid uniform
blayer attach "b_layer.6" face "face.321" "face.183" "face.184" "face.310" \
  "face.188" "face.190" "face.311" "face.195" "face.196" "face.314" \
  "face.201" "face.202" "face.315" "face.307" "face.225" "face.224" \
  "face.223" "face.221" "face.220" "face.216" "face.213" "face.212" \
  "face.211" "face.209" "face.208" "face.204" "face.308" "face.181" \
  "face.182" "face.309" "face.187" "face.189" "face.312" "face.193" \
  "face.194" "face.313" "face.199" "face.200" "face.25" "face.328" "face.227" \

```

```

"face.226" "face.222" "face.219" "face.218" "face.217" "face.215" \
"face.214" "face.210" "face.207" "face.206" "face.205" edge "edge.5" \
"edge.380" "edge.381" "edge.382" "edge.383" "edge.384" "edge.385" \
"edge.386" "edge.387" "edge.388" "edge.389" "edge.390" "edge.391" \
"edge.415" "edge.414" "edge.413" "edge.412" "edge.411" "edge.410" \
"edge.409" "edge.408" "edge.407" "edge.406" "edge.405" "edge.404" "edge.7" \
"edge.6" "edge.368" "edge.369" "edge.370" "edge.371" "edge.372" "edge.373" \
"edge.374" "edge.375" "edge.376" "edge.377" "edge.378" "edge.379" \
"edge.403" "edge.402" "edge.401" "edge.400" "edge.399" "edge.398" \
"edge.397" "edge.396" "edge.395" "edge.394" "edge.393" "edge.392" "edge.8" \
add
undo endgroup

/ Top Wall Edges
undo begingroup
blayer create first $blds_ chtop growth $blgrow_ chtop total $bltotal_ chtop rows
$blrows_ chtop transition $bltrans_ chtop \
  trows $bltrows_ chtop uniform
blayer attach "b_layer.7" face "face.228" "face.229" "face.230" "face.231" \
"face.232" "face.233" "face.234" "face.235" "face.236" "face.237" \
"face.238" "face.239" "face.240" "face.256" "face.255" "face.254" \
"face.253" "face.252" "face.251" "face.250" "face.249" "face.248" \
"face.247" "face.246" "face.245" "face.241" "face.242" "face.243" \
"face.244" edge "edge.521" "edge.447" "edge.448" "edge.522" "edge.455" \
"edge.454" "edge.523" "edge.459" "edge.460" "edge.524" "edge.468" \
"edge.467" "edge.757" "edge.466" "edge.465" "edge.470" "edge.469" \
"edge.461" "edge.462" "edge.463" "edge.464" "edge.453" "edge.458" \
"edge.457" "edge.456" "edge.449" "edge.450" "edge.451" "edge.452" add
undo endgroup

undo begingroup
blayer create first $blds_ chtop growth $blgrow_ chtop total $bltotal_ chtop rows
$blrows_ chtop transition $bltrans_ chtop \
  trows $bltrows_ chtop uniform
blayer attach "b_layer.8" face "face.283" "face.3" "face.286" "face.288" \
"face.290" "face.291" "face.294" "face.295" "face.298" "face.300" \
"face.302" "face.303" "face.306" "face.299" "face.305" "face.304" \
"face.301" "face.296" "face.297" "face.292" "face.293" "face.287" \
"face.289" "face.284" "face.285" "face.4" edge "edge.7" "edge.404" \
"edge.405" "edge.406" "edge.407" "edge.408" "edge.409" "edge.410" \
"edge.411" "edge.412" "edge.413" "edge.414" "edge.415" "edge.403" \
"edge.402" "edge.401" "edge.400" "edge.399" "edge.398" "edge.397" \
"edge.396" "edge.395" "edge.394" "edge.393" "edge.392" "edge.8" add
undo endgroup

undo begingroup

```

```

blayer create first $blids_ chtop growth $blgrow_ chtop total $bltotal_ chtop rows
$blrows_ chtop transition $bltrans_ chtop \
  trows $bltrows_ chtop uniform
blayer attach "b_layer.9" face "face.319" "face.318" "face.316" "face.317" edge \
  "edge.806" "edge.810" "edge.814" "edge.819" add
undo endgroup

/ Transitions
/ Into Dimple Inlet
undo begingroup
blayer create first $strands_ in growth $stransgrow_ in total $stranstotal_ in rows
$stransrows_ in transition $stranstrans_ in trows $stranstrows_ in \
  uniform
blayer attach "b_layer.10" face "face.7" "face.36" "face.34" "face.16" \
  "face.35" "face.37" "face.17" "face.40" "face.38" "face.18" "face.39" \
  "face.41" "face.44" "face.42" "face.21" "face.43" "face.45" "face.20" \
  "face.23" "face.48" "face.46" "face.24" "face.47" "face.49" edge "edge.29" \
  "edge.16" "edge.32" "edge.31" "edge.14" "edge.30" "edge.33" "edge.20" \
  "edge.36" "edge.35" "edge.18" "edge.34" "edge.24" "edge.40" "edge.39" \
  "edge.22" "edge.38" "edge.37" "edge.41" "edge.28" "edge.44" "edge.43" \
  "edge.26" "edge.42" add
undo endgroup

/ Dimple Edges into Bottom Wall of Channel - Spanwise Direction
undo begingroup
blayer create first $strands_ sid growth $stransgrow_ sid total $stranstotal_ sid rows
$stransrows_ sid transition $stranstrans_ sid trows $stranstrows_ sid \
  uniform
blayer attach "b_layer.11" face "face.183" "face.184" "face.182" "face.181" \
  "face.187" "face.189" "face.190" "face.188" "face.195" "face.196" \
  "face.194" "face.193" "face.199" "face.200" "face.202" "face.201" edge \
  "edge.16" "edge.32" "edge.14" "edge.30" "edge.34" "edge.18" "edge.36" \
  "edge.20" "edge.24" "edge.40" "edge.22" "edge.38" "edge.42" "edge.26" \
  "edge.44" "edge.28" add
undo endgroup

/ Edge Meshing
/ Dimples
/ Spanwise-Normal
undo begingroup
edge modify "edge.50" "edge.356" "edge.52" "edge.363" "edge.66" "edge.63" "edge.65"
"edge.68" "edge.79" "edge.82" \
  "edge.81" "edge.84" "edge.95" "edge.98" "edge.100" "edge.97" backward
edge picklink "edge.50" "edge.356" "edge.52" "edge.363" "edge.367" "edge.136" \
  "edge.359" "edge.285" "edge.66" "edge.63" "edge.65" "edge.68" "edge.79" "edge.82" \
  "edge.81" "edge.84" "edge.95" "edge.98" "edge.100" "edge.97" "edge.119" \

```

```

"edge.130" "edge.120" "edge.129" "edge.118" "edge.132" "edge.117" \
"edge.131" "edge.115" "edge.134" "edge.116" "edge.133"
edge mesh "edge.285" "edge.359" "edge.50" "edge.356" "edge.136" "edge.367" \
"edge.52" "edge.363" "edge.133" "edge.116" "edge.66" "edge.63" "edge.134"
"edge.115" \
"edge.65" "edge.68" "edge.131" "edge.117" "edge.79" "edge.82" "edge.132" \
"edge.118" "edge.81" "edge.84" "edge.129" "edge.120" "edge.95" "edge.98" \
"edge.130" "edge.119" "edge.100" "edge.97" \
successive ratio1 $growrate_dimp_span intervals $edgenum_dimp_span
undo endgroup

```

```

/ Streamwise-Normal

```

```

undo begingroup
edge modify "edge.51" "edge.365" "edge.93" "edge.94" "edge.335" "edge.244" "edge.83"
"edge.80" \
"edge.61" "edge.62" "edge.301" "edge.218"backward
edge picklink "edge.51" "edge.365" "edge.353" "edge.45" "edge.362" "edge.291" \
"edge.93" "edge.94" "edge.335" "edge.244" "edge.83" "edge.80" \
"edge.61" "edge.62" "edge.301" "edge.218" "edge.64" "edge.67" "edge.231" \
"edge.323" "edge.78" "edge.77" "edge.99" "edge.96"
edge mesh "edge.45" "edge.353" "edge.51" "edge.365" "edge.291" "edge.362" \
"edge.93" "edge.94" "edge.335" "edge.244" "edge.96" "edge.99" \
"edge.77" "edge.78" "edge.323" "edge.231" "edge.83" "edge.80" "edge.61" \
"edge.62" "edge.301" "edge.218" "edge.67" "edge.64"successive ratio1
$growrate_dimp_strm \
intervals $edgenum_dimp_strm
undo endgroup

```

```

/ Box Depth

```

```

undo begingroup
edge modify "edge.215" "edge.241" backward
edge picklink "edge.355" "edge.357" "edge.366" "edge.364" "edge.360" \
"edge.354""edge.215" "edge.241" "edge.103" "edge.102" "edge.234" \
"edge.101" "edge.104" "edge.227" "edge.88" "edge.87" "edge.221" "edge.86" \
"edge.85" "edge.71" "edge.70" "edge.208" "edge.69" "edge.72"
edge mesh "edge.354" "edge.360" "edge.364" "edge.366" "edge.357" "edge.355" \
"edge.72" "edge.69" "edge.208" "edge.70" "edge.71" "edge.215" \
"edge.85" "edge.86" "edge.221" "edge.87" "edge.88" "edge.227" "edge.104" \
"edge.101" "edge.234" "edge.102" "edge.103" "edge.241" \
successive ratio1 $growrate_dimpbox intervals $edgenum_dimpbox
undo endgroup

```

```

/ Legs

```

```

edge modify "edge.214" "edge.240" backward
undo begingroup
edge picklink "edge.202" "edge.199" "edge.197" "edge.196" "edge.193" \

```

```

"edge.203" "edge.214" "edge.240" "edge.235" "edge.232" "edge.242" \
"edge.238" "edge.236" "edge.222" "edge.219" "edge.229" "edge.228" \
"edge.225" "edge.223" "edge.209" "edge.206" "edge.216" "edge.212" \
"edge.210"
edge mesh "edge.203" "edge.193" "edge.196" "edge.197" "edge.199" "edge.202" \
"edge.210" "edge.212" "edge.214" "edge.216" "edge.206" "edge.209" \
"edge.223" "edge.225" "edge.228" "edge.229" "edge.219" "edge.222" \
"edge.236" "edge.238" "edge.240" "edge.242" "edge.232" "edge.235" \
successive ratio1 $growrate_dimp_rad intervals $edgenum_dimp_rad
undo endgroup

/ Channel
/ Small Stream-Wise Normal Edges
/ Bottom Wall
undo begingroup
edge modify "edge.9" backward
edge picklink "edge.9" "edge.789" "edge.430" "edge.431" \
"edge.432" "edge.764" "edge.763" "edge.426" "edge.425" "edge.424" \
"edge.762" "edge.761" "edge.436" "edge.437" "edge.438" "edge.760" \
"edge.783" "edge.759" "edge.420" "edge.419" "edge.418" "edge.758"
edge mesh "edge.758" "edge.418" "edge.419" "edge.420" "edge.759" "edge.9" \
"edge.783" "edge.760" "edge.438" "edge.437" "edge.436" "edge.761" \
"edge.762" "edge.424" "edge.425" "edge.426" "edge.763" "edge.764" \
"edge.432" "edge.431" "edge.430" "edge.789" \
bellshape ratio1 $grow_ch_strm_short_bell intervals $edgenum_ch_strm_short
undo endgroup

/ Top Wall
undo begingroup
edge modify "edge.12" "edge.497" "edge.501" "edge.502" "edge.506" "edge.507" \
"edge.508" backward
edge picklink "edge.12" "edge.497" "edge.501" "edge.502" "edge.506" \
"edge.507" "edge.508" "edge.790" "edge.512" "edge.513" "edge.514" \
"edge.500" "edge.784" "edge.518" "edge.519" "edge.520"
edge mesh "edge.12" "edge.520" "edge.519" "edge.518" "edge.784" "edge.497" \
"edge.500" "edge.501" "edge.502" "edge.514" "edge.513" "edge.512" \
"edge.506" "edge.507" "edge.508" "edge.790" \
bellshape ratio1 $grow_ch_strm_short_bell intervals $edgenum_ch_strm_short
undo endgroup

/ Medium Stream-Wise Normal Edges
undo begingroup
edge modify "edge.782" "edge.786" "edge.785" backward
edge picklink "edge.782" "edge.786" "edge.785" "edge.509" "edge.429" \
"edge.441" "edge.495" "edge.433" "edge.427" "edge.423" "edge.435" \
"edge.439" "edge.421" "edge.416"

```

```

edge mesh "edge.416" "edge.421" "edge.439" "edge.435" "edge.423" "edge.427" \
"edge.433" "edge.782" "edge.495" "edge.786" "edge.441" "edge.785" \
"edge.429" "edge.509" \
bellshape ratio1 $grow_ch_strm_med_bell intervals $edgenum_ch_strm_med
undo endgroup

/ Large Stream-Wise Normal Edges
undo begingroup
edge picklink "edge.510" "edge.511" "edge.505" "edge.504" "edge.503" \
"edge.515" "edge.516" "edge.517" "edge.499" "edge.498" "edge.428" \
"edge.434" "edge.422" "edge.440"
edge mesh "edge.440" "edge.422" "edge.434" "edge.428" "edge.498" "edge.499" \
"edge.517" "edge.516" "edge.515" "edge.503" "edge.504" "edge.505" \
"edge.511" "edge.510" \
successive ratio1 $grow_ch_strm_long1 ratio2 $grow_ch_strm_long2 intervals
$edgenum_ch_strm_long
undo endgroup

/ Span-wise Normal Connecting Edges
/ Inners
undo begingroup
edge picklink "edge.444" "edge.443" "edge.442" "edge.524" "edge.523" "edge.522"
edge mesh "edge.442" "edge.443" "edge.444" "edge.522" "edge.523" "edge.524" \
bellshape ratio1 $grow_ch_span_connect_bell intervals $edgenum_ch_span_connect
undo endgroup

/ Outers
undo begingroup
edge picklink "edge.772" "edge.771" "edge.770" "edge.769" "edge.768" \
"edge.767"
edge mesh "edge.767" "edge.768" "edge.769" "edge.770" "edge.771" "edge.772" \
successive ratio1 $grow_ch_span_out intervals $edgenum_ch_span_out
undo endgroup

/ Span-wise Normal Connecting Edges on Inlet and Outlet
undo begingroup
edge modify "edge.813" "edge.810" "edge.521" "edge.806" "edge.757" backward
edge picklink "edge.813" "edge.446" "edge.773" "edge.766" "edge.805" \
"edge.445" "edge.810" "edge.521" "edge.806" "edge.757" "edge.819" \
"edge.814"
edge mesh "edge.445" "edge.805" "edge.766" "edge.773" "edge.446" "edge.813" \
"edge.810" "edge.521" "edge.806" "edge.814" "edge.757" "edge.819" \
successive ratio1 $grow_ch_span_ie intervals $edgenum_ch_span_S
undo endgroup

/ Vertical Edge Meshing - ALL

```

```

undo begingroup
edge picklink "edge.815" "edge.804" "edge.807" "edge.676" "edge.672" \
"edge.668" "edge.665" "edge.662" "edge.658" "edge.650" "edge.646" \
"edge.644" "edge.641" "edge.638" "edge.635" "edge.811" "edge.673" \
"edge.669" "edge.666" "edge.661" "edge.656" "edge.654" "edge.653" \
"edge.651" "edge.647" "edge.643" "edge.640" "edge.637" "edge.633"
edge mesh "edge.633" "edge.637" "edge.640" "edge.643" "edge.647" "edge.651" \
"edge.653" "edge.654" "edge.656" "edge.661" "edge.666" "edge.669" \
"edge.673" "edge.811" "edge.635" "edge.638" "edge.641" "edge.644" \
"edge.646" "edge.650" "edge.658" "edge.662" "edge.665" "edge.668" \
"edge.672" "edge.676" "edge.807" "edge.804" "edge.815" \
bellshape ratio1 $grow_ch_hght_bell intervals $edgenum_ch_hght
undo endgroup

```

```

undo begingroup
edge picklink "edge.752" "edge.748" "edge.739" "edge.731" "edge.725" \
"edge.722" "edge.713" "edge.709" "edge.700" "edge.692" "edge.686" \
"edge.683" "edge.11" "edge.755" "edge.745" "edge.742" "edge.735" "edge.728" \
"edge.719" "edge.716" "edge.706" "edge.703" "edge.696" "edge.689" \
"edge.680" "edge.10"
edge mesh "edge.10" "edge.680" "edge.689" "edge.696" "edge.703" "edge.706" \
"edge.716" "edge.719" "edge.728" "edge.735" "edge.742" "edge.745" \
"edge.755" "edge.11" "edge.683" "edge.686" "edge.692" "edge.700" "edge.709" \
"edge.713" "edge.722" "edge.725" "edge.731" "edge.739" "edge.748" \
"edge.752" bellshape ratio1 $grow_ch_hght_bell intervals $edgenum_ch_hght
undo endgroup

```

```

/ Face Meshing
/ Dimples
/ Inner Box and Legs

```

```

face mesh "face.170" "face.171" "face.174" "face.173" "face.172" "face.63" \
"face.64" "face.56" "face.57" "face.65" "face.66" "face.79" "face.51" \
"face.50" "face.55" "face.52" "face.53" "face.54" "face.87" "face.88" \
"face.89" "face.90" "face.91" "face.92" "face.93" "face.86" "face.80" \
"face.81" "face.85" "face.82" "face.83" "face.84" "face.101" "face.100" \
"face.103" "face.102" "face.119" "face.120" "face.121" "face.122" \
"face.123" "face.124" "face.126" "face.116" "face.110" "face.111" \
"face.112" "face.113" "face.114" "face.115" "face.118" "face.117" \
"face.125" "face.127" "face.150" "face.151" "face.152" "face.153" \
"face.154" "face.155" "face.140" "face.141" "face.142" "face.143" \
"face.144" "face.145" "face.146" "face.149" "face.148" "face.147" \
"face.157" "face.156" map size 1
face mesh "face.67" "face.68" "face.69" "face.70" "face.71" "face.72" \
"face.94" "face.95" "face.96" "face.97" "face.98" "face.99" "face.128" \
"face.129" "face.130" "face.131" "face.132" "face.133" "face.158" \
"face.159" "face.160" "face.161" "face.162" "face.163" map size 1

```

/ Dimple Floor

undo begingroup

```
face delete "face.16" "face.35" "face.37" "face.7" "face.36" "face.34" \  
"face.26" "face.27" "face.18" "face.39" "face.41" "face.17" "face.40" \  
"face.38" "face.28" "face.29" "face.21" "face.43" "face.45" "face.20" \  
"face.44" "face.42" "face.30" "face.31" "face.24" "face.47" "face.49" \  
"face.23" "face.48" "face.46" "face.32" "face.33" onlymesh
```

```
face mesh "face.16" "face.35" "face.37" "face.7" "face.36" "face.34" \  
"face.26" "face.27" "face.18" "face.39" "face.41" "face.17" "face.40" \  
"face.38" "face.28" "face.29" "face.21" "face.43" "face.45" "face.20" \  
"face.44" "face.42" "face.30" "face.31" "face.24" "face.47" "face.49" \  
"face.23" "face.48" "face.46" "face.32" "face.33" map
```

undo endgroup

/ Inlet Face

undo begingroup

```
face delete "face.73" "face.74" "face.75" "face.76" "face.77" "face.78" \  
"face.104" "face.105" "face.106" "face.107" "face.108" "face.109" \  
"face.134" "face.135" "face.136" "face.137" "face.138" "face.139" \  
"face.164" "face.165" "face.166" "face.167" "face.168" "face.169" onlymesh
```

```
face mesh "face.73" "face.74" "face.75" "face.76" "face.77" "face.78" \  
"face.104" "face.105" "face.106" "face.107" "face.108" "face.109" \  
"face.134" "face.135" "face.136" "face.137" "face.138" "face.139" \  
"face.164" "face.165" "face.166" "face.167" "face.168" "face.169" map
```

undo endgroup

/ Channel

/ Odd Balls

undo begingroup

```
face delete "face.180" "face.185" "face.186" "face.191" "face.192" "face.197" \  
"face.198" "face.203" "face.327" "face.179" onlymesh
```

```
face mesh "face.180" "face.185" "face.186" "face.191" "face.192" "face.197" \  
"face.198" "face.203" "face.327" "face.179" map size 1
```

undo endgroup

/ Little Boxes

```
face mesh "face.321" "face.308" "face.181" "face.182" "face.309" "face.310" \  
"face.188" "face.190" "face.311" "face.312" "face.193" "face.194" \  
"face.313" "face.314" "face.201" "face.202" "face.315" "face.25" map size 1
```

/ Big Boxes

undo begingroup

```
face delete "face.183" "face.184" "face.187" "face.189" "face.195" "face.196" \  
"face.199" "face.200" onlymesh
```

```
face mesh "face.183" "face.184" "face.187" "face.189" "face.195" "face.196" \  
"face.199" "face.200" map
```



```
"face.199" "face.200" map
undo endgroup
```

```
/ Coopered Volumes
```

```
face mesh "face.229" "face.230" "face.241" "face.242" "face.243" "face.248" \
"face.233" "face.232" "face.245" "face.246" "face.247" "face.235" \
"face.236" "face.252" "face.251" "face.250" "face.249" "face.256" \
"face.239" "face.238" "face.253" "face.254" "face.255" "face.244" map size 1
```

```
/ Channel Cuts
```

```
face mesh "face.319" "face.228" "face.318" "face.231" "face.234" "face.237" \
"face.317" "face.240" "face.316" map size 1
```

```
/ Streamwise Normal Planes
```

```
/ Small
```

```
face mesh "face.325" "face.257" "face.258" "face.259" "face.263" "face.264" \
"face.265" "face.329" "face.281" "face.320" "face.272" "face.273" \
"face.274" "face.278" "face.279" "face.280" map size 1
```

```
/ Medium
```

```
face mesh "face.6" "face.323" "face.269" "face.268" map size 1
```

```
/ Large
```

```
face mesh "face.270" "face.271" "face.260" "face.261" "face.262" "face.275" \
"face.276" "face.277" "face.266" "face.267" map size 1
```

```
/ Top Wall Faces
```

```
undo begingroup
```

```
face delete "face.205" "face.206" "face.207" "face.210" "face.214" "face.215" \
"face.217" "face.218" "face.219" "face.222" "face.226" "face.227" "face.5" \
"face.328" "face.331" "face.307" "face.225" "face.224" "face.223" \
"face.221" "face.220" "face.216" "face.213" "face.212" "face.211" \
"face.209" "face.208" "face.204" "face.322" onlymesh
```

```
face mesh "face.205" "face.206" "face.207" "face.210" "face.214" "face.215" \
"face.217" "face.218" "face.219" "face.222" "face.226" "face.227" "face.5" \
"face.328" "face.331" "face.307" "face.225" "face.224" "face.223" \
"face.221" "face.220" "face.216" "face.213" "face.212" "face.211" \
"face.209" "face.208" "face.204" "face.322" "face.324" map
```

```
undo endgroup
```

```
/ Volume Meshing
```

```
/ Dimples
```

```
volume mesh "volume.7" "volume.6" "volume.14" "volume.16" "volume.8" \
"volume.9" "volume.10" "volume.11" "volume.12" "volume.2" "volume.28" \
"volume.29" "volume.38" "volume.3" "volume.22" "volume.23" "volume.24" \
```

```
"volume.25" "volume.26" "volume.27" "volume.45" "volume.46" "volume.55" \  
"volume.4" "volume.39" "volume.40" "volume.41" "volume.42" "volume.43" \  
"volume.44" "volume.62" "volume.63" "volume.72" "volume.5" "volume.56" \  
"volume.57" "volume.58" "volume.59" "volume.60" "volume.61" map size 1
```

```
/ Cooper Over Dimples
```

```
volume mesh "volume.73" cooper source "face.177" "face.65" "face.66" \  
"face.77" "face.76" "face.75" "face.74" "face.73" "face.78" size 1  
volume mesh "volume.74" cooper source "face.178" "face.102" "face.103" \  
"face.108" "face.107" "face.106" "face.109" "face.105" "face.104" size 1  
volume mesh "volume.75" cooper source "face.176" "face.125" "face.127" \  
"face.138" "face.137" "face.136" "face.135" "face.134" "face.139" size 1  
volume mesh "volume.76" cooper source "face.175" "face.157" "face.156" \  
"face.169" "face.165" "face.164" "face.168" "face.167" "face.166" size 1
```

```
/ Odd Balls
```

```
volume mesh "volume.103" "Channel" map size 1  
volume mesh "volume.84" "volume.83" "volume.89" "volume.90" "volume.96" \  
"volume.95" map size 1
```

```
/ Small Boxes
```

```
volume mesh "volume.102" "volume.77" "volume.78" "volume.79" "volume.81" \  
"volume.85" "volume.88" "volume.91" "volume.93" "volume.97" "volume.100" \  
"volume.105" "volume.101" "volume.104" map size 1
```

```
/ Big Boxes
```

```
undo begingroup  
volume delete "volume.80" "volume.82" "volume.86" "volume.87" "volume.92" \  
"volume.94" "volume.98" "volume.99" onlymesh  
volume mesh "volume.80" "volume.82" "volume.86" "volume.87" "volume.92" \  
"volume.94" "volume.98" "volume.99" map size 1  
undo endgroup
```

```
/ BOUNDARY CONDITIONS
```

```
/ Walls
```

```
physics create "DIMPLE_WALLS" btype "WALL" face "face.7" "face.37" "face.35" \  
"face.16" "face.34" "face.36" "face.27" "face.26" "face.17" "face.41" \  
"face.39" "face.18" "face.38" "face.40" "face.29" "face.28" "face.20" \  
"face.45" "face.43" "face.21" "face.42" "face.44" "face.31" "face.30" \  
"face.23" "face.49" "face.47" "face.24" "face.46" "face.48" "face.33" \  
"face.32"
```

```
physics create "BOTTOM_WALL" btype "WALL" face "face.308" "face.180" \  
"face.179" "face.321" "face.183" "face.184" "face.310" "face.186" \  
"face.188" "face.190" "face.311" "face.191" "face.195" "face.196" \  
"face.314" "face.198" "face.201" "face.202" "face.315" "face.203" \  
"face.327" "face.25" "face.200" "face.199" "face.197" "face.313" "face.194" \  
"
```

```

"face.193" "face.312" "face.192" "face.189" "face.187" "face.185" \
"face.309" "face.182" "face.181"
physics create "SIDE_WALLS" btype "WALL" face "face.4" "face.285" "face.284" \
"face.289" "face.287" "face.293" "face.292" "face.297" "face.296" \
"face.301" "face.304" "face.305" "face.299" "face.283" "face.3" "face.286" \
"face.288" "face.290" "face.291" "face.294" "face.295" "face.298" \
"face.300" "face.302" "face.303" "face.306"
physics create "TOP_WALL" btype "WALL" face "face.204" "face.322" "face.324" \
"face.205" "face.206" "face.207" "face.210" "face.214" "face.215" \
"face.217" "face.218" "face.219" "face.222" "face.226" "face.227" \
"face.328" "face.5" "face.331" "face.307" "face.225" "face.224" "face.223" \
"face.221" "face.220" "face.216" "face.213" "face.212" "face.211" \
"face.209" "face.208" "face.177" "face.178" "face.176" "face.175"

/ Periodic Inlet and Outlet
physics create "IE_1" btype "PERIODIC" face "face.1" "face.325"
physics create "IE_2" btype "PERIODIC" face "face.326" "face.6"
physics create "IE_3" btype "PERIODIC" face "face.282" "face.323"
physics create "IE_4" btype "PERIODIC" face "face.330" "face.281"

/ Interior
/ Double Dimple Cuts
physics create "DD_INT" btype "INTERIOR" face "face.159" "face.146" \
"face.162" "face.149" "face.129" "face.116" "face.132" "face.126" "face.95" \
"face.86" "face.98" "face.93" "face.68" "face.79" "face.71" "face.64"
physics create "DIMPLE_INT" btype "INTERIOR" face "face.143" "face.144" \
"face.145" "face.140" "face.141" "face.142" "face.153" "face.154" \
"face.155" "face.150" "face.151" "face.152" "face.148" "face.147" \
"face.160" "face.161" "face.163" "face.158" "face.113" "face.114" \
"face.115" "face.110" "face.111" "face.112" "face.122" "face.123" \
"face.124" "face.119" "face.120" "face.121" "face.118" "face.117" \
"face.131" "face.133" "face.128" "face.130" "face.83" "face.84" "face.85" \
"face.80" "face.81" "face.82" "face.90" "face.101" "face.91" "face.100" \
"face.92" "face.87" "face.88" "face.89" "face.97" "face.99" "face.94" \
"face.96" "face.53" "face.54" "face.55" "face.50" "face.51" "face.52" \
"face.173" "face.172" "face.63" "face.170" "face.171" "face.174" "face.70" \
"face.72" "face.67" "face.69" "face.57" "face.56"
physics create "DIMPLE_INLET" btype "INTERIOR" face "face.157" "face.156" \
"face.166" "face.167" "face.168" "face.169" "face.164" "face.165" \
"face.127" "face.125" "face.137" "face.138" "face.139" "face.134" \
"face.135" "face.136" "face.103" "face.102" "face.107" "face.108" \
"face.109" "face.104" "face.105" "face.106" "face.65" "face.66" "face.76" \
"face.77" "face.78" "face.73" "face.74" "face.75"

/ Channel Cuts
physics create "USELESS_INT" btype "INTERIOR" face "face.316" "face.240" \
"face.317" "face.280" "face.279" "face.278" "face.265" "face.264" \

```

```

"face.263" "face.274" "face.273" "face.272" "face.259" "face.258" \
"face.257" "face.318" "face.319" "face.320" "face.228" "face.231" \
"face.234" "face.237" "face.329" "face.268" "face.269"
physics create "DS_1" btype "INTERIOR" face "face.277" "face.262" "face.271"
physics create "DS_2" btype "INTERIOR" face "face.267" "face.276" "face.261" \
"face.270"
physics create "DS_3" btype "INTERIOR" face "face.266" "face.275" "face.260"
physics create "DIMPLE_SIDES" btype "INTERIOR" face "face.255" "face.254" \
"face.238" "face.239" "face.251" "face.250" "face.235" "face.236" \
"face.232" "face.233" "face.246" "face.247" "face.242" "face.243" \
"face.229" "face.230"
physics create "DIMPLE_CHANNEL_INLET" btype "INTERIOR" face "face.256" \
"face.252" "face.248" "face.241"
physics create "DIMPLE_CHANNEL_EXIT" btype "INTERIOR" face "face.253" \
"face.249" "face.245" "face.244"

```

#### / CONTINUUM TYPES

```

physics create "DIMPLE_1" ctype "FLUID" volume "volume.8" "volume.9" \
"volume.10" "volume.11" "volume.12" "volume.2" "volume.7" "volume.6" \
"volume.14" "volume.16"
physics create "DIMPLE_2" ctype "FLUID" volume "volume.22" "volume.23" \
"volume.24" "volume.25" "volume.26" "volume.27" "volume.28" "volume.29" \
"volume.38" "volume.3"
physics create "DIMPLE_3" ctype "FLUID" volume "volume.39" "volume.40" \
"volume.41" "volume.42" "volume.43" "volume.44" "volume.45" "volume.46" \
"volume.4" "volume.55"
physics create "DIMPLE_4" ctype "FLUID" volume "volume.56" "volume.57" \
"volume.58" "volume.59" "volume.60" "volume.61" "volume.62" "volume.63" \
"volume.72" "volume.5"
physics create "CHANNEL" ctype "FLUID" volume "volume.102" "volume.77" \
"volume.103" "volume.78" "volume.79" "volume.81" "volume.83" "volume.80" \
"volume.82" "volume.84" "volume.86" "volume.87" "volume.85" "volume.88" \
"volume.89" "volume.90" "volume.92" "volume.91" "volume.93" "volume.95" \
"volume.94" "volume.96" "volume.98" "volume.99" "volume.97" "volume.100" \
"volume.105" "Channel" "volume.104" "volume.101"
physics create "CHANNEL_DIMP" ctype "FLUID" volume "volume.73" "volume.74" \
"volume.75" "volume.76"

```

## D.2. Fluent Run Setup Journal (RANS)

```
#$ -cwd
#$ -l fluent=1
#$ -l mem_free=6G
#$ -ckpt fluent_ckpt
#$ -c 6:00:00
#$ -pe fluent_pe 2
fluent -sge -g -t $NSLOTS 3ddp <<EOF
file/read-case DD_LES_mesh_3.msh
grid/scale 0.001 0.001 0.001
grid/check
define/models/viscous ke-realizable y
define/periodic-conditions/pressure-gradient-specification -277 0 0 -1
solve/set/discretization-scheme/pressure 12
solve/set/discretization-scheme/mom 1
solve/set/discretization-scheme/k 1
solve/set/discretization-scheme/epsilon 1
solve/set/under-relaxation/body-force 0.5
solve/set/under-relaxation/density 0.5
solve/set/under-relaxation/pressure 0.15
solve/set/under-relaxation/mom 0.35
solve/set/under-relaxation/k 0.4
solve/set/under-relaxation/epsilon 0.4
solve/set/under-relaxation/turb-viscosity 0.5
solve/initialize/compute-defaults/all-zones
solve/initialize/set-defaults pressure 0
solve/initialize/set-defaults x-velocity 0
solve/initialize/set-defaults y-velocity 0
solve/initialize/set-defaults z-velocity -21
solve/initialize/list-defaults
solve/initialize/initialize-flow
file/write-case-data DD_LES_40k_run.gz
exit
yes
EOF
```

### D.3. LES 'Rampup' Journal

```
#$ -cwd
#$ -l fluent=1
#$ -l mem_free=3G
#$ -ckpt fluent_ckpt
#$ -c 5:00:00
#$ -pe fluent_pe 6
fluent -sge -g -t $NSLOTS 3ddp <<EOF
file/read-case-data DD_LES_40k_sss1
yes
solve/set/under-relaxation pressure 0.3
solve/set/under-relaxation density 0.9
solve/set/under-relaxation body-force 0.9
solve/set/under-relaxation mom 0.6
solve/monitors/residual/convergence-criteria 0.00001 0.000001 0.000001
0.000001
solve/initialize/init-flow-statistics
solve/set/time-step 0.0000055
solve/set/reporting-interval 5
solve/dual-time-iterate 500 20
Y
Y
Y
Y
file/write-case-data DD_LES_40k_ss3
Y
exit
yes
EOF
```



#### D.4. LES 'Statistic' Journal

```
#$ -cwd
#$ -l fluent=1
#$ -l mem_free=3G
#$ -ckpt fluent_ckpt
#$ -c 5:00:00
#$ -pe fluent_pe 6
fluent -sge -g -t $NSLOTS 3ddp <<EOF
file/read-case-data DD_LES_40k_ss2
yes
solve/set/under-relaxation pressure 0.3
solve/set/under-relaxation density 0.9
solve/set/under-relaxation body-force 0.9
solve/set/under-relaxation mom 0.6
solve/monitors/residual/convergence-criteria 0.00001 0.000001 0.000001
0.000001
solve/set/data-sampling y 20 y y
solve/initialize/init-flow-statistics
solve/set/time-step 0.0000055
solve/set/reporting-interval 5
solve/dual-time-iterate 4400 20
Y
Y
Y
Y
file/write-case-data DD_LES_40k_ss2
Y
exit
yes
EOF
```

D.5. LES 'Pictures-Out' Journal

```
#$ -cwd
#$ -l fluent=1
#$ -l mem_free=3G
#$ -ckpt fluent_ckpt
#$ -c 5:00:00
#$ -pe fluent_pe 6
fluent -sge -g -t $NSLOTS 3ddp <<EOF
file/read-case-data DD_LES_40k_ss2
yes
solve/set/under-relaxation pressure 0.3
solve/set/under-relaxation density 0.9
solve/set/under-relaxation body-force 0.9
solve/set/under-relaxation mom 0.6
solve/monitors/residual/convergence-criteria 0.00001 0.000001 0.000001
0.000001
file/auto-save/append-file-name-with time-step 6
file/auto-save/data-frequency 44
file/auto-save/data-frequency 0
file/auto-save/overwrite-existing-files n
solve/set/time-step 0.0000055
solve/set/reporting-interval 5
solve/dual-time-iterate 221 20
Y
Y
Y
Y
file/write-case-data DD_LES_40k_ss2
Y
exit
yes
EOF
```

**APPENDIX E: REDUCED DOMAIN RANS – FULL RESULT SET**

E.1. Reynolds Number = 40000

## Surface Nusselt Number

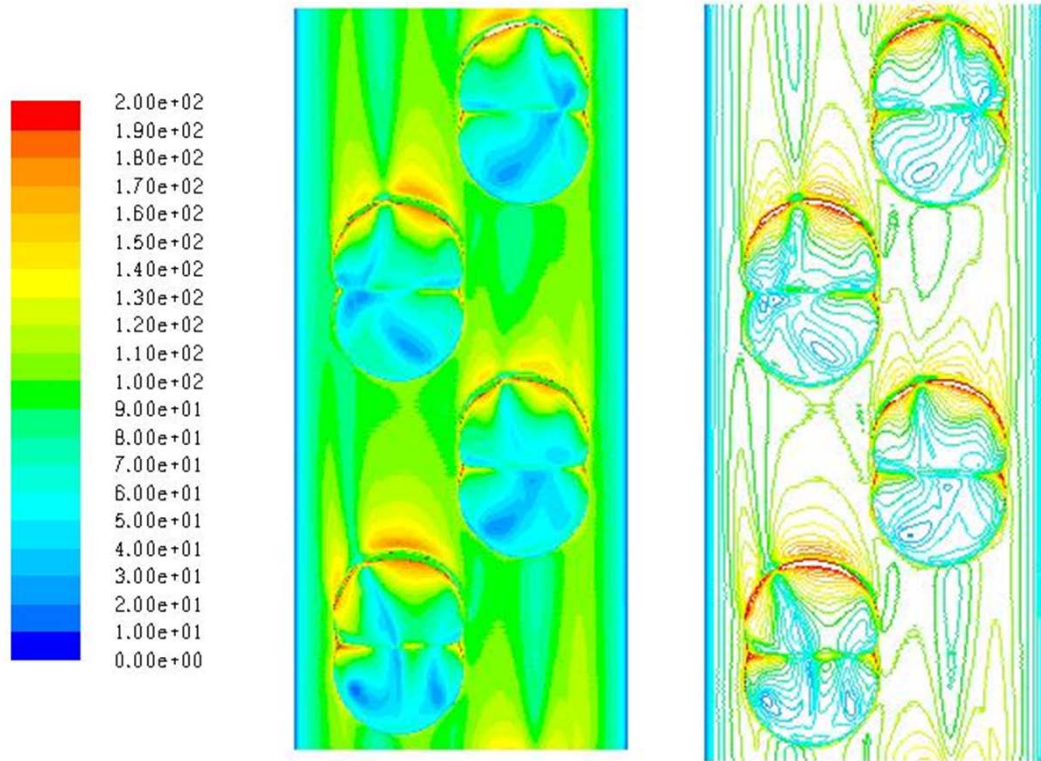


Figure E.1: Surface Heat Transfer Coefficient Contours, Bottom Wall –  $Re = 40000$

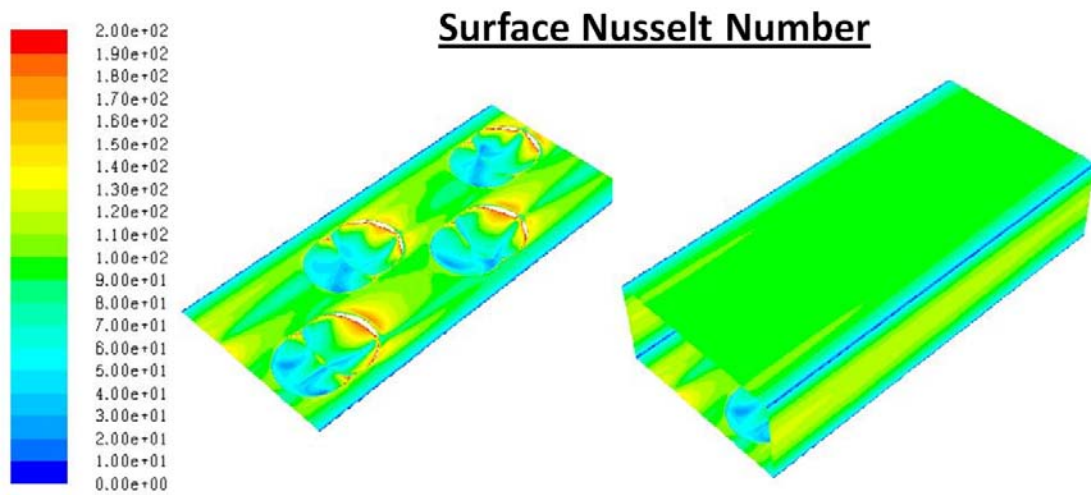
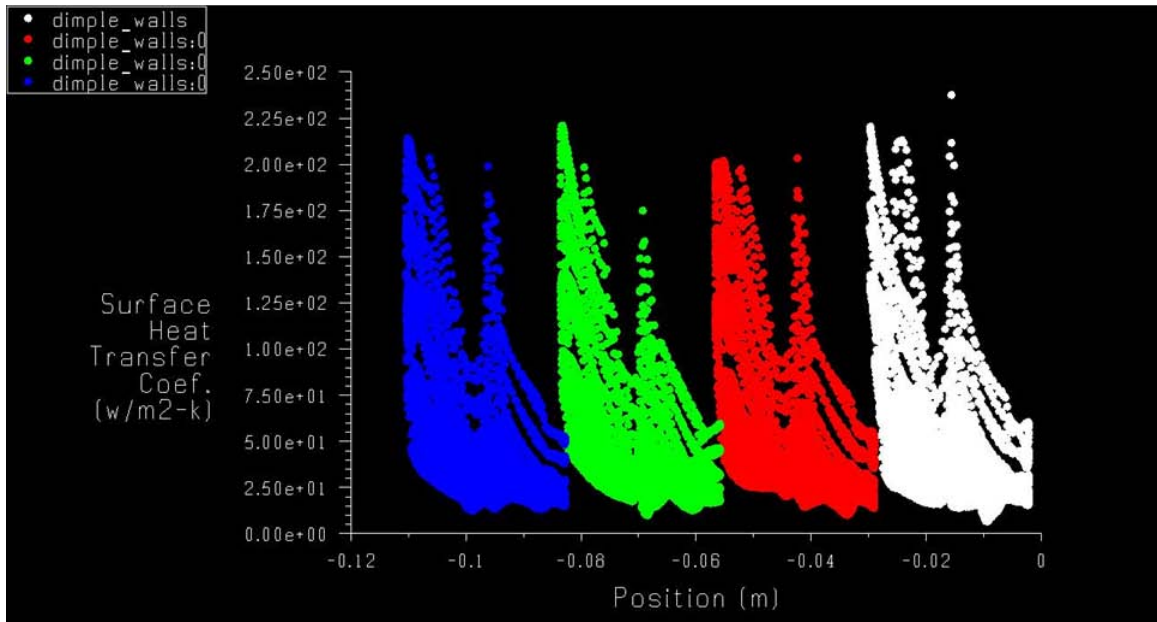


Figure E.2: Surface Heat Transfer Coefficient Contours –  $Re = 40000$



**Figure E.3: Surface Heat Transfer Coefficient as a Function of Streamwise Distance – Re = 40000**



# Static Pressure (Gauge) [Pa]

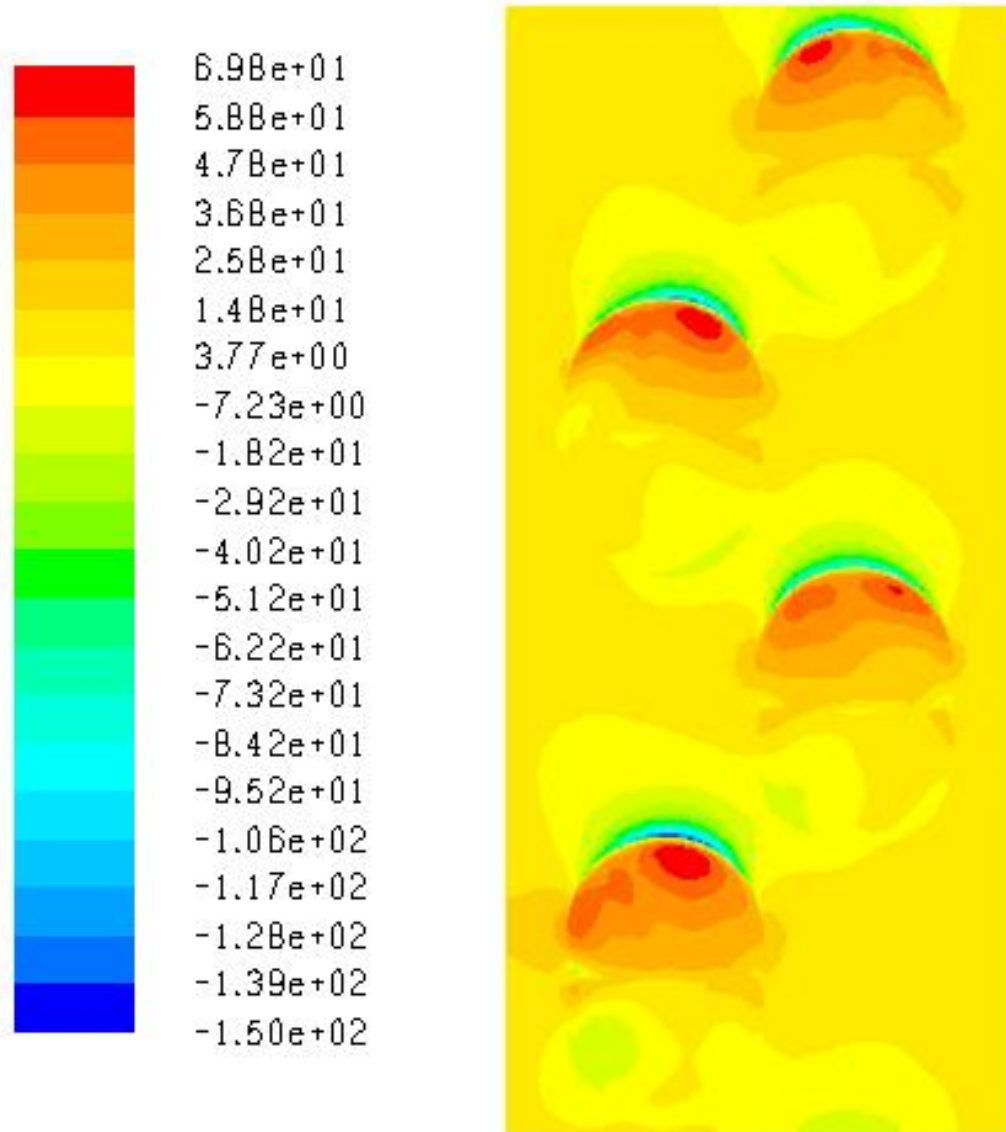


Figure E.4: Static Pressure Distribution over the Bottom Wall of the Channel – Re = 40000

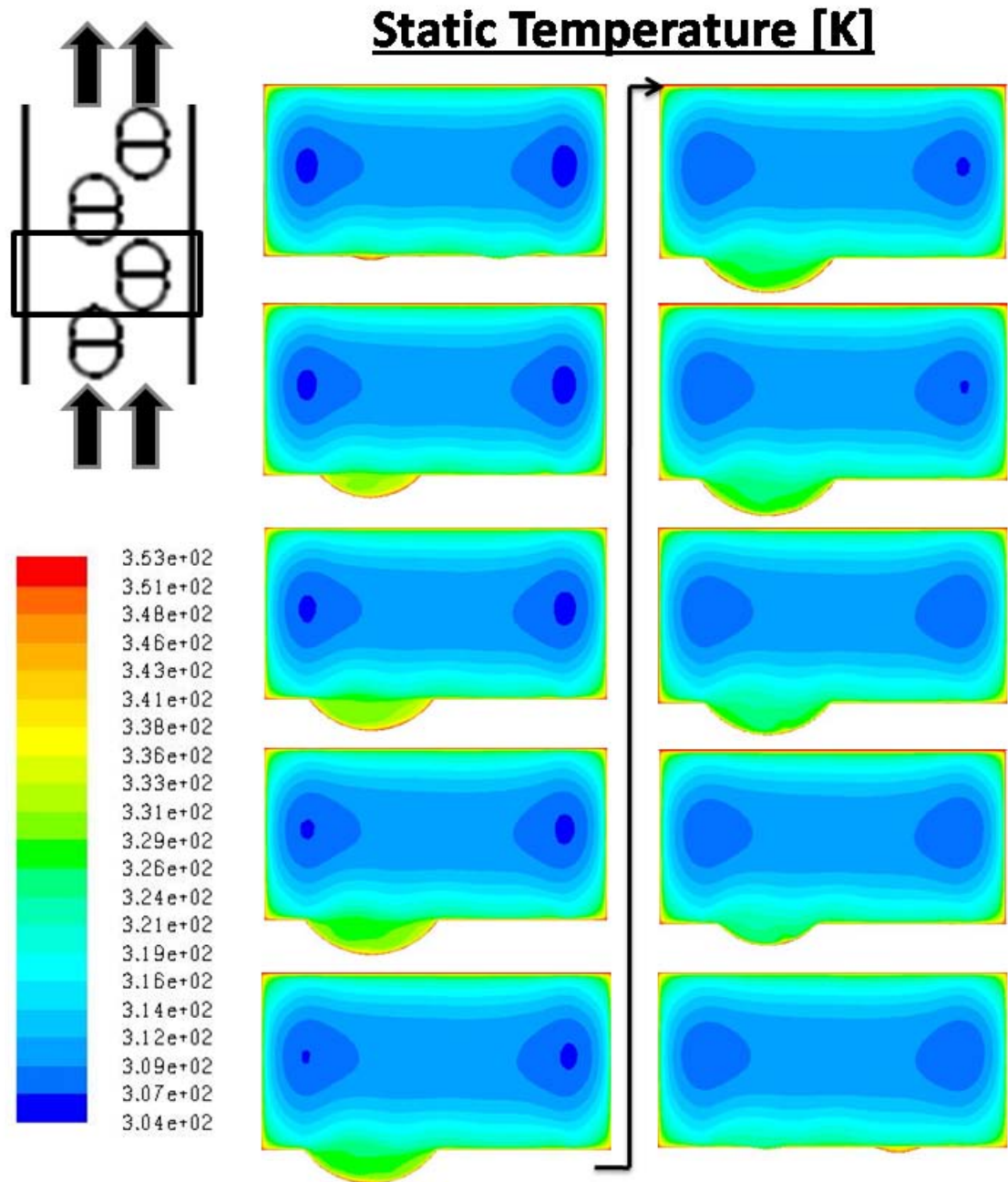


Figure E.5: Spanwise Profiles of Static Temperature –  $Re = 40000$

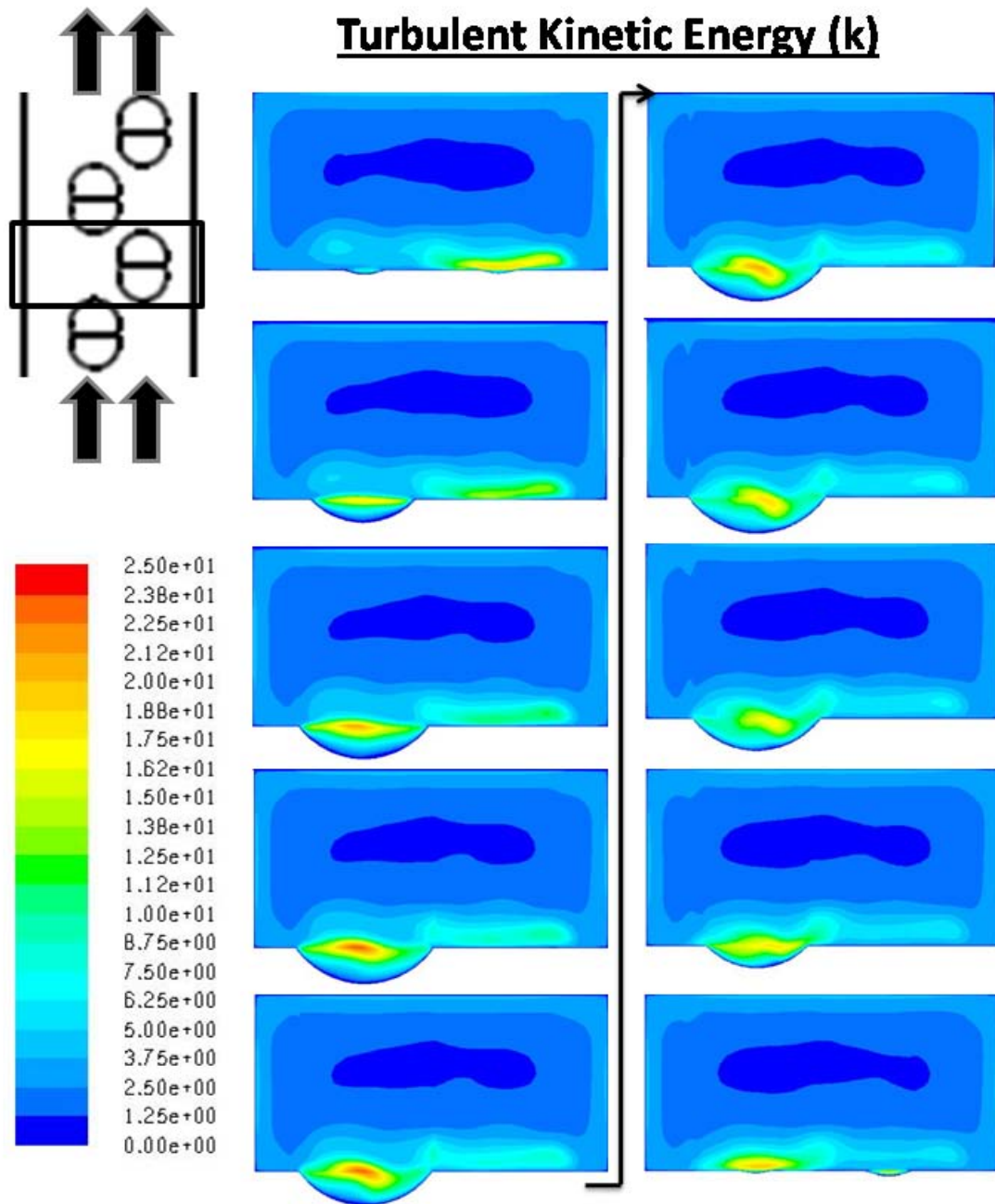


Figure E.6: Spanwise Profiles of Turbulent Kinetic Energy –  $Re = 40000$

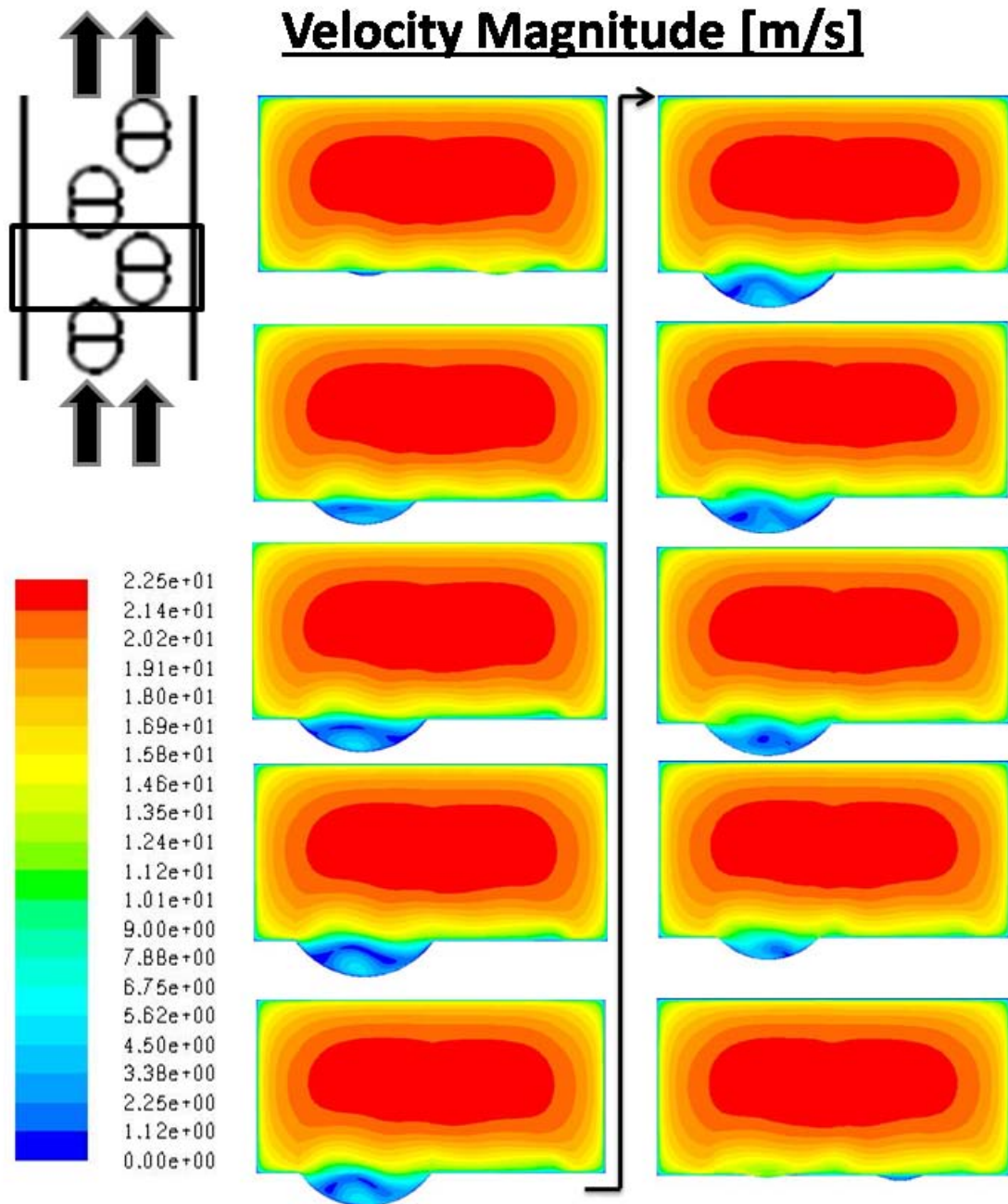


Figure E.7: Spanwise Profiles of Velocity Magnitude –  $Re = 40000$

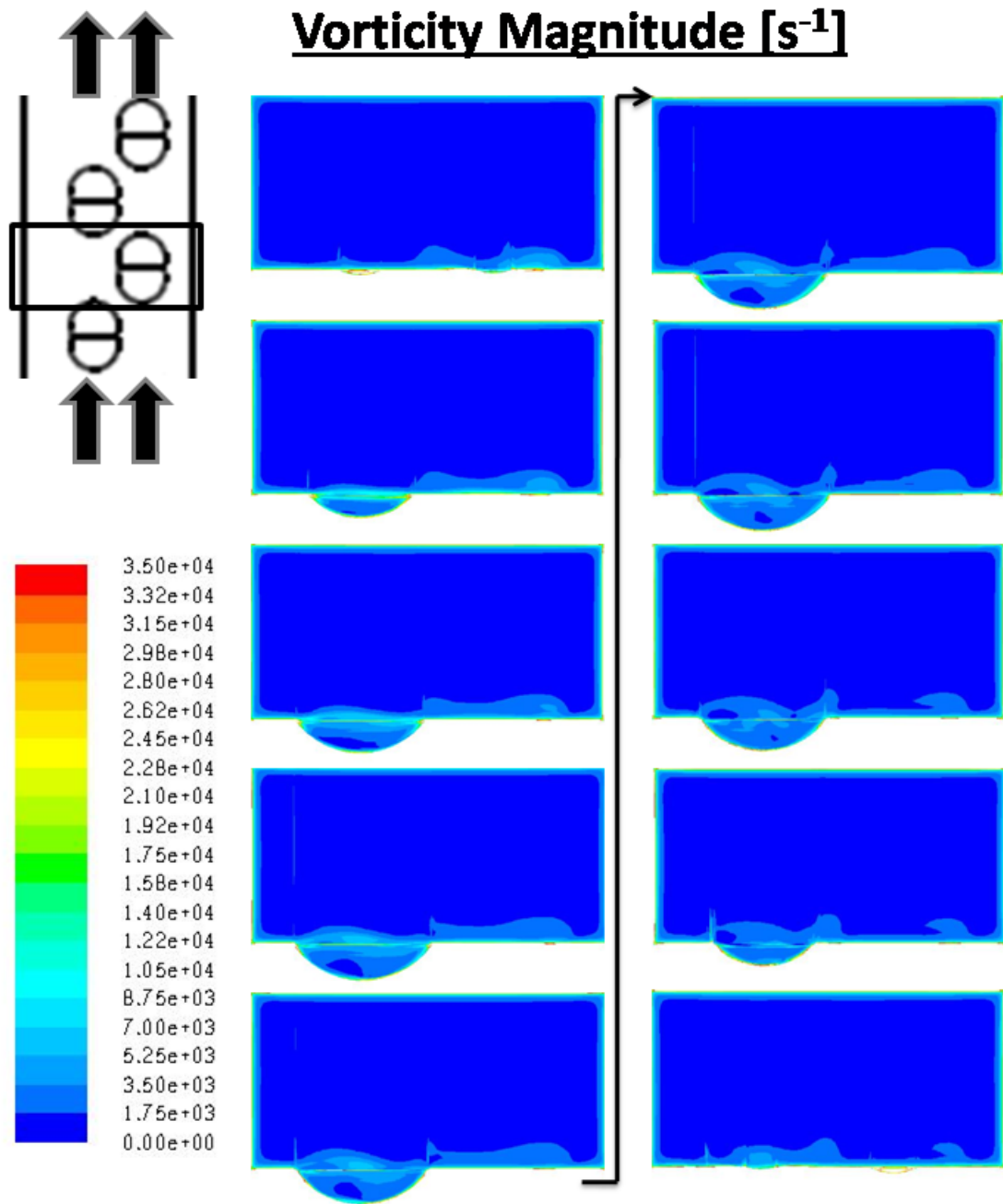
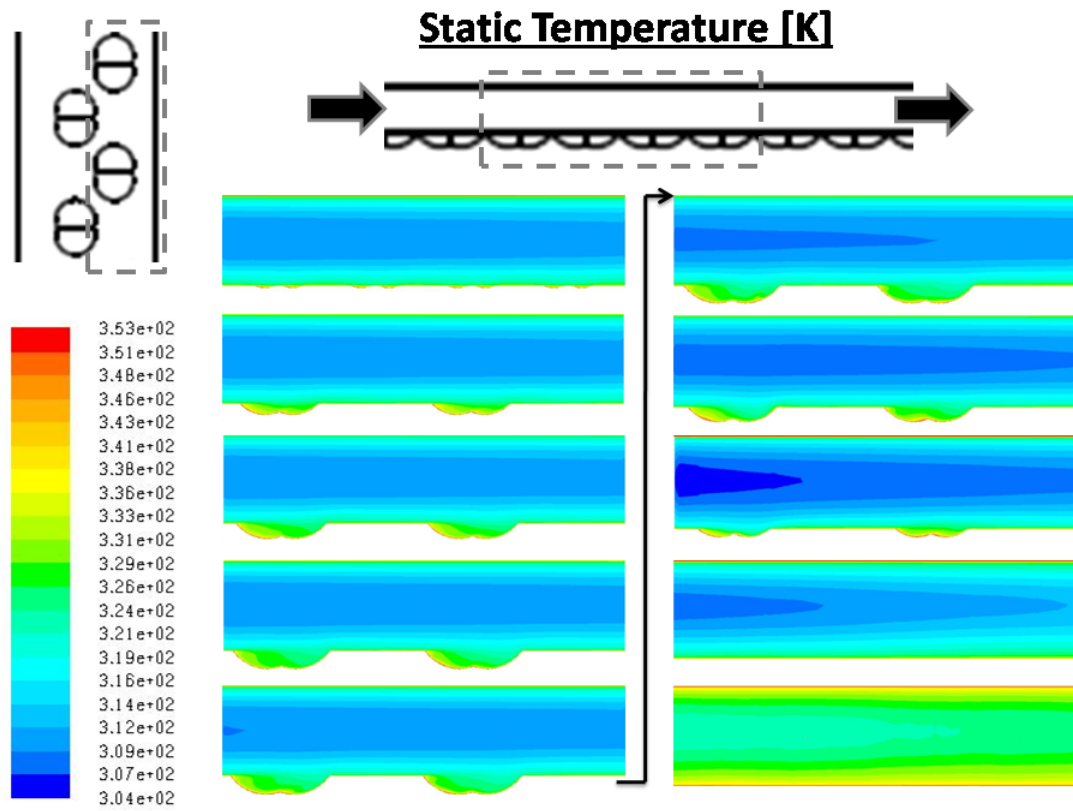
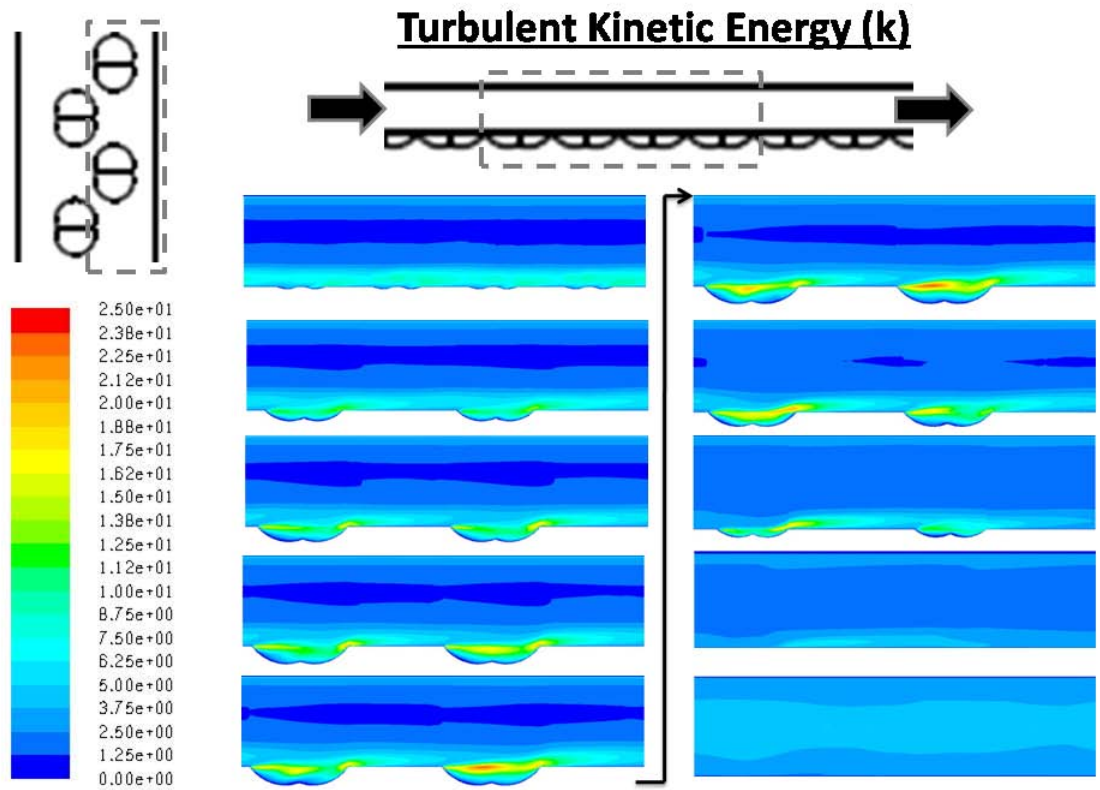


Figure E.8: Spanwise Profiles of Vorticity Magnitude – Re = 40000



**Figure E.9: Streamwise Profiles of Static Temperature – Re = 40000**





**Figure E.10: Streamwise Profiles of Turbulent Kinetic Energy – Re = 40000**

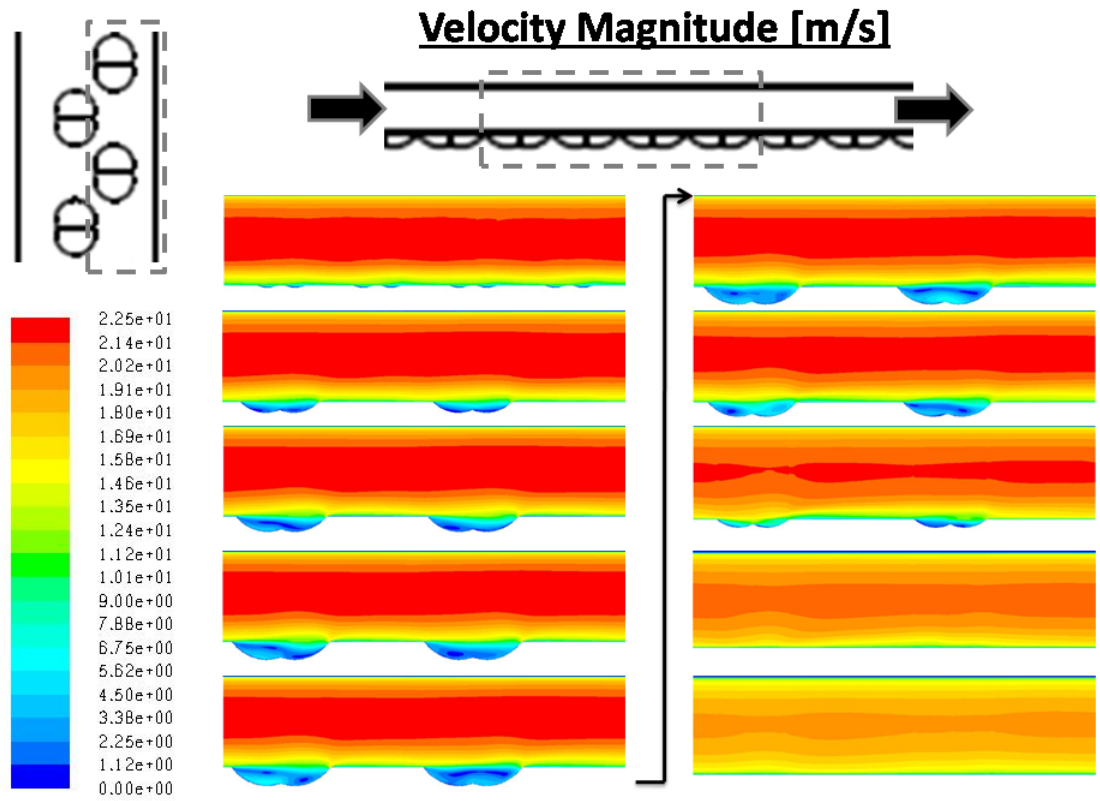


**Figure E.11: Streamwise Profiles of Velocity Magnitude – Re = 40000**



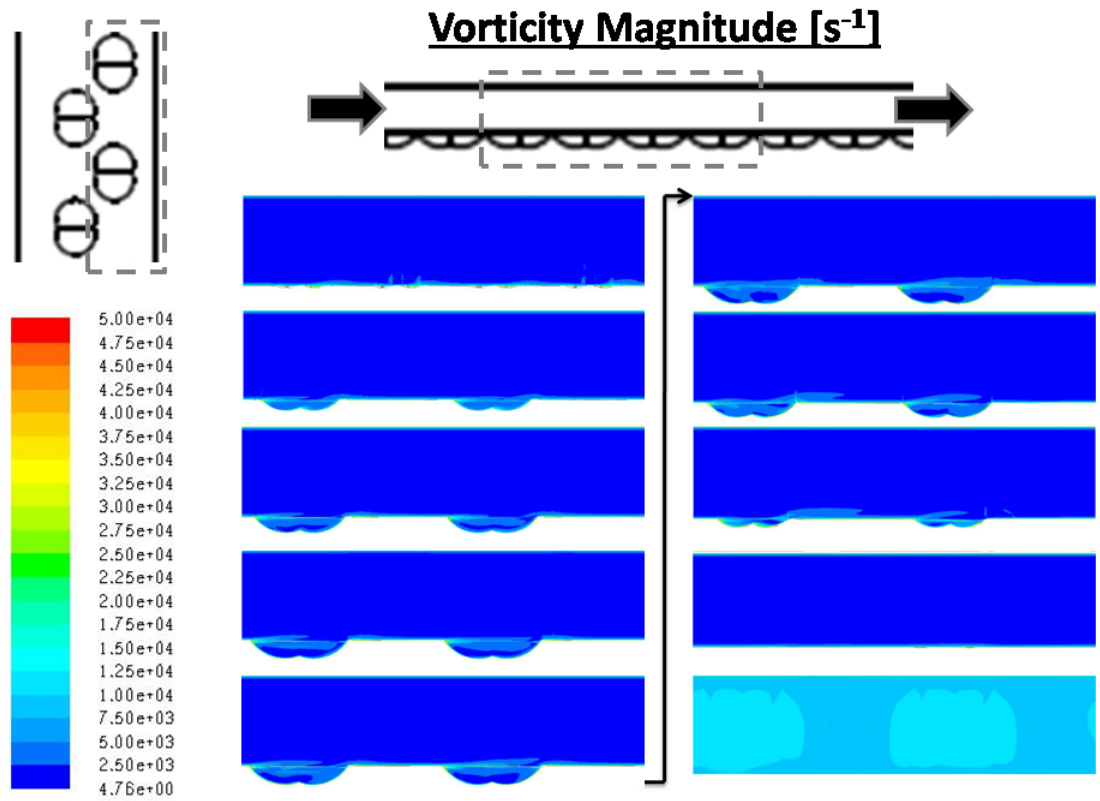


Figure E.12: Streamwise Profiles of Vorticity Magnitude – Re = 40000

E.2. Reynolds Number = 30000

# Surface Nusselt Number

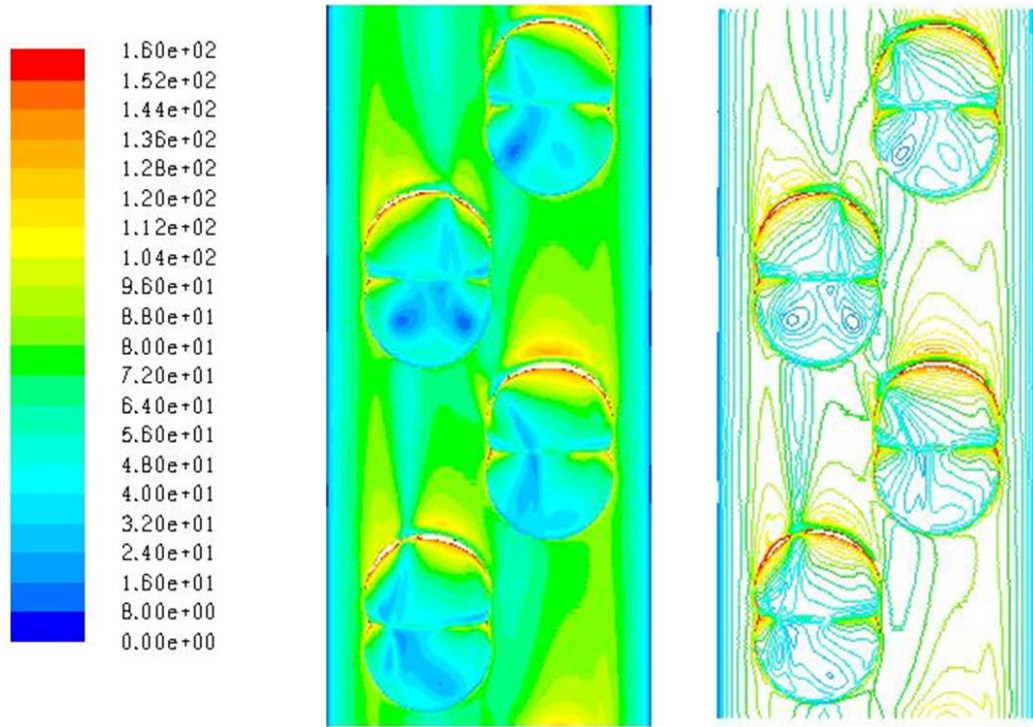
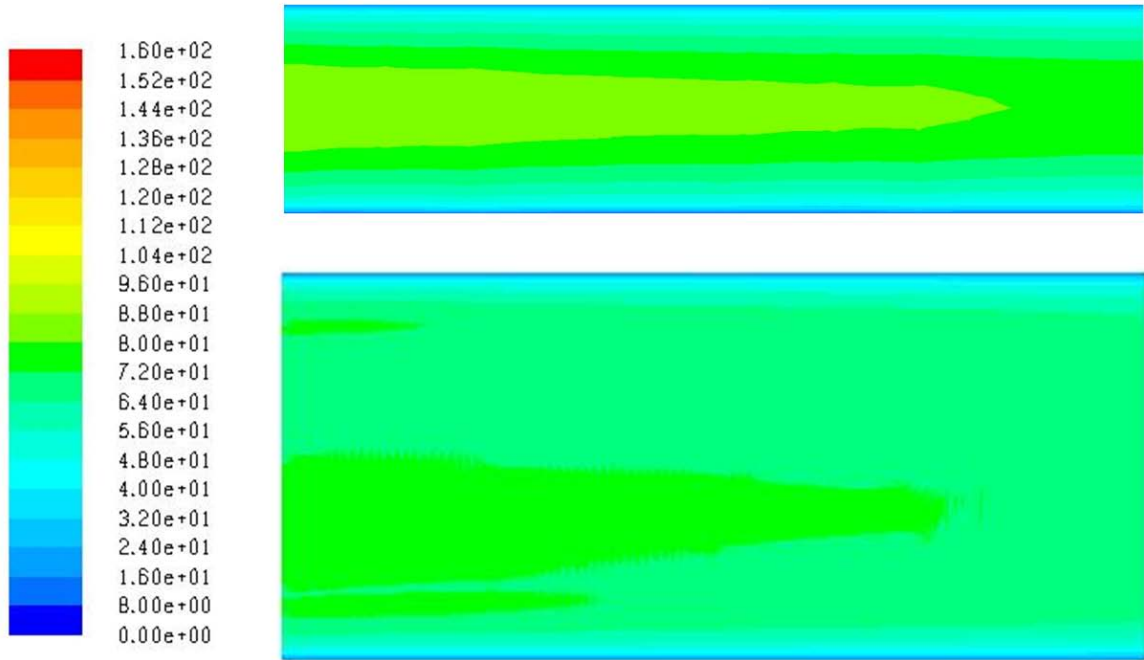
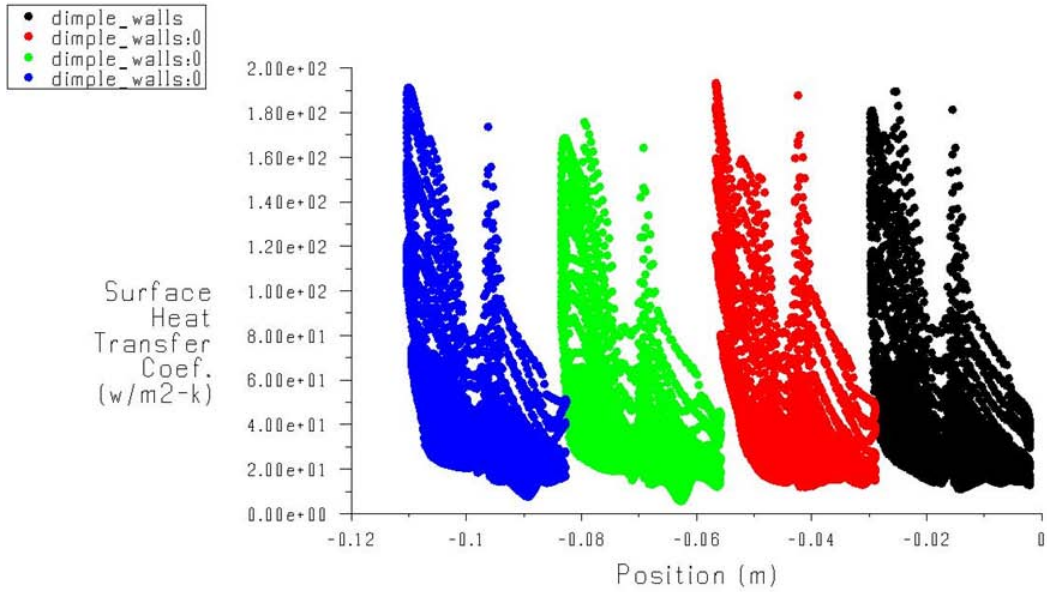


Figure E.13: Surface Heat Transfer Coefficient Contours, Bottom Wall– Re = 30000

## Surface Nusselt Number



**Figure E.14: Surface Heat Transfer Coefficient Contours, Side and Top Walls– Re = 30000**



**Figure E.15: Surface Heat Transfer Coefficient as a Function of Streamwise Distance – Re = 30000**

# Static Pressure (Gauge) [Pa]

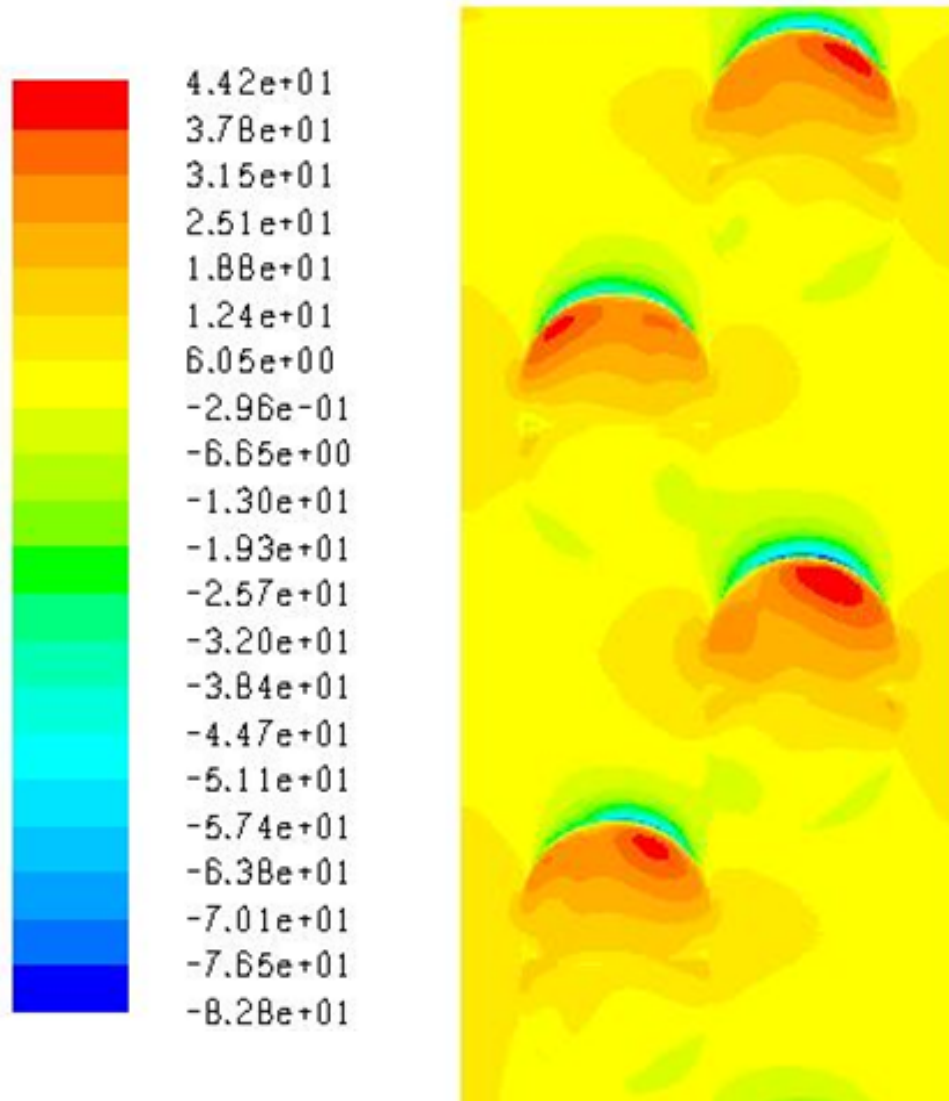
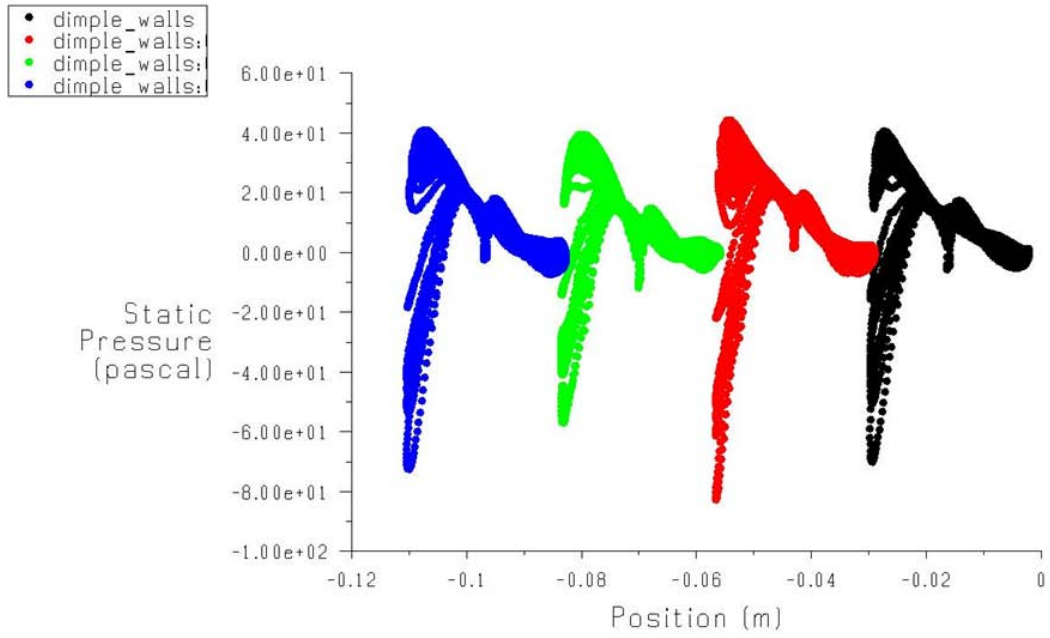


Figure E.16: Static Pressure Distribution over the Bottom Wall of the Channel –  $Re = 30000$



**Figure E.17: Static Pressure on the Dimple Surface as a Function of Streamwise Distance –  $Re = 30000$**

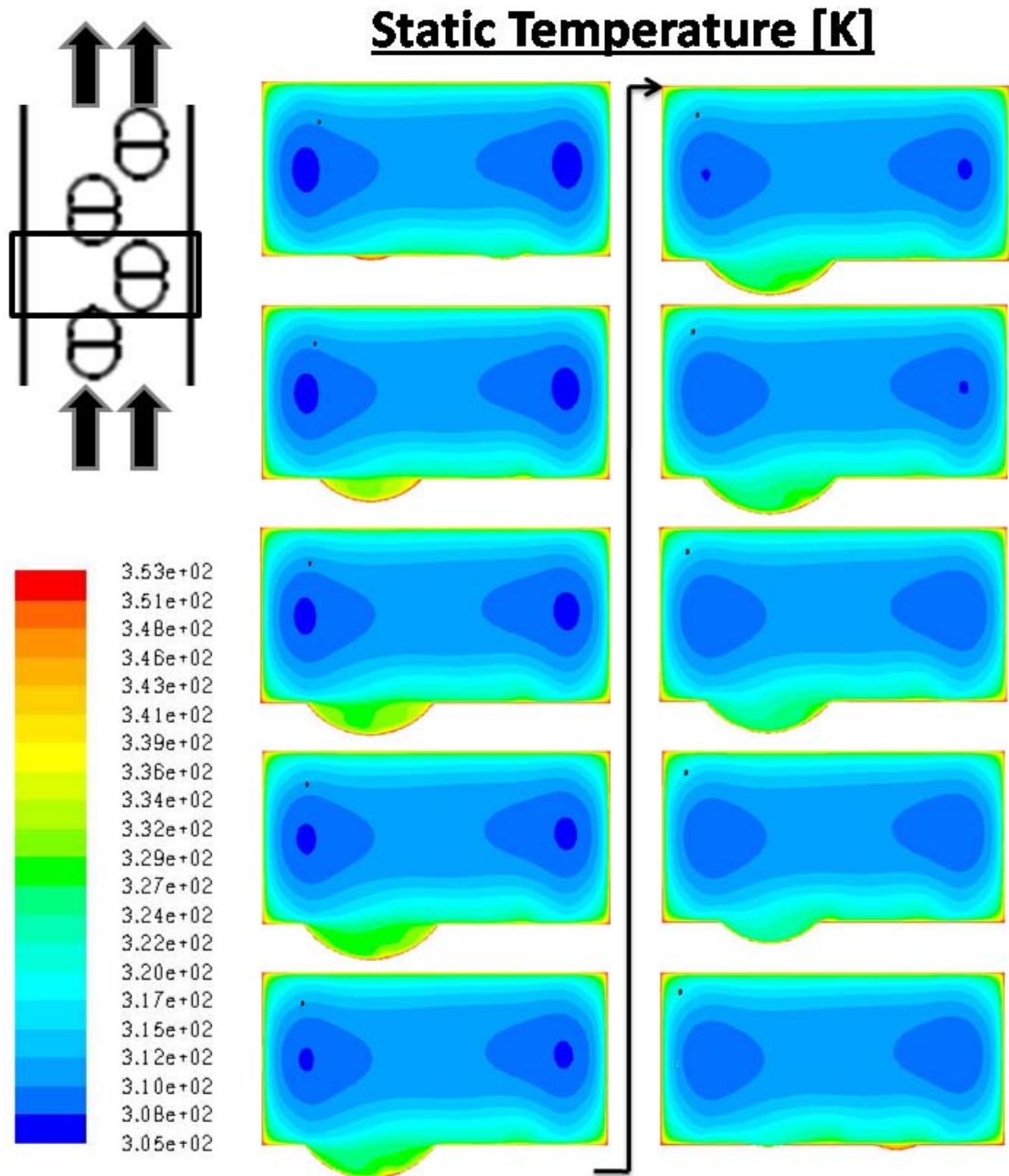


Figure E.18: Spanwise Profiles of Static Temperature –  $Re = 30000$



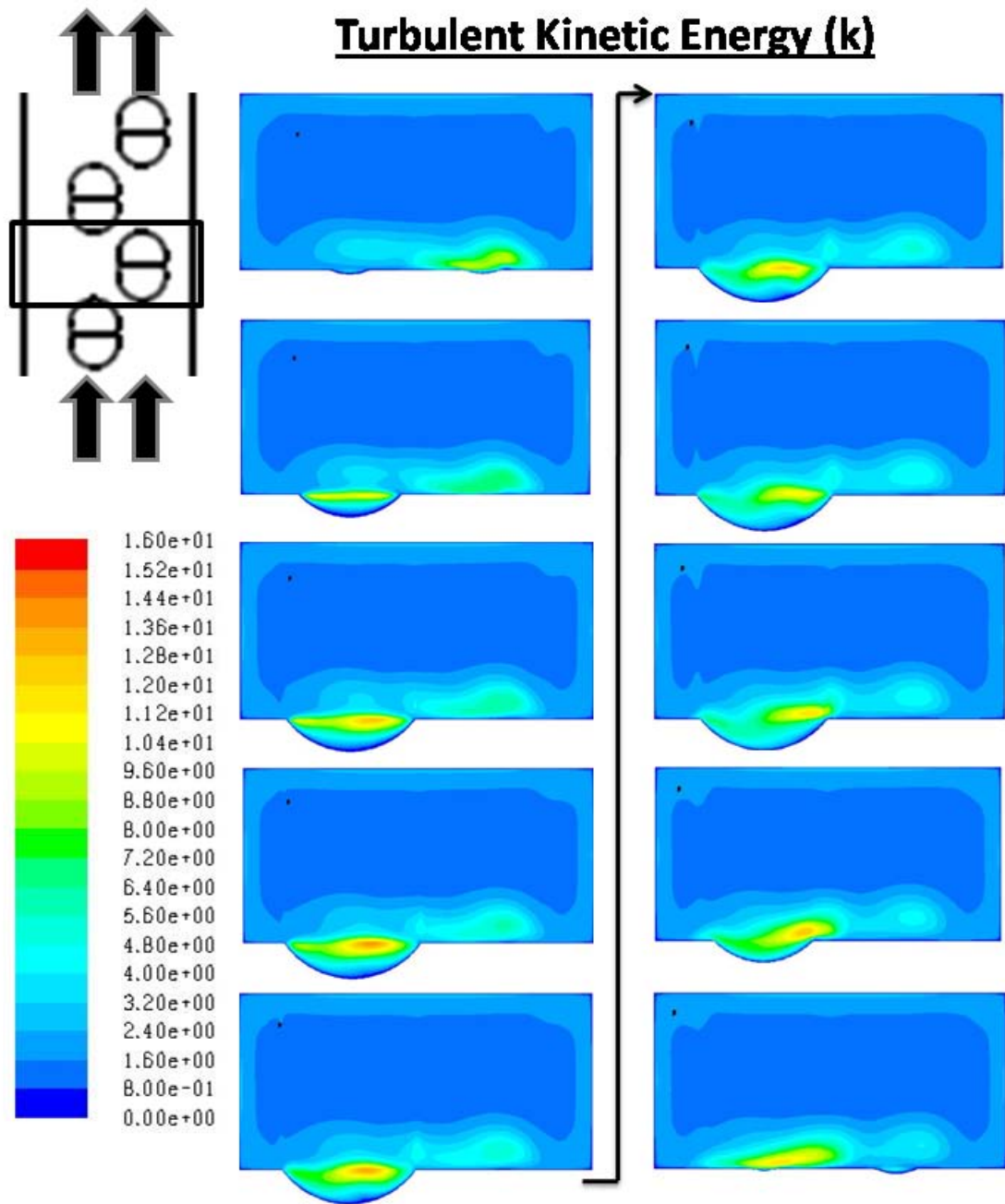


Figure E.19: Spanwise Profiles of Turbulent Kinetic Energy –  $Re = 30000$



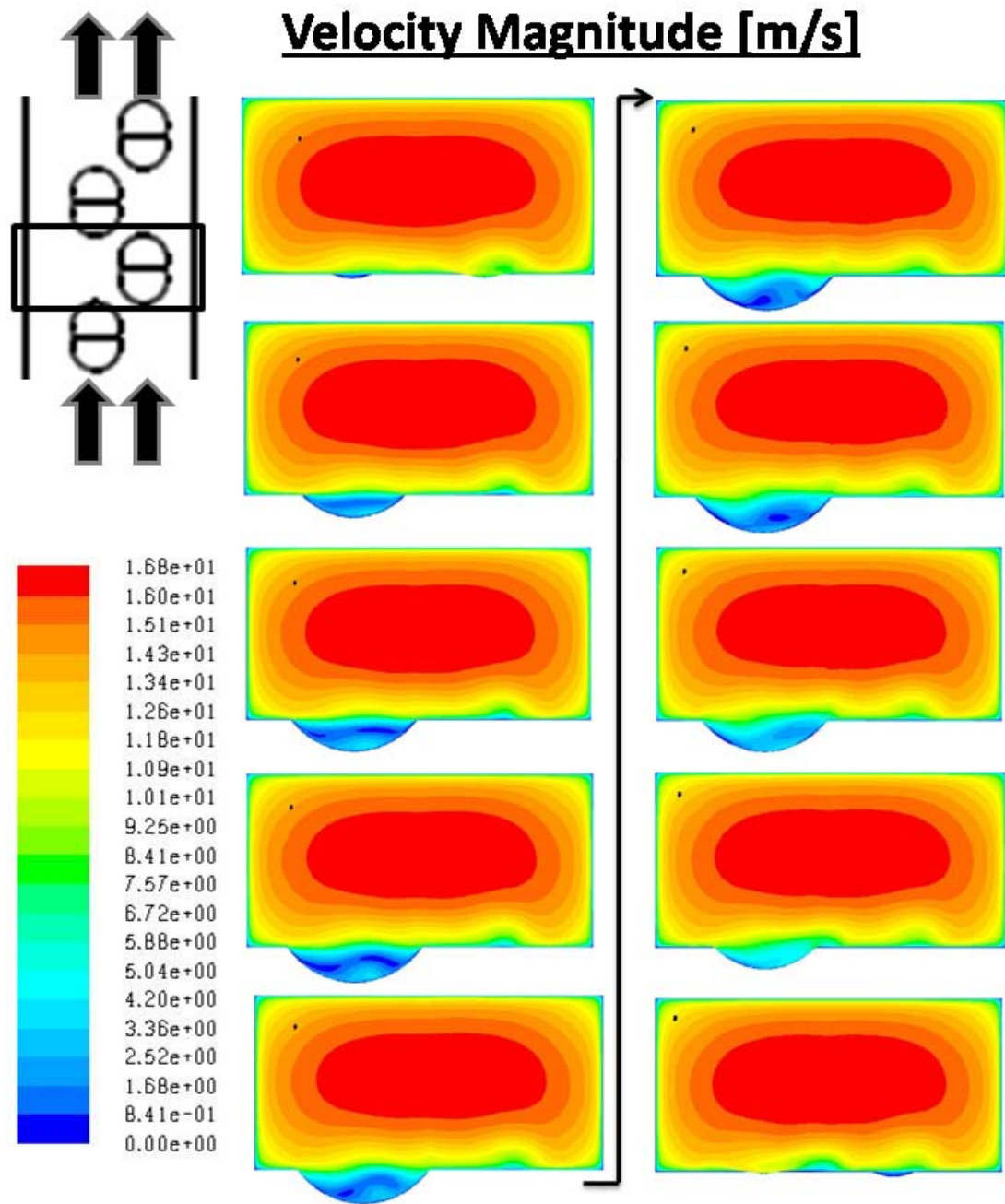
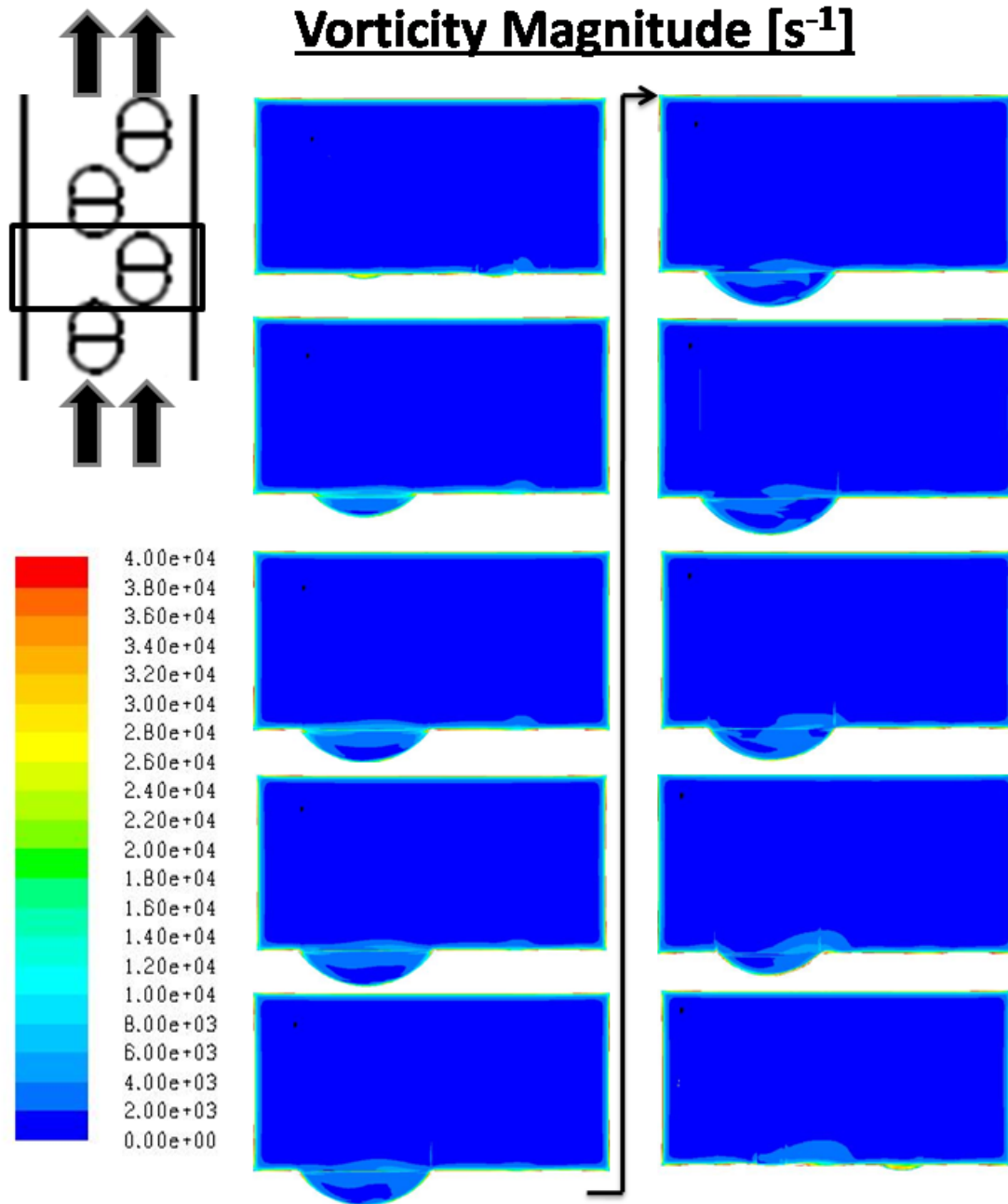
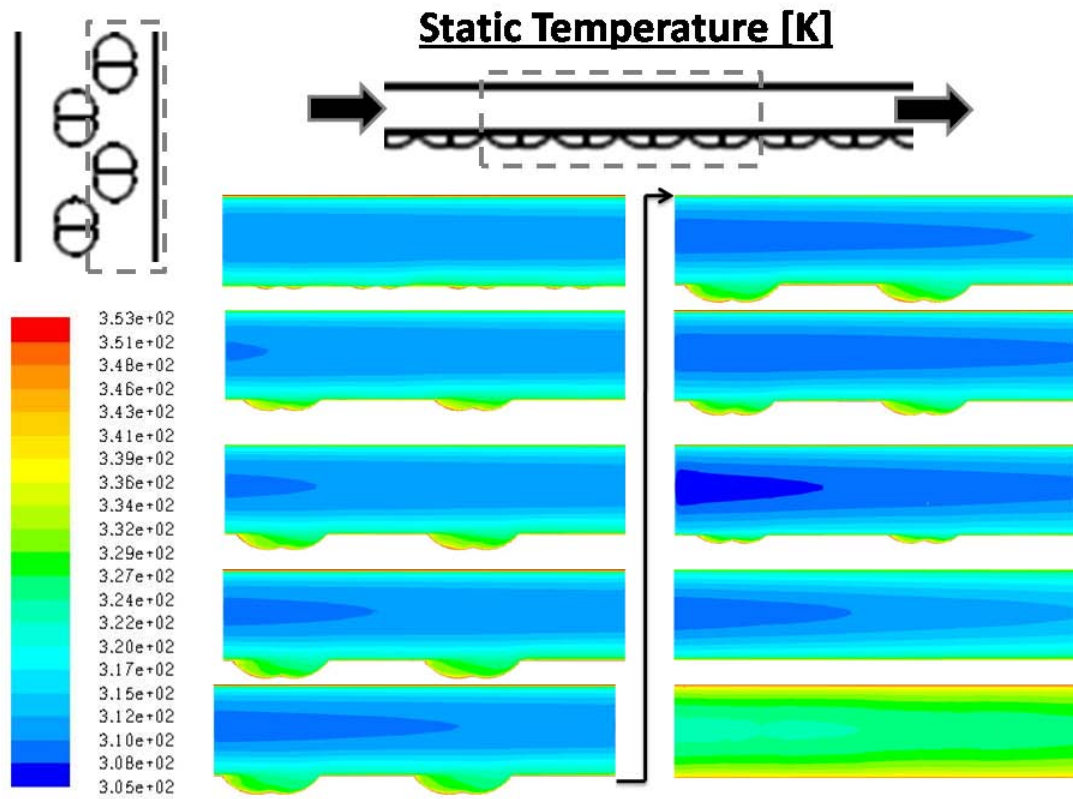


Figure E.20: Spanwise Profiles of Velocity Magnitude –  $Re = 30000$



**Figure E.21: Spanwise Profiles of Vorticity Magnitude –  $Re = 30000$**



**Figure E.22: Streamwise Profiles of Static Temperature – Re = 30000**

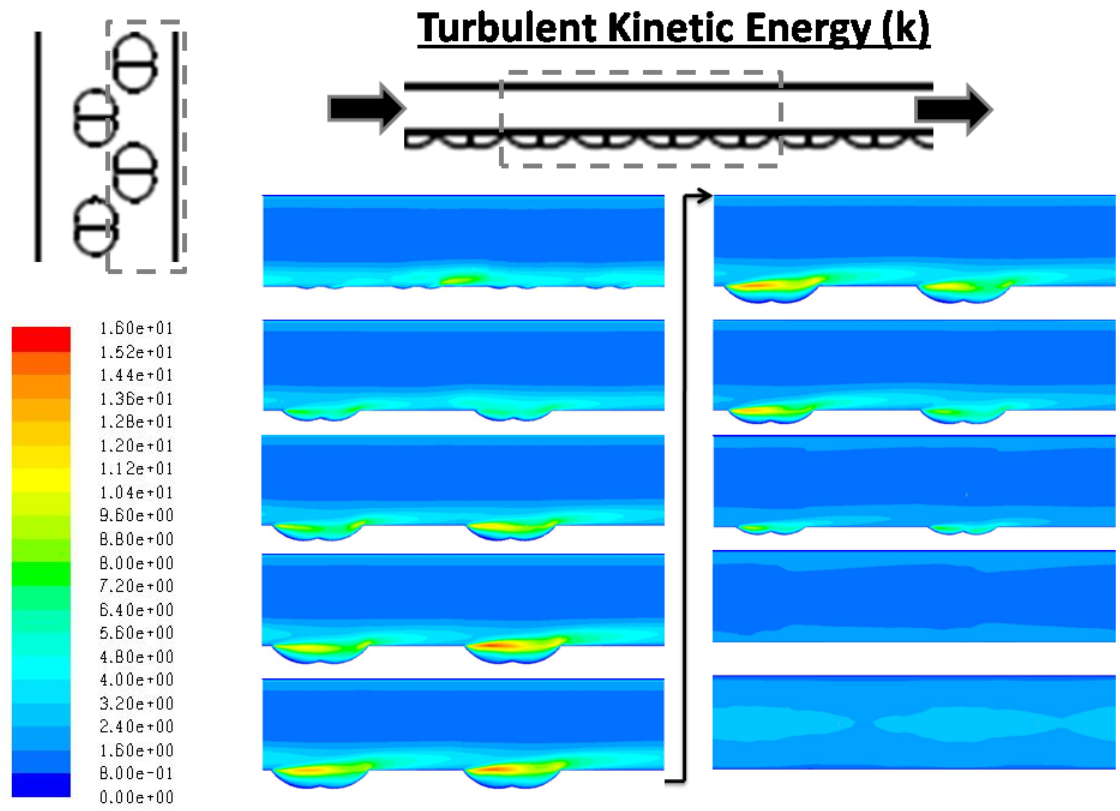


**Figure E.23: Streamwise Profiles of Turbulent Kinetic Energy – Re = 30000**





E.3. Reynolds Number = 20000

## Surface Heat Transfer Coefficient [W/(m<sup>2</sup>\*K)]

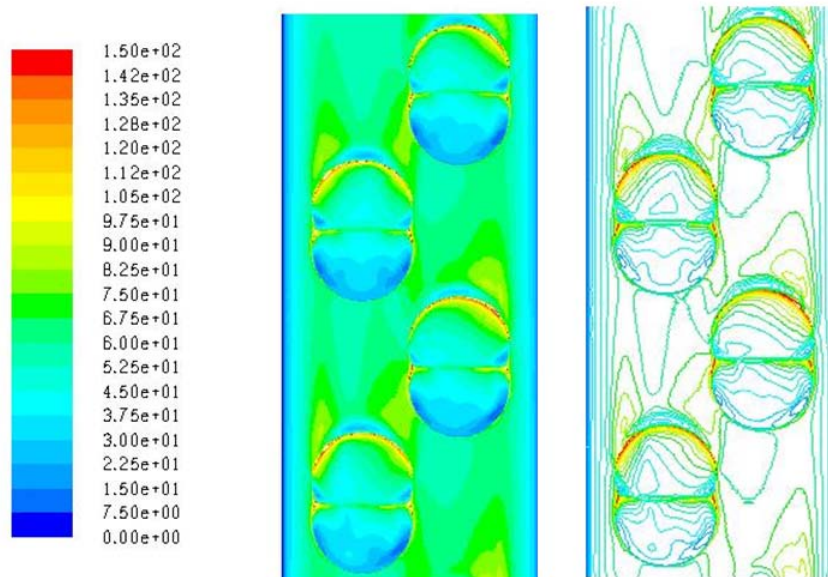


Figure E.26: Surface Heat Transfer Coefficient Contours, Bottom Wall– Re = 20000

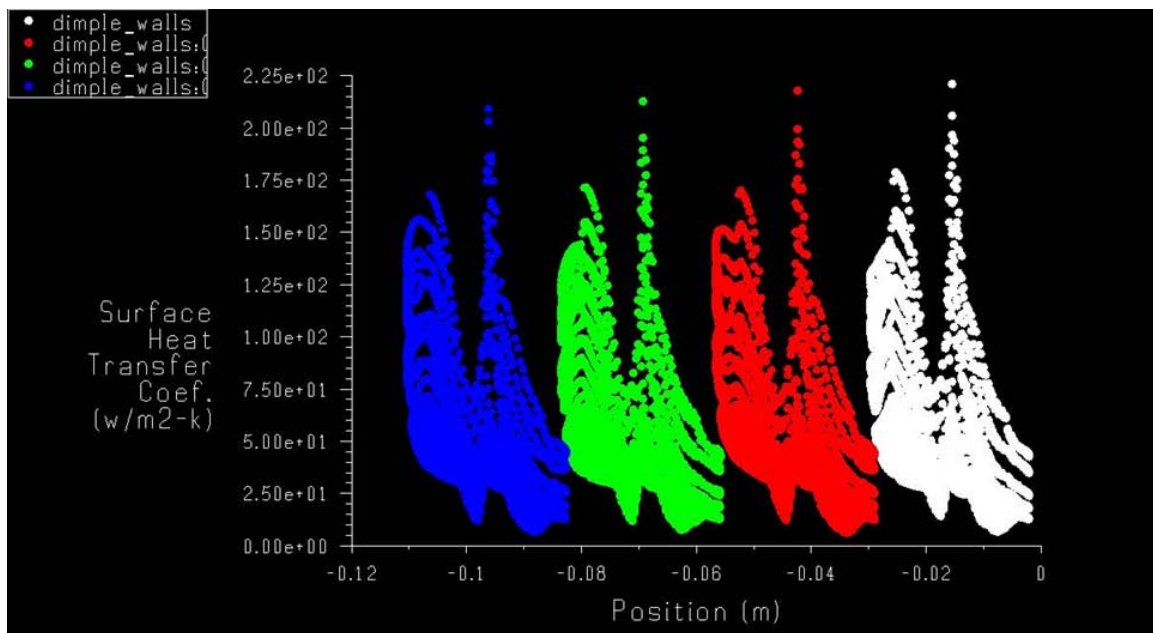


Figure E.27: Surface Heat Transfer Coefficient as a Function of Streamwise Distance – Re = 20000



# Static Pressure (Gauge) [Pa]

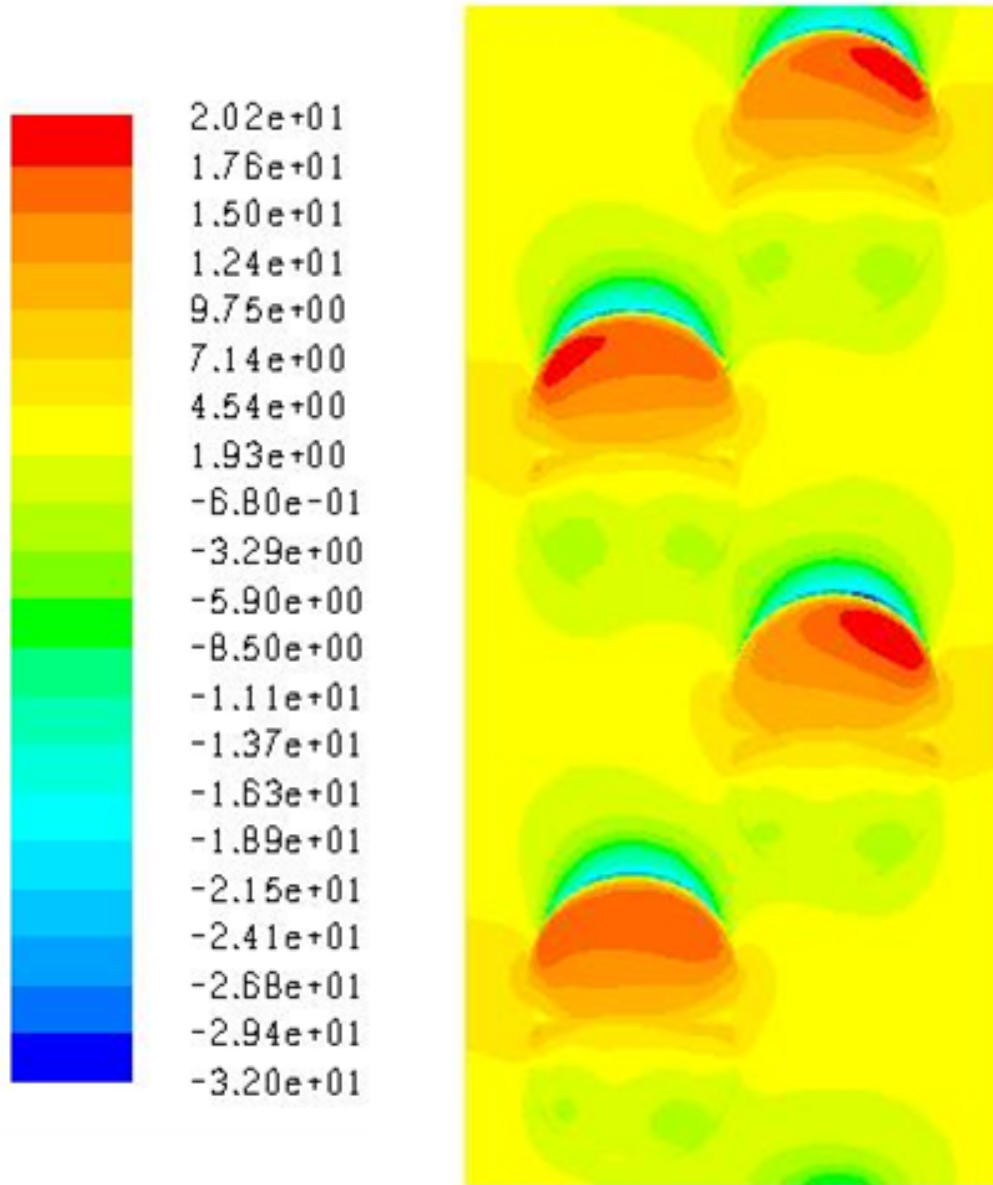
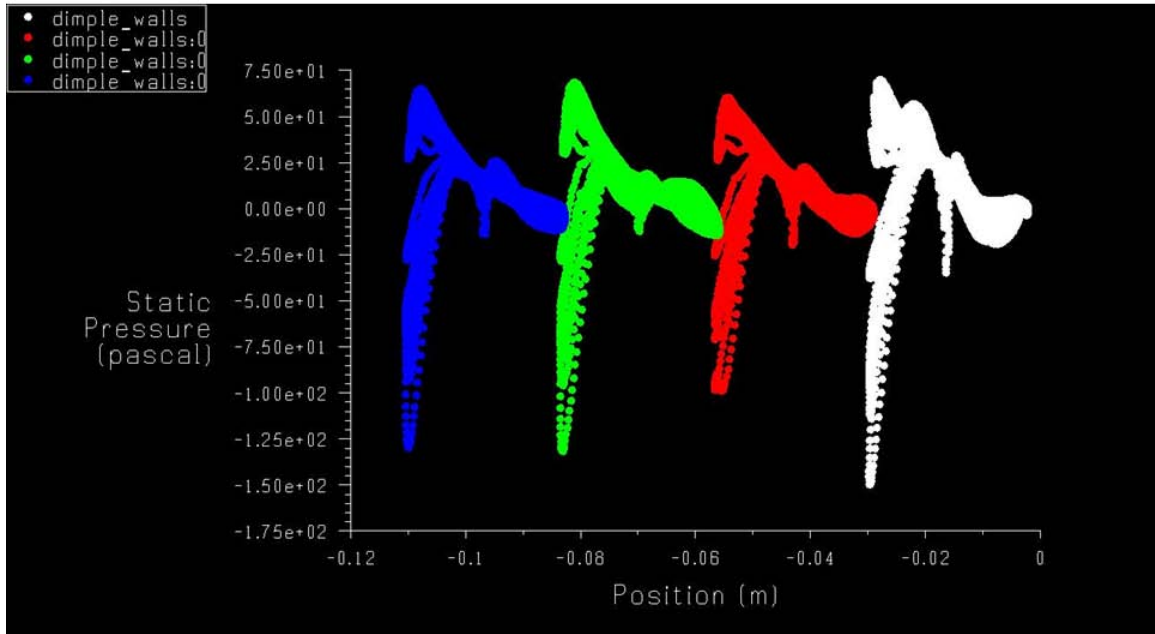
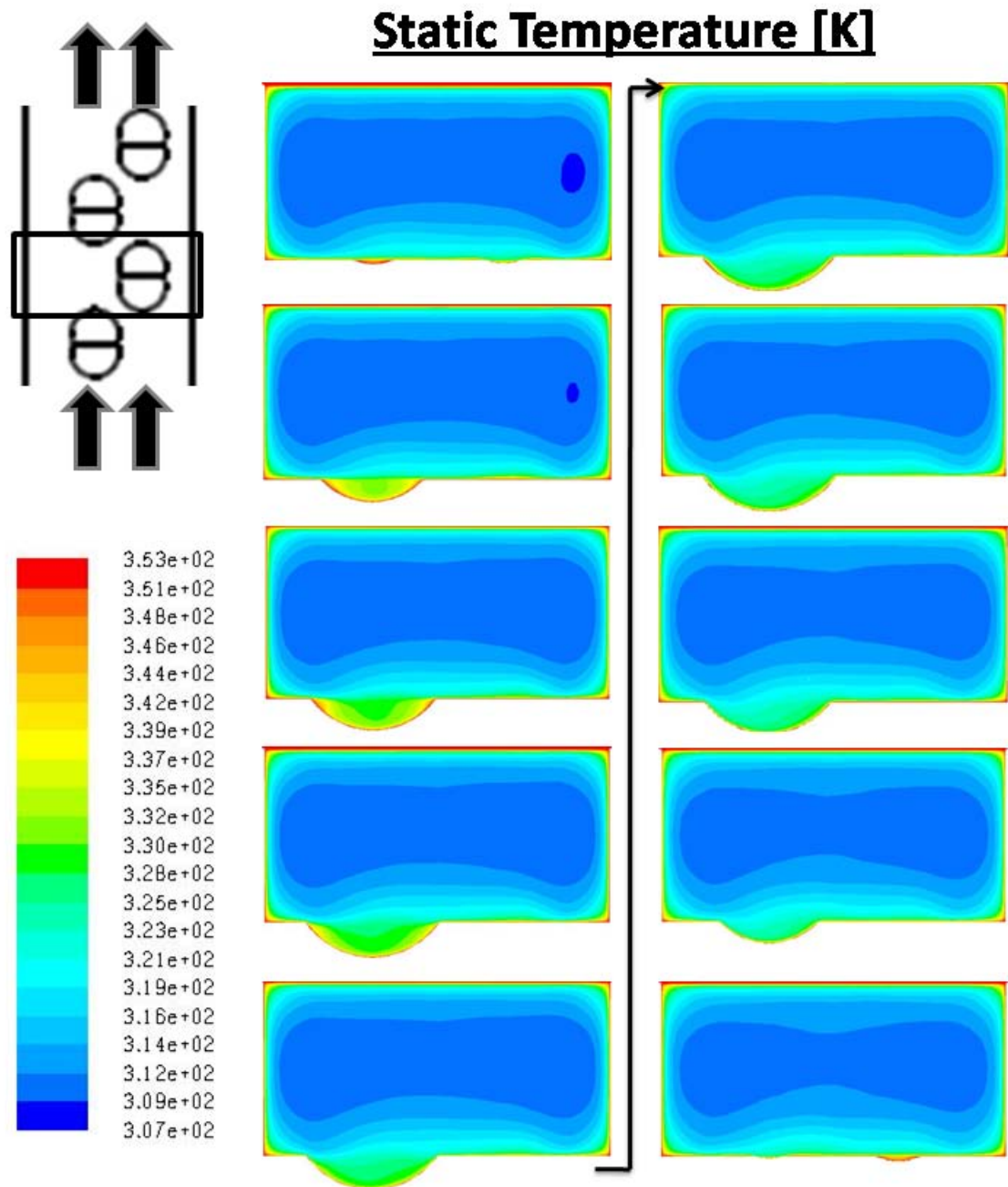


Figure E.28: Static Pressure Distribution over the Bottom Wall of the Channel –  $Re = 20000$



**Figure E.29: : Static Pressure on the Dimple Surface as a Function of Streamwise Distance –  $Re = 20000$**



**Figure E.30: Streamwise Profiles of Static Temperature – Double Dimples,  $Re = 20000$**

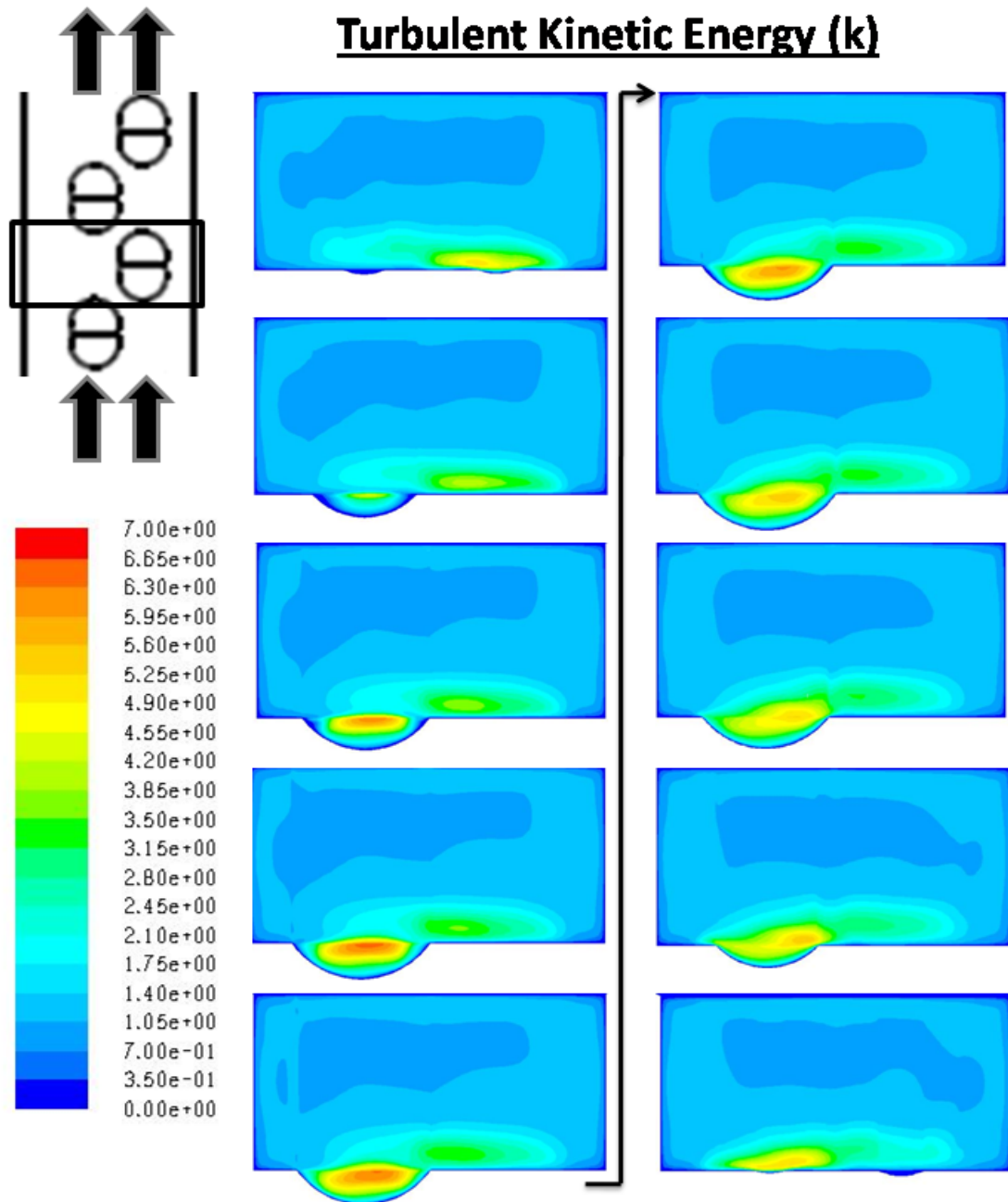


Figure E.31: Streamwise Profiles of Turbulent Kinetic Energy : Double Dimples, Re = 20000

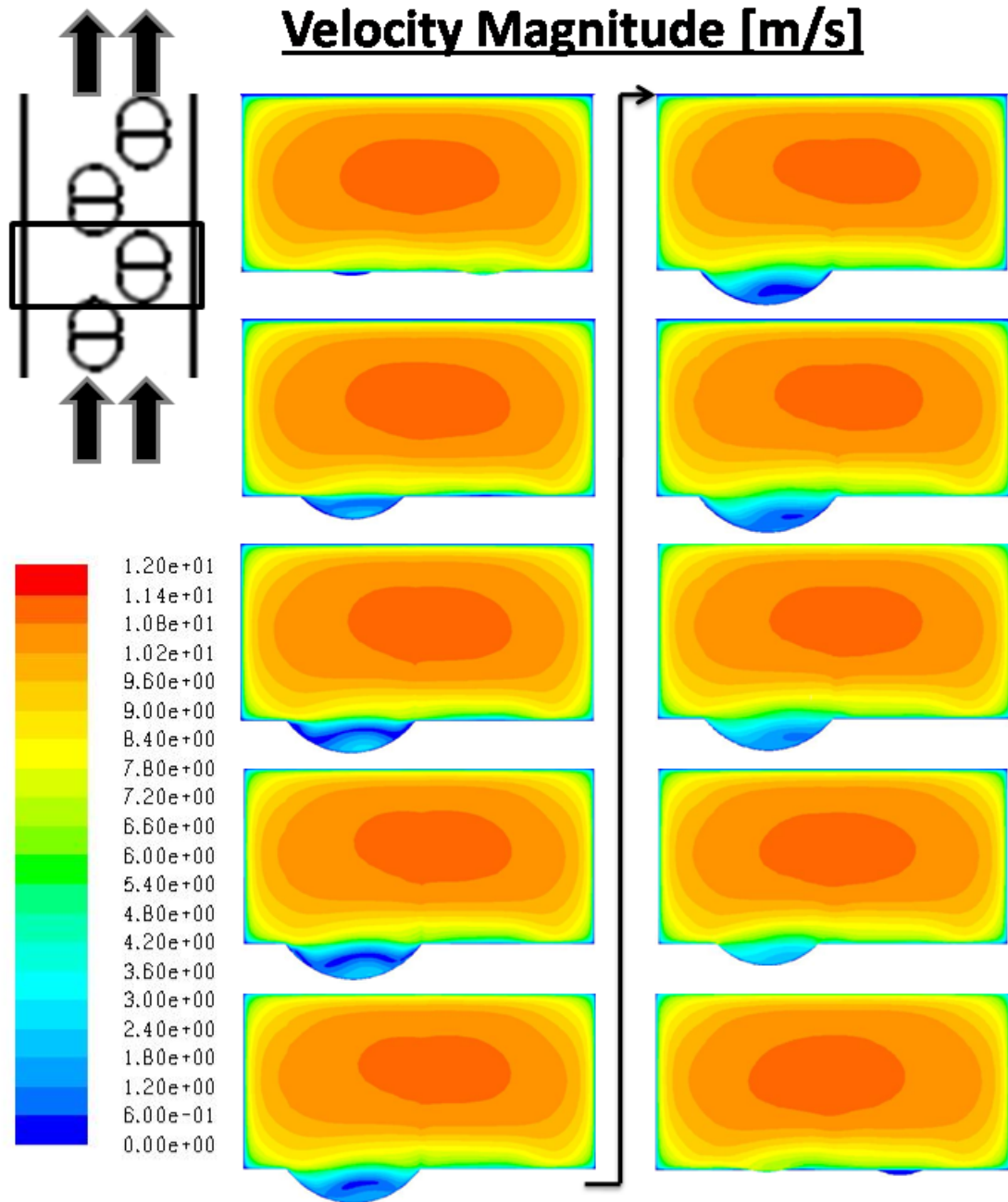


Figure E.32: Streamwise Profiles of Velocity Magnitude : Double Dimples, Re = 20000

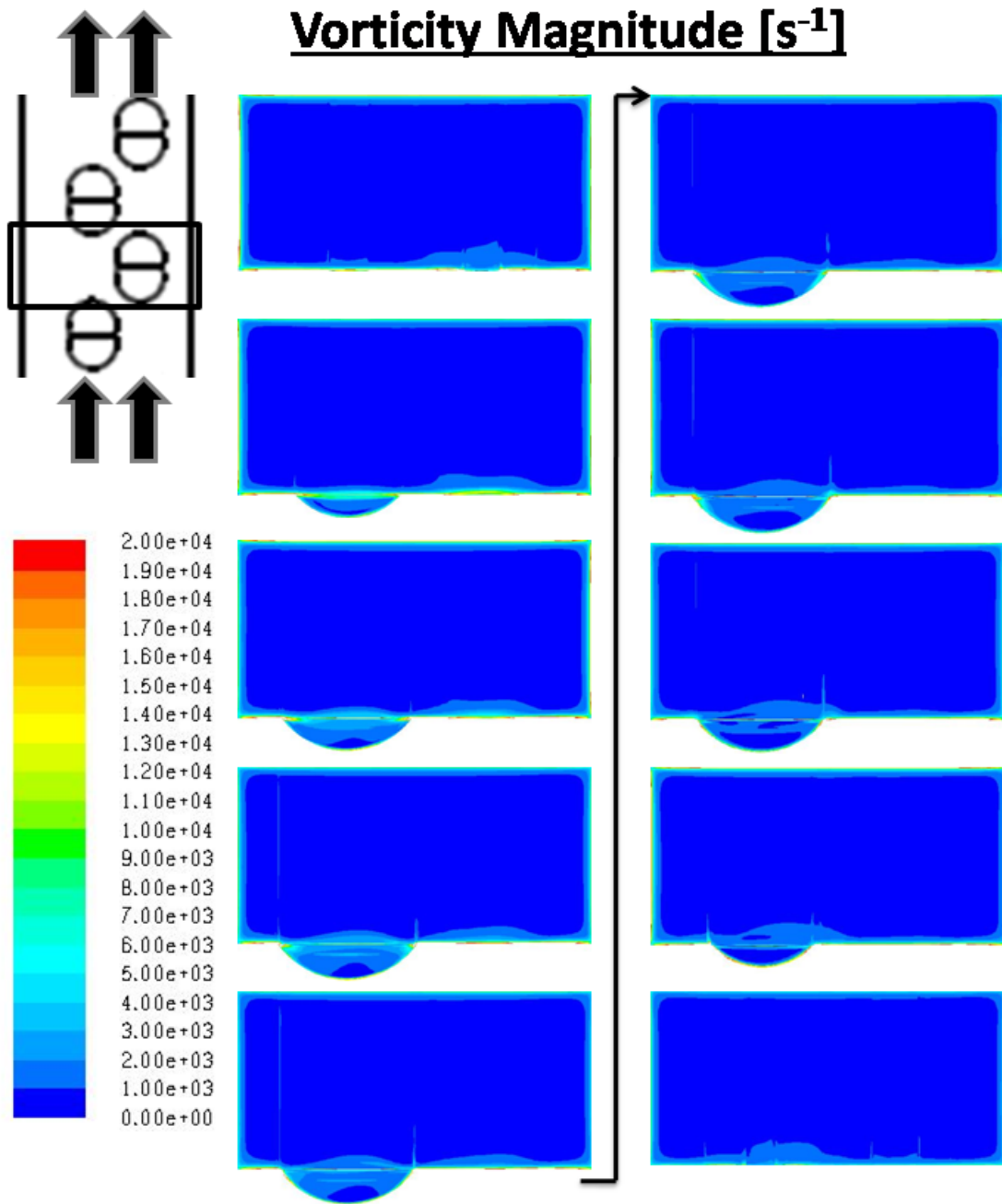


Figure E.33: Streamwise Profiles of Vorticity Magnitude : Double Dimples, Re = 20000

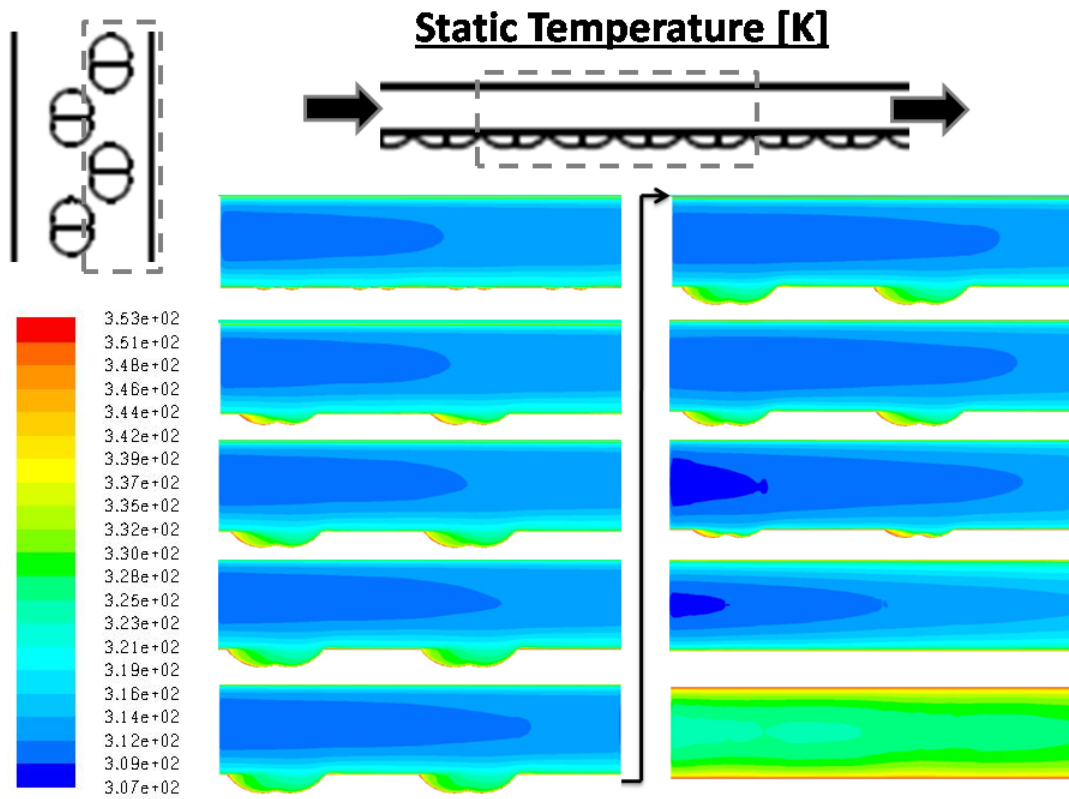
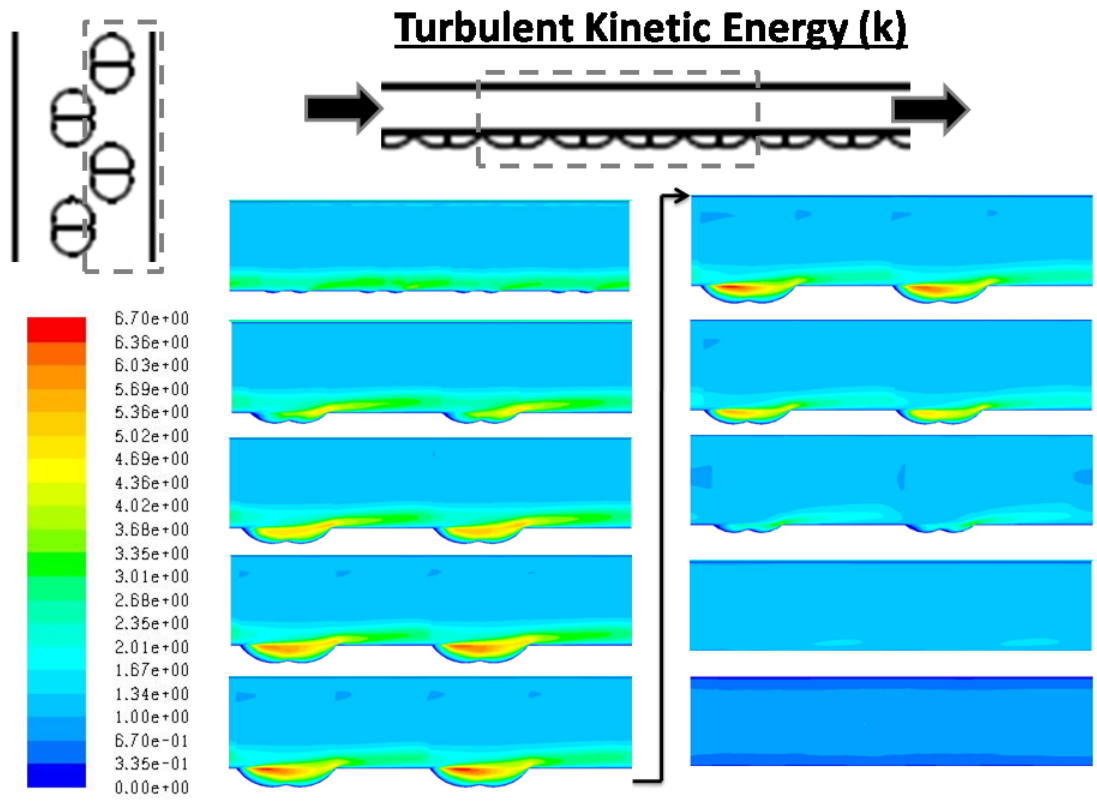


Figure E.34: Spanwise Profiles of Static Temperature : Double Dimples,  $Re = 20000$



**Figure E.35: Spanwise Profiles of Turbulent Kinetic Energy : Double Dimples, Re = 20000**



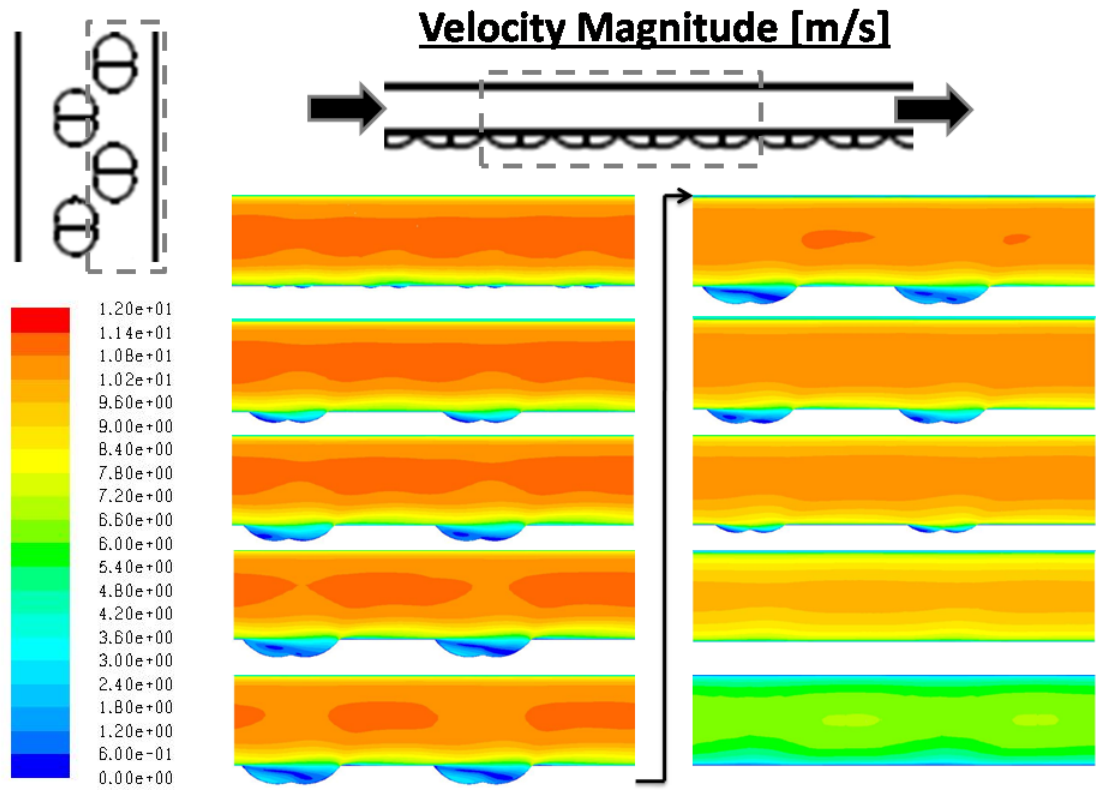
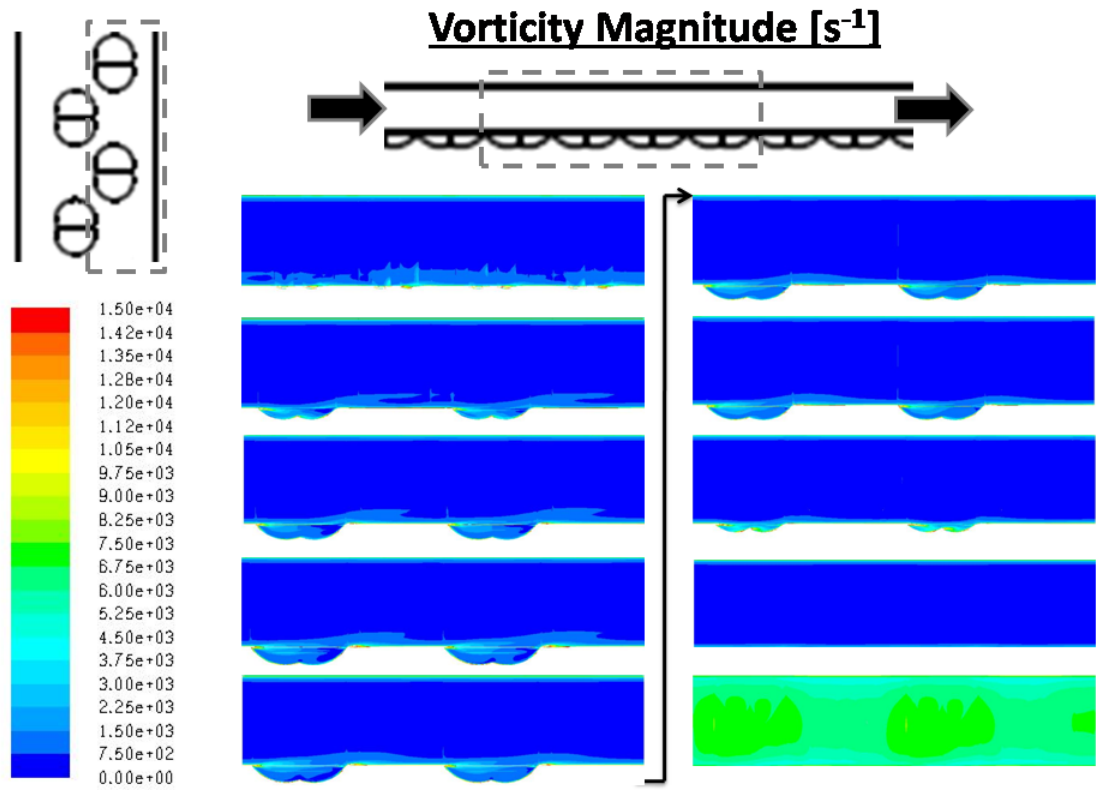


Figure E.36: Spanwise Profiles of Velocity Magnitude : Double Dimples, Re = 20000



**Figure E.37: Spanwise Profiles of Vorticity Magnitude – Double Dimples,  $Re = 20000$**

## APPENDIX F: LARGE EDDY SIMULATION – TRANSIENT RESULT SET

F.1. Velocity Contours – Positive x Streamwise Plane

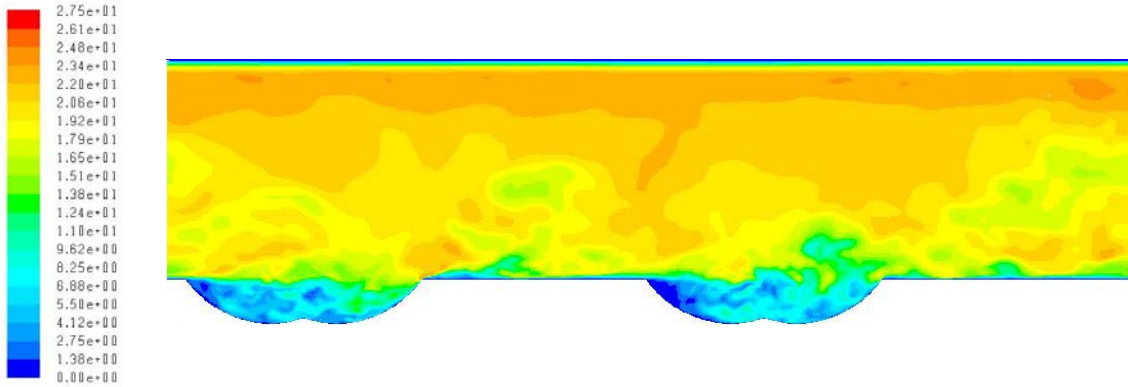


**Figure F.1: Transient Contours of Velocity – (+)X Plane, Time Step = 0s, Re = 40000**

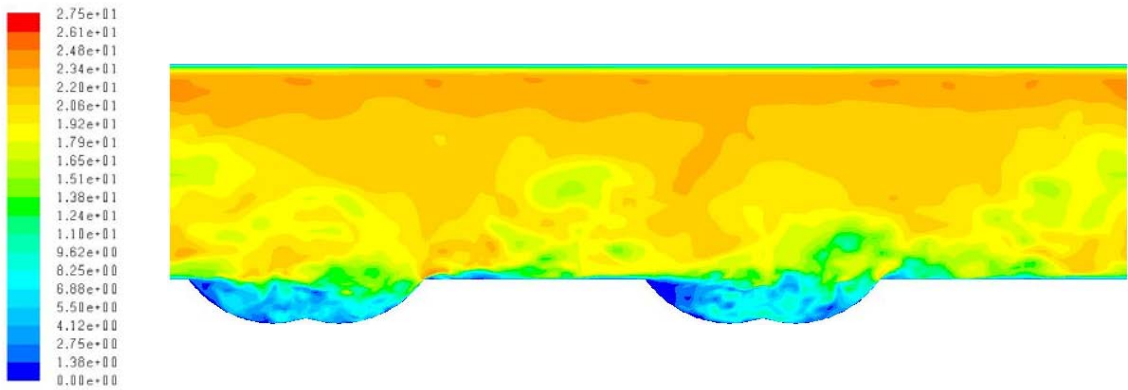


**Figure F.2: Transient Contours of Velocity – (+)X Plane, Time Step = 0.000242s, Re = 40000**

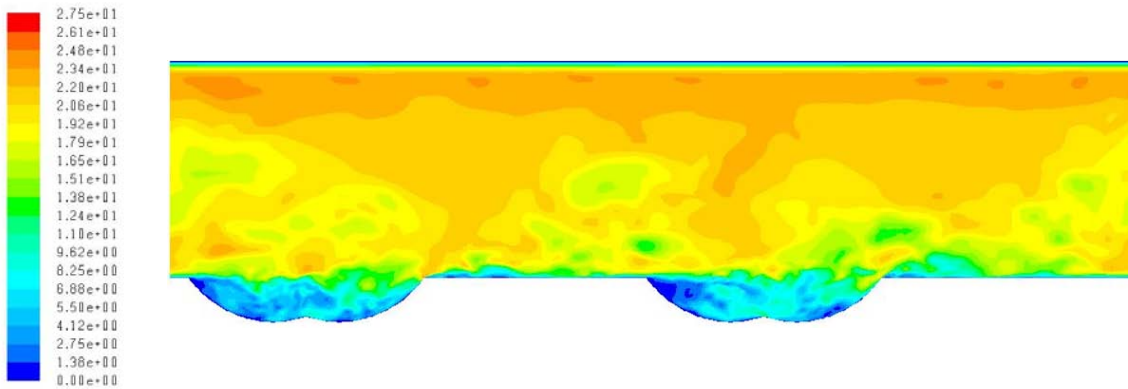


**Figure F.3: Transient Contours of Velocity – (+)X Plane, Time Step = 0.000484s, Re = 40000**

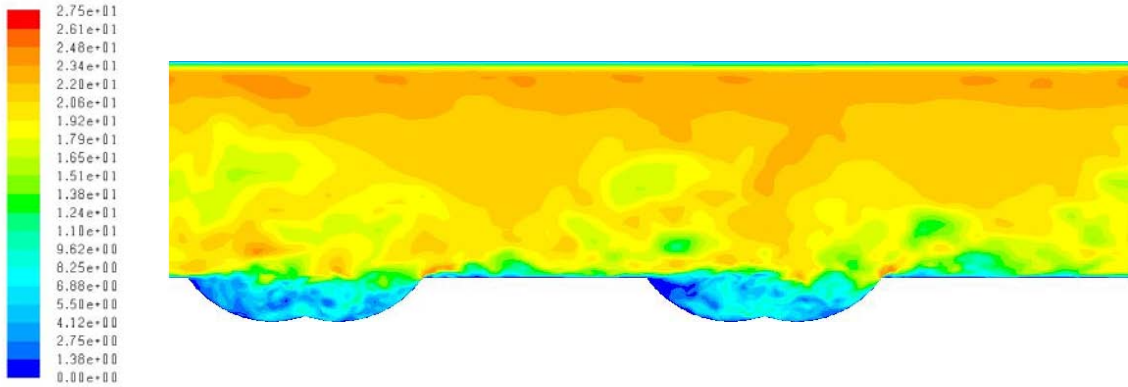


**Figure F.4: Transient Contours of Velocity – (+)X Plane, Time Step = 0.000726s, Re = 40000**

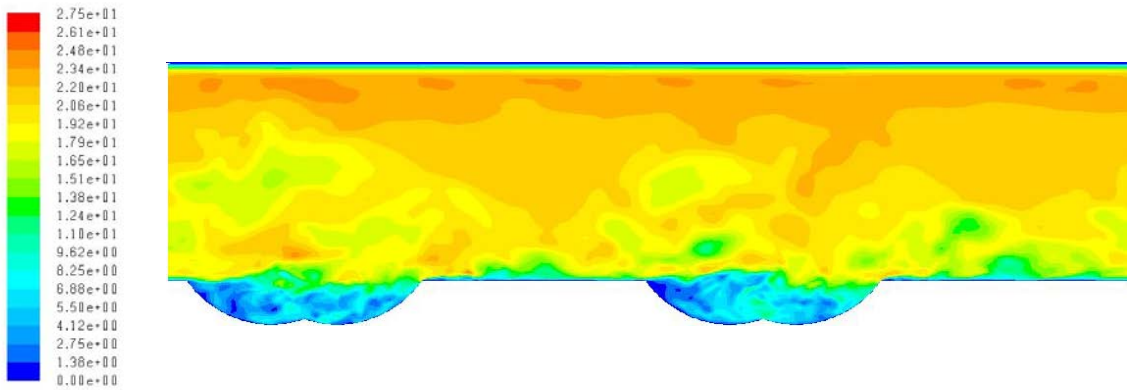


**Figure F.5: Transient Contours of Velocity – (+)X Plane, Time Step = 0.000968s, Re = 40000**

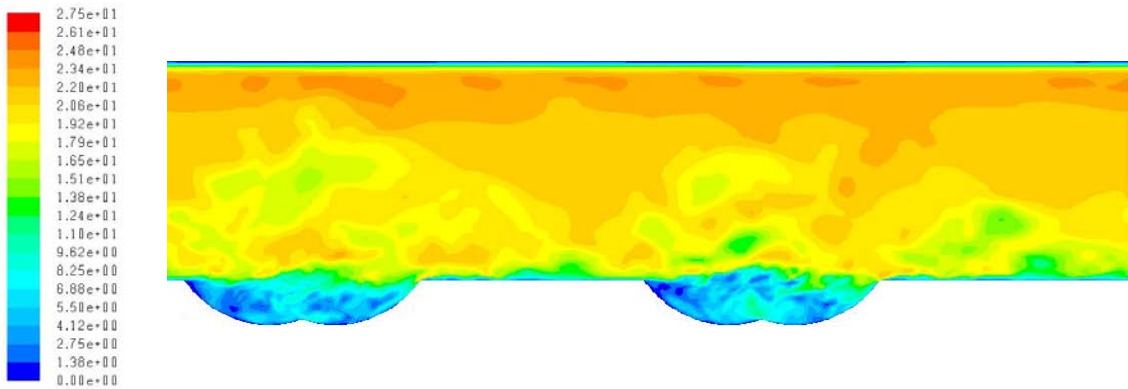


**Figure F.6: Transient Contours of Velocity – (+)X Plane, Time Step = 0.00121s, Re = 40000**

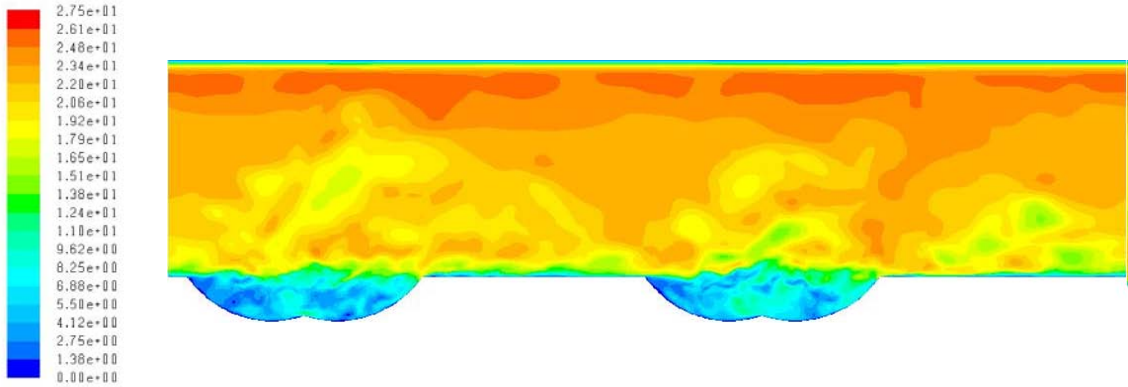


**Figure F.7: Transient Contours of Velocity – (+)X Plane, Time Step = 0.001452s, Re = 40000**

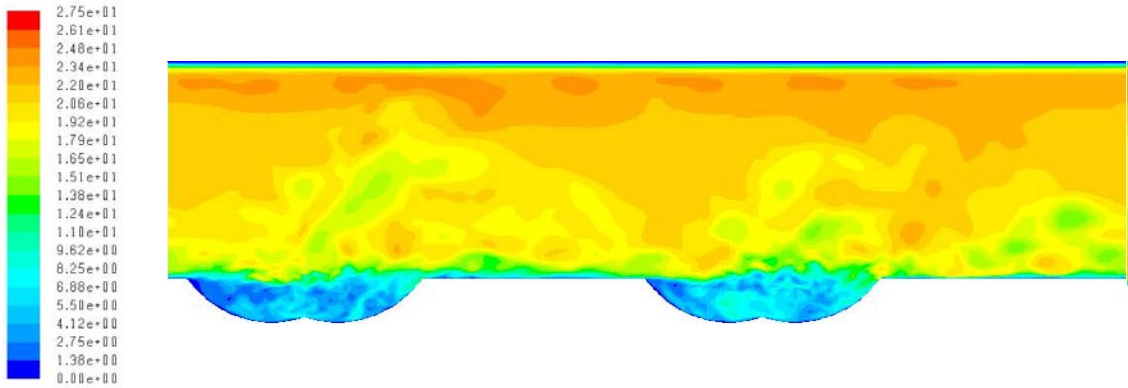


**Figure F.8: Transient Contours of Velocity – (+)X Plane, Time Step = 0.001694s, Re = 40000**

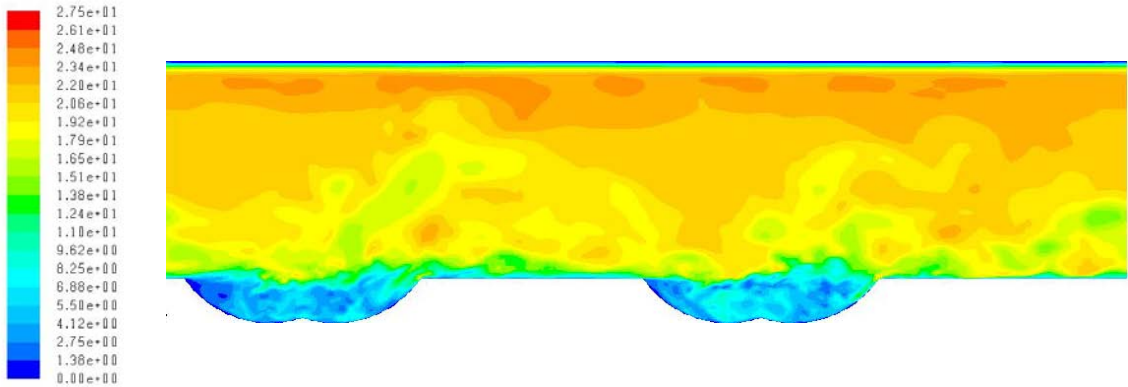


**Figure F.9: Transient Contours of Velocity – (+)X Plane, Time Step = 0.1936s, Re = 40000**

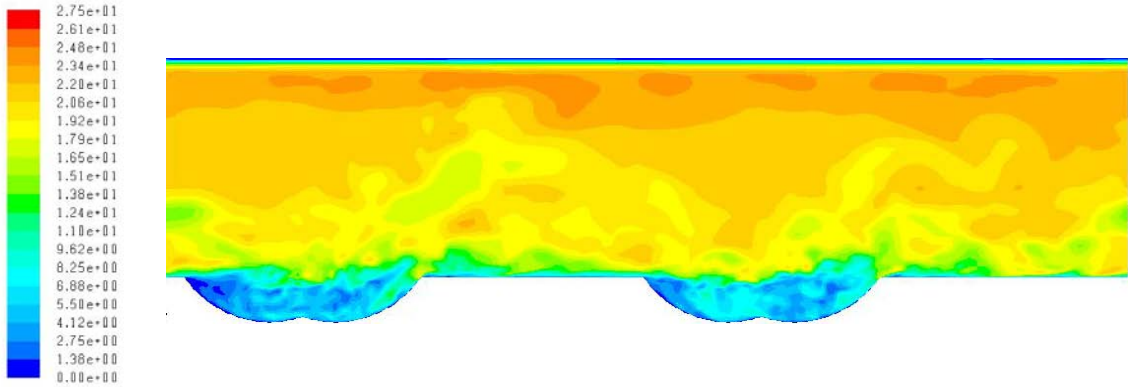


**Figure F.10: Transient Contours of Velocity – (+)X Plane, Time Step = 0.2178s, Re = 40000**

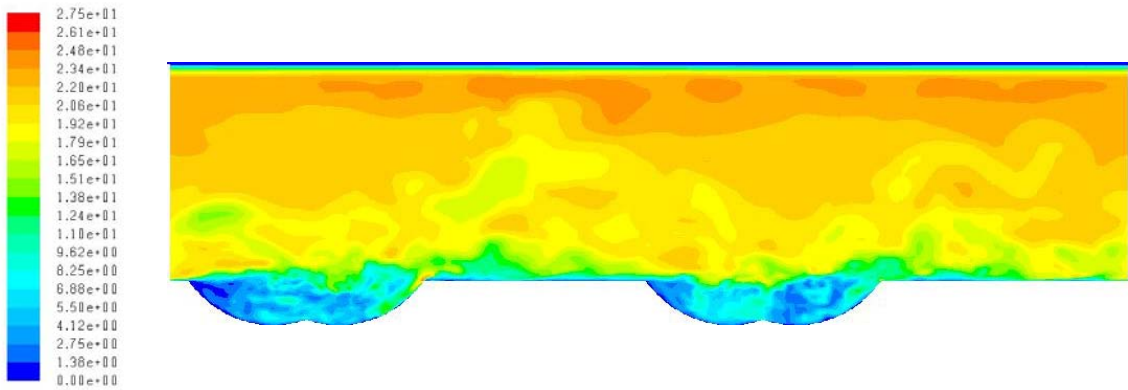


**Figure F.11: Transient Contours of Velocity – (+)X Plane, Time Step = 0.00242s, Re = 40000**

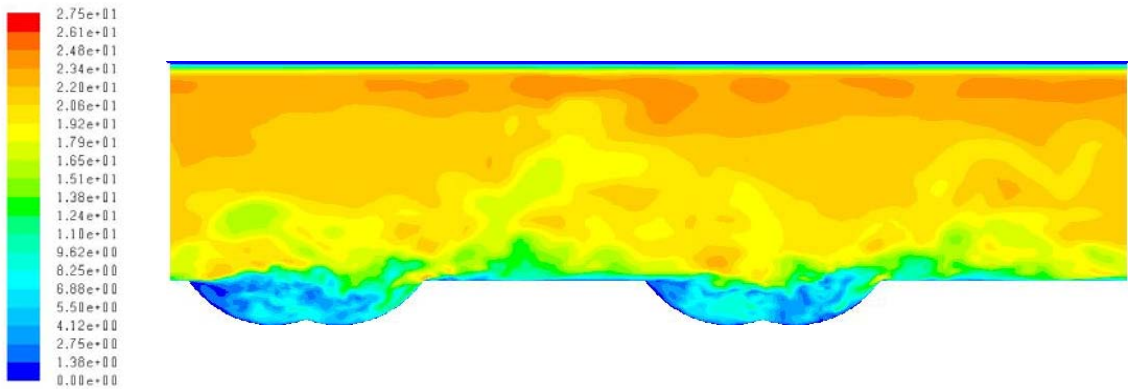


**Figure F.12: Transient Contours of Velocity – (+)X Plane, Time Step = 0.002662s, Re = 40000**



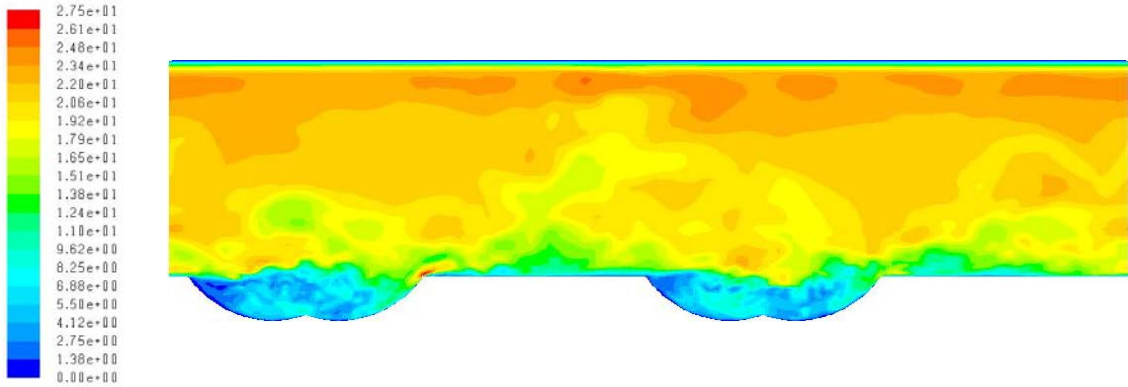


**Figure F.13: Transient Contours of Velocity – (+)X Plane, Time Step = 0.002904s, Re = 40000**

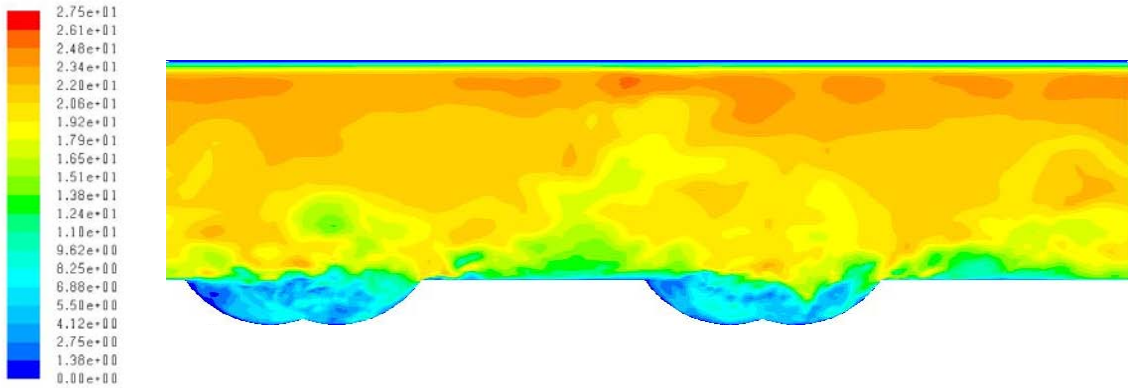


**Figure F.14: Transient Contours of Velocity – (+)X Plane, Time Step = 0.003146s, Re = 40000**

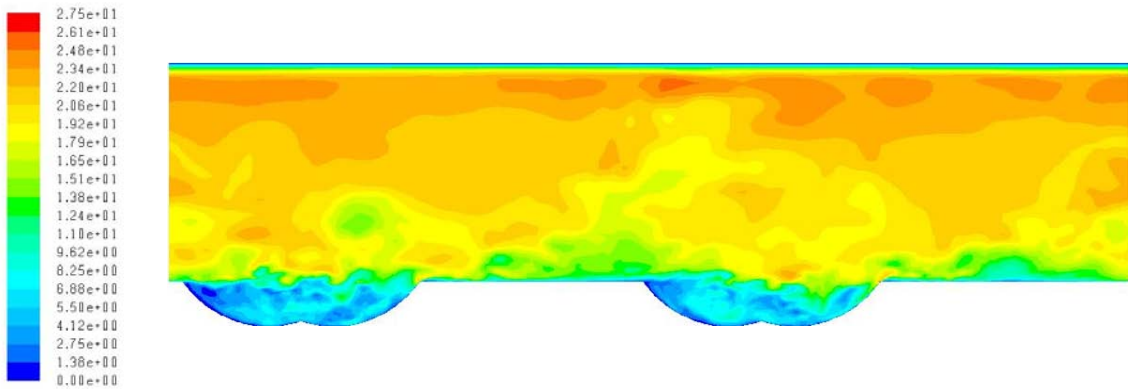


**Figure F.15: Transient Contours of Velocity – (+)X Plane, Time Step = 0.003388s, Re = 40000**

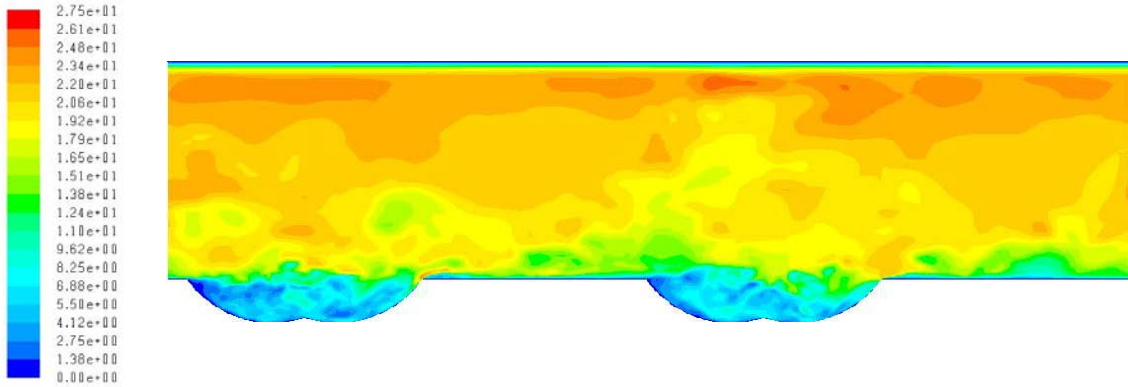


**Figure F.16: Transient Contours of Velocity – (+)X Plane, Time Step = 0.00363s, Re = 40000**

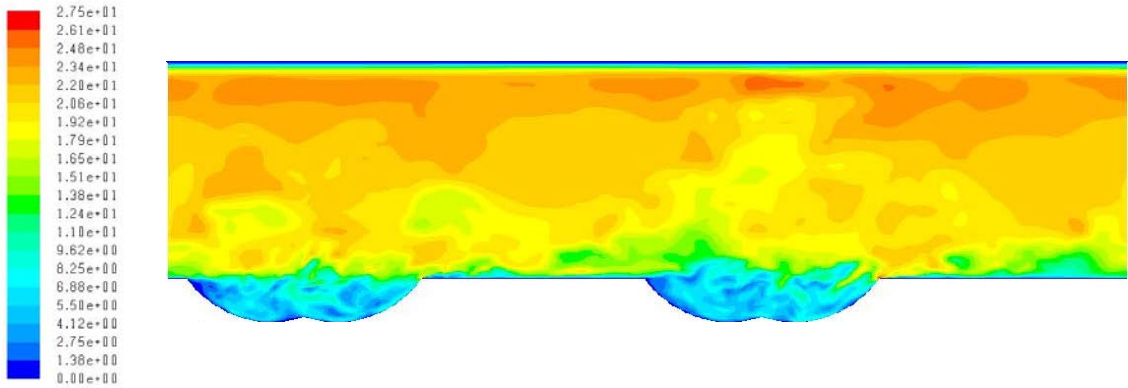


**Figure F.17: Transient Contours of Velocity – (+)X Plane, Time Step = 0.003872s, Re = 40000**

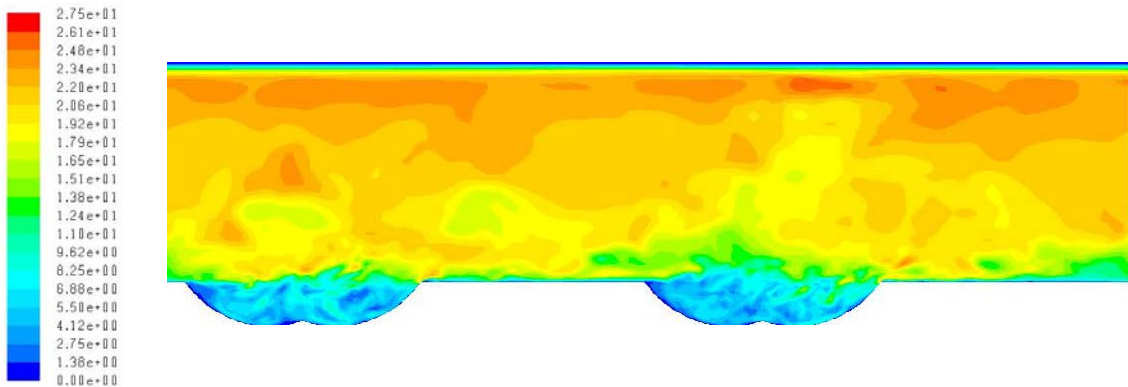


**Figure F.18: Transient Contours of Velocity – (+)X Plane, Time Step = 0.004114s, Re = 40000**

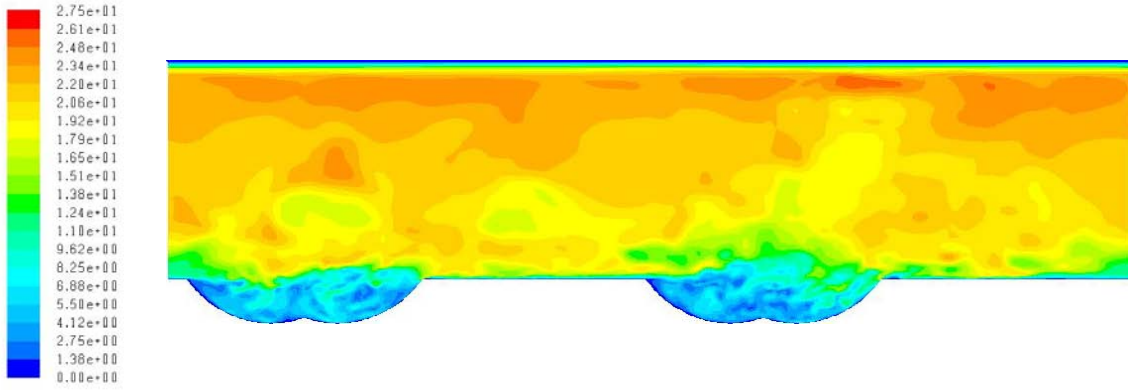


**Figure F.19: Transient Contours of Velocity – (+)X Plane, Time Step = 0.004356s, Re = 40000**

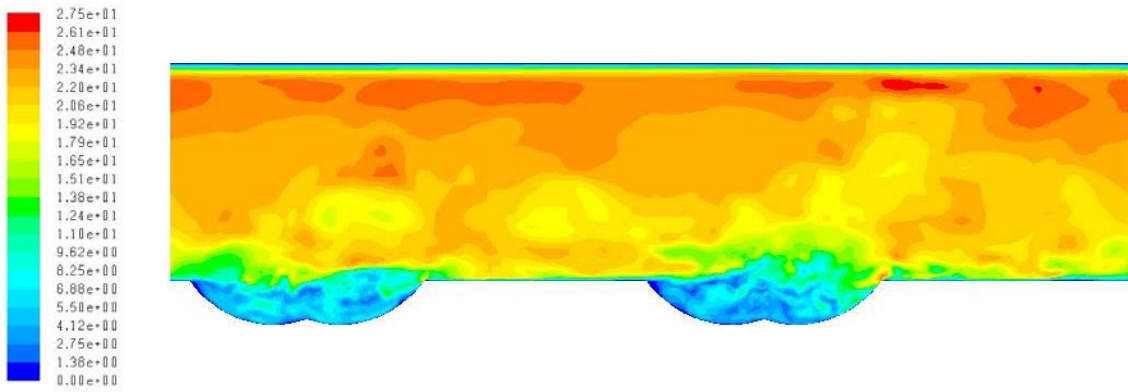


**Figure F.20: Transient Contours of Velocity – (+)X Plane, Time Step = 0.004598s, Re = 40000**

F.2. Velocity Contours – Spanwise Centerplane

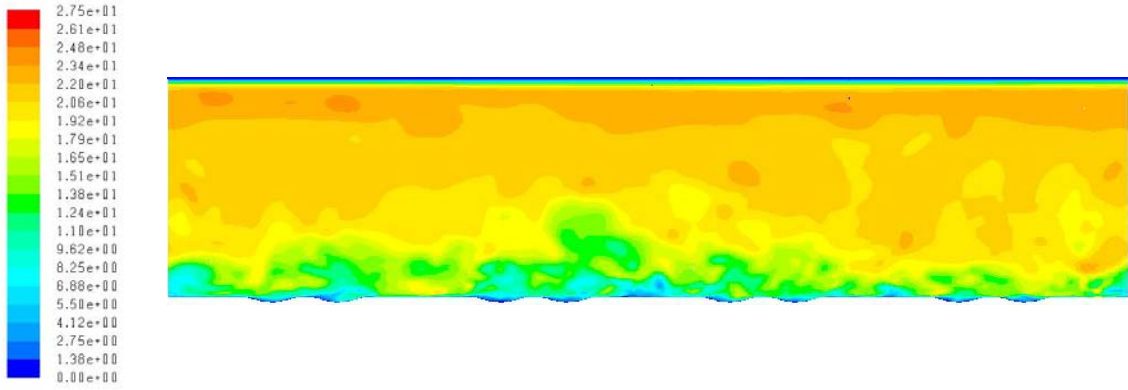


**Figure F.21: Transient Contours of Velocity – Spanwise Centerplane, Time = 0s, Re = 40000**

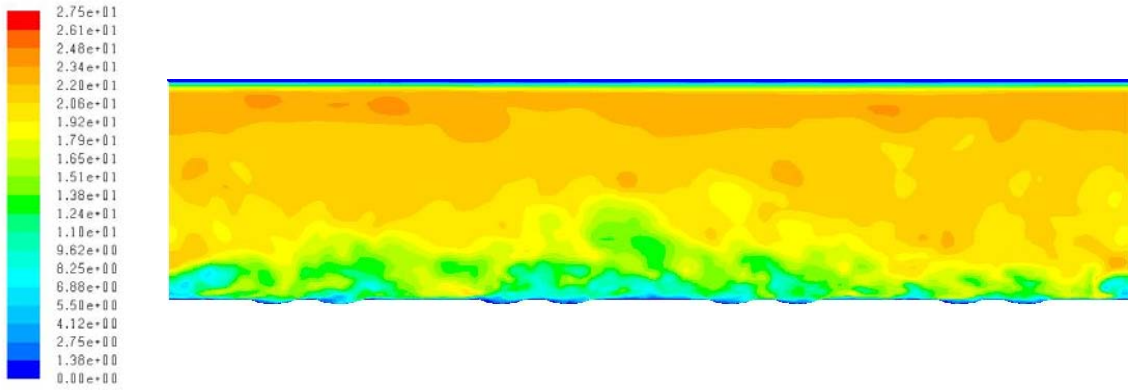


**Figure F.22: Transient Contours of Velocity – Spanwise Centerplane, Time = 0.000242s, Re = 40000**

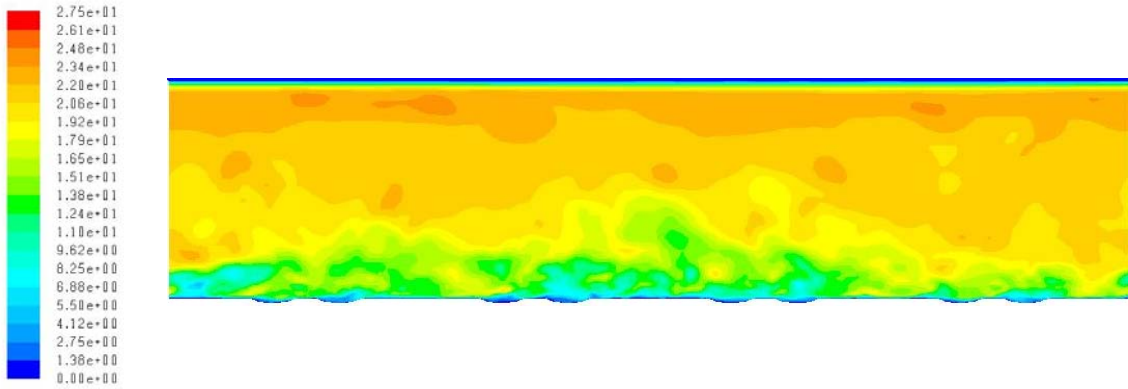


**Figure F.23: Contours of Velocity – Spanwise Centerplane, Time = 0.000484s, Re = 40000**

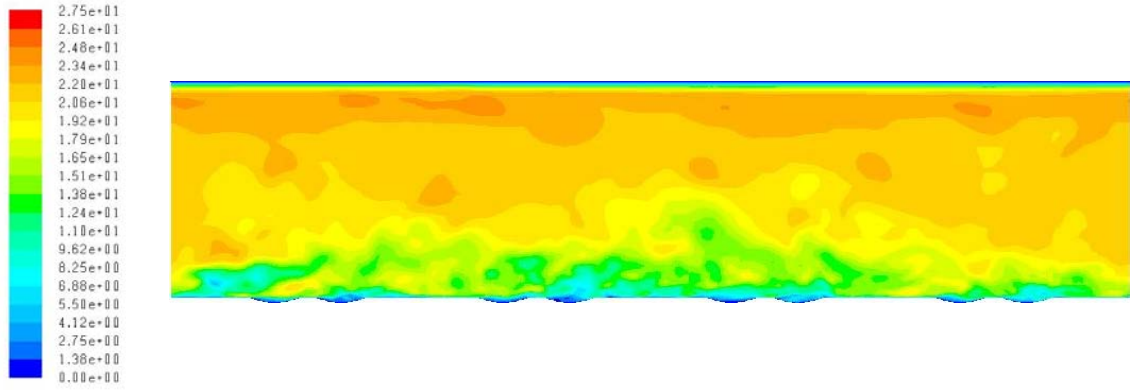


**Figure F.24: Transient Contours of Velocity – Spanwise Centerplane, Time = 0.000726s, Re = 40000**

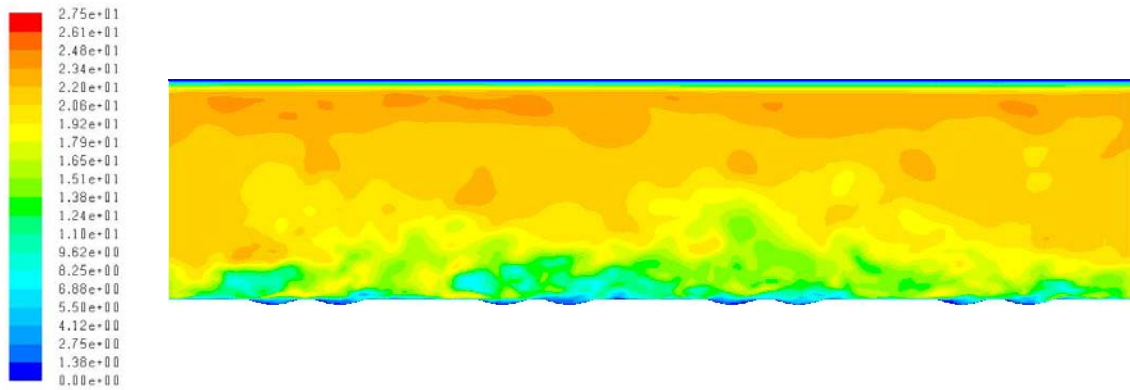


**Figure F.25: Transient Contours of Velocity – Spanwise Centerplane, Time = 0.000968s, Re = 40000**

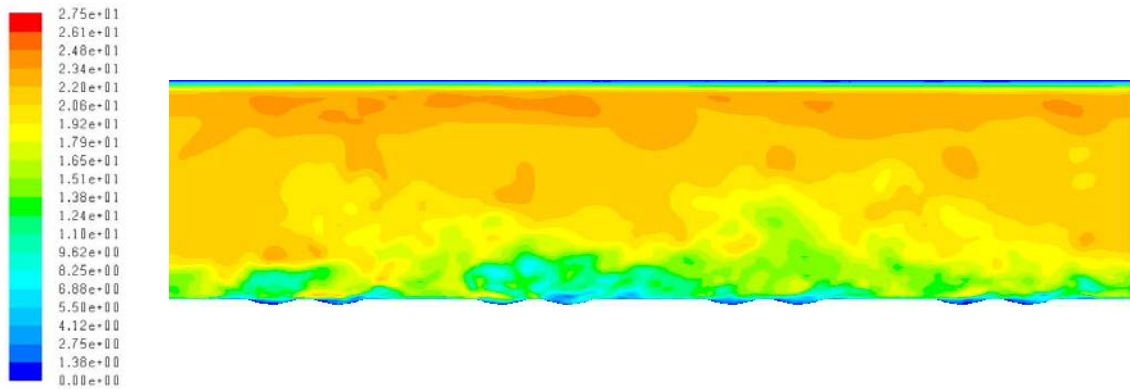


**Figure F.26: Transient Contours of Velocity – Spanwise Centerplane, Time = 0.00121s, Re = 40000**



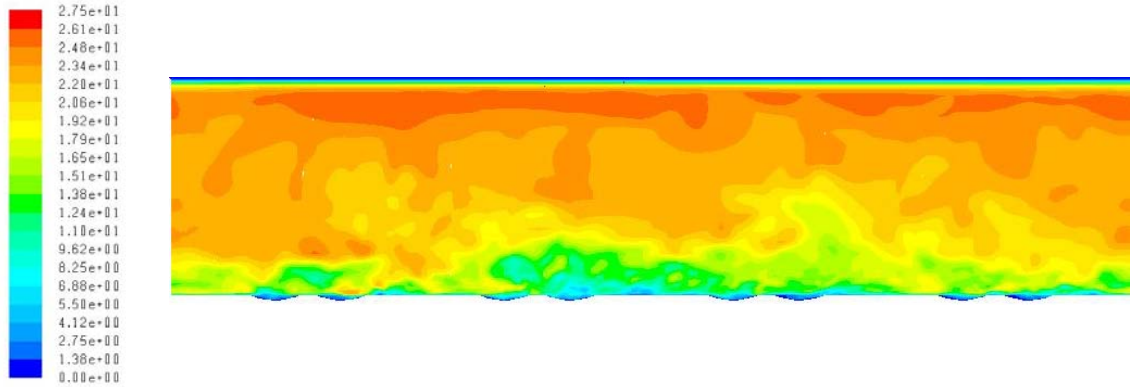


**Figure F.27: Transient Contours of Velocity – Spanwise Centerplane, Time = 0.001452s, Re = 40000**

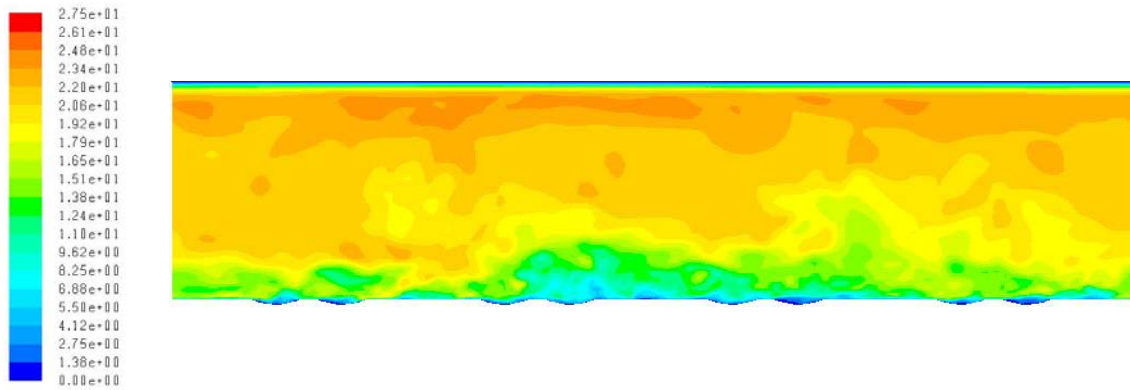


**Figure F.28: Transient Contours of Velocity – Spanwise Centerplane, Time = 0.001694s, Re = 40000**

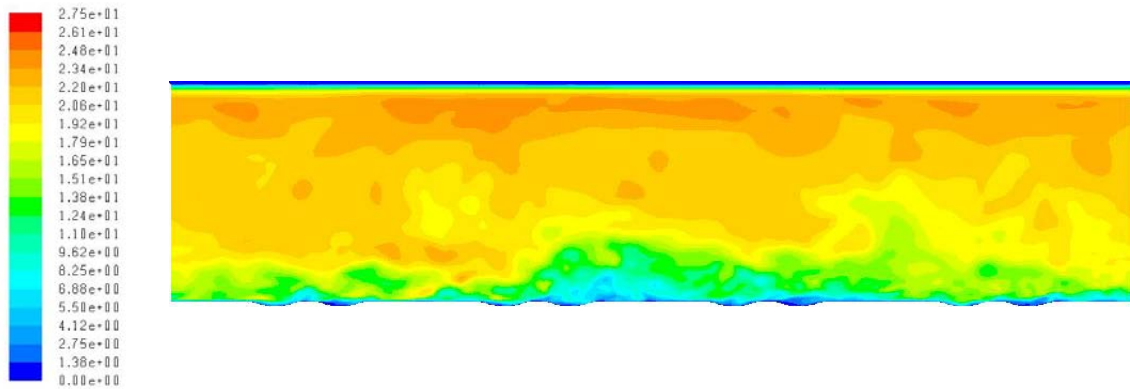


**Figure F.29: Transient Contours of Velocity – Spanwise Centerplane, Time = 0.001936s, Re = 40000**

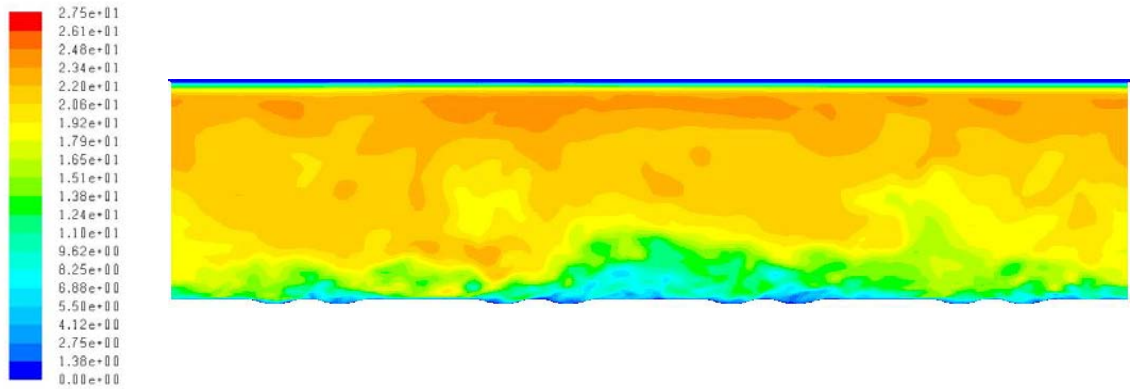


**Figure F.30: Transient Contours of Velocity – Spanwise Centerplane, Time = 0.002178s, Re = 40000**

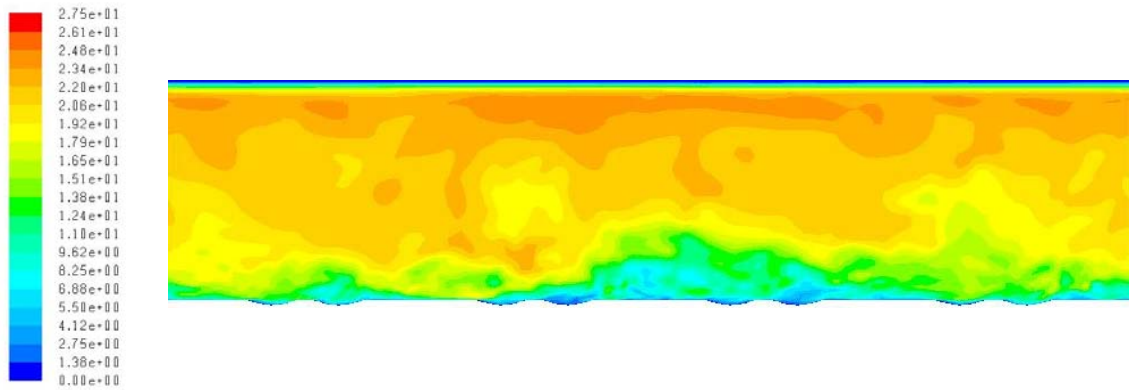


**Figure F.31: Transient Contours of Velocity – Spanwise Centerplane, Time = 0.0024 s, Re = 40000**

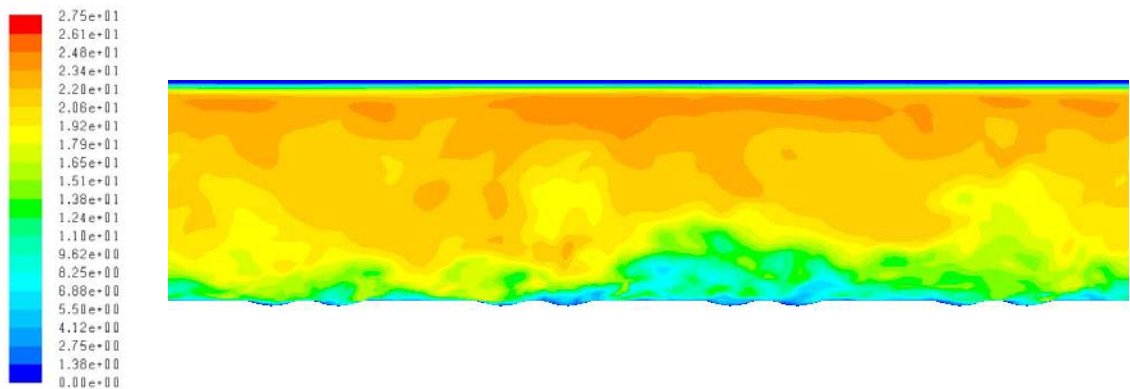


**Figure F.32: Transient Contours of Velocity – Spanwise Centerplane, Time = 0.002662s, Re = 40000**



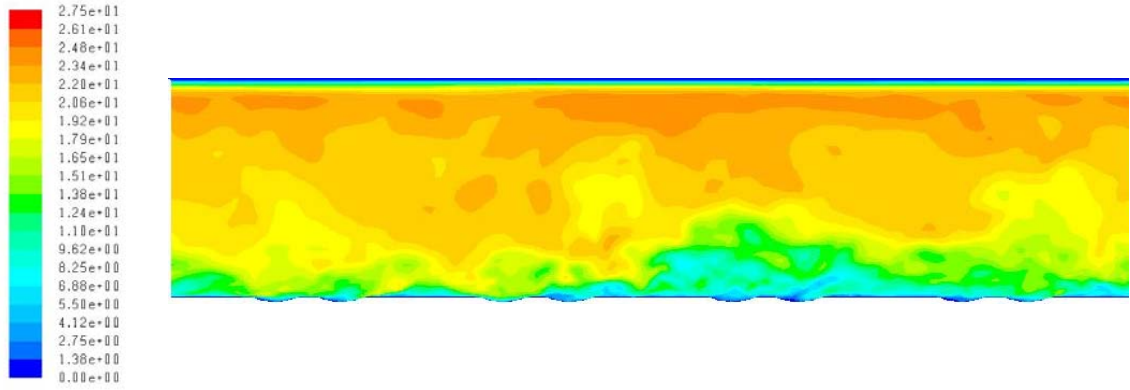


**Figure F.33: Transient Contours of Velocity – Spanwise Centerplane, Time = 0.002904s, Re = 40000**

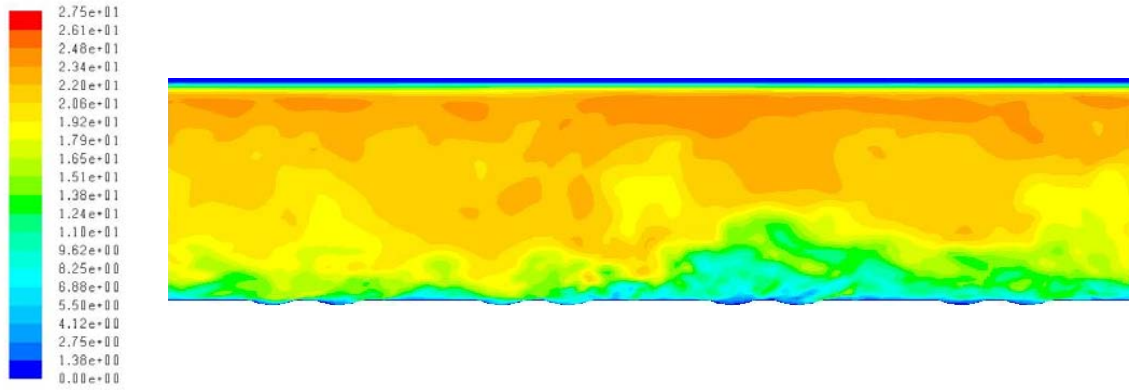


**Figure F.34: Transient Contours of Velocity – Spanwise Centerplane, Time = 0.003146s, Re = 40000**

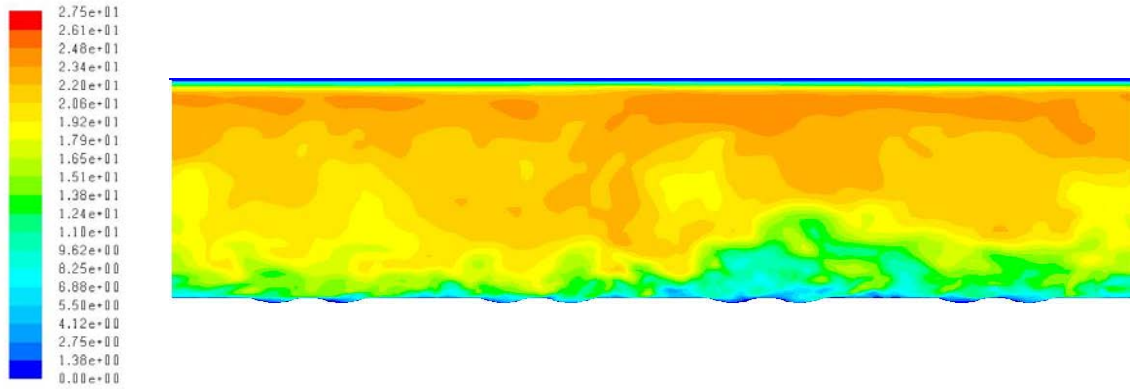


**Figure F.35: Transient Contours of Velocity – Spanwise Centerplane, Time = 0.003388s, Re = 40000**

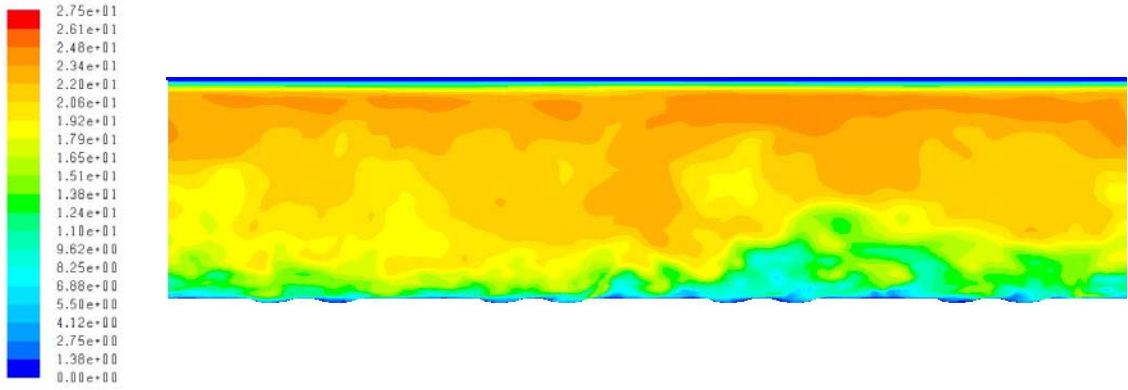


**Figure F.36: Transient Contours of Velocity – Spanwise Centerplane, Time = 0.00363s, Re = 40000**

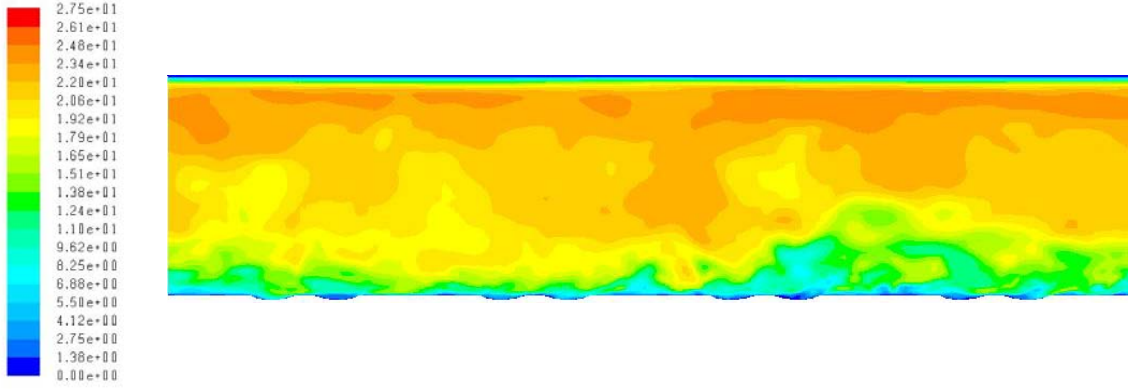


**Figure F.37: Transient Contours of Velocity – Spanwise Centerplane, Time = 0.003872s, Re = 40000**

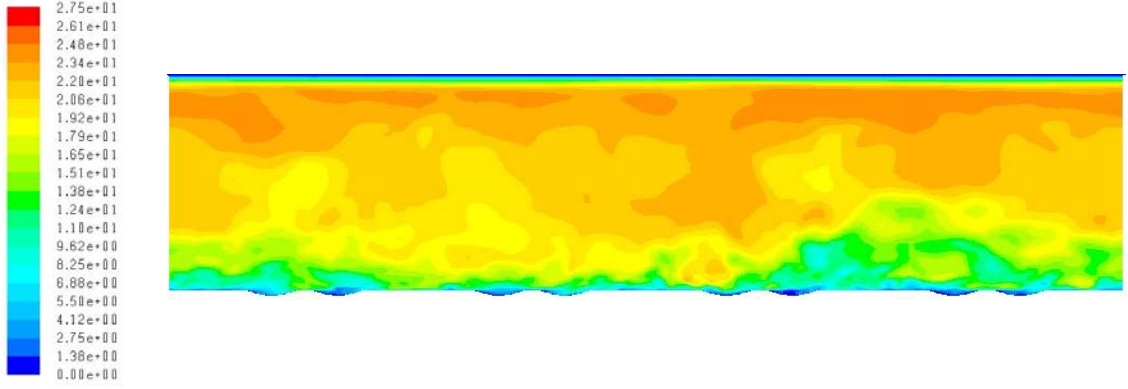


**Figure F.38: Transient Contours of Velocity – Spanwise Centerplane, Time = 0.004114s, Re = 40000**

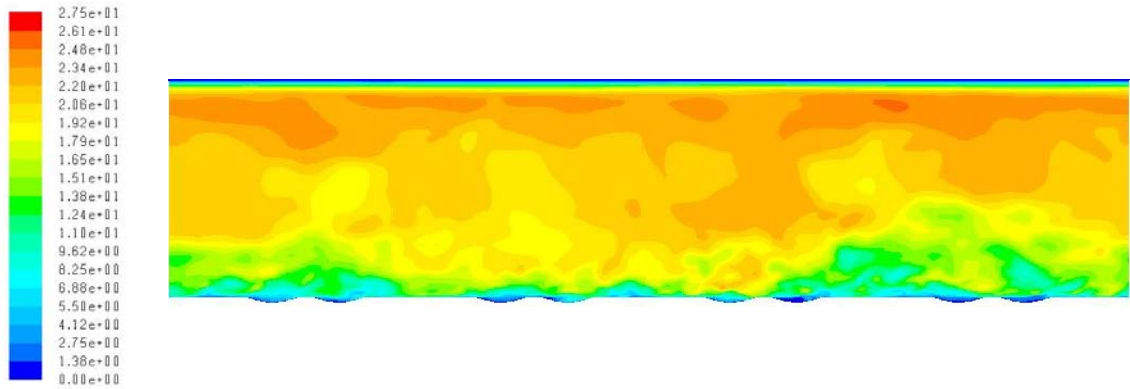


**Figure F.39: Transient Contours of Velocity – Spanwise Centerplane, Time = 0.004356s, Re = 40000**

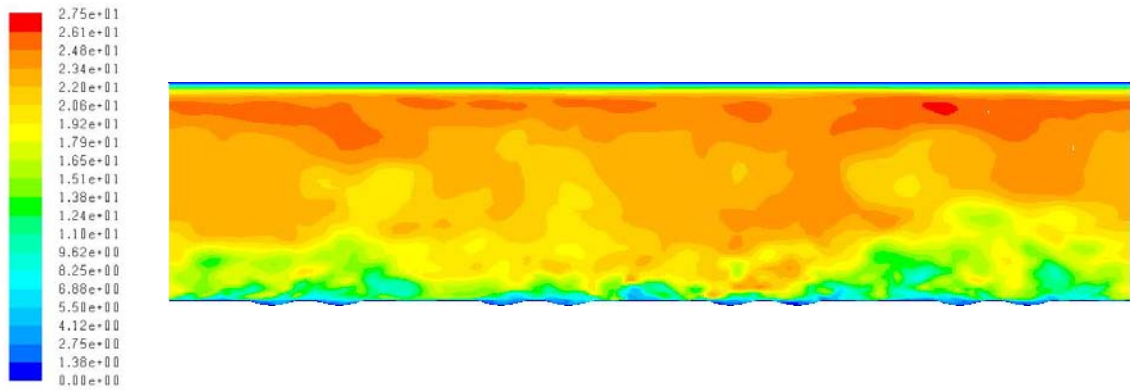


**Figure F.40: Transient Contours of Velocity – Spanwise Centerplane, Time = 0.004598s, Re = 40000**

### F.3. Velocity Contours – Negative x Streamwise Plane

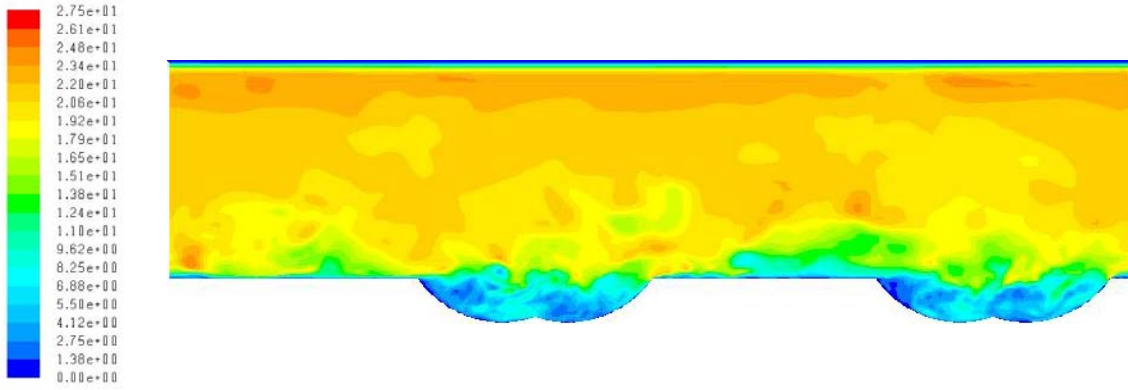


**Figure F.41: Transient Contours of Velocity – (-)X Plane, Time Step = 0s, Re = 40000**

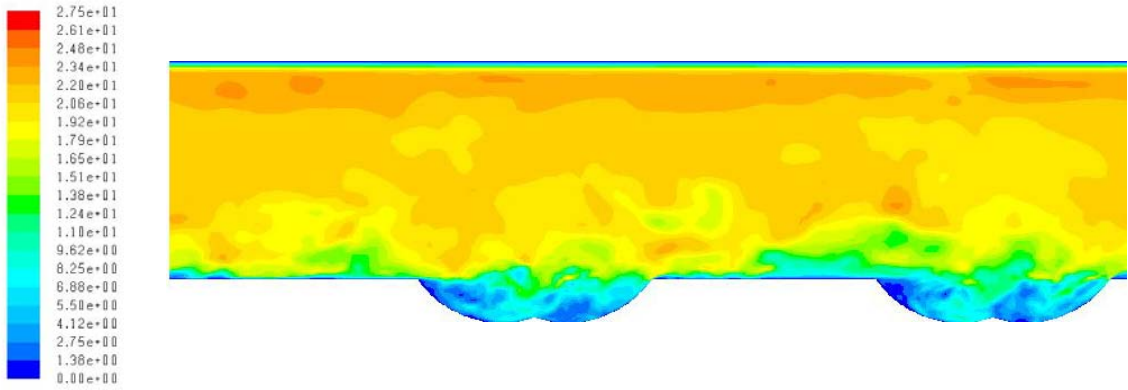


**Figure F.42: Transient Contours of Velocity – (-)X Plane, Time Step = 0.000242s, Re = 40000**

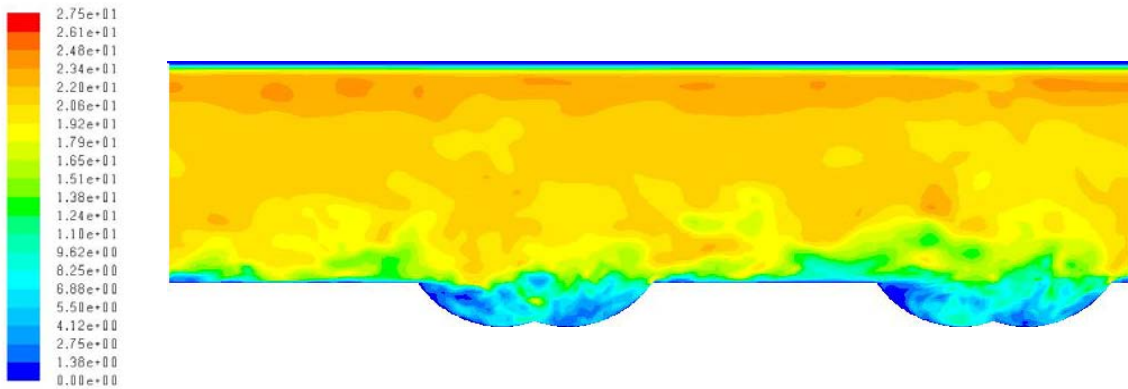


**Figure F.43: Transient Contours of Velocity – (-)X Plane, Time Step = 0.000484s, Re = 40000**

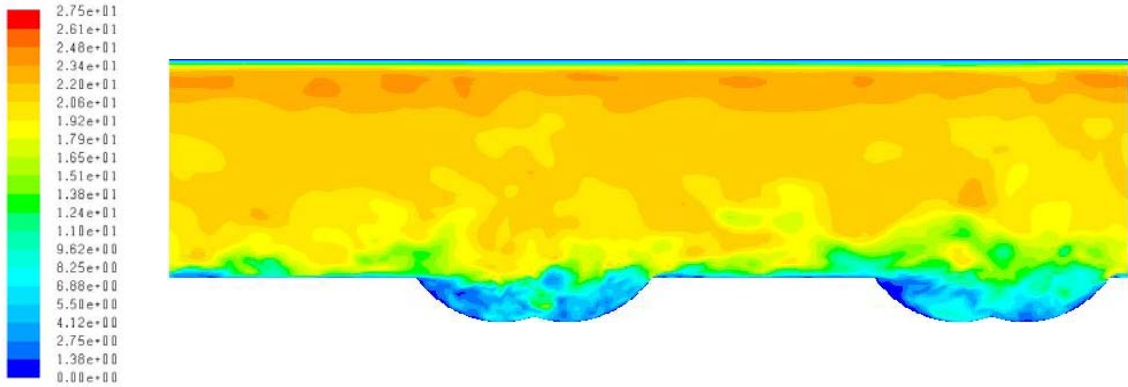


**Figure F.44: Transient Contours of Velocity – (-)X Plane, Time Step = 0.000726s, Re = 40000**

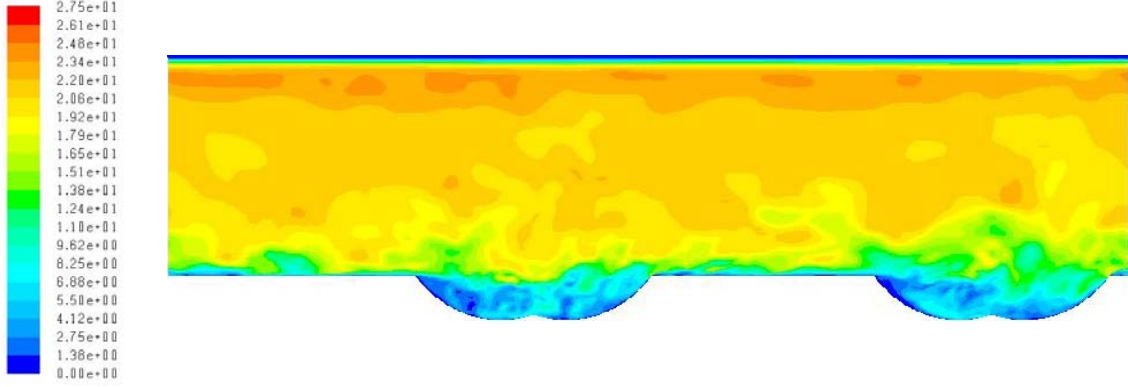


**Figure F.45: Transient Contours of Velocity – (-)X Plane, Time Step = 0.000968s, Re = 40000**

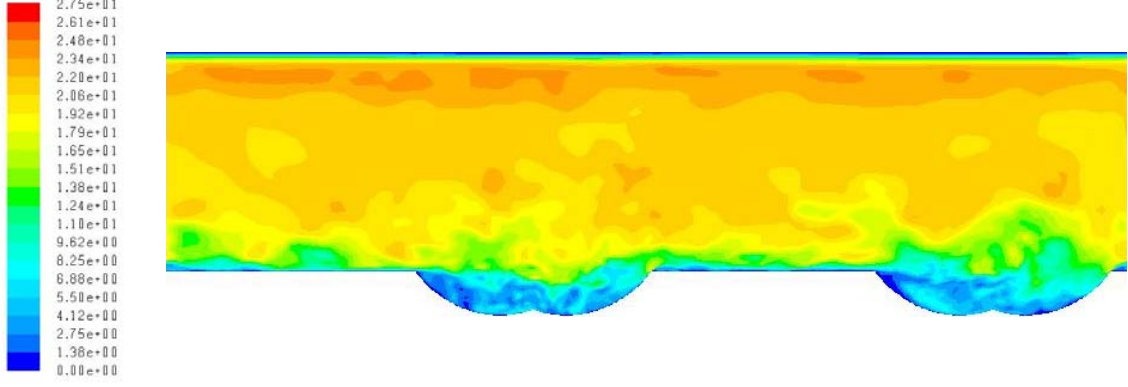


**Figure F.46: Transient Contours of Velocity – (-)X Plane, Time Step = 0.00121s, Re = 40000**



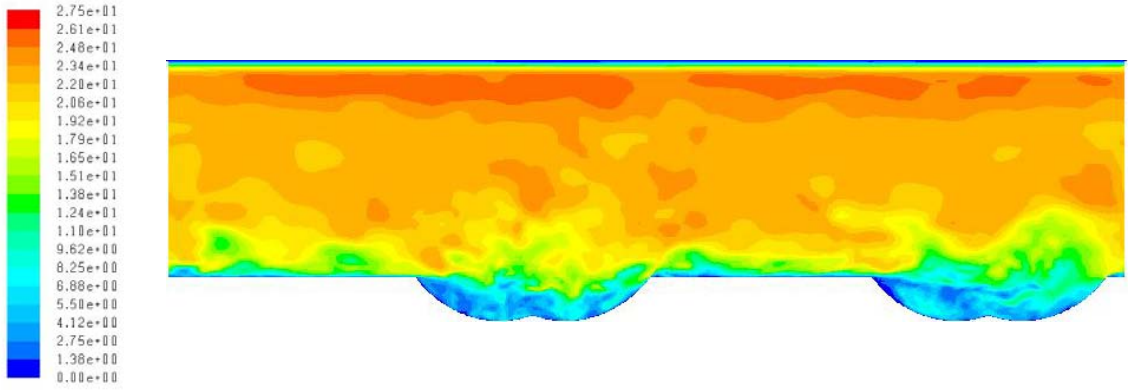


**Figure F.47: Transient Contours of Velocity – (-)X Plane, Time Step = 0.001452s, Re = 40000**

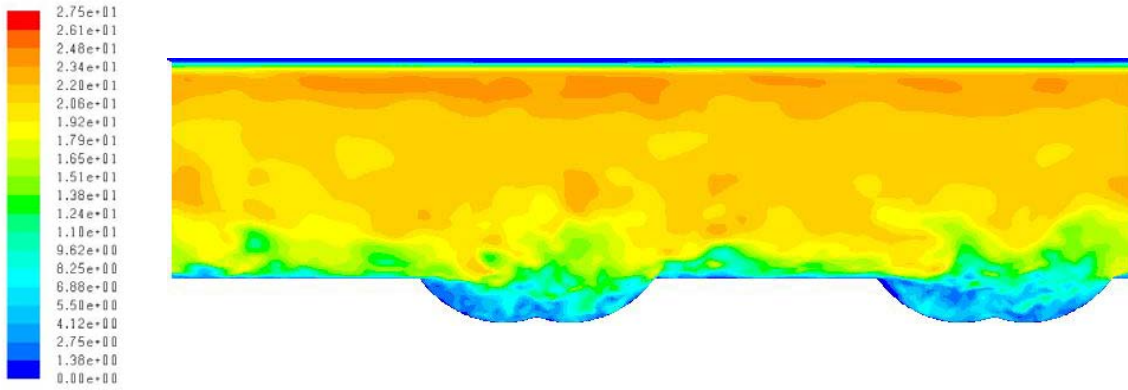


**Figure F.48: Transient Contours of Velocity – (-)X Plane, Time Step = 0.001694s, Re = 40000**

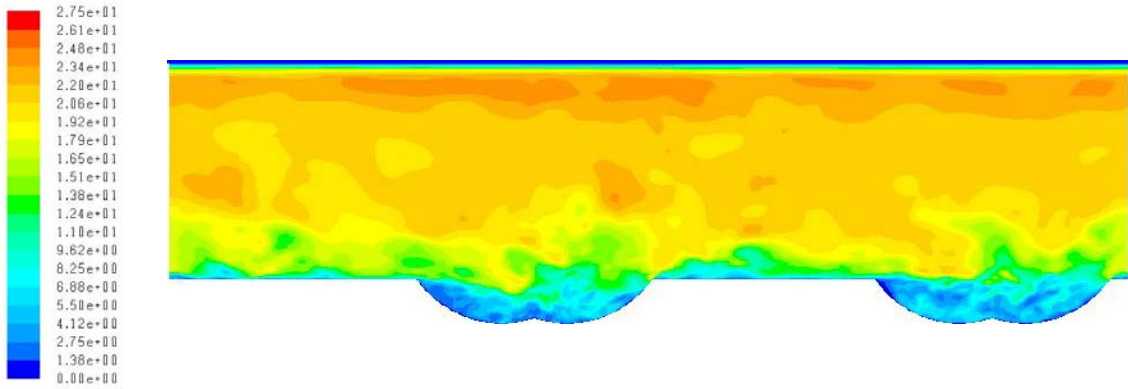


**Figure F.49: Transient Contours of Velocity – (-)X Plane, Time Step = 0.001936s, Re = 40000**

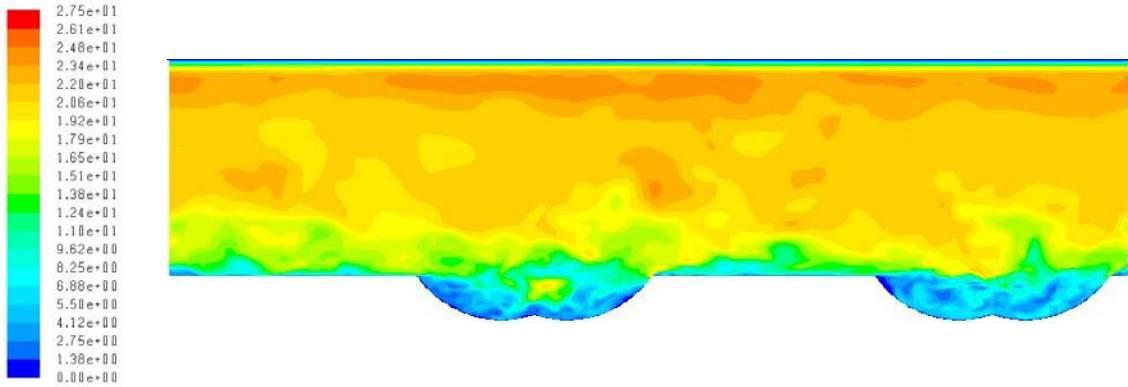


**Figure F.50: Transient Contours of Velocity – (-)X Plane, Time Step = 0.002178s, Re = 40000**

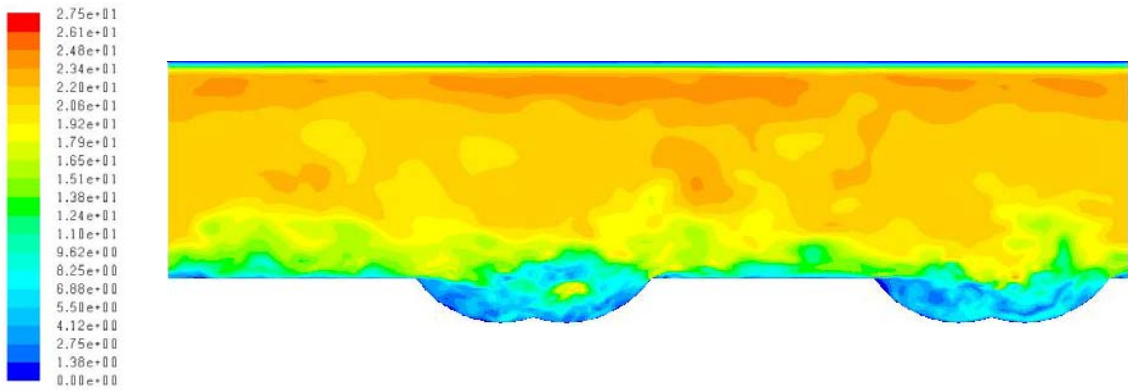


**Figure F.51: Transient Contours of Velocity – (-)X Plane, Time Step = 0.00242s, Re = 40000**

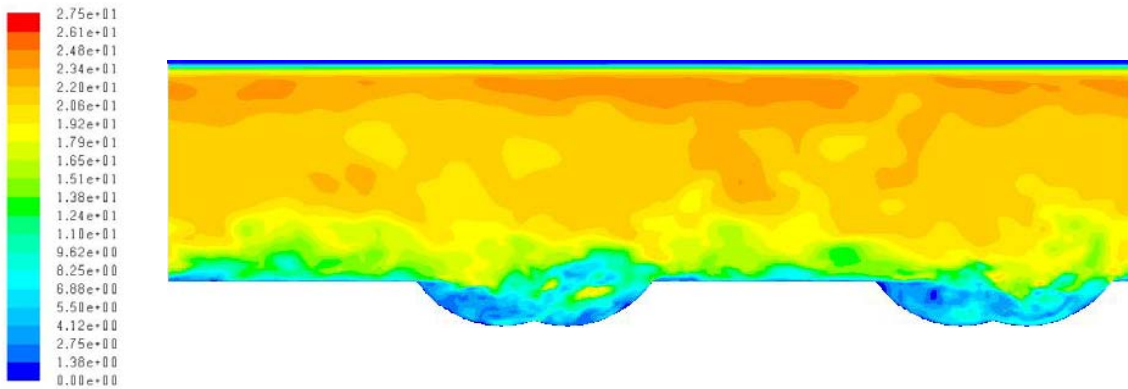


**Figure F.52: Transient Contours of Velocity – (-)X Plane, Time Step = 0.002662s, Re = 40000**



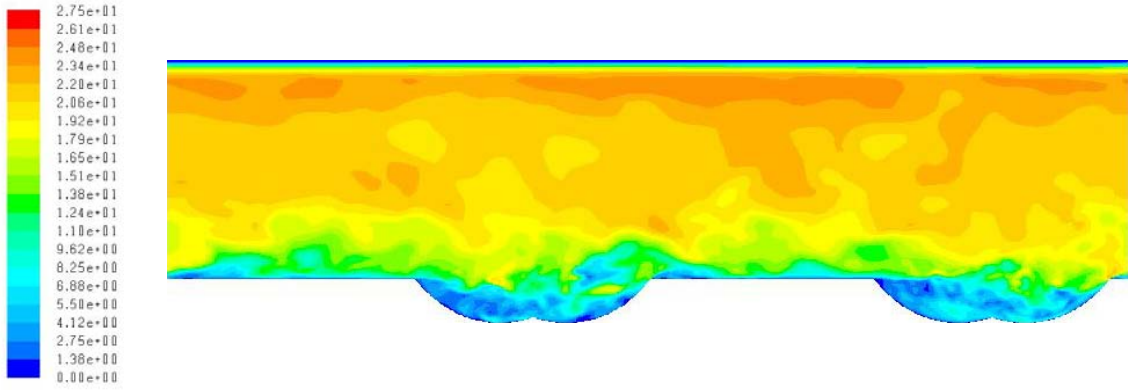


**Figure F.53: Transient Contours of Velocity – (-)X Plane, Time Step = 0.002904s, Re = 40000**

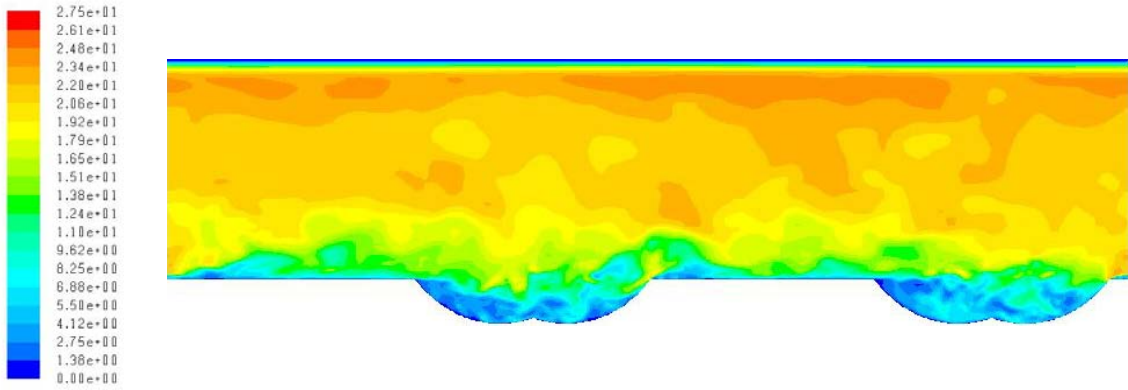


**Figure F.54: Transient Contours of Velocity – (-)X Plane, Time Step = 0.003146s, Re = 40000**

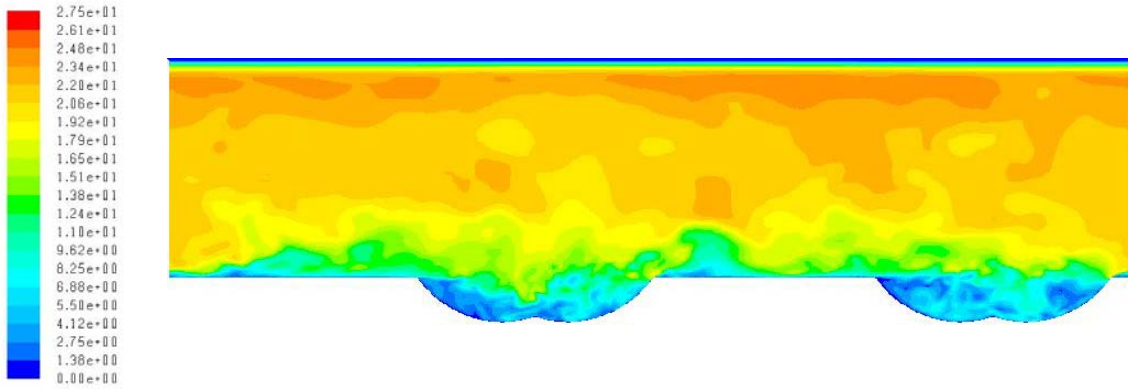


**Figure F.55: Transient Contours of Velocity – (-)X Plane, Time Step = 0.003388s, Re = 40000**

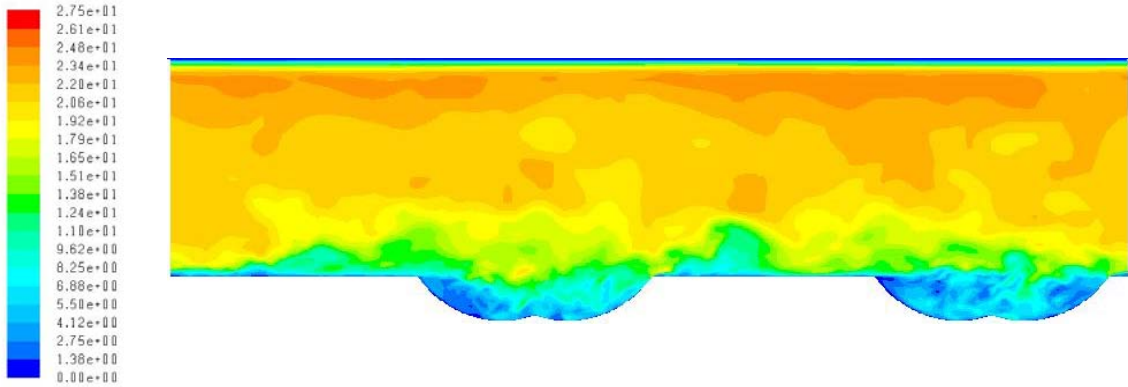


**Figure F.56: Transient Contours of Velocity – (-)X Plane, Time Step = 0.00363s, Re = 40000**

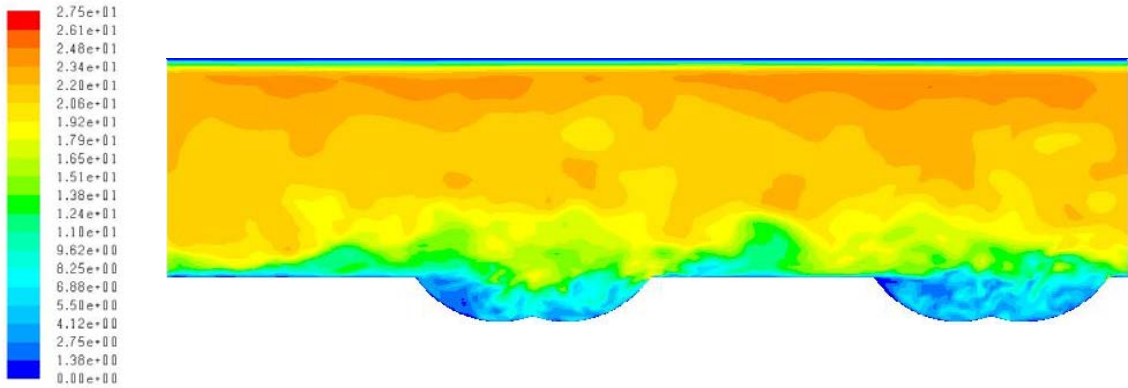


**Figure F.57: Transient Contours of Velocity – (-)X Plane, Time Step = 0.003872s, Re = 40000**

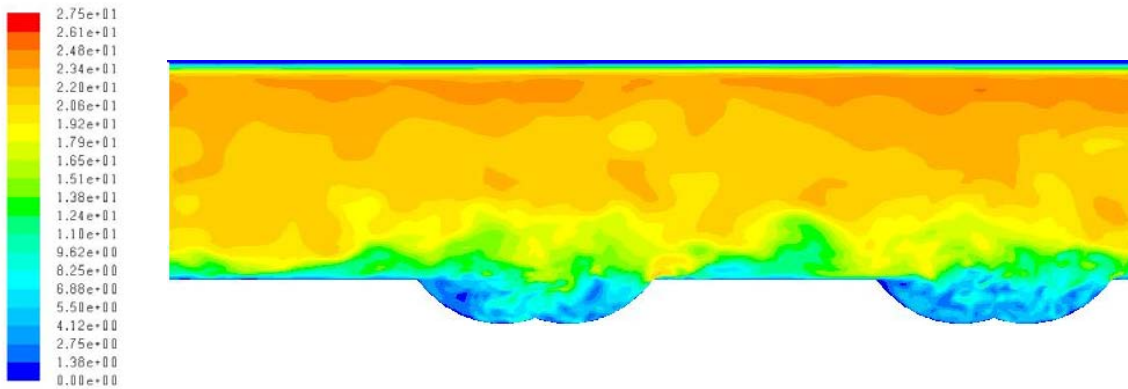


**Figure F.58: Transient Contours of Velocity – (-)X Plane, Time Step = 0.00411 s, Re = 40000**

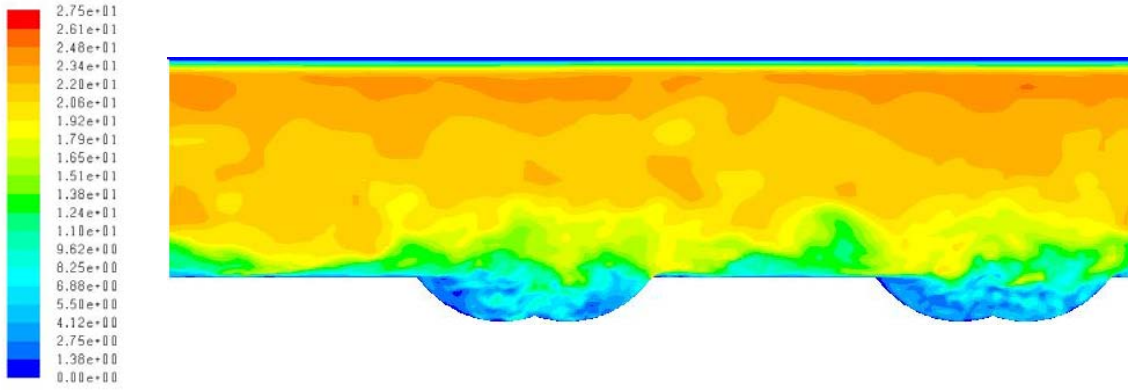


**Figure F.59: Transient Contours of Velocity – (-)X Plane, Time Step = 0.004356s, Re = 40000**

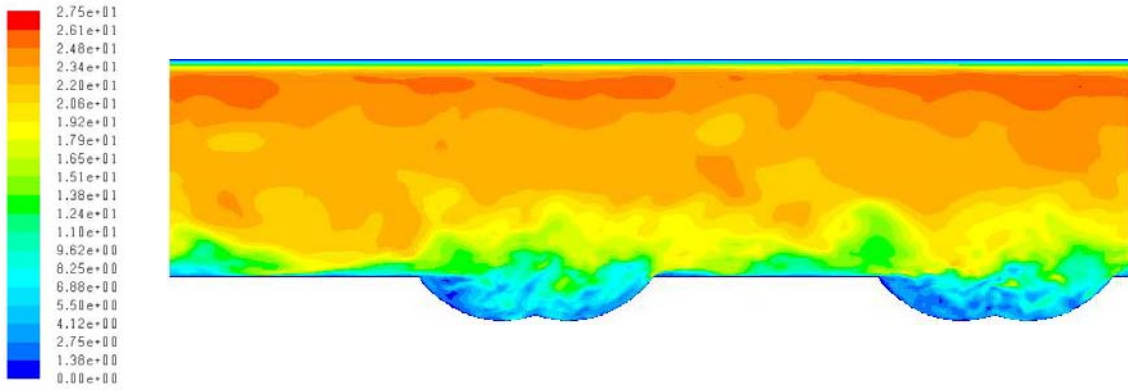


**Figure F.60: Transient Contours of Velocity – (-)X Plane, Time Step = 0.004598s, Re = 40000**

#### F.4. Vorticity Contours – Positive x Streamwise Plane

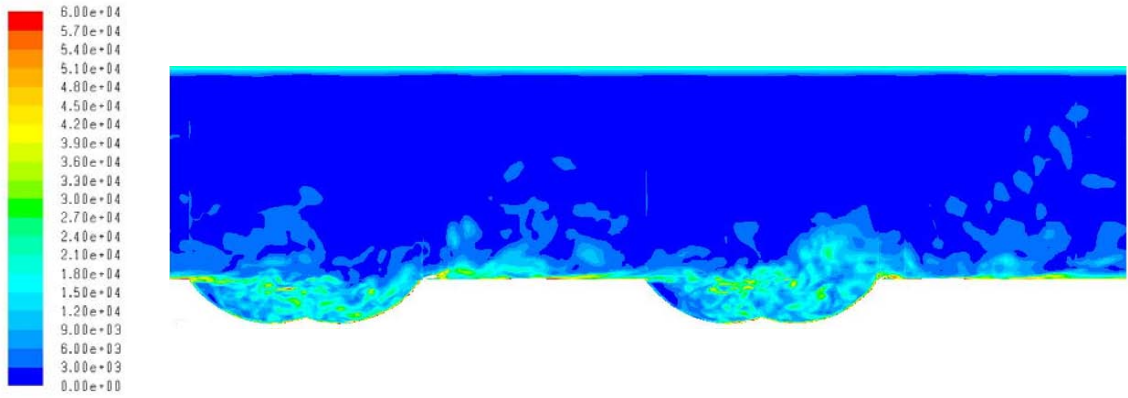


**Figure F.61: Transient Contours of Vorticity – (+)X Plane, Time Step = 0s, Re = 40000**

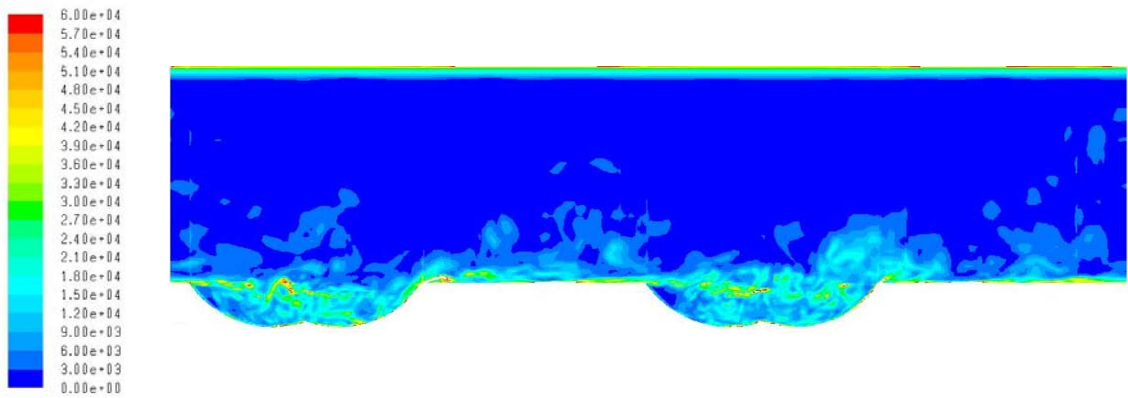


**Figure F.62: Transient Contours of Vorticity – (+)X Plane, Time Step = 0.000242s, Re = 40000**

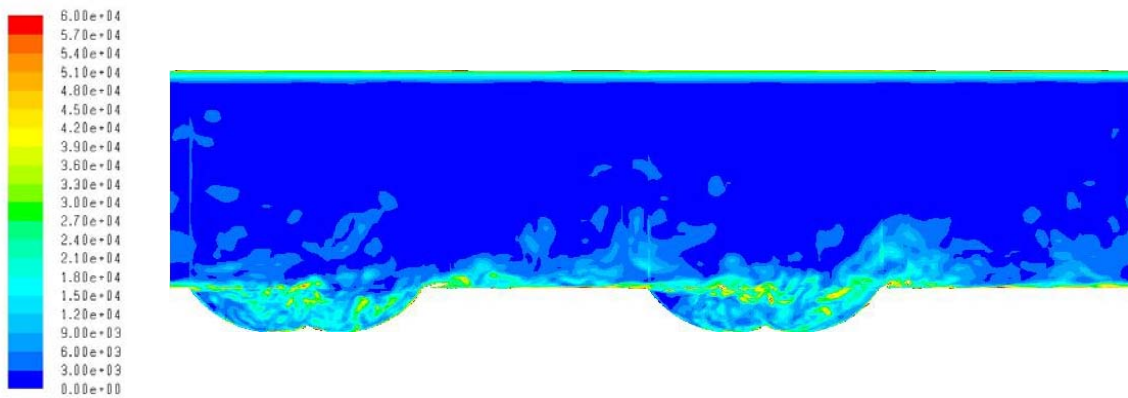


**Figure F.63: Transient Contours of Vorticity – (+)X Plane, Time Step = 0.000484s, Re = 40000**

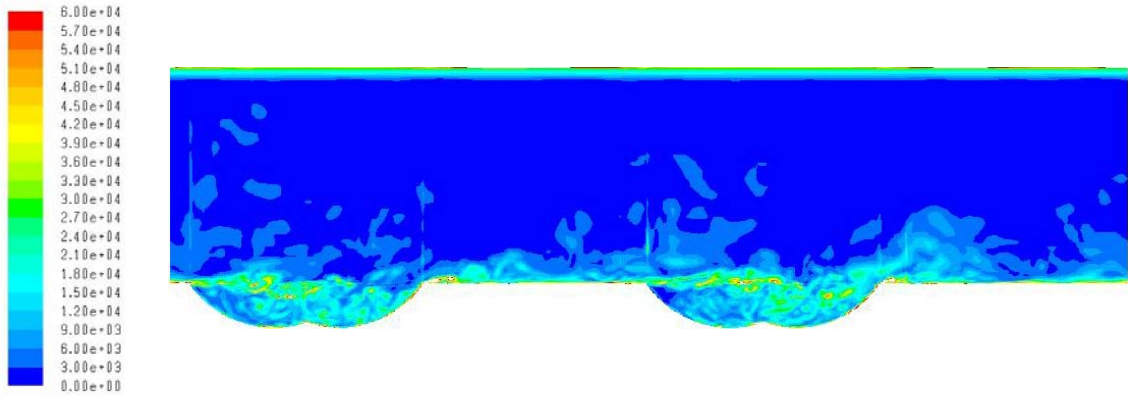


**Figure F.64: Transient Contours of Vorticity – (+)X Plane, Time Step = 0.000726s, Re = 40000**

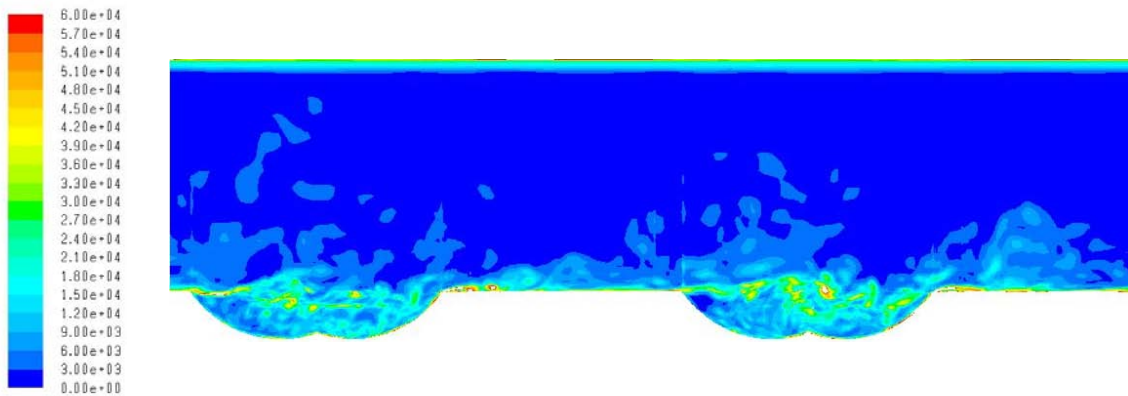


**Figure F.65: Transient Contours of Vorticity – (+)X Plane, Time Step = 0.000968s, Re = 40000**

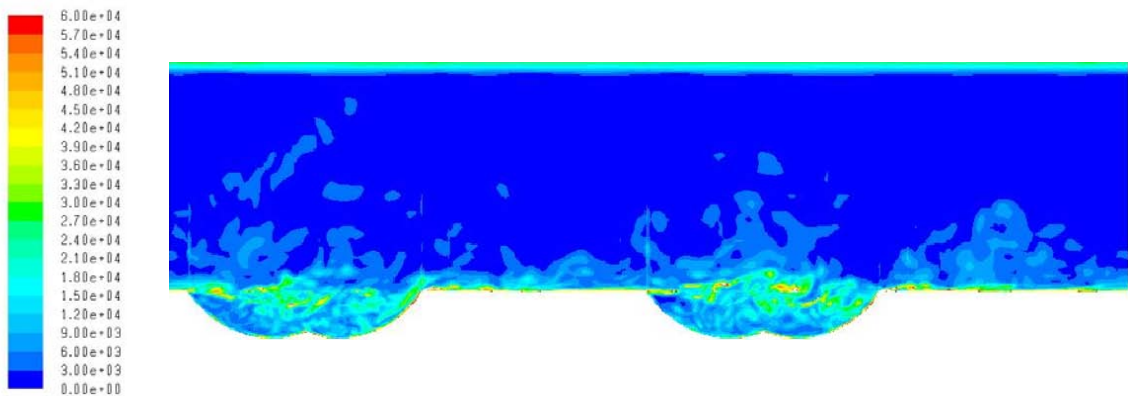


**Figure F.66: Transient Contours of Vorticity – (+)X Plane, Time Step = 0.00121s, Re = 40000**



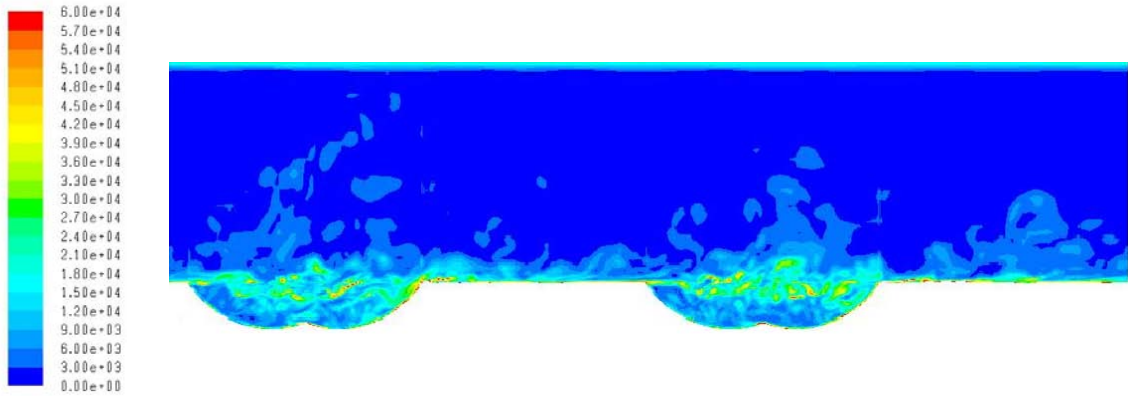


**Figure F.67: Transient Contours of Vorticity – (+)X Plane, Time Step = 0.001452s, Re = 40000**

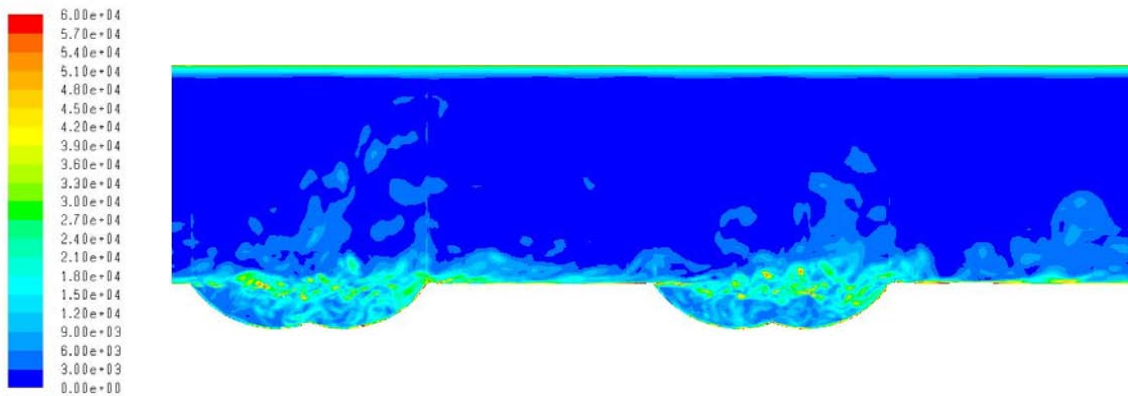


**Figure F.68: Transient Contours of Vorticity – (+)X Plane, Time Step = 0.001694s, Re = 40000**

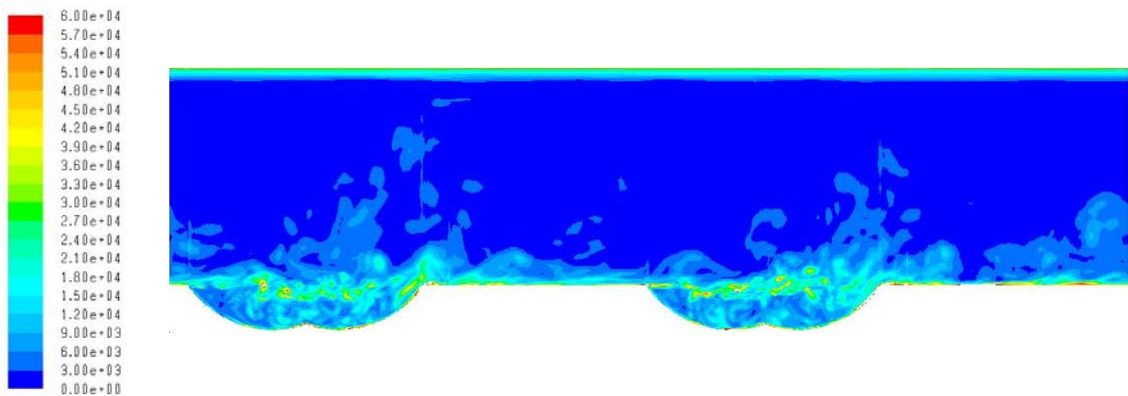


**Figure F.69: Transient Contours of Vorticity – (+)X Plane, Time Step = 0.001936s, Re = 40000**

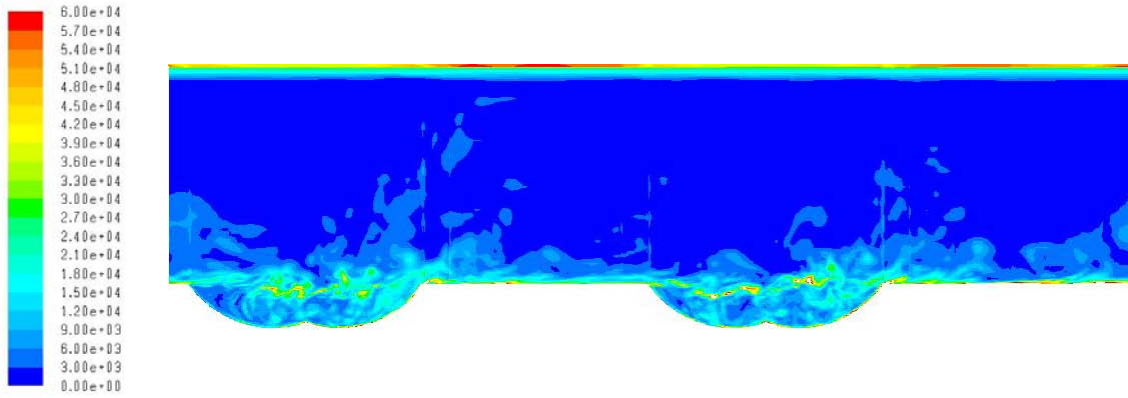


**Figure F.70: Transient Contours of Vorticity – (+)X Plane, Time Step = 0.002178s, Re = 40000**

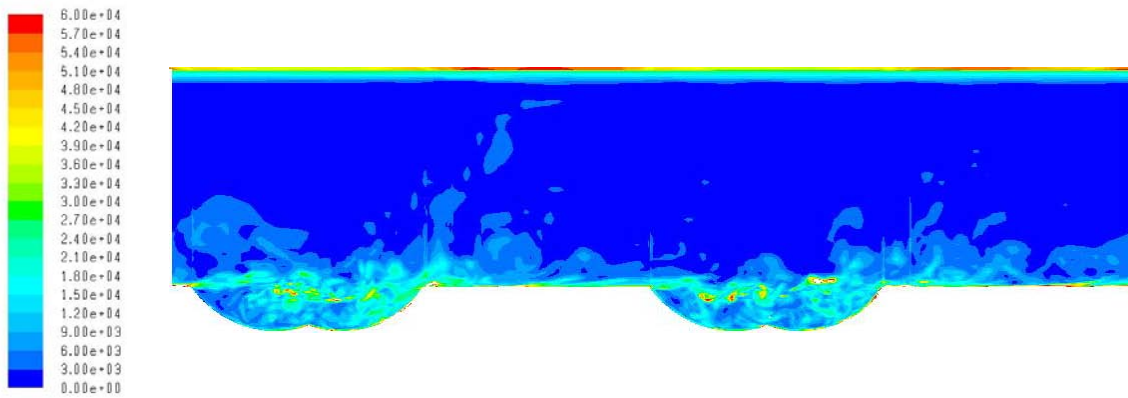


**Figure F.71: Transient Contours of Vorticity – (+)X Plane, Time Step = 0.00242s, Re = 40000**

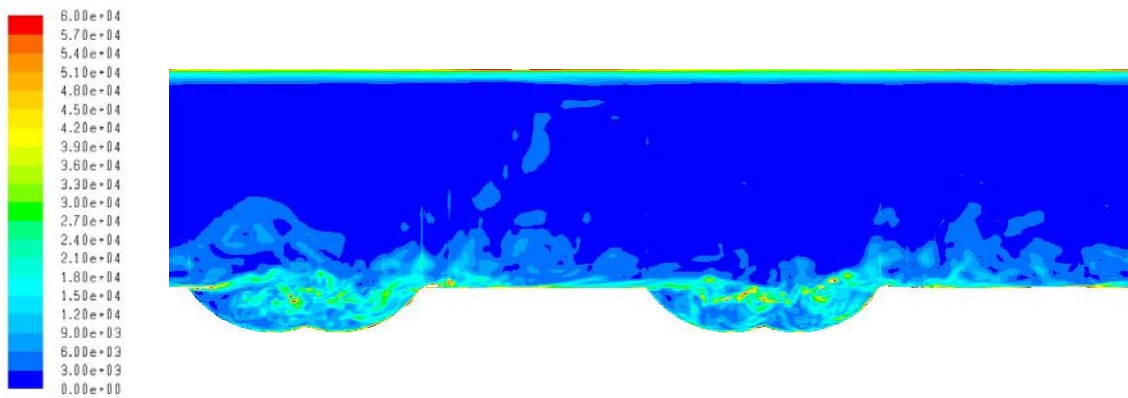


**Figure F.72: Transient Contours of Vorticity – (+)X Plane, Time Step = 0.002662s, Re = 40000**



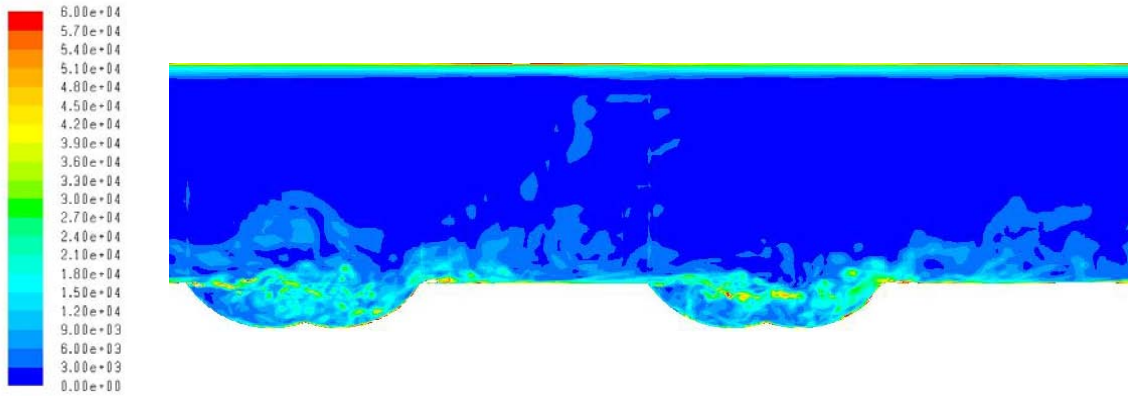


**Figure F.73: Transient Contours of Vorticity – (+)X Plane, Time Step = 0.002904s, Re = 40000**

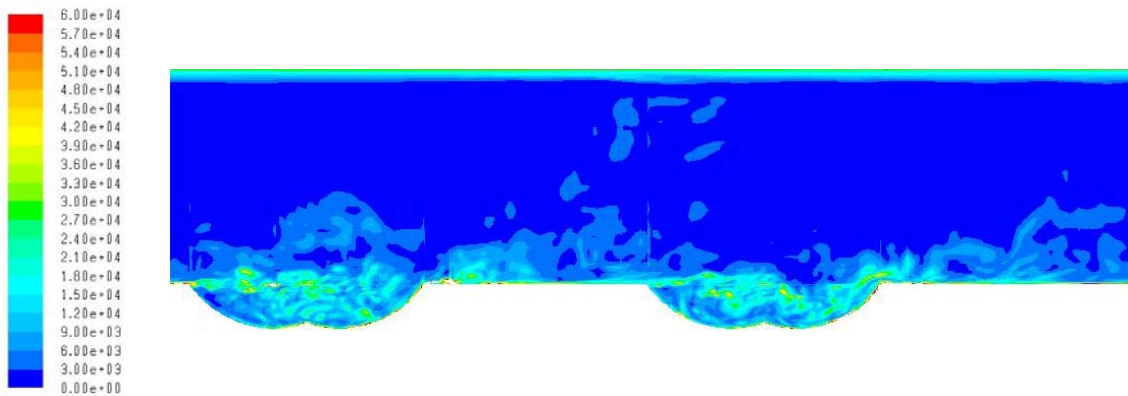


**Figure F.74: Transient Contours of Vorticity – (+)X Plane, Time Step = 0.003146s, Re = 40000**

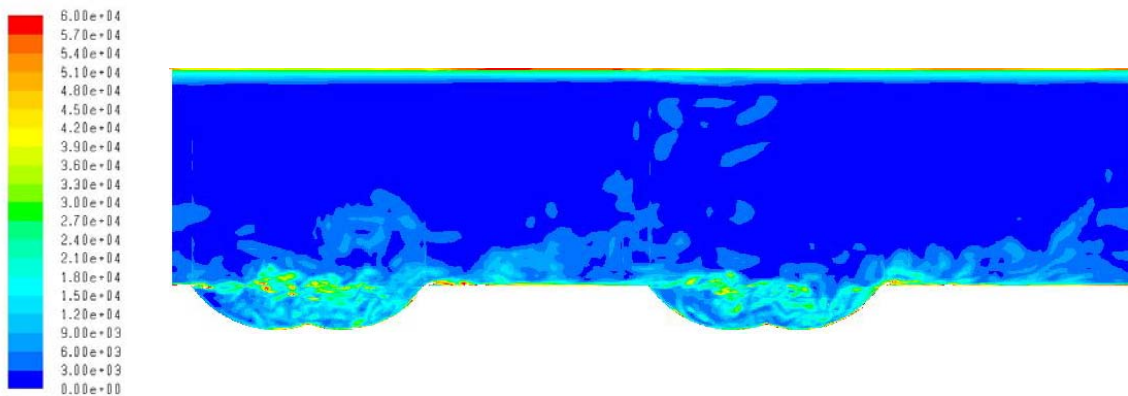


**Figure F.75: Transient Contours of Vorticity – (+)X Plane, Time Step = 0.003388s, Re = 40000**

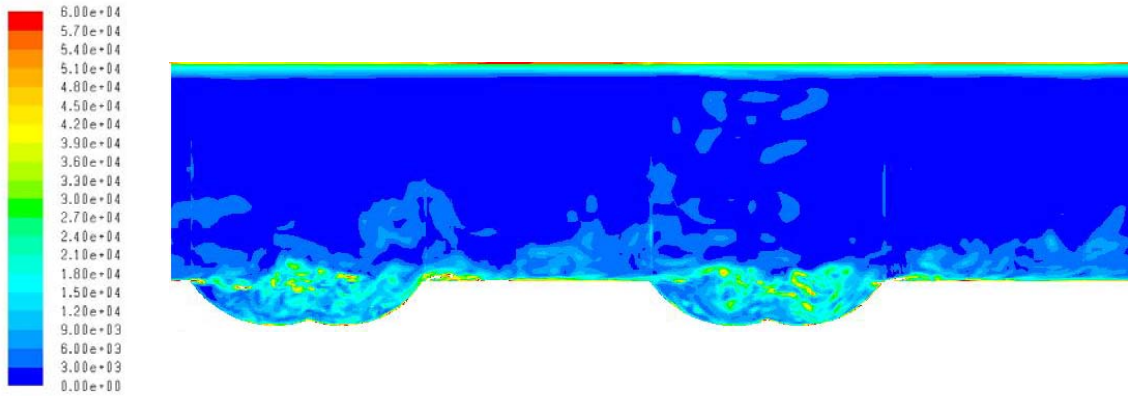


**Figure F.76: Transient Contours of Vorticity – (+)X Plane, Time Step = 0.00363s, Re = 40000**

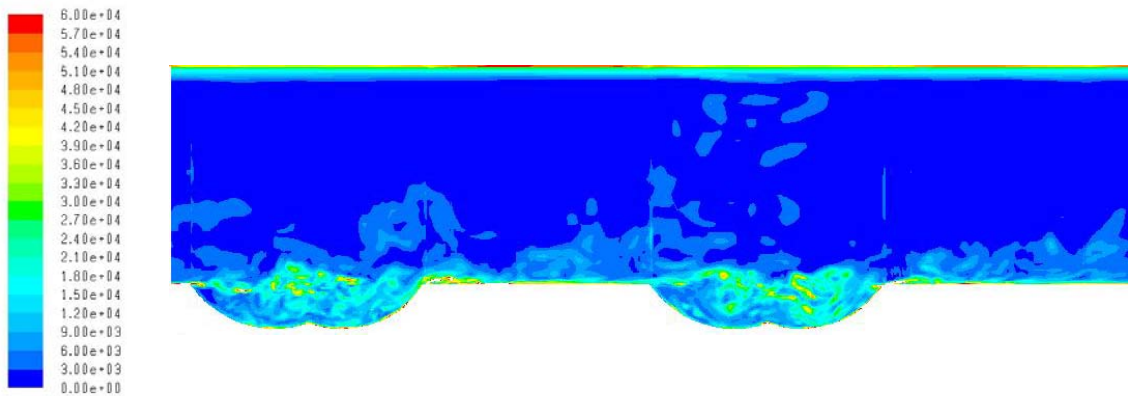


**Figure F.77: Transient Contours of Vorticity – (+)X Plane, Time Step = 0.003872s, Re = 40000**

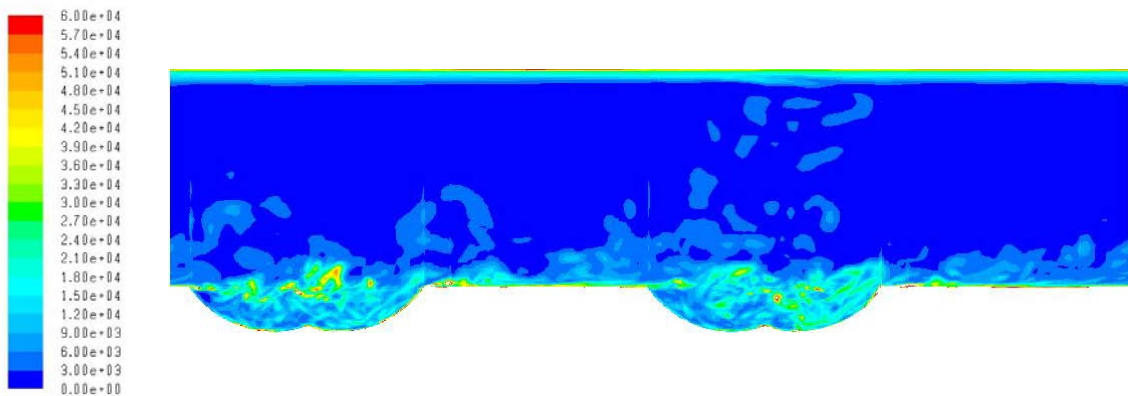


**Figure F.78: Transient Contours of Vorticity – (+)X Plane, Time Step = 0.004114s, Re = 40000**

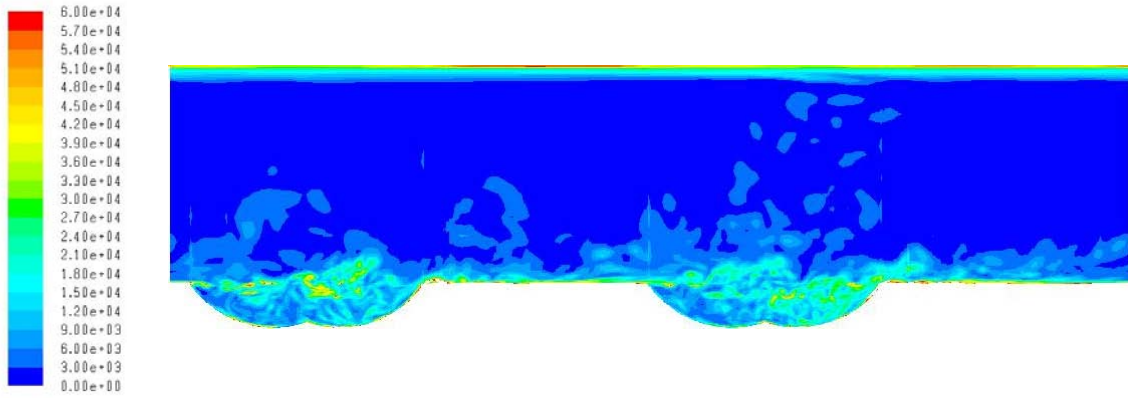


**Figure F.79: Transient Contours of Vorticity – (+)X Plane, Time Step = 0.004356s, Re = 40000**

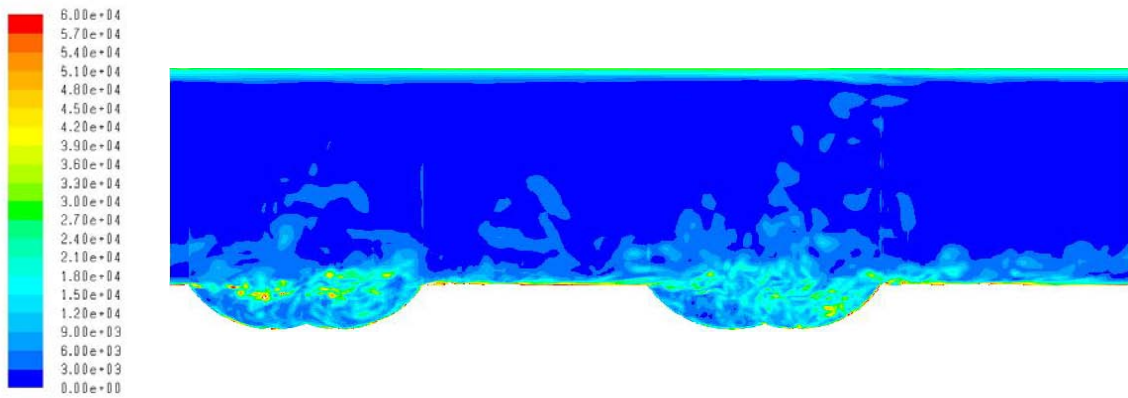


**Figure F.80: Transient Contours of Vorticity – (+)X Plane, Time Step = 0.004598s, Re = 40000**

F.5. Vorticity Contours – Negative x Streamwise Plane

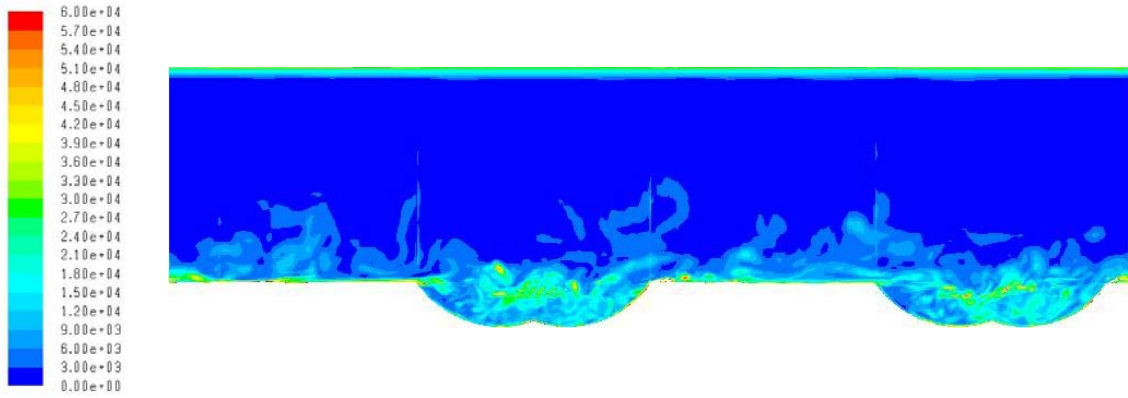


**Figure F.81: Transient Contours of Velocity – (-)X Plane, Time Step = 0s, Re = 40000**

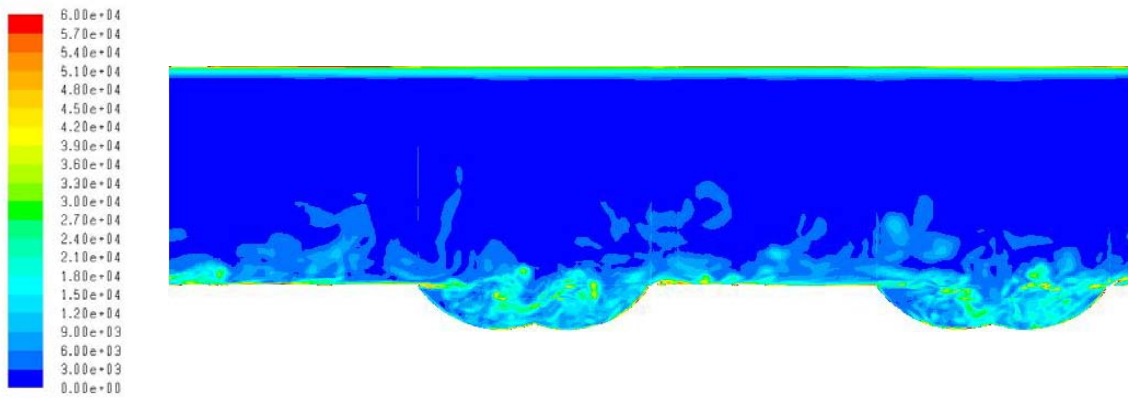


**Figure F.82: Transient Contours of Velocity – (-)X Plane, Time Step = 0.000242s, Re = 40000**

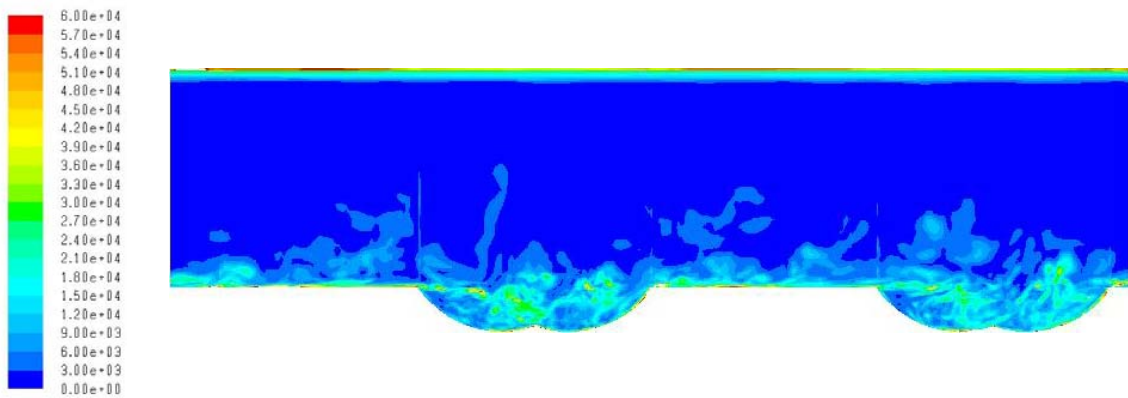


**Figure F.83: Transient Contours of Velocity – (-)X Plane, Time Step = 0.000484s, Re = 40000**

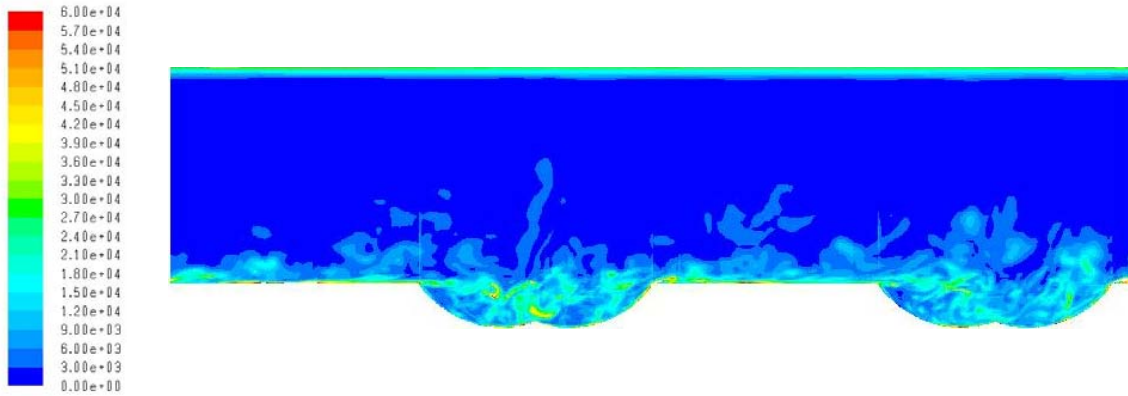


**Figure F.84: Transient Contours of Velocity – (-)X Plane, Time Step = 0.000726s, Re = 40000**

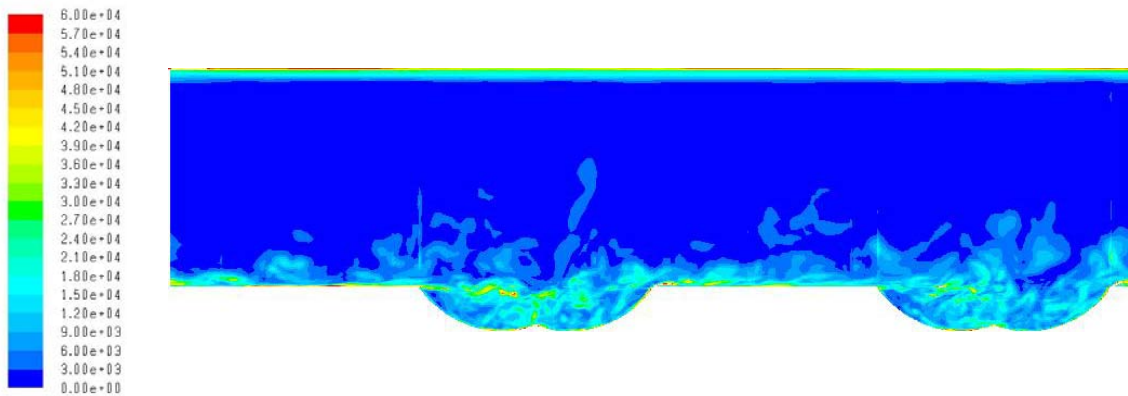


**Figure F.85: Transient Contours of Velocity – (-)X Plane, Time Step = 0.000968s, Re = 40000**

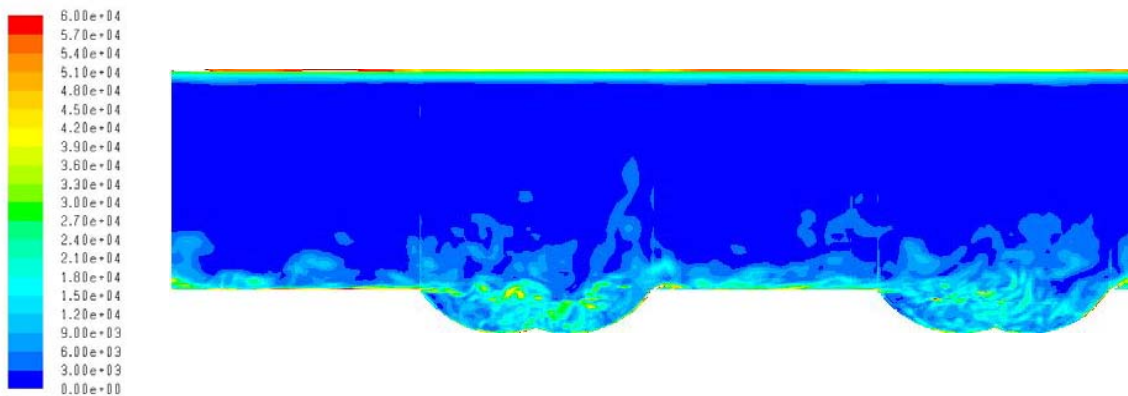


**Figure F.86: Transient Contours of Velocity – (-)X Plane, Time Step = 0.00121s, Re = 40000**



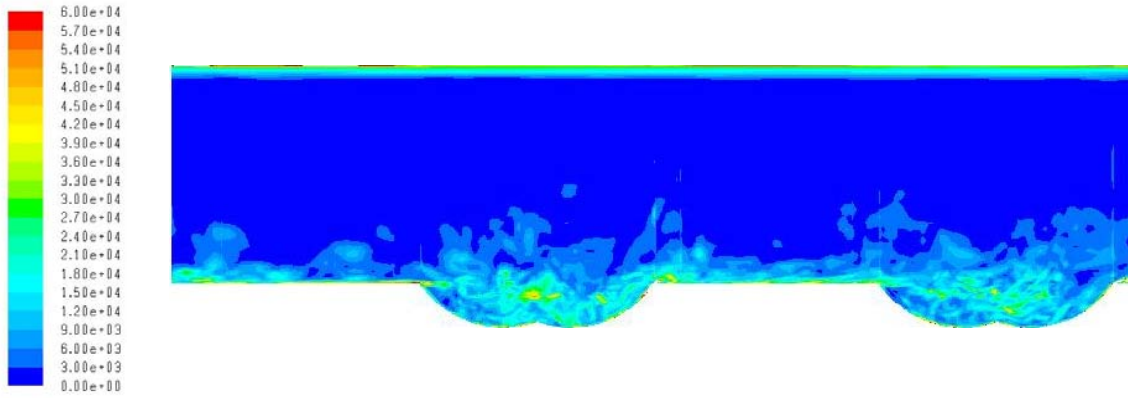


**Figure F.87: Transient Contours of Velocity – (-)X Plane, Time Step = 0.001452s, Re = 40000**

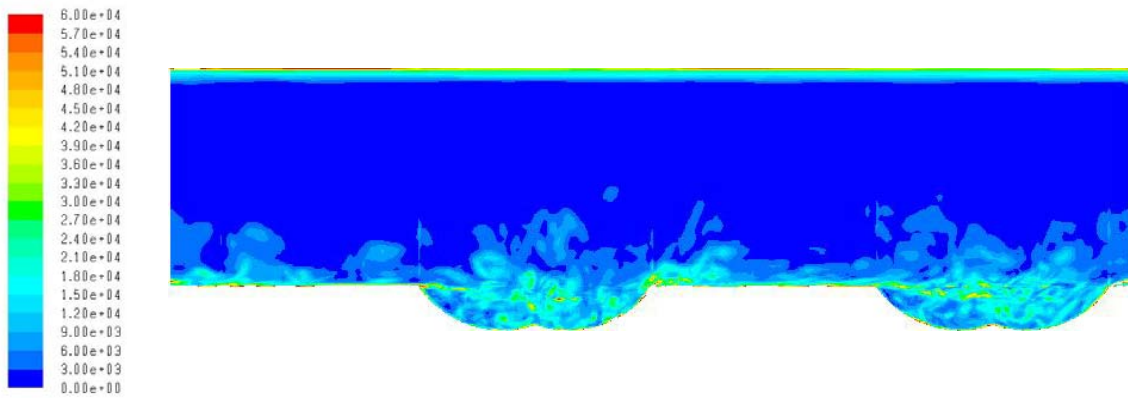


**Figure F.88: Transient Contours of Velocity – (-)X Plane, Time Step = 0.001694s, Re = 40000**

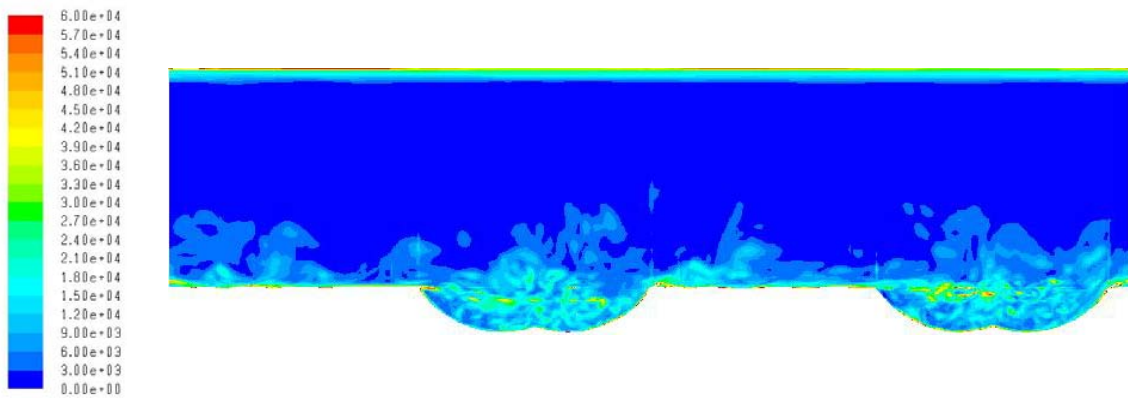


**Figure F.89: Transient Contours of Velocity – (-)X Plane, Time Step = 0.001936s, Re = 40000**

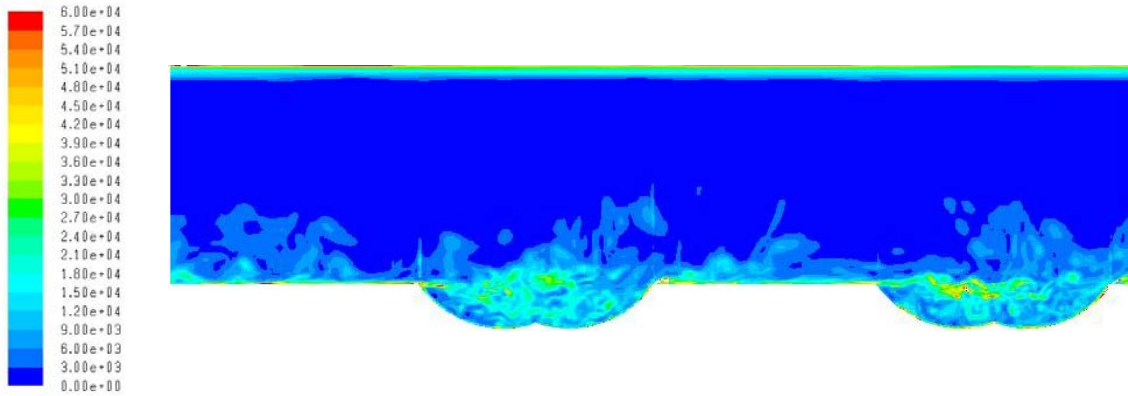


**Figure F.90: Transient Contours of Velocity – (-)X Plane, Time Step = 0.002178s, Re = 40000**

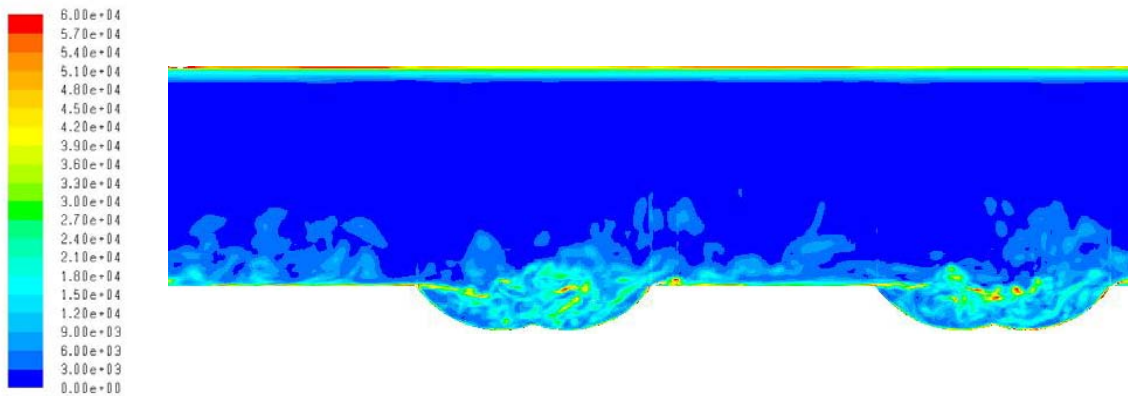


**Figure F.91: Transient Contours of Velocity – (-)X Plane, Time Step = 0.00242s, Re = 40000**

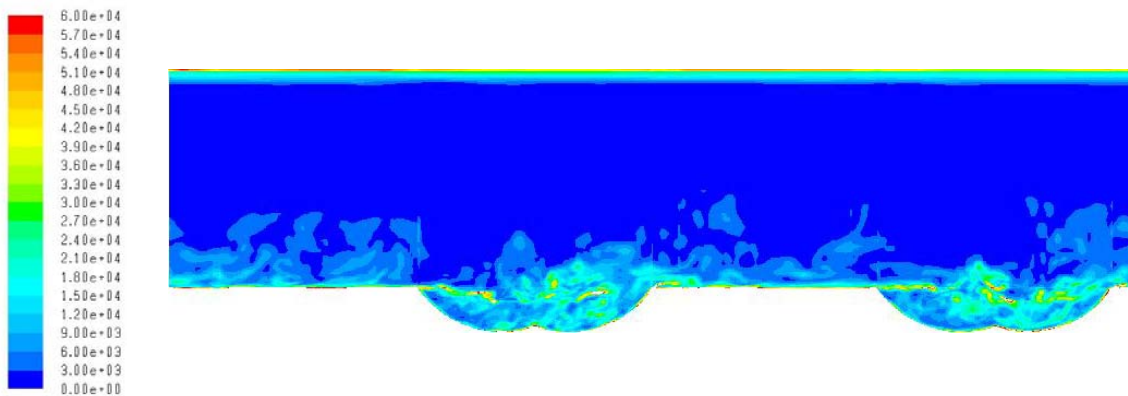


**Figure F.92: Transient Contours of Velocity – (-)X Plane, Time Step = 0.002662s, Re = 40000**



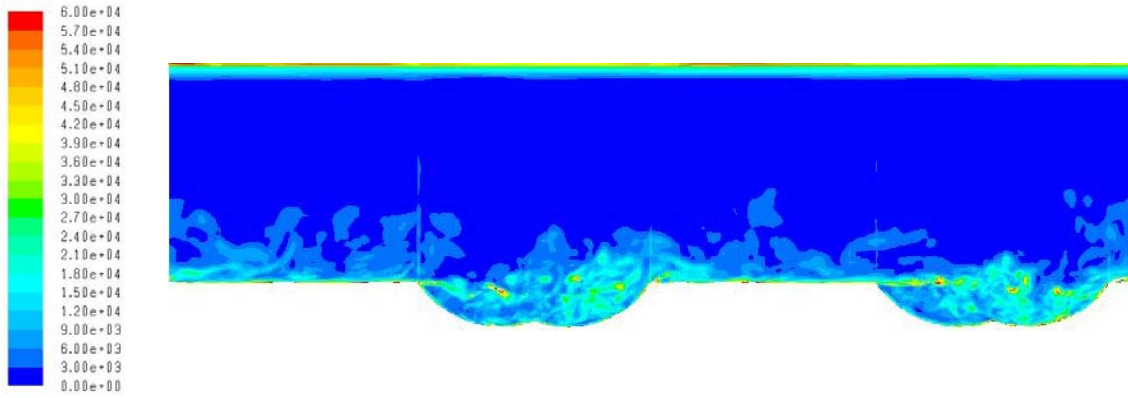


**Figure F.93: Transient Contours of Velocity – (-)X Plane, Time Step = 0.002904s, Re = 40000**

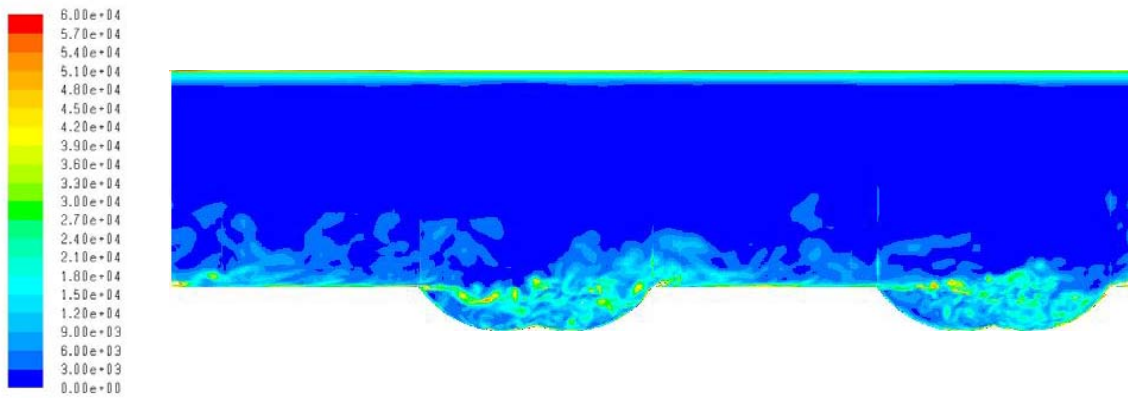


**Figure F.94: Transient Contours of Velocity – (-)X Plane, Time Step = 0.003146s, Re = 40000**

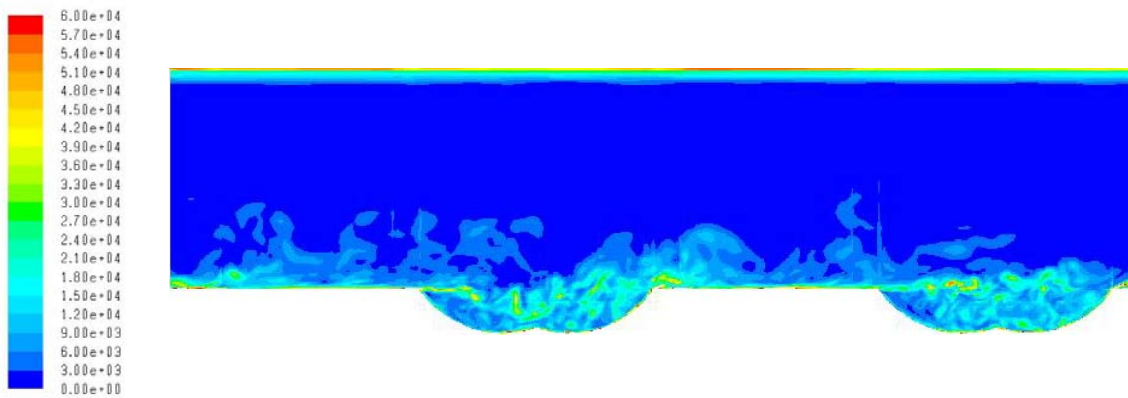


**Figure F.95: Transient Contours of Velocity – (-)X Plane, Time Step = 0.003388s, Re = 40000**

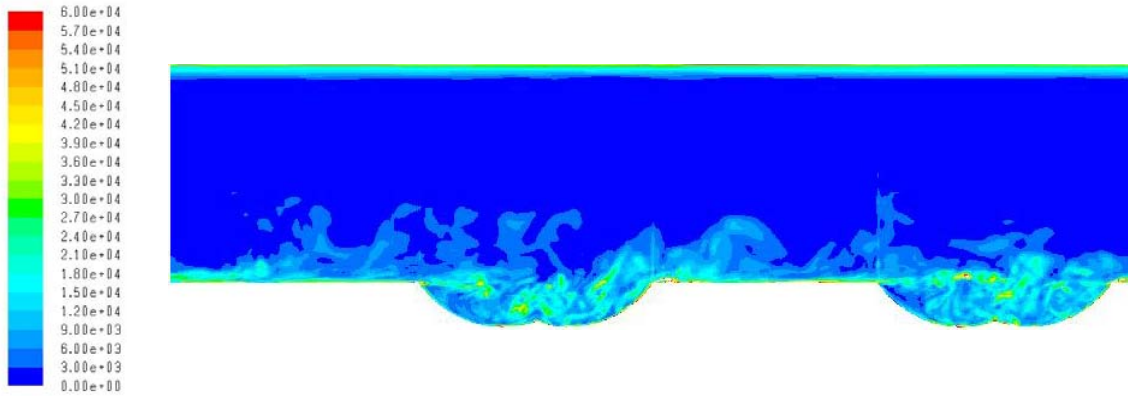


**Figure F.96: Transient Contours of Velocity – (-)X Plane, Time Step = 0.00363s, Re = 40000**

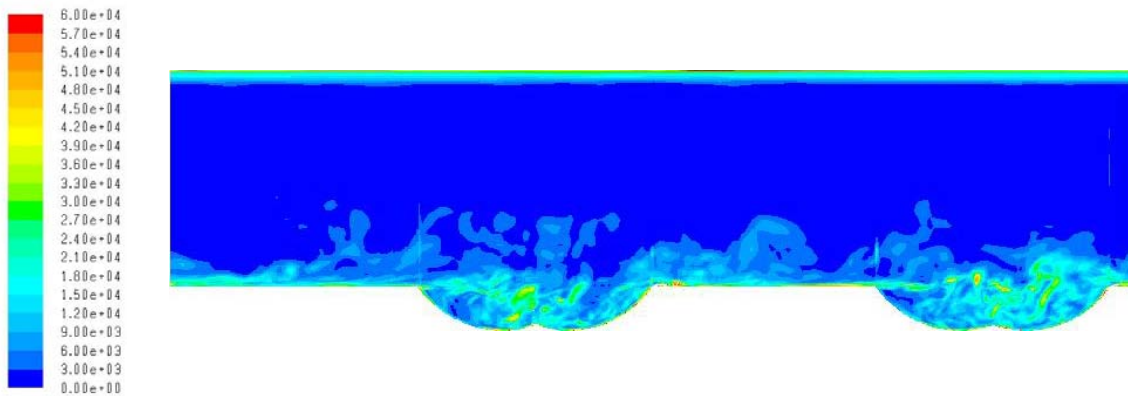


**Figure F.97: Transient Contours of Velocity – (-)X Plane, Time Step = 0.003872s s, Re = 40000**

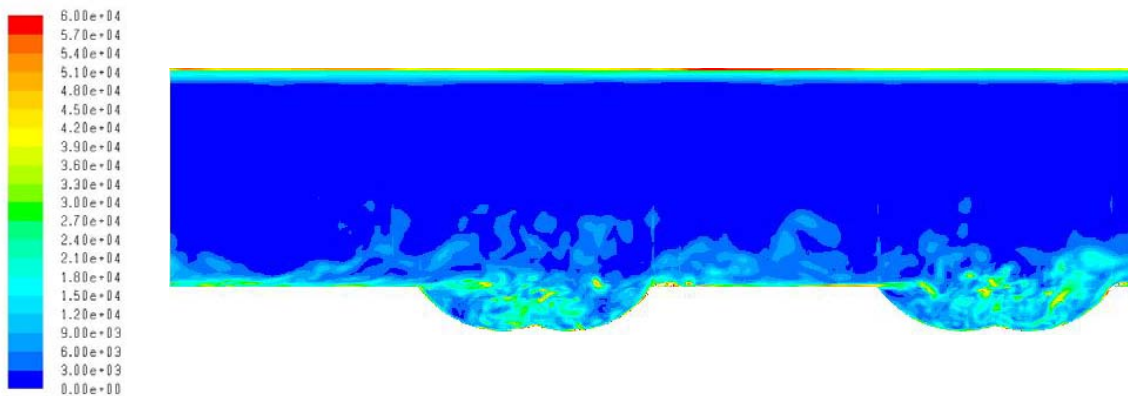


**Figure F.98: Transient Contours of Velocity – (-)X Plane, Time Step = 0.004114s, Re = 40000**

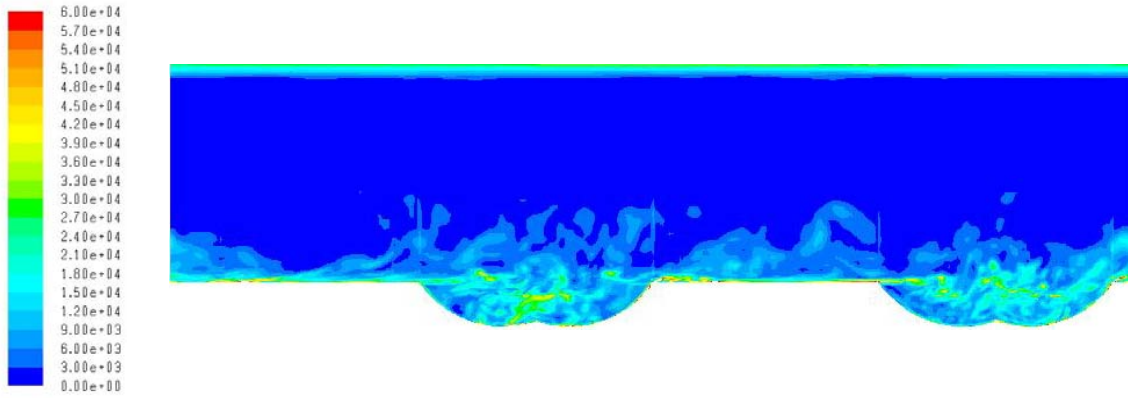


**Figure F.99: Transient Contours of Velocity – (-)X Plane, Time Step = 0.004356s, Re = 40000**

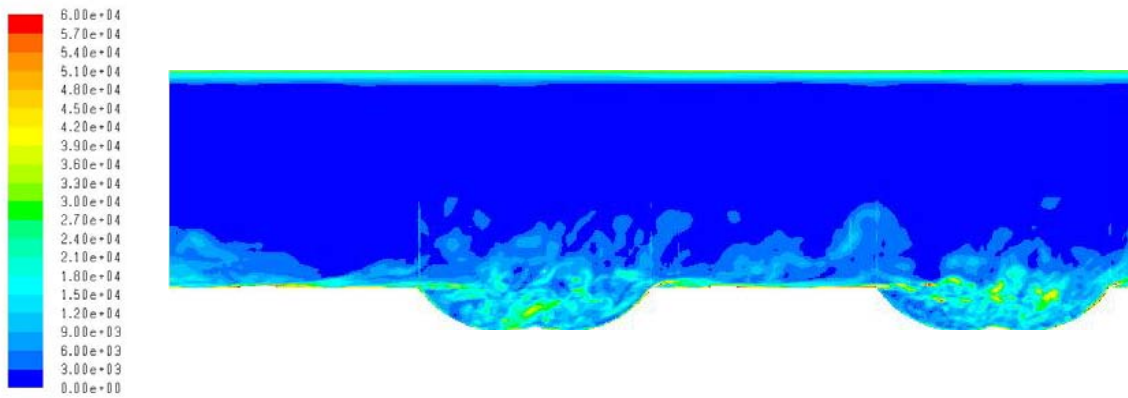


**Figure F.100: Transient Contours of Velocity – (-)X Plane, Time Step = 0.004598s, Re = 40000**

## APPENDIX G: VITA

Carson Daniel Slabaugh was born in Orlando, Florida on May 9, 1987, the son of Michael and Wanda. Carson was married to Hannah Renee Slabaugh on August 8, 2008. He received his Bachelor of Science in Mechanical Engineering from the University of Central Florida in May 2009 and is completing his Master of Science degree in Mechanical Engineering with this document. Carson will begin his doctoral work at Purdue University (West Lafayette, IN) in August, 2010 as a U.S. Department of Defense National Defense Science and Engineering Graduate Fellow. There he will be co-advised under the direction of Drs. Robert Lucht and William Anderson in the Maurice Zucrow High Pressure Combustion and Applied Laser Spectroscopy laboratories.

## REFERENCES

- Abreu, M. E., & Sood, V. M. (1998). *Patent No. 5758504*. United States of America.
- Afanasyev, V. N., Chudnovsky, Y. P., Leontiev, A. I., & Roganov, P. S. (1993). Turbulent Flow Friction and Heat Transfer Characteristics for Spherical Cavities on a Flat Plate. *Experimental Thermal and Fluid Science* , 7, 1-8.
- Al-Aqal, O. M. (2003). *Heat Transfer Distributions on the Walls of a Narrow Channel with Jet Impingement and Cross-Flow*. Doctoral Dissertation, University of Pittsburgh, Pittsburgh, PA.
- Bailey, J. C., & Bunker, R. S. (2002). Local Heat Transfer and Flow Distributions for Impinging Jet Arrays of Dense and Sparse Extent. *International Gas Turbine Conference and Exposition*. Amsterdam: International Gas Turbine Institute.
- Baskharone, E. A. (2006). *Principles of Turbomachinery in Air-Breathing Engines*. New York, New York, United States of America: Cambridge University Press.
- Basu, S. (2009). Thermochromic Liquid Crystals for Engineering Measurements. *University of Central Florida, Thermofluids Measurements Lecture*. Orlando.
- Baughn, J. W. (1995). Liquid Crystal Methods for Studying Turbulent Heat Transfer. *International Journal of Heat and Fluid Flow* , 16, 365-375.
- Belen'kiy, M. Y., Gotovskiy, M. A., Lekakh, B. M., Fokin, B. S., & Dolgushin, K. S. (1993). Heat Transfer Augmentation Using Surfaces Formed by a System of Spherical Cavities. *Heat Transfer Research* , 25 (2), 196-203.
- Box, G. E., Hunter, J. S., & Hunter, W. G. (2005). *Statistics for Experimenters*. Hoboken, New Jersey, USA: John Wiley and Sons.

- Casarsa, L. M., C., & Arts, T. (2002). Characterization of the Velocity and Heat Transfer Fields in an Internal Cooling Channel with High Blockage Ratio. *ASME 47th Annual International Gas Turbine Conference and Exposition*, (pp. 1-8). Amsterdam.
- Chandra, P. R., Alexander, C. R., & Han, J. C. (2003). Heat Transfer and Friction Behaviors in Rectangular Channels with Varying numbers of Ribbed Walls. *International Journal of Heat and Mass Transfer* , 46, 481-495.
- Chandra, P. R., Niland, M. E., & Han, J. C. (1997). Turbulent Flow Heat Transfer and Friction in a Rectangular Channel with Varying Numbers of Ribbed Walls. *ASME Journal of Turbomachinery* , 119, 374-380.
- Chang, S. W., Liou, T. M., Chiang, K. F., & Hong, G. F. (2008). Heat Transfer and Pressure Drop in Rectangular Channel with Compounding Roughness of V-Shaped Ribs and Deepend Scales. *International Journal of Heat and Mass Transfer* , 51, 457-468.
- Chang, S. W., Liou, T.-M., & Lu, M. H. (2005). Heat Transfer of Rectangular Narrow Channel with Two Opposite, Scale-Roughened Walls. *International Journal of Heat and Mass Transfer* , 48, 3921-2931.
- Chang, S. W., Yang, T. L., Huang, C. C., & Chiang, K. F. (2007, August). Endwall Heat Transfer and Pressure Drop in Rectangular Channels with Attached and Detached Circular Pin-Fin Array. *International Journal of Heat and Mass Transfer* , 1-13.
- Cho, H. H., Lee, S. Y., & Wu, S. J. (2001). The Combined Effect of Rib Arrangements and Discrete Ribs on Local Heat/Mass Transfer in a Square Duct. *ASME 46th*

- Annual International Gas Turbine and Aeroengine Congress and Exhibition*, (pp. 1-11). New Orleans, LA.
- Chupp, R., Helms, H., McFadden, P., & Brown, T. (1969). Evaluation of Internal Heat-Transfer Coefficients for Impingement-Cooled Turbine Airfoils. *Journal of Aircraft* , 6 (3), 203-208.
- Chyu, M. K. (1990). Heat Transfer and Pressure Drop for Short Pin-Fin Arrays with Pin-Endwall Fillet. *Journal of Heat Transfer* , 112 (4), 926-932.
- Chyu, M. K., & Natarajan, V. (1996). Heat Transfer on the Base Surface of Three-Dimensional Protruding Elements. *International Journal of Heat and Mass Transfer* , 39 (14), 2925-2935.
- Chyu, M. K., Emery, A. F., Downs, J. P., & Soechting, F. O. (1998). Determination of Local Heat Transfer Coefficients Based on Bulk Mean Temperature Using Transient Liquid Crystals Technique. *Experimental Thermal and Fluid Science* , 18, 142-149.
- Chyu, M. K., Hsing, Y. C., & Natarajan, V. (1998). Convective Heat Transfer of Cubic Fin Arrays in a Narrow Channel. *Journal of Turbomachinery* , 120 (2), 362-367.
- Chyu, M. K., Yu, Y., Ding, H., Downs, J. P., & Soechting, F. O. (1997). Concavity Enhanced Heat Transfer in an Internal Cooling Passage. *ASME 42nd International Gas Turbine and Aeroengine Congress and Exposition*, (pp. 1-7). Orlando, FL.
- Dailey, G. M. (2000). Aero Thermal Performance of Internal Cooling Systems in Turbomachines. *VKI Lecture Series* .



- Davis, L. B., Goodwin, W. W., & Steber, C. E. (1988). *Patent No. 4719748*. United States of America.
- Dittus, F. W., & Boelter, L. M. (1930). Heat Transfer in Automobile Radiators of the Tubular Type. *University of California Publications in Engineering* , 2, 443-461.
- Ecke, R. (2005). The Turbulence Problem: An Experimentalist's Perspective. *Los Alamos Science* , 29, 124-134.
- Ekkad, S. V., & Han, J.-C. (2000). A Transient Liquid Crystal Thermography Technique for Gas Turbine Heat Transfer Measurements. *Measurement Science and Technology* , 11, 957-968.
- Emery, A. F., Neighbors, P. K., & Gessner, F. B. (1980). The Numerical Prediction of Developing Turbulent Flow and Heat Transfer in a Square Duct. *Journal of Heat Transfer* , 102, 51-57.
- Eriksen, & Goldstein. (1974). Heat Transfer and Film Cooling Following Injection through Inclined Tubes. *ASME Journal of Heat Transfer* , 96, 239-245.
- Farina, D. J., Hacker, J. M., Moffat, R. J., & Eaton, J. K. (1994). Illuminant Invariant Calibration of Thermochromic Liquid Crystals. *Experimental Thermal and Fluid Science* , 9, 1-12.
- Florschuetz, L., Berry, R., & Metzger, D. (1980). Periodic Streamwise Variations of Heat Transfer for Inline and Staggered Arrays of Circular Jets with Crossflow of Spent Air. *Journal of Heat Transfer* , 102, 132-137.
- Florschuetz, L., Metzger, D., & Su, C. (1984). Heat Transfer Characteristics for Jet Array Impingement with Initial Crossflow. *Journal of Heat Transfer* , 106, 34-41.

- Florschuetz, L., Truman, C., & Metzger, D. (1981). Streamwise Flow and Heat Transfer Distributions for Jet Array Impingement with Crossflow. *Journal of Heat Transfer* , 103, 337-342.
- Gabour, L. A., & Lienhard, V. (1994). Wall Roughness Effects on Stagnation-Point Heat Transfer Beneath an Impinging Liquid Jet. *ASME Journal of Heat Transfer* , 116, 81-87.
- Gardon, R., & Akfirat, J. (1966). Heat Transfer Characteristics of Impinging Two-Dimensional Air Jets. *Journal of Heat Transfer* , 101-108.
- Gardon, R., & Cobonpue, J. (1962). Heat Transfer between a Flat Plate and Jets of Air Impinging on it. *Proceedings of the 2nd International Heat Transfer Conference, International Developments in Heat Transfer* (pp. 454-460). New York: ASME.
- Gillespie, D., Wang, Z., Ireland, P., & Kohler, S. (1996). Full Surface Local Heat Transfer Coefficient Measurements in a Model of an Integrally Cast Impingement Cooling Geometry. *IGTI Congress and Exposition*. Birmingham, UK.
- Gladden, H. J., & Simoneau, R. J. review and Assessment of the Database and Numerical Modeling for Turbine Heat Transfer. In I. D. E. Sokolowski (Ed.), *Toward Improved Durability in Advanced Aircraft Engine Hot Sections* (Vol. 2, pp. 39-55).
- Goldstein, R. J., Eckert, E. R., & Burgraf, F. (1974). Effects of Hole Geometry and Density on Three-Dimensional Film Cooling. *International Journal of Heat and Mass Transfer* , 17, 595-607.
- Golstein, R. J. Film Cooling. In *Advancement in Heat Transfer* (Vol. 7). New York: Academic Press.

- Grannis, V. B., & Sparrow, E. M. (1991). Numerical Simulation of Fluid Flow Through an Array of Diamond Shaped Pin Fins. *Numerical Heat Transfer* , 19 (A), 381-403.
- Griffith, T. S., Al Hadhrami, L., & Han, J.-C. (2003). Heat Transfer in Rotating Rectangular Cooling Channels (AR=4) With Dimples. *Journal of Turbomachinery* , 125, 555-563.
- Gromov, P. R., Zobnin, A. B., Rabinovich, M. I., & Sushchik, M. M. (1986). Creation of Solitary Vortices in a Flow Around Shallow Spherical Depressions. *Soviet Technical Physical Letters* , 12 (11), 1323-1328.
- Hallcrest. (1991). *Handbook of Thermochromic Liquid Crystal Technology*. Handbook, Hallcrest, Liquid Crystal Research, Glenview.
- Han, J. C., Glicksman, L. R., & Rohsenow, W. M. (1978). An Investigation of Heat Transfer and Friction for Rib-Roughened Surfaces. *International Journal of Heat and Mass Transfer* , 21 (7), 1143-1156.
- Han, J. C., Huang, J. J., & Lee, C. P. (1993). Augmented Heat Transfer in Square Channels with Wedge-Shaped and Delta-Shaped Turbulence Promoters. *Enhanced Heat Transfer* , 1 (1), 37-52.
- Han, J. C., Park, J. S., & Lie, C. K. (1984). *Heat Transfer and Pressure Drop in Blade Cooling Channels with Turbulence Promoters*. NASA.
- Han, J.-C., Dutta, S., & Ekkad, S. V. (2000). *Gas Turbine Heat Transfer and Cooling Technology*. New York, New York, United States of America: Taylor and Francis.

- Hay, N., Lampard, D., & Saluja, C. L. (1985). Effects of Cooling Films on the Heat Transfer Coefficient on a Flat Plate with Zero Mainstream Pressure Gradient. *ASME Journal of Engineering Gas Turbines Power* , 107, 104-110.
- Hippensteele, S. A., Russell, L. M., & Stepka, F. (1981). Evaluation of a Method for Heat Transfer Measurements and Thermal Visualization Using a Composite of a Heater Element and Liquid Crystals. *Annual Conference of Turbomachinery*.
- Hollworth, B. R., & Berry, R. D. (1978). Heat Transfer from Arrays of Impinging Jets with Large Jet-to-Jet Spacing. *ASME Journal of Heat Transfer* , 116, 352-357.
- Horlock, J. H., Watson, D. T., & Jones, T. V. (2001). Limitations on Gas Turbine Performance Imposed by Large Turbine Cooling Flows. *Journal of Engineering for Gas Turbines and Power* , 123, 487-494.
- Hrycak, P. (1983). Heat transfer from Round Impinging Jets to a Flat Plate. *International Journal of Heat Transfer* , 26, 1857-1865.
- Huang, Y., Ekkad, S., & Han, J. C. (1996). Detailed Heat Transfer Coefficient Distributions Under an Array of Impinging Jets with Coolant Extraction. *International Mechanical Engineering Congress and Exposition*. Atlanta, GA.
- Hucek, H. J. (1985). Aerospace Structural Metals Handbook. Metals and Ceramics Information Center, Battelle's Columbia Laboratories.
- Hwang, J. J., & Lu, C. C. (2000). Lateral-Flow Effect on Endwall Heat Transfer and Pressure Drop in a Pin-Fin Trapezoidal Duct of Various Pin Shapes. *ASME 45th International Gas Turbine and Aeroengine Congress and Exhibition*. Munich.

- Hwang, S. D., Kwon, H. G., & Cho, H. H. (2008). Heat Transfer with Dimple/Protrusion Arrays in a Rectangular Duct with a Low Reynolds Number Range. *International Journal of Heat and Fluid Flow* , 916-926.
- Ichimiya, K. (1995). Heat Transfer and Flow Characteristics of an Oblique Turbulent Impinging Jet within Confined Walls. *Journal of Heat Transfer* , 117, 316-322.
- Incropera, F. P., & Dewitt, D. P. (2006). *Fundamentals of Heat and Mass Transfer* (Vol. 6). John Wiley and Sons.
- Ireland, P. T. (1987). *Heat Transfer in Gas Turbines*. Oxford, U.K.: Oxford University.
- Ireland, P. T. (1999). Turbulent Heat Transfer Using Liquid Crystals. *International Journal of Heat and Fluid Flow* , 20, 355-367.
- Ireland, P. T., Neely, A. J., Gillespie, D. R., & Robertson, A. J. (1999). Turbulent Heat Transfer Measurements using Liquid Crystals. *International Journal of Heat and Fluid Flow* , 20, 355-367.
- Ireland, P., & Jones, T. (2000). Liquid Crystal Measurements of Heat Transfer and Shear Stress. *Measurement Science and Technology* , 11, 969-986.
- Isaev, S. A., Kornev, N. V., Leontiev, A. I., & Hassel, E. (2010). Influence of the Reynolds number and the spherical dimple depth on turbulent heat transfer and hydraulic loss in a narrow channel. *International Journal of Heat and Mass Transfer* , 53, 178-197.
- Isaev, S. A., Leontiev, A. I., Kudryatsev, N. A., & Pyshnyi, I. A. (2003). The Effect of Rearrangement of the Vortex Structure on Heat Transfer under Conditions of Increasing Depth of a Spherical Dimple on the Wall of a Narrow Channel. *Heat and Mass Transfer and Physical Gas Dynamics* , 41 (2), 229-232.

- Jeal, B. (1988). Moving Towards the Non-Metallic Aero-Engine. In *Rolls-Royce Magazine* (Vol. 25).
- Jorgensen, S. W., & Leahy, J. H. (2003). *Patent No. 6568187*. United States of America.
- Kercher, D., & Tabakoff, W. (1970). Heat Transfer by a Square Array of Round Air Jets Impinging Perpendicular to a Flat Surface Including the Effect of Spent Air. *Journal of Engineering for Power* , 92, 73-82.
- Kesarav, V. S., & Kozlov, A. P. (1995). *Heat Transfer Research* , 25, 156.
- Kim, K.-Y., & Choi, J.-Y. (2005). Shape Optimization of a Dimpled Channel to Enhance Turbulent Heat Transfer. *Numerical Heat Transfer* , 48, 901-915.
- Kline, S. J., & McClintock, F. A. (1953). *Mechanical Engineering* , 75, 3-8.
- Lakshminarayana, B. (1996). *Fluid Dynamics and Heat Transfer of Turbomachinery*. New York: John Wiley and Sons.
- Lau, S. C. (2001). Enhanced Internal Cooling of Gas Turbine Airfoils. (S. Sunden, & M. Faghri, Eds.) *Heat Transfer in Gas Turbines* , 109-175.
- Leinhart, H., Breuer, M., & Koksoy, C. (2008). Drag Reduction By Dimples? - A complementary experimental/numerical investigation. *International Journal of Heat and Fluid Flow* , 29, 783-791.
- Leonard, B. P. Computational Methods.
- Liao, B. (2000). *Study of the Effect of Jet Instability on Jet Impingement Heat Transfer with a Transient Liquid Crystal Technique*. Masters Thesis, University of Central Florida, Mechanical, Materials, and Aerospace Engineering, Orlando, FL.

- Ligrani, P. M., & Mahmood, G. I. (n.d.). Spatially-Resolved Heat Transfer and Flow Structure in a Rectangular Channel with Forty-Five Degree Angled Rib Turbulators. *Journal of Turbomachinery* .
- Ligrani, P. M., & Mahmood, G. I. (2003). Variable Property Nusselt Numbers in a Channel with Pin Fins. *Journal of Thermophysics and Heat Transfer* , 17 (1), 103-111.
- Ligrani, P. M., Harrison, H. L., Mahmood, G. I., & Mill, M. L. (2001). Flow Structure Due to a Dimple Depression in a Channel Surface. *Physics of fluids* , 13 (11), 3442-3451.
- Ligrani, P. M., Oliveira, M. M., & Blaskovich, T. (2003). Comparison of Heat Transfer Augmentation Techniques. *AIAA Journal* , 41 (3), 337-362.
- Ligrani, P. M., Wigle, J. M., Ciriello, S., & Jackson, S. (1994). Film Coolin From Holes with Compound Angle Orientations: Part 1 - Results Downstream of Two Staggered Roxes of Holes with 3-D Spanwise Spacing. *Journal of Heat and Mass Transfer* , 116, 341-352.
- Lin, Y. L., Shih, T. I.-P., & Chyu, M. K. (1999). Computation of Flow and Heat Transfer in a Channel with Rows of Hemispherical Cavities. *International Gas Turbine Conference and Exposition* (pp. 1-6). Indianapolis, IN: ASME.
- Lin, Z., Chou, Y., & Huang, Y. (1997). Heat Transfer Behaviors of a Confined Slot Jet Impingement. *International Journal of Heat and Mass Transfer* , 40, 1095-1107.
- Ling, J. P. (2005). *Development of Heat Transfer Measurement Techniques and Cooling Strategies for Gas Turbines*. Doctoral Dissertation, University of Oxford, Engineering Science, Oxford.

- Mahmood, G. I., & Ligrani, P. (2002). Heat Transfer in a Dimpled CHannel: Combined Influences of Aspect Ratio, Temperature Ratio, Reynolds Number, and Flow Structure. *International Journal of Heat and Mass Transfer* , 45, 2011-2020.
- Mahmood, G. I., Hill, M. L., Nelson, D. L., Ligrani, P. M., Moon, H. K., & Glezer, B. (2001). Local Heat Transfer and Flow Structure on and Above a Dimpled Surface in a Channel. *ASME Journal of Turbomachinery* , 123, 115-123.
- Mahmood, G. I., Won, S. Y., & Ligrani, P. M. (2002). *Local Nusselt Numbers and Flow Structure in a Rectangular Channel with Cylindrical Pin-Fins*. University of Utah, Department of Mechanical Engineering, Salt Lake City.
- Marcum, S., Gill, D. A., & Slentz, K. (2007). *Patent No. 7310938*. United States of America.
- Mark, H. (1958). *The Interaction of a Reflected Shock Wave in a Shock Tube*. NACA TM.
- McClevey, K. (2002, March). *Inventory of Electric Utility Powerplants 2000*. Retrieved August 2008, from Energy Information Administration: [http://www.eia.doe.gov/cneaf/electricity/ipp/ipp\\_sum.html](http://www.eia.doe.gov/cneaf/electricity/ipp/ipp_sum.html)
- Mehta, R. D., & Bradshaw, P. (1979). Technical Notes: Design Rules for Low Speed Wind Tunnels. *The Aeronautical Journal of the Royal Aeronautical Society* , 441-452.
- Metzger, D. E., & Fan, C. S. (1992). Heat Transfer in Pin Fin Arrays with Jet Supply and Large Alternating Wall Roughness Ribs. *ASME Fundamental and Applied Heat Transfer Research for Gas Turbine Engines* , 23-30.



- Metzger, D. E., & Haley, S. W. (1982). Heat Transfer Experiments and Flow Visualization for Arrays of Short Pin-Fins. *ASME International Gas Turbine and Aeroengine Congress and Exhibition*.
- Metzger, D. E., & Larson, D. E. (1986). Use of Melting Point Surface Coatings for Local Convection Heat Transfer Measurements in Rectangular Channel Flows with 90 degree Turns. *Journal of Heat Transfer* , 108, 48-54.
- Metzger, D. E., Barry, R. A., & Bronson, J. P. (1982). Developing Heat Transfer in Rectangular Ducts with Staggered Arrays of Short Pin-Fins. *Journal of Heat Transfer* , 104 (4), 700-706.
- Metzger, D. E., Fan, C. S., & Pennington, J. W. (1983). Heat Transfer and Flow Friction Characteristics of Very Rough Transverse Ribbed Surfaces with and without Pin Fins. *ASME/JSME Thermal Engineering Joint Conference Proceedings*, (pp. 429-435). Honolulu, Hawaii.
- Metzger, D., & Bunker, R. (1990). Local Heat Transfer in Internally Cooled Turbine Airfoil Leading Edge Regions: Part II - Impingement Cooling with Film Coolant Extraction. *Journal of Turbomachinery* , 112, 459-466.
- Metzger, D., & Korstad, R. (1972). Effects of Crossflow on Impingement Heat Transfer. *Journal of Engineering for Power* , 94, 35-41.
- Metzger, D., & R., K. (1972). Effects of Crossflow on Impingement Heat Transfer. *Journal of Engineering for Power* , 94, 35-41.
- Metzger, D., Baltzer, R., & Jenkins, C. (1972). Impingement Cooling Performance in Gas Turbine Airfoils including Effects of Leading Edge Sharpness. *Journal of Engineering for Power* , 92, 219-225.

- Moeller, S. M. (2000). *Patent No. 601850*. United States of America.
- Moon, H. K., O'Connell, T., & Glezer, B. (2000). Channel Height Effect on Heat Transfer and Friction in a Dimpled Passage. *Journal of Engineering Gas Turbine and Power* , 122, 307-313.
- Moustapha, H., Zelesky, M. F., Baines, N. C., & Japikse, D. (2003). *Axial and Radial Turbines*. Concepts ETI, Inc.
- Murzin, V. N., Stoklitskii, S. A., & Chebotarev, A. P. (1986). Creation of Solitary Vortices in a Flow Around Shallow Spherical Depressions. *Soviet Technical Physical Letters* , 12 (11), 547-549.
- Newton, P. J., Youyou, Y., Stevens, N. E., Evatt, S. T., Lock, G. D., & Owen, J. M. (2003). Transient Heat Transfer Measurements Using Thermochromic Liquid Crystal, Part 1. An Improved Technique. *International Journal of Heat and Fluid Flow* , 24, 14-22.
- Nguyen, C. Q., Rodriguez, S., Zuniga, H. A., Ho, S. H., & Kapat, J. S. (2009). Sensitivity Analysis of Flow Conditions and Geometric Parameters on the Film Cooling Effectiveness for a Flat Test Plate: Single Row of Cylindrical Holes. *Proceedings of the ASME Summer Heat Transfer Conference*. San Francisco, CA: ASME.
- Nie, J. H., & Armaly, B. F. (2002). Three-Dimensional Convective Flow Adjacent to Backward-Facing Step-Effects of Step Height. *International Journal of Heat and Mass Transfer* , 45, 2431-2438.
- Nordlund, R. S. (2005). *Patent No. 6890148*. United States of America.

- Owen, J. M., Newton, P. J., & Lock, G. D. (2003). Transient Heat Transfer Measurements Using Thermochromic Liquid Crystal. Part 2. Experimental Uncertainties. *International Journal of Heat and Fluid Flow* , 24, 23-28.
- Padet, J. (2005). Transient Convective Heat Transfer. *Journal of Brazilian Society of Mechanical Science and Engineering* , 1, 74-96.
- Patrick, W. V. (2005). *Computations of Flow Structures and Heat Transfer in a Dimpled Channel at Low to Moderate Reynolds Number*. Masters Thesis, Virginia Polytechnic University, Blacksburg, VA.
- Reiss, H., & Bolcs, A. (1999). Experimental Study of Showerhead Cooling on a Cylinder Comparing Several Configurations Using Cylindrical and Shaped Holes. *ASME International Gas Turbine Conference and Exposition*.
- San, J.-Y., Tsou, Y.-M., & Chen, Z.-C. (2007). Impingement Heat Transfer of Staggered Arrays of Air Jets Confined in a Channel. *International Journal of Heat and Mass Transfer* , 50, 3718-3727.
- Sarkar, A., & Florschuetz, L. W. (1992). Entrance Region Heat Transfer in a Channel Downstream of an Impinging Jet Array. *International Journal of Heat and Mass Transfer* , 35 (12), 3363-3374.
- Schukin, A. V., Kozlov, A. P., & Agachev, R. S. (1995). Study and Application of Hemispherical Cavities for Surface Heat Transfer Augmentation. *44th International Gas Turbine and Aeroengine Congress and Exposition*, (pp. 1-6). Houston, TX.

- Simoneau, R. J., & Simon, F. F. (1993). Progress Towards Understanding and Predicting Convection Heat transfer in the Turbine Gas Path. *International Journal of Heat and Fluid Flow* , 14 (2), 106-127.
- Simoneau, R. J., & Van Fossen, G. J. (1984). Effects of Location in an Array on Heat Transfer to a Short Cylinder in Cross Flow. *Journal of Heat Transfer* , 106 (1), 42-48.
- Snedeker, R. S., & Donaldson, C. D. (1966). Observation of Bistable Flow in a Hemispherical Cavity. *AIAA Journal* , 4 (4), 735-736.
- Son, C. M., Michaleis, M., Roberston, A. J., & Ireland, P. T. (1998). Detailed Heat Transfer Measurements in an Engine Representative Cooling System Using Liquid Crystals. *ASME International Mechanical Engineering Conference and Exposition*. Anaheim, CA, USA.
- Sparrow, E. M., & Cur, N. (1982). Turbulent Heat Transfer in a Symmetrically or Assymmetrically Heated Flat Rectangular Duct with flow Separation at Inlet. *Journal of Heat Transfer* , 104, 82-89.
- Sparrow, E. M., Ramsey, J. W., & Altemani, C. A. (1980). Experiments in In-Line Pin Rin Arrays and Performance Comparisons with Staggered Array. *Journal of Heat Transfer* , 102 (1), 44-50.
- Stasiek, J. A., & Kowalewski, T. A. (2002). Thermochromic Liquid Crystals Applied for Heat Transfer Research. *Opto-Electronics Review* , 10, 1-10.
- Stasiek, J. A., Jewartowski, M., & Collins, M. W. (2006). Liquid Crystal Thermography and True-Colour Digital Image Processing. *Optics and Laser Technology* , 38, 243-256.

- Sultanian, B. K. (2009). *EML 5402 - Turbomachinery*. Lecture Slides, University of Central Florida, Mechanical, Materials, and Aerospace Engineering, Orlando, FL.
- Suo, M. (1985). Aerothermo. (G. Ed. Oates, Ed.)
- Suo, M. Turbine Cooling. In G. O. Lab (Ed.), *Aerothermodynamics of Aircraft Gas Turbine Engines*.
- Syred, N., Khalatov, A., Kozlov, A., Shchukin, A., & Agachev, R. (2001). Effect of Surface Curvature on Heat Transfer and Hydrodynamics within a Single Hemispherical Dimple. *Journal of Turbomachinery* , 123 (3), 609-613.
- Tabakoff, W., & Clevenger, W. (1972). Gas Turbine Blade Heat Transfer Augmentation by Impingement of Air Jets Having Various Configurations. *Journal of Engineering for Power* , 92, 51-60.
- Taslim, M. E., Li, T., & Spring, S. D. (1998). Measurements of Heat Transfer Coefficients and Friction Factors in Passages Rib-Roughened on All Walls. *Journal of Turbomachinery* , 120 (3), 564-570.
- Terekhov, V. I., Kalinina, S., & Mshvidobadze, Y. (1995). *Russian Journal of Engineering Thermophysics* , 5, 11.
- Thole, K., Gritsch, M., Schulz, A., & Wittig, S. (1996). Flow Field Measurements for Film Cooling Holes with Expanded Exits. *ASME International Gas Turbine Conference and Exposition*.
- Uzol, O., & Camci, C. (2001). Elliptical Pin Fins as an Alternative to Circular Pin Fins for Gas Turbine Blade Cooling Applications. Part 1: Endwall Heat Transfer and Total Pressure Loss Characteristics. *ASME 46th International Gas Turbine and Aeroengine Congress and Exhibition*. New Orleans.

- Uzol, O., & Camci, C. (2001). Elliptical Pin Fins as an Alternative To Circular Pin Fins For Gas Turbine Blade Cooling Applications. Part 2: Wake Flow Field Measurements and Visualization Using Particle Image Velocimetry. *ASME 46th Annual International Gas Turbine and Aeroengine Congress and Exhibition*. New Orleans, LA.
- Van Fossen, G. J. (1982). Heat Transfer Coefficients for Staggered Arrays of Short Pin Fins. *Journal of Engineering for Power* , 104 (2), 268-274.
- von Wolfersdorf, J., Hoecker, R., & Hirsch, C. (1998). A Data Reduction Procedure for transient Heat transfer Measurements in Long Internal Coolin Channels. *Journal of Heat Transfer* , 120, 314-321.
- W., B. A., & Van Frossen, G. J. (1984). Length to Diameter Ratio and Row Number Effects in Short Pin Fin Heat Transfer. *Journal of Engineering for Gas Turbines and Power* , 106 (1), 241-245.
- Wagner, G., Kotulla, M., Ott, P., Weigand, B., & von Wolfersdorf, J. (2005). The Transient Liquid Crystal Technique: Influence of Surface Curvature and Finite Wall Thickness. *ASME Journal of Turbomachinery* , 127, 175-182.
- Wang, T., Lin, M., & Bunker, R. S. (2005). Flow and Heat Transfer of Confined Impingement Jet Colling Using a 3-D Transient Liquid Crystal Scheme. *International Jounral of heat and Mass Transfer* , 48, 4887-4903.
- Wang, Z., Ireland, P. T., Kohler, S. T., & Chew, J. W. (1998). Heat Transfer Measurements to a Gas Turbine Cooling Passage with Inclined Ribs. *Journal of Turbomachinery* , 120 (1), 63-69.

- Zhak, V. D. (1995). The Taylor-Goertler Vortices and Three-Dimensional Evolution in a Cavity. *Russian Journal of Engineering Thermophysics* , 5, 165-176.
- Zhao, J. B., Chew, Y. T., & Khoo, B. C. (2004). Experimental Studies on Hydrodynamic resistance and flow pattern of a narrow flow channel with dimples on the wall. *ASME International Mechanical Engineering Congress and Exhibition*. Anaheim, CA, USA.
- Zukauskas, A. (1972). Heat Transfer from Tubes in Cross Flow. *Advances in Heat Transfer* , 8, 96-160.